

AGARD-R-723

AGARD-R-723

AD-A160 718

AGARD

ADVISORY GROUP FOR AEROSPACE RESEARCH & DEVELOPMENT

7 RUE ANGELE 92200 NEUILLY SUR SEINE FRANCE

AGARD REPORT No.723

Aircraft Drag Prediction and Reduction

DTIC
ELECTE
OCT 29 1985
S A

MP: FILE COPY

NORTH ATLANTIC TREATY ORGANIZATION



DISTRIBUTION AND AVAILABILITY
ON BACK COVER

This document has been approved
for public release and sale; its
distribution is unlimited.

28 01 87

NORTH ATLANTIC TREATY ORGANIZATION
ADVISORY GROUP FOR AEROSPACE RESEARCH AND DEVELOPMENT
(ORGANISATION DU TRAITE DE L'ATLANTIQUE NORD)

AGARD Report No.723

AIRCRAFT DRAG PREDICTION AND REDUCTION

The material assembled in this report was prepared under the combined sponsorship of the von Kármán Institute and the Fluid Dynamics Panel of AGARD and was presented as an AGARD Special Course at the von Kármán Institute, Rhode-St-Genèse, Belgium on 20—23 May 1985 and NASA Langley, USA on 5—8 August 1985.

THE MISSION OF AGARD

The mission of AGARD is to bring together the leading personalities of the NATO nations in the fields of science and technology relating to aerospace for the following purposes:

- Exchanging of scientific and technical information;
- Continuously stimulating advances in the aerospace sciences relevant to strengthening the common defence posture,
- Improving the co-operation among member nations in aerospace research and development;
- Providing scientific and technical advice and assistance to the North Atlantic Military Committee in the field of aerospace research and development;
- Rendering scientific and technical assistance, as requested, to other NATO bodies and to member nations in connection with research and development problems in the aerospace field;
- Providing assistance to member nations for the purpose of increasing their scientific and technical potential;
- Recommending effective ways for the member nations to use their research and development capabilities for the common benefit of the NATO community.

The highest authority within AGARD is the National Delegates Board consisting of officially appointed senior representatives from each member nation. The mission of AGARD is carried out through the Panels which are composed of experts appointed by the National Delegates, the Consultant and Exchange Programme and the Aerospace Applications Studies Programme. The results of AGARD work are reported to the member nations and the NATO Authorities through the AGARD series of publications of which this is one.

Participation in AGARD activities is by invitation only and is normally limited to citizens of the NATO nations.

The content of this publication has been reproduced directly from material supplied by AGARD or the authors.

Published July 1985

Copyright © AGARD 1985
All Rights Reserved

ISBN 92-835-1507-2



Printed by *Specialised Printing Services Limited*
40 Chigwell Lane, Loughton, Essex IG10 3TZ

PREFACE

With diminishing world fuel supplies, and a global increase in fuel price over the last ten years, the reduction of aircraft drag has become a technology of major importance to aircraft manufacturers. Likewise, advances in test and evaluation techniques have facilitated the accurate evaluation of drag and led to concurrent developments in drag prediction methods. A noteworthy development is the use of a number of novel flow control methods which, through either passive or active interaction with the flow physics, can lead to substantial drag reductions.

This special course covers some of the more recent progress in drag reduction, measurement and prediction. The topics presented discuss the different sources and contributions to aircraft drag with particular emphasis on those areas in which significant new developments have taken place.

The course begins with a general review of drag reduction technology. Then the possibility of reduction of skin friction through control of laminar flow is discussed, with design aspects of laminar flow control hardware included. The other possibility of skin friction reduction through modification of the structure of the turbulence in the boundary layer is also discussed.

Methods for predicting and reducing the drag of external stores, of nacelles, of fuselage protuberances, and of fuselage afterbodies are then presented.

Transonic drag rise, the prediction of viscous and wave drag by a method matching inviscid flow calculations and boundary layer integral calculations, and the reduction of transonic drag through boundary layer control are also discussed.

Accession For
NTIS CR-81
DTIC 71
UNCLASSIFIED
DATE 10/10/81
BY [Signature]



SPECIAL COURSE STAFF

Special Course Director: Dr A.S.W Thomas
D72-74, Z 403
Lockheed Georgia Co.
86 South Cobb Drive
Marietta, GA 30063
United States

LECTURERS

Mr D.M.Bushnell
Head, Viscous Flow Branch
High-Speed Aerodynamics Division
NASA Langley Research Center
Hampton VA 23665
USA

Mr M.C.Fischer
ACEE Project Office
Mail Stop 158
NASA Langley Research Center
Hampton VA 23665
USA

Dr J.Hackett
D72-74, Z 403
Lockheed Georgia Co.
86 South Cobb Drive
Marietta, GA 30063
USA

Mr R.C.Lock
Aerodynamics Department
Royal Aircraft Establishment
Farnborough, Hants GU14 6TD
UK

M. Ph. Poisson-Quinton
ONERA
B.P. 72
92322 Châtillon
France

Dr W.S.Saric
Mechanical & Aerospace Engineering
Arizona State University
Tempe, AZ 85287
USA

Dr Ing. E.Stanewsky
DFVLR
Bunsenstrasse 10
3400 Göttingen
Federal Republic of Germany

LOCAL COORDINATOR

Professor M.Carbonaro
Von Kármán Institute for Fluid Dynamics
Chaussée de Waterloo 72
B-1640 Rhode-Saint-Genèse
Belgium

AGARD REPRESENTATIVE

Mr R.H.Rollins II
Fluid Dynamics Panel Executive
7 rue Ancelle
92200 Neuilly-sur-Seine
France

CONTENTS

	Page
PREFACE	iii
SPECIAL COURSE STAFF	iv
	Reference
AIRCRAFT DRAG REDUCTION TECHNOLOGY – A SUMMARY by A.S.W.Thomas	1
BOUNDARY LAYER TRANSITION: T-S WAVES AND CROSS-FLOW MECHANISMS by W.S.Saric	2
LAMINAR FLOW CONTROL WITH SUCTION: THEORY AND EXPERIMENT by W.S.Saric	3
DESIGN CONSIDERATIONS FOR APPLICATION OF LAMINAR FLOW CONTROL SYSTEMS TO TRANSPORT AIRCRAFT by A.L.Braslow and M.C.Fischer	4
TURBULENT DRAG REDUCTION FOR EXTERNAL FLOWS by D.M.Bushnell	5
PARASITIC AND INTERFERENCE DRAG PREDICTION AND REDUCTION by Ph. Poisson-Quinton	6
RECENT DEVELOPMENTS IN THREE-DIMENSIONAL WAKE ANALYSIS by J.E.Hackett and A.Sugavanam	7
VORTEX DRAG AND ITS REDUCTION* by J.E.Hackett	8
COMPUTATIONAL DRAG ANALYSIS AND MINIMIZATION* by J.W.Slooff	9
PREDICTION OF THE DRAG OF WINGS AT SUBSONIC SPEEDS BY VISCOUS/INVISCID INTERACTION TECHNIQUES by R.C.Lock	10
TRANSONIC DRAG RISE AND DRAG REDUCTION BY ACTIVE/PASSIVE BOUNDARY LAYER CONTROL by E.Stanewsky and P.Krogmann	11

*Not available at time of printing.

AIRCRAFT DRAG REDUCTION TECHNOLOGY — A SUMMARY

by

Andrew S W Thomas
Advanced Flight Sciences
Lockheed-Georgia Company
Marietta, Georgia, 30063
USA

SUMMARY

This paper presents a review of the current techniques of aircraft viscous drag reduction and some of the more recent developments that have taken place in this technology. The various sources and relative contributions of aircraft drag are described including skin friction drag, pressure drag, interference drag and lift induced drag. In the discussion, emphasis is given to the physical processes that lead to these drag contributions, followed by a discussion of methods of reducing the impact of these drag sources. Finally some brief discussion is presented to show how innovative and optimized aircraft configurations can lead to drag benefits.

1. INTRODUCTION.

Since the early seventies and the subsequent trend in world fuel prices (Figure 1), aircraft drag reduction technology has become of prime importance to military and civilian operators. For example, a 10% drag reduction on a large military transport aircraft is estimated to have the potential to save up to 13 million gallons of fuel per aircraft over the lifetime of the aircraft. Considering also that US domestic operators spent a staggering 2.1 billion dollars on fuel in 1976 alone, it is clear that enormous benefits are to be derived from drag reduction technology. Additionally, with the very high cost of acquisition of new aircraft, existing fleet lifetimes are being extended and derivative designs are now coming on to the marketplace. Thus, retrofittable drag reduction technologies are critically important.

The aerodynamic forces experienced at the surface of an aircraft may be either tangential to the surface or normal to the surface and both will contribute to the total drag on the body. The interrelation and development of these forces is shown in Figure 2. The only tangential force that is present is the viscous skin friction due to the development of boundary layers over the surfaces. The development of the normal forces, i.e. pressures normal to the surface, is more complex and, as Figure 2 shows, these can arise from a number of contributions. Firstly, there is the pressure field modification due to the displacement thickness of the boundary layers and possible formation of regions of separation (and which, with the skin friction, constitutes the profile drag). Next, there are pressure forces that arise from the formation of vortices in the wake and which may further modify the flow around the body. This is termed vortex drag. If compressibility effects are present, then there are additional pressure forces due to the compressibility effects and the presence of waves in the flow.

The non-zero integrated streamwise component of these pressure forces constitutes the pressure drag on the aircraft. Because lifting conditions are present, there is a strong component of the lift-dependent vortex drag which in conjunction with a smaller amount of lift-dependent profile drag gives rise to the so-called induced drag.

Although the relative importance of different drag sources varies for each aircraft type and mission that is flown, a representative breakdown is shown in Figure 3. The important contributors to the total drag are the following:

- (1) Skin friction drag due to viscous boundary layer formation.
- (2) Lift induced drag due to the conserved circulation developed around the wings.
- (3) Pressure drag due to the open separation in the afterbody and other regions.
- (4) Interference effects between aerodynamic components.
- (5) Wave drag due to compressibility effects at near-sonic flight conditions.
- (6) Miscellaneous effects such as roughness effects and leakage, etc.

All these drag sources contribute to the total drag by different relative amounts for different types of aircraft and the breakdown in Figure 3 corresponds to the case of a large subsonic transport of the type flown by most major airlines. The greatest contribution arises from turbulent skin friction drag, a fact that has provided the impetus for most of the friction drag reduction work that will be described. The next most significant contribution arises from the lift induced drag and this, added with the friction drag, accounts for about 85% of the total aircraft drag. Interference drag, wave drag, trim drag to balance the aircraft, and miscellaneous effects account for the remainder. In drag reduction studies, it might be argued that it is more worthwhile to address only the more significant drag contributions. However, this is not necessarily the case because very often it is easier to obtain much greater percentage reductions in the smaller drag sources than in the larger contributions. For example a 50% reduction in afterbody drag is feasible and might represent a 5% total drag reduction. To achieve the same total drag reduction through skin-friction reduction alone may be a much more difficult task.

The purpose of this paper is to review and summarize the various aircraft drag reduction technologies that are currently being explored. Compressibility effects and transonic wave drag reduction will not be discussed explicitly and instead, emphasis will be given mostly to the drag sources associated with viscous flows. This is because viscous flow drag reduction technology is the area that has advanced most rapidly in recent years and which is currently receiving the greatest attention. The discussion will therefore concentrate on skin friction reduction, afterbody drag reduction, induced drag reduction and interference drag reduction. Finally, some brief discussion will be given to show how innovative aerodynamic configurations can be exploited to achieve low drag characteristics.

2. SKIN FRICTION DRAG REDUCTION.

For the reduction of skin friction drag, either of two different philosophies may be followed. The first is to capitalize on the low friction characteristics inherent to laminar boundary layers and to delay transition on the

wetted surfaces as much as possible. This is the approach that has been followed in the laminar flow control programs that were undertaken in England (summarized in Ref. 1) after the second war and later in the United States at Northrup (Ref. 2) and more recently at NASA Langley (Ref. 3). An alternative philosophy for friction reduction that has recently emerged is to accept the inevitability of turbulent flow and to attempt to modify or interact with the turbulent structures to reduce the friction (Ref. 4).

2.1 Laminar Flow Control (LFC).

Although laminar flow control is a generic term, it has, by association, come to mean the maintenance of laminar flow through the use of wall suction. The suction may be in the form of distributed porosity over the surface (Refs. 5 and 6) or in the form of a series of spanwise-running slots (Refs. 5, 7 and 8). The suction is not sufficient to suppress any existing turbulence, but serves to modify the curvature of the laminar velocity profile which in turn reduces the amplification of any instability waves in the boundary layer that grow and lead to the formation of turbulence. As depicted in Figure 4, local friction can be reduced to about 20% of its turbulent value and with sufficient care, laminar flow can be maintained up to Reynolds numbers of the order of 60 million. An extensive bibliography of the literature describing LFC can be found in Reference 2.

The current Lockheed concept for an LFC aircraft is shown in Figure 5 taken from Ref. 9. Control is only exercised on the wing surfaces because of the greater difficulty of maintaining laminar flow at the high fuselage Reynolds numbers as well as the problems of surface discontinuities at the windows. The suction units for this configuration are mounted in the lower fuselage at the wing root and the propulsion engines are mounted in the tail to minimize noise and vibration on the wings. The real benefits of such a configuration must be evaluated against the performance of an equivalent advanced turbulent aircraft and, as Figure 6 (from Ref. 9) shows, these benefits are greater for long stage lengths and represent a 27% performance improvement. Whether or not this is sufficient to justify the higher acquisition and maintenance costs of a new fleet of such aircraft will depend largely on future fuel price developments.

While the feasibility of LFC has been known for a long time, the system does suffer from a number of design, manufacturing and maintainability problems as depicted in Figure 7. An essential problem with any laminar flow condition is its susceptibility to dirt and other particulates, such as insect debris accumulating near the leading edge during low altitude flight. These can trip the flow to turbulence which will then spread over a wide area of the wing. To avoid this, close manufacturing tolerances must be followed and some kind of in flight cleaning system (Ref. 9) or leading-edge protection must be employed (Ref. 10).

From an aerodynamic viewpoint, probably the greatest difficulty lies in being able to confidently predict where transition will occur. The design procedure requires that the boundary-layer characteristics, with suction, first be accurately determined using a boundary-layer analysis of the type in Ref. 11. This is followed by a stability analysis to determine the amplification of the instability waves in the flow (Ref. 12).

A fundamental difficulty is that the stability analysis is based upon a set of linearized small-disturbance equations so that the actual amplitudes cannot be calculated, but the amplification can. Furthermore, the receptivity of the flow to the free stream disturbances that drive the instabilities is also not well known (Ref. 13). The problem, therefore, is analogous to predicting the output of an amplifier given its gain, but knowing nothing of its input signal level.

To circumvent these difficulties, empirical transition criteria must be used, such as the e^N criterion (Ref. 14), which assumes that transition takes place once the amplification ratio (or system gain) exceeds some critical threshold given by the value of e^N . The critical values of N are typically 11-12 for the mid-chord regions dominated by quasi-two-dimensional Tollmien-Schlichting instability (Ref. 15), and 10-11 for the crossflow instability that originates most severely near a swept-wing leading edge (Ref. 14).

In order to derive the optimal efficiency of the LFC system it is best to minimize the suction quantities that are required and this generally requires a careful iteration of the design procedure that has been described. Furthermore, the way that the suction is achieved can have a bearing on the overall system efficiency both from an aerodynamic and a structural weight penalty viewpoint. One approach is to use discrete slots as in Figure 5, or through the use of strips of porous material as an integral part of the wing surface. The porous strips have been studied in References 16 and 17, and it has been demonstrated that discrete suction through porous strips can be as effective as suction distributed continuously over a greater streamwise length. Both the suction approaches have been critically evaluated in work that has been undertaken at Lockheed-Georgia (K.C. Cornelius, private communication). As Figure 8 shows, it has been demonstrated through stability measurements that the suction slots have a greater stabilizing influence, for a given suction flow rate, than do the porous strips. Naturally, other parameters such as skin structural integrity must also be considered before a final choice of surface type can be made.

2.2 Natural Laminar Flow (NLF).

The simplest technique for maintaining laminar flow over a surface is to capitalize on the stabilizing effect that favorable pressure gradients have on laminar boundary layers (Ref. 18). In order to implement NLF on a wing, it is necessary to bring the point of maximum thickness as far aft as possible so as to create extensive regions of favorable pressure gradient over the wing surface as depicted in Figure 9. The concept can be employed without the need for considering the attendant weight and structural penalties associated with the LFC suction system and, from an aerodynamic point of view, the design procedures are similar to those used in LFC (including the inherent empiricism).

A number of low-speed aircraft are currently flying with NLF (Ref. 19), although in some cases this has been fortuitous. In a high-speed application where good transonic cruise is needed, additional design considerations arise. For example, permissible wing sweep is limited by the onset of crossflow instability at the leading edge. Also, in order to rise to the correct pressure at the trailing edge after a large region of favorable gradient, large adverse gradients are necessary and these can lead to strong shocks and a wave drag penalty or the possibility of separation. Careful design studies are needed to minimize these detrimental effects.

2.3 Hybrid Laminar Flow Control (HLFC).

A compromise LFC system that avoids some of the problems associated with LFC and NLF is the Hybrid Laminar Flow Control System (HLFC) shown in Figure 10. This is a mix of the other two systems and suction is applied only at the leading edge to minimize crossflow instability. Control of the instabilities in the mid-chord region is achieved with tailoring of the pressure gradient as with NLF. In this way a larger wing sweep can be achieved for transonic flight than with NLF, and the weight penalties are not as great as for LFC. Also, the suction orifices at the leading edge can double as a leading-edge-cleanser discharge system to prevent accumulation of dirt and insects during the low-altitude climbout.

2.4 Wall Cooling.

Another favorable physical effect that could conceivably be exploited in a drag reduction scheme is by the use of wall cooling (Ref. 20). As Figure 11 (adapted from Ref. 22) shows, a reduction in surface skin temperature can lead to significant increases in the minimum critical Reynolds number. This is not because the kinematic viscosity goes up (the reverse is true), but arises because the heat transfer modifies the viscosity distribution across the boundary layer which causes the mean profiles to become more full, thereby increasing their stability. This has been substantiated by the flat plate experiments of Ref. 20 for Tollmien-Schlichting type disturbances. However, the calculations in Ref. 21 have shown that while the same is true for crossflow-type instabilities, the effect is much smaller as depicted by the growth curves in Figure 12.

In order to implement such a concept, a very large heat sink is needed. One possibility would be to use liquid hydrogen in the cryogenic state to fuel the aircraft (Refs. 22 and 23). To maintain the laminar flow, the fuel would be circulated just below the wing surface as a preheater to the combustion process. The same effect could be achieved if liquid methane was used.

2.5 Active Wave Suppression (Wave Cancellation).

The transition control concepts that have been described are passive and do not require a dynamic interaction with the flow. A new transition control concept that has been suggested and tested under laboratory conditions (Refs. 24, 25, 26 and 27) is by the use of active wave suppression or wave cancellation. The idea is to detect any low amplitude pre-transitional instability waves in the flow and then to introduce a control disturbance that is of equal amplitude and 180 degrees out of phase with the original disturbance. In principle, superposition should then remove the primary disturbances from the flow.

To date, the concept has only been evaluated under low speed conditions but significant increases in the transition Reynolds numbers have been reported. An example of the streamwise amplitude history of an instability wave, with and without the control disturbance is shown in Figure 13, and a smoke-wire visualization of the corresponding flow conditions is shown in Figure 14 (from Ref. 27). These demonstrate that while an impressive degree of control of the two-dimensional disturbances is possible, some residual three-dimensional disturbances remain in the flow and that these bring about transition.

The reason for this is that transition arises from complex wave interactions between a primary disturbance and three-dimensional disturbances that have their origins with the free stream (Ref. 28). Thus, while the control disturbance removes most of the energy of the primary disturbance, the now amplified three-dimensionalities still remain. Therefore, any real implementation of the concept will probably require a complex three-dimensional control system, even for two-dimensional flow. Whether or not this is possible at the very high instability growth rates characteristic of flight Reynolds numbers remains to be determined.

3. TURBULENT SKIN FRICTION REDUCTION.

An alternative approach to the reduction of skin friction is based not upon trying to maintain laminar flow, but instead on attempting to modify the turbulence in some way so as to reduce friction. Possible approaches may be passive, as in the case of the riblets and large eddy breakup devices etc., or active as in the case of the synthetic boundary layer. These efforts are still quite new and arose largely from a series of ongoing tests that were begun at NASA Langley during the late seventies (Ref. 4).

3.1 Riblets.

Because it is known that the near wall structure of a turbulent boundary layer is dominated by streaks of streamwise vortices with an average spacing of $z^+ \approx 100$, it has been argued that changing the surface geometry with micro-grooves should spatially lock the structures which may alter the momentum transport characteristics and reduce the skin friction. Studies have therefore been made of the friction characteristics of a boundary layer that develops over surfaces with various geometries of small streamwise grooves carved into them (Ref. 29). As shown in Figure 15, it has been demonstrated that local drag reductions of the order of 10% are indeed possible, despite the increase in wetted area. The optimized groove spacing is of the order of ten wall units. Also, sharp pointed grooves tend to perform better than grooves with rounded peaks (Ref. 29).

Because the optimized groove spacing is about an order of magnitude less than the streak spacing, it is difficult to picture them as interacting with the streaks and experimental studies have been made to look at the characteristics of the turbulence that develops over the grooved surfaces (Refs. 30, 31). These studies have attempted to measure the mean turbulent bursting frequency and conditional averages of the velocity fluctuations during the bursting process, since this activity is a measure of the turbulence production mechanism. One example, that of the mean turbulence bursting frequency is shown in Figure 16 taken from Reference 30. Some apparent change is indicated due to the presence of the riblets. Unfortunately, there is a fundamental difficulty in objectively defining the turbulence activity thresholds that are used to measure when a turbulent burst is taking place. Therefore, whether or not the changes in Figure 16 accurately represent flow structure changes associated with the drag reduction is difficult to say.

An alternative model for the drag reduction is proposed in Reference 31 and is based upon the idea that the drag reduction does not arise from a direct interaction with the turbulence structure, but arises instead because of the way the viscous fluid flows over the ribbed surface. The flow in the valley of the grooves is at low Reynolds number

and is creeping in character and the local wall shear is low. Because of the mean velocity gradient, the wall shear is higher at the top of the rib as found in the data of Ref. 30. If the geometry is right, the low shear dominates and, even though the wetted area is increased, and a net drag reduction results. In this model, any turbulence changes are then merely a passive attendant to the wall shear change, rather than a direct cause. This would also serve to explain why the sharp groove tips have better drag reducing characteristics since they minimize the surface area exposed to high shear.

The multi-colored dye visualizations shown in Figure 17, from Ref. 31, show the inhibited lateral spreading of the flow in the grooves and its creeping nature. By themselves they do not prove the proposed model, but they are certainly consistent with that view. More detailed experimental studies of the flow field within the grooves as well as numerical simulations are needed to resolve this question.

3.2 Large Eddy Breakup Devices, Manipulators (LEBU).

Another very promising concept for the reduction of turbulent skin friction is by the use of plates or fences inserted into the boundary layer flow. Friction reductions of the order of 20% have been recorded downstream of the devices (Refs. 32-36) and because it has been suggested that the devices break up the large scale structures of the flow, they have been referred to as large eddy breakup devices (LEBU). The term turbulence manipulator may be more appropriate.

The boundary-layer development downstream from a set of thin plates immersed in a flow is depicted in Figure 18 taken from Ref. 4. The change in slope of the curve of momentum thickness development is representative of friction changes by virtue of the momentum integral equation. There is a device drag penalty that must be paid before a break-even point is reached, but thereafter a net drag reduction can be achieved. The best drag reduction configuration for these devices appears to be thin airfoil shapes to minimize the device drag. They should be of the order of the local boundary layer thickness in streamwise extent and located at about 80% of the boundary layer thickness from the wall. Tandem devices also appear to perform well and the geometrical characteristics of the devices are critically important for good performance (Ref. 34).

At present there is some controversy over the mechanism behind the observed drag reductions. The first investigations suggested that the devices serve to break up the large eddies of the flow and the smoke-wire visualizations in Figure 19 (from Ref. 35) show that while large eddy structures are clearly visible in the uncontrolled flow, they are not apparent in the controlled flow. This is perhaps surprising in view of the fact that logarithmic behavior is still evident in mean flow measurements of the controlled flow (Ref. 33). However, conclusions about structural features should not be based on streakline data alone and measurements of correlations and length scales are needed to clarify this issue.

An alternative description for the behavior of the devices has recently been proposed in Ref. 36. In that model, the large eddies are viewed as conglomerations of smaller scale hairpin vortices and the wake eddies of the manipulator interact with these hairpins in such a way so as to inhibit wallward motions. Thus, it is the introduction of new structures into the flow rather than the destruction of existing ones that is important. Flow visualization data seem to support this interpretation and it is consistent with the continued existence of logarithmic behavior in the velocity profiles. However, the examination was based on manipulators that were quite thick and which consequently had large wakes.

An important fundamental issue with the devices is how long the drag reduction effect will persist in the downstream direction. The indications from Ref. 34 are that the flow does indeed return to an uncontrolled state after about 150 boundary layer thicknesses downstream of the device. Whether or not further devices can be used to reimplement control is an issue that remains to be examined.

3.3 Other Surface Geometry Effects.

In addition to the ribs, a number of other surface geometry effects are receiving attention as possible friction reduction concepts. Among these are streamwise surface curvature, transverse surface waves and transverse micro-grooves.

While concave curvature increases near wall turbulence intensities through the Görtler instability, convex curvature appears to reduce intensities and skin friction (Ref. 37). The mechanism for this is not clear and Ref. 4 suggests that the effect is mostly due to a change of the outer eddies. An alternative and quite plausible possibility, is that if the near wall streaks themselves arise from a Görtler rotational instability due to local streamline curvature as suggested by Ref. 38, then it is possible that the convex wall curvature changes the streamline curvature to suppress these structures. Whatever the case, it does appear that there is a very long relaxation distance of low drag after regions of convex curvature which can be exploited in a drag reduction scheme.

If the scale of the curvature is reduced and made periodic, transverse surface waves result. This has been suggested as a possible drag reduction scheme since measurements over surfaces with low amplitude waves and wavelengths of the order of the boundary layer thickness have shown friction reductions (Ref. 39). Unfortunately, the static pressure distribution over the wall shifts in phase relative to the surface wave and there is an attendant pressure drag (Refs. 40 and 41). NASA Langley experiments on non-symmetric surface waves have attempted to minimize this effect, but no net drag reductions have yet been reported and the wall shear reductions appear to be diminished (Ref. 40). For the case of moving (compliant) sinusoidal wavy walls beneath turbulent boundary layers the situation is not clear and is currently under investigation. Numerical simulations suggest that there may be drag reductions for the case of wave speeds approaching the free stream velocity (Refs. 42 and 43), but for passive compliant surfaces, careful experiments have shown no net drag reductions in air (Ref. 44).

Another transverse surface geometry that is receiving attention is to use closely spaced transverse cavities (D type roughness, Ref. 45) of small scale to reduce drag (Ref. 4). These have been referred to as micro-air bearings with an implication that small vortices recirculate in the cavities providing low shear stress to the external flow at the lip of the cavity. As with wavy walls, there is an attendant pressure drag, and the vortex structures, if they do form at these low Reynolds numbers, will not be stable and will periodically burst out of the cavities giving rise to pulses in the pressure drag. This may explain why no net drag reductions have been achieved. Ref. 4 suggests that these cavities in conjunction with some other device (LEBU's, streamwise vortex generators etc.) to minimize the eruptions may be a viable approach.

3.4 The Synthetic Boundary Layer.

In a unique series of experiments, Coles and Savas (Ref. 46) have shown that it is possible to create turbulence with large scale structures that are spatially and temporally periodic. This was achieved using an array of turbulent spot generators in a laminar boundary layer driven at the appropriate frequency and relative phase. This is a form of controlled transition and has been suggested as a possible means of creating stable turbulent flows of reduced skin friction. This is currently under examination at Lockheed-Georgia (Ref. 47) and tests at NASA Langley (Ref. 48) have shown local friction modifications. As with the LEBU's, a fundamental issue that remains to be resolved is whether or not the flow will remain in the modified state ad infinitum, or whether it will ultimately relax back to some uncontrolled state.

Although the concept is dynamic in character, it could conceivably be implemented by a purely passive means. This is because periodic disturbances are not necessarily the only way to produce periodic arrays of spots. Indeed, it has been found that an array of periodic spots will arise from a small non-moving pin placed on the wall beneath a laminar boundary layer. Thus, an appropriately spaced (streamwise and spanwise) array of such pins could be used to produce the desired phase and frequency of spots. Since the pins are small ($<0.3 d$) and in a region of low velocity laminar flow, their device drag might also be quite low.

4. AFTERBODY DRAG REDUCTION.

4.1 Separation Control as a Means of Drag Reduction.

For the reduction of the drag associated with the separated flow of generic streamlined shapes, concepts such as the use of vortex generators have been in use for many years. Recently, however, a number of novel flow control methods have been developed. For example, Ref. 49 describes a technique whereby it is possible to use a disk mounted in the wake region of a bluff body (Fig. 21) to lock a vortex in the wake. This gives rise to some pressure recovery on the afterbody which in turn reduces the total drag. The same technique has also been used with considerable success to reduce forebody drag (Ref. 50). Likewise, tests at NASA Langley have shown that transverse grooves on a tapered afterbody can reduce drag (Ref. 51, Figure 21,22) as can large streamwise grooves (Ref. 52, Figure 23). In each case the vortex structure set up within the grooves changes the near wall momentum transfer to modify the separation point. In one case the vortex structure is transverse to the flow, while in the other a streamwise vortex system is present. Control of separated flows can also be achieved by periodic re-energizing of the near wall flow using, for example, the embedded rotating cam devices suggested in Ref. 53.

Direct base suction has been suggested as a drag reduction scheme since it does reduce the wake region. However, as shown in Ref. 54 high drag inevitably results due to the low pressure created at the base of the body. In any case prodigious amounts of suction are invariably required.

If the geometry of the body allows the flow in the afterbody region to be attached, then these kinds of flow control concepts are not necessary. Instead, inverse design procedures can be used to devise shapes that have a prescribed low skin friction from which the required body shape can be determined. This approach is based upon a Stratford type (Ref. 55) flow that has low wall shear, but a penalty is paid in the higher pressure drag that can result with the thicker boundary layers. Some optimization is therefore necessary. Ref. 56 describes the procedures and resulting shapes for axisymmetric flows and Ref. 57 describes similar calculations for 3-D wings with prescribed skin friction. More work in the area of 3-D flows would be useful since it may be possible to define optimized shapes by minimizing the drag producing streamwise component of skin friction while allowing the cross-stream component to vary as needed to keep the flow attached.

4.2 Upswept Fuselages - The Real Problem.

In order to meet operational requirements and take-off rotation, it is necessary that the aircraft aft fuselage have upsweep as depicted in Figure 24. This gives rise to a flowfield that is fundamentally different from the closed separations typical of bluff bodies and limits the applicability of some of the separation control methods that have been described. In order to implement any drag reduction scheme, it is important that the physics of this flowfield be correctly understood.

The important characteristics of the flow field typical of upswept fuselages are also shown in Figure 24. It is characterized by a 3-D boundary layer with significant crossflow regions on the fuselage. This boundary layer separates into a pair of counter rotating vortices trailing downstream. The flow is analogous to the flow about a missile at high angle of attack or the flow over a delta wing, although in the present case a hard separation line does not exist.

The total drag associated with this kind of flow can be split into two components. First, there is the pressure drag that arises because of the reduced pressures on the lower surface of the fuselage. In addition, there is a considerable loss of flow energy in the form of rotational kinetic energy of the vortex structures and this is manifested as a vortex drag component. (This loss is analogous to the lift induced drag that can be related to the tip vortex structures behind a wing.) Depending upon the geometry of the aircraft, the relative contributions of each may vary.

An important point to be made is that the other aerodynamic components can interfere with this flow and compound, or possibly relieve the drag problem. Wing downwash is the most severe contributor to this effect since it changes the effective upsweep angle. Externally mounted gear pods, if present, can also feed vorticity to the trailing vortex structure. Accurate drag definition therefore requires testing and optimization of complete aircraft configurations.

A survey of the wake structure behind a fuselage with large upsweep and large drag is shown in Figure 25. The wake vortex structure is clearly in evidence. These data were recorded with 5-hole pressure probes and the corresponding data for a low upsweep fuselage with much less drag are shown in Figure 26. The reduction in the intensity of the wake vortex system is evident. These kinds of data are very useful for drag reduction studies since integration of the crossflow velocities enables the vortex drag to be determined and integration of the wake total pressure enables the pressure drag to be found (Ref. 58). This information is therefore of much greater utility than force measurements alone.

For reducing the drag associated with this kind of flowfield, the best approach is to attempt to optimize the geometry of the configuration at the design stage. Thus, high up-sweep angles should be avoided. Also, slender fuselages with little or no flatness in cross-section should be used since these minimize the area exposed to the low pressure. An example of the importance of the geometry is shown in Figure 27 where a tail cone was added to a blunt fuselage to reduce its drag (Ref. 59). As can be seen a significant drag reduction is obtained, presumably through a reduction in the size of the separation region.

In many applications it is not possible to optimize the geometry due to the need to meet structural and operational requirements and significant amounts of vortex drag can sometimes result. One very good approach for reducing the drag, and one which is finding application as a retrofit to existing aircraft, is by the use of strakes. These were first fitted to a Short-Belfast strategic transport (Ref. 60) and are shown in Figure 28 for a Lockheed C-130 Hercules aircraft. Essentially these are small vertical plates or fins placed beneath the fuselage and embedded in the vortex flow. They act to reduce the intensity of the swirl of the vortex structures and so reduce the vortex drag. To be effective the devices must be optimized since they carry a skin friction and weight penalty. It might be added that the same devices can be used to control the vortex flow over forebodies (Ref. 61).

The utility of some of the other separation control concepts that were mentioned previously has not yet been evaluated for these kinds of fuselages and this would appear to be an area for fruitful research. Also, modification of the structure of the incoming boundary layer that separates and feeds vorticity to the vortices is an area that warrants examination.

5. LIFT-INDUCED DRAG REDUCTION.

Lift induced drag arises primarily because the lift producing circulation around the airfoil leads to a sheet of trailing vorticity in the wake which rolls up into a pair of counterrotating vortices. This vortex structure is concentrated at the tips and induces a downwash over the wing which reduces the effective angle of attack. Therefore, to achieve the same lift, it is necessary to tip the wing back which rotates the lift vector away from the vertical thereby producing a component of drag force (Ref. 62). As in the case of the afterbody flow, this drag is manifested in the wake as rotational kinetic energy. The minimum induced drag is achieved for an elliptical lift distribution across the span which also corresponds to the case of constant wing downwash.

To reduce the induced drag, wings of large aspect ratio should be used since these enable the tip vortex structures to be separated which reduces the strength of the average induced flow between them. However, a point that is not well appreciated is that for the same chord, this will also lead to a weight penalty that may offset the drag reduction. In fact, the selection of optimal aspect ratio is intimately tied to the criteria used to define aircraft geometry. This is discussed in Ref. 9 and as Figure 29 from that reference shows, optimal wing aspect ratio for a transport aircraft varies from 7.5 for minimum acquisition cost, to 9.8 for minimum gross weight, to 12.0 for minimum direct operating cost, and to 15.2 for minimum fuel. At present aspect ratios as large as 15.2 are not structurally feasible but the importance of aspect ratio is clear.

Other techniques for the reduction of induced drag include various wing tip devices, tip blowing, span extension and active controls for load relief.

5.1 Wing-Tip Devices.

Winglets.

It has long been recognized that the addition of tip mounted surfaces to a wing can reduce and diffuse the vortex structures arising from the tips. Induced drag reductions result, but these may be offset by unfavorable interference and viscous effects. The winglet concept shown in Figure 30 is one of the most promising of these concepts and can be thought of as a device to increase the effective span of the wing. As shown in the Figure, the winglet is a small wing mounted in the swirling flow at the wing tip. The lift on the winglet acts as a sideforce and, with proper positioning of the winglet, it will have a thrust component in the stream direction. As with the afterbody strakes, the structure of the vortices is somewhat diffused due to the winglets. Most of the development work for these kinds of devices has been undertaken at NASA Langley and is described in References 64 and 65.

The computed spanwise lift and drag distributions for a wing with and without winglets are shown in Figure 31 (from Ref. 63). As can be seen, there will be an increase in wing root bending moment due to both the increased wing loading and the winglet loading. This may limit the utility of winglets as retrofittable devices. A nose down pitching moment can also occur due to the above center thrust location and this can lead to a trim drag penalty. In addition there are attendant increases in other forms of drag such as skin friction drag and interference drag at the junction region. Thus, while typical total drag reductions of the order of 3-6% may result, comparable performance can in some cases be achieved by a simple tip extension (Ref. 63).

For best performance, proper design of the winglets is clearly very important and some specific design details are discussed in References 63, 65, 66 and 67. These may be summarized as follows:

- (1) For good supercritical performance, the winglet should be tapered and swept aft. It should be mounted behind the region of lowest pressure of the main wing to minimize interference effects.
- (2) Some outward cant is desirable and helps to minimize interferences at the junction.
- (3) As Figure 32 shows (from Ref. 63), smooth fillets should be used between the wing tip and the winglet or smaller drag reduction benefits might result.
- (4) From Ref. 65, some toe-out of the winglet is needed due to the inflow angles at the wing tip. This is also desirable since it reduces the likelihood of winglet stall during sideslip.
- (5) Although the drag reduction increases with winglet span, it is less than linear (Ref. 66). Therefore, the optimal winglet height must be a trade-off between the improved aerodynamics and the increased moments due to the larger moment arms.
- (6) In principle winglets can be mounted above or below the wing, but operational requirements and ground clearances favor upper mounts. A smaller winglet below and ahead of the main winglet is desirable for preventing stall on the main winglet at high lift conditions (Ref. 65).

It might also be mentioned that winglets confer other favorable characteristics, besides drag reductions, which might

be important. Among these are the better control of the spreading and dispersal of particulates behind agricultural aircraft and improved hanger and ground maneuvering clearances for large aircraft. In certain integrated aircraft designs they can also act as control surfaces (see, for example some of the configurations in Ref. 20).

Vortex Diffuser Vanes.

Another concept that is similar to the winglet and which attempts to extract some of the rotational energy from the tip vortices are the vortex diffuser vanes devised at Lockheed-Georgia (Ref. 68). The device is shown schematically in Figure 33 and operates on the same principles as winglets. The advantage of these devices is that the aft mount places them in a region of more intense vortex flow with the possibility of greater energy recovery. Figure 34 shows the reduction in crossflow kinetic energy that can be achieved using a two-vane version of the device. The total integrated reduction for this test condition was 19%.

Another advantage to the rear mount of the vanes is that unfavorable wing interference effects are minimized. Furthermore, unlike for winglets, some inward cant appears to be desirable for optimal aerodynamic performance and as Figure 35 from Ref. 68 shows, this can, under certain circumstances, lead to a reduction in wing-root-bending moment rather than an increase.

Wing-Tip Sails.

A logical extension of the tip devices that have been described is the use of multiple winglets or vanes as suggested by Spillman (Ref. 69). These are shown in Figure 36. These are referred to as sails and are mounted in a spiral array around the wing tip. They are similar to the tip feathers of some species of soaring birds. Induced drag reductions of up to 30% have been reported and for best performance, the array should be essentially horizontal rather than vertical and rearward mounts seem to be preferable. The angle between each successive vane should be about 15 to 20 degrees and four vanes with spans no more than 30% of the wing chord are recommended (Ref. 69). A larger number of vanes is to be avoided, presumably due to the increased interference and viscous losses.

Wing-Tip Devices versus Wing-Tip Extensions.

A fundamental issue with the devices that have been described is whether or not it is better to fit some kind of wing tip device in preference to merely extending the wing tips. This question can not be answered in generality and each configuration must be examined for its weight penalty, bending moment increases, structural integrity as well as the likely vortex drag reductions.

The example described in Ref. 65 has shown that winglets were to be preferred over tip extensions but that case was for quite short tip extensions. The example quoted in Ref. 63 indicates that in order to get 5% drag reduction with tip extensions then a 12% increase in aspect ratio is needed. Such an increase is likely to be heavier than the use of winglets optimized for the same drag reduction. This is because the winglets generally have a smaller chord than the wing tip. From Ref. 68 it is shown that an important correlating parameter is the lift coefficient at the tip. Thus, wings that carry considerable outboard loading are good candidates for wing tip devices.

Comparative analyses of wing tip extensions, winglets, vortex diffusers and tip sails are given in Ref. 63, and the findings are summarized in Figure 37. The even trade lines are for an equal percentage reduction in drag and in bending moment at the wing root and correspond closely to the lines of constant lift coefficient. The added area for each device was kept equal in all cases. The data do not show a clear preference for winglets over tip extensions and overall, the sails showed the best drag reduction for a given area increase. These data apply, however, only to a low aspect ratio wing, and similar data for large aspect ratio, tapered wings may yield differing results.

5.2 Wing-Tip Blowing.

Because of the poorer performance that is obtained from devices such as winglets at off-design conditions, an alternative that has been suggested is to use spanwise-blown jets of air at the tips to increase the effective span (Ref. 70). The idea may have originated with tip blowing as a means of vortex wake hazard alleviation where improvements in L/D were also observed (Ref. 71). Increases in the normal force coefficient of about 0.1 have been reported for quite modest blowing rates. The main advantage of the concept lies in being able to vary the blowing and to be able to select the desired blowing ports in order to get the best performance at any particular flight condition. System studies are needed to determine whether or not the weight of ducting and the effect of the bleed from the engine are sufficient to outweigh the benefits of the concept.

An alternative form of blowing that has been suggested is described in Ref. 63 and is to blow the jets of air in the streamwise direction so as to breakup the tip vortex structure. Measurements of the vortex structure in the wake do show structural changes (Ref. 63), but it does appear that the benefits of the concept level off at higher blowing rates and a tradeoff must be made between blowing energy requirements and the drag reduction.

A logical development of this concept is to mount engines at the wing tips and to use the fan exhaust to break up the tip vortex structure. Whitcomb (Ref. 65) has reported induced drag reductions of the order of one-third with such a configuration on a wing that has significant outboard loading. A large part of this arises from the end-plate effect of the nacelle itself and would be less for a tapered wing. Also, there would be flutter and other structural problems associated with such an installation.

5.3 Active Controls for Load Alleviation

Installation of any wing-tip device, including direct wing-tip extensions, leads to the possibility of undesirable increases in the wing-root-bending moments. Indeed, this essentially limits the amount of tip extension that can be fitted to an aircraft to reduce its induced drag. One possible way to avoid this is to use controlled aileron deflections to off-load the outer wing panels during certain critical phases of the flight when large bending moments are present. To do this requires a sophisticated active control system and three possible applications can be considered (Ref. 72):

- (1) Use of symmetric aileron deflections to reduce wing loads during maneuver,
- (2) Use of aileron deflections to reduce the wing elastic response to gust loads, and,

(3) Use of the horizontal stabilizer to reduce the overall airplane response to gusts.

Concepts such as these enable the peak wing loadings to be reduced which enable tip extensions to be added to an aircraft for the same cruise loadings. Alternatively, they enable the weight of the wing structure to be reduced so that the lift (and hence the drag) may be reduced.

The active control concept is currently finding application on the Lockheed L-1011 and has enabled 4.5 foot wing-tip extensions to be added to the aircraft (Figure 38) with no change to the fundamental wing structure. Appropriately distributed accelerometers are used to provide the required inputs to the control systems which in turn drive the aileron servos. The consequent reduction in the induced drag represents about a 3% increase in fuel efficiency for the aircraft.

6. INTERFERENCE DRAG REDUCTION.

Detrimental interference effects usually arise when aerodynamic components are mated together to complete a configuration such that the configuration drag is may be greater than the sum of the drag of the individual components. Very often however, it is possible to capitalize on interference effects to get favorable drag benefits. A very simple example of a favorable interference is given in Ref. 73 where it is shown that the drag of two disks in tandem is less than that for a single disk. For aircraft, the important drag producing interferences are the regions of juncture flow at the wing-root, empennage and pylon junctions etc., and the interferences between the engine mounting and the wing flows.

6.1 Juncture Flow Interferences.

The juncture regions of the various aerodynamic components of an aircraft all lead to a drag penalty and various examples are cited in Refs. 73 through 79. This juncture drag is due to the occurrence of an unfavorable modification of the local pressure field and the additional rapid straining of the vorticity of the incoming boundary layer that usually leads to the formation of vortices in the juncture regions. The flowfield in an unfileted juncture region is shown in Figure 39 and has long been known to be characterized by the formation of a horseshoe vortex structure ahead of the junction. Careful filleting can reduce these effects, and Ref. 73 gives an example of reducing the drag at the juncture of two struts by more than an order of magnitude with careful fairing. Even with fairings, however, a vortex structure may still ultimately form in the downstream corner regions with its attendant energy loss.

The importance of the geometry to these kinds of flows is also shown by the examples in Figure 40 (from Ref. 59) that correspond to a wing root and an externally mounted gear pod. It is evident that significant drag reductions can be obtained from careful design. At present, the optimized design of these kinds of juncture regions must rely heavily on the use of wind tunnel evaluations and empirical engineering methods. This is because computational methods are not yet sufficiently advanced to correctly account for the complex three-dimensional viscous and transonic effects that are present. Indeed, in many cases only a 3-D Navier-Stokes simulation will provide sufficient accuracy to enable favorable designs to be developed theoretically.

6.2 Engine Installation Effects.

Interferences between the engine/nacelle flow and the wing flow can represent a major source of interference drag and some specific examples are given in Refs. 80-83. Part of this drag is due to juncture of the pylon, but a large contribution also arises from the presence of the pressure field of the nacelle and the suction and exhaust flows. This is especially true for some of the large fan engines that are now being used (Refs. 84, 85). As a consequence, the positioning of the engine installation can lead to either favorable or unfavorable influences and each installation configuration may have its own merits. For example, Ref. 65 gives two examples where optimizing the engine installation can reduce drag. In one case, that of an underwing mount, careful positioning of the pylon inhibits the spanwise flow induced by the tip vortex system and reduces the induced drag. In the other case, that of a forward-overwing mount, the entrained flow of the exhaust accelerates the upper surface air to enhance the lift. As Figure 41 from that reference shows, induced drag reductions can be obtained through the reduced loadings on the other regions of the wing. Some recent work has also shown that, an aft-slung-underwing mount (Ref. 86) might be a particularly promising concept because the engine is in a region of lower velocity and has less unfavorable interference with the lift producing flow over the wing than does a forward lower mount.

The work in Refs. 87 and 88 has shown, however, that for conventional configurations, the geometry of the installation, the capture ratio and the exhaust velocity all have a bearing on the problem. Subtle variations in these parameters can lead to either beneficial or detrimental effects. Computational methods are currently being developed by industry and government agencies (Refs. 87 and 88) which will enable more optimized engine installations to be developed and some of the recent developments in the area of propulsion system design and installation can be found in Ref. 89.

7. INNOVATIVE AIRCRAFT CONFIGURATIONS.

Because drag reduction techniques are providing drag decreases in smaller and smaller increments, an additional area that warrants some mention is the use of innovative aerodynamic configurations (as opposed to aerodynamic concepts) to reduce the drag penalty and fuel consumption associated with transporting a given amount of load over a given flight mission. This is not a viscous flow drag reduction problem per se, but novel configurations do have the possibility of reducing fuel consumed per tonnage of load carried.

A number of these concepts are shown in Figures 42 through 44, and each is designed with some specific aerodynamic or structural advantage in mind. Thus, the spanloader in Figure 42 (from Ref. 9) is designed to have large aspect ratio and reduced fraction of afterbody drag. The control surface at the wing tips provide an added advantage as winglets. Unfortunately, the operation of such a configuration will require much larger runways and taxi areas than currently available and the high acquisition cost of the system would limit its application under current airline economics.

An alternative method for achieving high span that is receiving considerable interest at the present is to use tandem fuselages as shown in Figure 43 (from Ref. 9). The advantage of this configuration is that because the load is concentrated at two points rather than one, then it is possible to significantly reduce the wing-root bending moment.

and consequently the structural weight of the wing box over that of an equivalent large single-body aircraft. The studies in Ref. 9 suggest that this may be as great as a 7% reduction.

The configuration shown in Figure 44 (from Ref. 90), is less extreme and utilizes over-the-wing engines to enhance the wing circulation. The engines are mounted on canards to avoid pylon/wing interferences and because the canards can also act as an auxiliary control surfaces, the empennage size can be reduced.

Use of full canard control surfaces, rather than tail mounted surfaces is also desirable from a drag point of view, because, for static stability and balance, conventional configurations require a download on the horizontal control surface at the tail. This must be balanced by higher wing lift and an attendant drag. For the canard configuration, the canard control surface produces an upload, but the aircraft will be inherently dynamically unstable. Application of an active control system to provide stability will eliminate this problem and the induced drag will be lessened than that for the aft-control surface configuration. The problem is that control system failure may lead to an unflightworthy condition. (The original Wright Flyer flew in this mode, but the instability responses were so slow that the pilot could correct for them.)

Use of active controls on conventional configurations has already been mentioned in the context of load relief, but there is an additional benefit to be derived with relaxed static stability (RSS). If appropriate dynamic and active control surface deflections are available, it is possible to allow the center of gravity to be moved further aft and relax the stability of the aircraft. Smaller control surface sizes are then permissible and the skin-friction drag can be reduced. Figure 45 (from Ref. 70) shows that for the L-1011 aircraft, the benefits that can be derived by utilizing relaxed static stability amount to a 40% reduction in the size of the horizontal stabilizer.

ACKNOWLEDGEMENT

The author is indebted to Dr. Joe Vadyek, Dr. J.E. Hackett, Mr. Geoff Webber, Mr. Roy Lange and Prof. Spiro Lekoudis for advice and guidance in the preparation of this paper. Thanks are also due to Ms. Shelby Christophers for the typing of the manuscript.

REFERENCES

1. Head, M.R., History of Research on Boundary Layer Control for Low Drag in U.K., in *Boundary Layer and Flow Control*, Vol 1, G.V. Lachmann (Ed.), Pergamon Press, 1961, p 104.
2. Pfenninger, W., *Laminar Flow Control Laminarization*, AGARD Report No. 654, Special Course on Concepts for Drag Reduction, 1977, Paper No. 3.
3. Wagner, R.D., Maddalon, D.V. and Fischer, M.C., Technology Development for Laminar Boundary Layer Control on Subsonic Transport Aircraft, presented at the AGARD symposium on Improvement of Aerodynamic Performance Through Boundary Layer Control and High-Lift Systems, Brussels, Belgium, May 21-23, 1984.
4. Bushnell, D.M., Turbulent Drag Reduction for External Flows, AIAA Paper No. 83-0227, 1983.
5. Gregory, N., Research on Suction Surfaces for Laminar Flow, in *Boundary Layer and Flow Control*, Vol 2, G.V. Lachmann (Ed.), Pergamon Press, 1961, p104.
6. Thelander, J.A., Allen, J.B., and Welge, H.R., Aerodynamic Development of Laminar Flow Control on Swept Wings using Distributed Suction Through Porous Surfaces, ICAS Paper No. 82-5.1.2, 1982.
7. Lange, R.H., Design Integration of Laminar Flow Control for Transport Aircraft, AIAA Paper No. 83-2440, 1983.
8. Thomas, A.S.W. and Cornelius, K.C., Investigation of a Laminar Boundary Layer Suction Slot, AIAA Journal, Vol 20, No. 6, p790, 1981.
9. Lange, R.H., Trends in Very Large Aircraft Design and Technology, AIAA Paper No. 80-0902, 1980.
10. Pearce, W.E., Progress at Douglas on Laminar Flow Applied to Commercial Transport Aircraft, ICAS Paper No. 82-1.5.3, 1982.
11. Cebeci, T., Kaups, K. and Ramsey, J., A General Method for Calculating Three-Dimensional Compressible Laminar and Turbulent Boundary Layers on Arbitrary Wings, NASA CR-277, 1977.
12. Srokowski, A.J. and Orszag, S.A., Mass Flow Requirements for LFC Wing Design, AIAA Paper No. 77-1222.
13. Reshotko, E., Boundary Layer Stability and Transition, *Annual Review of Fluid Mechanics*, Vol. 8, p311, 1976.
14. Malik, M.R. and Orszag, S.A., Comparison of Methods for Prediction of Transition by Stability Analysis, AIAA Paper No. 80-1375.
15. Van Ingen, J.L., Transition, Pressure Gradient, Suction, Separation and Stability Theory, AGARD Conference on Laminar-Turbulent Transition, AGARD-CP-224, p20.1, 1977.
16. Reynolds, G.A. and Saric, W.S., Experiments on the Stability of the Flat-Plate Boundary Layer with Suction, AIAA Paper No. 82-1026, 1982.
17. Reed, H.L. and Nayfeh, A.H., Stability of Flow over Plates with Porous Suction Strips, AIAA Paper No. 81-1280, 1981.
18. Saric, W.S. and Nayfeh, A.H., Nonparallel Stability of Boundary Layers with Pressure Gradients and Suction, AGARD Conference on Laminar-Turbulent Transition, AGARD-CP-224, p6.1, 1977.

19. Holmes, B.J. and Obara, C.J., Observations and Implications of Natural Laminar flow on Practical Airplane Surfaces, ICAS paper No. 82-5.1.1, 1982.
20. Kachanov, Y.S., Koslov, V.V. and Levchenko V. Ya., Experimental Study of The Influence of Cooling on The Stability of Laminar Boundary Layers, *Izvestia Sibirskogo Otdielenia Ak. Nauk SSSR, Seria Technicheskikh Nauk*, Novosibirsk, No. 8-2, p75, 1974.
21. Lekoudis, S.G., The Stability of a Boundary Layer on a Swept Wing with Wall Cooling, *AIAA Paper No.*, 79-1495, 1979.
22. Reshotko, E., Drag Reduction by Cooling in Hydrogen Fueled Aircraft, *Journal of Aircraft*, Vol. 16, No. 9, p584-590, 1979.
23. Brewer, D.G., The Case for Hydrogen Fueled Transport Aircraft, *Astronautics and Aeronautics*, Vol. 12, No. 5, p40-51, 1974.
24. Liepmann, H.W., Brown, G.L. and Nosenchuck D.M., Control of Laminar-Instability Waves Using a New Technique, *J. Fluid Mech.*, Vol 118, p187, 1982.
25. Liepmann, H.W. and Nosenchuck D.M., Active Control of Laminar-Turbulent Transition, *J. Fluid Mech.*, Vol 118, p201, 1982.
26. Malling, R.W., Tollmien-Schlichting Wave Cancellation, *Physics of Fluids*, Vol. 24, p979, 1981.
27. Thomas, A.S.W., The Control of Boundary-Layer Transition Using a Wave Superposition Principle, *J. Fluid Mech.*, Vol. 137, p233, 1983.
28. Saric, W.S. and Thomas, A.S.W., Experiments on the Subharmonic Route To Turbulence in Boundary layers, *Proceedings of the International Symposium on Transition (to be published)*, Kyoto, Japan, Sept., 1983.
29. Walsh, M.J. and Lindemann, A.M., Optimization and Application of Riblets for Turbulent Drag Reduction, *AIAA Paper No. 84-0347*, 1984.
30. Hooshmand, A., Youngs, R.A., Wallace, J.M. and Balint, J.-L., An Experimental Study of Changes in The Structure of Turbulent Boundary Layer Due to Surface Geometry Changes, *AIAA Paper No. 83-0230*, 1983.
31. Gallagher, J.A. and Thomas, A.S.W., Turbulent Boundary Layer Characteristics Over Streamwise Grooves, *AIAA Paper No. 84-2185*, 1984.
32. Corke, T.C., Nagib, H.M. and Guezennec, Y.G., A New View on Origin, Role and Manipulation of Large Scales in Turbulent Boundary Layers, *NASA CR No. 165861*, 1982.
33. Bertelrud, A., Truong, T.V. and Avellan, F., Drag Reduction in Turbulent Boundary Layers Using Ribbons, *AIAA Paper No. 82-1370*, 1982.
34. Anders, J.B., Hefner, J.N. and Bushnell, D.M., Performance of Large-Eddy Breakup Devices at Post-Transitional Reynolds Numbers, *AIAA Paper No. 84-0345*.
35. Corke, T.C., Guezennec, Y.G. and Nagib, H.M., Modification of Drag of Turbulent Boundary Layers Resulting from Manipulation of Large-Scale Structures. In *Viscous Flow Drag Reduction*, edited by Hough G.R., Vol 72, *Progress in Astronautics and Aeronautics*, 1980.
36. Mumford, J.C. and Savil, A.M., Parametric Studies of Flat Plate Turbulence Manipulators Including Direct Drag Results and Laser Flow Visualization, presented at the *ASME Fluids Engineering Symposium*, Feb. 12-16, New Orleans, 1984.
37. So, R.M.C. and Mellor, G.L., An Experimental Investigation of Turbulent Boundary Layers Along Curved Surfaces, *NASA CR No. 1940*, 1972.
38. Brown, G.L. and Thomas, A.S.W., Large Structure in a Turbulent Boundary Layer, *Physics of Fluids*, Vol. 20, No. 10, Pt. 2, p243, 1977.
39. Kendall, J.M., The Turbulent Boundary Layer Over a Wall With Progressive Surface Waves, *J. Fluid Mech.*, Vol. 41, p259, 1970.
40. Lin, J.C., Walsh, M.J., Watson, R.D. and Balasubramanian, R., Turbulent Drag Characteristics of Small Amplitude Rigid Surface Waves, *AIAA Paper No. 83-0228*, 1983.
41. Sengupta, T. and Lekoudis, S.G., Calculation of Turbulent Boundary Layers Over Moving Wavy Surfaces, *AIAA Paper No. 83-1670*, 1983.
42. Sengupta, T., Turbulent Boundary Layers Over Rigid and Moving Wavy Surfaces, Ph.D Dissertation, School of Aerospace Engineering, Georgia Institute of Technology, in preparation, 1984.
43. Kuhn, G.D., Moin, P., Kim, J. and Ferziger, J., Turbulent Flow in a Channel with a Wall with Progressive Surface Waves, in *Symposium on Laminar and Turbulent Boundary Layers Control, Modification and Marine Applications*, New Orleans, February, 1984.
44. McMichael, J.M., Klebanoff, P.S. and Mease N.E., Experimental Investigation of Drag on a Compliant Surface. In *Viscous Flow Drag Reduction*, edited by Hough G.R., Vol 72, *Progress in Astronautics and Aeronautics*, 1980.
45. Mulhearn, P.J., Turbulent Flow Over a Periodic Rough Surface, *Physics of Fluids*, Vol 21., p1113, 1978.

46. Coles, D. and Savas, O., Interactions for Regular Patterns of Spots in a Laminar Boundary Layer. In Laminar-Turbulent Transition, Eppler, R. and Fasel, H. (Editors), Springer-Verlag, Berlin, 1980.
47. Chambers, F.W., Preliminary Measurements of a Synthetic Turbulent Boundary Layer, Lockheed-Georgia Research Report No. LG82RR0009, 1982.
48. Goodman, W.L., Attempts to Alter Turbulent Large Eddy Structure Through Emmons Spot Modification, Washington Drag Reduction Symposium Abstracts, p65, 1982.
49. Little, B.H. and Whipkey, R.R., Locked Vortex Afterbodies, Journal of Aircraft, Vol. 16, No. 5, p296, 1979.
50. Roshko, A. and Koenig, K., Interaction Effects on the Drag of Bluff Bodies in Tandem. In Aerodynamic Drag Mechanisms of Bluff Bodies and Road Vehicles, Sovran, G., Morel, T. and Mason, W.T., (Editors), Plenum Press, 1978.
51. Howard, F.G., Goodman, W.L. and Walsh, M.J., Axisymmetric Bluff-Body Drag Reduction using Circumferential Grooves, Presented at the AIAA Applied Aerodynamics Conference, Danvers, Mass., July, 1983.
52. Juass, B., Howard, F.G., Weinstein, L. and Bushnell, D., Longitudinal Grooves for Bluff-Body Drag Reduction, AIAA Journal, Tech. Notes, Vol. 19, No. 4, p535, 1981.
53. Viets, H., Piatt, M. and Ball, M., Boundary Layer Control by Unsteady Vortex Generation, Proceedings of ASME Symposium on Aerodynamics of Transportation, p223, ASME, New York.
54. Brogna, S.J. and Hawkes, R.J., Effect of Base Suction on Subsonic Drag of Bluff Bodies, Journal of Aircraft, Vol. 15, No. 7, p443, 1978.
55. Stratford, B.S., The Prediction of Separation of the Turbulent Boundary Layer, J. Fluid Mech., Vol. 5, No. 1, p1, 1959.
56. Smith, A.M.O., Stokes, T.R. and Lee, R.S., Optimum Tail Shapes for Bodies of Revolution, J. Hydronautics, Vol. 15, No. 1, p67, 1981.
57. Lekoudis, S.G., Radwan, S.F., and Sankar, N.L., A Method for Designing Three-Dimensional Configurations with Prescribed Skin Friction, AIAA Paper No. 84-0526.
58. Hackett, J.E., Phillips, C.G. and Lilley, D.E., Three-Dimensional Wake Flow Measurements for a Wing and a Bluff Car-Like Body, Lockheed-Georgia Engineering Report, LG81ERO201, 1981, (prepared under NSF Grant No. ENG-7900891).
59. Webber, G.W., Aerodynamic Development for Efficient Military Cargo Transports, AIAA Paper No. 83-1822, 1983.
60. McCluney, B., Improving the Belfast, Flight International, 3 Aug., 1967.
61. Polhamus, E.C. and Spreemann, K.P., Effect of High Subsonic Speeds on the Static Stability and Vertical-Tail-Load Characteristics of a Complete Model Having a Delta Wing, NACA RM L157k15a, 1958.
62. Perkins, C.D. and Hage, R.E., Airplane Performance Stability and Control, John Wiley and Sons, New York, 1953.
63. Webber, G.W. and Dansby, T., Wing tip Devices for Energy Conservation and Other Purposes - Experimental and Analytical Work in Progress at Lockheed-Georgia Company, Canadian Aeronautics and Space Journal, Vol. 29, No. 2, p105, 1983.
64. Whitcomb, R.T., A Design Approach and Selected Wind-Tunnel Results at High Subsonic Speeds for Wing-Tip Mounted Winglets, NASA TN D-8260, 1976. (See also NASA TN D-8624, 8627, 8473, 8474, 8478 for specific details of winglet development.)
65. Whitcomb, R.T., Methods for Reducing Subsonic Drag Due to Lift, Paper No. 2 of AGARD Special Course on Concepts for Drag Reduction, AGARD Rept. No. 654, 1977.
66. Darel, I., Eliraz, Y. and Barnett, Y., Winglets Development at Israel Aircraft Industries, ICAS Paper No. 80-12.5, 1980.
67. Gifford, R.V. and van Dam, C.P., The Design Integration of Wingtip Devices for Light General Aviation aircraft, ICAS Paper No. 82-1.4.4, 1982.
68. Hackett, J.E., Vortex Drag Reduction by Aft-Mounted Diffusing Vanes, ICAS Paper No. 80-13.4, 1980.
69. Spillman, J.J., The Use of Wingtip Sails to Reduce Vortex Drag, Aeronautical Journal, Paper No. 618, p387, 1978.
70. Wu, J.M., Vakili, A. and Chen, Z.L., Wing Tip Jets Aerodynamic Performance, ICAS Paper No., 82-5.6.3, 1982.
71. Poppelton, E.D., Effect of Air Injection Into Core of Trailing Vortex, Eng. Notes, J. of Aircraft, Vol. 8, No. 8, 1971.
72. Foss, R.L. and Lewolt, J., Use of Active Controls for Fuel Conservation of Commercial Transports, AIAA Paper No. 77-1220, 1977.
73. Hoerner, S.F., Fluid Dynamic Drag, published by the author, New Jersey, 1958.
74. Kuchemann, D., Some Remarks on the Interference Between a Swept Wing and a Fuselage. In Aerodynamic Interference, AGARD-CP-71-71, Paper No. 1, 1971.

75. Weber, J., Interference Problems on Wing-Fuselage Combinations, Part 1, RAE-TR-69130, 1969.
 76. Weber, J. and Joyce, M.G., Interference Problems on Wing-Fuselage Combinations, Part 2, RAE-TR-71179, 1971, Part 3, RAE-TR-73189 and Part 4, RAE-TR-73190, 1974.
 77. Yoshino, F., An Experimental Investigation of the Effect of Fuselage on Wing Characteristics, Princeton University Rcpt. No. AMS-TR-1151, Prepared for the Office of Naval Research, 1975.
 78. Gersten, K., Corner Interference Effects, AGARD Rept. No. 299, 1959.
 79. Sopher, R., Design of a Fairing for the Junction of Two Wings, J. Aircraft, Vol. 4, No. 4, p379, 1967
 80. Patterson, J.C., Wind Tunnel Studies of Nacelle Interference Drag at High Subsonic Speeds Including the Effect of Powered Jets, NASA SP-124, Paper No. 18, p259, 1966.
 81. Runckel, J.F., Aerodynamic Interference Between Exhaust System and Airframe, AGARD CP-71-71, Paper No. 15, 1971.
 82. Ewald, B., Airframe-Engine Interaction for Engine Configurations Mounted Above the Wing, AGARD CP-159, 1975.
 83. Hess, J.L. and Faulkner, S.M., Determination of Low Speed Interference Effects by Superposition, AGARD CP-71-71, Paper No. 24, 1971.
 84. Aldridge, S.E. and Nye, J.L., Experimental Results of High Bypass Ratio Turbofan and Wing Aerodynamic Interference, AGARD CP-71-71, Paper No. 23, 1971.
 85. Swan, W.C. and Sigilla, A., The Problem of Installing a Modern High Bypass Engine on Twin Jet Transport Aircraft, AGARD CP-124, Paper No. 17, 1973.
 86. The Effect of Underwing Aft-Mounted Nacelles on the Characteristics of a High-Wing Transport, NASA-Langley Rept. No. 1-15664, 1984, to be published.
 87. Atta, E.H. and Vadyak, J., A Grid Embedding Transonic Flow Analysis Computer Program for Wing/Nacelle Configurations, NASA-CR-166529, 1983.
 88. Vadyak, J. and Atta, E.H., A Computational Program for the Calculation of Three-Dimensional Transonic Nacelle/Inlet Flowfields, NASA-CR-166528, 1983.
 89. Aerodynamics of Power Plant Installation, AGARD-CP-301, 1981.
 90. Krenz, G. and Hilbig, R., Aerodynamics Concepts for Fuel-Efficient Transport Aircraft, ICAS Paper No. 82-1.5.2, 1982.
-

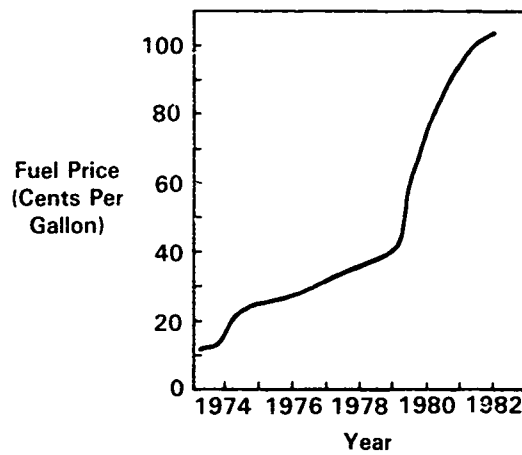


Figure 1. Trend in world fuel prices.

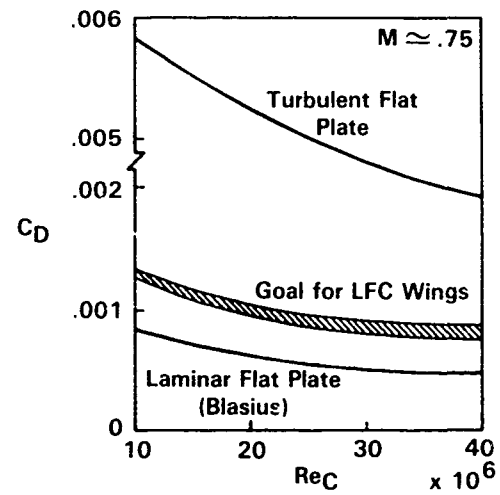


Figure 4. Skin friction goal for LFC surfaces.

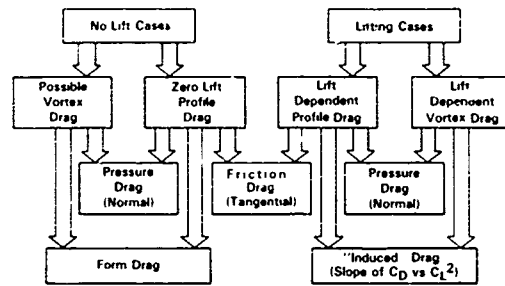


Figure 2. Sources and terminology of drag contributions.

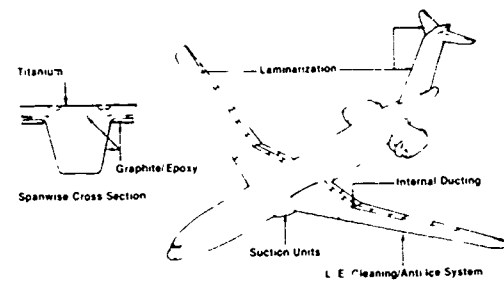


Figure 5. The Lockheed LFC aircraft concept (Ref. 9).

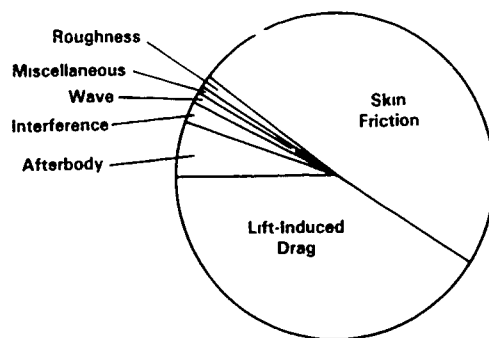


Figure 3. Contributions of different drag sources for a typical transport aircraft.

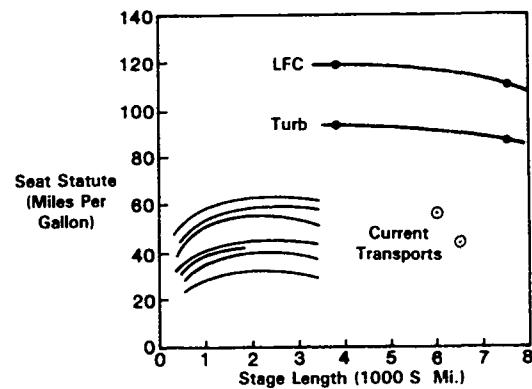


Figure 6. Fuel efficiency - current transports versus an advanced LFC aircraft and an advanced turbulent aircraft (Ref. 7).

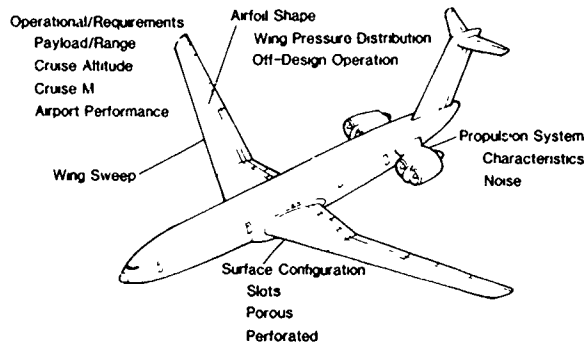


Figure 7(a). Factors affecting LFC design (Ref. 7).

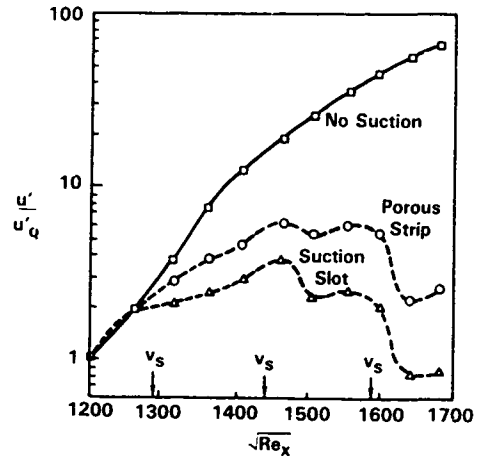


Figure 8. Instability wave growths for suction through a slot or through a wide porous strip.

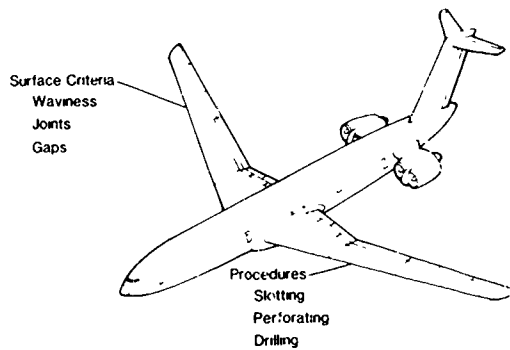


Figure 7(b). Factors affecting LFC manufacturing (Ref. 7).

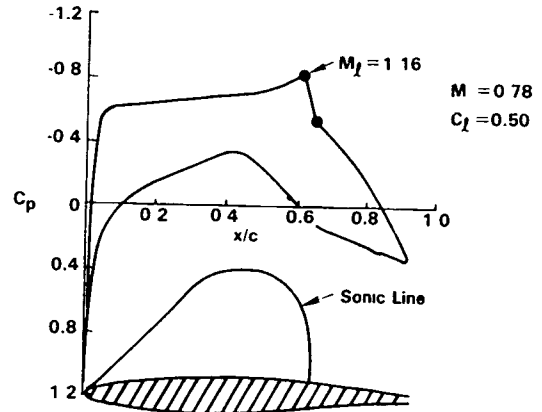


Figure 9. Wing geometry and surface pressures characteristic of a Natural Laminar Flow wing.

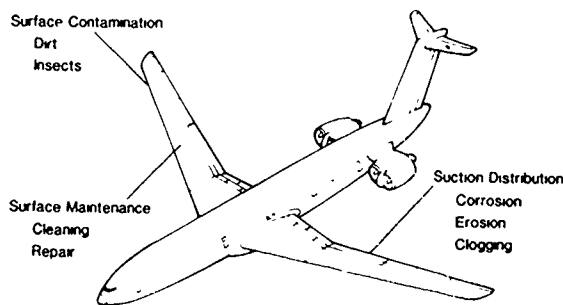


Figure 7(c). Factors affecting LFC operations (Ref. 7).

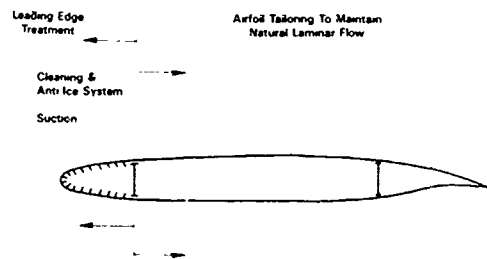


Figure 10. The Hybrid Laminar Flow Control concept.

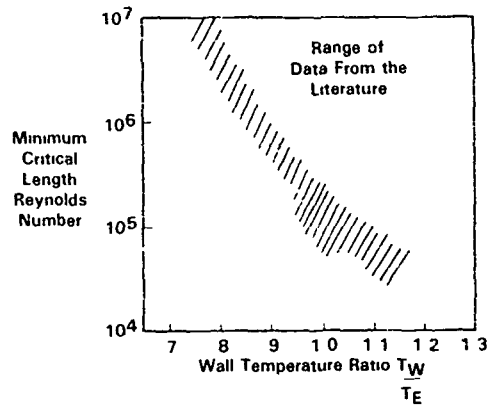


Figure 11. The effect of wall cooling on transition Reynolds numbers (Ref. 21).

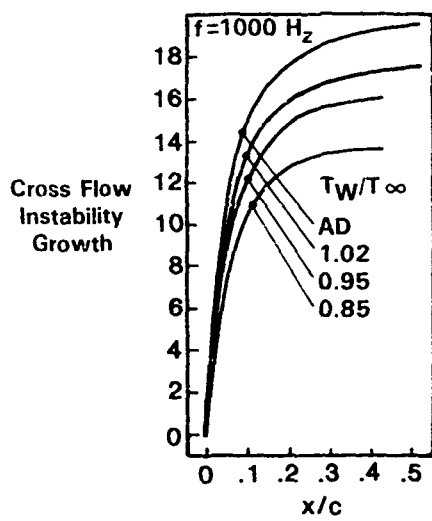


Figure 12. Crossflow instability growth for different wall temperatures (Ref. 22).

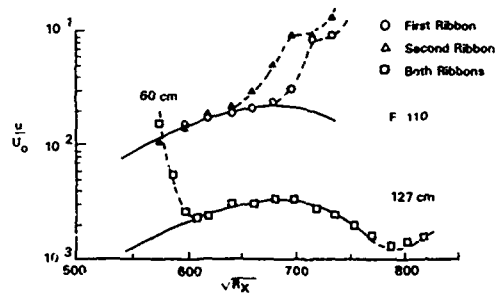
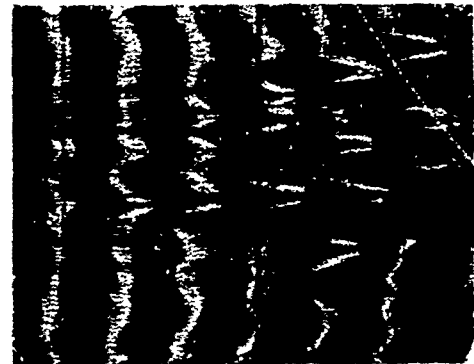
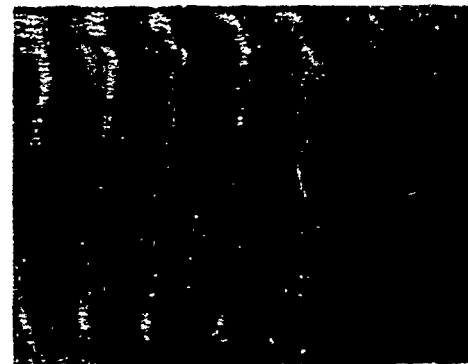


Figure 13. Instability wave growth with and without a control disturbance being present (Ref. 28).



(a)



(b)

Figure 14. Smoke wire visualization of (a) uncontrolled and (b) controlled instability waves (Ref. 28).

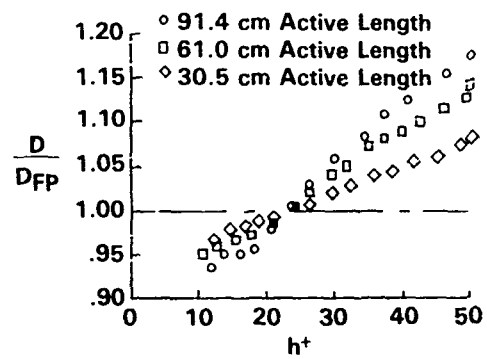


Figure 15. Drag reduction over riblet surface (Ref. 30).

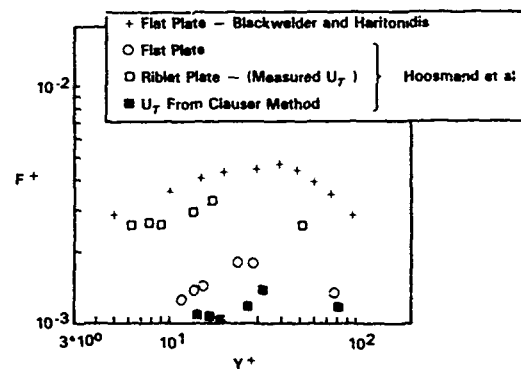


Figure 16. Turbulent bursting frequency over riblet surface (Ref. 31).



(a)



(b)

Figure 17. Multi-colored dye visualization of the flow over (a) a flat plate surface and (b) a riblet surface. Flow is from left.

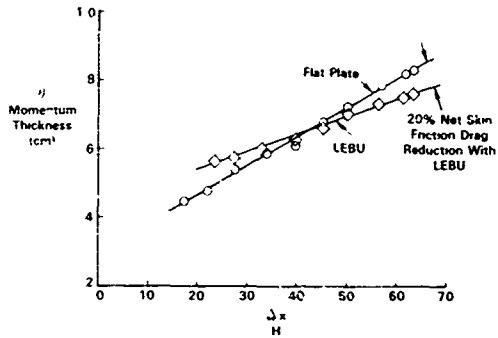
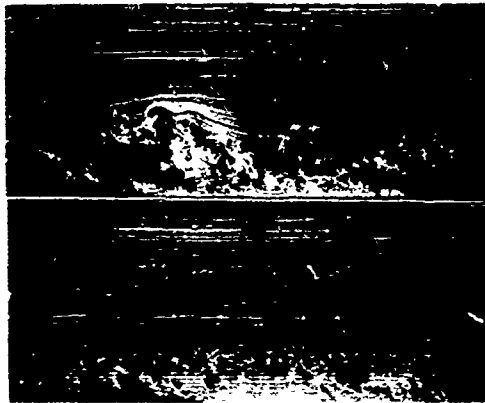


Figure 18. Boundary layer development downstream of a LEBU (Ref. 36).



(a)

(b)

Figure 19. Smoke wire visualizations of (a) controlled and (b) uncontrolled turbulent boundary layer structure (Ref. 36). Flow is from right to left.

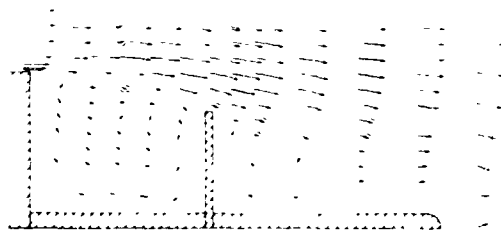


Figure 20. Locked vortex afterbody flow control (Ref. 49).

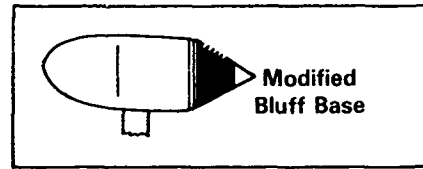
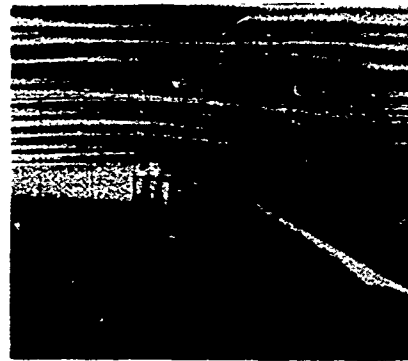


Figure 21. Transverse grooves for afterbody drag reduction (Ref. 51).



(a)



(b)

Figure 22. Flow visualization of the flow over an afterbody (a) with and (b) without transverse grooves (Ref. 51).

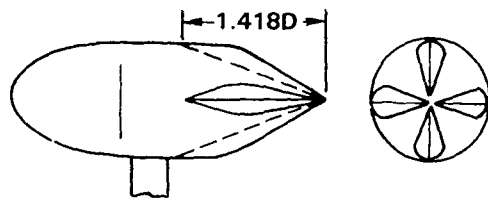


Figure 23. Streamwise grooves for afterbody drag reduction (Ref. 52).

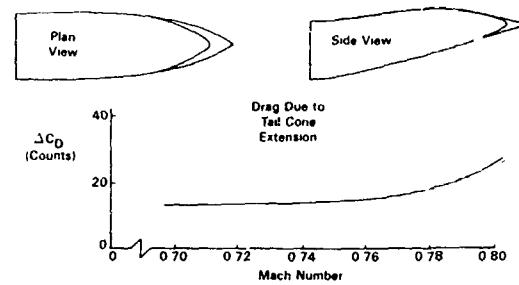


Figure 27. The use of a tail cone to reduce afterbody drag (Ref 59).

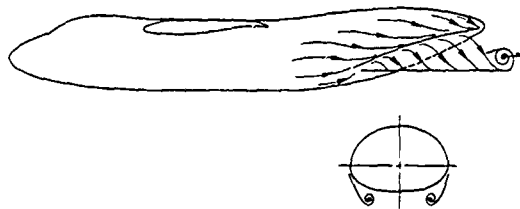


Figure 24. The vortex wake behind an upswept afterbody.

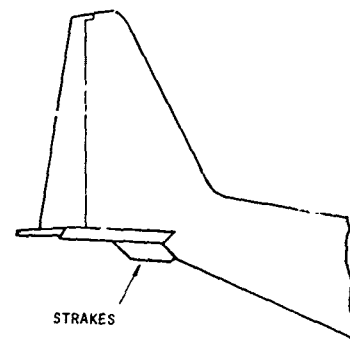


Figure 28. The drag reducing strakes on the C-130 aircraft.

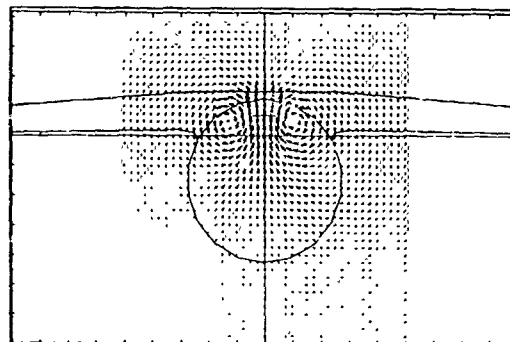


Figure 25. Crossflow velocities in the wake of a highly upswept fuselage.

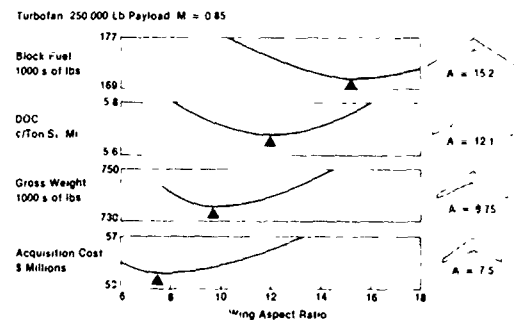


Figure 29. Effect of wing aspect ratio (Ref. 9).

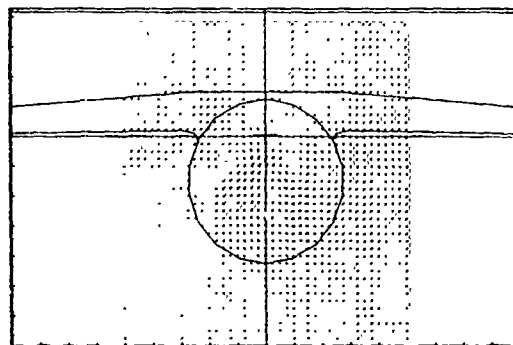


Figure 26. Crossflow velocities in the wake of a fuselage with low upsweep.

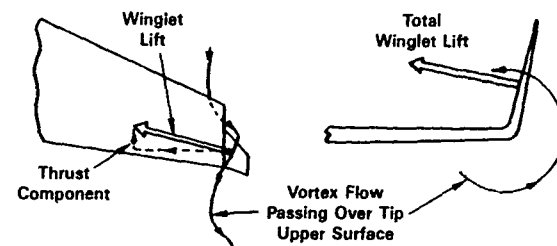
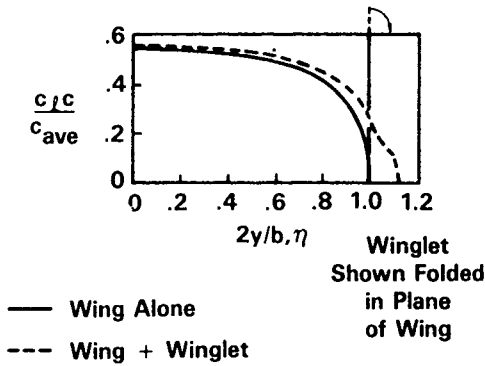


Figure 30. Winglets for drag reduction (Ref 63).

a. Spanwise Lift Distribution



b. Spanwise Drag Distribution, Near Field

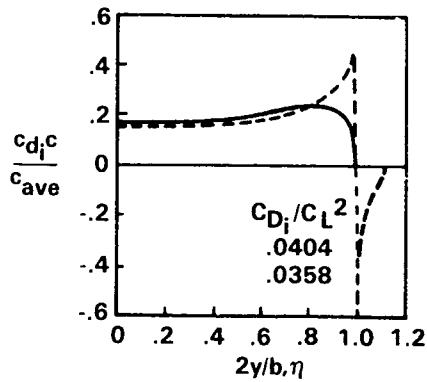


Figure 31. Spanwise lift and drag components for a wing with and without winglets.

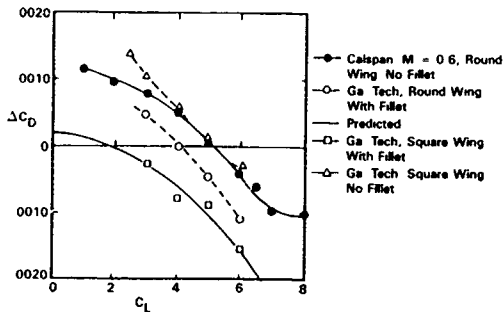


Figure 32. Winglet performance with and without appropriate filleting.

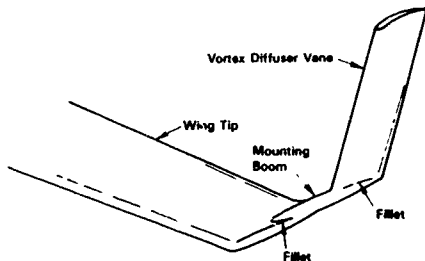


Figure 33. The vortex diffusing vane (Ref. 68).

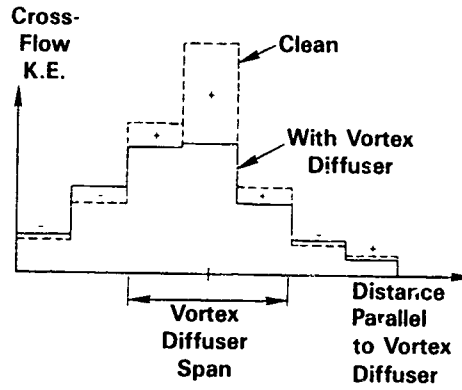


Figure 34. The reduction in crossflow kinetic energy available from vortex diffusing vanes (Ref. 68).

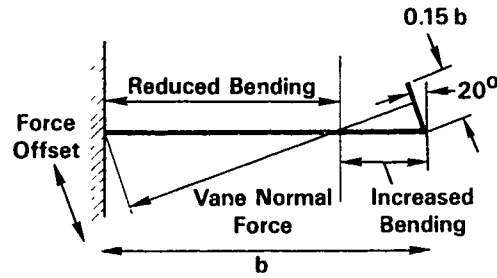


Figure 35. Possible reduction in wing-root bending with vortex diffusing vanes (Ref. 68).

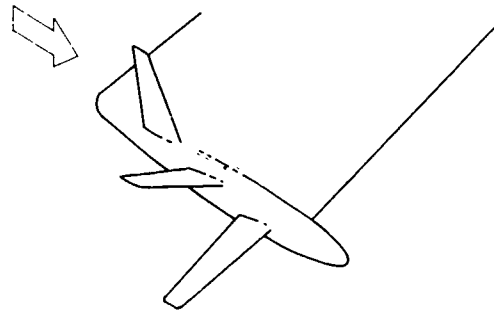


Figure 36. Wing-tip sails for drag reduction.

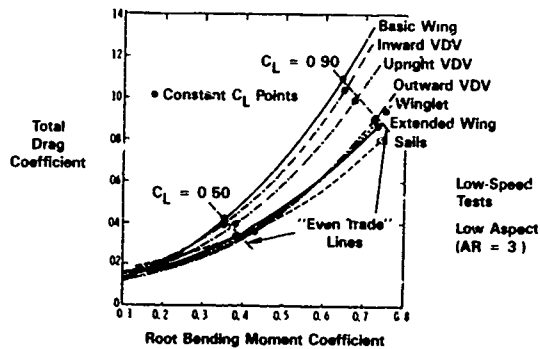


Figure 37. Comparative performance of various wingtip devices and tip extensions (Ref. 63).

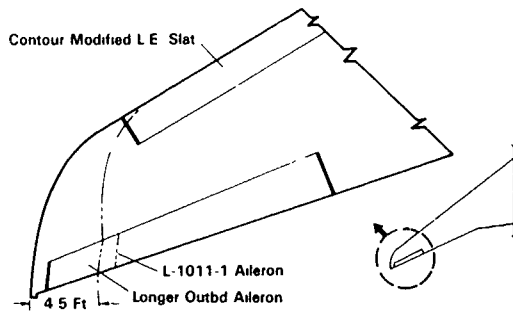


Figure 38. Wing-tip extensions for the L-1011 aircraft with active controls (Ref. 70).



Figure 39. The horseshoe vortex structure ahead of an unfilleted junction.

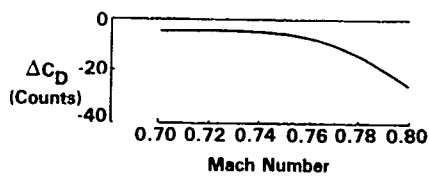
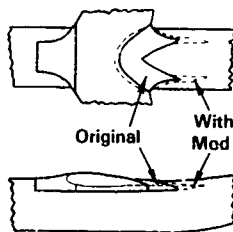
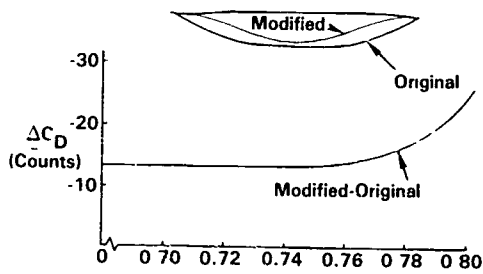


Figure 40. Reduction of juncture drag with filleting.

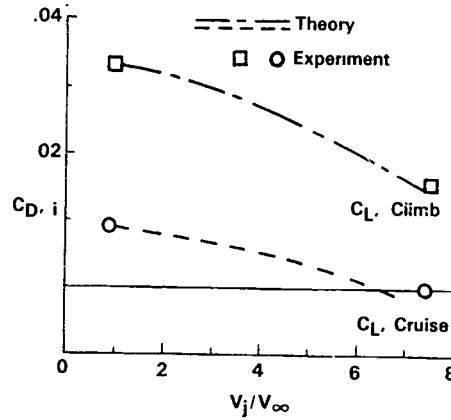
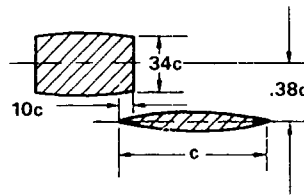


Figure 41. Induced drag reduction with an over wing engine mount (Ref. 65).

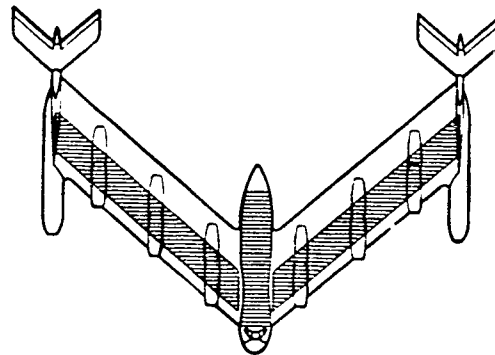


Figure 42. The spanloader concept (Ref. 9).

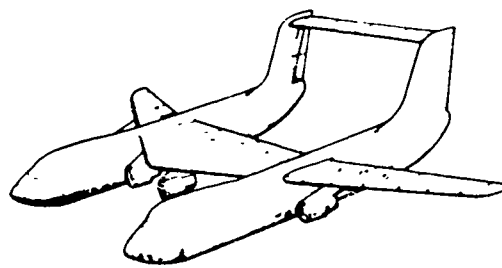


Figure 43. The tandem fuselage concept (Ref. 9).

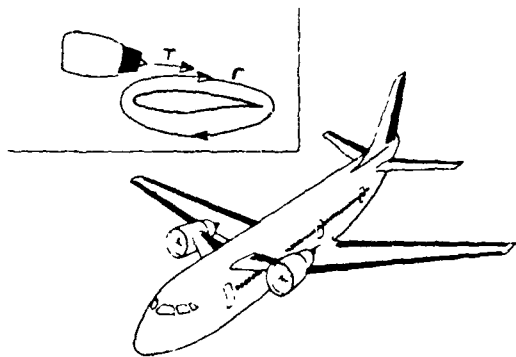


Figure 44. Canard mounted engines for performance improvements (Ref. 90).

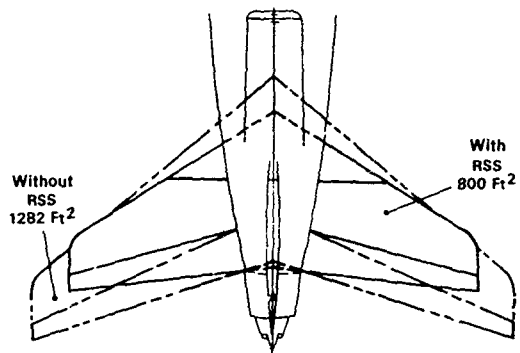


Figure 45. Reduction in control surface size through relaxed static stability (Ref. 70).

BOUNDARY-LAYER TRANSITION: T-S WAVES AND CROSSFLOW MECHANISMS

by

William S. Saric

Mechanical and Aerospace Engineering
 Arizona State University
 Tempe, AZ 85287

SUMMARY

The basic instability mechanisms are discussed from an elementary standpoint considering only boundary layers in external flows. The current state-of-the-art of boundary-layer transition prediction is reviewed and by using recent results, it is shown that a number of unique transition mechanisms exist and each can play a different role in the breakdown to turbulence. The control of the stability and transition characteristics of a particular flow field requires thoroughly understanding the details of these breakdown mechanisms.

NOMENCLATURE

A	: disturbance amplitude
A_0	: amplitude at $R=R_0$, usually Branch I
a	$= \alpha_r/R = \nu/U_0 \lambda_x$: dimensionless chordwise wavenumber
b	$= \beta_r/R = \nu/U_0 \lambda_z$: dimensionless spanwise wavenumber
C_p	: pressure coefficient
D	$= d/dy$
F	$= \omega/R = 2\pi\nu f/U_0^2$: dimensionless frequency
f	: dimensional frequency [hz]
H	$= \delta^*/\theta$: shape factor
i	$= \sqrt{-1}$
k	$= k_r = ik_i$: complex wavenumber vector, ($k \equiv \alpha$ for 2-D)
k_r	: (α_r, β_r) wavenumber vector
k_i	: (α_i, β_i) growth-rate vector
L	: length scale
N	$= \ln(A/A_0)$: amplification factor
P	: basic-state pressure normalized by ρU_0^2
p'	: disturbance-state pressure
Q	: basic-state dependent variable
q'	: disturbance-state dependent variable (i.e. u', v', w' , or p')
R	$= \sqrt{R_x} = U_0 \delta_r/\nu$: boundary-layer Reynolds number
R_I, R_{II}	: Branch I and II neutrally stable Reynolds numbers
R_0	: initial boundary-layer Reynolds number, usually Branch I
R_x	$= U_0 x^2/\nu$: x-Reynolds number or chord Reynolds number
$R_{c,f}$	$= W_{t,max} \delta_{10}/\nu$: crossflow Reynolds number
T	: temperature [°K]
U	: basic-state chordwise velocity normalized by U_0
U_0	: freestream velocity, [m/s], (normalizing velocity)
U_t	: component parallel to inviscid flow over swept wing [m/s]
U_t^{invisc}	: inviscid flow velocity over swept wing [m/s]
u', v', w'	: disturbance velocity field normalized by U_0
$ u' $: rms of u'
V	: basic-state, normal-to-the-wall velocity normalized by U_0
V_0	: blowing or suction velocity at the wall [m/s]
W	: basic-state spanwise velocity normalized by U_0
W_t	: crossflow velocity, [m/s], (perpendicular to U_t)
$W_{t,max}$: maximum of crossflow velocity [m/s]
x, y, z	: chordwise, normal-to-the-wall, and spanwise coordinates normalized by δ_r
x^*, y^*, z^*	: dimensional coordinates [m]
x_t, z_t	: coordinates tangent to and perpendicular to the inviscid velocity vector
y_{max}	: location of maximum crossflow velocity
α	$= \alpha_r + i\alpha_i$: chordwise complex wavenumber normalized by δ_r
α_r	$= 2\pi\delta_r/\lambda_x$
β	$= \beta_r + i\beta_i$: spanwise complex wavenumber normalized by δ_r
β_r	$= 2\pi\delta_r/\lambda_z$
δ	: boundary-layer thickness, [m], at $U/U_0 = 0.99$
δ_r	$= \sqrt{\nu x^*}/U_0$: boundary-layer reference length, [m], (normalizing length)
δ^*	: displacement thickness [m]
δ_{10}	: largest thickness where $W_t/W_{t,max} = 10\%$ [m]
η	$= y^*/\delta_r = y$: boundary-layer coordinate
θ	$= \int (\alpha dx + \beta dz - \omega dt)$: phase function

θ	: momentum thickness [m]
λ_x	: chordwise wavelength [m]
λ_z	: spanwise wavelength [m]
μ	: dynamic viscosity [ns/m ²]
ν	: kinematic viscosity [m ² /s]
ρ	: density [kg/m ³]
ϕ	: disturbance streamfunction amplitude, $\phi = \phi(y)$
ϕ'	: disturbance streamfunction, $\phi' = \phi'(x,y,z,t)$
ω	: $2\pi f\delta_r/U_0$: dimensionless circular frequency

1. INTRODUCTION

This lecture on boundary-layer stability and transition comes at the beginning of the course on Aircraft Drag Prediction and Reduction and serves as a tutorial on the basic concepts of stability and transition. During March 26-30, 1984, an AGARD-VKI Special Course on Stability and Transition of Laminar Flow was held at VKI (AGARD Report No. 709). During that course, the written lectures by Arnal (1984), Mack (1984b), Reshotko (1984a,b), Poll (1984b), and Herbert (1984b,c) covered vast amounts of detail. Therefore it will not be necessary to present here a detailed research document with complete references but rather it is possible to rely on this considerable collection of information. Before presenting a detailed review of these proceedings, some basic ideas will be discussed.

In fluids, turbulent motion is usually observed rather than laminar motion because the Reynolds number range of laminar motion is generally limited. The *transition* from laminar to turbulent flow occurs because of an incipient instability of the basic flow field. This instability intimately depends on subtle, and sometimes obscure, details of the flow. The process of transition for *boundary layers in external flows* can be qualitatively described using the following (albeit, oversimplified) scenario.

Disturbances in the freestream, such as sound or vorticity, enter the boundary layer as steady and/or unsteady fluctuations of the basic state. This part of the process is called *receptivity* (Morkovin, 1969) and although it is still not well understood, it provides the vital initial conditions of amplitude, frequency, and phase for the breakdown of laminar flow. Initially these disturbances may be too small to measure and they are observed only after the onset of an instability. The type of instability that occurs depends on Reynolds number, wall curvature, sweep, roughness, and initial conditions. The initial growth of these disturbances is described by *linear* stability theory. This growth is weak, occurs over a viscous length scale, and can be modulated by pressure gradients, mass flow, temperature gradients, etc. As the amplitude grows, three-dimensional and nonlinear interactions occur in the form of *secondary* instabilities. Disturbance growth is very rapid in this case (now over a convective length scale) and breakdown to turbulence occurs.

Since the linear stability behavior can be calculated, transition prediction schemes are usually based on linear theory. However, since the initial conditions (receptivity) are not generally known, only correlations are possible and, most importantly, these correlations must be between two systems with similar environmental conditions.

At times, the initial instability can be so strong that the growth of linear disturbances is *by-passed* (Morkovin, 1969) and turbulent spots or secondary instabilities occur and the flow quickly becomes turbulent. This phenomenon is not well understood but has been documented in cases of roughness and high freestream turbulence. In this case, transition prediction schemes based on linear theory fail completely.

The literature review follows the outline of the process described above and begins with Reshotko (1984a) on receptivity (i.e. the means by which freestream disturbances enter the boundary layer). In this paper, Reshotko summarizes the recent work in this area and points out the difficulties in understanding the problem. Indeed, the receptivity question and the knowledge of the initial conditions are the key issues regarding a transition prediction scheme.

Mack (1984b) is actually a monograph on boundary-layer stability theory and should be considered required reading for those interested in all aspects of the subject. It covers 58 pages of text with 170 references. In particular, his report updates the three-dimensional (3-D) material in Mack (1969), covering in large part Mack's own contributions to the area. This lecture will rely on Mack (1984b) to some extent since all of the basic details for deriving, analyzing, and solving the stability equations for 2-D flows, compressible flows, and 3-D flows are given. The discussion on suction stabilization for laminar flow control is limited, but this is covered in some detail in the next lecture (Saric, 1985).

The two papers of Herbert (1984b,c) cover the problems of secondary instabilities and nonlinearities i.e. those aspects of the breakdown process that follow the growth of linear disturbances. Two-dimensional waves do not completely represent the breakdown process since the transition process is *always* three-dimensional in bounded shear flows. Herbert describes the recent efforts in extending the stability analysis into regions of wave interactions that produce higher harmonics, three-dimensionality, subharmonics, and large growth rates--all harbingers of transition to turbulence. More is said about this in section 5.

The paper by Arnal (1984) is an extensive description and review of transition prediction for two-dimensional flows that covers 34 pages of text and over 100 citations. A description of different mechanisms that cause transition such as Tollmien-Schlichting (T-S) waves, Görtler vortices, and turbulent spots is given. The effects that modulate the transition behavior are presented. These include the influence of freestream turbulence, sound, roughness, pressure gradient, suction, and unsteadiness. A good deal of the data comes from the work of the group at ONERA/CERT part of which has only been available in report form. The different transition criteria that have been developed over the years are described in Chapter II. This paper is of interest to the aircraft systems designer from the standpoint of giving an overall historical perspective of transition phenomena and their anfractuous nature.

Poll (1984b) extends the description of the transition territory to 3-D flows. When the basic state is three-dimensional, not only are 3-D disturbances important, but different types of instabilities can occur. Poll concentrates on the problems of leading-edge contamination and crossflow vortices, both of which are of interest to the designer. The history of these problems as well as the recent work on transition prediction and control schemes are discussed. Additional discussion of 3-D flows is presented in section 4.

Reshotko (1984b) reviews the application of stability and transition information to problems of drag reduction and in particular, laminar flow control. He discusses some of the laminar flow control issues which are not covered in the next lecture (Sarić, 1985). A portion of his work is also devoted to the issues of *viscous simulation*. Reshotko (1985) also addresses problems of transition control that are of interest here.

The objective of this report is to provide the basic ideas and results of stability and transition research in order that the reader can understand laminar flow control for aircraft systems. The above referenced reports by Reshotko, Mack, Herbert, Arnal, and Poll are relied on to provide the details of the research in this area.

2. LINEAR STABILITY EQUATIONS

In this section, the stability analysis of three-dimensional disturbances in an incompressible *parallel* boundary-layer flow, without curvature, is presented. The *basic state* velocity vector, $\underline{V} = (U, V, W)$, is defined by the following one-dimensional flow:

$$U = U(y), \quad V = 0, \quad W = W(y) \quad (1)$$

where U is the chordwise velocity component, W is the spanwise velocity component, and y is the coordinate normal to the wall.

It is, of course, an incongruity to speak of a parallel boundary-layer flow since no such thing can exist except under very special circumstances. However, the parallel-flow assumption is an important first approximation to the actual two-dimensional basic-state problem because the Reynolds number is very large. It is beyond the scope of this lecture to discuss non-parallel stability effects so the reader is referred to Mack (1984b) for a summary. Likewise, the role of compressibility in subsonic flows is minor and all of the essential physical ideas are represented in the flow of Eq.(1).

The stability equations are obtained by superposing small disturbances on the basic state in the following way:

$$\begin{aligned} u^*/U_0 &= U + u'(x, y, z, t) \\ v^*/U_0 &= v'(x, y, z, t) \\ w^*/U_0 &= W + w'(x, y, z, t) \\ p^*/\rho U_0^2 &= P + p'(x, y, z, t) \end{aligned} \quad (2)$$

where u^* , v^* , w^* , and p^* satisfy the complete dimensional Navier-Stokes equations, ($'$) denotes dimensionless disturbance quantities, and capital letters denote dimensionless basic-state quantities. Equation (2) is substituted into the Navier-Stokes equations which are made dimensionless by introducing the length scale L . The basic-state velocity components also satisfy the usual Navier-Stokes equations so that basic-state solution drops out. Thus, equations in terms of the disturbance velocities result which are simplified by making the additional approximation that products of disturbance quantities are neglected. This results in the following set of *linear* disturbance equations:

$$\frac{\partial u'}{\partial x} + \frac{\partial v'}{\partial y} + \frac{\partial w'}{\partial z} = 0 \quad (3)$$

$$\frac{\partial u'}{\partial t} + U \frac{\partial u'}{\partial x} + W \frac{\partial u'}{\partial z} + v' \frac{dU}{dy} + \frac{\partial p'}{\partial x} - \frac{1}{R} \nabla^2 u' = 0 \quad (4)$$

$$\frac{\partial v'}{\partial t} + U \frac{\partial v'}{\partial x} + W \frac{\partial v'}{\partial z} + \frac{\partial p'}{\partial y} - \frac{1}{R} \nabla^2 v' = 0 \quad (5)$$

$$\frac{\partial w'}{\partial t} + U \frac{\partial w'}{\partial x} + W \frac{\partial w'}{\partial z} + v' \frac{dW}{dy} + \frac{\partial p'}{\partial z} - \frac{1}{R} \nabla^2 w' = 0 \quad (6)$$

where the Reynolds number is given by $R = U_0 L / \nu$ for the time being. The question of *stability* is one of whether the solution set of Eqs.(3)-(6) contain disturbances that grow or decay in space (or time).

The disturbance equations are linear and the coefficients are only functions of y . This suggests a solution in terms of separation of variables using normal modes (i.e. exponential solutions in terms of the independent variables x, z, t) that would reduce Eqs.(3)-(6) to ordinary differential equations. One possible normal mode is the single wave:

$$q'(x, y, z, t) = q(y) \exp[i(\alpha x + \beta z - \omega t)] + C.C. \quad (7)$$

where C.C. stands for complex conjugate, q' represents any of the disturbance quantities of Eq. (2), α is the chordwise wavenumber, β is the spanwise wavenumber, and ω is the frequency. Here, α and β are in general complex and given by $\alpha = \alpha_r + i\alpha_i$, and $\beta = \beta_r + i\beta_i$, and ω is real. The amplitude function $q(y)$ is complex and q' is real.

The parallel-flow assumption is essentially a local one in that, at each chord location, U and W are re-evaluated and L is chosen to be the boundary-layer reference length $L = \delta_x = \sqrt{\nu x^3 / U_0}$. In this case, α , β , and R depend on the chordwise position, x^* . Therefore, the use of Eq.(7) is not rigorously correct and the phase function, Θ , must be introduced to define the normal mode as:

$$q'(x, y, z, t) = q(y) \exp(i\Theta) + C.C. \quad (8)$$

where

$$\frac{\partial \Theta}{\partial x} = \alpha \quad (9)$$

$$\frac{\partial \Theta}{\partial z} = \beta \quad (10)$$

$$\frac{\partial \Theta}{\partial t} = -\omega \quad (11)$$

This step can be rigorously justified using a non-parallel analysis (e.g. Gaster, 1974; Saric and Nayfeh, 1977). Substitution of Eq.(8) into Eqs.(3)-(6) gives

$$i\alpha u + i\beta w + Dv = 0 \quad (12)$$

$$i(\alpha U + \beta W - \omega)u + (DU)v + i\alpha p - \frac{1}{R}(D^2 - k^2)u = 0 \quad (13)$$

$$i(\alpha U + \beta W - \omega)v + Dp - \frac{1}{R}(D^2 - k^2)v = 0 \quad (14)$$

$$i(\alpha U + \beta W - \omega)w + (DW)v + i\beta p - \frac{1}{R}(D^2 - k^2)w = 0 \quad (15)$$

where $D \equiv d/dy$ and $k^2 = \alpha^2 + \beta^2$.

Although Eqs.(12)-(15) look like a 6th-order system of equations, they can be combined into a single 4th-order equation called the *Orr-Sommerfeld* equation.

$$D^4 v - 2k^2 D^2 v + k^4 v - iR[(\alpha U + \beta W - \omega)(D^2 v - k^2 v) - \alpha(D^2 U)v - \beta(D^2 W)v] = 0 \quad (16)$$

When the definition, $k\bar{U} = \alpha U + \beta W$ is used, Eq.(16) immediately resembles the 2-D form of the Orr-Sommerfeld equation as

$$(D^2 - k^2)^2 v - ikR[(\bar{U} - \omega/k)(D^2 - k^2)v - (D^2 \bar{U})v] = 0 \quad (17)$$

with boundary conditions

$$v(0) = Dv(0) = 0, \quad v(y \rightarrow \infty) \rightarrow 0 \quad (18)$$

Thus, *all* of the 3-D stability characteristics for the class of flows defined by Eq.(1), can be found by solving Eq.(17). This is the subject of the next two sections. The extension of Eq.(17) to the case of nonparallel flows is formally done by Nayfeh (1980)

3. T-S WAVES

For tutorial purposes, the disturbance state is restricted to two dimensions with $W \equiv 0$, $\beta = 0$, and $k = \alpha = \alpha_r + i\alpha_i$. The 2-D instability to be considered is a *viscous* instability in that the boundary-layer velocity profile is stable in the inviscid limit and thus, an increase in viscosity (a decrease in Reynolds number) causes the instability to occur. All of this is contained within the framework of Eqs.(17)-(18). This mechanism is inappropriately called the *Tollmien-Schlichting* instability after two of its very early investigators. The historical development of this work is given in Mack (1984b).

Equations (17)-(18) are linear and homogeneous and form an eigenvalue problem which consists of determining α ($=k$) as a function of frequency, ω , Reynolds number, R , and the basic state, $U(y)$. The Reynolds number is usually defined as

$$R = U_0 \delta_r / \nu = \sqrt{R_x} \quad (19)$$

and is used to represent distance along the surface. In general, $\delta_r = \sqrt{\nu x^* / U_0}$ is the most straightforward reference length to use because of the simple form of Eq.(19) and because the Blasius variable, η , in $2f\eta\eta' + f\eta\eta'' = 0$ is the same as y in the Orr-Sommerfeld equation. The reader will still find the archaic use of δ^* and θ as reference lengths so care must be taken in comparing data; in using these lengths, additional constants must be carried around.

When comparing the solutions of Eq.(17) with experiments, the dimensionless frequency, F , is introduced as

$$F = \omega/R = 2\pi f / U_0 \quad (20)$$

where f is the frequency in Hertz.

Usually, an experiment designed to observe T-S waves and to verify the 2-D theory is conducted in a low-turbulence wind tunnel ($u'/U_0 \approx 0.02\%$ to 0.06%) on a flat plate with zero pressure gradient (determined from $H = \delta^*/\theta = 2.59$ and not from pressure measurements) where the virtual-leading-edge effect is taken into account by carefully controlled boundary-layer measurements. Disturbances are introduced by means of a 2-D vibrating ribbon using single-frequency, multiple-frequency, step-function, or random inputs (Costis and Saric, 1982) taking into account finite-span effects (Mack, 1984a). Hot wires measure the $U + u'$ component of velocity in the boundary layer and d-c coupling separates the mean from the fluctuating part. In comparing with the theory, v in Eq.(17) is proportional to the disturbance streamfunction so that u' is proportional to $\partial v / \partial y$. The frequency, F , for single-frequency waves remains a constant.

Figure 1 shows the data of the mean flow and disturbance flow measurements from a routine single-frequency experiment conducted by the author at VPI & SU. These data are compared with the Blasius solution and a solution of the Orr-Sommerfeld equation (17) as shown with the solid lines. In comparing the disturbance measurements (of rms u') and theory (of $|\partial v / \partial y|$) both profiles are normalized by their respective maximum values. The agreement between theory and experiment is quite good and illustrates that the 2-D problem is well understood. The fact that the wave amplitude is $1.5\%U_0$ while still remaining linear and 2-D is discussed in section 5. The disturbance signature of figure 1 is a recognizable characteristic of T-S waves. The sharp zero and second maximum of $|u'|$ occur because of a 180° phase shift in the region of the critical layer. This shape is quite unlike a turbulence distribution or even a 3-D, T-S wave.

When the measurements of figure 1 are repeated along a series of chordwise stations, the maximum amplitude varies as shown in the schematic of figure 2. At constant frequency, the disturbance amplitude initially decays until the Reynolds number at which the flow first becomes unstable is reached. This point is called the *Branch I* neutral stability point and is given by $R_{I,1}$. The amplitude grows exponentially until the *Branch II* neutral stability point is reached which is given by $R_{II,1}$. The locus of $R_{I,1}$ and $R_{II,1}$ points as a function of frequency gives the *neutral stability curve* shown in figure 3. For $R > 600$ the theory and experiment agree very well for Blasius flow. For $R < 600$ the agreement is not as good because the theory is influenced by nonparallel effects and the experiment is influenced by low growth rates and nearness to the disturbance source. Virtually all problems of practical interest have $R > 1000$ in which case the parallel theory seems quite adequate (Saric and Nayfeh, 1977).

In order to compare the stability behavior of figure 2 with theory, Eq.(8) is interpreted locally to have the form of Eq.(7) and is rewritten in the following form:

$$v'(x, y, t) = v(y)[\exp(-\alpha_1 x)] \exp[i(\alpha_r x - \omega t)] \quad (21)$$

which shows $-\alpha_1$ as the spatial growth rate. Depending on the sign of this term, the flow is said to be stable or unstable, i.e. if $\alpha_1 > 0$, the disturbances grow exponentially in the streamwise direction and the neutral points are determined by finding the R at which $\alpha_1 = 0$. From the eigenvalues of Eq.(17), figure 3 is $\alpha_1(R, F) = 0$. Recall that Eq.(7) is said to only hold locally (within the quasi-parallel flow approximation) since $\alpha = \alpha(R, F)$. In this case, Eqs.(9) (11) are integrated along the surface to give:

$$\theta(x, t) - \theta(x_0, t) = \int_{x_0}^x \alpha dx - \omega t \quad (22)$$

Since x and R are related through Eq.(19), Eq.(22) can be written as

$$\theta(R, t) - \theta(R_0, t) = 2 \int_{R_0}^R \alpha dR - \omega t \quad (23)$$

where R_0 is the starting point of the integration. Equation (23) is used in Eq.(8) in order to see how much the disturbance has changed from R_0 to R . The real part of θ in Eq.(23) is just the phase and does not contribute to amplitude growth. Thus the change in amplitude of the disturbance is carried by the imaginary part of θ as shown in Eq.(24).

$$\exp[i(\theta - \theta_0)] = [\exp(2 \int_{R_0}^R \alpha_r dR)] \exp[i(2 \int_{R_0}^R \alpha_i dR - \omega t)] \quad (24)$$

In order to determine the relative amplitude ratio, A/A_0 , or as most commonly done, the amplification factor, N , Eq.(24) is used in Eq.(8) to obtain:

$$N = \ln(A/A_0) = -2 \int_{R_1}^R \alpha_i(R) dR \quad (25)$$

where R_1 is the Reynolds number at which the constant-frequency disturbance first becomes unstable (Branch I of the neutral stability curve) and A and A_0 are the disturbance amplitudes at R and R_1 .

The basic design tool is the correlation of N with transition Reynolds number, R_T , for a variety of observations. The correlation will produce a number for N (say 9) which is now used to predict R_T for cases in which experimental data are not available. This is the celebrated e^N method of Smith and von Ingen (e.g. Arnal, 1984; Mack, 1984b). The basic LFC technique changes the physical parameters and keeps N within reasonable limits in order to prevent transition. As long as laminar flow is maintained and the disturbances remain linear, this method contains all of the necessary physics to accurately predict disturbance behavior. As a transition prediction device, the e^N method is certainly the most popular technique used today. It works within some error limits *only* if comparisons are made with experiments with identical disturbance environments. Since no account can be made of the initial disturbance amplitude this method will always be suspect to large errors and should be used with extreme care. When bypasses occur, this method does not work at all. This discussion is continued at the end of section 5.

Mack (1984b) and Arnal (1984) give examples of growth-rate and e^N calculations showing the effects of pressure gradients, Mach number, wall temperature, and three dimensionality for a wide variety of flows. These reports contain the most up-to-date stability information.

4. CROSSFLOW VORTICES

Three-dimensional flows offer a rich dessert of instability mechanisms and the 3-D boundary-layer flow over the swept-wing is no exception. This type of flow is susceptible to four types of instabilities that lead to transition. They are leading-edge contamination, streamwise instability, centrifugal instability, and the topic of this section, crossflow instability. Leading-edge contamination occurs along the attachment line and is caused by disturbances that propagate along the wing edge (Poll 1979, 1984a,b). Streamwise instability is associated with the chordwise component of flow and is quite similar to processes in two-dimensional flows, where T-S waves generally develop. This usually occurs in zero or positive pressure-gradient regions on a

wing. Centrifugal instabilities occur in the shear flow over a concave surface and appear in the form of Görtler vortices (Floryan and Saric, 1979; Hall, 1983). Attachment-line contamination problems are important for transition control but not discussed here because of the existing reviews cited above. On the other hand, a review of Görtler vortices may be beyond the goals of this lecture.

The focus of this section is on the crossflow instability which occurs in strong negative pressure gradient regions. In the leading-edge region both the surface and flow streamlines are highly curved. The combination of pressure gradient and wing sweep deflects the inviscid-flow streamlines inboard as shown in the schematic of figure 4. This mechanism re-occurs in the positive pressure gradient region near the trailing edge. Because of viscous effects, this deflection is made larger in the boundary layer, and causes *crossflow*, i.e. the development of a velocity component inside the boundary layer that is perpendicular to the inviscid-flow velocity vector. This is illustrated in the schematic of figure 5. The crossflow profile has a maximum velocity somewhere in the middle of the boundary layer, going to zero on the plate surface and at the boundary-layer edge. This profile exhibits an inflection point (a condition which is known to be dynamically unstable) causing so-called crossflow vortex structures to form with their axes in the streamwise direction. These crossflow vortices all rotate in the same direction. Descriptions of this instability are given in the classic paper by Gregory, Stuart and Walker (1955) and in the reports by Mack (1984b) and Poll (1984b). Since this is an inchoate area of research at the present time, a more detailed review of the current work is given with emphasis on the results that have appeared since the AGARD special course in March, 1984.

In the past ten years considerable progress has been achieved in calculating the stability characteristics of three-dimensional flows. The state-of-the-art transition prediction method still involves linear stability theory coupled with an e^m transition prediction scheme (Mack, 1984b, Poll, 1984b). Malik and Poll (1984) extend the stability analysis of three-dimensional flows, analyzing the flow over a yawed cylinder, to include curvature of the surface and streamlines. They show that curvature has a very stabilizing effect on the disturbances in the flow. This is compared with the experimental results of Poll (1984a) which show good agreement with the transition prediction scheme. They also find that the most highly amplified disturbances are traveling waves and not stationary waves. This is in disagreement with Malik, Wilkinson and Orszag (1981) who showed for the rotating disk that the fixed disturbances produced the highest amplification rates. Here again Malik and Poll (1984) obtain good agreement with Poll's (1984a) recent experimental work where Poll identifies a highly amplified traveling wave around one kHz near transition. Malik and Poll obtain N factors for the fixed-frequency disturbances between 11 and 12 which agreed with the work of Malik, Wilkinson and Orszag (1981) on the rotating disk. In both cases (the disk and cylinder), when the extra terms involving curvature and Coriolis effects are omitted in the stability analysis, the N factors are much larger which illustrates the need to do the realistic stability calculations.

Michel, Arnal and Coustols (1984) develop transition criteria for incompressible two- and three dimensional flows and in particular for the case of a swept wing with infinite span. They correlate transition onset on the swept wing using three parameters: a Reynolds number based on the displacement thickness in the most unstable direction of flow, the streamwise shape parameter, and the external turbulence level. They simplify the problem by not including curvature effects and assuming locally parallel flow and even with these simplifications, the comparison with experiment shows good agreement.

The current experimental work of Poll (1984a) focuses on the crossflow instability where he shows that increasing yaw has a very destabilizing effect on the flow over a swept cylinder. He characterizes the instability in two ways. The first is by *fixed* disturbances visualized by either surface evaporation or oil-flow techniques. These disturbances are characterized by regularly spaced streaks aligned approximately in the inviscid-flow direction, leading to a "saw-tooth" pattern at the transition location. The second way is with unsteady disturbances in the form of a large-amplitude high-frequency harmonic wave at frequencies near one kHz. At transition near the wall surface, he obtains disturbance amplitudes greater than 20% of the local mean velocity. Initially he tries to use two parameters to predict transition. They are the crossflow Reynolds number (R_{cf}) and a shape factor based on the streamwise profile. However, based on the results of his research, he found that two parameters alone are not enough to predict transition, and that one needs at least three parameters to accurately describe the crossflow instability.

Michel, Arnal, Coustols and Juillen (1984) present some very good experimental results on the crossflow instability, conducted on a swept airfoil model. By surface visualization techniques they show regularly spaced streaks that are aligned practically in the inviscid-flow direction, with a "saw-tooth" pattern near the transition area. They perform hot-wire measurements on the stationary waves. Their results show a spanwise variation of the boundary layer before transition that becomes chaotic in the transition region. The variations are damped in the turbulent region. From their boundary-layer measurements they deduce that the ratio of λ_z/δ is nearly constant and equal to 4, where λ_z is the spanwise wavelength and δ the physical boundary-layer thickness. They also find a small peak in the spectra around one kHz (like Poll, 1984a), which is due to a streamwise instability. In addition to this they provide some theoretical work on the secondary velocities, and show counter rotating vortices in the streamwise direction. However, when these components are added to the mean velocities the vortices are no longer clearly visible. Even with all this progress there are very little experimental data with which to compare the theoretical models.

A major unanswered question concerning swept-wing flows is the interaction of crossflow vortices with T-S waves. If the vortex structure continues aft into the mid-chord region where T-S waves are amplified, some type of interaction could cause premature transition. In fact, the unsteadiness at transition observed by Poll and Michel et al. could be due to this phenomenon. Indeed early LFC work of Bacon et al. (1962) show a somewhat anomalous behavior of transition when sound is introduced in the presence of crossflow vortices. It is well known that streamwise vortices in a boundary layer strongly influence the behavior of other disturbances. Nayfeh (1981) shows that Görtler vortices produce a double-exponential growth of T-S waves. Herbert and Morkovin (1980) show that the presence of T-S waves produces a double-exponential growth of Görtler vortices, while Floryan and Saric (1980) show a similar behavior for streamwise vortices interacting with Görtler vortices. Reed (1984) analyzes the crossflow/T-S interaction in the leading-edge region by using a parametric-resonance model. Reed shows that the interaction of the crossflow vortices with T-S waves produces a double exponential growth of the T-S waves. The results of Bacon, Pfenninger and Moore (1962) and Reed (1984) clearly show the need to experimentally study problems of this kind. These papers are discussed later in the context of the results from Saric and Yeates (1985).

Saric and Yeates (1985) established a three-dimensional boundary layer on a flat plate that is typical of infinite swept-wing flows. This is done by having a swept leading edge and contoured walls to produce the pressure gradients. The experimentally measured C_p distribution is used along with the 3-D boundary-layer code of Kaups and Cebeci (1977) to establish the crossflow experiment and to compare with the theory. Some of the results of Saric and Yeates (1985) are discussed below because they illustrate that not everything is as it should be in three-dimensional boundary layers.

4.1 Boundary-Layer Profiles

Detailed measurements of the inviscid-flow velocities in the chordwise and spanwise directions are conducted (Saric and Yeates, 1985) using hot-wire anemometry. Straight-wire and slant-wire probes are used to obtain the velocity components (U,W). The vector sum of U and W forms the velocity vector which describes the inviscid streamlines over the plate and establishes the tangential direction, x_t , with respect to the x-axis. Where applicable, the experimental results are compared to the theoretical calculations (Kaups and Cebeci, 1977) of the mean flow, not as a test of the theory, but as a verification that a typical swept-wing flow is established.

Boundary-layer profiles are taken at different locations along the plate with both the slant-wire and straight-wire probes. Reduction of both the straight-wire and slant-wire data at one location produces a crossflow profile which provides comparison with the theory. Initially a boundary-layer profile is taken with a straight-wire probe and then repeated with a 45° slant-wire probe. The direction of x_t is obtained from these measurements. The velocity components (U,W) are then transformed, placing the new component U_{ct} in the direction of the inviscid-flow velocity vector. Finally boundary-layer profiles, parallel and transverse to the inviscid-flow velocity vector, are obtained. The velocity component perpendicular to the inviscid-flow velocity vector is called the crossflow velocity. By definition, since the crossflow profile is perpendicular to the edge velocity, the crossflow velocity is zero in the inviscid flow. From this profile a *crossflow Reynolds Number* is calculated. It is defined (Pfenninger, 1977) as

$$R_{cf} = \frac{\delta_{10} W_{t,max}}{\nu}$$

where δ_{10} is the largest of the heights at which the crossflow velocity is 10% of the maximum value, and $W_{t,max}$ is the absolute value of the maximum crossflow velocity.

Figure 6 is a normalized boundary-layer plot of U_t and W_t at $x = 170\text{cm}$ from the leading edge with a reference velocity of 10m/s . Similar measurements were taken every 5 cm in the chord direction and the data shown here have the least scatter. These results are compared with the theoretical calculations of the Kaups-Cebeci (1977) code using the experimental pressure distribution. In general, at low values of crossflow (closer to the leading edge) the experimental results tend to agree with the theory in the magnitude of the crossflow and the location above the test surface where the maximum of crossflow occurs. Further back, the magnitude of crossflow begins to differ, but the location of the maximum crossflow is still in good agreement. However, a slight reversal of flow near the wall appears in the data of both these cases that does not appear in the theory and is due to experimental error in trying to extract out such small differences in the data. The scatter in all the data is due to resolving small differences of large numbers after each is interpolated from a straight-wire and slant-wire profile and then transformed into the U_t and W_t directions. The profile of figure 6 has very little scatter but differs from the theory in both magnitude and location of the maximum crossflow primarily because the experiment has a higher than anticipated value of crossflow velocity because of the wall modifications. Even though the experimental model does not quite represent an infinite swept wing, the differences between the theory and experiment are minor in light of the objective of establishing a thick crossflow-velocity boundary layer.

4.2 Spanwise Measurements of Vortices

Disturbance measurements of the mean flow are conducted (Saric and Yeates, 1985) within the boundary layer by making a spanwise traverse (parallel to the leading edge) of the hot wire at a constant y location with respect to the plate. These measurements are carried out at many different x and y locations using two different mean velocities. The results show a steady vortex structure with a dominant spanwise wavelength of approximately 0.5 cm. Figure 7 shows a typical spanwise measurement at $x = 160$ cm for a reference velocity of 10 m/s. In this region, the structure is well defined and shows large spanwise variations. The corresponding spectrum for this disturbance measurement is shown in figure 8. It shows a sharp peak at a wavelength of about 0.5 cm, but it also shows a broad peak at a larger wavelength, generally at a lower amplitude. The cause of this broad peak at the larger wavelength is explained by the linear-theory predictions (Dagenhart, 1981) for crossflow vortices. This 0.5 cm wavelength does not agree with the flow-visualization results of the next section nor with the theoretical calculations of the MARIA code (Dagenhart, 1981). However, the reason for the disagreement may be known and is given by Reed (1985). This is discussed later.

Moving back in x (aft of $x = 200$ cm) toward the transition location, the spanwise variations decrease and the structure begins to show signs of unsteadiness. These changes are thought to be due to some type of interaction with weakly growing T-S waves.

4.3 Flow Visualization

A type of flow visualization employed in the experiment is a sublimation technique. In this procedure, a solution of trichloroethane and naphthalene is sprayed directly onto the plate surface. The trichloroethane acts as a solvent when mixed with the solid naphthalene crystals and once the solution is sprayed on the plate, the solvent quickly evaporates leaving the solid naphthalene. The test conditions are set and surface patterns on the plate are observed and photographed as the naphthalene sublimates.

This flow-visualization technique shows that there exists a crossflow vortex structure on the swept flat plate. Figure 9 shows typical surface patterns that develop. This vortex structure is made visible because of the differential sublimation of the naphthalene according to variations of the surface shear stress. The pattern of disturbance vortices is nearly equally spaced and aligned approximately in the inviscid-flow direction. The wavelength of the vortices is on the scale of 1 cm and this spacing agrees quite well with the calculated wavelength from the MARIA code. The fact that on cold days it took 45 minutes to establish the vortex structure gives every indication that the vortices are steady until the transition region is approached. The conditions did not permit accurate enough measurements to provide information on the chordwise variation of wavelength as reported by Michel, Arnal, Coustols, and Juillen (1984).

4.4 Determination of Spanwise Wavelength

The flow visualization photograph of Figure 9 clearly indicates a spanwise wavelength of 1 cm on the surface. On the other hand, the spectra of the hot-wire measurements (taken near Y_{max}) show a dominant sharp peak at 0.5 cm and a smaller broad-band peak at 1 cm. This apparent incongruity can be explained with the wave interaction theory of Reed (1985), who uses the actual test conditions of this experiment. Reed shows that it is possible for a parametric resonance to occur between a previously amplified 0.5 cm vortex and a presently amplified 1 cm vortex and that measurements taken near the maximum of the crossflow velocity would show a strong periodicity of 0.5 cm. Moreover, Reed's wall-shear calculations and v - w streamline calculations show the 0.5 cm periodicity dying out near the wall and the 1 cm periodicity dominating.

Interactions of this sort are apparently not unusual. The experiments of Bacon, Pfenninger and Moore (1962) are crossflow stability experiments that show a shift to smaller spanwise wavelengths when sound is introduced into the flow. The sound could enhance the vortex-vortex interaction discussed above or could be the result of a vortex-TS wave interaction of the type proposed by Reed (1984).

4.5 Summary

The spanwise boundary-layer measurements of Saric and Yeates (1985) show a steady spanwise variation in the mean flow with a wavelength of about 0.5 cm with smaller variations at a 1.0 cm wavelength. Flow visualization using a sublimation technique show a fixed surface pattern with a spanwise wavelength of about 1 cm. This 1 cm wavelength agrees quite well with the linear stability of Dagenhart (1981) while the 0.5 cm is accounted for by Reed (1985). In all cases the vortex structure appears to be steady until transition is approached.

These phenomena are not observed by Michel et al. (1984) who measure phenomena not measured by Poll nor Saric and Yeates. All of this serves notice that stability and transition phenomena are extremely dependent on initial conditions.

5. SECONDARY INSTABILITIES AND TRANSITION

There are different possible scenarios for the transition process, but it is generally accepted that transition is the result of the uncontrolled growth of unstable three-dimensional waves. For swept-wing flows, this growth occurs because of the

interactions of 3-D waves with either of the two basic instabilities discussed in sections 3 and 4 of this lecture. Secondary instabilities with T-S waves are reviewed in some detail by Herbert (1984b, 1985) and those with crossflow by Reed (1984, 1985). Therefore, only a brief outline is given here in order to give the reader some perspective of the different types of breakdown.

5.1 Secondary Instabilities

The occurrence of three-dimensional phenomena in an otherwise two-dimensional flow is a necessary prerequisite for transition (Tani, 1981). Such phenomena were observed in detail by Klebanoff et al. (1962) and were attributed to a spanwise differential amplification of T-S waves through corrugations of the boundary layer. The process leads rapidly to spanwise alternating "peaks" and "valleys", i.e., regions of enhanced and reduced wave amplitude, and an associated system of streamwise vortices. The peak-valley structure evolves at a rate much faster than the (viscous) amplification rates of T-S waves. The smoke-streakline photograph (Saric and Thomas, 1984) in figure 10 clearly shows the rapid sequence of events after the onset of "peak-valley splitting". The unstable waves are observed to be two-dimensional until the 160 cm location when the pattern breaks down very quickly. This represents the path to transition under conditions similar to Klebanoff et al. (1962) and is called a *K-type* breakdown. The A-shaped (Hama and Nutant, 1963) spanwise corrugations of streaklines, which correspond to the peak-valley structure of amplitude variation, are a result of weak 3-D displacements of fluid particles across the critical layer and precede the appearance of Klebanoff's "hair-pin" vortices. This has been supported by hot-wire measurements and a Lagrangian-type streakline prediction code (Saric and Thomas, 1984). Note that the A vortices are ordered in that peaks follow peaks and valleys follow valleys.

Different types of three-dimensional transition phenomena recently observed (e.g. Kachanov et al. 1977; Kachanov and Levchenko, 1984; Saric and Thomas, 1984; Saric et al. 1984) are characterized by *staggered* patterns of peaks and valleys (see figures 11 and 12) and by their occurrence at very low amplitudes of the fundamental T-S wave. This pattern also evolves rapidly into transition. These experiments showed that the subharmonic of the fundamental wave (a necessary feature of the staggered pattern) was excited in the boundary layer and produced either the resonant wave interaction predicted by Craik (1971) as shown in figure 11 (called the *C-type*) or the secondary instability of Herbert (1983) as shown in figure 12 (called the *H-type*). Spectral broadening to turbulence with self-excited subharmonics has been observed in acoustics, convection, and free shear layers and was not identified in boundary layers until the results of Kachanov et al. (1977). This paper re-initiated the interest in subharmonics and prompted the simultaneous verification of C-type resonance (Thomas and Saric, 1981; Kachanov and Levchenko, 1984). Subharmonics have also been confirmed for channel flows (Kozlov and Ramazanov, 1984) and by direct integration of the Navier-Stokes equations (Spalart, 1984). There is visual evidence of subharmonic breakdown before Kachanov et al. (1977) in the work of Hama (1959) and Knapp and Roache (1968) which was not recognized as such at the time of their publication. The recent work on subharmonics is found in Herbert (1983a,b, 1984a,b) and Saric, Kozlov and Levchenko (1984).

The important issues that have come out of the subharmonic research is that the secondary instability depends not only on disturbance amplitude, but on phase and fetch as well. Fetch means here the distance over which the T-S wave grows in the presence of the 3-D background disturbances. If T-S waves are permitted to grow for long distances at low amplitudes, subharmonic secondary instabilities are initiated at disturbance amplitudes of less than $0.3\%U_0$. Whereas, if larger amplitudes are introduced, the breakdown occurs as K-type at amplitudes of $1\%U_0$. Thus, there no longer exists a "magic" amplitude criterion for breakdown.

5.2 Transition Prediction and Control

When the recent work on subharmonics is added to the discussion at the end of section 3 on the limitations of the e^N method, one indeed has an *uncertainty principle for transition* (Morkovin, 1978). Transition prediction methods will remain conditional until the receptivity problem is adequately solved and the bypass mechanisms are well understood. In the mean time, extreme care must be exercised when using correlation methods to predict transition. Additional problems of transition prediction and control are discussed by Reshotko (1985). The main principle of laminar flow control is to keep the disturbance levels low enough so that secondary instabilities and transition do not occur. Under these conditions, linear theory is quite adequate and e^N methods can be used to calculate the effectiveness of a particular LFC device.

The idea of transition control through active feedback systems is an area that has received considerable recent attention (Liepmann and Nosenchuck, 1982; Thomas, 1983; Kleiser and Laurien, 1984, 1985; Metcalfe et al., 1985). The technique consists of first sensing the amplitude and phase of an unstable disturbance and then introducing an appropriate out-of-phase disturbance that cancels the original disturbance. In spite of some early success, this method is no panacea for the transition problem. Besides the technical problems of the implementation of such a system on an aircraft, the issue of three-dimensional wave cancellation must be addressed. As Thomas (1983) showed, when the 2-D wave is canceled, all of the features of the 3-D disturbances remain to cause transition at yet another location. Some clear advantage over passive systems have yet to be demonstrated for this technique.

6. REFERENCES

- Arnal D. 1984. Description and prediction of transition in two-dimensional incompressible flow *AGARD Report No. 709* (Special course on stability and transition of laminar flows) VKI, Brussels.
- Bacon, J.W. Jr., Pfenninger, W. and Moore, C.R. 1962. Influence of acoustical disturbances on the behavior of a swept laminar suction wing. Northrup Report NOR-62-124.
- Costis, C.E. and Saric, W.S. 1982. Excitation of wave packets and random disturbances in a boundary layer. V.P.I. & S.U. Report No. VPI-E-82.26
- Craik, A.D.D. 1971. Nonlinear resonant instability in boundary layers. *J. Fluid Mech.* vol. 50, 393.
- Dagenhart, J.R. 1981. Amplified crossflow disturbances in the laminar boundary layer on swept wings with suction. *NASA TP-1902*.
- Floryan, J.M. and Saric, W.S. 1979. Stability of Görtler vortices in boundary layers. *AIAA Paper No. 79-1497 and AIAA J.*, vol. 20, 316.
- Floryan, J.M. and Saric, W.S. 1980. Wavelength selection and growth of Görtler vortices. *AIAA paper no. 80-1376 and AIAA J.*, vol. 22, 1529.
- Gaster, M. 1974. On the effects of boundary-layer growth on flow stability. *J. Fluid Mech.*, vol. 66, 465.
- Gregory, N., Stuart, J.T. and Walker, W.S. 1955. On the stability of three-dimensional boundary layers with applications to the flow due to a rotating disk. *Phil. Trans. Roy. Soc. Lon.*, vol. A248, 155.
- Hall, P. 1983. The linear development of Görtler vortices in growing boundary layers. *J. Fluid Mech.*, vol. 130, 41.
- Hama, F.R. 1959. Some transition patterns in axisymmetric boundary layers. *Phys. Fluids*, vol. 2, 664.
- Hama, F.R. and Nutant, J. 1963. Detailed flow-field observations in the transition process in a thick boundary layer. *Proc. 1963 Heat Trans. Fluid Mech. Inst.*, 77.
- Herbert, T. 1983a. Secondary instability of plane channel flow to subharmonic three-dimensional disturbances. *Phys. Fluids*, vol. 26, 871.
- Herbert, T. 1983b. Subharmonic three-dimensional disturbances in unstable plane shear flows. *AIAA Paper No. 83-1759*.
- Herbert, T. 1984a. Analysis of the Subharmonic Route to Transition in Boundary Layers. *AIAA Paper No. 84-0009*.
- Herbert, T. 1984b. Secondary instability of shear flows. *AGARD Report No. 709* (Special course on stability and transition of laminar flows) VKI, Brussels.
- Herbert, T. 1984c. Nonlinear effects in boundary-layer stability. *AGARD Report No. 709* (Special course on stability and transition of laminar flows) VKI, Brussels.
- Herbert, T. 1985. Three-dimensional phenomena in the transitional flat-plate boundary layer. *AIAA Paper No. 85-0489*.
- Herbert, T. and Morkovin, M. V. 1980. Dialogue on bridging some gaps in stability and transition research. *Laminar-Turbulent Transition*, ed. R. Eppler and H. Fasel, Springer.
- Kachanov, Yu.S., Kozlov, V.V. and Levchenko, V.Ya. 1977. Nonlinear development of a wave in a boundary layer (in Russian). *Mekhanika Zhidkosti i Gaza*, no. 3, 49.
- Kachanov, Yu.S. and Levchenko, V.Ya. 1984. Resonant interactions of disturbances in transition to turbulence in a boundary layer. *J. Fluid Mech.*, vol. 138, 209. (in Russian in 1982).
- Kaups, K. and Cebeci, T. 1977. Compressible laminar boundary layers with suction on swept and tapered wings. *J. Aircraft*, vol. 14, 661.
- Klebanoff, P.S., Tidstrom, K.D. and Sargent, L.M. 1962. The three-dimensional nature of boundary-layer instability. *J. Fluid Mech.*, vol. 12, 1.
- Kleiser, L. and Laurien, E. 1984. Three-dimensional numerical simulation of laminar turbulent transition and its control by periodic disturbances. *Proc. 2nd IUTAM Symp. Laminar-Turbulent Transition*, Novosibirsk, USSR.
- Kleiser, L. and Laurien, E. 1985. Numerical investigation of interactive transition control. *AIAA Paper No. 85-0566*.

- Knapp, C.F. and Roache, P.J. 1968. A combined visual and hot-wire anemometer investigation of boundary-layer transition. *AIAA J.*, vol. 6, 29
- Kozlov, V.V. and Ramazanov, M.P. 1984. Development of finite amplitude disturbances in a Poiseuille flow. *J. Fluid Mech.*, vol. 147, 149.
- Liepmann, H.W. and Nosenchuck, D.M. 1982. Active control of laminar-turbulent transition. *J. Fluid Mech.*, vol. 118, 201.
- Mack, L.M. 1969. Boundary-layer stability theory. Jet Propulsion Lab. Rpt. 900-277, Rev. A.
- Mack, L.M. 1984a. Line sources of instability waves in a Blasius boundary layer. *AIAA Paper 84-0168*.
- Mack, L.M. 1984b. Boundary-layer linear stability theory. *AGARD Report No. 709* (Special course on stability and transition of laminar flows) VKI, Brussels.
- Malik, M.R. and Poll, D.I.A. 1984. Effect of curvature on three-dimensional boundary layer stability. *AIAA Paper No. 84-1672*.
- Malik, M.R., Wilkinson, S.P. and Orszag, S.A. 1981. Instability and transition in rotating disk flow. *AIAA J.*, vol. 19, 1131.
- Metcalfe, R.W., Rutland, C., Duncan, J.H. and Riley, J.J. 1985. Numerical simulations of active stabilization of laminar boundary layers. *AIAA Paper No. 85-0567*.
- Michel, R., Arnal, D. and Coustols, E. 1984. Stability calculations and transition criteria in two- or three-dimensional flows. *Proc. 2nd IUTAM Symp. on Laminar-Turbulent Transition*, Novosibirsk.
- Michel, R., Arnal, D., Coustols, E. and Juillen, J.C. 1984. Experimental and theoretical studies of boundary layer transition on a swept infinite wing. *Proc. 2nd IUTAM Symp. on Laminar-Turbulent Transition*, Novosibirsk.
- Morkovin, M.V. 1969. On the many faces of transition. *Viscous Drag Reduction* ed. C.S. Wells, Plenum.
- Morkovin, M.V. 1978. Instability, transition to turbulence and predictability. *AGARDograph No. 236*.
- Nayfeh, A.H. 1980. Three-dimensional stability of growing boundary layers. *Laminar-Turbulent Transition*, ed. R. Eppler and H. Fasel, Springer.
- Nayfeh, A.H. 1981. Effect of streamwise vortices on Tollmien-Schlichting waves. *J. Fluid Mech.*, vol. 107, 441.
- Pfenninger, W. 1977. Laminar flow control - Laminarization. *AGARD Report No. 654*, (Special Course on Drag Reduction).
- Poll, D.I.A. 1979. Transition in the infinite swept attachment line boundary layer. *Aeronautical Quart.*, vol. XXX, 607.
- Poll, D.I.A. 1984a. Some observations of the transition process on the windward face of a yawed cylinder. Cranfield College of Aeronautics Report 8407.
- Poll, D.I.A. 1984b. Transition description and prediction in three-dimensional flows. *AGARD Report No. 709* (Special course on stability and transition of laminar flows) VKI, Brussels.
- Reed, H.L. 1984. Wave interactions in swept-wing flows. *AIAA paper no. 84-1678*.
- Reed, H.L. 1985. Disturbance-wave interactions in flows with crossflow. *AIAA Paper No. 85-0494*.
- Reshotko, F. 1984a. Environment and receptivity. *AGARD Report No. 709* (Special course on stability and transition of laminar flows) VKI, Brussels.
- Reshotko, F. 1984b. Laminar flow control - Viscous simulation. *AGARD Report No. 709* (Special course on stability and transition of laminar flows) VKI, Brussels.
- Reshotko, F. 1985. Control of boundary-layer transition. *AIAA Paper No. 85-0562*.
- Saric, W.S. 1985. Laminar Flow Control With Suction: Theory and Experiment. *Proc. AGARD Special Course on Aircraft Drag Prediction and Reduction*, VKI, Belgium.
- Saric, W.S., Kozlov, V.V. and Levchenko, V.YA. 1984. Forced and unforced subharmonic resonance in boundary-layer transition. *AIAA Paper No. 84-0007*.
- Saric, W.S. and Nayfeh, A.H. 1977. Nonparallel stability of boundary layers with pressure gradients and suction. *AGARD C-P No. 224*, 6.

- Saric, W.S. and Thomas, A.S.W. 1984. Experiments on the subharmonic route to transition. *Turbulence and Chaotic Phenomena in Fluids*, ed. T. Tatsumi, North-Holland.
- Saric, W.S. and Yeates, I.G. 1985. Experiments on the stability of crossflow vortices in swept-wing flows. *AIAA Paper No. 85-0493*.
- Spalart, P.R. 1984. Numerical simulation of boundary-layer transition. *NASA TM-85984*.
- Tani, I. 1981. Three dimensional aspects of boundary layer transition. *Proc. Indian Acad. Sci., vol. 4, 219*.
- Thomas, A.S.W. 1983. The control of boundary-layer transition using a wave superposition principle. *J. Fluid Mech., vol. 137, 233*.
- Thomas, A.S.W. and Saric, W.S. 1981. Harmonic and subharmonic waves during boundary-layer transition. *Bull. Amer. Phys. Soc., vol. 26, 1252*.
- Wazzan, A.R., Okamura, T.T. and Smith, A.M.O. 1968. Spatial and temporal stability charts for the Falkner-Skan boundary-layer profiles. Douglas Aircraft Co. Report No. DAC-67086.

ACKNOWLEDGEMENTS

The author would like to thank Dr. H. Reed for her helpful comments and suggestions during the course of writing these lectures. The author is also grateful to Dr. T. Herbert for his comments and ideas during our collaboration at VPI & SU.

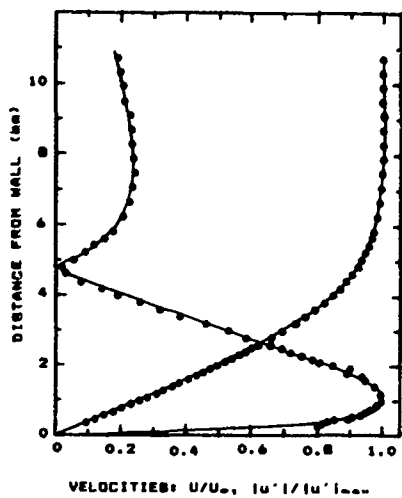


Figure 1. Comparison of theory (solid line) with experiments (circles) for mean velocity and disturbance amplitude versus y . $F = 56.4 \times 10^{-6}$, $R = 780$ for $f = 50\text{Hz}$ and $U_\infty = 9.6\text{m/s}$. In this case $|u'|_{\text{max}} = 1.52U_\infty$.

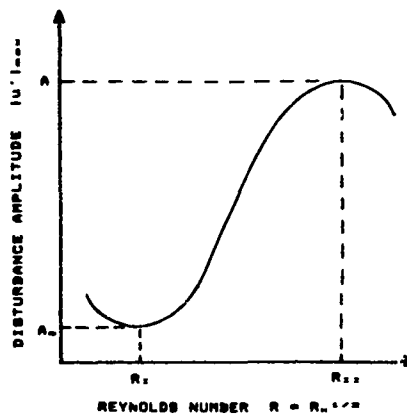


Figure 2. Schematic of typical disturbance amplitude growth as a function of Reynolds number. R_1 and R_2 are the Branch I and II neutral stability points.

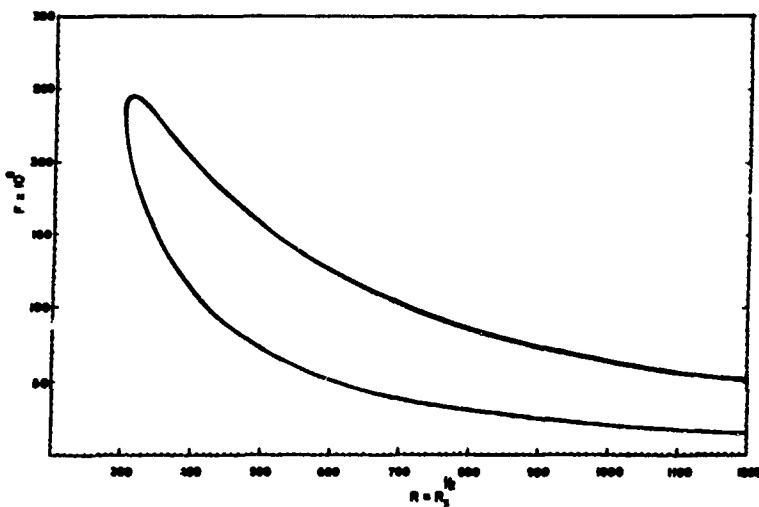


Figure 3. Neutral Stability Curve for Blasius Boundary Layer from Parallel Stability Theory

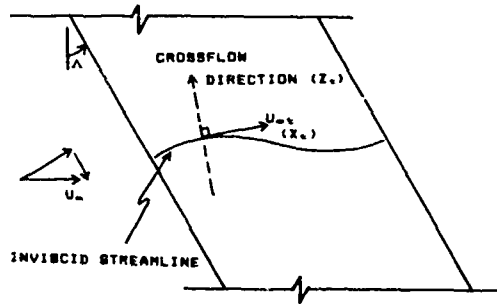


Figure 4. Schematic of flow over a swept wing

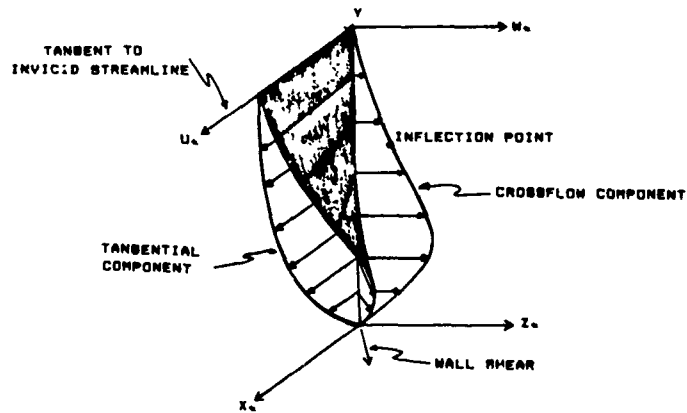


Figure 5. Schematic of velocity components on a swept wing illustrating the definition of crossflow velocity.

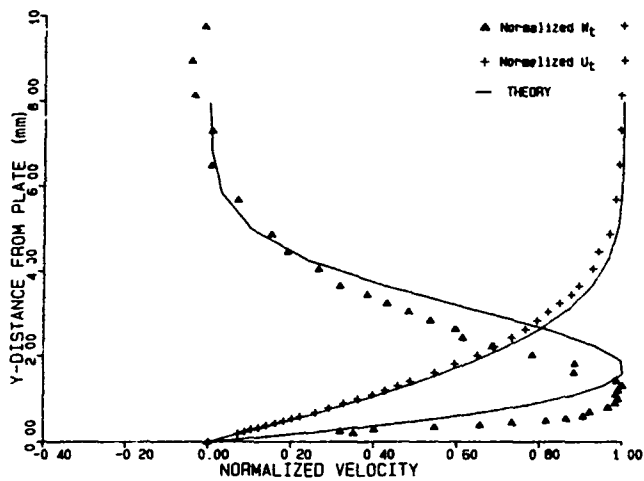


Figure 6. Tangential Velocity, U_x/U_{∞} , and Crossflow Velocity, W_z/W_{∞} , at $x = 170\text{cm}$ and $U_{\infty} = 10\text{m/s}$.

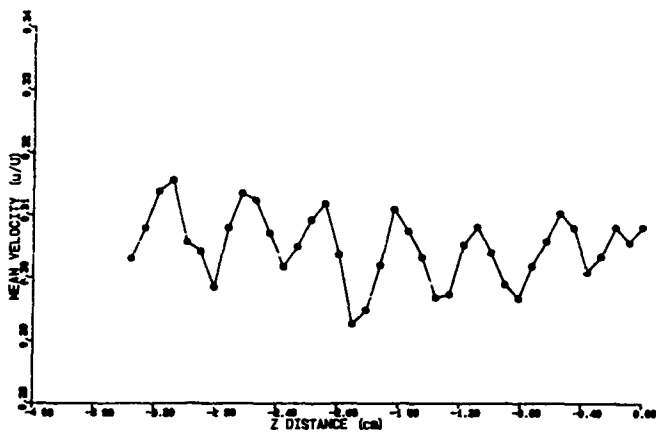


Figure 7. Spanwise Variation of Mean Flow at $x = 160\text{cm}$ and $U_{\infty} = 10\text{m/s}$.

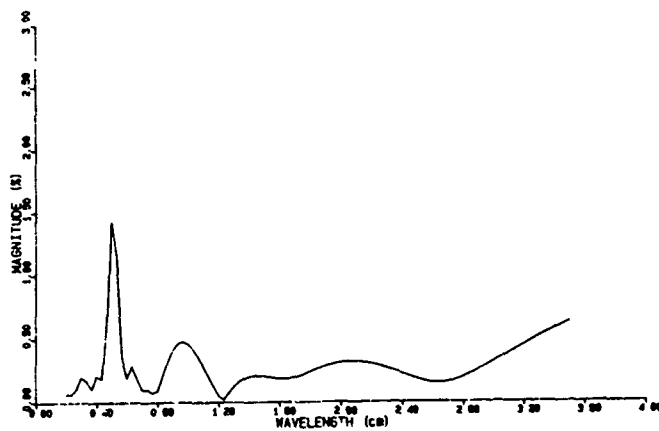


Figure 8. Spanwise Spectrum of Disturbance Measurements at $x = 160\text{cm}$ and $U_{\infty} = 10\text{m/s}$.

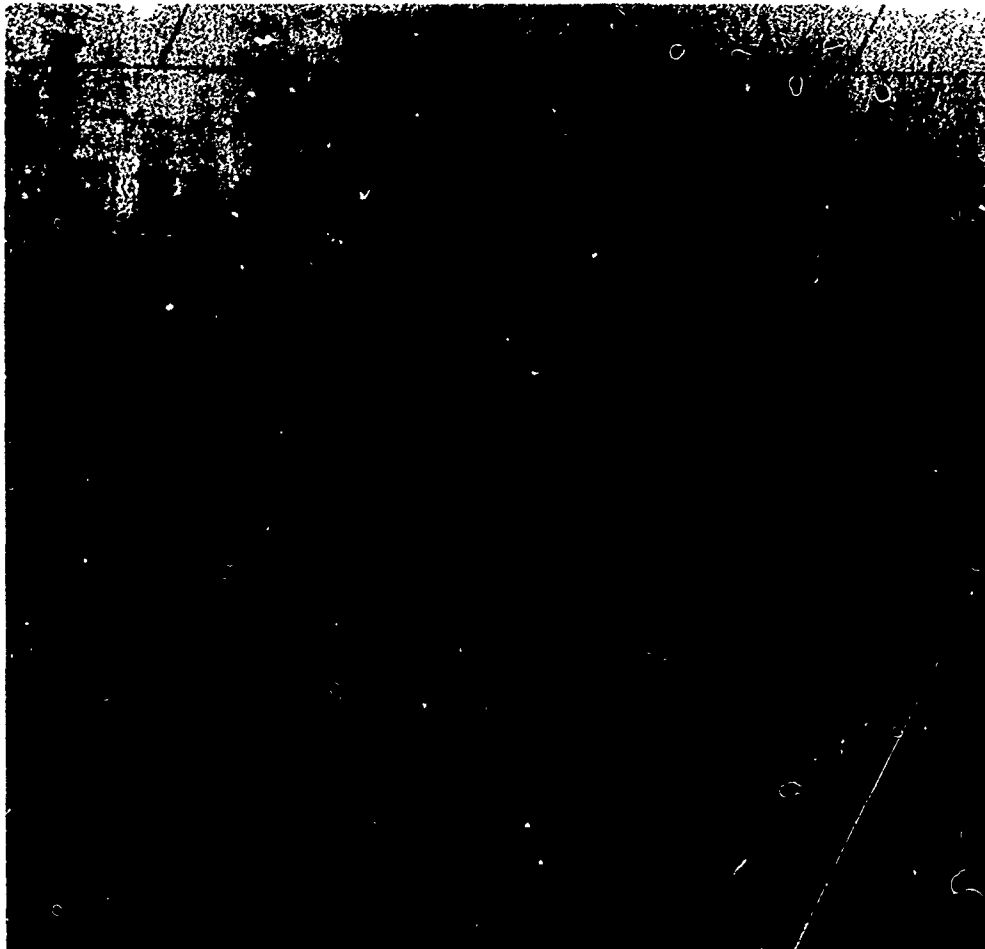


Figure 9. Naphthalene Surface Patterns. Flow from left to right.



Figure 10. K-type breakdown. Distance from leading edge shown in cm. The vibrating ribbon is at $x = 48\text{cm}$. The smokewire is at $x = 138\text{cm}$ which is $R = 784$. Branch II for $F = 83 \times 10^{-4}$ is $x = 170$ ($R = 870$). $U_\infty = 6.6 \text{ m/s}$ and $f = 39\text{Hz}$. Chordwise wavenumber $a = \alpha/R = 0.22 \times 10^{-3}$, spanwise wavenumber $b = \beta/R = 0.33 \times 10^{-3}$, $b/a = 1.5$. Maximum rms u' at Branch II is approx. 1%.



Figure 12. H-type breakdown. Same as figure 10 except u' at Branch II is approx. 0.4%. At $R = 1000$, $b = 0.32 \times 10^{-3}$, $b/a = 1.46$.



Figure 11. C-type breakdown. Same as figure 10 except u' at Branch II is approx. 0.3%. At $R = 1000$, $b = 0.15 \times 10^{-3}$, $b/a = 0.67$.

LAMINAR FLOW CONTROL WITH SUCTION: THEORY AND EXPERIMENT

by

William S. Saric

Mechanical and Aerospace Engineering
Arizona State University
Tempe, AZ 85287

SUMMARY

The concept of boundary-layer stabilization with weak wall suction is introduced at a basic level and the means for calculating the effects of suction are described. The historical development of this technique is reviewed and the state-of-the-art of theory and experiment is covered. Some problems associated with the implementation of suction into aircraft boundary layers are discussed.

1. INTRODUCTION

The advent of higher fuel costs in the mid-1970's prompted initiation of the Aircraft Energy Efficiency program (ACEE) within NASA in 1976 (Provinelli et al., 1976). This program has supported drag-reduction activity in all aspects of aircraft design (e.g. Pfenninger et al., 1980) and has been recently summarized by Wagner and Fischer (1983) and Braslow and Fischer (1985). One important aspect of this program is *Laminar Flow Control* (LFC), which is an attempt to maintain laminar boundary layers on the wing surfaces by delaying transition to turbulence.

The attractiveness of LFC is a subsequent decrease in the skin friction of 60-80% when the boundary layer is laminar instead of turbulent. In commercial transport aircraft, the viscous drag accounts for 50% of the overall drag. If fully laminar flow can be maintained on the wings, overall drag is reduced by 25%.

The feasibility and effectiveness of viscous drag reduction in aircraft via LFC has been demonstrated through the extensive research efforts of Pfenninger and co-workers over the last forty years. This work has been summarized in the lecture notes of Pfenninger (1977) which are required reading for anyone interested in LFC. The reports of Bushnell and Tuttle (1979) and Tuttle and Maddalon (1982) are rather complete bibliographies that catalog all of the important LFC papers and thus it is not necessary here to survey all of the literature. Moreover, the lectures by Thomas (1985) and Braslow and Fischer (1985) bring the current technology up to date.

The objective of this report is to describe in some detail the role of wall suction and pressure gradients in delaying transition on aircraft systems. The state-of-the-art in predicting the effectiveness of suction is described and some technical issues regarding the implementation of suction are discussed. The LFC roles of heating and cooling are not discussed, since they are not considered to be aircraft applications and excellent surveys on the topics already exist. For example, the heating and cooling applications in LFC systems are reviewed by Reshotko (1978, 1979, 1984b, 1985).

2. STABILIZATION MECHANISMS

Given the caveats described in the first lecture (Saric, 1985b), the process of laminar-turbulent transition is generally the result of the uncontrolled growth of small disturbances. A number of instability mechanisms may be in operation in the boundary layer, and together these eventually lead to transition. The job here in describing the transition process is made easier by the recent monograph-like AGARD Special Course on the subject (Arnal, 1984; Mack, 1984b; Reshotko, 1984a,b; Poll, 1984; Herbert, 1984b,c). Therefore, only a brief outline is given here.

One type of instability to be considered is the viscous instability with respect to laminar boundary-layer disturbances, called *Tollmien-Schlichting* (T-S) waves (e.g. Arnal, 1984; Mack, 1984b; Saric, 1985b). These waves are initially two-dimensional and are selectively amplified or damped depending on Reynolds number and frequency. This instability is most important in the mid-chord region where the C_p distribution may be flat or decelerating. A second type of instability results when a three-dimensional flow exhibits an inflectional velocity profile (in this case due to crossflow on swept wings). The resulting *inviscid* instability becomes more important as sweep angle increases and dominates in the leading-edge region where the crossflow is maximal (e.g. Mack, 1984b; Poll, 1984; Saric, 1985b). This instability is characterized by streamwise vortices all having the same sense of rotation that are called *crossflow* (C-F) vortices. Another possible inviscid instability mechanism depends on the nature of the wall curvature. The presence of concave curvature and the accompanying centrifugal forces give rise to the Görtler instability (e.g. Floryan and Saric, 1979; Hall, 1982, 1983). In this case the instability is in the form of counter-rotating streamwise vortices called Görtler

vortices. Finally, there is the case of leading-edge contamination (Poll, 1984) which involves the propagation along the attachment line of disturbances that originate from local disturbances or from the turbulent boundary layer on the fuselage.

The principle behind LFC is to keep the growth of these disturbances within acceptable limits so that 3-D and nonlinear effects do not cause breakdown to turbulence. With this philosophy, one only deals with *linear* disturbances and thus, the difficulties with transition prediction do not directly arise. The manner in which LFC works can be described using the following example of Reshotko (1984b, 1985).

It is well known that the velocity-profile curvature term in the Orr-Sommerfeld equation, $-(\partial^2 U / \partial y^2) \phi$, is an important driver of the stability behavior. In fact, it is more important than unmeasurable changes in the mean velocity itself. The boundary-layer flow can be made *more stable* by making the curvature term *more negative* near the wall. In the notation of Saric (1985b), the boundary-layer momentum equation can be evaluated near the wall, as shown in Eq.(1), and used to illustrate the stabilizing effects of different LFC techniques.

$$\rho V_0 \partial U / \partial y + dP/dx - (d\mu/dT)(\partial T/\partial y) \partial U / \partial y = \mu \partial^2 U / \partial y^2 \quad (y \approx 0) \quad (1)$$

Equation (1) shows that wall suction ($V_0 < 0$), favorable pressure gradient ($dP/dx < 0$), cooling in air ($d\mu/dT > 0$, $\partial T/\partial y > 0$), and heating in water ($d\mu/dT < 0$, $\partial T/\partial y < 0$) all tend to stabilize the boundary layer by making the curvature term more negative.

It should be pointed out that these are very sensitive mechanisms and that even *weak* suction or *weak* pressure gradients produce strong effects. For example, a Falkner-Skan pressure gradient of $\beta = +0.1$ (which can only be measured by comparing a 6.6% change in the shape factor, δ^*/θ , from Blasius) increases the minimum critical x-Reynolds number by a factor of 9 (e.g. Wazzan, Okamura, and Smith, 1968). At the same time, average suction velocity ratios of $V_0/U_0 \approx 10^{-3} - 10^{-4}$ are not unusual for LFC applications and can, for example, reduce relative amplitude growth from e^{26} to e^5 at $F = 10 \times 10^6$ (Saric and Nayfeh, 1977). That the system works is evidenced by the fact that the X-21 achieved laminar flow at chord Reynolds numbers of 47×10^6 with a 20% decrease in overall drag (Pfenninger, 1977).

Present designs for supercritical energy-efficient airfoils have LFC systems with a porous region near the leading edge. Generally, suction is applied near the leading edge of a swept wing in order to control leading-edge contamination and crossflow instabilities (Wagner, Maddalon and Fischer, 1984). Appropriate shaping of the pressure distribution stabilizes mid-chord instabilities (Wagner and Fischer, 1984). This arrangement is called a *hybrid* LFC system in that it combines *active* LFC (suction) with *passive* LFC (pressure gradient).

3. TWO-DIMENSIONAL DISTURBANCES

The mid-chord region is expected to be dominated by two-dimensional T-S waves so it serves as a good high-Reynolds-number reference for describing the stability calculations. In general, there have been no difficulties in predicting the stabilizing effects of pressure gradients since the mean-flow calculations are well in hand (Kaups and Cebeci, 1977). The situation with regard to suction has not been as straightforward. Although the theory up to the mid-70's was adequate to predict the general nature of the effects of suction for continuously distributed suction cases (e.g. Saric and Nayfeh, 1977; Srokowski and Orszag, 1977; Lekoudis, 1979), the capability for calculating the mean flow (and its stability) over finite-width suction strips was still unknown. Moreover, it was thought at the time to use suction slots or strips in the mid-chord region. The abrupt change in wall boundary conditions for this type of flow raised all sorts of questions regarding the adequacy of distributed-suction calculations to account for the upstream influence and non-parallel effects of slots or strips. This situation prompted a series of theoretical works by Nayfeh and co-workers and a parallel experimental program which together, put the cap on the understanding of stabilization with suction of two-dimensional T-S waves (Reed and Nayfeh, 1981; Reynolds and Saric, 1982).

3.1 Theory

The objective of the theory of Reed and Nayfeh (1981) was to not only determine the effectiveness of suction for LFC, but to determine the optimal number, spacing, and mass flow rate through finite suction strips, taking into account all of the changes in the mean flow. Because of the sensitivity of the stability problem, it is necessary to calculate the basic state as accurately as possible. Nayfeh and El-Hady (1979) used a nonsimilar boundary-layer code to solve the mean flow. However, nonsimilar boundary-layer calculations fail to account for the upstream influence of the suction slot. On the other hand, solutions of the Navier-Stokes equations or of the interacting boundary-layer equations usually require prohibitively large amounts of computer time and storage as well as having difficulties at high Reynolds numbers.

Reed and Nayfeh (1981) used the linearized triple-deck, closed-form solutions of Nayfeh, Reed and Ragab (1980) for the flow over porous suction strips. It will be shown

below that these results compare well with interacting-boundary-layer solutions and with the experimental data of Reynolds and Saric (1982). Moreover, they developed an elegant and workable optimization scheme for idealizing the location of the suction strips; a result that was also experimentally confirmed.

3.1.1 Disturbance State

The stability equations are formulated in the usual way by superposing small disturbances on the basic state to form total flow quantities, Q^* , in the following way.

$$Q^*(x,y,t) = Q(y) + q'(x,y,t) \quad (2)$$

where $Q(y)$ is a basic-state quantity such as a velocity component that only depends on the coordinate normal to the surface and $q'(x,y,t)$ represents a small unsteady disturbance quantity such as velocity or pressure.

These total flow quantities are substituted into the Navier-Stokes equations, the solution of the basic state drops out, and the equations are linearized (e.g. Mack, 1984b). These linear partial differential equations are locally separable in x and t with the separation of variables solution given by:

$$q'(x,y,t) = q(y)\exp[i(kx-\omega t)] \quad (3)$$

where k and ω are the dimensionless streamwise wavenumber and frequency, respectively, normalized with respect to the boundary-layer reference length, $\delta_r = \sqrt{\nu x/U_0}$, and the freestream velocity, U_0 . Here ω is real and $k = k_r + ik_i$ is complex.

Substitution of Eq.(3) into the linearized partial differential equations results in the Orr-Sommerfeld equation for the streamfunction ϕ :

$$(D^2 - k^2)^2\phi - iR[(kU - \omega)(D^2 - k^2)\phi - k(D^2U)\phi] = 0 \quad (4)$$

with boundary conditions:

$$\phi(0) = D\phi(0) = 0, \quad \phi(y \rightarrow \infty) \rightarrow 0 \quad (5)$$

where $D = d/dy$. Equations (4)-(5) are linear and homogeneous and form an eigenvalue problem which consists of determining k as a function of frequency, Reynolds number, and the basic state. The Reynolds number is usually defined as

$$R = U_0 \delta_r / \nu = \sqrt{Re_x} \quad (6)$$

and is used to represent distance along the surface. When comparing the solutions of Eq.(4) with experiments, the reduced frequency, F , is introduced as

$$F = \omega/R = 2\pi f\nu/U_0^2 \quad (7)$$

where f is the frequency in Hertz.

In order to interpret the stability behavior, Eq.(3) is rewritten in the following form:

$$\phi'(x,y,t) = \phi(y)[\exp(-k_i x)]\exp[i(k_r x - \omega t)] \quad (8)$$

which shows $-k_i$ as the spatial growth rate. Depending on the sign of this term, the flow is said to be stable or unstable, i.e. if $-k_i > 0$, the disturbances grow exponentially in the streamwise direction. Recall that Eq.(8) is said to only hold locally (within the quasi-parallel flow approximation) since $k = k(R)$ and R represents the streamwise coordinate (Mack, 1984b).

Equation (8) can be integrated along the surface to determine the relative amplitude ratio, A/A_0 , or as most commonly done, the amplification factor, N .

$$N = \ln(A/A_0) = -2 \int_{R_0}^R k_i(R) dR \quad (9)$$

where R_0 is the Reynolds number at which the constant-frequency disturbance first becomes unstable (Branch I of the neutral stability curve) and A and A_0 are the disturbance amplitudes at R and R_0 . As mentioned in the previous lecture, the basic design tool is to keep N within reasonable limits in order to prevent transition. This is the celebrated e^N method (Arnal, 1984; Mack, 1984b).

3.1.2 Stability Calculations

The eigenvalue problem is solved with the appropriate basic state used as input (Reed and Nayfeh, 1981). Justification for using the usual homogeneous boundary conditions on the disturbance velocity (Eq. 5) over the porous sections follows the work of Gaponov (1971) and Lekoudis (1978).

Figures 1 and 2 are comparisons between the growth-rate calculations made with three different techniques and the Blasius flow as reference. Figure 1 is a low-Reynolds-number calculation of the growth rate for the case of a flat plate with one porous strip of width 20mm centered at a distance of 300mm from the leading edge. The x -Reynolds number at the center of the strip is 1×10^5 and the dimensionless flow rate through the suction strip is $V_0/U_0 = -2.3 \times 10^{-4}$. A disturbance with a dimensionless frequency $F = 2\pi f y/U_0^2 = 210 \times 10^{-6}$ is superposed on the mean flow. This figure shows good agreement between the linear triple-deck model and the more complicated interacting boundary-layer solution. The nonsimilar calculations are poor in comparison due primarily to the impulsive imposition of the wall-suction boundary condition. Figure 2 has the same geometry and suction level as figure 1 except the strip is at $Re_x = 10^6$ and the disturbance frequency is $F = 40 \times 10^{-6}$. A small upstream influence is observed and a significant reduction in growth rate is shown in the vicinity of the strip even for such a small suction level.

The elegance of the linear triple-deck solution is that multiple-strip configurations can be considered with ease. Reed and Nayfeh first developed a perturbation technique to determine the correction to the Blasius-flow growth rate at x_1 due to a strip centered at x_1 that has a unit suction velocity. The result is a set of influence coefficients, a_{ij} , that can be used in a superposition technique to calculate the growth rates at locations x_j modulated by the presence of a number of porous suction strips at x_i with suction velocities V_{0i} . The local amplification factors are found similarly. Since the a_{ij} are independent of the suction levels, an optimization scheme for minimizing the amplification factor is possible.

These results were used by Reynolds and Saric (1982) to reduce the parameter space in their experiments and to provide a basis for a comparison between the theory and the experiment. The remainder of the theoretical results are discussed along with the experiments.

3.2 Experiments

Much of the work of Pfenninger and co-workers (Pfenninger, 1977) was concerned primarily with the implementation of wall suction through narrow ($\approx 100\mu\text{m}$ width) slots. This motivated the detailed experiments of Kozlov et al. (1978) and Thomas and Cornelius (1981) who measured the flow field and stability characteristics downstream of the suction slot. The two-dimensional nature of the suction slot offers a number of distinct advantages over the use of holes (see section 5) as well as over 2-D suction strips (Thomas, 1985). Although the issue is not settled, design considerations may dictate the use of porous strips ($\approx 20\text{mm}$ width) as the suction device (Braslow and Fischer, 1985).

The objective of the experiments of Reynolds and Saric (1982) was to conduct careful and thorough measurements of the effects of suction strips on boundary-layer stability and thus provide a data base for theoretical models. The experiments were conducted on a flat plate fitted with porous suction panels. The porous-panel surface material was a woven stainless steel material of 80 x 700 mesh with a 80 x 80 mesh backing layer. The substructure was divided into spanwise flutes that manifold the airflow. With this configuration, the suction distribution was varied on each panel from continuous suction over 254mm to discrete suction with 16mm strips. Later, Saric and Reed (1983) performed additional experiments by using porous panels made of the perforated Titanium skin (63 μm holes on 635 μm centers) that is presently considered for LFC systems. They found the results of Reynolds and Saric (1982) qualitatively unchanged with this new material, the titanium surface gave more consistent results, and the agreement between theory and experiment was better.

3.2.1 Disturbance Measurements

In Reynolds and Saric (1982), detailed hot-wire measurements were made of the mean flow and of the disturbance flow in the low-turbulence wind tunnel at VPI&SU. The disturbances were introduced by means of a vibrating ribbon. This technique permits the introduction of a wide variety of initially two-dimensional disturbances (Costis and Saric, 1982) and is a valuable tool provided the ribbon span is long enough (Mack, 1984a).

Figure 3 (with data taken from Reynolds and Saric) shows the mean-flow velocity profile, $U(y)$, and the rms disturbance velocity profile, $|u'(y)|$, downstream of a single suction strip (16mm wide) located at $x = 1.94m$ from the leading edge. The suction velocity was $V_0/U_0 = 5.7 \times 10^{-3}$ at a freestream velocity of 15m/s. The dimensionless frequency was $F = 20 \times 10^{-6}$ and the strip was at a x -Reynolds number of 1.8×10^6 . Measurements were taken at $Re_x = 1.9 \times 10^6$. The theory of Reed and Nayfeh (1981) is superposed on the data with good agreement.

A composite of the experimental data from a no-suction case and figure 3 is shown in figure 4. The disturbance amplitudes have been normalized to have their maxima equal to 1.0. The unnormalized $|u'|_{max}$ are $0.55U_0$ and $1.2U_0$ with and without suction, respectively. One observes only a slight change in the mean flow velocity profile whereas a more pronounced distortion of the normalized disturbance velocity profile is present and the disturbance energy is redistributed to a region of higher dissipation.

In the following presentation of the data, the disturbance amplitude at a given streamwise station was expressed in terms of the integral of $|u'|$ across the boundary layer given by.

$$A(x) = \int_0^{\infty} |u'(x,y)|/U_0 dy \quad (10)$$

Integration of the disturbance profile using Eq.10 is a more desirable method for the evaluation of the disturbance behavior than the usual single-point measurements for a number of reasons. First, the non-parallel effects in the boundary layer are minimized when compared to single-point measurements conducted along constant y or constant y/δ (e.g. Gaster, 1974; Saric and Nayfeh, 1977). In addition, the experimental errors of scatter that are inherent in single-point measurements are reduced by integration of the disturbance profile. Finally, integration allows profile shape changes due to suction to be included in the measurement.

Figure 5 shows the corresponding disturbance amplitude behavior as a function of Reynolds number for the conditions of figure 3 with and without suction. The amplitudes have been normalized to the initial Reynolds-number measurement, $A_0 = A(R_0)$, which in terms of maximum rms u' , was $|u'|_{max} \approx 0.05U_0$. In this case the suction was strong enough to cause decay from a region ahead of the strip to 20 δ downstream. Of particular interest is that the theory predicted the upstream influence rather closely and in general did very well against the experiments. Other measurements were conducted at lower suction levels and with multiple-strip configurations. In each case the theory agreed with the data in every aspect.

3.2.2 Optimization Theory and Experiment

To obtain an efficient suction-strip configuration, Reed and Nayfeh (1981) minimized the amplification factor N , while maintaining constant mass flow rate. Other optimization choices are possible with the theory and some may be more desirable from a system standpoint e.g. minimize drag with constant mass flow. However, the first choice was the easiest to verify experimentally. Their perturbation solution showed that suction should be concentrated not in the region of maximum growth rate, but further upstream near Branch I of the neutral stability curve.

Figure 6 is a direct test of the optimization scheme and contains three sets of data. The first is the no suction case as a reference. The second is a configuration with 7 strips open on one panel and 3 strips open on another with a flow unit Reynolds number of $.923 \times 10^6 m^{-1}$. The third is the same suction configuration except at a flow unit Reynolds number of $.769 \times 10^6 m^{-1}$. This lower flow velocity shifts the suction strips to a lower boundary-layer Reynolds number (closer to Branch I) while keeping everything else more or less constant. The suction levels and the location of the strips are shown on the figure. The theory agrees with the experiment in all respects. Moreover, this figure was duplicated by Saric and Reed (1983) at a later time with perforated titanium panels.

It appears that the theory provides an adequate tool for predicting the suction requirements for LFC systems in so far as two-dimensional T-S waves are concerned. In the remaining sections, other problems on the application of the suction technique are discussed.

4. THREE-DIMENSIONAL DISTURBANCES

The most important consideration in LFC with suction is the leading-edge region where the both the basic state and the disturbance state are three-dimensional and crossflow disturbances are expected to dominate. The question is not one of whether or not suction will stabilize the flow. The calculations of Floryan and Saric (1983) show that typical LFC suction levels will stabilize Görtler vortices and the crossflow problem should not be much different. The real question is what are the C-F disturbances doing.

As described in the first lecture, the recent work of Saric and Yeates (1985), Reed (1984, 1985), Malik and Poll (1984), and Michel et al. (1984) have raised more questions with regard to crossflow instabilities. Whether these vortices are: (1) steady or

with regard to crossflow instabilities. Whether these vortices are: (1) steady or unsteady, (2) interacting with T-S waves, (3) interacting with other C-F vortices, (4) changing wavelength, and (5) always co-rotating or counter-rotating are questions that need to be resolved. Do nonparallel effects in the leading-edge region strongly influence the C-F problem to the extent that a complete 3-D, nonparallel analysis (e.g. Nayfeh, 1980) should be used? Moreover, do the C-F vortices provide the spanwise modulation required to produce the rapid growth of secondary instabilities predicted by Nayfeh (1981), Herbert and Morkovin (1980) and Floryan and Saric (1980)? Needless to say, the C-F problem is still one of active consideration by a number of investigators.

5. SUCTION THROUGH HOLES

One possible candidate for a porous surface is perforated titanium with a sub-assembly manifold slot (Pearce, 1982; James and Maddalon, 1984). This has the advantage over surface slots because the skin remains a continuous structural member. An important characteristic of such a surface is that it contributes only a small perpendicular pressure drop when suction is applied. In the leading-edge region, the streamwise pressure gradient may be strong enough across a manifold slot to cause outflow in the aft region of the manifold while inflow occurs in the forward region. The effects of outflow on boundary-layer transition were investigated by Saric and Reed (1983) in a preliminary study following the work of Reynolds and Saric (1982). They showed that blowing was indeed destabilizing. In order to avoid the problems of outflow destabilization, it has been suggested that one either lower the manifold pressure or decrease the number of holes. It is generally accepted that, in any case, it may be necessary to increase the local flow rate and perhaps increase the hole spacing over present designs. This is called the *oversuction* problem.

There are a number of important and *inseparable* stability and transition issues arising from oversuction in holes that are not present when one uses slots. Some of them are: (1) the creation of streamwise vortices at each suction hole as the flow rate increases, (2) the creation of resonant spanwise scales when the hole spacing is changed, (3) the different roles that issues (1)-(2) play with regard to destabilizing C-F vortices or T-S waves or the C-F/T-S interaction. These topics are discussed below in the light of the fact that there is a dearth of solid experimental data and theoretical models to guide the designer and researcher.

5.1 Local Streamwise Vortices

Streamwise vorticity is the major source of three-dimensional disturbances within the boundary layer that cause secondary instabilities leading to transition (Saric and Thomas, 1984; Herbert, 1985). Other analyses (Nayfeh, 1981; Herbert and Morkovin, 1980; Floryan and Saric 1980) have shown that certain types of spanwise modulations of the mean flow produce additional amplification that results in double exponential growth of disturbances i.e. $A \approx \exp(\exp(\sigma x))$. The importance of the control of three-dimensionality in boundary-layer stability is only now being understood (Nayfeh, 1980; Saric, 1985a) and must be part of any laminarization work. Since the usual stability theory does not include interactions *between* 3-D disturbances, one would expect premature transition and failure of the e^N method in this case.

The flow over a hole with suction resembles in principle the flow over a finite wing with lift (or more appropriately, a circular disk at angle of attack) in that a pair of tip vortices are generated. As the suction velocity increases in the hole, the coupling of the local 3-D flow with the streamwise flow intensifies the vortex structure. The key result in the early Northrop work (Goldsmith, 1953; Goldsmith, 1954; Meyer and Pfenninger, 1955; Goldsmith, 1957) was that an increase in suction velocity destabilized the flow through a basic instability of the vortex structure.

These phenomena may be parameterized by a *hole Reynolds number*, $R_D = V_0 D / \nu$, and the *velocity ratio*, $r_v = V_0 / U_0$, where V_0 is the average velocity through the suction hole, D is the hole diameter, and U_0 is the freestream velocity. An equivalent way of expressing the hole Reynolds number is with the volumetric flow rate, Q . Thus: $R_D = 4Q / \pi D \nu$. Other important parameters are the *boundary-layer Reynolds number*, $R = U_0 \delta / \nu$, the *unit Reynolds number*, $R' = U_0 / \nu$, and the *thickness ratio*, δ / D . What is unknown at this time are the threshold values of R_D and r_v that cause the appearance of streamwise vortices. Moreover, it is not known at what strength and spanwise scaling these vortices begin to effect the stability behavior.

In the experiments of Saric and Reed (1983), there was no apparent effect on stability when the hole Reynolds number, R_D , was increased beyond 200. In these experiments R_D and r_v were chosen to be typical LFC applications but R , R' , and δ / D were off the mark.

The Northrop experiments varied hole spacing, number of holes, freestream velocity, suction velocity, hole diameter, and location of holes. They contributed a vast amount of data over different ranges of parameters. Only a few highlights will be summarized here. It was observed that a pair of vortices were shed from each hole for both an isolated hole and a row of holes. At low suction rates, the flow was undisturbed in all cases. For a row of closely spaced holes with an increased suction rate, the trailing vortices of adjacent holes linked together to form horseshoe vortices which grew with time and then shed downstream followed by the formation of new horseshoe vortices. The

result was a continuous series of horseshoe vortices forming between holes and shedding downstream. From the Northrop data, it appears that this *instability of the vortex pattern* (although it was not called that) occurred in the range $370 < R_0 < 720$ with a velocity ratio, r_v , approaching 1. These suction levels are probably a bit high and the experiments relied on qualitative measurements that would not, of course, be considered to be state of the art today. As with the Saric and Reed work, the unit Reynolds number and the thickness ratio, δ/D , were not in the proper range. However, this work is very valuable in pointing out the extreme sensitivity of boundary-layer stability to small changes in hole spacing, hole diameter, and flow rate.

5.2 Resonant Spanwise Scales

The use of discrete suction holes produces a weak spanwise nonuniformity of the mean flow. Spanwise nonuniformities of the order of T-S wavelengths, λ_{TS} , or of the order of C-F vortex wavelengths, λ_{CF} , can produce resonant wave interactions (Saric and Thomas, 1984; Saric and Yeates, 1985; Reed, 1984, 1985; Herbert, 1983, 1984a,b,c, 1985)). For T-S waves, $\lambda_{TS} \approx 5\delta$, whereas for C-F vortices, $\lambda_{CF} \approx \delta$. When the hole spacing, L , is around 1 mm, there is little chance of resonant T-S interaction, but there is indeed a chance for C-F interaction in the flight case. The experiments of Saric and Yeates (1985) and the theory of Reed (1985) demonstrate the strong possibility of C-F interactions that changes the usual stability behavior. Moreover, if one increases the hole spacing in order to obtain a larger pressure drop across the surface, critical hole-spacing lengths for T-S wave interactions may be reached. The Northrop experiments (Goldsmith, 1957) demonstrated a significant sensitivity to hole spacing and orientation. Their qualitative data showed that the critical suction levels for tripping the flow were lower in the case of a number of rows of holes than in the case of a single hole or a single row of holes. What are missing here are hard data coupled with theoretical predictions that define the extent of this problem.

6. CONCLUSIONS

The understanding of the effects of suction and pressure gradients on the stability of T-S waves is well in hand. Computational tools exist that can be used with confidence by the designer. The issues with regard to the leading-edge problem that include crossflow vortices and leading-edge contamination are not as well understood. The shift of LFC suction techniques from slots to holes may cause problems of secondary boundary-layer destabilization.

7. REFERENCES

- Arnal D. 1984. Description and prediction of transition in two-dimensional incompressible flow. *AGARD Report No. 709* (Special course on stability and transition of laminar flows) VKI, Brussels.
- Bushnell, D.M. and Tuttle, M.H. 1979. Survey and bibliography on attainment of laminar flow control in air using pressure gradient and suction - Volume I. *NASA RP-1035*.
- Braslow, A.L. and Fischer, M.C. 1985. Design considerations for application of laminar flow control hardware and systems for transport aircraft. *Proc. AGARD Special Course on Aircraft Drag Prediction and Reduction*, VKI, Belgium.
- Costis, C.E. and Saric, W.S. 1982. Excitation of wave packets and random disturbances in a boundary layer. V.P.I. & S.U. Report No. VPI-E-82.26.
- Floryan, J.M. and Saric, W.S. 1979. Stability of Görtler vortices in boundary layers. *AIAA Paper No. 79-1497 and AIAA J.*, vol. 20, 316.
- Floryan, J.M. and Saric, W.S. 1980. Wavelength selection and growth of Görtler vortices. *AIAA Paper No. 80-1376 and AIAA J.*, vol. 22, 1529.
- Floryan, J.M. and Saric, W.S. 1983. Effects of suction on the Görtler instability of boundary layers. *AIAA J.*, vol. 21, 1635.
- Gaponov, S.A. 1971. Influence of the characteristics of a porous wall on the stability of a boundary layer (in Russian). *Izv. Sib. Otd. Akad. Nauk SSSR*, No. 3, 21.
- Gaster, M. 1974. On the effects of boundary-layer growth on flow stability. *J. Fluid Mech.*, vol. 66, 465.
- Goldsmith, J. 1953. Preliminary experiments on laminar boundary layer suction through circular holes at high Reynolds numbers and low turbulence. Northrop Report BLC-23.
- Goldsmith, J. 1954. Additional experiments on laminar boundary layer suction through circular holes at high Reynolds numbers and low turbulence. Northrop Report BLC-28.

- Goldsmith, J. 1957. Critical laminar suction parameters for suction into an isolated hole or a single row of holes. Northrop Report BLC-95, NAI-57-529.
- Hall, P. 1982. Taylor-Görtler vortices in fully developed or boundary-layer flows: linear theory. *J. Fluid Mech.*, vol. 124, 475.
- Hall, P. 1983. The linear development of Görtler vortices in growing boundary layers. *J. Fluid Mech.*, vol. 130, 41.
- Herbert, T. 1983. Subharmonic three-dimensional disturbances in unstable plane shear flows. *AIAA Paper No. 83-1759*.
- Herbert, T. 1984a. Analysis of the Subharmonic Route to Transition in Boundary Layers. *AIAA Paper No. 84-0009*.
- Herbert, T. 1984b. Secondary instability of shear flows. *AGARD Report No. 709* (Special course on stability and transition of laminar flows) VKI, Brussels.
- Herbert, T. 1984c. Nonlinear effects in boundary-layer stability. *AGARD Report No. 709* (Special course on stability and transition of laminar flows) VKI, Brussels.
- Herbert, T. 1985. Three-dimensional phenomena in the transitional flat-plate boundary layer. *AIAA Paper No. 85-0489*.
- Herbert, T. and Morkovin, M. V. 1980. Dialogue on bridging some gaps in stability and transition research. *Laminar-Turbulent Transition*, Springer-Verlag.
- James R.L. Jr. and Maddalon, B.V. 1984. Airframe technology for aircraft energy efficiency. *NASA-TN-85749*.
- Kaups, K. and Cebeci, T. 1977. Compressible laminar boundary layers with suction on swept and tapered wings. *J. Aircraft*, vol. 14, 661.
- Kozlov, V.V., Levchenko, V.Ya. and Scherbakov, V.A. 1978. Growth of disturbances in a boundary layer with a suction slot (in Russian). *Ucheniye Zapiski TsAGI*, vol. 9, 99.
- Lekoudis, S.G. 1978. Stability of boundary layers over permeable surface. *AIAA Paper No. 78-203*.
- Lekoudis, S.G. 1979. Stability of three-dimensional boundary layers with suction. *AIAA Paper No. 79-0265*.
- Mack, L.M. 1984a. Line sources of instability waves in a Blasius boundary layer. *AIAA Paper 84-0168*.
- Mack, L.M. 1984b. Boundary-layer linear stability theory. *AGARD Report No. 709* (Special course on stability and transition of laminar flows) VKI, Brussels.
- Malik, M.R. and Poll, D.I.A. 1984. Effect of curvature on three-dimensional boundary layer stability. *AIAA Paper No. 84-1672*.
- Meyer, W.A. and Pfenninger, W. 1955. Preliminary report on the flow field due to laminar suction through holes. Northrop Report BLC-75, NAI-55-290.
- Michel, R., Arnal, D., Coustols, E. and Juillen, J.C. 1984. Experimental and theoretical studies of boundary layer transition on a swept infinite wing. *Proc. 2nd IUTAM Symp. on Laminar-Turbulent Transition*, Novosibirsk.
- Nayfeh, A.H. 1980. Three-dimensional stability of growing boundary layers. *Laminar-Turbulent Transition*, ed: R. Eppler and H. Fasel, Springer.
- Nayfeh, A.H. 1981. Effect of streamwise vortices on Tollmien-Schlichting waves. *J. Fluid Mech.*, vol. 107, 441.
- Nayfeh, A.H. and El-Hady, N.M. 1979. An evaluation of suction through porous strips for laminar flow control. *AIAA Paper No. 79-1494*.
- Nayfeh, A.H., Reed, H.L. and Ragab, S. 1980. Flow over plates with suction through porous strips. *AIAA Paper No. 80-1416*.
- Pearce, W.E. 1982. Progress at Douglas on laminar flow control applied to commercial transport aircraft. *Proc. 13th Congress ICAS/AIAA*, Seattle, WA.
- Pfenninger, W. 1977. Laminar flow control - Laminarization. *AGARD Report No. 654*, (Special course on drag reduction) VKI, Brussels.
- Pfenninger, W., Reed, H.L. and Dagenhart, J.R. 1980. Design considerations of advanced supercritical low drag suction airfoils. *Viscous Flow and Drag Reduction*, vol. 72. *Prog. Astro. and Aero.*, 249.

- Poll, D.I.A. 1984. Transition description and prediction in three-dimensional flows. *AGARD Report No. 709* (Special course on stability and transition of laminar flows) VKI, Brussels.
- Provinelli, F.P., Klineberg, J.M. and Kramer, J.J. 1976. Improving aircraft energy efficiency. *Astro. and Aero.*, Vol. 14, No. 2.
- Reed, H.L. 1984. Wave interactions in swept-wing flows. *AIAA Paper No. 84-1678*.
- Reed, H.L. 1985. Disturbance-wave interactions in flows with crossflow. *AIAA Paper No. 85-0494*.
- Reed, H.L. and Nayfeh, A.H. 1981. Stability of flow over plates with porous suction strips. *AIAA Paper No. 81-1280 and AIAA J. (in press)*.
- Reshotko, E. 1978. Heated boundary layers. *Proc. 12th Symposium on Naval Hydrodynamics*, Nat'l Acad. Sci., Washington, D.C.
- Reshotko, E. 1979. Drag reduction by cooling in hydrogen-fueled aircraft. *J. Aircraft*, vol. 16, 584.
- Reshotko, E. 1984a. Environment and receptivity. *AGARD Report No. 709* (Special course on stability and transition of laminar flows) VKI, Brussels.
- Reshotko, E. 1984b. Laminar flow control - Viscous simulation. *AGARD Report No. 709* (Special course on stability and transition of laminar flows) VKI, Brussels.
- Reshotko, E. 1985. Control of boundary-layer transition. *AIAA Paper No. 85-0562*.
- Reynolds, G.A. and Saric, W.S. 1982. Experiments on the stability of a flat-plate boundary layer with suction. *AIAA Paper No. 82-1026 and AIAA J. (in press)*.
- Saric, W.S. 1985a. Stability and transition in bounded shear flows. *Proc. Perspectives in Fluid Mechanics*, Caltech, (Jan. 1985).
- Saric, W.S. 1985b. Boundary-Layer Transition: T-S Waves and Crossflow Mechanisms. *Proc. AGARD Special Course on Aircraft Drag Prediction and Reduction*, VKI, Belgium.
- Saric, W.S. and Nayfeh, A.H. 1977. Nonparallel stability of boundary layers with pressure gradients and suction. *AGARD C-P No. 224*, 6.
- Saric, W.S. and Reed, H.L. 1983. Effect of suction and blowing on boundary-layer transition. *AIAA Paper No. 83-0043 and AIAA J. (in press)*.
- Saric, W.S. and Thomas, A.S.W. 1984. Experiments on the subharmonic route to transition. *Turbulence and Chaotic Phenomena in Fluids*, ed: T. Tatsumi, North-Holland.
- Saric, W.S. and Yeates, L.G. 1985. Experiments on the stability of crossflow vortices in swept-wing flows. *AIAA Paper No. 85-0493*.
- Srokowski A. and Orszag, S.A. 1977. Mass flow requirements for LFC wing design. *AIAA Paper No. 77-1222*.
- Thomas, A.S.W. and Cornelius, K.C. 1981. Investigation of a laminar boundary layer suction slot. *AIAA J.*, vol. 20, 790.
- Thomas, A.S.W. 1985. Aircraft drag reduction technology - A summary. *Proc. AGARD Special Course on Aircraft Drag Prediction and Reduction*, VKI, Belgium.
- Tuttle, M.H. and Maddalon, D.V. 1982. Laminar Flow Control (1976-1982). *NASA-TN-84496*.
- Wagner, R.D. and Fischer, M.C. 1983. Developments in the NASA transport aircraft laminar flow program. *AIAA Paper No. 83-0090*.
- Wagner, R.D. and Fischer, M.C. 1984. Fresh attack on laminar flow. *Aerospace America*, (March 1984), 72.
- Wagner, R.D., Maddalon, D.V. and Fischer, M.C. 1984. Technology development for laminar boundary control on subsonic transport aircraft. *AGARD C-P 365*, 16.
- Wazzan, A.R., Okamura, T.T. and Smith, A.M.O. 1968. Spatial and temporal stability charts for the Falkner-Skan boundary-layer profiles. Douglas Aircraft Co. Report No. DAC-67086.

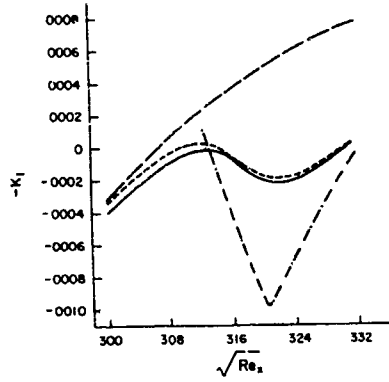


Figure 1. Spatial growth rate $-k_i$ versus R ($=\sqrt{Re_s}$). Single strip with $V_0/U_0 = 2.3 \times 10^{-4}$, $F = 21 \times 10^{-6}$. From Reed and Nayfeh (1981).

- Linear Triple Deck
- - - Interacting Boundary Layer
- · - Nonsimilar
- - - Blasius

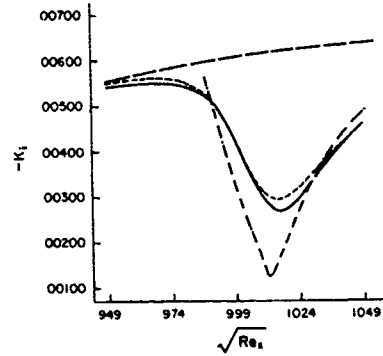


Figure 2. Spatial growth rate $-k_i$ versus R ($=\sqrt{Re_s}$). Single strip with $V_0/U_0 = 2.3 \times 10^{-4}$, $F = 40 \times 10^{-6}$. From Reed and Nayfeh (1981).

- Linear Triple Deck
- - - Interacting Boundary Layer
- · - Nonsimilar
- - - Blasius

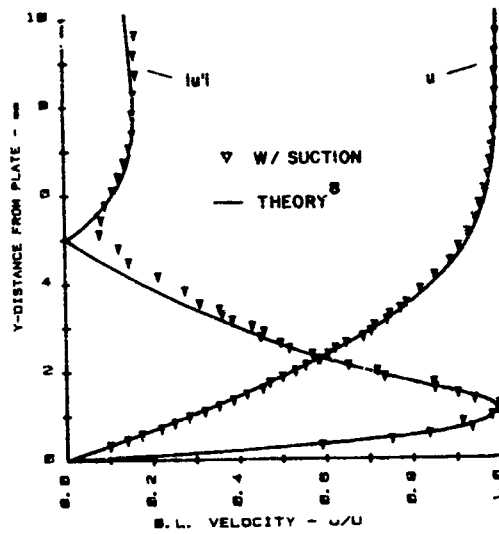


Figure 3. Profiles of Mean Velocity $U(y)/U_0$ and Disturbance Velocity $|u'(y)|/|u'|_{max}$ at $R = 1380$, $V_0/U_0 = 3.7 \times 10^{-3}$ at $R = 1340$, $F = 20 \times 10^{-6}$. Data from Reynolds and Beric (1982). Theory from Reed and Nayfeh (1981).

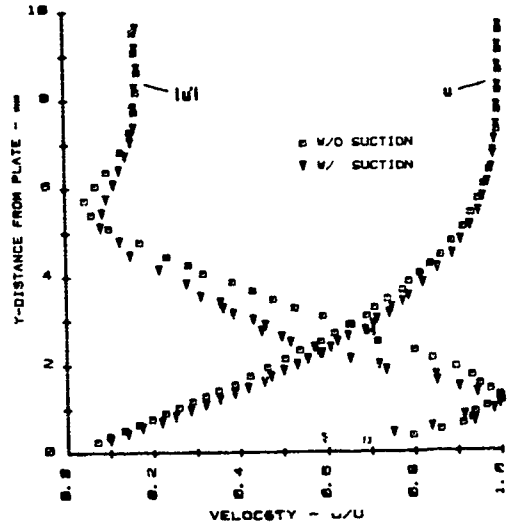


Figure 4. Profiles of Mean Velocities $U(y)/U_0$ and Disturbance Velocities $|u'(y)|/|u'|_{max}$ With and Without Suction at $R = 1380$. Conditions of Figure 3.

DESIGN CONSIDERATIONS FOR APPLICATION OF LAMINAR FLOW CONTROL SYSTEMS
TO TRANSPORT AIRCRAFT

by
Albert L. Braslow* and Michael C. Fischer
NASA Langley Research Center
Hampton, Virginia 23665

SUMMARY

Research and development in laminar-flow control (LFC) has been intensive in the past 10 years since the "oil crisis" of the early 1970's. The prospects for the implementation of the technology on commercial transports are now better than at any time in the past.

This paper briefly summarizes the current status of the laminar-flow control technology. Factors that have previously inhibited the application of LFC are first reviewed. Involved are the effects of atmospheric ice crystals, surface irregularities, acoustical environment, and off-design operating conditions. Aircraft design trends that are different from turbulent aircraft are discussed as are various design requirements unique to the LFC systems. Current design approaches for the principal LFC systems are reviewed. These include the system for protection of the leading-edge region from surface contamination and icing and the system for removal of a portion of the boundary-layer air. The latter includes consideration of both multiple spanwise suction slots and distributed perforations and required differences between the wing-box and leading-edge box regions.

NOMENCLATURE

a	wave amplitude
AR	aspect ratio
b	wing span or slot depth
BPR	engine bypass ratio
c	chord
C_D	total airplane drag coefficient
C_{D_i}	induced drag coefficient
C_{D_o}	profile drag coefficient
C_L	aircraft lift coefficient
ΔC_N	slot spacing
C_p	surface pressure coefficient
C_{p_s}	slot pressure drop coefficient
C_q	suction flow coefficient
C_l	airfoil lift coefficient
d	perforated hole diameter
D_i	induced drag
DOC	direct operating cost
EMD	equivalent melted diameter
FL	field length
FVR	fuel volume ratio
g	gap width
GASP	global atmospheric sampling program
h	step height
k	roughness height
L	lift
LECF	leading edge crossflow
LFC	laminar flow control
M	Mach number
q_∞	free stream dynamic pressure
Q	surface porosity
R_k	Reynolds number based on roughness height
R_w	Reynolds number based on slot width
R/ft	unit Reynolds number
s	perforated hole spacing
S	area of wing or tail
S_f	flap deflection
t	wing thickness
TECF	trailing edge crossflow
TIC _F	fraction of time-in-clouds for a flight
TIC _R	average fraction of time-in-clouds for a given route

*Required

TOGW	takeoff gross weight
T-S	Tollmien Schlichting
U	velocity
V_w	velocity of sucked flow through surface
w	slot width
W	aircraft weight
W_b	wing box weight
W_b/W_{REF}	relative wing box weight
W/S	wing loading
x	distance from leading edge
$(X/C)_L$	fraction of wing chord laminarized
z	sucked height
β_w	slot design parameter defined as $\frac{b}{WR_w}$
δ	boundary-layer thickness
ρ	density
μ	viscosity
λ	wave length
Λ	wing sweep at $\frac{1}{4}C$

Subscripts

crt	critical conditions
e	boundary-layer edge conditions
MAX	maximum value
SUB	subsurface conditions
THEOR	theoretical value
w	conditions at wall
z	conditions at sucked height
∞	free stream conditions

INTRODUCTION

Fuel costs comprise a major portion of air transport operating costs. Thus, energy efficiency is an essential design goal for transport aircraft. Technology for maintenance of a laminar boundary layer over extensive regions of aircraft surfaces during the cruise phase of flight offers great benefits in fuel efficiency and direct operating cost. NASA and the American air transport industry have been cooperating since 1976 in a comprehensive program to expedite introduction of laminar-flow technology into production aircraft.

An immense background of information had been developed at the time of the decision to reactivate efforts to apply laminar-flow control to aircraft. See Reference 1 for an extensive survey and bibliography on these pioneering efforts. Although this information established and verified basic concepts, no applications had been made to either commercial or military aircraft because the technology for a reliable and economically practical application was inadequate and the fuel-cost savings at that time did not warrant the time and effort required to bring the technology to a state of readiness for application. Advances in materials and manufacturing technology and large increases in the relative cost of fuel since the hiatus in LFC activities commenced in the mid 1960's fostered the reactivation of an LFC program. The program was formulated to focus on the industry needs and concerns regarding a reliable and economically practical application of laminar-flow technologies. The factors of concern are indicated in Figure 1.

They include sweep, where laminar-flow control experience with the high values required for high-speed transports is very limited, and airfoil shape, where new "supercritical" type profiles desired for high subsonic speeds must be accommodated. The advanced airfoils are required so that LFC aircraft can retain the projected performance advantage over advanced-technology turbulent aircraft. Efficient suction distributions are necessary to minimize the size and power requirements of the suction-system components, the laminar skin friction, and sensitivity to surface roughness. Also, alternatives for surface openings must be evaluated. The very fine openings of the suction system must not unduly corrode or clog and must be cleanable and repairable. New materials currently available must be manufacturable to close shape and smoothness tolerances without excessive cost. The sensitivity of the laminar boundary layer to adverse operational influences such as accumulation of insects or dirt, erosion, foreign-object damage, and engine noise must be attenuated. Finally, the degree to which atmospheric ice particles will impact the performance of a fleet of laminar-flow control aircraft must be known.

This paper briefly reviews some of the advances made during the recent program in these areas of concern that had previously inhibited the application of LFC.

FACTORS AFFECTING LFC VIABILITY
Atmospheric Ice Crystals

During flight tests of the X-21 laminar-flow control airplane (Ref. 2), a factor that adversely affected retention of laminar flow was the existence of ice particles in cirrus clouds or haze. When penetrating light cirrus clouds or haze at typical cruise

conditions, laminar flow was partially degraded or erratic. At cruise altitudes, cirrus clouds are comprised mainly of ice crystals indicating that the crystals are detrimental to the maintenance of laminar flow. A theory was developed (Ref. 3) to explain and predict the effect of ice particle encounter on the maintenance of laminar flow. It was theorized that turbulent vortices shed by ice particles in the boundary layer will trigger boundary-layer transition for certain combinations of particle size, concentration, and residence time in the boundary layer. Figure 2, adapted from this analysis, illustrates the combinations that affect laminar flow at an altitude of 40,000 ft for a Mach number of 0.75. Columnar ice particles, for which the analysis was made, with an equivalent melted diameter of less than $33 \mu\text{m}$ will not cause boundary-layer transition at any ambient concentration level (region 1). For particles larger than $33 \mu\text{m}$ EMD, particle concentrations smaller than about $500 \text{ particles/m}^3$ produce no effect on maintaining laminar flow (region 2). As particle concentrations increase above about $500/\text{m}^3$ (for EMD greater than $33 \mu\text{m}$), there is an increasingly detrimental effect on laminar flow (regions 3 and 4). The critical values of particle size and concentration are functions of airfoil leading-edge shape and aircraft speed and altitude, all of which affect the number of ice particles that penetrate the boundary layer. Quantitative validation of the regions of Figure 2 for several flight conditions await planned flight research.

Based upon the available theory, however, the magnitude of the cloud problem on operational LFC aircraft has been assessed. Firstly, all available meteorological data were studied to determine the probability of cloud encounter as a function of altitude, season of the year, and geographic location. Secondly, estimates were made of the probability of laminar-flow loss along various airline route/altitude profiles.

The desired cloud-encounter data did not exist in documented form but, fortunately, unanalyzed cloud data were available from the NASA CASP (Global Atmospheric Sampling Program) archive. As part of the GASP effort, some 88,000 cloud-encounter measurements on more than 3000 Boeing 747 airliner flights were obtained during 1975-79 and are presented in References 4 and 5. These reports, as well as Reference 6, also include estimates of average cloud-cover statistics for several long-distance airline routes. Statistics for seven high-density airline routes are presented in Table I.

In the table, for each route/altitude band, parameter values are given for: the number of flights actually in the sample; TIC_P , the sample average percentage time-in-clouds for the route; $P(\text{TIC}_P < 1\%)$, and $P(\text{TIC}_P < 5\%)$, the modeled probabilities that the average time-in-clouds will be below 1 and 5%, respectively; $P(\text{TIC}_P > 5\%)$, $P(\text{TIC}_P > 10\%)$, $P(\text{TIC}_P > 25\%)$, and $P(\text{TIC}_P > 50\%)$, the modeled probabilities that the route-average time-in-clouds will equal or exceed 5, 10, 25, and 50%, respectively. All probabilities are expressed as percentages.

In an example of using Table I, on the California-Hawaii route, in the 28,500 ft to 33,500 ft altitude band there were 22 flights in the sample, and the route-average time-in-clouds is 9.4%. There is a 52.4% probability of being in clouds for more than 5% of the route, a 32.5% probability of being in clouds for 10 percent or more of the route, but only an 8.9% probability that one-quarter or more of the route will lie within clouds. There is only a 1.2% probability that half or more of the route will be in cloud. In the 33,500-38,500 ft altitude band a much larger sample - 177 flights - was available for this route. It is noted that the respective parameter values are all much lower than for the preceding band. For the 38,500-43,500 ft altitude band there were only 2 flights in the sample - insufficient data to derive reliable statistics.

Based on these results, conservative estimates of the probable loss of laminar flow on major airline routes were made. Conservatism was introduced by assuming that all cloud encounters cause total loss of laminar flow and that the percentage loss of laminar flow on a given flight is equal to the percentage of time spent within cloud on that flight. It was also assumed that no cloud avoidance measures are taken. Figure 3 is an example of the potential laminar-flow loss on some of the major airline routes. It is now apparent from the results, such as Figure 3, that cloud encounters during cruise of long-range air transports are not frequent enough to invalidate the large improvement in fuel usage attainable through application of LFC.

Surface Conditions

The sensitivity of laminar flow to surface irregularities, especially at high Reynolds numbers, is well known. The establishment, therefore, of appropriate tolerances for the manufacturing and maintenance of LFC airplane surfaces is of principal importance. The primary types of surface irregularities are waviness, two-dimensional type discontinuities such as steps and gaps, and three-dimensional type protuberances such as rivets, fasteners, and insect debris.

Surface Waviness

The basic criteria for permissible surface waviness are presented in Reference 7. A simplified relationship in general agreement with Reference 7 was presented in

Reference 8 as $\frac{a}{\lambda} = \left(\frac{59000C \cos^2 \Lambda}{\lambda(R_c)^{1.5}} \right)^{1/2}$ for single two-dimensional waves parallel to the

wing span. For multiple waves parallel to the wing span, the tolerance limits are one-third of that for single waves. For chordwise waves, the permissible wave amplitude is twice as high as for spanwise waves. A quantitative example of permissible wave amplitude for a representative LFC airplane wing sweep and cruise altitude and Mach number is presented as Figure 4. These waviness criteria were originally derived for airfoils with a maximum local Mach number of about 1.04. The current LFC study airplane designs utilize supercritical airfoils with higher maximum local Mach numbers. Wave criteria for such airfoils with more extensive local supersonic flow will almost certainly be more strict. Adverse effects of surface waves under these conditions might involve: 1) a decrease in local external pressure sufficient to induce outflow of air, with a resultant premature transition, for the design value of internal suction-duct pressure and flow rate; 2) a change in pressure distribution which can influence the growth of boundary-layer disturbances; and 3) generation of a pressure wave that reflects to the airfoil from the sonic line which might induce immediate or forward transition movement in the vicinity of the reflection. Establishment of a general criterion for waviness on airfoils with large regions of supercritical flow, therefore, is obviously impossible. Insight to necessary tolerances for each particular airfoil, suction configuration, and flight condition can be obtained with pressure distribution and boundary-layer stability calculations using up-to-date computer techniques, as was done for many cases in this program.

Two-Dimensional Type Discontinuities

Tolerance criteria for two-dimensional type discontinuities are reported in Reference 8 and presented in Figure 5. Some typical results using these criteria are presented in Figure 6. The step and gap equations used do not account for distance of the discontinuity from the wing leading edge. Even with suction, the boundary layer increases in thickness with downstream distance with a resultant decreased sensitivity to surface disturbances. Figure 7 presents criteria obtained from Reference 7 that account for distance in a very limited way. Typical results using these equations are presented in Figure 8. For determination of permissible tolerances, it appears wise to use the method that predicts the smallest allowables for each type of discontinuity with a unit Reynolds number at least as large as the maximum in the cruise envelope. Even then, the tolerance goals used were smaller to allow for the probable increased sensitivity of the boundary layer to surface discontinuities in the supersonic region of supercritical airfoils and in regions where significant crossflow prevails.

Three-Dimensional Type Protuberances

Use of the transition criterion for three-dimensional type surface roughness $R_{k_{crt}}$ on unswept wings is reviewed in Reference 9. A low value of $R_{k_{crt}}$ was generally used in this program (about 200) to provide some conservatism for an indicated adverse effect of sweep, as previously noted. Some typical allowable roughness heights are presented in Figure 9.

Acoustics

One of the disturbance inputs that influences the ability to attain laminar flow is the aircraft's own noise environment. The noise incident upon the airplane surfaces may be conveniently categorized into three major source groups, as indicated in Figure 10 with their subsources. The major source groups are the airframe noise sources, the propulsion system noise sources, and the laminar-flow control systems noise sources. Considerable progress has been made in the last decade regarding the understanding and prediction of airplane noise generation and in improvements to the acoustic criteria for maintenance of laminar flow.

Reference 10 developed general procedures for prediction of noise levels incident upon the surfaces of future subsonic commercial air transports during cruise. A summary and explicit definitions of these prediction methods are contained in Reference 11.

In the area of acoustic criteria for laminar flow, with the exception of a few ad hoc experiments on sound-induced boundary-layer transition, the only sets of data available from an engineering application point of view are those developed during the X-21 research and development program. The X-21 program data were derived from turbulence-induced transition and, therefore, do not account for the spectrum or directionality of the sound field. In Reference 10, the existing criteria were improved with the use of a semi-empirical method that includes the sensitivity to frequency and directionality. The empirical constant defines the level to which the acoustically-induced boundary-layer disturbance must amplify before transition starts and varies with the amount of suction. A quantitative example of results obtained with this method is presented in Figure 11. For each of five chordwise stations, the critical sound pressure level spectra are presented for sound incident on an airfoil in the same direction as the mean flow, i.e., sound directionality of 0°. The sensitivity of critical SPL to noise frequency is evident. This frequency sensitivity was not apparent, of course, from the spectrally integrated X-21 criteria, which are superimposed on Figure 11. This comparison indicates that sound pressure levels may exceed the X-21 criteria values

except in rather limited ranges of noise frequency where boundary-layer disturbances are most amplified. Other results in Reference 10 indicate that the amount of boundary-layer suction and the suction distribution affect not only the depth of the critical SPL spectrum but also the critical frequency and the critical region along the chord.

Operations

Effects of Off-Design Flight Conditions

During cruise, a transport airplane usually flies at a constant altitude until sufficient fuel has been used to allow the cruise altitude to increase by an increment of usually 4000 ft. The design lift coefficient is that required for the initial cruise altitude. As fuel is burned, the C_L decreases from the design value until the step climb returns it to the design value. An indication of the effect of lift coefficient on the chordwise pressure distribution and, more importantly, on the required suction velocity distribution is presented in Figures 12 and 13, respectively. The burn off of fuel with a reduction in C_L during constant-altitude flight causes no problem for the suction system. Cruise flight at lower than design Mach number, however, should be avoided because the increase in required C_L (Fig. 14) causes a large penalty in suction (Fig. 15).

Effect of Loss of Laminar Flow on Flight Characteristics

An example of chordwise pressure distribution normal to the leading edge at design flight conditions and with the design chordwise extent of laminar flow is presented in Figure 16 as the solid line. If laminar flow is lost, the section lift coefficient at the original angle of attack decreases about 20% (dashed line). To maintain a constant lift coefficient, the angle of attack must increase about 0.8° (solid line with circles). The pressure distribution indicates formation of a shock on the upper surface which would adversely affect the ability to restore laminar flow when the cause of the initial loss of laminar flow is removed. A small deflection of a 15% chord trailing-edge flap, however, was found to be adequate to maintain the local lift coefficient with no change in angle of attack and no formation of upper-surface shock (Fig. 17). Such a segmented trailing-edge trim flap can, therefore, be used satisfactorily to compensate for any local disruption of laminar flow in flight.

Effect of Loss of Laminar Flow on Airplane Range

An area of concern frequently expressed regarding the viability of LFC transports is the ability either to reach the scheduled city-pair range in event of loss of laminar flow or to return safely to the point of origination or to an alternate airport. The airplane design studies of this program and associated economic benefits and costs included allowances for increased reserve fuel as compared with turbulent airplane requirements. Assumptions and results for one of the airplane designs studied follows.

For the 6500 nmi study airplane, fuel reserves were increased above the international fuel reserve requirements to 1) permit loss of laminar flow due to weather phenomena during 6% of the mission cruise time; 2) permit flight against a 50-knot wind and allow for fuel efficiency variations with a 2% fuel penalty; and 3) increase the 200 nmi diversion distance included in the international reserves to 390 nmi (6% of the design range). With these modified fuel reserve assumptions, Figure 18 presents the sensitivity of range to intermittent loss of laminar flow for the basic design point takeoff weight, payload, cruise speed, and cruise altitude. With no laminar loss, the attainable range is 6550 nmi. With a 50% loss of laminar flow, similar to complete laminar loss at the critical mid point of the 6500 nmi mission, if no prior loss of laminar flow had been suffered, a range of 5800 nmi is attainable. After use of the diversion-distance fuel allowance, only a small part of the 10% contingency fuel reserve (equivalent to more than 600 nmi for this airplane) would be required to reach the original destination. Considerable flexibility exists, therefore, in establishment of a revised flight plan, if desired. Also, more of the range reduction may be recovered by revision of cruise Mach number and altitude to more fuel-efficient values.

Effect of Fuel Cost on Direct Operating Cost

Each of the study LFC airplanes of the present program used approximately 20% less fuel than advanced turbulent airplanes designed for the same payload/ range missions. The benefit of the fuel savings in terms of reductions in direct operating costs depends, of course, on the cost of fuel. An example of the sensitivity of DOC reduction due to LFC as a function of fuel cost is presented in Figure 19 for an airplane with laminar flow to 70% chord on both surfaces and for one with laminar flow to 85% chord on the upper surface only. The economic benefit of LFC increases rapidly with rising fuel costs for either design approach.

LFC System Operation

The in-flight operation of an LFC airplane differs from turbulent airplanes by the addition of a leading-edge protection system and a boundary-layer air suction system. Operation of the leading-edge protection system is limited to ground operation during takeoff roll and the initial portion of the climb (to about 5000 ft altitude) and during final descent and landing. The suction system is designed for laminarization during cruise only and, therefore, will be operable only at and near cruise speed and altitudes. Both systems will be automated to the extent that actuation of a single control would be required for in-flight operations.

AIRCRAFT DESIGN TRENDS AND REQUIREMENTS UNIQUE TO LFC Suction Requirements

Laminar-flow airfoils for transport aircraft have two principal types of boundary-layer instabilities to consider in their design in determination of the amount of suction required to maintain laminar flow. In the leading- and trailing-edge regions of swept wings (regions of strong favorable and adverse pressure gradients), there are disturbance modes which are sensitive to the strong crossflow velocity profile. This type of instability is characterized as inviscid because the instability results from the presence of an inflection point in the crossflow profile. This condition causes formation of crossflow vortices which have their axes in the streamwise direction and which rotate in the same sense. The second type of instability on a swept wing, known as a Tollmien-Schlichting wave, has a direction of propagation close to the local boundary-layer edge flow direction and under certain conditions exhibits viscous instability. Tollmien-Schlichting waves are sensitive to Reynolds number and the shape of the mean velocity profile. Tollmien-Schlichting disturbances generally occur in the mid-chord region where the pressure gradient is flat or slightly adverse. A third type of instability mechanism which can trigger turbulent flow on swept wings is leading-edge turbulence contamination which is caused by disturbances that propagate down the wing leading edge along the attachment line. This type of instability can be controlled by proper treatment of the inboard leading edge, such as concentrated local suction in the attachment line region or tailoring of the leading-edge radius, and will not be discussed further in this paper. Taylor-Görtler instabilities, associated with surface concavities, did not exist in the laminarized regions of this study.

Figure 20 illustrates the regions where the crossflow and Tollmien-Schlichting types of disturbances predominate and shows how suction applied in the proper amount can control the disturbance growth rates to prevent their exceeding an allowable amplification rate. The design process (Fig. 21) generally involves development of an airfoil shape which has the desirable pressure distribution and use of an advanced transonic wing code to develop a wing shape with very similar desirable pressure distributions. The next step is to assume an initial suction distribution based on previous experience and to use the wing coordinates, suction distribution and design conditions (M , Re , etc.) to compute 3-D laminar boundary-layer profiles. These profiles are then input into an advanced boundary-layer stability code where the disturbance amplification levels are computed and compared to the upper limit allowed (determined from existing transition criteria). If the stability levels are unacceptable, an iterative process follows wherein the initial suction distribution is changed and the amplification rates are recomputed. Once the stability levels are considered acceptable, the suction requirements are known and the LFC system design can proceed.

To minimize the penalties associated with a laminar-flow suction system and to maximize the aerodynamic benefits, it is important to minimize the suction flow required to maintain allowable disturbance growth rates, with a small additional allowance for conservatism and off-design operation. Excessive suction requirements result in increased suction drag, larger duct volume requirements, excessive surface suction-slot or porous-suction regions, and increased aircraft weight. Fortunately, advanced boundary-layer stability codes, e.g., Reference 12, predict lower suction requirements than earlier methods.

Wing Sweep

The selection of wing sweep for an LFC aircraft is different from that for a turbulent aircraft. For turbulent airplanes, experience indicates the most efficient designs for high subsonic cruise speeds involve wing sweep angles between 25° and 35° . For LFC airplanes, however, sweep has a very powerful adverse effect due to increased crossflow instability, increased spanwise turbulence contamination along the front attachment line, and increased sensitivity of the laminar boundary layer to external disturbances. A compromise is necessary, therefore, for the LFC airplane. Figures 22 and 23 from Reference 13 illustrate the trade relations among sweep, thickness, and relative wing weight. Figure 22 indicates the outboard wing thickness ratio required to achieve a given cruise Mach number as a function of wing sweep angle. The lower sweep angles desired for easier laminarization require thinner wings which Figure 23 indicates will, in combination with the lower sweep, increase the relative weight of the basic wing structure. A sweep of about 25° is required to approach a minimum wing weight for a long-range cruise Mach number of 0.80. Figure 24 shows results of a wing-sweep trade study as a function of wing loading. In addition to an increase in airplane gross weight, decreased sweep also significantly increases the fuel burned but has no significant impact on wing loading or high-altitude cruise trends.

Wing Loading and Aspect Ratio

Definition of the other principal geometric features of the wing first requires definition of some design criteria. Principal airplane design guidelines for a baseline airplane wing study conducted in this program included: near minimum airplane direct operating cost with moderate block fuel penalty; moderate aspect ratio to assure sufficient LFC duct volume and provide adequate design flexibility; and fuel volume in the wing and wing center section. It is important first to review qualitatively the direction in which the wing loading of a laminar-flow airplane wing tends. At the maximum value of lift to drag ratio, close to that desired for high-speed cruise, the induced drag approximately equals the friction drag. For a laminar wing, with its friction drag lower than for a turbulent wing, it is desirable, therefore, to reduce the induced drag

relative to a turbulent airplane in order to maximize the laminar benefits. The induced drag D_i can be reduced by increasing the wing span b . ($D_i = \frac{W^2}{\pi b}$) as derived from $D_i = C_{D_i} q S = \frac{C_L^2}{\pi AR} q S$ and $W = L = C_L q S$). For a constant wing area S , however, which is attained by decreasing the wing chord C as span is increased, the wing weight increases which offsets some of the fuel saved from the lower induced drag. If one were to decrease the chord a lesser amount, thereby allowing the wing area to increase with a resultant approach to a constant aspect ratio, the increase in wing weight might be less but the total drag decrease attained from the lower induced drag is reduced by the increased friction drag of the larger wing area. Because the friction drag increase due to increased wing area is much lower for a laminar wing than for a turbulent wing, the laminar wing design tends towards an increased span and an increased area and, therefore, a reduced wing loading for the same weight.

The following series of figures are quantitative examples of the effects of wing loading and aspect ratio on the important airplane performance parameters mentioned previously with consideration given to the important design constraints of FAA field length limit and fuel volume. The values presented are strictly dependent upon the airplane design mission and are included only to indicate trends and considerations. For a given airplane size, the adequacy of available fuel volume is best judged with the parameter fuel volume ratio FVR. This parameter is the ratio of available fuel volume to that required to fly the design mission range with fuel reserves at constant altitude carrying the full passenger payload. In this study, a value of FVR of 1.1 was chosen as a constraint for design conservatism to allow a possible increase of required suction duct volume as the design progressed. Figure 25 gives FVR results for a matrix of airplanes sized for a cruise altitude of 40,000 ft and a cruise Mach number of 0.8. A field length limit of 10,000 ft, selected for the airplane designs of this study, is superimposed to complete delineation of a boundary which defines wing loading/aspect ratio combinations which are excluded from consideration by the FVR and field length constraints. Figure 26 indicates that the minimum direct operating cost DOC lies at the intersection of the fuel/field length limit lines. The variation of DOC with aspect ratio AR is fortunately rather flat at the intersection. After establishment of engine bypass ratio and cruise power ratio from trade studies, Figure 27 led to selection of a near-optimum aspect ratio of 11.6 based on DOC, a value that also meets the guideline for moderate aspect ratio. The near-optimum DOC choice, however, is not the optimum from a fuel-usage viewpoint, as indicated in Figure 28. Selection of an aspect ratio of 14 rather than 11.6, for example, decreases fuel usage by 6%. The technical risks of such a choice would be considerably greater and the small portion of total flights that would be flown at the maximum range with full passenger payload did not appear to justify use of such a high aspect ratio at the current state of the art of structures and materials.

Cruise Mach Number and Altitude

The effect of cruise Mach number and altitude on DOC is presented in Figure 29. Although DOC decreases with increased M , greater wing sweep is required which, as discussed previously, aggravates the leading-edge spanwise turbulence contamination problem and the adverse effects of boundary-layer crossflow instability and external disturbances. Increased cruise altitude, with the associated reduced unit Reynolds number, is very desirable from the point of view of reduced sensitivity of the laminar boundary layer to all disturbances. The effect of an increase in cruise altitude on DOC, however, is adverse, as indicated in Figure 29. The figure also indicates that a progressively greater DOC penalty occurs as altitude is increased above 40,000 ft.

Chordwise Extent of Laminarization

The reduction of profile drag by extending the percentage of chord laminarized is an obvious way of decreasing fuel usage. The penalties in LFC system weight, cost, and complexity are less obvious. For practical design of conventional-looking transports, these penalties are significant enough to limit the chordwise extent of laminarization to a value below the theoretical ideal of full-chord laminar flow. The following figures indicate general trends for conventional transport arrangements with chordwise extent of laminarization but absolute values vary with design mission and aircraft geometry. The design variation of suction flow with chordwise position, a principal input to these general trends, is represented in Figure 30.

Figure 31 illustrates the increase in LFC system weight with increasing $(X/C)_L$. Aircraft gross weight decreases at first with increasing $(X/C)_L$ and then increases rapidly with a further increase in $(X/C)_L$. The trend is consistent with the trend of wing area with $(X/C)_L$ and results directly from a smaller wing volume available for fuel when the increased suction ducting volume required toward the rear of the wing is considered (Fig. 30). A continuously favorable effect of increased laminarization on the wing and tail profile drag coefficients, the total airplane profile drag coefficient, and the total airplane drag coefficient is shown in Figure 32. The rate of decrease in drag coefficient slows as laminarization approaches full chord. When the required increase in wing area is considered for laminarization past about half chord (Fig. 31), however, the total drag of each component, as represented by $C_D S$ in Figure 33, reaches a minimum at $(X/C)_L$ of about 0.80 and then increases. This drag variation with $(X/C)_L$ along with the airplane gross weight variation with $(X/C)_L$ (Fig. 31) result in a

minimization of both block fuel and direct operating cost (DOC) at an aft position of laminarization considerably ahead of the trailing edge - in the order of 80%C for minimum block fuel and 70%C for DOC, depending upon the fuel price (Fig. 34). As a result of these trends and other considerations, each contractor involved in these studies elected to terminate laminar flow considerably ahead of the trailing edge.

Limiting Laminarization to Upper Surface

Because of the difference in skin friction between the upper and lower wing surfaces due to the differences in local velocities, it is possible to obtain nearly the same drag reduction by laminarization of only the upper surface to 80% chord as can be obtained by laminarization of both surfaces to 70% chord (Fig. 35). This is an interesting approach to application of LFC which provides significant simplifying advantages that compensate for the higher drag coefficient. Conventional access panels to wing leading- and trailing-edge systems and fuel tanks can be provided for inspection and maintenance purposes without disturbing any LFC surface. Laminarized surfaces in areas susceptible to foreign-object damage are eliminated. The possibility of fuel leakage into the LFC panels and ducting is avoided. The initial cost and maintenance costs are reduced. A shield for contamination avoidance can be deployed forward of the wing leading edge which can be retracted into the unlaminarized lower surface when not required. The contamination-avoidance shield will be discussed in more detail later.

CURRENT DESIGN APPROACHES Leading-Edge Protection Systems

Questions are continuously raised about the significance of airborne insects on the practicality of attaining and retaining laminar flow in flight. Are insects really a problem for transport aircraft? If so, isn't that sufficient reason to dispute the practicality of laminar-flow concepts? Is there any effective method of eliminating the adverse effects of insects if they are, in fact, significant?

With respect to the first question, the degree to which insects may be a problem varies with geographic location, season of the year, and local atmospheric conditions. The fact that insects do, in fact, adhere in the wing leading-edge region is evident from observations of transport and other aircraft as well as from some flight tests with a Jetstar airplane made specifically for this purpose in this program. Figure 36 presents the maximum height of insect accretion permissible in the most sensitive regions near the wing leading edge for no premature boundary-layer transition at a cruise Mach number of 0.8, as obtained for unswept wings from Reference 14. It is possible that even these low values may be somewhat optimistic in that a limited amount of data indicates an aggravating effect of wing sweep on permissible roughness (Ref. 13). The favorable effect on permissible height of increased cruise altitude is indicated.

A conservative assumption was made in this program that insect accumulations could be significant, at least for some seasons and geographical locations, so that efforts were made to develop practical means for alleviating the adverse effect. Results to this point in time are quite encouraging. The first part of the program involved flight tests at the NASA-Dryden Flight Research Facility with a Jetstar airplane under airline operating flight conditions. The Jetstar was instrumented to detect transition on the outboard leading-edge flap and equipped with a system to wet the leading edge in flight (Fig. 37). The significant results were: use of superslick or hydrophobic coatings does not offer a complete solution; low cruise temperatures and high cruise Mach numbers are ineffective in a hoped-for erosion of accumulated insect residue; wetting the wing leading-edge region during insect encounter is effective in prevention of insect accumulation although washing the surface after insect accumulation did not sufficiently remove the residue (Ref. 15). Follow-on wind-tunnel tests (Ref. 16) of liquid ejection through a combination liquid ejection-air suction slot system indicated an effectiveness of surface wetting in prevention of insect adhesion to the surface (Fig. 38). Use of a freezing-point depressant as the wetting fluid provides the dual function of anti-icing.

A second leading-edge protection approach offering promise was developed for the LFC concept with laminarization of the upper surface only (Ref. 17). In this case, a retractable shield is used as the primary contamination avoidance device. The shield, which also serves as a leading-edge high-lift device, provides line-of-sight protection of the wing leading edge from insect impingement (Fig. 39). A supplemental freezing-point depressant is sprayed on the wing upper surface to provide an additional precaution against insect adhesion and to provide protection against icing. Insect trajectory analyses and wind-tunnel tests indicate complete shielding of the upper surface during climb and other high angle-of-attack conditions. The supplemental spray is required to shield against small insects during operation at low angles of attack such as during take-off roll and descent. Flight validation in simulated airline flight profiles will be accomplished for both of these approaches to alleviate the potential insect-contamination problem (Ref. 18).

Suction System

The objective of the suction system is to maintain laminar boundary-layer flow through an efficient removal of part of the low-energy boundary-layer air on the surface. The system design must satisfy the stringent requirements for surface smoothness and waviness, must be compatible with production-environment manufacturing procedures and with in-service inspection, maintenance, and repair capabilities, and must provide a high degree of reliability with imposition of minimum airframe weight and cost.

penalties. The basic elements of the system include the suction surface through which the air is sucked, a system for metering the level and distribution of the ingested flow, a ducting system for collecting the flow, and pumping units which provide sufficient compression to discharge the suction flow at a velocity at least as high as the airplane velocity (Fig. 40).

Although the schematic of Figure 40 illustrates the use of multiple slots, the suction surface may be also fabricated with a porous material or perforated. Early studies of numerous methods of fabricating porous surfaces using various materials failed to yield surfaces that could be satisfactory for both structural and aerodynamic requirements. The program then concentrated on development of surfaces with multiple spanwise slots and with perforations. Very careful design analyses are required for either of these surface types because of the nonuniformity of required suction over the chord and span of a wing, in combination with external variations in surface pressure.

Multiple Slots

Slot Configuration Considerations The design of multiple suction slots must provide flow characteristics that are predictable, stable, uniform along the length of the slots, and free from flow disturbances that would interfere with laminarization. Criteria for slot design developed to meet these requirements are reported in Reference 7. Figure 41 defines the design criteria and a brief description follows. The goal for the parameter $\frac{w}{z}$, the ratio of the slot width to the sucked height, is a range from 1.0 to 1.4. These approximate limits are indicative of slot stability but may be exceeded up to a value of about 2 if the minimum slot width is limited by fabrication considerations. It is desirable to maintain the ratio of the velocity in the boundary layer at the sucked height to the velocity at the edge of the boundary layer U_z/U_e as low as practicable (< 0.3) to limit the influence of suction on the flow outside the sucked boundary layer. The value of β_w should exceed approximately 0.0075. For lower values, separated flow from the forward slot lip may not reattach in the slot with a resultant undesirable destabilizing oscillating flow. The reader should be aware that some references define β_w as $\frac{4b}{wR_w}$ rather than $\frac{b}{wR_w}$. The value of C_{ps} should exceed approximately 0.02 to provide sufficiently uniform flow along the slot and to damp out disturbances from metering holes and acoustic disturbances beneath the slot. The slot Reynolds number R_w is based on the slot width and flow conditions and is indicative of slot-flow stability. The lower the value of R_w , the more viscous and steady the slot flow and the less susceptible the external flow is to slot and internal disturbances. An R_w less than 100 is the goal.

The criteria parameters are interrelated and dependent upon the influences of differences in flight conditions. An analysis of the governing equations of each design criterion (Ref. 16) indicated that β_w , w/z , C_{ps} , and U_z/U_e could all be expressed in terms of slot Reynolds number R_w and slot width w , and properties associated with a specific chordwise location X/C . Evaluation of slot spacing ΔC_N requirements for distributed suction indicated that spacing could be expressed in terms of only R_w and the local distributed-suction rate. A plot of the limiting values of the design criteria, therefore, could be made in terms of R_w as a function of w for each X/C and a plot of the corresponding slot spacing in terms of R_w as a function of ΔC_N for each X/C could be constructed. A sample plot of this very useful interrelationship of the design criteria and slot spacing is shown in Figure 42.

In this sample figure, the upper point within the design boundaries is more favorable from construction considerations than the lower point in that a fewer number of wider slots is required. The lower point, however, is not as close to the U_z/U_e limit and, therefore, is preferable from the performance viewpoint. The final design process involves compromises between the production and performance considerations as the range of cruise design and cruise off-design conditions and wing locations are considered.

Wing Box A crucial concern in the definition of a practical production LFC transport is the wing structural design. Initial studies were performed (Refs. 13, 16, and 17) to define future LFC transports and the required systems. Structural slotted concepts were selected, and structural, flow and environmental testing were performed to establish concept feasibility (Fig. 43). Structural components were subjected to lightning strikes, corrosion, impact damage and icing. Other tests included moisture exposure, fatigue, residual strength, and compression tests. Figure 44 illustrates there were no significant problems with lightning strikes, corrosion, foreign-object damage and icing. Repair techniques with hand-held tools were developed. These tests demonstrated the feasibility of manufacturing slotted LFC panels within the permissible step/waviness tolerances and developed the needed manufacturing technology for thick graphite/epoxy structures. Considerable effort was devoted to developing methods for producing slots in titanium skins. Methods evaluated included electro-discharge machining, electron-beam cutting, water jet, laser, chem-milling and sawing. The most consistent slot widths were made with the sawing technique which was selected as the approach in these studies.

The slotted wing-box design, illustrated in Figure 45, employs extensive use of graphite epoxy (G/E) composite materials. The primary load-carrying structure is thick G/E wing skin stiffened with integral G/E hat section stiffeners. Titanium sheet, with spanwise slots, is bonded to the G/E wing skins. Suction air passes through the slots

into small plenums molded into the G/E skins and through metering holes to spanwise ducts formed by the hat stiffeners. At every other rib station, the suction air is metered into ducts formed by rib caps of truss ribs. The rib-cap ducts penetrate the front spar web to transfer the suction air into trunk ducts in the leading-edge box. The trunk ducts collect the suction air into independently driven suction pump units located under each wing root. Laminar flow is maintained to 75% chord on upper and lower wing surfaces.

To evaluate the design, an extensive fabrication and testing program (Fig. 46) was undertaken that examined materials, adhesives, cure process variables, structural characteristics, and fabrication techniques. Numerous specimens of a materials verification series (consisting of 68 specimens) have been fabricated and tested. Processes for fabrication of thick G/E skin panels with up to 40 plies and molded slot plenums were developed that produced void free laminates with excellent structural properties. Critical details of the wing surface design were selected for developing manufacturing procedures. The four specimens selected were (the concept selection series in Fig. 46): a rib duct to wing surface element; an integral spar cap section; a chordwise splice joint; and a spar-cap/chordwise splice joint. These specimens were also structurally tested and confirmed design analyses. Fatigue and compression tests performed on the concept verification specimens (Fig. 46) verified the structural feasibility of the design.

For the slotted approach, manufacturing studies, based in part upon the experience gained in the structural specimen fabrication, was a major effort. The data base accrued allowed an assessment of manufacturing costs which was used to reassess benefits evaluated in initial studies reported in Reference 16. A comparison of features of the slotted baseline LFC aircraft with an advanced turbulent aircraft is presented in Figure 47. The turbulent aircraft is designed for the same mission as the LFC aircraft and employs the same technology level. The LFC aircraft has a gross take-off weight that is 8.5% lower than the turbulent aircraft and burns 21.7% less fuel. While the acquisition cost is \$2.4 million higher per aircraft, fuel usage per year indicates that the LFC systems cost would be offset in the first six months of operations with annual fuel cost savings thereafter of nearly \$4 million per aircraft, assuming a fuel price of \$1.50 per gallon.

Leading-Edge Box The leading-edge region of a laminar-flow wing represents a difficult technical and design challenge. The leading edge is subject to insect impacts (as previously discussed), foreign object damage, erosion, and ice contamination. The required systems for protection from insect contamination and anti-icing must be designed to perform synergistically with the required suction system in the limited volume available. These problems are exacerbated by the fact that suction requirements are large in the leading edge due to the need to control the boundary-layer crossflow instabilities present. These large suction requirements may in turn mean that design criteria are pushed to the limit or exceeded, that slots be closely spaced or that porous surfaces be designed with special considerations for pressure drop and chordwise inflow/outflow.

As for the case of the slotted wing-box design, many slotted leading-edge concepts were evaluated (Ref. 16). The approach selected evolved as a result of extensive design studies and development testing. These studies focused on addressing special concerns associated with systems and structures, including development of leading edge insect/anti-icing protection systems and development of practical, reliable structures which meet the more stringent external smoothness and waviness requirements of the leading edge. Evaluation of the slotted suction-panel designs also included considerations of suction duct efficiency, weight, cost, integrity, manufacturability and repairability. Concepts were fabricated and flow tested to evaluate and improve upon configurations of slot, slot plenum, collector ducts and metering holes. Structural specimens were subjected to tension, compression, bending and fatigue tests. Repairability tests were also performed. The slotted leading-edge concept selected (Refs. 16 and 19) is illustrated in Figure 48 and involves suction through fine spanwise slots (0.004 inch width) on both the upper and lower surfaces to the front spar. No leading-edge high-lift device is required. A 0.016 inch thick titanium outer sheet is bonded to a sandwich substructure of graphite epoxy face sheets with a Nomex honeycomb core. The suction flow is routed through the structure by a combination of slot ducts, metering holes and collector ducts embedded in the honeycomb. Six slots in the leading edge serve the dual purpose of providing a protective fluid film for both insect protection and anti-icing. These slots are purged of fluid during climbout and join the other suction slots for laminarizing the boundary layer in cruise. The feasibility of this concept for protecting the leading edge against insect residue was verified in wind-tunnel tests as discussed in an earlier section. Flight evaluation of the slotted leading-edge concept is currently in progress (Ref. 18).

Perforated Surface

Perforation Configuration Considerations The aerodynamic feasibility of perforated suction surfaces at transport flight conditions has not yet been completely established. The aerodynamic uncertainty regarding perforated surfaces involves the possibility of premature transition due to introduction of perforation-induced disturbances, which, based on limited previous data for circular holes, is dependent upon perforation geometry (diameter, spacing) and suction flow rate in combination with the unit and length Reynolds numbers.

Based on previous tests and physical reasoning, the perforation configuration parameters that are most significant to the ability to maintain large extents of laminar flow are: δ/d , the ratio of the boundary-layer thickness to perforation diameter, which should be as large as possible; R_d , a local Reynolds number based on the velocity through a hole and the hole diameter, which should be as small as possible; and s/d , the ratio of hole spacing to hole diameter, which should be equal to about 10. Results of hand calculations based on unswept flat-plate boundary layers for simplicity are presented in Figures 49, 50, and 51 to indicated principal trends. The ratio δ/d is plotted against chordwise location from the leading edge of an unsucked flat plate at a unit Reynolds number of $1 \times 10^6/\text{ft}$ in Figure 49 for perforation diameters of 0.0040, 0.0028, 0.0020, and 0.0014 in. Regardless of suction flow requirements, the decrease of δ/d near the leading edge is obvious and the need to decrease d is apparent. The absence of a rigid criterion on the minimum permissible value of δ/d led to the concern about the maximum permissible d in the thin boundary-layer region near leading edges. The hole diameter Reynolds number R_d is plotted against suction flow coefficient C_q in Figure 50 for the same hole diameters with spacings of 0.010, 0.020, and 0.040 in. These data are cross plotted against hole spacing for two values of C_q in Figure 51. Figures 50 and 51 indicate that for any given value of C_q , as d is decreased (as desired for larger δ/d), the hole spacing s must be decreased in order to decrease R_d as desired. Fortunately, this trend is compatible with the previous experimental determination that a small spacing of the holes with respect to the hole diameter is required to minimize formation of undesirable vortices at each individual hole. The previous data indicated that a value of s/d of about 10 should be satisfactory.

From the preceding trends, it is apparent that to maximize δ/d and minimize R_d while maintaining s/d at about 10, it is necessary to minimize hole diameter. The smallest diameter holes developed in the current program with clean edges and a satisfactory variation of diameter through the material were produced with the electron-beam technique. Photomicrographs of the selected configuration are presented in Figure 52. Low-speed wind-tunnel tests of this configuration in the critical leading-edge region yielded laminar flow. These tests were made at a unit Reynolds number of $1.2 \times 10^6/\text{ft}$ whereas the value for transport flight at 38,000 ft altitude at a Mach number of 0.8 is 1.68×10^6 . An increase in unit Reynolds number decreases δ/d and increases R_d for a given perforation geometry (d and s), both in an adverse direction. Laminar flow was also attained in the wind tunnel at the lower R/ft , however, with larger perforations of 0.004 in. diameter, which increases the confidence that laminar flow will be obtained at the larger flight value of R/ft with the smaller perforations of 0.0026 in. in the leading-edge region. A question still remains as to the possibility of a continual reinforcement of hole disturbances as suction through holes is continued downstream.

Another design consideration that requires careful analysis is that of appraising the relationships between perforated-surface porosity, the subsurface suction pressure, and the integrated suction flow rate in regions where the chordwise pressure gradient is steep, e.g., in the wing leading-edge region. The interrelationships among these variables are illustrated in Figure 53. The value Q has been defined as the surface porosity in terms of flow quantity per unit area for a given pressure differential across the surface.

To prevent outflow of air in any given flute (a condition to be avoided because of severe adverse impact on transition), the subsurface flute pressure P_{sub} must be equal to or lower than P_2 , the lowest external pressure over the chordwise extent of the flute. For the value of $P_{\text{sub}} = P_2$, a porosity of Q_{max} is required for the integrated suction flow rate across the flute to be equal to the integrated theoretical design value. For a porosity greater than Q_{max} , the integrated flow rate is greater than the theoretical value required. More suction than required is to be avoided as indicated in a previous section. If the porosity is lower than Q_{max} , attainment of an integrated flow rate equal to the theoretical value requires a subsurface pressure P_{sub} lower than the minimum external pressure P_2 . For this case, some inflow - rather than zero flow - occurs at the minimum pressure station 2. This case also gives a smoother suction velocity profile than that obtained with more porous surfaces and an increased tolerance to external pressure variations resulting from surface contour variations, spanwise design variations, and off-design conditions.

The chordwise widths of the open flute areas and of the blocked surface areas affect the porosity--pressure drop-flow rate relationships. For example, an increase in the ratio of open flute chord to blocked chord necessitates a lower surface porosity so that the higher pressure drop across the surface required for no outflow (higher external pressure differential subtended by the flute) will not increase the integrated flow rate above the theoretical value due to the resultant increase in suction velocity. A decrease in open-chord ratio, of course, results in the opposite effects.

Surface Panel The selected perforated surface (Ref. 17) was fabricated of 0.025 in. thick 6AL4V titanium alloy sheet drilled by Pratt and Whitney Aircraft using EB-perforating equipment produced by Steigerwald Strahltechnik GMBH in Germany. The taper of the holes shown in Figure 52 is a natural outcome of the EB process and attenuates the possibility of clogging the holes from surface particles. The Steigerwald chart of Figure 54 confirms that the selected configuration is pushing the

state of the art with respect to hole size and material thickness and that the hole production rate is quite rapid. Figure 52 shows that the holes are of true circular shape at the outer surface. The EB-perforated surface was bonded directly to a corrugated fiberglass substructure to form a simple LFC glove panel (Fig. 55).

Selection of the final glove panel arrangement was preceded by much fabrication development and environmental and structural testing. Results indicate that the EB-perforated titanium glove panel provides a tough, corrosion-resistant, effectively smooth, and easily cleaned LFC surface that can be worked satisfactorily to strain levels corresponding to those of an advanced-technology wing structure. This conclusion is partially based on the types of environmental tests indicated in Figure 56. Examples of results are presented in Figures 57 and 58. Figure 57 shows the reduction of porosity of an EB-perforated titanium sheet after a long-duration exposure to a contaminating environment on a building roof near an airport. The original porosity was completely restored by a simple steam cleaning from the outer surface with a simple hand-held steam-cleaning wand. The curves of Figure 58 show that the impact resistance of the EB-perforated titanium sheet is better than that of a thicker 7075-T6 aluminum alloy sheet material commonly used for airplane leading edges.

Wing Box The main wing box (Refs. 17 and 20) is formed by internal blade-stiffened graphite epoxy wing covers (Fig. 59). Suction panels are gloved to the main wing box and suction air collection is external to the wing box. The EB-perforated titanium sheet is bonded to a fiberglass sandwich panel with a corrugated core forming flutes for subsurface airflow transfer. The impervious bond areas divide the panel surface such that perforated-strip suction occurs at the surface. The suction panels are attached to generally chordwise oriented blades on the outer surface of the wing-box cover. These blades form ducts for suction air collection into trunk ducts in the leading-edge box. This collection scheme is advantageous, over for example spanwise air collection, because the quantity of airflow and the collection distance are such that the ducts can be comparatively shallow with a minimum loss in structural depth. Wing bending efficiency, therefore, is only slightly compromised. Behind the rear spar and in the leading-edge box, air collection is in spanwise ducts. In the development of the perforated-surface wing-box concept, emphasis was placed on the structural development of practical suction panels, as indicated in the previous section. The assumption was made that sufficient technology for the primary wing structure will evolve from other ongoing programs.

Leading-Edge Box With the selection of suction on the upper surface only, the elimination of suction systems and the stringent surface smoothness requirements from the lower surface permits the use of a Krueger leading-edge protection shield and high-lift device. A principal problem in the design of the leading-edge box was the definition of a geometry that would provide for both the air suction system and the Krueger flap in the limited volume available. Figure 60 is a schematic of the selected arrangement (Refs. 17, 21 and 22). Similar to the wing-box region described in the previous section, the concept for the perforated leading-edge surface is a perforated-strip approach with about 60% of the surface perforated and about 40% blocked where the skin bonds to the land area of the corrugated substructure. The suction ducts or flutes collect the sucked air which is routed to the suction source. Spray nozzles are mounted on the Krueger underside to supplement the insect-protection capability of the shield or to provide a coating of anti-icing fluid for leading-edge icing protection. A system for purging fluid from the suction flutes and surface perforations is provided, if required. The leading edge of the shield itself is provided icing protection through the use of a commercially available ice-protection system manufactured by TKS, Ltd. The perforated leading-edge concept is undergoing flight evaluation in the same program as the slotted leading-edge concept (Ref. 18).

Natural Laminar Flow and Hybrid Laminar-Flow Control

While this paper addresses systems for laminar-flow control, i.e., the maintenance of laminar flow to large chordwise extents by active wall suction, the systems developed for the leading-edge region are equally applicable for natural laminar-flow and hybrid laminar-flow-control concepts. More limited regions of laminar flow than that possible with laminar-flow control may be attainable through design with favorable pressure gradients over part of the wing (decreasing surface pressures in the direction of the flow). Adverse cross-flow effects induced by sweep of the leading edge, necessary for cruise at high subsonic speeds, limit the extent of natural laminar flow attainable. Recent boundary-layer stability analyses, however, indicate that wing sweep angles up to about 17°, corresponding to a lower cruise speed than today's transports, may be permissible. Verification of the analytical predictions is being pursued in a flight-test program of a natural laminar-flow airfoil incorporated in partial gloves on the wings of a variable-sweep airplane. Results will help define the types of airplane for which natural laminar flow may be feasible. For any type, smoothness of surface finish and contour must be provided as well as leading-edge protection from insect-residue and ice accumulation, as in the case for laminar-flow control.

A combination of the principles for laminar-flow control and natural laminar flow may find application to large high-speed transports (Fig. 61). Suction in the leading-edge region, where the cross flow due to sweep is large, may be used to control the cross-flow disturbances, and favorable pressure gradients, not large enough to induce unacceptable cross flow, may be used aft of the front spar to maintain natural laminar flow to the vicinity of midchord (Ref. 23). Such a hybrid approach may provide more extensive laminar flow than possible with natural laminar flow at high sweeps, and has

the advantage of avoiding the complexities associated with providing suction in the region of the wing torsion box where fuel is stored. Analysis of the feasibility of this hybrid concept is underway.

CONCLUDING REMARKS

Results of this program to date indicate that LFC configurations utilizing either slotted-surface or perforated-surface structural arrangements should result in practical LFC transport aircraft that provide substantial reductions in fuel usage and direct operating costs as compared with equally advanced turbulent configurations. Continued efforts are necessary for further development of efficient LFC structures and for flight validation of LFC reliability and economics under realistic operating conditions.

REFERENCES

1. Bushnell, Dennis M., and Tuttle, Marie H.: Survey and Bibliography on Attainment of Laminar Flow Control in Air Using Pressure Gradient and Suction. NASA Reference Publication 1035, Vol. I, Sept. 1979.
2. White, R. C., Sudderth, R. W., and Wheldan, W. G.: Laminar Flow Control on the X-21. *Astronautics and Aeronautics*, July 1966.
3. Hall, G. R.: On the Mechanics of Transition Produced by Particles Passing Through an Initially Laminar Boundary Layer and the Estimated Effect on the LFC Performance of the X-21 Aircraft. Northrop Corp., Oct. 1964.
4. Nastrom, G. D., Holdeman, J. D., and Davis, R. E.: Cloud-Encounter and Particle-Concentration Variabilities from GASP Data. NASA TP-1886, Dec. 1981.
5. Jaspersen, W. H., Nastrom, G. D., Davis, R. E., and Holdeman, J. D.: GASP Cloud- and Particle-Encounter Statistics, and Their Application to LFC Aircraft Studies. Volume I, Analysis and Conclusions and Volume II, Appendixes. NASA Technical Memorandum 85835, Oct. 1984.
6. Davis, R. E., and Fischer, M. C.: Cloud Particle Instrumentation for the Laminar Flow Control Leading Edge Flight Test. AIAA Paper No. 83-2734, Nov. 1983.
7. Staff, LFC Engineering Section: Final Report on LFC Aircraft Design Data, Laminar Flow Control Demonstration Program. NOR 67-136, Northrop Corporation, Norair Division, June 1967. (Available from DDC as AD819317).
8. Nenni, J. P. and Gluyas, G. L.: Aerodynamic Design and Analysis on an LFC Surface. *Astronautics and Aeronautics*, July 1966.
9. von Doenhoff, A. E. and Braslow, A. L.: The Effect of Distributed Surface Roughness on Laminar Flow. Lachman, G. V., *Boundary Layer Control-Its Principles and Applications*, Vol. 2, Pergamon Press, 1961.
10. Swift, G. and Munger, P.: A Study of the Prediction of Cruise Noise and Laminar Flow Control Noise Criteria for Subsonic Air Transports. NASA CR159104, Aug. 1979.
11. Tibbetts, J. G.: Near-Field Noise Prediction for Aircraft in Cruising Flight-Methods Manual. NASA CR159105, Aug. 1979.
12. Stokowski, A. J. and Orszag, S. A.: Mass Flow Requirements for LFC Wing Design. AIAA Paper No. 77-1222, Aug. 1977.
13. BCAC Preliminary Design Department: Evaluation of Laminar Flow Control System Concepts for Subsonic Commercial Transport Aircraft. NASA Contractor Report 158976, Dec. 1978.
14. Braslow, A. L. and Knox, E. C.: Simplified Method For Determination of Critical Height of Distributed Roughness Particles for Boundary-Layer Transition at Mach Numbers From 0 to 5. NACA TN 4363, Sept. 1958.
15. Fisher, D. F. and Peterson, J. B., Jr.: Flight Experience on the Need and Use of Inflight Leading-Edge Washing for a Laminar Flow Airfoil. AIAA Paper 78-1512, Aug. 1978.
16. Lockheed-Georgia Company: Evaluation of Laminar Flow Control System Concepts for Subsonic Commercial Transport Aircraft. NASA Contractor Report 159253, Sept. 1980.
17. Pearce, W. E.: Evaluation of Laminar Flow Control Systems Concepts for Subsonic Commercial Transport Aircraft. Executive Summary. NASA CR 159251, June 1983.
18. Fischer, M. C., Wright, A. S., Jr., and Wagner, R. D.: A Flight Test of Laminar Flow Control Leading-Edge Systems. NASA TM 85712, Dec. 1983.
19. Etchberger, F. R.: Laminar Flow Control Leading Edge Glove Flight - Aircraft Modification Design, Test Article Development, and Systems Integration. NASA CR-172136, Nov. 1983.

20. Pearce, W. E.: Progress at Douglas on Laminar Flow Control Applied to Commercial Transport Aircraft. Presented at NASA-Dryden Flight Research Center, Sept. 1981.
21. McNay, D. and Allen, J.: Laminar Flow Control Leading Edge Glove Flight Test Article Development. Presented at the NASA-Dryden Flight Research Center, Sept. 1981.
22. Anon., Douglas Aircraft Company Staff, Laminar Flow Control Leading Edge Glove Flight Test Article Development. NASA CR 172137, Nov. 1984.
23. Wagner, R. D., Maddalon, D. V., and Fischer, M. C.: Technology Development for Laminar Boundary Layer Control on Subsonic Transport Aircraft. AGARD-CP-365, Aug. 1984.

TABLE I.- PROBABILITY OF ENCOUNTERING VARIOUS LEVELS OF AVERAGE CLOUDINESS ON SEVEN LONG-RANGE AIRLINE ROUTES, AS ESTIMATED FROM A GAMMA PROBABILITY DISTRIBUTION

Route	Altitude, kft					
	28.5-33.5		33.5-38.5		38.5-43.5	
California - Hawaii	22	52.4	177	37.2	2	
	9.4	32.5	5.5	17.4		
	17.3	8.7	24.7	2.1		
	47.6	1.2	62.8	=0		
East Coast - West Coast (USA)	3		58	46.2	13	14.0
			7.5	25.9	2.4	2.8
			20.1	5.3	41.3	=0
			53.8	0.4	86.0	=0
West Coast - Northwest Europe	6	53.8	26	16.9	26	17.8
	9.9	34.0	2.7	4.0	2.8	4.4
	16.7	9.9	38.6	0.1	37.7	0.1
	46.2	1.4	83.1	=0	82.2	=0
East Coast - Northwest Europe	38	52.1	99	47.7	24	23.1
	9.3	32.2	7.9	27.4	3.4	7.1
	17.5	8.7	19.5	6.0	33.5	0.3
	47.8	1.1	52.3	0.6	76.9	=0
Australia - SE Asia	16	49.4	20	51.0	No data	
	8.4	29.2	8.9	30.9		
	18.7	7.0	18.0	7.9		
	50.6	0.7	49.0	0.9		
West Coast - Japan (westbound)	4		30	26.2	14	12.1
			3.8	9.1	2.2	2.1
			31.3	0.5	43.5	=0
			73.8	=0	87.9	=0
West Coast - Japan (eastbound)	No data		12	51.0	29	24.7
			8.9	30.9	3.6	8.1
			18.0	7.9	32.3	0.3
			49.0	0.9	75.3	=0

Code: No. of flights	P(TIC _P > 5 %), %
TIC _R , %	P(TIC _P > 10 %), %
P(TIC _P < 1 %), %	P(TIC _P > 25 %), %
P(TIC _P < 5 %), %	P(TIC _P > 50 %), %



Figure 1. Factors affecting laminar flow

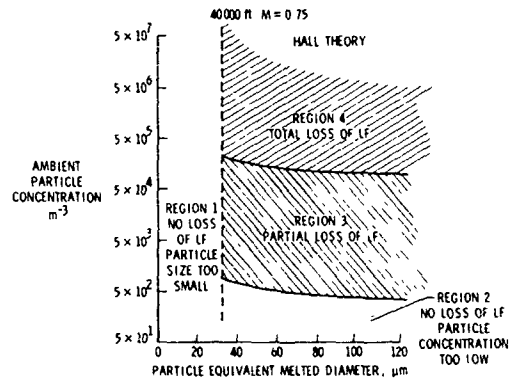


Figure 2. Effect of atmospheric ice crystals on laminar flow

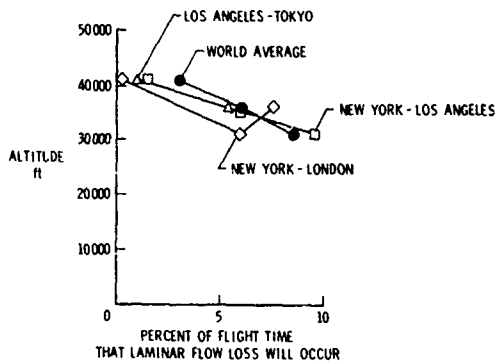


Figure 3. Potential laminar flow loss without flight management

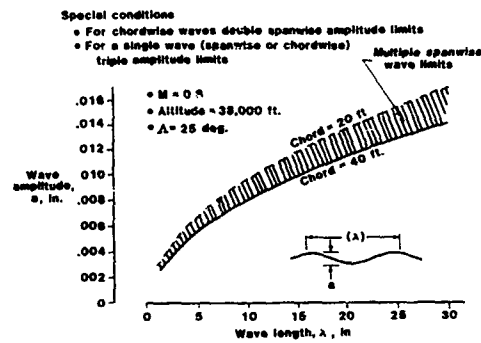


Figure 4. Typical permissible surface waviness

FORWARD FACING STEPS

ALLOWABLE STEP HEIGHT FROM

$$\frac{R}{FT} \times h, FT. = 1800$$

WHERE h = STEP HEIGHT

AFT FACING STEPS

ALLOWABLE STEP HEIGHT = 1/2 VALUE FOR FORWARD FACING STEP

GAPS (FLOW ACROSS)

ALLOWABLE GAP WIDTH FROM

$$\frac{R}{FT} \times g, FT. = 15,000$$

WHERE g = GAP WIDTH

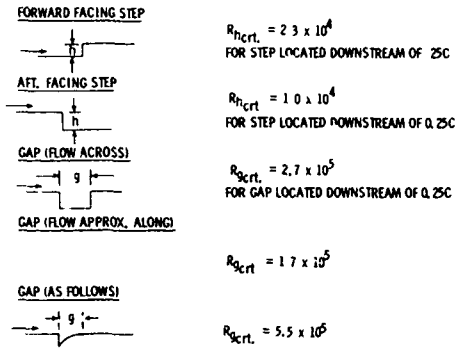
GAPS (FLOW ALONG)

GAPS WITH FLOW ALONG GAP SHOULD DEFINITELY BE AVOIDED (CRITERION = 1/7 g FOR FLOW ACROSS GAP) FROM NORAIR ORAL REVIEW

Figure 5. Tolerance criteria for two-dimensional type surface discontinuities - independent of distance from leading edge

	M _∞ = .8	M _∞ = .8	M _∞ = .8
ALTITUDE = 20 000 ft.	ALTITUDE = 30 000 ft.	ALTITUDE = 38,000 ft.	
Re _∞ /ft. = 3.16 x 10 ⁶	Re _∞ /ft. = 2.25 x 10 ⁶	Re _∞ /ft. = 1.68 x 10 ⁶	
FORWARD FACING STEP	h, INCHES = .007	.010	.013
AFT FACING STEP	h, INCHES = .0035	.005	.0065
GAP (FLOW ACROSS)	g, INCHES = .057	.080	.107
GAP (FLOW ALONG)	g, INCHES = .008	.011	.015

Figure 6. Typical permissible two-dimensional type surface discontinuities - from Figure 5 criteria



NOTE ABOVE EXPRESSIONS ARE FOR h OR g IN INCHES

Figure 7. Tolerance criteria for two-dimensional type surface discontinuities - somewhat dependent on distance from leading edge

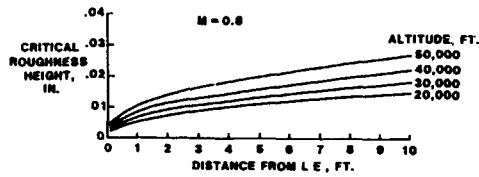


Figure 9. Typical permissible three-dimensional type surface protuberances

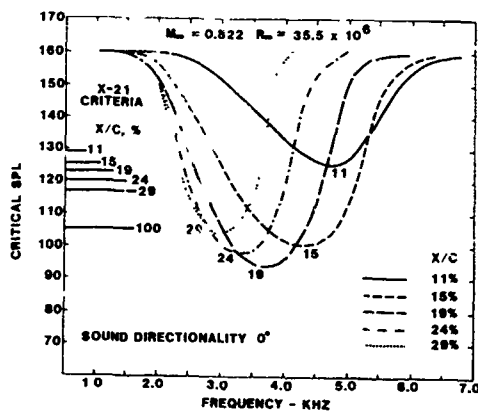


Figure 11. Sensitivity of critical SPL to noise frequency

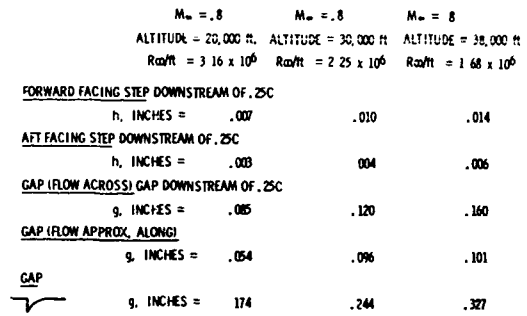


Figure 8. Typical permissible two-dimensional type surface discontinuities - from Figure 7 criteria

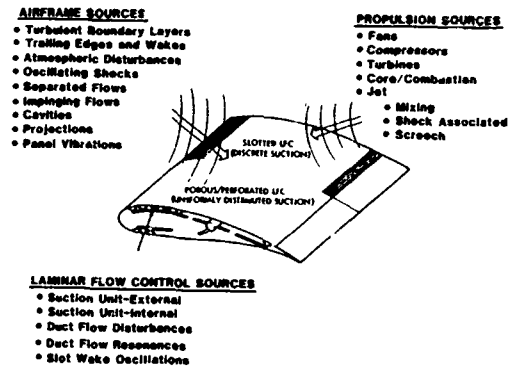


Figure 10. Noise sources on LFC aircraft

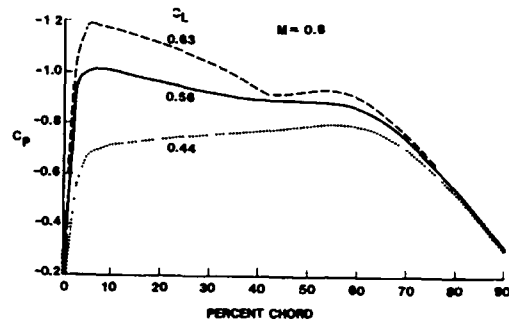


Figure 12. Effect of lift coefficient on upper surface chordwise pressure distribution

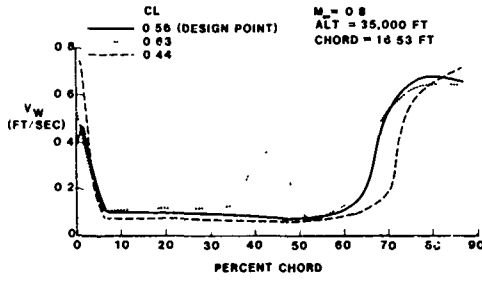


Figure 13. Effect of lift coefficient on upper surface suction requirements

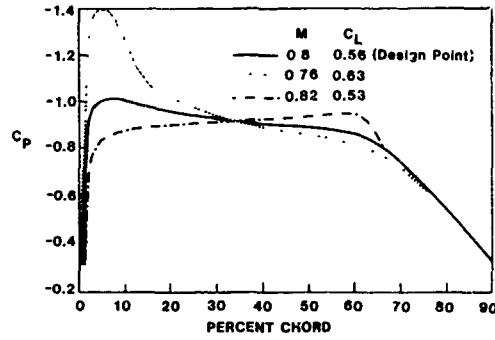


Figure 14. Effect of Mach number on upper surface chordwise pressure distribution; constant aircraft weight and altitude

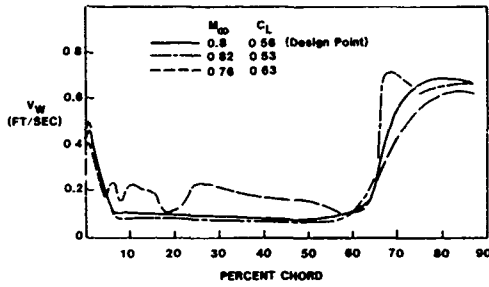


Figure 15. Effect of Mach number on upper surface suction requirements; constant aircraft weight and altitude

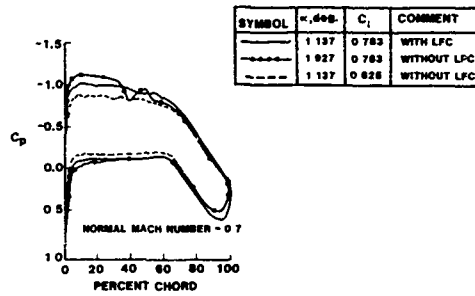


Figure 16. Effect of loss of laminar flow on upper surface chordwise pressure distribution

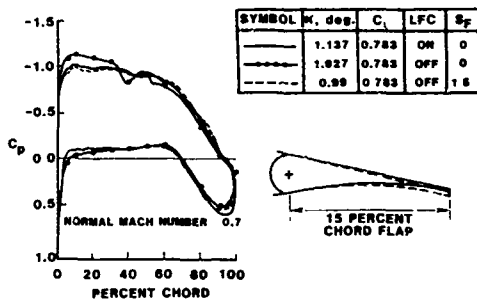


Figure 17. Effect of trailing edge flap on upper surface chordwise pressure distribution with loss of laminar flow

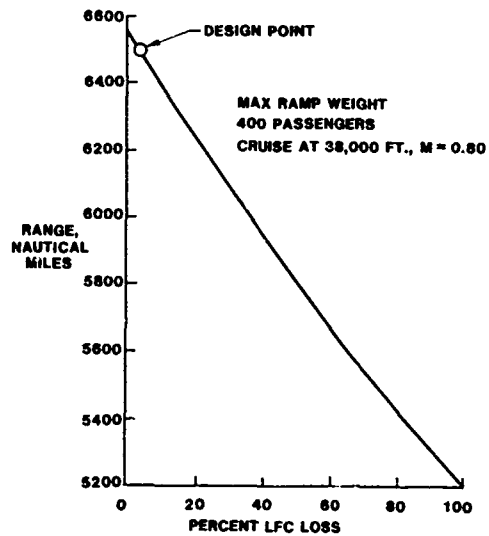


Figure 18. Effect of loss of laminar flow on aircraft range

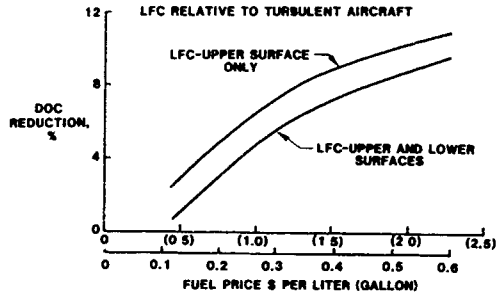


Figure 19. Effect of fuel cost on aircraft direct operating cost

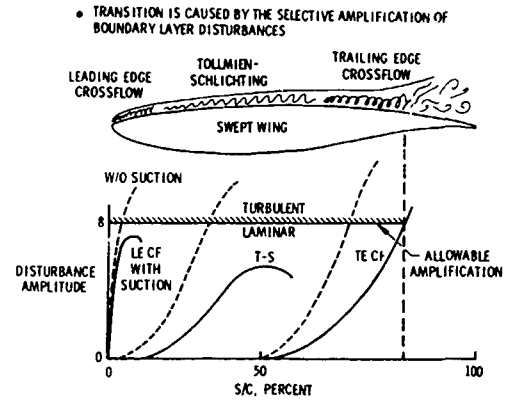


Figure 20. Schematic of effect of suction on crossflow and Tollmien-Schlichting disturbance growth

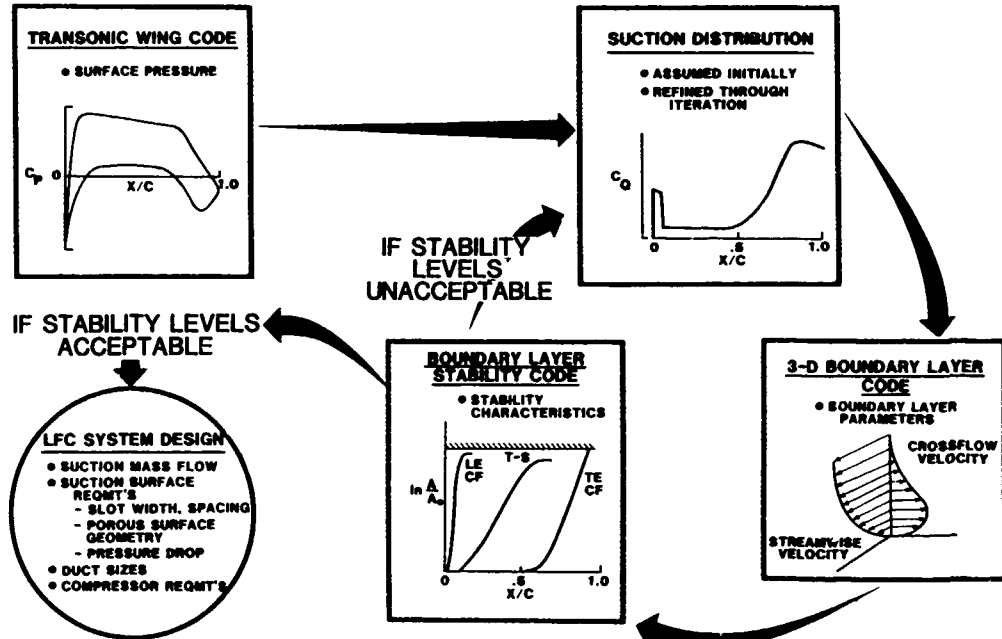


Figure 21. Block diagram of LFC wing design methodology

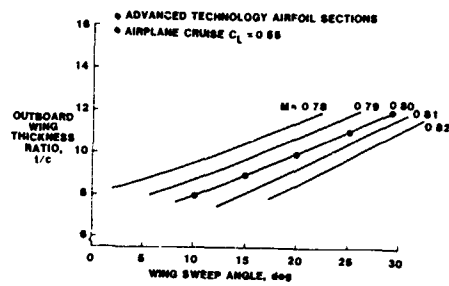


Figure 22. Relationship between wing thickness and wing sweep

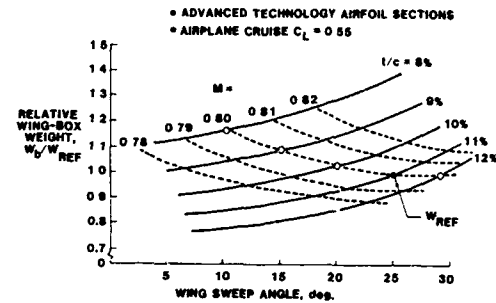


Figure 23. Relationship between relative wing-box weight and wing sweep

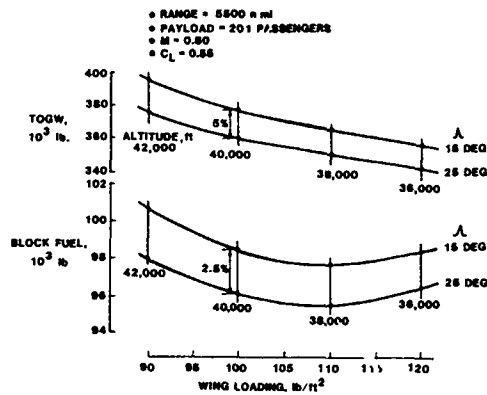


Figure 24. Results of a wing-sweep trade study as a function of wing loading

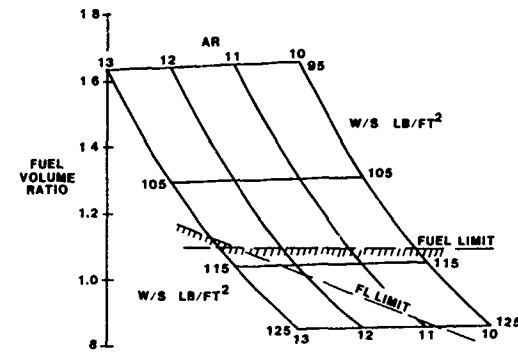


Figure 25. Fuel volume ratios for a matrix of airplanes; 0.8 Mach number, 40,000 feet altitude

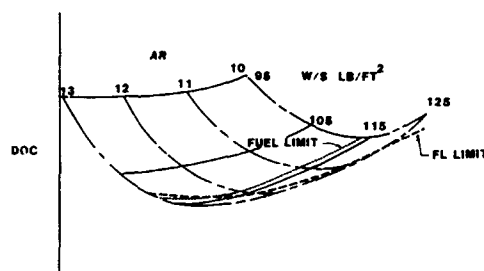


Figure 26. Direct operating costs for a matrix of airplanes; 0.8 Mach number, 40,000 feet altitude

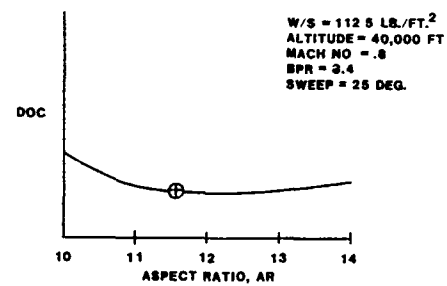


Figure 27. Sensitivity of direct operating cost to aspect ratio

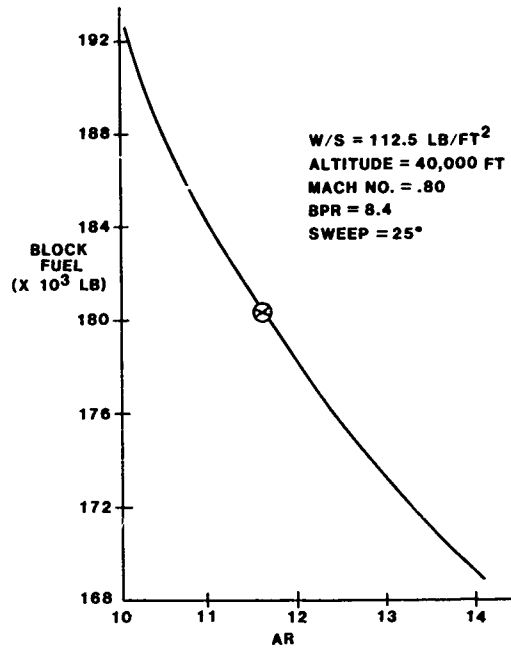


Figure 28. Sensitivity of block fuel to aspect ratio

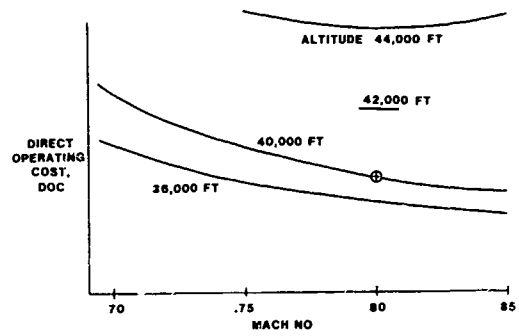


Figure 29. Effect of cruise Mach number and altitude on direct operating cost

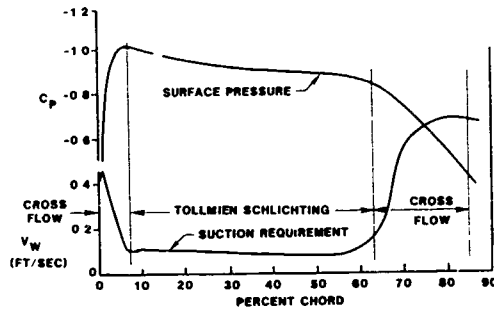


Figure 30. Design point variation of surface pressure coefficient and suction flow velocity with chordwise position

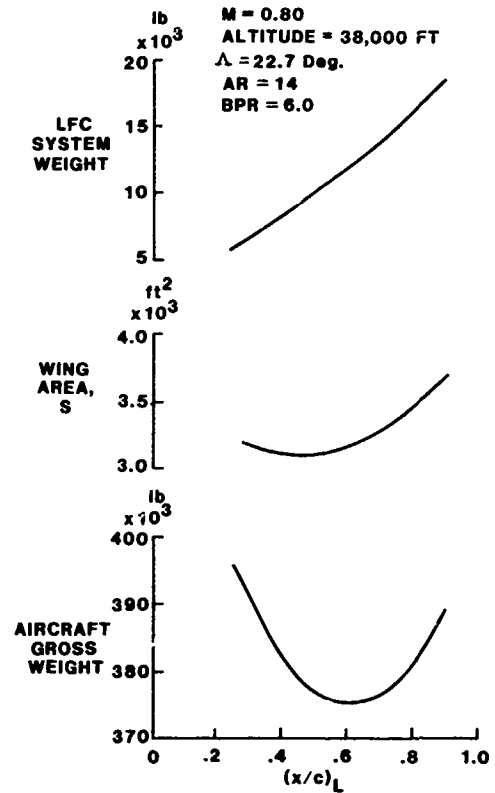


Figure 31. Effect of chordwise extent of laminarization on wing area and LFC system and aircraft weight

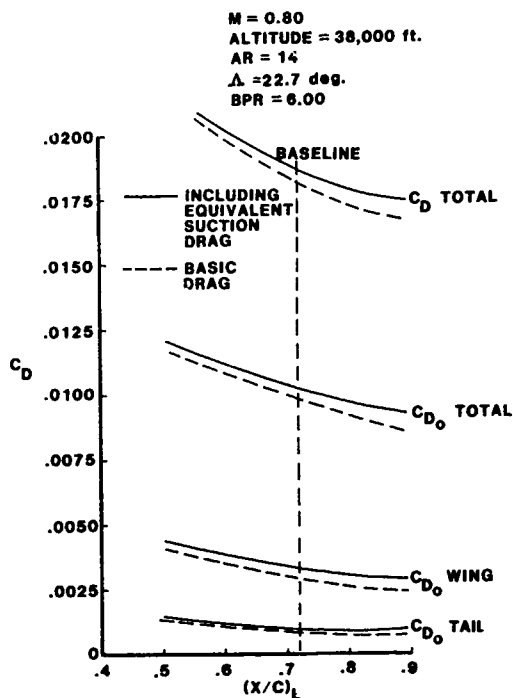


Figure 32. Effect of chordwise extent of laminarization on various component drag coefficients

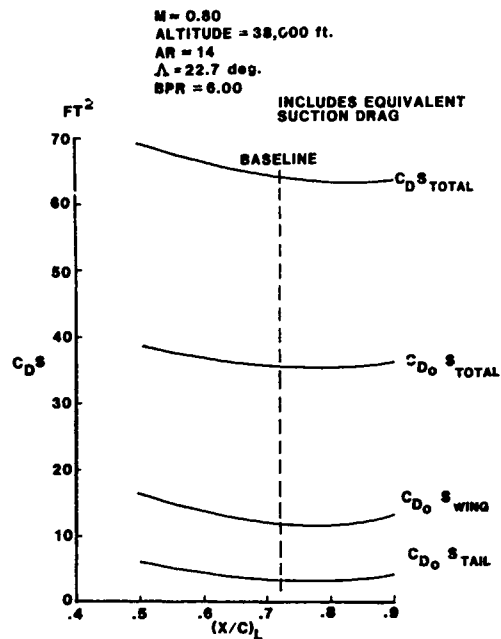


Figure 33. Effect of chordwise extent of laminarization on various component total drags

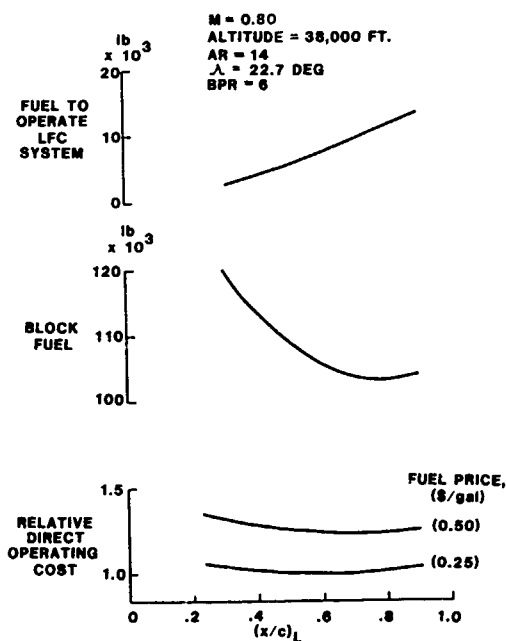


Figure 34. Effect of chordwise extent of laminarization on fuel and cost parameters

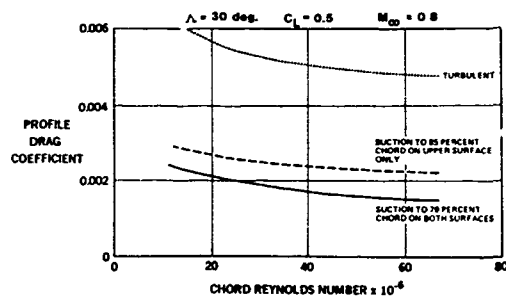


Figure 35. Effect on profile drag coefficient of limiting laminarization to upper surface

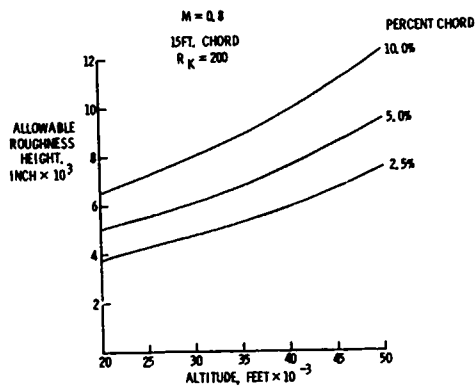
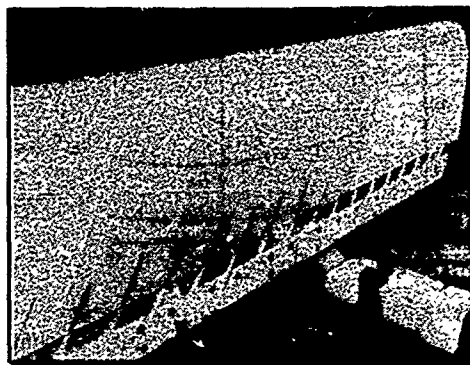
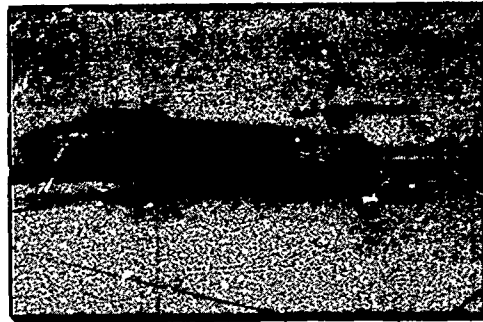


Figure 36. Allowable three-dimensional type roughness near wing leading edge

NASA JETSTAR



L.E. UPPER SURFACE
WITH TOTAL HEAD TUBES.



L.E. LOWER SURFACE
WITH WATER SPRAY NOZZLES

Figure 37. Leading-edge contamination flight test

- 30 deg. swept model
- Insects injected into freestream
- Velocities up to 154 kts.
- Angle-of-attack to 15 deg.



Conclusion - Fluid dispensed through slots in leading edge provided protective surface film on the upper and lower surfaces which prevented insects from adhering

Figure 38. Swept wing wind-tunnel model for evaluation of liquid dispensing through slots for protection of leading edge

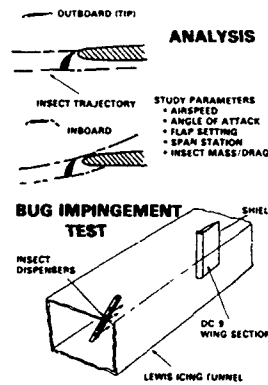


Figure 39. Leading-edge Krueger/insect shield analyses and wind-tunnel tests

RESULTS

KRUEGER EFFECTIVE AS LINE OF SIGHT SHIELD FOR HEAVY INSECTS

ONLY LIGHTEST INSECTS IMPINGE CRITICAL AREA FOR INBOARD STATIONS AT HIGH FLAP SETTINGS

SUPPLEMENTAL LIQUID FILM SYSTEM NEEDED FOR SOME AREAS

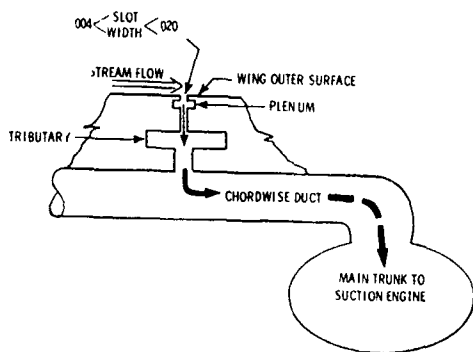


Figure 40. Schematic of basic suction system elements

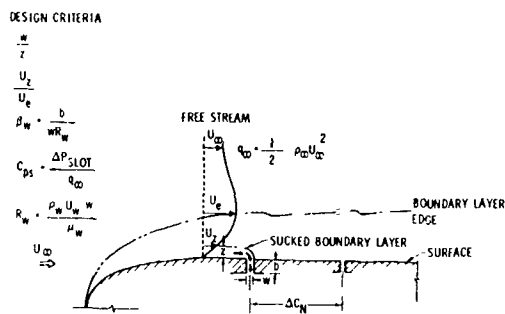


Figure 41. Slotted-surface schematic and design criteria

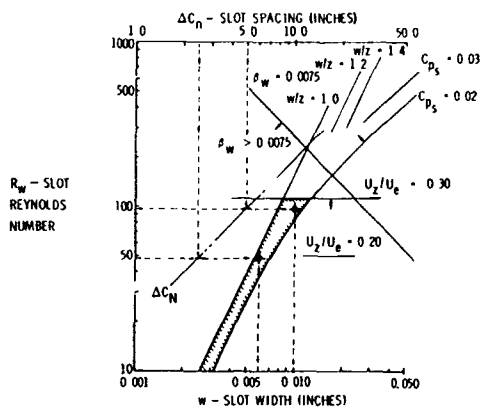


Figure 42. Typical slot criteria envelope

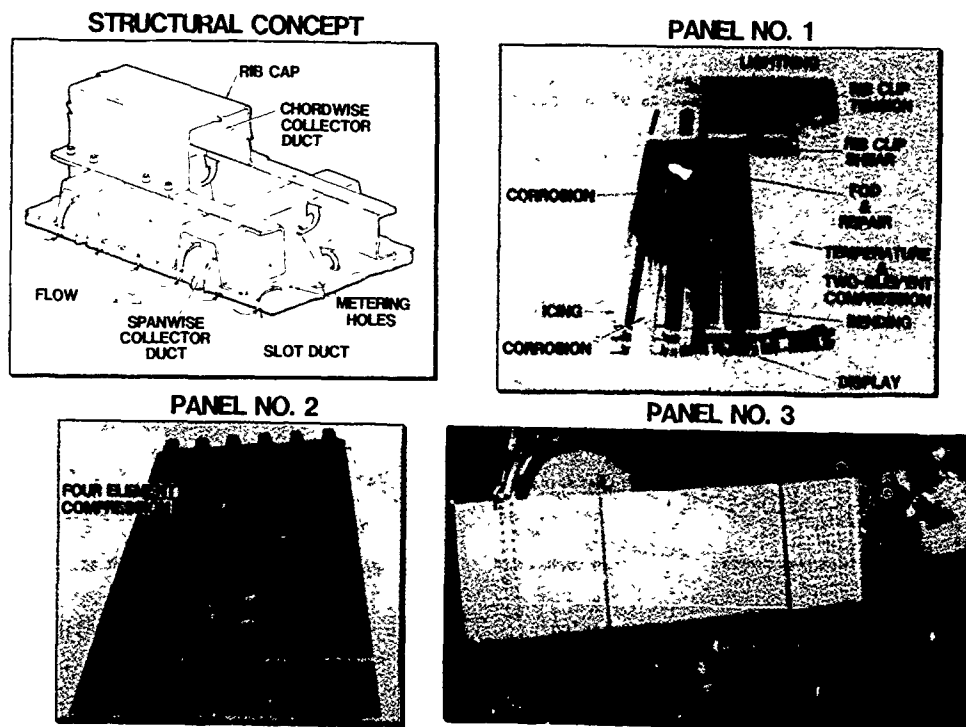


Figure 43. Evaluation tests of slotted-suction concept

- CONCEPT WITHSTANDS LIGHTNING STRIKE, NO CATASTROPHIC FAILURE, SURFACE REPAIRABLE
- CORROSION, ICING, LOW TEMP. NO SIGNIFICANT PROBLEM
- FOREIGN OBJECT IMPACT ONLY A PROBLEM OVER A SLOT (UNSUPPORTED TITANIUM SKIN)
- DAMAGED SLOT CAN BE REPAIRED TO ORIGINAL CONDITION USING HAND HELD TOOLS
- DEMONSTRATED FEASIBILITY OF MANUFACTURING LFC PANEL WITHIN PERMISSABLE STEP/WAVINESS TOLERANCES
- DEVELOPED MANUFACTURING TECHNOLOGY FOR THICK GRAPHITE/EPOXY STRUCTURES

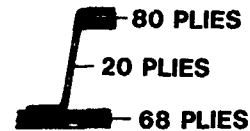
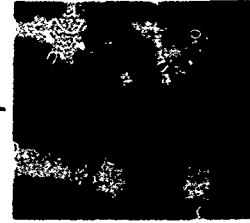


Figure 44. Results of structural development of slotted-suction concept

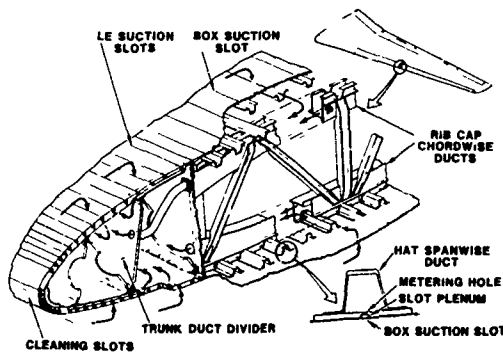


Figure 45. Slotted wing-box design

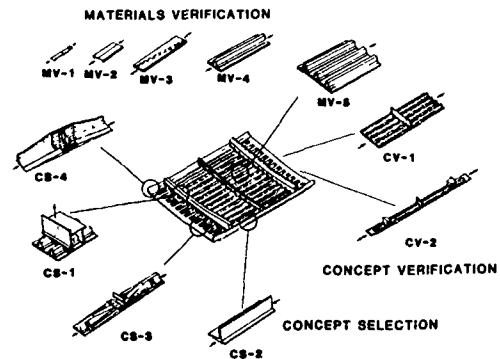


Figure 46. Slotted wing-box fabrication and testing program

M=0.8
400 PASSENGERS
6500 N. M. RANGE

	ADVANCED TURBULENT	LFC	% CHANGE
• TOGW (LBS.)	645,073	590,496	-8.5
• FUEL BURN (LL'S.)	274,073	214,711	-21.7
• ACQUISITION COST (\$M)	79.2	81.1	+2.4
• INCREMENTAL LFC A/C COST (\$M)	—	1.9	—
• INCREMENTAL FUEL COST PER YEAR (\$M) (@ \$1.50 PER GAL. FUEL)	3.9	—	—

Figure 47. Comparison of a slotted LFC aircraft with an advanced turbulent aircraft

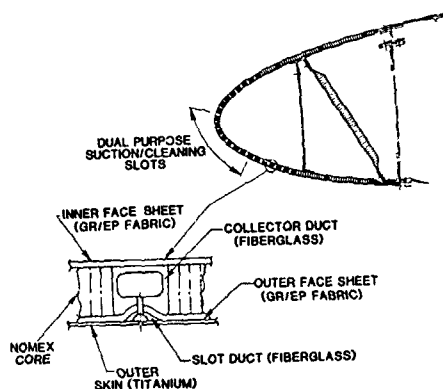


Figure 48. Slotted leading-edge box design

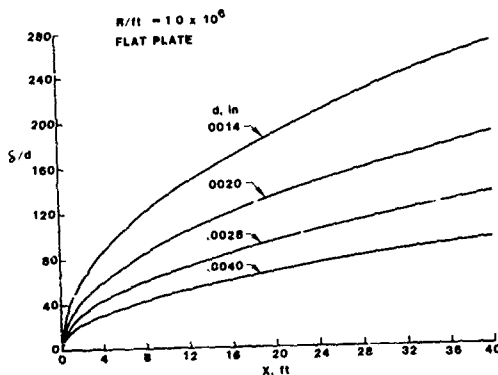


Figure 49. Variation of boundary-layer thickness to perforation diameter ratio with chordwise position

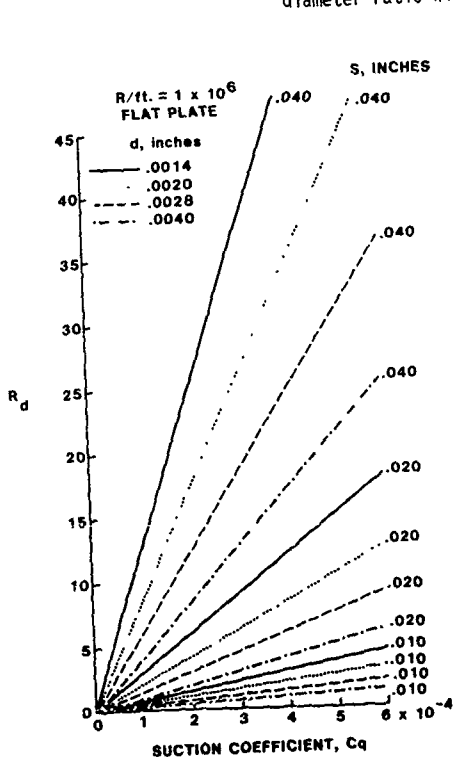


Figure 50. Variation of perforation diameter Reynolds number with suction flow coefficient

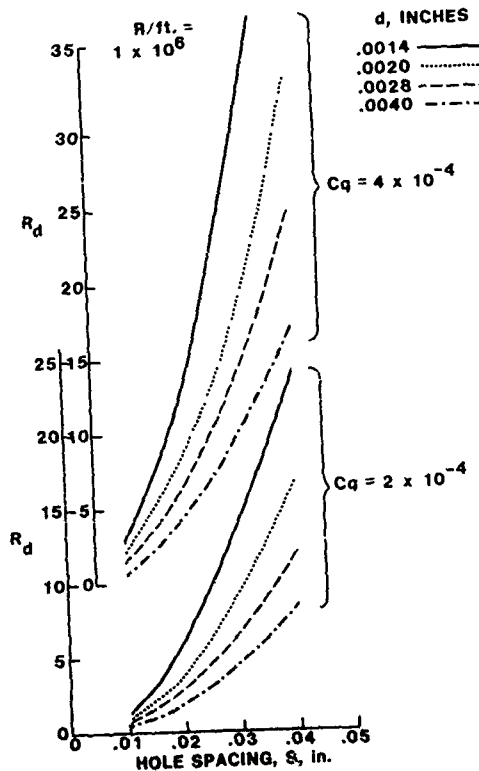


Figure 51. Variation of perforation diameter Reynolds number with perforation spacing

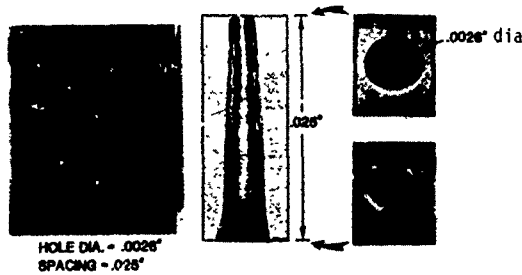


Figure 52. Photomicrographs of electron-beam drilled perforations in 0.025 inch thick titanium sheet

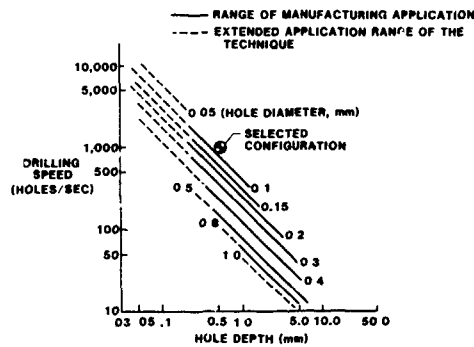


Figure 54. Electron-beam drilling speeds

STRUCTURAL and BOND STRENGTHS

- SALT SPRAY EXPOSURE
- HUMIDITY EXPOSURE
- -60°F to 180°F TEMPERATURE EXTREMES
- PRIMED and UNPRIMED SURFACES

FOREIGN OBJECTS DAMAGE TOLERANCE

- IMPACT TESTING

ELECTRICAL PROPERTIES

- LIGHTNING CURRENT TRANSFER TESTS
- 105 KA RESTRIKE TESTS

CONTAMINATION and CLEANING CHARACTERISTICS

- AIRPORT EXPOSURE TESTING
- GLYCOL CLEANING TESTS
- STEAM CLEANING
- RAIN EROSION

Figure 56. Evaluation tests of perforated suction concept

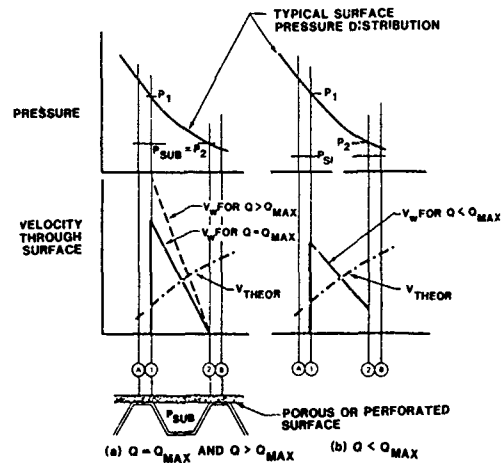


Figure 53. Effect of perforated surface porosity on chordwise variation of suction through surface

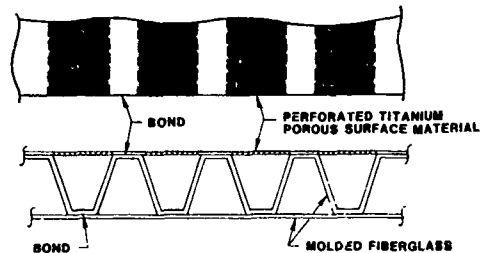


Figure 55. Electron-beam perforated surface glove panel

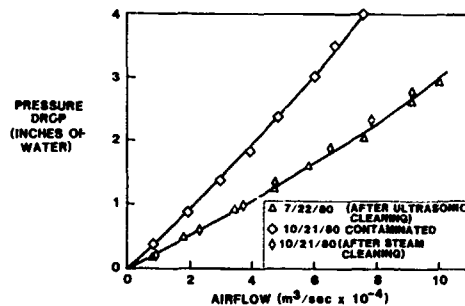


Figure 57. Effect of contamination and cleaning of EB-perforated panel; 0.0026 inch diameter perforations in 0.025 inch thick titanium sheet

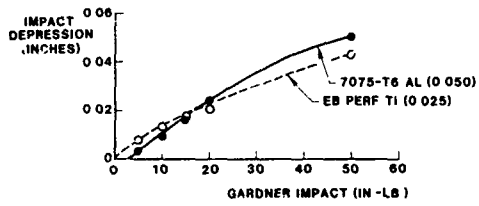


Figure 58. Impact resistance of EB perforated titanium sheet

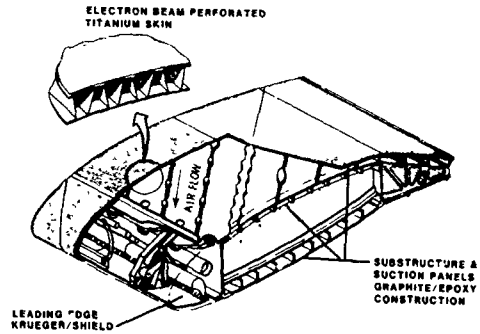


Figure 59. Perforated suction panels grafted to the wing box

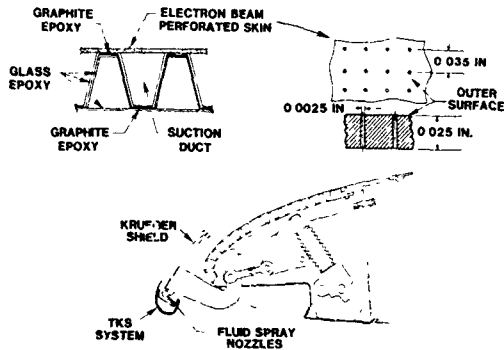


Figure 60. Perforated leading-edge box design

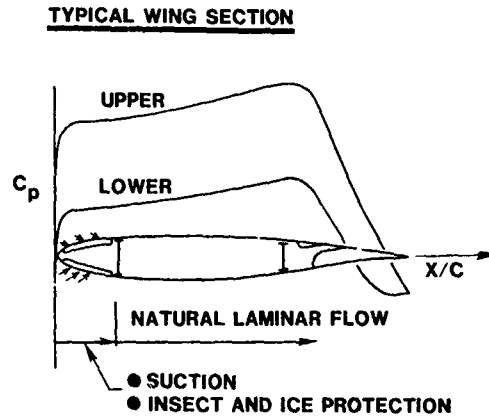


Figure 61. Hybrid laminar flow control wing concept

TURBULENT DRAG REDUCTION FOR EXTERNAL FLOWS

D. M. Bushnell*
 NASA Langley Research Center
 Hampton, VA 23665

ABSTRACT

Paper presents a review and summary of turbulent drag reduction approaches applicable to external flows. Because relatively recent and exhaustive reviews exist for laminar flow control and polymer (hydrodynamic) drag reduction, the paper focuses upon the emerging areas of non-planar geometry and large-eddy alteration. Turbulent control techniques for air generally result in modest (but technologically significant) drag reductions (order of 20 percent or less) whereas hydrodynamic approaches can yield drag reductions the order of 70 percent. Paper also includes suggestions for alternative concepts and optimization of existing approaches.

NOMENCLATURE

a	land width for micro air bearings
C	chord
C_D	drag coefficient
C_F	local skin friction coefficient
C_F^+	area averaged skin friction coefficient
D^*	total drag
f	pipe friction factor
F^*	$\rho_w v_w / \rho U_w$
h^*	$(HU_w / \nu)^{1/2} (C_F / 2)^{1/2}$
H	device height
M	Mach number
R	longitudinal radius of curvature
R_C	chord Reynolds number
R_G	gas Reynolds number
R_L	body length Reynolds number
R_x	Reynolds number based upon local surface distance
R_θ	momentum thickness Reynolds number
s_θ	riblet transverse wavelength
S	slot height
s^+	$(sU_w / \nu) (C_F / 2)^{1/2}$
U, V	longitudinal and normal velocity components
x, y	curvilinear coordinates along and normal to the surface, respectively
Δx	downstream surface distance
δ	boundary layer thickness
η	loading ratio
θ	momentum thickness
λ	wavelength
ν	kinematic viscosity
ρ	density

Subscripts

g	gas
J	slot flow
O	reference flat plate condition
P	pressure drop
s	gas + solids
W	wall value
*	free stream

INTRODUCTION

Previous research on "form" or "pressure" drag reduction and roughness control decreased the zero-lift drag coefficient of most air and underwater bodies to very low values (nearly that of attached viscous flow). In fact, skin friction reduction is currently considered a major "barrier Problem" to the further optimization of most aerodynamic and hydrodynamic bodies, whether platforms or weapons. Viscous drag accounts for (a) approximately 50 percent of CTOL aircraft and surface ship drag, (b) the order of 70 percent of the drag for most underwater bodies, and (c) nearly all of the pumping power for long distance pipelines. Typical benefits resulting from a sizable reduction in viscous drag include design options for (a) longer range, (b) reduced fuel volume/cost/weight, and (c) increased speed. As an example, a 20 percent reduction in fuselage skin friction drag for the U.S. CTOL civilian aircraft transport fleet translates into a yearly fuel saving approaching 400 million dollars. This estimate does not include additional savings and increased performance from either DOD or surface ship/pipeline

*Head, Viscous Flow Branch, High-Speed Aerodynamics Division

applications. Therefore, the "leverage" in this area of research (viscous drag reduction) is quite considerable and justifies the study of "unusual," or "high risk" approaches on an exploratory basis, e.g., "so little is known about the nature of turbulent boundary layers, and so much benefit would accrue to aviation from a reduction in turbulent skin friction, that all avenues for its reduction should be thoroughly examined" (Ref. 1).

A basic question concerning skin friction reduction is whether the "unmodified" viscous flow over the bulk of the body is laminar or turbulent. Three problem regimes can be readily identified. In the first, the body Reynolds number is relatively low (order of 10^6 or less) and, in the absence of transition "promoters" such as adverse pressure gradients, three-dimensional flow, roughness, waviness, stream disturbances, etc., the boundary layer flow is laminar. For this case ($R_L < O(10^6)$) the viscous drag reduction problem is one of reducing laminar skin friction. Applicable techniques include (1) reducing the tangential momentum accommodation coefficient, e.g., introducing a slip velocity at the surface (Ref. 2), (2) use of convex longitudinal curvature (Ref. 3), (3) adverse longitudinal pressure gradients, and (4) fluid injection through the wall. Each of these, except for the slip layer (Ref. 4), can be included in design tradeoffs using state-of-the-art computational techniques. The major difficulties with skin friction reduction for laminar flows are (1) the consequent increased tendency toward separation for an already "separation sensitive" flow and (2) increased probability of transition (for adverse pressure gradient and injection options).

A second problem regime typically embraces body Reynolds numbers from 1×10^6 to 10×10^6 (or greater). In this regime large portions of the vehicle can be subjected to transitional flow, and the obvious drag reduction ploy is to delay this transition process for as long as possible. Typical techniques include (Ref. 5) (1) wall suction, (2) favorable pressure gradient (on two-dimensional or axisymmetric bodies), (3) wall heating (in water) or cooling (in air) and (4) compliant surfaces (in water) (Ref. 6). These laminar flow control (LFC) techniques can be quite successful, with laminar flow occurring up to $R_L = 25 \times 10^6$ and even higher (Ref. 7). However, there are residual questions concerning maintenance and reliability (failure modes) associated with LFC, exacerbated by the relatively large parameter space of possible transition "spoilers" (e.g., Fig. 1). An extremely important consideration in LFC is the occurrence of "unit Reynolds numbers" in the range of $3 \times 10^6/\text{ft}$ or less, thereby allowing reasonable roughness tolerances.

The third problem regime concerns bodies with Reynolds numbers in excess of 10×10^6 , e.g., where the boundary layer flow is generally turbulent. This third problem class includes many applications of technological interest (transport aircraft, missiles, submarines, torpedoes) and is the principle focus of the present paper. Figure 2 indicates schematically the difference in philosophy (and payoff) between LFC and turbulent drag reduction. Wings and other appendages (empennage, control/dive planes, etc.) may have Reynolds numbers low enough for LFC (and the consequent large local drag reduction payoff). However, fuselages (which are responsible for approximately 50 percent of the friction drag) are generally at too large a Reynolds number for LFC and therefore something else, perhaps some alteration of the turbulence structure, is usually required. Indeed, the area of turbulent drag reduction could be looked upon as part of a larger discipline termed "turbulence control." Historically, the research in the turbulence control area has focused upon the (perhaps simpler) area of turbulence amplification, primarily for heat transfer augmentation, separation delay, and increased combustion efficiency. The opposite side of the turbulence control question is the present subject of turbulence diminution or drag reduction.

It is of interest that techniques developed for turbulent drag reduction can, in many instances, be employed for other purposes such as self-noise reduction (Ref. 8), cavitation inhibition, increased performance of airborne laser, telescope and IR windows, alteration of hydrodynamic wave drag (Ref. 9), heat transfer optimization (Ref. 10), improved hull boundary layer - propellor interaction, flow separation control in shock-boundary interactions (Ref. 11), and reduction of attached flow form drag (Ref. 12).

Previous summaries in the area of turbulent drag reduction include References 13 to 26. Much of the information in these references concerns "polymers," (or other additives, see Ref. 27) which are primarily applicable to water (as opposed to air) flows and can provide large skin friction reductions (up to O(70 percent)). In view of the BHRA review in this area (Ref. 17) the present paper will concentrate upon newer (and generally air-applicable) turbulent drag reduction techniques, such as the non-planar geometry approaches which first surfaced in the 1979 time frame (see Ref. 18).

The present paper is an update of Reference 22 and summarizes the current state-of-the-art in the area of turbulent drag reduction for external flows (excluding, as stated previously, the polymer case). The presentation is organized around the influence or physics of the various approaches, including (1) reduction of near-wall momentum, (2) alteration of conditions within or upstream of the boundary layer, (3) alteration of the local wall boundary conditions, and (4) use of a stabilizing body force. Since this field is evolving at a rapid rate, and in the absence of a strong theoretical base for turbulent shear flows, much of what is stated herein concerning (1) drag reduction mechanisms and (2) techniques which have not yet achieved actual net drag reduction (experimentally) is speculative, and included primarily as a tentative guide to further experimentation and optimization. It should be noted that the internal flow problem, because

of the mass flow constraint, may react quite differently from the external flows discussed herein. As an example, fluid injection from the surface decreases drag and excites turbulence fluctuations in external flows whereas surface injection leads to a higher shear and eventual relaminarization in the fully developed internal case (Ref. 28).

STRUCTURE AND SENSITIVITY OF TURBULENT BOUNDARY LAYERS

Before discussing the various approaches used to control (reduce) turbulent drag, it is of interest to briefly examine the structure of the turbulence one is trying to modify. A schematic of the typical wall turbulence flow modules is indicated on Figure 3. This information is a result of both detailed flow visualization and "conditional sampling" measurements conducted over the past 20 years, particularly at Stanford University (e.g., Refs. 19 and 29-31).

The turbulence production process appears to be composed of at least three different scales of motion; a large outer scale (which for low R_L , is evidently the residue of the Emmors spots (Ref. 32), intermediate scales, sometimes referred to as typical or Falco eddies with dimension the order of 100 wall units, and a near wall region where the Reynolds stress is produced (in a very intermittent fashion) by a process termed "bursting." Within the wall region quasi-stationary weak longitudinal (counter-rotating) vortices exist with an individual dimension the order of 30 to 40 wall units and an average transverse spacing of approximately 100 wall units. The wall streak structures and the intermittent turbulent production events (or "bursts") in the near wall region are generally referred to as "coherent structures" in the wall boundary layer. The bursting occurs randomly in space and time, but does have identifiable scales and frequency. The bursts are at least partially induced by the upwelling associated with the counter-rotating wall region vortices (wall streaks). Turbulence production, which is a violent ejection of fluid from the wall region, is preceded by the somewhat more gradual formation, at approximately 20 to 30 wall units from the surface, of an inflection in the instantaneous longitudinal velocity profile.

What is agreed concerning this turbulence production process is the stages, scales, and frequency of the burst cycle and the presence, scales, and structure of the wall streaks. What is not clear is the origin of the ubiquitous wall streaks, and details of the inter-relationship(s) between the three (or more) scales involved (outer, Falco or "typical" and inner regions).

One approach to the turbulent drag reduction problem is to attempt to interfere either with some component of the turbulence production cycle (e.g., breakup the large eddies, stabilize the instantaneous inflectional profile, etc.) or to alter the communication between the various scales. At a minimum, the "coherent structure" information provides scales and frequencies which one can use in inventing and applying turbulence suppression concepts. In fact, Liepmann in Reference 33 states, "Probably the most important aspect of the existence of deterministic structures in turbulent flow is the possibility of turbulence control by direct interference with these large structures. Such control could lead to very significant technological advances."

Narasimha (Ref. 28) indicates that wall turbulence can indeed be altered fairly easily. "We may conclude by remarking on 'How easy it appears to be to suppress turbulence' -- whether you suck or blow, squeeze or bend, heat or cool, or do any of a vast number of other things to it, turbulence can be destroyed, or at least disabled, provided the operation is done properly." For several years, Professor Kline of Stanford has made a hobby of collecting a list of known first order influences upon turbulent flows (Ref. 34). A modified form of his list is shown on Figure 4 and indicates the large number of possible "knobs" one has available when attempting to produce a net turbulent drag reduction. Many of these influences will be discussed in detail in subsequent portions of the present paper. Additional possible variables in the turbulence control problem include (a) combinations of influences and their relative phasing, (b) the rate at which effects are applied or removed (equilibrium/non-equilibrium turbulence structure), and (c) the length scale of the application ($\delta/10$, δ , 10δ , etc.). It is relatively easy, using the items on Figure 4 (or anything which puts a large momentum defect into the boundary layer), to locally reduce skin friction (i.e., a separated flow has a negative skin friction). The present paper focuses upon techniques which do (or might) provide net drag reductions.

TURBULENT DRAG REDUCTION APPROACHES BASED UPON REDUCING THE NEAR WALL LONGITUDINAL MOMENTUM

Having just, in the previous section, discussed how one may be able to obtain net drag reductions by suppressing turbulence production, we begin the actual drag reduction discussions with a series of approaches which generally increase turbulence intensity, yet reduce local skin friction. These methods are aimed particularly at altering, by brute force, the longitudinal velocity gradient at the wall; i.e., driving the flow toward separation. It should be noted that these techniques increase δ and hence (unseparated) form drag. In many cases the form drag increase can be greater than the skin friction reduction.

Adverse Pressure Gradient

This drag reduction approach is extremely straightforward. When an adverse pressure gradient is designed into the body geometry, the flow near the wall is retarded and the skin friction reduced. In fact, not only is C_f lowered, but so is the local dynamic pressure and therefore the viscous drag force can be considerably diminished. The conventional "end point" of this philosophy is the so-called "Stratford Distribution" (Refs. 35 and 36) where the boundary layer is kept quite close to separation over a long distance. The adverse pressure gradient approach is locally applicable to almost any body, but severe problems occur when one tries to approach the limit of a nearly separated condition. The most obvious difficulty is one of off-design sensitivity; e.g., flow separation and consequent large drag increases can easily occur due to small angle-of-attack excursions. A "standby" separation control device could perhaps be utilized to overcome this off-design difficulty.

Nevertheless, in spite of these problems there have been several applications of the nearly separating condition, in particular to high performance airfoils (yielding lift-to-drag ratios of over 100 (Ref. 37)) and in diffusers. As stated previously, this approach can be applied locally, and in a moderate manner, to produce a net gain. In particular, very long wavelength waviness (e.g., waisted body results may produce as much as a 10 percent benefit (Ref. 33)). (Adverse pressure gradient effects will surface again under the subject of "wavy walls.") The effect of an adverse pressure gradient upon the turbulence itself is well known, both the rms turbulence intensity and wall burst frequency is increased (Ref. 39) probably due to a biasing (strengthening) of the instantaneous near wall inflections discussed previously. However, although the turbulence is in fact enhanced, the skin friction drag is reduced.

Wall Mass Transfer

Slot Injection. - This drag reduction approach essentially replaces, for some distance downstream, the actual free stream velocity which the wall senses by a lower value imposed by injecting low momentum fluid in a tangential direction at the surface from a discrete slot (Ref. 40 and Fig. 5)). A simple description of this method is the use of a "wall wake" as opposed to a "wall jet." The latter is utilized in some high lift devices to keep the flow attached. In the present context, the interest is in driving the flow toward separation; hence, the use of a wall wake. The initial skin friction level and the downstream relaxation rate are a function of the slot velocity ratio, with lower slot velocities (which use less mass flow) giving lower initial skin friction but faster recovery (Fig. 6 (Ref. 40)). The lowest surface-integrated skin friction generally occurs for a slot velocity ratio in the neighborhood of 0.3 (Fig. 7 (Ref. 40)). Obviously, repeated slots could be used to keep the skin friction low beyond the influence of the first slot.

The force balance for the slot approach is shown on Figure 8. The major problem with the slot injection method for drag reduction is securing a "low loss" source of air. Simple sums indicate that a net drag reduction is extremely problematical if one has to pay free stream intake ram drag for the injected air. There are, however, several possible sources of "low loss" air including (a) LFC suction air from the wings and empennage, (b) fuselage relaminarization suction air (discussed in a later section of the present paper), (c) (passive) bleed air for separation control (discussed in connection with "convex curvature" effects and in Ref. 41), (d) mass flux from local suction within the boundary layer (also discussed herein, however, much more speculative than some of the other sources mentioned), and (e) mass injection at the leading edge of transonic wings to allow thicker, more efficient sections. Figure 9, (Ref. 42), indicates the computed C_f distribution over a transport fuselage resulting from the injection, through a single slot, of LFC (wing and empennage) suction air. Note that C_f can be reduced where the unmodified levels are the highest (forward portion of the fuselage).

There is a strong possibility that the drag reduction efficiency of the slot injection method can be further enhanced. The extent of the low skin friction region is dictated by the rate of mixing in the shear layer between the slot and boundary layer flows. There exists a rapidly developing technology involving the control of such turbulent free shear layers (e.g., Refs. 43-45) which could be applied to the slot problem and which may result in up to a factor of two increase in surface area exposed to the lowest skin friction levels. Also, pulsed injection could perhaps be utilized to reduce the mass flow requirement for a given drag reduction (ref. 46).

Distributed Normal Injection. - This approach also involves mass injection from the wall, but in this case the injection occurs approximately normal to the surface in a distributed manner (porous or perforated geometry). Obviously there exist possibilities for situations in-between the slot (tangential, highly localized) and wall or distributed (normal, continuous) injection. Calculations (Ref. 47) indicate that a surface with quite discrete normal injection is nearly as effective as the distributed normal injection case.

The amount of drag reduction obtainable from distributed normal injection is indicated on Figure 10 (Ref. 48). The basic problem with this technique is the same as for slot injection, a low loss source of air is required. The possible air sources mentioned in connection with slot injection could also be employed for the continuous, normal injection case. However, research in Reference 49 indicated, on the basis of amount

of drag reduction per pound of injected air, that slot injection can be more efficient than normal injection. This may be at least partially due to the injected air thrust recovery obtainable in the slot case (see Fig. 8). As an aside, Soviet studies of a system with alternating regions of suction and injection (which requires no net mass addition) indicate net drag increases (Refs. 50, 51).

The influences of normal injection upon the mean and turbulent velocity fields are somewhat similar to those of adverse pressure gradient. The near wall mean longitudinal velocity profile can become highly inflected near the wall and the turbulence intensity increases (e.g., Ref. 52).

Ion Wind

This technique is quite new with initial exploratory studies documented in Reference 53. The basic concept is to attempt to "turn around" a phenomenon which has been known for many years (Ref. 54). If one places electrodes above a boundary layer and creates a corona discharge between the electrodes and the plate, it is possible to induce, due to the non-uniform electric field near the electrodes, a mean molecular motion directed away from the electrodes and toward the plate. The experimentally observed effects of such an electric wind upon the boundary layer are what one would expect, the boundary layer is thinned and convective heating (and presumably skin friction) is increased (e.g., Refs. 55 and 56). Also, transition can be delayed (Ref. 57). The literature in this area is quite extensive. Only a very small ion concentration is required to initiate the corona (or glow) discharge and reasonably large mean velocities (several meters/sec) can be induced. However, sharp electrodes (which stay sharp) are necessary.

In all of the previous ion wind research, the electrodes were placed above the plate. In the present context of drag reduction, the ion wind is studied with a reversed geometry, the electrodes are placed on (in) the wall (Ref. 53). If the discharge is either to space (virtual ground) or to a ground on the wall farther downstream, the electrostatic body force in the normal momentum equation should induce a larger mean normal velocity in the vicinity of the wall. As there is no net mass transfer through the surface, this larger mean normal velocity can only appear at the expense of the average longitudinal velocity component and therefore one might reasonably expect some drag reduction. The fact that the ion wind is induced in the wall region, where the longitudinal velocity is lower than the external value, may increase the Mach number range over which the ion wind velocity is of sufficient magnitude to affect the flow (Ref. 55).

In the present, very early, stage of the ion wind drag reduction studies, all that is known for certain is that there are many potentially serious questions and some intriguing possibilities. The questions (or critical issues) include (a) the amount of power required to produce a measurable drag reduction, (b) possible destabilization of the turbulence due to the discrete electrode spacing and the inherent pulsing of the discharge (Ref. 58), and (c) whether a large enough normal velocity can be induced close enough to the surface to significantly affect drag. The intriguing possibilities include (a) utilizing the static electricity (streaming potential) which builds up on an aircraft in flight to furnish some or all of the required electric field (up to 600 kv, this is now dissipated at discharge points to avoid large scale arcing/ball lightning (Ref. 59 and 60), and (b) utilization of the polar molecules in the nearly 180 lbs/min of cabin flush air to create a corona discharge at lower power (Ref. 61). Favorable effects of altitude and photo-ionization should also be studied. Initial experiments indicate an exquisite sensitivity to moisture content in the airstream. As of now, the ion wind is only a possibility requiring further investigation. Also of interest are related studies of α and β particle injection from the wall (Refs. 62 and 63). This somewhat similar boundary condition change results in a small drag reduction, which may be due to a mechanism similar to that postulated herein for the ion wind (particle impacts providing increased normal velocity near the wall).

Boundary Layer "Thickeners"

As stated in a previous section, approaches which increase momentum thickness usually result in a lower local skin friction level. The basic problem with such methods include the drag of the device used to thicken the viscous flow and larger δ /form drag. Examples of apparently successful utilization of the thickener approach include the favorable influence of aircraft length upon viscous drag (the forward portion of the fuselage increases the boundary layer thickness so that the drag on the aft end is quite low) and the swordfish "sword" (where the high skin friction region occurs on a portion of the body with small wetted area (Ref. 6). Recent research in West Germany (Ref. 64) and previous work by Lang (Ref. 21) suggest the use of an energy extraction device (a wind turbine) at the front end of the fuselage to thicken the viscous flow (reduce momentum near the surface). This shaft energy is then transmitted and added to the main aircraft propulsion system. The essence of this approach (Ref. 64) is that the thickening process should be one of useful energy extraction rather than deleterious drag. Variations on this same theme, such as small scale transverse shaft turbines placed within the boundary layer itself have evidently not yet been investigated. The concept of useful energy extraction for subsequent viscous drag reduction requires considerable further innovation and research.

TURBULENT DRAG REDUCTION APPROACHES BASED UPON ALTERING CONDITIONS WITHIN THE BOUNDARY LAYER

The Philosophy for this class of methods is somewhat new. Historically, local wall region modifications have constituted the favored "approach of choice" for drag reduction. The methods considered in the present group are based upon modification of the flow in the outer portion of the turbulent boundary layer.

Large-Eddy Breakup Devices

Large-eddy breakup devices (termed "manipulators" in Ref. 65 and "ribbons" in Ref. 66), constitute probably the most exciting and promising single recent development in turbulent drag reduction. The genesis of the large-eddy breakup idea is a 1977 paper by Yagnik and Acharya (Ref. 67). Evidently Yagnik initially suggested such a concept in 1968 (Ref. 68). "Hence it can be concluded that if a stationary, impervious, thin bar is introduced in an eddy of a fluid of low viscosity, there will be a noticeable change in the flow, although the diameter of the rod may be small in comparison with the diameter of the eddy." "The constraining effect can be used as an inexpensive and highly effective method of control of vortices."

Simple estimates indicated that net reductions would not be possible with the Yagnik et al. screen device (see also Refs. 70 and 71) and therefore a search was begun for a lower drag configuration which would still break up large eddies. Initial tests in early 1978 with various sized honeycombs (Ref. 72) indicated that sizable downstream drag reductions were possible (with much lower device drag than a screen) but still no net drag reduction, at least within 50 δ downstream. Around this time frame Nagib at Illinois Institute of Technology, drawing upon his extensive expertise in free stream turbulence management (e.g., Ref. 73), suggested trying only a very few horizontal elements. Initial IIT (Ref. 74) and NASA Langley (Ref. 72) results on such devices both indicated that the device drag was recovered (from downstream skin friction reductions) at a distance of approximately 40 δ . Additional IIT work (Ref. 65) carried further downstream obtained (1) a net drag reduction of up to 20 percent (Fig. 12) and (2) a decrease in burst frequency of approximately 18 percent. Reference 66 and Langley work (Ref. 69) obtained more modest net reductions (0.5%) for essentially the IIT device geometry (but not at the same chord Reynolds number, which turns out to be crucial).

In the meantime, a "vortex unwinding" mechanism (Ref. 75) was identified as a probable mechanism to explain the apparent success of such few elements (Ref. 72). Basically, the element could act as a low Reynolds number airfoil on a gusty day. As the gust (turbulent rotational motion) approaches the leading edge, a starting vortex is induced which is phase locked with, and of opposite sense to, the incoming gust. The resultant downstream flow therefore contains only smaller scale motions. The IIT flow visualization (Refs. 74 and 65) indicates this expected behavior, the larger outer scales being much reduced. Also, the fact that the skin friction is decreased along with the outer eddies is strong circumstantial evidence for an outer-to-wall communication which is of first order importance to the burst cycle.

More recent LEBU work (Refs. 76-87) indicates consistent results for the amount of local skin friction reduction (0(20 percent - 30 percent)) produced downstream of a tandem set of plates. Of particular importance is the observation first made in Reference 76 that the altered boundary layer relaxes back to undisturbed drag levels in the order of 120 δ downstream of the device. At this point another device would have to be placed to "do it again." On a typical CTOL fuselage 120 δ corresponds to the 0(50 ft.). Of particular interest in the recent work is the realization of the importance of having a high device chord Reynolds number to avoid inordinately high device (separation) drag (Ref. 83, see also Ref. (88)). The results from Reference 80 indicate up to 25 percent net reductions are possible for thin devices at high device chord Reynolds number. This geometry produces minimum device drag and hence greatest net drag reduction. Unfortunately, these thin devices are inefficient for CTOL application due to the large device support drag (vertical supports would have to be placed every few δ apart circumferentially/spanwise). Thicker, flight capable airfoil shaped devices were therefore developed at NASA Langley (Ref. 83). These elements are 10³ stiffer than the conventional thin plate devices while still providing 8 percent net drag reduction. From current indications, the higher chord Reynolds numbers associated with flight should make these devices ever more efficient.

Several drag reduction mechanisms have been postulated to explain the drag reduction effectiveness of these devices (e.g., Ref. 84). These include (1) blocking effect of the embedded impervious surface, (2) device mean momentum wake (a portion of which could induce "negative production" of turbulence, (3) incident turbulence distortion due to the device average flow field, (4) the unwinding mechanism already mentioned and (5) the downstream influence of control vortices shed from the device trailing edge. The latter is favored in Reference 82. The recent IIT research (Refs. 85, 86) and consistent experimental observations (Ref. 83) indicate that the device (1) affects the large eddies and (2) acts at the device site, rather than downstream. This suggests a combination of mechanisms 1-4 above, as opposed to mechanism 5. It should be noted that preliminary flight tests of LEBU devices have already been carried out (Ref. 87).

Conclusions thus far in the large-eddy breakup device area include (a) thin elements are required to keep the pressure drag low (held as tension members rather than

beams to reduce support strut drag, (b) the element chord should be the order of δ with (c) the height of the outer element the order of 8δ and (d) no more than two horizontal elements preferably in tandem. Thick (Airfoil) devices are probably required for CTOL application (Ref 83). Also for the $R_\theta < O(6000)$ the actual net drag reduction obtainable from a small number of horizontal elements is dependent upon the particular transition process of the experiment. This is reasonable as Wygnanski et al (Ref. 32) and IIT (Ref. 65) suggest that the large eddies for $R_\theta < 10^4$ are the remnants of the transitional Emmons spots.

Aside from drag reduction, there exist several intriguing possible applications for the "turbulence control" offered by large-eddy breakup devices. These applications (which should be investigated) include (a) decreased distortion of laser signals beamed through fuselage boundary layers, (b) lower self noise on hydrodynamic and aerodynamic bodies, and (c) reduction of noise radiation from turbulent eddy-propellor interactions (also possible increased propulsor efficiency). In addition, these LEBU devices could probably be employed in conjunction with other drag reduction approaches to obtain increased overall performance (several such combinations are discussed in subsequent sections of the present paper).

Local Suction Within the Boundary Layer

The only research of this type known to the author is Reference 89, which was a study of highly localized suction through an enlarged pitot tube. The results of Reference 89 indicate that quite large suction rates were required to alter the turbulence, but the suction was so localized that the results are not definitive. The suggestion is that exploratory tests might be tried on large-eddy breakup type devices with suction through the leading edge, the lateral surfaces, the trailing edge, or a combination thereof. There is no firm rationale for expecting a net drag reduction; but since the experiment has evidently not yet been tried, it may yield some interesting turbulence control/alteration results. Sreenivasan suggested (at the Drag Reduction Symposium in Washington, DC, September 13-17, 1982) that control of the v' fluctuation field is probably the most effective means of altering the outer turbulent flow. In terms of overall efficiency, the v' control offered by large-eddy breakup devices (impervious surfaces in the flow) is probably more favorable than employing active suction.

Modification of Emmons Spot Formation

As mentioned in connection with the large-eddy breakup devices, there exists some evidence which indicates that the larger scale turbulent boundary layer motions (at least for $R_\theta > 6 \times 10^3$) may be produced by the transitional Emmons spot production process (Ref. 32). Also, observations of turbulence intensity (e.g., Ref. 9C) indicate higher levels close to the end of transition and, at high speeds, the velocity profile "N factor" decreases with distance from the end of transition (Ref. 91). Therefore, there is little doubt that the transitional (Emmons spot production) process can result in high levels of turbulence activity which slowly decrease with distance once the Emmons spots have merged (nominal end of transition). If this is the case, then an obvious turbulent drag reduction approach would be to attempt to alter these transitional spots in their region of formation. The observation in References 76 and 83 that large eddies "heal" in $O(120\delta)$ suggests that this approach would be of only limited usefulness as it could not be repeated (only go through transition once, usually).

A simple-minded possibility is that, in the transitional region, the Emmons spots (which appear to be convecting "islands" of fully turbulent flow in a "laminar sea" (Ref. 92) contain more virulent motions than their remnants in the "asymptotic" ($R_\theta > 10^4$) region due to the low intensity (laminar) surrounding flow. A crude analogy might be the favorable effect of open space upon plant growth.

Possible experiments to check this simplex reasoning include (1) examining the boundary layer downstream of a transition region induced by a forward or backward facing step, where the transition is completed within the free shear layer bounding the separated flow region (this should bypass the Emmons spot formation region altogether but might not reduce intensity levels) and (2) promoting "instant transition," for example, by pulsing air jets through a transverse line of closely spaced holes in the surface at the longitudinal position of the first "natural" Emmons spots. The purpose of the latter experiment would be to induce the spots to form simultaneously at the same longitudinal location and quite close together, thereby eliminating the "laminar sea." Preliminary experiments along these lines at Langley by Goodman (Refs. 93 and 23) indicate lower skin friction levels in the low R_θ ($R_\theta < 10^4$) region for particular driver amplitude and frequency values as well as indication of smaller scales from "flow visualization." Other related experiments (without the close spanwise spacing) indicate little effect (Ref. 94). An additional piece of relevant physics is the Klebanoff et al. "calming effect" caused by the passage of an artificially-induced Emmons spot (Ref. 95).

Large Eddy Substitution

This is also a relatively new area, suggested in Reference 84 with initial studies documented in References 96 and 97. The basic concept is to control/replace the usual

Large-Eddy Structures with control vortices shed from various fixed Bodies. In Reference 96 the control vortices are "stationary" and longitudinal, and provide stabilizing streamline (as opposed to wall) curvature. Once the outer turbulence is organized and altered by these input vortices the organized motion is "unwound" (using a vortex generator of the opposite circulation) and the flow relaxes back to an undisturbed state. The "unwinding" is necessary as the steady pumping action of the embedded input vortices increases mean shear. In Reference 97 a transverse cylinder is used in the outer region with a control (LEBU-like) plate placed above it to force the shedding of unsteady transverse control vortices of the sign opposite to the dominant boundary layer vorticity. Many other realizations of this approach are possible, using various types of bodies/classes of control vortices. From the results thus far this method provides, at the very least, opportunities for wall turbulence control. Net drag reductions, if obtainable, are still quite far in the future.

TURBULENT DRAG REDUCTION APPROACHES BASED UPON ALTERATION OF THE WALL BOUNDARY CONDITION

These methods are based primarily upon the following query: "Is it correct that the lowest drag occurs (in zero pressure gradient) for a smooth, flat surface, or is there some micro-geometry which (while conventionally a roughness) might alter the turbulence wall production processes in a net favorable manner?" The LEBU results already discussed indicate that it is indeed possible to lower net drag using nonplanar geometry. This section of the paper discusses nonplanar geometry approaches for the wall region, along with affects of wall motion and wall slip.

Riblets

The micro-geometry associated with the riblet approach consists of small longitudinal striations in the surface. The basic concept arose from the drag reduction which occurs at the apex of Isoscles Triangle ducts (Ref. 98) and involves creation of a highly viscous sub-region in the transverse direction which alters the formation and growth/bursting of the wall streak. Additional considerations include the possible alteration of the transverse pressure field and a quasi-two-dimensionalization of the very near wall flow. Since the grooves are flow-aligned, parasitic form drag is minimal but the wetted area is considerably increased. From Reference 99, the drag is considerably reduced over the riblet valley and increased somewhat over the peak. A potpourri of riblet models tested at Langley is given on Figure 13 (Refs. 100-103). Experimentally, the optimal drag reducing surface is also one of the first ones tried, the sawtooth arrangement indicated at the upper left of Figure 13. Research on this riblet concept indicates (a) net drag reductions are possible if the height and spacing of the grooves are the order of the individual wall streak dimensions (approximately 30 wall units (Fig. 14)), (b) net drag reductions of up to 10 percent can be obtained on sharp tip v-groove surfaces (Fig. 15), (c) rms turbulence intensity near the surface is reduced, but burst frequency is not (Ref. 102, 104) although a burst frequency reduction was observed in Reference 105 and (d) riblet surfaces can provide increases in heat transfer (0(38%)) with essentially no increase in "pumping power", Reference 106. Data taken at Lenigh (Ref. 107) indicate that the wall streaks tend to align themselves over the riblets, at least in the range of spacing greater than 50 wall units. Confirmatory data for riblet drag reduction are available in References 108 and 109.

Of interest in connection with these riblets is that fast sharks have a surface covering of dermal denticles with flow-aligned keels having nearly an optimal riblet spacing Ref. 110. These keels are lined up peak to peak down the body, developed relatively recently in the fossil record and (as the shark grows) the keel-to-keel spacing does not change, the fish merely adds keels onto the sides of the denticles. There is no prima-facie evidence that these dermal keels on the shark do, in fact, act as drag-reducing riblets. For the denticle-keel combination there are indeed alternative drag reduction mechanisms which include their acting as a guide for polymer (slime) deposition into the near wall region (see also Ref 109).

The application of riblets need not involve tedious and delicate surface machining. In one concept, thin (low specific gravity) films could be inexpensively extruded through dies with the correct geometry and attached with adhesive to the surface. Smooth Surface films of this type have already been tested on aircraft (Ref. 111) and found in the flight tests to be satisfactory in terms of maintainability, uv degradation and cycle life. An interesting further possibility is the use of three-dimensional riblet configurations. The surface morphology of Marlin (Ref. 112) can be crudely likened to an array of non-aligned flattened half-cones pointing backward. This configuration gives the impression of diverging flow (in a three-dimensional sense) which, from Reference 113, may damp the wall streaks

Bubbles

This approach is suitable for liquids only and involves placing a gas "slip layer" between the surface and the liquid. Due primarily to the lower density of the gas layer large drag reductions are possible (Ref. 121). This is an ancient concept, with patents dating back to the last century. Historically, the major problem with the implementation of this approach has been the instability of the air film. Very large air envelopes obviously have very large buoyancy difficulties/instabilities while smaller

bubbles can induce roughness effects if the surface coverage is not uniform. Nevertheless, sizable local drag reductions have been obtained (Fig. 16, Ref. 114), in this case using electrolysis for bubble production. A net drag reduction using the electrolysis approach is problematical; however, other techniques for gas or vapor production (including surface boiling (Ref. 115) and "cavities" (Refs. 116 and 117)) indicate considerable promise, especially for high-speed operation.

Relatively recent Soviet research seems to have provided an answer to several of the bubble difficulties (Ref. 118). Their basic approach was to utilize distributed air injection through microporous surfaces to produce a relatively uniform covering of very small bubbles. Using this method, quite large (O(70%)) reductions in skin friction were obtained with relatively low gas flow rates. The application of this technology to surface ships would be quite straightforward, involving an external skin through which compressed atmospheric air is continuously (in surface space and time) injected. Soviet estimates indicate a possible O(30) percent decrease in installed horsepower and there are additional possibilities for reduced fouling drag and fouling maintenance costs if water is kept away from the hull surface, even while berthed (this would also increase aeration/O₂ content of normally oxygen deficient harbor waters). Experiments at Penn State by Merkle et al (Refs. 119-122 indicate large drag reductions over a sizable parameter range, i.e., the reduction is rather easily obtained. To circumvent the large quantities of air/gas required an attempt should be made (using surface chemistry, Ref. 123) to create (as an end point) a "mono-layer" of microbubbles on the surface which would provide a slip velocity directly with minimum gas usage.

Compliant Walls (Interactive Wall Motion)

The status of compliant walls for turbulent drag reduction is, as usual, murky. Soviet research reported in Reference 6 indicates that, in water, several types of "soft" surfaces can (in the linear instability region) both increase the lower critical Reynolds number and decrease the amplification rate of unstable disturbances but even these data are now in question (Ref. 124). The data and analyses cited in References 18 and 125 indicate that there are no reproduced experiments, at least to the date of this writing, which indicate sizable (greater than 5 percent) net drag reduction for compliant surfaces under turbulent boundary layers, either in air or water. The Soviets have reported some recent favorable results (Refs. 126 and 184 as has Taylor et al at Applied Physics Lab (Ref. 127) but these have not yet been confirmed. Due to the tremendous density difference between air and any reasonable surface material, the compliant wall approach is probably confined to water for the foreseeable future. (See also Ref. 128 for an acoustically-orientated prescription for compliant wall design.)

Relaminarization Using Massive Wall Suction

This method is of particular interest to the CTOL fuselage drag problem. A conceptual layout is indicated on Figure 17. The forward portion of the fuselage is typically characterized by a host of excrescences, including windshield wipers, bugs, probes, attachment points and access hatches. The basic concept is to "writeoff" this forward portion of the flow as transitional/turbulent and subsequently relaminarize the boundary layer downstream of the cockpit using massive suction. Maintenance suction and/or wall cooling would be required further downstream to maintain the laminar condition.

Pfenninger (Ref. 129) successfully carried out a series of relaminarization experiments applicable to this concept but found it necessary to ingest the entire mass flow in the boundary layer (up to 1.5%) to capture all of the "superlayer" fluctuating vorticity. Suction of less than this amount compromised and complicated the downstream maintenance LFC problem. The key ingredients to maximizing the overall system efficiency of this approach are (1) ingesting the minimum mass flow consistent with downstream maintenance LFC and (2) obtaining maximum pressure recovery in the suction inlet.

There exist several possibilities for optimizing the fuselage relaminarization approach. The most obvious is to place the massive suction forward of the minimum pressure region on the fuselage. This placement performs two functions: (a) places the initial (thin and tender) laminar flow region in a stabilizing favorable pressure gradient and (b) should lower the required pumping power (and possibly allow for selfbled to the side of the fuselage where slot injection might be utilized in regions where laminar flow could not readily be maintained, such as the wing juncture contamination zone). Another optimization possibility is to design the aircraft for minimum disruption of fuselage LFC from the wing-induced pressure field (providing this could be accomplished without unduly altering the wing efficiency). Historically, alterations in the wing and fuselage design for interference have been in favor of the wing. As a "blue sky" possibility, the maintenance laminar flow could be made somewhat easier on passenger aircraft by replacement of the windows with a smooth skin and providing the passengers with a small video screen giving a pilot's-eye-view (or a view in any other direction) using the recent advances in microelectronics.

A final optimization possibility is to "preprocess" the fuselage boundary layer through a large-eddy breakup device (see previous section) which should, by altering the superlayer structure and thickness, reduce the suction mass flow requirements and therefore possibly increase the overall system efficiency. Research on this last possibility is currently underway at NASA Langley. Closing arguments in favor of downstream

fuselage relaminarization include (a) possibility of using cooling (from liquid H_2 fuel) as a maintenance LFC technique (not feasible for swept wings (Ref. 130)), (b) greatly reduced problems from "insect remains," (insects impinge in the nose region, which is turbulent anyway) and (c) reduced roughness sensitivity compared to the swept wing case (Ref. 131).

Non-Interactive Wall Motion

This boundary condition change is meant to be distinct from the compliant wall approach. The essence of the latter is that the wall motion is, somehow, tied to the turbulent motions and/or burst process within the flow. In the non-interactive wall motion case (as defined herein), the wall simply translates in the downstream direction. The wall geometry could be either flat or wave shaped.

Typical drag reductions for rectilinear wall motion with a flat wall geometry are shown on Figure 18 (Ref. 132). The rectilinear wall motion in the stream direction essentially acts as a slip boundary condition and reduces the mean shear. The end point of such wall motion ($U_{wall} = U$) is zero boundary layer thickness and zero mean shear. If the moving wall has a wave-shaped geometry, it is even possible to produce thrust with this approach (for a large enough wall velocity). However, for $U_w < U$ the wavy surface usually has an additional pressure drag component (e.g., Ref. 133) not present in the flat wall case.

The application of downstream moving walls to actual systems for turbulent drag reduction is probably not feasible except in very specialized circumstances. In fact, as a general observation, turbulence control approaches which require moving solid objects are generally extremely difficult in practice (due to inertia and fatigue considerations) and may result in drag increases due to periodic eddy shedding (from oscillatory object motions). However, as noted in connection with the postulated drag reduction mechanism for large-eddy breakup devices, it is not necessary for objects to move in order to force a time-dependent interaction with the turbulence. The fact that the turbulence itself is unsteady automatically ensures unsteady flow interactions even with stationary objects.

Micro Air Bearings

The approach is highly speculative, but does bring to light (in fact makes us of) several apparent anomalies in the literature. The first of these is a reduced Reynolds stress level measured near the wall over a "D" type roughness (Ref. 134). This special type of rough surface consists of closely spaced spanwise cavities. Near-wall flow visualization over such surfaces indicates an absence of wall streaks over the cavities (Ref. 135) and an intermittent eruption of cavity fluid (Ref. 136), the latter perhaps due to strafing from the "typical eddies."

A second apparent anomaly is the very low drag (essentially laminar skin friction) over such surfaces in laminar flow (Fig. 19, unpublished NASA Langley data by L. M. Weinstein, see also Ref. 137; e.g., in the absence of the turbulence-induced cavity eruption (Ref. 138)). The inference from the foregoing information is that the innate drag over moderate-sized D-type roughness may be quite low, providing that the cavity eruptions (which presumably cause space and time variable pulses of pressure drag) can be reduced. Possible approaches to the reduction of these cavity eruptions include (a) use of large-eddy breakup devices (see previous discussions on LEBU's) and (b) use of imbedded (co-rotating?) vortex generators. The latter device is suggested by data in Reference 139, which indicate that wall shear stress fluctuations are significantly reduced downstream of such imbedded vortex generators (see also Ref. 140 for remarks on partial substitution of longitudinal vortex structures for the usual transverse (horseshoe?) turbulent "vortex" motions). Moreover, Reference 141 indicates that such longitudinal structures can survive for large streamwise distances. Simplistically, one may be partially substituting "stable" three-dimensional longitudinal vortex structures for unsteady horseshoe/ring/transverse vortex motions; i.e., utilizing a more stable type of flow structure to "insulate" the wall from a portion of the turbulent chaos. Therefore, the micro-air bearing approach conceptually combines both a wall boundary condition change (substitution of intermittent pressure drag for attached skin friction) and a flow field alteration method (LEBU, imbedded vortex generator or ?) to reduce the level of intermittent pressure drag. Whether net drag reductions can be obtained is, of course, problematical, but the research (currently on-going at Langley) is of considerable interest for the turbulent drag reduction of rough surfaces (e.g., ship hulls). Initial data (Ref. 142) indicate no net drag decreases for the LEBU cavity combination.

TURBULENT DRAG REDUCTION APPROACHES BASED UPON USE OF A STABILIZING BODY FORCE

Longitudinal Convex Curvature

Reference 143 provides a premiere discussion of the effects of longitudinal wall curvature upon turbulent boundary layers. The general result is that concave longitudinal curvature increases turbulence intensity and generally produces Gortler vortices imbedded in the turbulent flow (which greatly increases mean entrainment/drag). The effects of convex curvature are, however, very favorable with large decreases in

turbulence intensity and skin friction (Fig. 20 (Ref. 144)). Moreover, quite small curvature inputs ($\delta/R \sim 0(.1)$) produce tremendous effects. There exist indications that the convex curvature affects primarily the large, outer eddies (e.g., Refs. 145 and 146). Simplistically, therefore, convex curvature should have effects similar to the large eddy-breakup devices discussed previously, with ultra long downstream relaxation distances. That such is the case is indicated on Figure 21. The skin friction distributions shown are in the downstream relaxation region; e.g., downstream of the end of the curvature region (Ref. 147), downstream of the LEBU (Ref. 65), or downstream of other (conventional) boundary condition changes (Ref. 69).

The data on Figure 21 indicate that convex curvature does indeed tend to act in a similar fashion to large-eddy breakup devices. In fact, heat transfer data (Ref. 148) downstream of convex curvature indicates relaxation distances in the 50 δ range. The necessary criteria to ensure sizable downstream distances of low drag (due to convex curvature) are (a) δ/R in the range of .01 to 1 (note the lower level on Figure 22 for the larger δ/R , (b) the curvature must be applied downstream of the end of transition (so that all of the large eddies are in place to be modified), and (c) the curvature must be applied over a surface distance the order of 15δ or greater. These criteria were deduced from the available Stanford data (Refs. 147 and 148). Also of interest, from Reference 149 is that, at least locally, convex curvature also damps turbulence in the supersonic case, something that LEBU devices may not do.

Simplex concepts for application of convex longitudinal curvature for turbulent drag reduction are shown on Figure 22. The basic tricks are (1) to deal, at least initially, with the nose regions of axisymmetric bodies such as fighters or missiles (which are fairly slender), and (2) to first establish the end of transition on a forebody with small wetted area (somewhat similar to the swordfish case (Ref. 6)) and then process the boundary layer through a short ($\Delta x/\delta < 10$) region of concave curvature on the way to the convex portion. The critical observation is that the limited extent of the concave curvature region may not allow formation of any lasting alterations to the turbulent structure. Research on both subsonic and supersonic convex curvature approaches is currently underway at NASA LaRC.

In addition to longitudinal (x-y) curvature there are obviously curvature possibilities in two other planes, transverse (y-z) and "in-plane" (x,z). For external flows convex transverse curvature is a second order effect compared to the longitudinal case (requires $\delta/R + 1$ or greater) which acts similar to favorable pressure gradients, drag is increased with increasing δ/R , with relaminarization for large enough values. In-plane curvature results have, in some cases, indicated reduction in both turbulence scale and drag (Ref. 150) but the experiments are not yet "clean" in the sense that the curvature is not the only major parameter affecting the flow. For the swept wing transition problem in-plane curvature is stabilizing (Ref. 151)

Fibers and Other Particles, Plus MHD

The bulk of the drag reduction research on fibers and particles is for liquid flows (see Refs. 17, 152, and 153). The situation in liquids appears to be the following: large length-to-diameter particles (fibers) can provide reasonably large drag reductions (0(20 percent to 50 percent)), but spherical particles generally do not. In gases, spherical particles sometimes give drag reductions up to 50 percent or greater (Fig. 23 from Ref. 154) and sometimes not. Fibers have evidently never been tried in air flows. Some evidence (Refs. 155 and 156) indicates that the particle drag reductions in air may be due to the electrostatically induced formation of chains of particles or fibers. This explanation may also apply to some of the liquid data, where mixtures of blue clay particles (non-fibers) provided a drag reduction (Ref. 157). Blue clay is known to be electrostatically active. The bulk of the data therefore seems to indicate that long length-to-diameter fibers, either mechanically introduced or electrostatically formed from particles, are responsible for drag reduction in turbulent flows.

A possible explanation for fibrous drag reduction is that the fibers provide a distributed anisotropic body force. If one assumes (reasonably) that the fibers are approximately aligned with and follow the main flow, there then exists a large fiber Reynolds number difference in the streamwise and cross-stream directions (based upon pulsation velocity). This in turn gives rise to large directional differences in the drag coefficient which the particle induces upon the pulsation velocity field. This heuristic model suggests that the longitudinal velocity fluctuations should be affected much less than those in the cross-stream directions. Since shear flow turbulence is a three-dimensional phenomena, the possible "mono-dimensionalizing" effects of a fiber-induced anisotropic distributed body force should be to alter the turbulence production and reduce drag.

The application of fiber drag reduction to external flows is not straightforward, due to the innately non-circulatory nature of the problem. Conceptually, one could inject particles near the nose and then attempt to recover them near the tail of the body for recirculation, but this simplex approach demands non-realistic fiber capture efficiencies (as well as energy for fiber return). A possible (but still improbable) approach would be to form fibers from the fuel, use the fibrous fuel for drag reduction (utilizing nose injection and subsequent boundary layer transit), and then collect fuel plus boundary layer into an engine at the tail for subsequent combustion.

Another body force which tends to mono-dimensionalize the turbulence is MHD related. Practically any value for skin friction between laminar and turbulent is possible in magnetic fluids depending upon the level of the applied DC magnetic field (e.g., Ref. 158). Since these particular data (Ref. 158) are for a magnetic field aligned with the mean flow, the magnetic force can only directly affect radial and tangential velocity fields, which are entirely fluctuational (obviously radial and tangential mean velocity components are zero in a developed pipe flow). Transverse fields are also effective (Refs. 159, 160). Unfortunately, MHD control requires a magnetic fluid which is singularly lacking in the usual external flow problems, except perhaps (weakly) for sea water. Super-conducting magnets may, in fact, allow turbulent boundary layer control/drag reduction in hydrodynamic applications; e.g., Reference 161.

Wall Cooling

As is well known in geophysical flows, buoyancy forces can either stabilize, or destabilize, turbulent shear flows. For air, wall cooling tends to stabilize, with the amount of stabilization indicated, for example, by the local gradient Richardson number. A value greater than 0.05 generally indicates the beginning of measurable effects, with a value of 0.5 indicating major stabilization (Ref. 162). This approach could conceivably be of interest on aircraft utilizing liquid hydrogen (cryogenic) fuel where a sizable heat sink is readily available. In a large scale, low-speed boundary layer experiment, wall cooling provided an 18 percent skin friction reduction (Ref. 163). Unfortunately, if one estimates from the Richardson number the free-stream velocity range over which such stabilization is operative, the numbers are disappointingly low (less than $O(10)$ fps) for even the extreme case of liquid nitrogen wall cooling. Therefore, the wall cooling approach is evidently suitable only for specialized applications. On the other hand, the well known decrease in skin friction due to wall heating (primarily due to wall density reduction, in air) can be utilized locally (using waste propulsion heat) e.g., Reference 12.

SOME INTERESTING APPROACHES WHICH EVIDENTLY MAY NOT PROVIDE NET DRAG REDUCTION

Passive Porous Walls

One would expect that relaxing the wall impenetrability condition, (without imposing a net mass flux through the surface) might alter the near-wall turbulence production cycle, with the extent and type of alteration perhaps a function of the detailed micro-geometry of the surface. Research on high pressure drop passive porous surfaces (Refs. 164 and 165) and noise absorbing walls with considerably less pressure drop (Ref. 166) indicates that the net effect of relaxing wall impenetrability (without net mass transfer) is to increase skin friction drag. Recent research at Langley (Ref. 167) indicates that the drag increase is due to unsteady pressure forces on the edges of the perforations. Non-normal orientations of the surface openings have not yet been evaluated.

Such passive porous surface may be useful for flow separation control by allowing self bleed of boundary layer displacement thickness buildup (e.g., Ref. 168). In a related problem steady-state computations (Ref. 47) and experiments (Refs. 50, 51) of spatially-adjacent (alternating) regions of suction and blowing also indicate net drag increases.

Oscillatory Longitudinal Curvature and Pressure Gradients (Wavy Walls)

The original impetus for the wavy wall studies at Langley (Refs. 38, 169, and 170 and 171) was the apparent average skin friction reductions obtained by Kendall (Ref. 133, 20 percent, Fig. 24) and Sigal (Ref. 172, 10 percent) over wavy walls with $\lambda/\delta \sim O(1)$. Computations in Reference 170 indicated that these reductions were probably due to periodic partial relaminarization approaching each wave crest, caused by the coincidence of large favorable pressure gradient and convex curvature influences.

The major problem with wavy walls for drag reduction is the attendant pressure drag, caused by a downstream phase shift in the oscillatory pressure distribution for $\lambda \sim O(\delta)$. This pressure drag is larger than the skin friction reduction usually obtainable over the wave. A Langley investigation into non-sinusoidal wave shapes with possibly lower pressure drag culminated in a family of skewed waves with gradual (straight) downstream-facing slopes and much steeper upstream facing surfaces (Fig. 25). However, initial tests of such surfaces suggest that the surface modifications necessary to reduce pressure drag have also apparently nullified much of the viscous drag reduction. Therefore, although we can now design wavy surfaces with essentially flat plate drag levels, a sizable net drag reduction may not be obtainable. Net benefits the order of 10 percent do evidently accrue from the use of "marco" waves ($\lambda/\delta \gg 1$) where $C_{D,p} = 0$ (see section entitled "Adverse Pressure Gradient" and Ref. 38).

Wall Turbulence "Sieves" and "Furry" Surfaces

A particularly simplex concept for reducing the intensity of turbulent motions near the wall is to "sieve" them through a local (wall region) breakup device. Results from Reference 139 (using restricted length vertical plates placed quite close together and

horizontal "small eddy" breakup devices placed close to the surface) indicate sizable drag reductions downstream, but estimates of the device drag penalty indicate net drag increases (at least thus far). Since this approach deals with the near wall region, the downstream relaxation distances are much shorter than for the large-eddy breakup devices discussed previously (Ref. 69). Further work on the Sandborn type devices (Ref. 139) is probably warranted. If the sieves are distributed continuously over the body surface and moreover the device elements are flexible, then one has a "furry" (Ref. 173) or "wheatfield" type of wall treatment (Refs. 174-180). This latter type of surface is of obvious interest to boundary layer meteorologists. The general conclusion, thus far, from the work on long, thin, closely packed and flexible wall roughnesses such as fur and wheat or rice indicates (a) that the overall drag increases substantially due to the increased effective wetted area contributed by the multitudinous individual elements and (2) the elements undergo a vibratory limit-cycle motion (at their characteristic frequency) and this "compliant-wall like" response usually feeds back into the turbulent boundary layer structure as a destabilization.

CONCLUDING REMARKS

Turbulent drag reduction is beginning to provide a viable and probably less sensitive alternative to laminar flow control for viscous drag reduction, particularly for fuselages and other bodies. The relatively recent (within the last 20 years) studies of "coherent structures" in wall boundary layers provide, for the first time, guidelines as to scales, frequencies, and possible mechanisms which might be used to control the turbulence structure and perhaps provide a net drag reduction.

An important (but simple) concept is that the turbulent drag reduction approach must be tailored to the particular application. For example, there are several very powerful techniques available for water flows (e.g., polymers and bubbles/gas layer (and perhaps compliant walls)) which have no counterpart in the air flow case. The air problem is much more difficult, with current approaches providing 5 to 20 percent type reductions as opposed to the 50 to 70 percent levels obtainable in water. Within the water-only approaches, the bubble method is particularly interesting for surface ships where a large reservoir of air (the atmosphere) is readily available for compressing and injecting.

Aside from relaminarization, for air flow applications the "best" current approaches appear to be nonplanar geometries: (1) large-eddy breakup devices (20 percent thus far for low speeds), (2) convex curvature (at low speeds, reductions in the 20 percent range appear to be obtainable, although this has not yet been demonstrated), and (3) riblets (10 percent). On a localized basis, adverse pressure gradients and slot injection can probably provide meaningful reductions, along with the old standbys of wall heating and porous wall injection, depending again upon the application. The remaining techniques are mainly applicable only to very specialized situations; e.g., wall cooling (very low speeds) MHD (magnetic flowing media) and fibers (requires fiber availability or a recirculating system). It should be noted that very little research is yet available for combinations of methods. Limited data for the riblet/LEBU combination (Ref. 103) indicates that the drag reductions are nearly additive, and various combinations of polymer systems have been attempted (polymers and particles (Ref. 181), polymers and magnetically controlled particles (Refs. 182), polymer and air film (Ref. 183) and polymer and compliant walls (Ref. 184). In addition to the drag reduction techniques discussed herein, there are several passive approaches available which lead to "relaminarization" (Ref. 28), such as a favorable pressure gradient. Also, the combined "thicker" and energy extraction methods remain to be explored fully.

Some possibility exists for development of a "smart wall." Since the wall pressure signature of the preburst flow is known (e.g., Ref. 185), this could be sensed and used to trigger a real-time wall (or flow field) reaction designed to alter/modify the burst process (see Refs. 186-188). The correct phase relation is the critical issue, simply pulsing at some average frequency is not suitable/effective (see Refs. 189, 190). The obvious problem with this approach is the extremely small scales and attendant high frequencies associated with the turbulent boundary layer wall production processes. (The ion wind or an electric approach might have the necessary spatial and temporal response for a "real time" feedback control system in air). For the water case phased control is evidently feasible (Ref. 188).

Finally, the turbulence modification and drag reduction approaches discussed herein are probably a small subset of the real range of possibilities. A key to uncovering other (perhaps better) techniques is to approach the problem from the viewpoints of turbulence control and invention. Much of the previous turbulence research was of the passive (study what exists) type. This is a plea for more active (e.g., control/invention) studies. The research aimed at basic understanding should continue, but significant increases in understanding often result from attempts to control for technological purposes.

REFERENCES

1. Schairer, G. S.: Some Opportunities for Progress in Aircraft Performance. 27th Wright Brothers Lecture, AIAA Journal of Aircraft, Vol. 1, No. 2, March-April 1964, pp. 49-70.
2. Steinheil, E.; Scherber, W.; Seidl, M.; and Rieger, H.: Investigations on the Interaction of Gases and Well-Defined Solid Surfaces With Respect to Possibilities for Reduction of Aerodynamic Friction and Aerothermal Heating. (Domier-System GmbH, Friedrichshafen, West Germany) In: Rarefied Gas Dynamics; International Symposium, 10th, Aspen, Co, July 18-23, 1976, Technical Papers, Part I. New York, AIAA 1977, pp. 589-602.
3. Narasimha, Roddam; and Ojba, S. K.: Effect of Longitudinal Surface Curvature on Boundary Layers. Journal of Fluid Mechanics, Vol. 29, Part I, 1967, pp. 187-199.
4. Gampert, B.; Homann, K.; and Rieke, H. B.: The Drag Reduction in Laminar and Turbulent Boundary Layers by Prepared Surfaces With Reduced Momentum Transfer. Israel Journal of Technology, Vol. 18, 1980, pp. 287-292.
5. Hefner, Jerry N.; and Bushnell, Dennis M.: An Overview of Concepts for Aircraft Drag Reduction. AGARD Report No. 654, Oct. 1975, pp. 1-1 - 1.30.
6. Kozlov, L. F.; and Babenko, V. V.: Eksperimental Issledovaniya Propranichogo Sloya. Institute of Hydromechanics, Kiev, U.S.S.R., 1978.
7. Bushnell, Dennis M.; and Tuttle, Marie H.: Survey and Bibliography on Attainment of Laminar Flow Control in Air Using Pressure Gradient and Suction, Vol. 1. NASA RP 1035, December 1979.
8. Beeler, George B.: Influence of a Tandem Large-Eddy Breakup Device on Tubulent Wall Pressure Fluctuations. To be published in AIAA Journal.
9. Calisal, S. M.: An Attempt to Detect the Importance of Turbulent Boundary Layer in Ship Wave Resistance. AD No. A089174; 19th American Towing Tank Conference, University of Michigan, Ann Arbor, MI, July 1980.
10. Lindemann, A. Margrethe: Turbulent Reynolds Analogy Factors of Stacked Large-Eddy Breakup Devices. Submitted to the AIAA Journal of Spacecraft and Rockets.
11. Goodman, Wesley L.; Morrissette, E. Leon; and Hussaini, M. Yousuff: Shock-Boundary Layer Interaction Separation Control. Presented at the AIAA Shear Flow Control Conference, Boulder, Colorado, March 12-14, 1985, AIAA Paper No. 85-0523.
12. Lin, John C.: Effect of Wall Temperature Control on Low-Speed Axisymmetric Body Drag. M.S. Thesis, Old Dominion University, Dec. 1984.
13. Fifth Symposium on Naval Hydrodynamics, Ship Motions and Drag Reduction. Office of Naval Research, Department of the Navy, ACR-112, 1964.
14. Viscous Drag Reduction. Proceedings of the Symposium on Viscous Drag Reduction held at the LTV Research Center, Dallas, TX. September 24-25, 1968. Edited by C. Sinclair Wells. Plenum Press, New York, 1969.
15. Proceedings of the International Conference on Drag Reduction 1974. Editor, N. G. Coles, BHRA Fluid Engineering, Cranfield, Bedford, England, September 1974.
16. Drag Reduction. Papers Presented at the Second International Conference on Drag Reduction. University of Cambridge, Aug. 31-Sept. 2, 1977, BHRA Fluid Engineering.
17. White, A.; and Hemmings, J. A. G.: Drag Reduction by Additives. Review and Bibliography. BHRA Fluid Engineering, 1976.
18. Viscous Flow Drag Reduction. AIAA Progress in Astronautics and Aeronautics, Vol. 72. Edited by Gary R. Hough, 1980.
19. Structure of Turbulence and Drag Reduction. Edited by F. N. Frenkiel, M. T. Landahl, and J. L. Lumley. International Union of Theoretical and Applied Mechanics Symposium 1976, American Institute of Physics. Phys. of Fluids, Vol. 20, No. 10, Pt. 2, October 1977.
20. Special Course on Concepts for Drag Reduction. AGARD-R-654, von Karman Institute, Rhode-St-Genese, Belgium, march 28-April 1, 1977.
21. Lang, T. G.: Torpedo Drag Reduction. U.S. Naval Ordnance Test Station, NAVORD Report 6451, May 1959.
22. Bushnell, Dennis M.: Turbulent Drag Reduction for External Flows. Presented at the AIAA 21st Aerospace Sciences Meeting, Reno, Nevada, January 10-13, 1983, AIAA Paper No. 83-0227.

23. Bushnell, D. M.; Anders, J. B.; Walsh, M. J.; and McInville, R. V.: Turbulent Drag Reduction Research. Presented at AGARD Conference on Improvement of Aerodynamic Performance Through Boundary Layer Control and High Lift Systems, Brussels, Belgium, May 21-23, 1984. AGARD-CP-365.
24. Bushnell, D. M.: NASA Research on Viscous Drag Reduction II. Presented at ASME Symposium on Laminar Turbulent Boundary Layers, Energy Sources Technology Conference, New Orleans, Louisiana, Feb. 12-16, 1984, pp. 93-98. FED-Vol. 11.
25. Thomas, Andrew S. W.: Aircraft Drag Reduction Technology. Presented at AGARD Conference on Improvement of Aerodynamic Performance Through Boundary Layer Control and High Lift Systems, Brussels, Belgium, May 21-23, 1984. AGARD-CP-365.
26. Narasimha, R.; and Sreenivasan, K. R.: The Control of Turbulent Boundary-Layer Flows. Presented at the AIAA Shear Flow Control Conference in Boulder, Colorado, March 12-14, 1985. AIAA Paper No. 85-0517.
27. Aslanov, P. V.; Maksyutenko, S. N.; Povkh, I. L.; Simonenko, A. P.; and Stupin, A. B.: Turbulent Flows of Solutions of Surface-Active Substances. Fluid Dynamics, Vol. 15, No. 1, 1980, pp. 27-33.
28. Narasimha, R.; and Sreenivasan, K. R.: Re'aminarization of Fluid Flows. Advances in Applied Mechanics, Vol. 19. Edited by Chia-Shun Vih, Academic Press, 1979.
29. Coherent Structure of Turbulent Boundary Layers. Editors, C. R. Smith and D. E. Abbott. AFOSR/Lehigh University Workshop, November 1978.
30. Cantwell, B. J.: Organized Motion in Turbulent Flow. Annual Reviews of Fluid Mechanics, 1981, V. 13, pp. 457-515.
31. Hussain, A. K. M. F.: Coherent Structures - Reality and Myth. Physics of Fluids, V. 26, No. 10, October 1983, pp. 2816-2850.
32. Zilberman, M.; Wygananski, I.; and Kaplan, R. E.: Transitional Boundary Layer Spot in a Fully Turbulent Environment. IUTAM Symposium 1976, Structure of Turbulence and Drag Reduction, Physics of Fluids, V. 20, No. 10, 1977, pp. S258-S271.
33. Liepmann, H. W.: The Rise and Fall of Ideas in Turbulence. American Scientist, Vol. 67, 1979, pp. 221-228.
34. Proceedings of the 1980-81 AFOSR-HTTM-Stanford Conference on Complex Turbulent Flows, 1982.
35. Stratford, B. S.: Prediction of Separation of the Turbulent Boundary Layer. Journal of Fluid Mechanics, 1959, pp. 1-16.
36. Sparangenberg, W. G.; Rowland, W. R.; and Mease, N. E.: Measurements in a Turbulent Boundary Layer Maintained in a Nearly Separating Condition. Fluid Mechanics of Internal Flow. Proceedings of the Symposium on the Fluid Mechanics of Internal Flow, General Motors Research Laboratories, Warren, Michigan, 1965, pp. 110-151.
37. Charmichael, B. H.: Application of Sailplane and Low-Drag Underwater Vehicle Technology to the Long-Endurance Drone Problem. AIAA/MIT/SSA Second International Symposium on the Technology and Science of Low Speed and Motorless Flight, Cambridge, MA, Sept. 11-13, 1974. Paper No. 74-1036.
38. Lin, John C.; Weinstein, L. M.; Watson, R. D.; and Balasubramanian, R.: Turbulent Drag Characteristic of Small Amplitude Rigid Surface Waves. Presented at the AIAA 21st Aerospace Sciences Meeting, Reno, Nevada, January 10-13, 1983. Paper No. 83-0228.
39. Schraub, F. A.; and Kline, S. J.: A Study of the Structure of the Turbulent Boundary Layer With and Without Longitudinal Pressure Gradients. Report MD-12, Thermosciences Division, Department of Mechanical Engineering, Stanford University, Stanford, CA, March 1965.
40. Cary, A. M., Jr.; Bushnell, D. M.; and Hefner, J. N.: Slot Injection for Skin-Friction Drag Concepts for Drag Reduction, presented at the von Karman Institute, Rhode-St-Genese, Belgium, March 28-April 1, 1977, pp. 5-1 - 5-11.
41. Wiedemann, J.; and Gersten, K.: Drag Reduction Due to Boundary-Layer Control by Combined Blowing and Suction. Presented at AGARD Conference on Improvement of Aerodynamic Performance Through Boundary Layer Control and High Lift Systems, Brussels, Belgium, May 21-23, 1984. AGARD CP-365.
42. Howard, F. G.; Hefner, J. N.; and Srokowski, A. J.: Multiple Slot Skin Friction Reduction. Journal of Aircraft, Vol. 12, No 9, Sept. 1975, pp. 753-754.

43. Oster, D.; Wagnanski, I.; Oziomba, B.; and Fiedler, H.: On the Effect of Initial Conditions on the Two-Dimensional Turbulent Mixing Layer. Lecture Notes in Physics. Structure and Mechanisms of Turbulence 1, Proceedings of the Symposium on Turbulence. Technische Universitat Berlin, Aug. 1977, Springer-Verlag, New York, 1978, pp. 48-64.
44. Vlasov, Ye. V.; and Genevskiy, A. S.: Bilateral Character of Acoustic Action on Free Turbulent Jets. NASA TT F-16658, November 1975.
45. Zaman, K. B. M. O.; and Hussain, A. K. M. F.: Turbulence Suppression in Free Shear Flows by Controlled Excitation. Presented at the AIAA 13th Fluid and Plasma Dynamics Conference, July 1980, Snowmass, CO. Paper No. AIAA 80-1338.
46. Spangler, Jack F.: Effects of Periodic Blowing Through Flush Transverse Slots on Turbulent Boundary Layer Skin Friction. NASA CR-634, October 1966.
47. Watson, R. D.; and Balasubramanian, R.: Wall Mass Transfer and Pressure Gradient Effects on Turbulent Skin Friction. AIAA Journal, V. 22, No. 1, January 1984, pp. 143-145.
48. Bushnell, D. M.; Watson, R. D.; and Holley, B. B.: Influence of Mach Number and Reynolds Number on Skin Friction Reduction due to Wall Injection. Engineering Note, AIAA Journal of Spacecraft and Rockets, Col. 12, No. 8, August 1975, pp. 506-508.
49. Schetz, Joseph A.; and Van Overeem, Johannes: Skin Friction Reduction in Supersonic Flow By Injection Through Slots, Porous Sections and Combinations of the Two. NASA CR-2491, March 1975.
50. Leont'ev, A. I.; Puzach, V. G.; Komarov, V. P.; Ermolaev, I. K.; Dubina, N. V.; and Fadeev, V. A.: Friction at the Surface of a Plate With Simultaneous Injection and Suction of Gas. Journal of Engineering Physics, Vol. 33, No. 2, pp. 204-209, August 1977.
51. Leont'ev, A. I.; Puzach, V. G.; Komarov, V. P.; Ermolaev, I. K.; and Dubina, N. V.: Drag of a Plate With Simultaneous Unequal Mass Blowing and Suction. Journal of Engineering Physics, Bol. 43, No. 1, pp. 5-9, July 1982.
52. Wooldridge, C. E.; and Muzzy, R. J.: Boundary Layer Turbulence Measurements With Mass Addition and Combustion. AIAA Journal, Vol. 4, No. 11, Nov. 1966, pp. 2009-2016.
53. Malik, Mujeeb, R.; Weinstein, Leonard M.; and Hussaini, M. Yousuff: Ion Wind Drag Reduction. Presented at the AIAA 21st Aerospace Sciences Meeting, Reno, Nevada, January 10-13, 1983. Paper No. 83-0231.
54. Robinson, Myron: A History of the Electric Wind. American Journal of Physics, Vol. 4, No. 5, May 1962, pp. 366-372.
55. Velkoff, H. R.; and Godfrey, R.: Low Velocity Heat Transfer, Vol 10, February 1979, pp. 157-163.
56. Velkoff, H. R.; and Kulacki, F. A.: Electrostatic cooling. ASME Paper No. 77-DE-36, May 1977, pp. 1-17.
57. Ketchum, Jeffery J.; and Velkoff, Henry R.: An Experimental Investigation of the Effect of Electrically Induced Controlled Frequency Perturbations on Boundary Layer Transition. Ohio State University, Technical Report No. 5, June 1967.
58. Hopfinger, E. J.; and Gosse, J. P.: Charge Transport by Self-Generated Turbulence in Insulating Liquids Submitted to Unipolar Injection. The Physics of Fluids, vol. 14, No. 8, August 1971, pp. 1671-1682.
59. Nanevicz, J. E.: Alleviation Techniques for Effects of Static Charging on Avionics. AGARD Atmospheric Electrical Aircraft Interaction, 1980.
60. Nanevicz, J. E.: Static Electricity Phenomena: Theory and Problems. Conference on Certification of Aircraft for Lightning and Atmospheric Electricity Hazards, ONERA - Chatillon, France, Sept. 14-21, 1978.
61. Zykov, E. V.; and Zykov, V. A.: Impurity-Initiated Unipolar Gas Flow. State Pedagogic Institute, Armavir. Translated from Teplofizika Vysokikh Temperatur, Vol. 11, No. 3, May-June 1973, pp. 585-586.
62. Kestin, J.; and Shah, V. L.: The Effect of Long-Range Intermolecular Forces on the Drag of an Oscillating Disk and on the Viscosity of Gases. Technical Report AFFDL-TR-68-86, January 1968.
63. Clark, J.; Field, J. E.; and Wilby, W. A.: Reduction of Aerodynamic Drag. University of Cambridge, Interim Scientific Report No. 1, AFOSR-79-0057, May 1980.

64. Lobert, C.: Drag Reduction by Means of Active Boundary Layer Thickening. Presented at the 23rd Annual Israel Conference on Aviation and Astronautics, Tel Aviv and Haifa, Israel, February 1981, pp. 233-241.
65. Corke, T. C.; Nagib, H. M.; and Guezennec, Y. G.: A New View on Origin, Role and Manipulation of Large Scales in Turbulent Boundary Layers. Illinois Institute of Technology, NASA CR-165861, February 1982.
66. Bertelrud, A.; Truong, T. V.; and Avellan, F.: Drag Reduction in Turbulent Boundary Layers Using Ribbons. AIAA 9th Atmospheric Flight Mechanics Conference, August 1982, San Diego, CA. AIAA Paper No. 82-1370.
67. Yajnik, K. S.; and Acharya, M.: Nonequilibrium Effects in a Turbulent Boundary Layer Due to the Destruction of Large Eddies. Lecture Notes in Physics, Structure and Mechanisms of Turbulence, Proceedings of the Symposium on Turbulence held at the Technische Universitat Berlin, August 1977, Springer-Verlag, New York, 1978, pp. 249-260.
68. Yajnik, K.; and Lieber, Paul: Fundamental Properties of Eddies. Seventh Symposium Naval Hydrodynamics, Rome, Italy, August 25-26, 1968, pp. 435-457.
69. Hefner, Jerry N.; Anders, John B.; and Bushnell, D. M.: Alteration of Outer Flow Structures for Turbulent Drag Reduction. Presented at the AIAA 21st Aerospace Sciences Meeting, Reno, Nevada, Jan. 10-13, 1983.
70. Yajnik, K. S.; Acharya, M.; and Sundaram, S.: Non-equilibrium Effects in a Turbulent Boundary Layer. First Asian Congress of Fluid Mechanics, December 1980, Indian Institute of Science Bangalore.
71. Yajnik, K. S.; Sandaram, S.; and Acharya, M.: Observations on Large Scale Motions in Highly Disturbed Boundary Layers. Structure of Complex Turbulent Shear Flow, IUTAM Symposium, Marseille, 1982.
72. Hefner, Jerry N.; Weinstein, Leonard M.; and Bushnell, Dennis M.: Large-Eddy Breakup Scheme for Turbulent Viscous Drag Reduction. Viscous Flow Drag Reduction, Vol. 72. Presented at the Symposium on Viscous Drag Reduction, Dallas, Texas, November 1979.
73. Loehrke, R. I.; and Nagib, H. M.: Experiments on Management of Free Stream Turbulence. AGARD Report No. 598, September 1972.
74. Corke, T. C.; Guezennec, Y.; and Nagib, H. M.: Modification in Drag of Turbulent Boundary Layers Resulting from Manipulation of Large-Scale Structures. Viscous Flow Drag Reduction. Presented at the Symposium on Viscous Drag Reduction, Dallas, TX, November 1979, pp. 128-143.
75. Liss, A. Yu.; and Ulolttsev, A. A.: Influence of Vortex-Wing Interaction on Reducing Vortex Induction. Izvestiya Vuz. Aviatsionnaya Tekhnika, Vol. 16, No. 3, 1973, pp. 5-10.
76. Anders, J. B.; Hefner, J. N.; and Bushnell, D. M.: Performance of Large-Eddy Breakup Devices at Post-Transitional Reynolds Numbers. Presented at the AIAA 22nd Aerospace Sciences Meeting, January 9-12, 1984, Reno, NV, Paper No. 84-0345.
77. Nguyen, V. D.; Dickinson, L.; Jean, Y.; Chalifour, Y.; Anderson, J.; Lemay, J.; Haerberle, D.; and Larose, G.: Some Experimental Observations of the Law of the Wall Behind Large-Eddy Breakup Devices Using Servo-Controlled Skin Friction Balances. Presented at the AIAA 22nd Aerospace Sciences Meeting, January 9-12, 1984, Reno, Nevada. Paper No. 84-0346.
78. Nguyen, V. D.; Dickinson, J.; Lemay, J.; Provencal, Y.; Jean, Y.; and Chalifour, Y.: The Determination of Turbulent Skin Friction Behind Flat Plate Turbulence Manipulators Using Servo-Controlled Balances. Presented at the 14th ICAS Congress, Toulouse, September 9-14, 1984.
79. Lemay, J.; Provencal, D.; Gourdeau, R.; Nguyen, V. D.; and Dickinson, J.: More Detailed Measurements Behind Turbulence Manipulators Including Tandem Devices Using Servo-Controlled Balances. Presented at the AIAA Shear Flow Control Conference, Boulder, Colorado, March 12-14, 1985. Paper NO. 85-0521.
80. Nagib, H. M. et al: Management of Turbulent Flow Structures in Boundary Layers Aimed at Drag Reduction. NASA CR-174491, May 1984.
81. Falco, R. E.: A Study of the Effects of LEBU Devices on Turbulent Boundary Layer Drag. Final Technical Report for 11-1-81 to 10-31-82.
82. Mumford, J. C.; and Savill, A. M.: Parametric Studies of Flat Plate, Turbulence Manipulators Including Direct Drag Results and Laser Flow Visualization. Presented at ASME Symposium on Laminar Turbulent Boundary Layers, Energy Sources Technology Conference, New Orleans, Louisiana, February 12-16, 1984, pp. 41-52.

83. Anders, J. B.; and Watson, R. D.: Airfoil Large-Eddy Breakup Devices for Turbulent-Drag Reduction. Paper presented at the AIAA Shear Flow Control Conference, Boulder, Colorado, March 12-14, 1985. Paper No. 85-0520.
84. Bushnell, Dennis M.: Body-Turbulence Interaction. Presented at the AIAA 17th Fluid Dynamics, Plasmadynamics and Lasers Conference, Snowmass, Colorado, June 25-27, 1984. AIAA Paper No. 84-1527.
85. Plesnick, M. W.; and Nagib, H. M.: New Drag Reduction in Turbulent-Boundary Layers Resulting from Optimized Manipulation. Presented at the AIAA Shear Flow Control Conference, Boulder, Colorado, March 12-14, 1985. Paper No. 85-0518.
86. Guezennec, Y. G.; and Nagib, H. M.: Documentation of Mechanisms Leading to New-Drag Reduction in Manipulated Turbulent-Boundary Layers. Presented at the AIAA Shear Flow Control Conference, Boulder, Colorado, March 12-14, 1985. Paper No. 85-0519.
87. Bertelrud, Arild: Full Scale Experiments into the Use of Large-Eddy-Breakup Devices for Drag Reduction on Aircraft. Presented at AGARD Conference on Improvement of Aerodynamic Performance Through Boundary Layer Control and High Lift Systems, Brussels, Belgium, May 21-23, 1984. AGARD-CP-365.
88. Carmichael, B. H.: Low Reynolds Number Airfoil Survey, Vol. 1. NASA CR-165803, November 1981.
89. Yuu, Shinichi: Experimental Study of Turbulent Flow Near a Suction Tube. AIAA Journal, Vol. 18, No. 2, 1980, pp. 222-223.
90. Harvey, W. D.; Bushnell, D. M.; and Beckwith, I. E.: on the Fluctuating Properties of Turbulent Boundary Layers for Mach Numbers up to 9.0. NASA TN D-5496, 1969.
91. Johnson, C. B.; and Bushnell, D. M.: Review and Evaluation of N Power Law Velocity Profiles as Applied to Experimental Turbulent Boundary Layer Data. NASA TN D-5733, 1970.
92. Gad-El-Hak, Mohamed; Blackwelder, Ron F.; and Riley, James J.: On the Growth of Turbulent Regions in Laminar Boundary Layers. Journal of Fluid Mechanics, Vol. 110, 1981, pp. 73-95.
93. Goodman, Wesley L.: Emmons Spot Forcing for Turbulent Drag Reduction. AIAA Journal, Vol. 23, No. 1, January 1985, pp. 155-157.
94. Chambers, F. W.: Synthetically-Generated, Turbulent-Boundary Layer Development and Structure. Presented at the AIAA Shear Flow Control Conference, Boulder, Colorado, March 12-14, 1985. Paper No. 85-0534.
95. Schubauer, G. B.; and Klebanoff, P. S.: Contributions on the Mechanics of Boundary Layer Transition. NACA TN-3489, September 1955.
96. McGinley, C. B.; and Beeler, G. B.: Large-Eddy Substitution Via Vortex Cancellation for Wall-Turbulence Control. Presented at the AIAA Shear Flow Control Conference, Boulder, CO, March 12-14, 1985. Paper No. 85-0549.
97. Goodman, W. L.: The Effect of Opposing-Unsteady Vorticity on the Turbulent Structures in Wall Flow. Presented at the AIAA Shear Flow Control Conference, Boulder, CO, March 12-14, 1985. Paper No. 85-0550.
98. Carlson, L. W.; and Irvine, T. F., Jr.: Fully Developed Pressure Drop in Triangular Shaped Ducts. Journal of Heat Transfer, November 1961, pp. 441-444.
99. Hooshmand, A.; Youngs, R. A.; Wallace, J. M.; and Balint, J.-L.: An Experimental Study of Changes in the Structure of a Turbulent Boundary Layer Due to Surface Geometry Changes. AIAA Paper No. 83-0320.
100. Walsh, M. J.; and Weinstein, L. M.: Drag and Heat Transfer on Surfaces With Small Longitudinal Fins. Presented at the AIAA 11th Fluid and Plasma Dynamics Conference. AIAA Paper No. 78-1161, Seattle, WA, July 1978.
101. Walsh, Michael J.: Drag Characteristics of V-Groove and Transverse Curvature Riblets. Viscous Flow Drag Reduction. Presented at the Symposium on Viscous Drag Reduction, Dallas, Texas, Nov. 1979. Progress in Astronautics and Aeronautics AIAA, Vol. 72, 1980, pp. 168-184.
102. Walsh, Michael J.: Turbulent Boundary Layer Drag Reduction Using Riblets. Presented at the AIAA 12th Aerospace Sciences Meeting, Orlando, FL, January 1982. AIAA Paper No. 82-0169.
103. Walsh, M. J.; and Lindemann, A. M.: Optimization and Application of Riblets for Turbulent Drag Reduction. Presented at the AIAA 22nd Aerospace Sciences Meeting, Reno, Nevada, January 9-12, 1984. AIAA Paper No. 84-3468.

104. Bacher, E. V.; and Smith, C. R.: A Combined Visualization-Anemometry Study of the Turbulent-Drag Reducing Mechanisms of Triangular Micro-Groove Surface Modifications. Presented at the AIAA Shear Flow Control Conference, Boulder, CO, March 12-14, 1985. Paper No. 85-0548.
105. Gallagher, J. A.; and Thomas, A. S. W.: Turbulent Boundary Layer Characteristics Over Streamwise Grooves. Presented at the AIAA 2nd Applied Aerodynamics Conference, August 21-23, 1984, Seattle, WA. AIAA 84-2185.
106. Lindemann, A. Margrethe: Turbulent Reynolds Analogy Factors for Non-Planar Surface Microgeometries. To be published in AIAA Journal of Spacecraft and Rockets, July-August 1985.
107. Johansen, John B.: The Effects of Sublayer Scale Streamwise Surface Modifications on Turbulent Boundary Layers. Masters Thesis, Lehigh University, Dept. of Mechanical Engineering and Mechanics, November 1982.
108. Nitschke, Petra: Experimentelle Untersuchung der turbulenten Stromung in glatten and langsgerrillten kohren. Max-Planck-Institut for Stromungsforschung, Göttingen, April 1983.
109. Bechert, D. W.; Rief, W. E.; and Hoppe, G.: On the Drag Reduction of the Shark Skin. Presented at the AIAA Shear Flow Control Conference, Boulder, CO, March 12-14, 1985. Paper No. 85-0546.
110. Bigelow, Henry B.; Farfante, Isabel Perez; and Schroeder, William C.: Fishes of the Western North Atlantic Part 1. Sears Foundation for Marine Research, Yale University, New Haven, 1948.
111. Dreitinger, Richard L.; and Middleton, David B.: Aircraft Surface Coatings for Drag Reduction/Erosion Protection. SAE Technical Paper Series. Aerospace Congress and Exposition, Anaheim, CA, October 1981.
112. Aleyev, Yu. G.: Nekton. Dr. W. Junk b.v. Publishers - The Hague, 1977.
113. Smits, A. J.; Eaton, J. A.; and Bradshaw, P.: The Response of a Turbulent Boundary Layer to Lateral Divergence. Journal of Fluid Mechanics, Vol. 94, Part 2, 1979, pp. 243-268.
114. McCormick, M. E.; and Bhattacharyya, R.: Drag Reduction of a Submersible Hull by Electrolysis. Naval Engineers Journal, April 1973, pp. 11-16.
115. Gay, Archibald: Film Boiling Heat Transfer and Drag Reduction. General Dynamics, Conv. Air Aerospace Division. Report AD 722428, 1971.
116. Reduction in Drag of Submerged Bodies by Partial Enclosure in Gaseous Cavities. United Aircraft Corporation Technical Report - AD 340908, June 1963.
117. Turpin, Francis J.; and Blaes, Viggo A.: Experimental Investigation of a Low Drag Sidewall Development Program. Hydronautics, Inc., Technical Report 920-1, November 1969.
118. Bogdevich, V. G.; Evseen, A. R.; Malyuga, A. G.; and Migirenko, G. S.: Gas-Saturation Effect on Near-Wall Turbulence Characteristics. Second International Conference on Drag Reduction, Aug.-Sept. 1977, pp. D2-25-D2-37.
119. Merkle, C. L.; Madavan, N. K.; and Deutsch, S.: Reduction of Turbulent Skin Friction by Microbubbles. Physics of Fluids, Vol. 27, No. 2, February 1984, pp. 356-363.
120. Merkle, C. L.; Madavan, N. K.; and Deutsch, S.: The Effects of Porous Material on Microbubble Skin Friction Reduction. Presented at the AIAA 22nd Aerospace Sciences Meeting, Reno, Nevada, June 9-12, 1984, AIAA Paper No. 84-0348.
121. Madavan, N. K.; Merkle, C. L.; and Deutsch, S.: Numerical Investigations into the Mechanisms of Microbubble Drag Reduction. Laminar Turbulent Boundary Layers, American Society of Mechanical Engineers, Vol. 11, pp. 31-40, February 1984.
122. Drag Reduction by Microbubbles: Current Research Status. Presented at the AIAA Shear Flow Control Conference, Boulder, Colorado, March 12-14, 1985. AIAA Paper No. 85-0537.
123. Turbulence Phenomena: An Introduction to the Eddy Transfer of Momentum, Mass, and Heat, Particularly at Interfaces. Davies, J. T.: "Eddies at Film-Covered Surfaces pp. 250-272, 1972.
124. Carpenter, P. W.; and Garrad, A. D.: The Hydrodynamic Stability of Flow Over Kramer-Type Compliant Surfaces. Part 1. Tollmien-Schlichting Instabilities. University of Exeter, Technical Note 83/1, July 1983.

125. Bushnell, Dennis M.; Hefner, Jerry N.; and Ash, Robert L.: Effect of Compliant Wall Motion on Turbulent Boundary Layers. AGARD Report No. 654. Special Report on Concepts for Drag Reduction. June 1977, pp. 9-1 - 9-26.

126. Kanarskiy, M. V.; and Teslo, A. P.: Turbulent Flow Over a Plate With a Compliant Surface. Fluid Mechanics, Soviet Research, Vol. 9, No. 5, September-October 1980.

127. Taylor, Thomas D.; and Hurdiss, David A.: Drag Reduction Studies by Compliant Surfaces and Surface-Active Substances. John Hopkins APL Technical Digest, Jan.-Mar. 1984, pp. 56-58.

128. Roebuck, Ian: Mutual Impedance Effects in Active Noise Control and the Possibility of Extracting Energy From Turbulence. Presented at Meeting on Acoustics of Turbulent Flows, Euromech 142, Lyon, France, 1981.

129. Pfenninger, W.; and Bacon, John W., Jr.: Investigation of Methods for Re-Establishment of a Laminar Boundary Layer From Turbulent Flow. Prepared under Navy, Bureau of Naval Weapons, Contract No. 63-076-c, Report No. NOR 65-48, February 1965.

130. Lekoudis, S.: The Stability of the Boundary Layer on a Swept Wing With Wall Cooling. AIAA 12th Fluid and Plasma Dynamics Conference, Williamsburg, Virginia, July 23-25, 1979. AIAA Paper No. 79-1495.

131. Pfenninger, Werner: Laminar Flow Control Laminarization. AGARD Report No. 654. Special Course on Concepts for Drag Reduction. June 1977, pp. 3-1 - 3-75.

132. Roper, A. T.; and Gentry, G. L., Jr.: Analysis of a Turbulent Boundary Layer Over a Moving Ground Plane. NASA TN D-6788, July 1973.

133. Kendall, J. M.: The Turbulent Boundary Layer Over a Wall With Progressive Surface Waves. Journal of Fluid Mechanics, Vol. 41, Part 2, 1970, pp. 259-281.

134. Mulhern, P. J.: Turbulent Flow Over a Periodic Rough Surface. Physics of Fluids, Vol. 21, No. 7, July 1978, pp. 1113-1115.

135. Liu, C. K.; Kline, S. J.; and Johnston, J. P.: An Experimental Study of Turbulent Boundary Layer on Rough Walls. Report MD-15, Stanford, California, July 1966.

136. Townes, Harry W.; and Sabersky, Rolk H.: Experiments on the Flow Over a Rough Surface. International Journal Heat Mass Transfer, Vol. 9, Pergamon Press, 1966, pp. 729-738.

137. Gatski, T. B.; and Grosch, C. E.: Embedded Cavity Drag in Steady and Unsteady Flows. Presented at the AIAA 22nd Aerospace Sciences Meeting, Reno, Nevada, January 9-12, 1984.

138. Reiman, Thomas C.; and Sabersky, Rolk H.: Laminar Flow Over Rectangular Cavities. International Journal Heat Mass Transfer, Vol. 11, Pergamon Press, 1968, pp. 1083-1085.

139. Sandborn, V. A.: Aerodynamics Control of Surface Shear Stress Fluctuations in Turbulent Boundary Layers. Department of Civil Engineering, Colorado State University, April 1981.

140. Smits, A. J.; Young, S. T. B.; and Bradshaw, P.: The Effect of Short Regions of High Surface Curvature on Turbulent Boundary Layers. Imperial College, London, Journal of Fluid Mechanics (1979), Vol. 94, Part 2, pp. 209-242.

141. Sprangler, J. G.; and Wells, C. S., Jr.: Effect of Spiral Longitudinal Vortices on Turbulent Boundary Layer Skin Friction. NASA CR-145, December 1964.

142. Bandyopadhyay, P. R.: Performance of Wall-Drag Reducing Outer-Layer Devices in Rough-Wall Boundary Layers. Presented at the AIAA Shear Flow Control Conference, Boulder, Colorado, March 12-14, 1985. Paper No. 85-0558.

143. Bradshaw, P.: Effects of Streamline Curvature on Turbulent Flow. AGARDograph No. 169, London, August 1973.

144. So, Ronald M. C.; and Mellor, George L.: An Experimental Investigation of Turbulent Boundary Layers Along Curved Surfaces. NASA CR-1940, April 1972.

145. Maroney, R. N.: Measurements of Turbulent Boundary Layer Growth Over a Longitudinally Curved Surface. Colorado State University, THEMIS Technical Report No. 25, January 1974.

146. Shivaprasad, B. G.; and Ramaprian, B. R.: Some Effects of Longitudinal Wall-Curvature on Turbulent Boundary Layers. Symposium on Turbulent Shear Flows, April 1977, University Park, PA, pp. 9.21-9.28.

147. Gillis, Jay Colin: Turbulent Boundary Layer on a Convex, Curved Surface. Ph.D. Thesis, Stanford University, June 1980.

148. Simon, T. W.; Moffat, R. J.; Johnston, J. P.; and Kays, W. M.: Turbulent Boundary Layer Heat Transfer Experiments: Convex Curvature Effects, Including Introduction and Recovery. Report No. HMT-32, November 1980.
149. Thomann, H.: Effect of Streamwise Wall Curvature on Heat Transfer in a Turbulent Boundary Layer. *Journal of Fluid Mechanics*, Vol. 33, Part 2, 1968, pp. 283-292.
150. Pontikos, N. S.: The Structure of Three-Dimensional Turbulent Boundary Layers. Ph.D. Thesis, Imperial College, London, September 1982.
151. Malik, M. R.; and Poll, D. I. A.: Effect of Curvature on Three-Dimensional Boundary Layer Stability. Presented at the AIAA 17th Fluid Dynamics, Plasmadynamics and Lasers Conference, Snowmass, Colorado, June 25-27, 1984. AIAA Paper No. 84-1672.
152. Radin, I.; Zakin, J. L.; and Patterson, G.: Drag Reduction in Solid-Fluid Systems. *AICHE Journal*, Vol. 21, No. 2, Mar. 1975, pp. 358-381.
153. Hoyt, J. W.: Turbulent Flow of Drag-Reducing Suspensions. NUC TP 299, July 1972.
154. Pfeffer, R.; and Rosetti, S. J.: Experimental Determination of Pressure Drop and Flow Characteristics of Dilute Gas-Solid Suspensions. NASA CR-1894, August 1971.
155. Radin, I.: Solid-Fluid Drag Reduction. Ph.D. Thesis, University of Missouri-Rolla, 1974.
156. Soo, S. L.; and Trezek, G. J.: Turbulent Pipe Flow of Magnesia Particles in Air. *I&EC Fundamentals*, Vol. 5, 1966.
157. Povkin I. L.; Bolonov, N. J.; and Eidel'man, A. Ye.: The Average Velocity Profile and the Frictional Loss in Turbulent Flow of an Aqueous Suspension of Clay. *Fluid Mechanics -- Soviet Research*, Vol. 8, No. 2, March-April 1979, pp. 118-124.
158. Fraim, Freeman W.; and Heiser, William H.: The Effect of a Strong Longitudinal Magnetic Field on the Flow of Mercury in a Circular Tube. *Journal of Fluid Mechanics*, Vol. 33, Part 2, 1968, pp. 397-413.
159. Reed, Claude B.; and Lykoudis, Paul S.: The Effect of a Transverse Magnetic Field on Shear Turbulence. *Journal of Fluid Mechanics*, Vol. 89, Part 1, 1978, pp. 147-171.
160. Branover, H.; and Claesson, S.: Some Peculiarities of Turbulence Suppression by Magnetic Fields and Their Use for Magnetic Flow Control in Liquid Metals. Presented at the Third Beer-Sheva International Seminar on Magnetohydrodynamic Flows and Turbulence, Ben-Gurion University of the Negev, Beer-Sheva, Israel, March 23-27, 1981.
161. Anderson, Gordon F.; and Wu, Yung-Kuang: Drag Reduction by Use of MHD Boundary-Layer Control. *Journal of Hydronautics*, Vol. 5, No. 4, pp. 150-152.
162. Ueda, Hiromasa; Mitsumoto, Shigeki; and Komori, Satoru: Buoyancy Effects on the Turbulent Transport Processes in the Lower Atmosphere. *Quarterly Journal Royal Meteorol. Soc.*, Vol. 107, No. 453, July 1981, pp. 561-579.
163. Arya, S. P. S.: Buoyancy Effects in a Horizontal Flat-Plate Boundary Layer. *Journal of Fluid Mechanics*, Vol. 68, Part 2, 1975, pp. 321-343.
164. Schetz, J. A.; and Kong, F.: Turbulent Boundary Layer Over Solid and Porous Surfaces With Small Roughness. AIAA 19th Aerospace Sciences Meeting, St. Louis, Missouri, January 1981. AIAA Paper No. 81-0418.
165. Kong, F. Y.; and Schetz, J. A.: Turbulent Boundary Layer Over Porous Surfaces With Different Surface Geometries. AIAA 20th Aerospace Sciences Meeting, Orlando, Florida, January 1982. AIAA Paper No. 41-0050.
166. Boldman, Donald R.; and Brinich, Paul F.: Skin Friction on a Flat Perforated Acoustic Liner. *AIAA Journal*, Vol. 14, No. 11, November 1976, pp. 1656-1659.
167. Wilkinson, S. P.: Influence of Wall Permeability on Turbulent Boundary Layer Properties. Presented at the AIAA 21st Aerospace Sciences Meeting, Reno, Nevada, January 10-13, 1983. AIAA Paper No. 83-0294.
168. Bahi, Lakhdar: Passive Shock Wave/Boundary Layer Control for Transonic Supercritical Airfoil Drag Reduction. Ph.D. Dissertation, Rensselaer Polytechnic Institute, May 1982.
169. Cary, Aubrey M., Jr.; Weinstein, Leonard M.; and Bushnell, Dennis M.: Drag Reduction Characteristics of Small Amplitude Rigid Surface Waves. *Viscous Flow Drag Reduction*, Vol. 72. Presented at the Symposium on Viscous Drag Reduction, Dallas, Texas, November 1979, pp. 144-167.

170. Balasubramanian, R.; Cary, Aubry M., Jr.; Bushnell, Dennis M.; and Ash, Robert L.: Influence of Transverse Surface Waves on Turbulent Boundary Layers. Fifth Biennial Symposium on Turbulence, University of Missouri-Rolla, October 1977.
171. Lin, John C.; Walsh, Michael J.; and Balasubramanian, R.: Drag of Two-Dimensional Small-Amplitude Symmetric and Asymmetric Wavy Walls in Turbulent Boundary Layers. NASA TP-2318, June 1984.
172. Sigal, A.: An Experimental Investigation of the Turbulent Boundary Layer Over a Wavy Wall. Ph.D. Thesis, California Institute of Technology, 1971.
173. Kurbatov, B. V.; and Mordvinov, Yu. Ye.: Hydrodynamic Resistance of Semiaquatic Mammals. Moscow Zoologicheskii Zhurnal, Vol. 53, No. 1, 1974, pp. 104-110.
174. Finnigan, J. J.: Turbulence in Waving Wheat. I. Mean Statistics and Honami. Boundary Layer Meteorology, Vol. 15, 1979, pp. 181-211.
175. Finnigan, J. J.: Turbulence in Waving Wheat. II. Structure of Momentum Transfer. Boundary Layer Meteorology, Vol. 16, 1979, pp. 213-236.
176. Maitani, T.: An Observational Study of Wind-Induced Waving of Plants. Boundary Layer Meteorology, Vol. 16, 1979, pp. 49-65.
177. Inoue, Kimio; and Uchijima, Zenbei: Experimental Study of Microstructure of Wind Turbulence in Rice and Maize Canopies. Bull. Natl. Inst. Agric. Sci., Vol. 26, 1979, pp. 1-88.
178. Munro, D. S.; and Oke, T. R.: Aerodynamic Boundary-Layer Adjustment Over a Crop in Neutral Stability. Boundary-Layer Meteorology, Vol. 9, 1975, pp. 53-61.
179. Thom, A. S.: Momentum Absorption by Vegetation. Quart. J. R. Met. Soc., 1971, Vol. 97, pp. 414-428.
180. Finnigan, J. J.; and Mulhearn, P. J.: Modeling Waving Crops in a Wind Tunnel. Boundary Layer Meteorology, 1978, Vol. 14, pp. 253-277.
181. Metzner, A. B.: Polymer Solution and Fiber Suspension Rheology and Their Relationship to Turbulent Drag Reduction. Physics of Fluids, Vol. 20, No. 10, October 1977, pp. S145-S149.
182. Potemkin, V. F.; and Dreytser, G. A.: Method for Controlling the Turbulent Boundary Layer. Soviet Patent No. 909384, Applied 3/14/80, Published 2/28/82.
183. Giles, W. B.: Air Film Drag Reduction With Viscoelastic Additives. July 15, 1969, Patent No. 3,455,266.
184. Semenov, B. N.; Kulik, V. M.; Lopyrev, V. A.; Mironsov, B. P.; Poguda, I. S.; and Yushmanova, T. I.: Combined Effect of Small Amounts of Polymers Added to a Flow and of Surface Pliability on Turbulent Friction. Seriya Tekhnicheskikh Nauk, November 1984, pp. 89-94.
185. Burton, Thomas E.: The Connection Between Intermittent Turbulent Activity Near the Wall of a Turbulent Boundary Layer With Pressure Fluctuations at the Wall. Massachusetts Institute of Technology prepared for Naval Ship Research and Development Center, June 1974.
186. Alshamani, K. M. M.; Livesey, J. L.; and Edwards, F. J.: Excitation of the Wall Region by Sound in Fully Developed Channel Flow. AIAA Journal, Vol. 20, No. 3, 1982, pp. 334-339.
187. Wilkinson, S. P.; and Balasubramanian, R.: Turbulent-Burst Control Through Phase-Locked Travelling Surface Depression. Presented at the AIAA Shear Flow Control Conference, Boulder, Colorado, March 12-14, 1985. AIAA Paper No. 85-0536.
188. Nosenchuck, D. M.; and Lynch, M. K.: Active Control of Low-Speed Streak Bursting in Turbulent Spots. Presented at the AIAA Shear Flow Control Conference, Boulder, Colorado, March 12-14, 1985. AIAA Paper No. 85-0535.
189. Bushnell, Dennis M.: Turbulence Sensitivity and Control in Wall Flows. Presented at ICASE - Theoretical Approaches to Turbulence Workshop, Virginia Beach, Virginia, October 10-12, 1984.
190. Arakeri, J.; and Narasimha, R.: Effect of Pulsed Slot Suction on a Turbulent Boundary Layer. AIAA Journal, Vol. 21, No. 2, February 1983, pp. 306-307.

- ROUGHNESS
 - DISCRETE
 - DISCONTINUOUS
 - TWO-DIMENSIONAL
 - THREE-DIMENSIONAL
 - STEPS
 - GAPS
 - PARTICLE IMPACT/EROSION
 - CORROSION
 - LEAKAGE
- WALL WAVINESS
 - TWO-DIMENSIONAL
 - THREE-DIMENSIONAL
 - SINGLE WAVE
 - MULTIPLE WAVE
 - DISTORTION UNDER LOAD
- SURFACE AND DUCT VIBRATION
- ACOUSTIC ENVIRONMENT
 - ATTACHED FLOW
 - SEPARATED FLOW
 - PROPULSION SYSTEM
 - VORTEX SHEDDING
- STREAM FLUCTUATIONS AND VORTICITY
 - PROPELLER WAKES
 - OCEAN SURFACE
 - BODY WAKES (FISH/AIRCRAFT)
 - HIGH SHEAR AREAS (WEATHER FRONTS/ JET STREAM EDGES/OCEAN CURRENTS)
- PARTICLES
 - ICE CLOUDS
 - RAIN
 - ALGAE
 - SUSPENSIONS
 - FAUNA (INSECTS FISH ETC)
- LFC SYSTEM-GENERATED DISTURBANCES
 - VORTEX SHEDDING (BLOCKED SLOTS, HOLES, PORES)
 - ACOUSTIC OR CHUGGING
 - PORE DISTURBANCES
 - NON-UNIFORMITIES

Fig. 1. - Possible stream/wall disturbances critical to boundary layer transition/LFC.

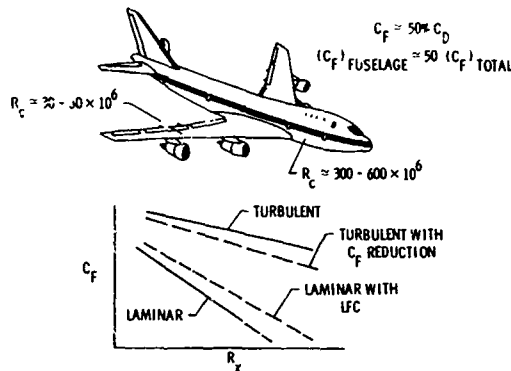


Fig. 2. - Turbulent skin friction reduction.

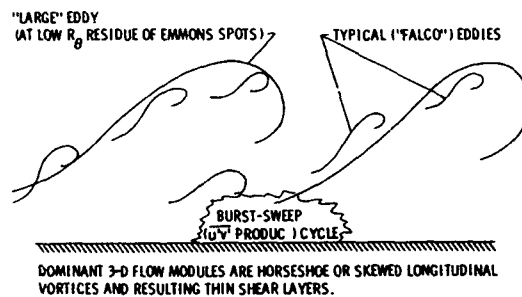


Fig. 3. - Schematic of wall turbulence production flow modules and events.

- PRESSURE GRADIENT
- CORIOLIS FORCES
- WALL CURVATURE
- WALL ROUGHNESS
- COMPLIANT WALLS (WALL MOTION)
- ENERGY RELEASE, CHEMICAL REACTION
- PROXIMITY TO TRANSITION/ REYNOLDS NO
- SHOCK INTERACTION
- DENSITY STRATIFICATION (E.G. BUOYANCY PROBLEM)
- ADDITIVES (POLYMERS, FIBERS)
- COMPRESSIBILITY (DENSITY VARIATION)
- TWO PHASE FLOW
- EHD & MHD FORCES
- STREAM OSCILLATIONS
- WALL PERMEABILITY/ MICROGEOMETRY

Fig. 4. - Known parameters having a first order influence upon two-dimensional turbulent boundary layer structure.

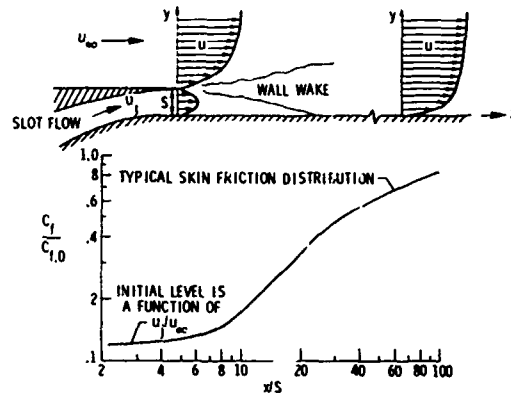


Fig. 5. - Skin-friction drag reduction by tangential slot injection.

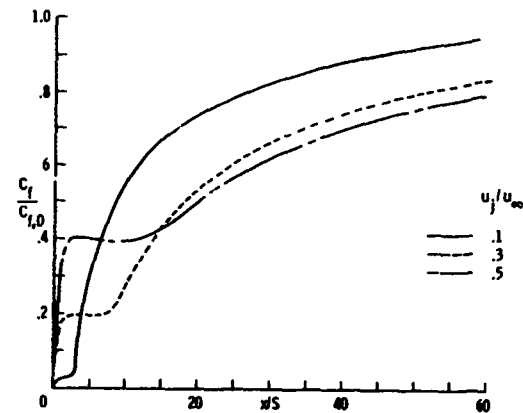


Fig. 6. - Predicted effect of slot velocity ratio.

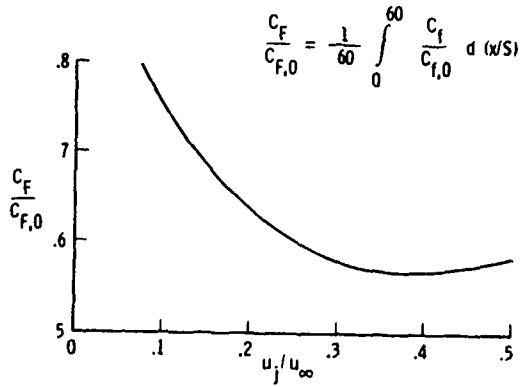


Fig. 7. - Influence of slot velocity on integrated skin-friction drag downstream of slot.

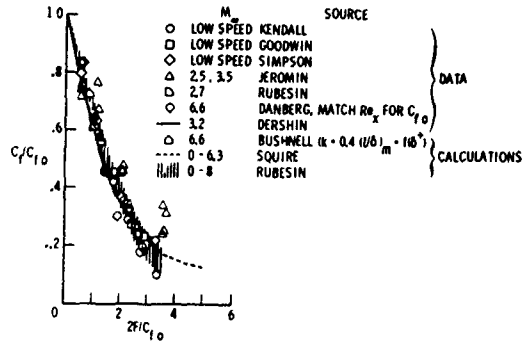


Fig. 10. - Influence of wall injection on turbulent skin friction.

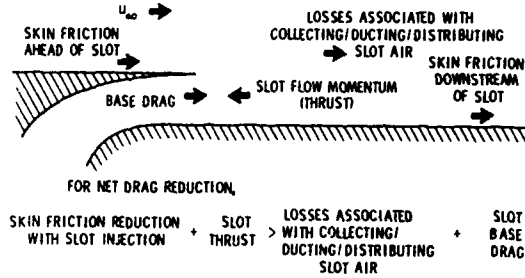


Fig. 8. - Force balance associated with slot injection.

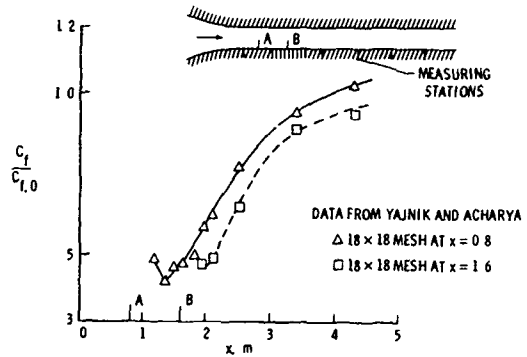


Fig. 11. - Skin friction reduction downstream of screen boundary layer fences.

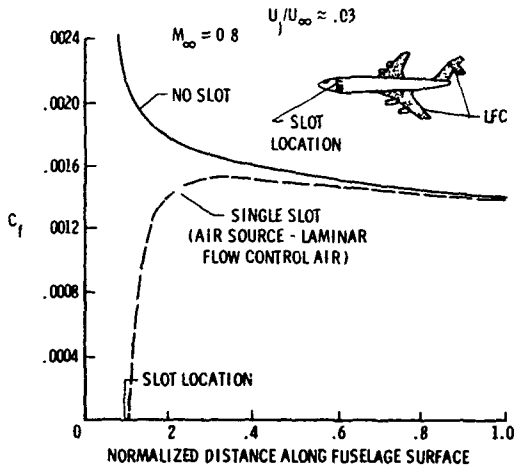


Fig. 9. - Slot injection skin friction reduction on transport fuselage.

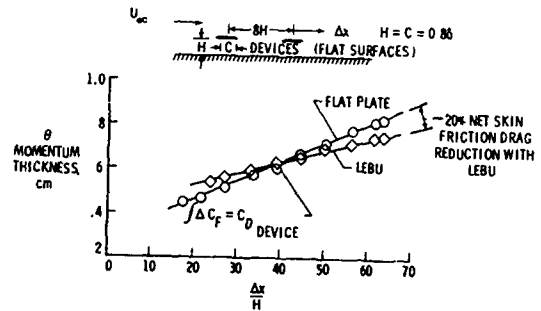


Fig. 12. - Large-eddy breakup devices for turbulence control and viscous drag reduction.

	NO. OF MODELS	HEIGHT RANGE	SPACING RANGE	DESCRIPTION
	11	.025- .102 cm	.025- .315 cm	SYMMETRIC V-GROOVE
	7	.005- .051	.051- .343	RECTANGULAR
	2	.025- .051	.114	SPACED TRIANGULAR
	3	.025- .051	.051- .147	RIGHT ANGLE RIB
	3	.025- .051	.051- .101	PEAK CURVATURE
	3	.025	.051	VARIOUS DEGREES OF VALLEY CURVATURE
	3	.051- .07	.01- .07	PEAK AND VALLEY CURVATURE
	1	.025	.051	NOTCHED PEAK
	1	.025	.102	SPACED V-GROOVE
	5	.025- .051	.058- .117	UNSYMMETRIC V-GROOVE

Fig. 13. - Riblet models tested at NASA LaRC.

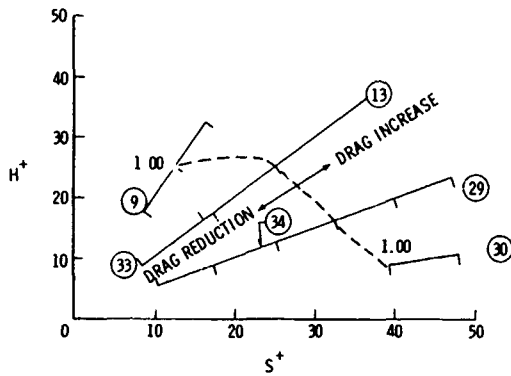


Fig. 14. - Drag reduction region of H^+ and S^+ for v-groove riblets.

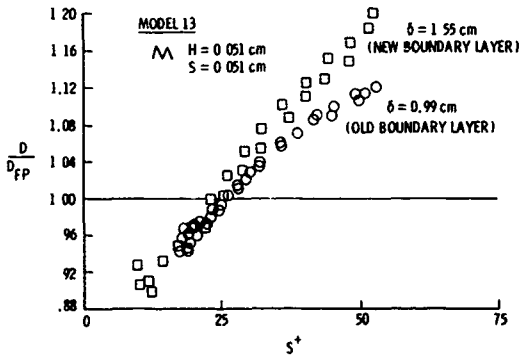


Fig. 15. - V-groove riblet drag reduction.

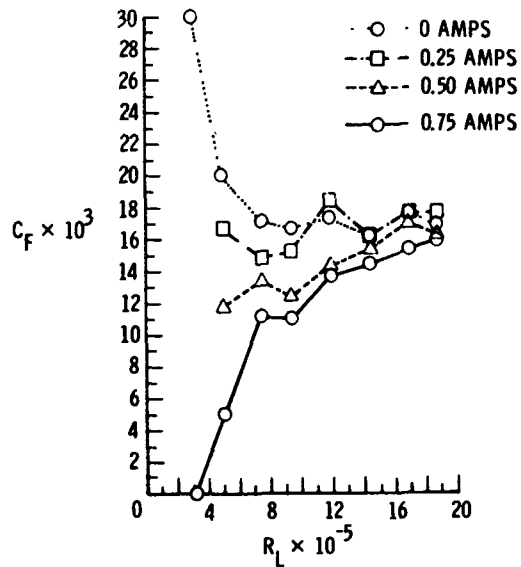
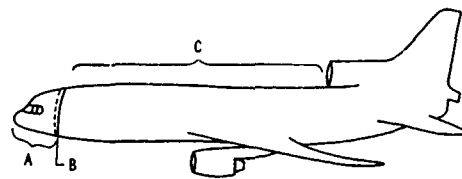


Fig. 16. - Effect of water electrolysis on drag.



A - TURBULENT NOSE REGION (BUGS, WINDSHIELD WIPERS, ETC)
 B - MASSIVE SUCTION REGION (APPROXIMATELY 1.56 B_L SUCTION REQUIRED TO ENSURE ABSENCE OF EXTERNAL TURB BOUNDARY LAYER REMNANTS)
 REQUIREMENT - LOW ΔP SURFACE
 C - MAINTENANCE LFC (SUCTION OR COOLING (H_2 FUEL = 2-D T S WAVES))

Fig. 17. - General concept, fuselage relaminarization research.

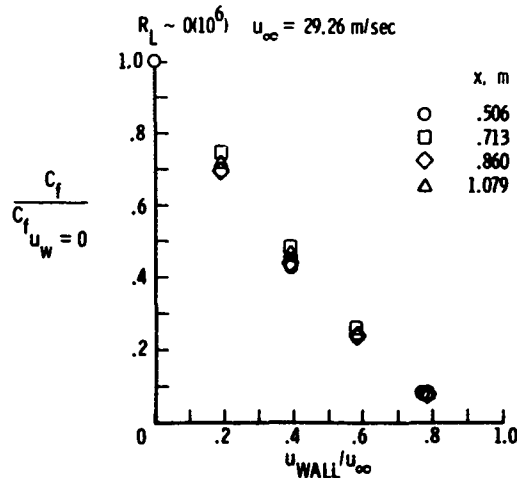


Fig. 18. - Skin-friction drag reduction with rectilinear wall motion.

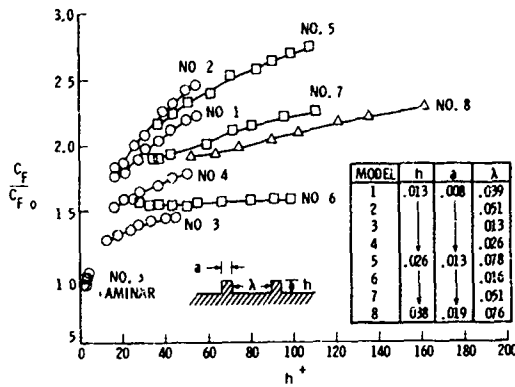


Fig. 19. - Drag of micro-air-bearing models.

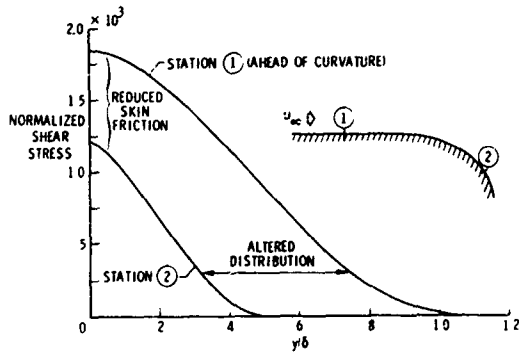


Fig. 20. - Influence of convex curvature on turbulent shear stress.

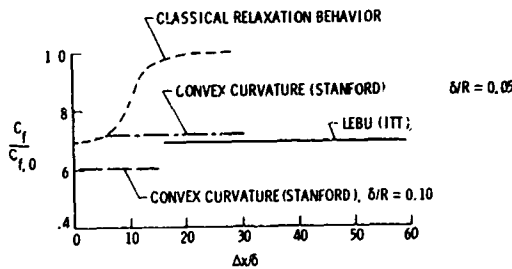


Fig. 21. - Effect of convex curvature and LEBU devices on downstream skin friction.

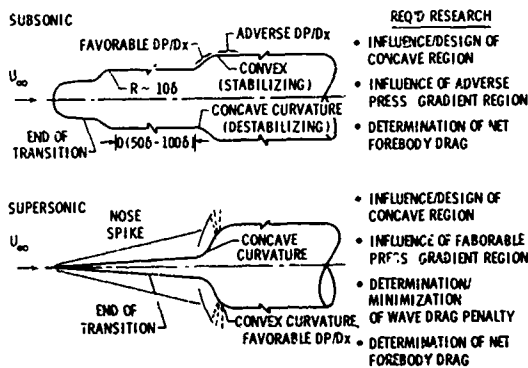


Fig. 22. - Conceptual applications of convex curvature for turbulent drag reduction.

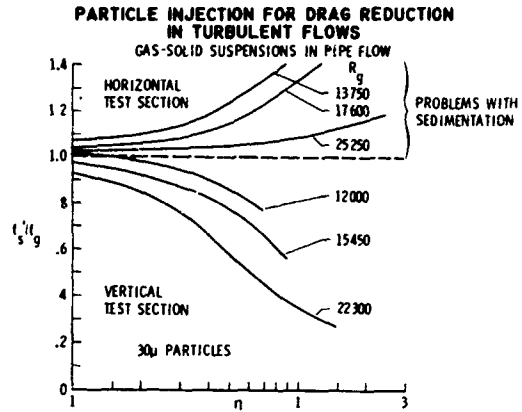


Fig. 23. - Particle injection for drag reduction in turbulent flows. Gas-solid suspensions in pipe flow.

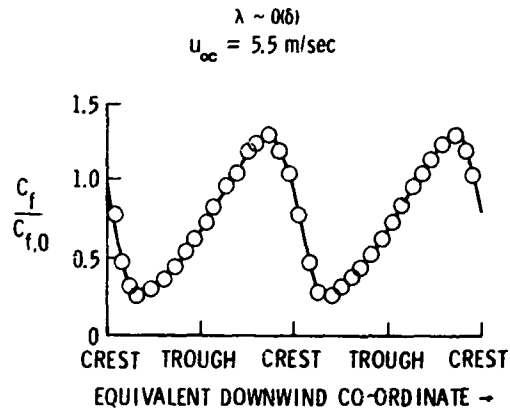


Fig. 24. - Effect of transverse stationary waves on skin friction, δ = λ.

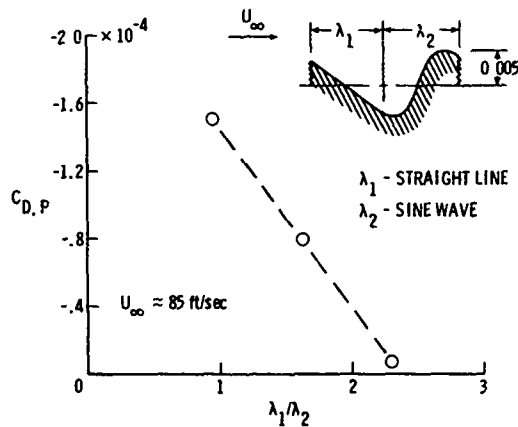


Fig. 25. - Pressure drag for nonsymmetric waves straight ramp/sine wave.

PARASITIC AND INTERFERENCE DRAG PREDICTION AND REDUCTION

by Ph. POISSON-QUINTON,
Senior Advisor, ONERA, Fr.

ABSTRACT

For a realistic evaluation of the total drag of an Aircraft, we must add to the drag due lift (+ wave drag) and to the friction drag of the "clean" configuration, some other drag components:

- Parasitic Drag related to excrescences, leaks, etc., and to local flow separations;
- Interference Drag related to wing/fuselage, propulsive nacelle/wing or fuselage, external stores/wing or fuselage, etc.

Although a precise prediction of such drag terms is still difficult to obtain in wind-tunnel testing -and even more by calculation-, a large number of typical trends are available to the designer to avoid too large penalties on transport or combat Aircraft at the preliminary design stage; several examples are given to illustrate these trends, together with some optimisation methods.

In this presentation, we have used a lot of results already given in various AGARD Reports and some more recent unpublished data.

The paper is split in five parts, illustrated by self-comprehensive charts:

- Introduction to "other" drag components,
- Excrescence drag components,
- Aircraft drag due to airframe aerodynamic interferences,
- Propulsion/Airframe interferences,
- External stores/Airframe interferences.

I - INTRODUCTION TO "OTHER" DRAG COMPONENTS

An excellent NASA-Langley paper [1] was given during an AGARD/VKI special course on "concepts for drag reduction" in 1977, from which is taken the Figure 1 illustrating the various drag components listed on table (b); the graphs (c) and (d) show that the drag build-up is very different for subsonic and supersonic "clean" configurations; and inside these two categories, there are again large differences between well-streamlined subsonic or supersonic transport (where a very good cruise L/D is vital for a "decent" operational efficiency) and a helicopter (large parasitic drag), or a supersonic fighter (large wave drag, even without external stores); in fact, for many cases, the "minor" drag components are quite large!

To improve the aerodynamic efficiency of a subsonic transport configuration, it is possible to act on the two terms of its polar curve (Fig. 2), with less minimum drag and less induced drag: parasitic and interference drag components are minor terms in both of these components, but still important for a better fuel economy, ranging from 3 to 5% [2].

To compare the aerodynamic performance of various existing civil or military transport Aircraft, or future projects, it is convenient to look at their effective parabolic polar curve at the cruise condition, i.e. at their maximum lift-to-drag ratio (where $\overline{C}_{Do} = \overline{C}_{Di}$, by definition):

- with $\overline{C}_{Do} = C_f \frac{S_{\text{wetted surface}}}{S_{\text{reference wing}}}$,

where C_f is an effective friction drag taking into account parasitic and interference terms at zero lift,

- and with $\overline{C}_{Di} = \frac{CL^2}{\pi \cdot e \cdot R}$,

where e is a "span efficiency factor", which integrates also various parasitic/interference drag terms increasing with the angle of attack.

The Figure 3 [2] shows that it is possible to draw a mean curve through various experimental points obtained from flight results for well-known operational Airliners: $(L/D)_{\text{max}} = 14 \text{ b} / \sqrt{S_{\text{wet}}}$. (the not-so-streamlined military cargos are below this mean curve); here the convenient experimental terms used are: $e = 0.75$ and $\overline{C}_f = 0.003$ respectively.

This equivalent skin friction value \overline{C}_f is obtained from a survey shown on Figure 4b relative to various subsonic transport or bomber Aircraft; for typical combat Aircraft, the \overline{C}_f value is equal or larger than 0.0035 (Fig. 4c); in fact, the summation of the form drag (flow separation induced by viscous effect) and interference drag (mutual interaction between various aircraft components, increases by about 50% the turbulent friction drag (flat plate) calculated with the Karman-Schoenherr method (Fig. 4a); these charts are taken from a recent comprehensive synthesis by USAF/FDL [9].

II - EXCRESCENCE DRAG COMPONENTS

Estimates of typical roughness and excrescence drag contributions for the C-5A military transport at cruise regime are given on Figure 5 [1, 3], which amount for about 3.5% of the total drag: 30% of the roughness drag is attributable to steps, ridges and gaps and about 25% due to mass transfer in and out of the Aircraft skin (vents, pressure leaks, air conditioning, etc.).

Estimates of various parasitic drag: steps, ridge, gaps are based on fundamental wind-tunnel investigations (mainly from a RAE-Bedford program 4, 5), and illustrated on Figure 6: such roughness drags can be much greater than the turbulent skin friction on a smooth flat plate, even if such excrescence are small relative to the boundary-layer thickness: the rear facing step drag (b) is about one-half that of the forward-facing steps, whereas the ridge drag (c) is twice that of the forward-facing step; these excrescence drags largely increase from subsonic to supersonic regime.

Two such typical excrescence estimates on an Airbus-type fuselage [7] are illustrated on Figure 7 for only one forward-facing step (3 mm sheet-metal joint, Fig. 7a): half a count drag; and for an anti-collision light (h = 75 mm, Fig. 7b): 5/100 count.

Roughness drag breakdown for a typical transport Aircraft wing was estimated by the Boeing Company [1] and illustrated on Figure 8a; by bonding a plastic film over only 50% of the surface area (Fig. 8b), the total drag of such A/C could be reduced by 0.7%; covering a T-33 A/C wing model with a 5-mil Kapton plastic film has reduced the drag (measured in a NASA-Langley pressurized tunnel) by 12 to 40%, depending upon the Reynolds number (Fig. 8c). The quite severe drag due to control surface gap can be appreciably reduced by decreasing the airfoil thickness by 15% just ahead of the aileron: a 76% gap drag reduction is shown on Figure 8d.

Every Aircraft manufacturer is deeply involved with parasitic drag reduction during the development of their projects: for example, Figure 9 illustrates the evolution of the total parasitic drag on the Airbus A/C family [7]: more than 3% gain on the total Aircraft drag from the A-300 prototype to the A-320 project...

Even during the operational life of a subsonic transport Aircraft, it is rewarding for an Airline Company to undertake periodically an "Aerodynamic clean-up" operation on their fleet (about 0.5% block fuel-saving, see ref. [2]).

III - AIRCRAFT DRAG DUE TO AERODYNAMIC INTERFERENCES

"Aerodynamic interference in Aircraft is defined as the change in the flow over given elements of the configuration due to the presence of one or more of the other elements; such interference is mainly severe with transonic flow" (H. Yoshihara [8]).

To show how large can be this parasitic interference drag, it is interesting to begin with an USAF/FDL study, undertaken some years ago for improving the drag of the C-141 military cargo-Aircraft [2]; wind-tunnel tests have shown that it would be possible to reduce its cruise drag by about 8% (Fig. 10) thanks to minor modifications around the wing-fuselage juncture at the landing-gear pods, and by a small wing-tip extension: the corresponding fuel saving for the C-141 fleet would be so important that the cost of modifications would be paid by only one year fuel-saving!

III,1 - Wing-Fuselage interference

This wing-body juncture is particularly critical on high-wing configurations, as shown on Figure 11, where the redesign of the top-fuselage shape and a well design wing-root fairing has given a substantial drag reduction at cruise conditions (see B. Haines contribution in Ref. [8]).

Since few years, thanks to the computational Fluid Dynamics development, it is possible to optimize the wing-fuselage juncture at the preliminary design stage, as illustrated on Figure 12 for a low-wing/fuselage "active" fairing, which reduces the supercritical flow on the wing root upper-surface (see J. Sloof contribution in Ref. [8]).

Another examples, taken in the same Ref. [8] and relative to Airbus-type root-fairing optimization, are illustrated on Figure 13: for example, about 2% cruise drag saving has been obtained between the A-300 and A-310 fillet designs.

III,2 - Fuselage drag improvement

Another example of a rewarding redesign of the fuselage shape on a cargo-Aircraft project [10] is given on Figure 14: thanks to fuselage tail-cone extension, and to gear-pod and wing fillet modifications, the total drag was reduced by 50 counts at cruise condition, after extensive computation and wind-tunnel testing by Lockheed-Georgia Company.

The parasitic drag due to the rear-fuselage shape is always an important item in the drag build-up: two good examples given by Aerospatiale [7] are shown on Figure 15:

- During the project development of the ATR-42 commuter Aircraft in wind-tunnel, a gain of 1% on the cruise drag was obtained by extending the rear part of the fuselage (Fig. 15a);

- During the development of the Concorde project, it appeared mandatory to improve the drag of the prototype, and one of the important decisions was to extend the rear-fuselage cone for improving the supersonic cruise drag by 1% (Fig. 15b); Such "small" gain at $M = 2$ on A/C drag was vital for the supersonic-transport payload, as illustrated on Figure 16b. Several other modifications between the Concorde prototype and the production A/C are indicated on Figure 16c, a part of them being made for drag reduction at $M = 2$ cruise (extended fuselage nose, extended elevons and rudder trailing-edge, extended fin leading-edge, etc.).

III,3 - Wing-tip optimization for drag reduction

Here, the main objective is to reduce the induced drag by increasing the effective aspect-ratio: a well known favorable interference effect has been obtained through "winglets" fitted at the wing-tip [13], but with some drawback (increased friction drag, increased wing bending-moment, flutter risk, etc.); an elegant compromise has been recently installed on the Airbus A-310-300 with some small "wing-tip fences" integrated on the tip fairings (Fig. 17a), which give a 1.5% drag reduction, already demonstrated in flight [7].

Other solutions to reduce the induced drag [2] are: to fit a small jet-engine at the wing-tip (Fig. 17b), or to install a blowing slot on the tip fairing, to reduce the tip vortex development (Fig. 17c).

III,4 - Helicopter Airframe drag reduction

For various reasons, many helicopter fuselages have a poor rear-shape, which gives an important drag penalty; an interesting experimental study in wind-tunnel was recently undertaken at the University of Bristol by Prof. Seddon [11] to analyse the various types of flow occurring at the rear base of typical helicopter fuselages: as shown on Figures 18a and b, the two main parameters acting on the types of flow are the fuselage angle of attack and the rear-fuselage upsweep angle. When decreasing the angle of attack for a given upsweep angle, the "eddy flow" regime is suddenly changed into a "vortex flow" regime, which results in much larger parasitic drag; and the same trend appears when reducing the upsweep angle for a given angle of attack. In such conditions, it is possible to draw a critical boundary between the two flow regimes in the (upsweep, incidence) plane which indicates the favorable low drag zones (Fig. 18c).

A similar critical boundary appears for a tapered base instead of the previous untapered fuselage base, as shown on Figure 18d, where two other boundaries are also indicated.

This high drag vortex flow regime can be reduced by a spoiler fitted on the bottom of the base (Fig. 18e) or suppressed by a series of small deflectors fitted all along the lateral corners of the base (Fig. 18f); such simple devices greatly improve the fuselage drag at negative incidences (high-speed regime).

Since few years, the helicopter manufacturers are more aware of potential gains on total drag with a better aerodynamic design [2]; a typical example of such gains obtained between the first Aerospatiale "Dolphin" prototype and the production model is given on Figure 19: a 25% drag reduction through numerous improvements on the fuselage, the rotor hub, the engine inlets, and a retractable landing-gear installation.

III,5 - Wave-drag reduction through area-ruling

One of the most revolutionary process to improve the transonic drag rise (and to avoid a lot of transonic troubles) before crossing Mach one was first proposed in the fifties by R. Whitcomb, from NACA-Langley [12]; and this very simple method was then successfully applied to almost all high-speed military Aircraft; this evolution appears clearly on Figure 20, which gives the transonic drag jump as a function of the equivalent fineness ratio calculated for a number of Aircraft [9]. The price to pay for crossing the sonic barrier has continuously decreased up to almost attain the value given by a SEARS-HAAS minimum-sonic-drag-body. On this Figure 20, it should be observed that for the B-58 bomber, the drag jump is less for the configuration with a well integrated pod under fuselage than for the clean configuration; we shall see other examples of favorable stores/weapons interference in Section V.

The usefulness of the sonic area-rule for large aspect-ratio transport Aircraft type was demonstrated by NASA on a modified F8-U with a supercritical wing perfectly integrated on a smooth axial cross-section distribution; it is interesting to note that in the early seventies (pre-fuel-crisis), near-sonic transport configurations were envisaged [2]. A Boeing wind-tunnel study for a successor to the B-747 has demonstrated a drag divergence at $M = 0.98$ instead of $M = 0.87$ for the conventional B-747 (Fig. 21), but obtained by a very sophisticated (and certainly expensive) airframe area ruling.

IV - PROPULSIVE NACELLES/AIRFRAME INTERFERENCE

In this section are reviewed some difficult interference problems arising from propulsive nacelle installation on two types of Aircraft: subsonic transport with various Turbo-fans or prop-fans locations, and supersonic transport/bomber.

IV,1 - Turbo-fan installation drag on conventional subsonic transport

Figure 22 illustrates the case of underwing nacelle arrangements [1]; the wing-pylon-nacelle flow field (Fig. 22a) is influenced by the engine positioning (Fig. 22b), the more ahead longitudinal location being the most favorable because a better local area-ruling and a less supercritical channel flow between nacelle and wing. Wing leading-edge contouring and pylon trailing-edge contouring (Fig. 22c) are shown to have either favorable or adverse effects on the interference drag, depending on the flight Mach number.

Even at low speed, some adverse interference sometimes appear when the high lift devices are deployed: on Figure 22d, a strong boundary-layer separation, which occurred in the front of the slat, was cured by a small strake fitted on the nacelle: this device induces a vortex which siphons off the low energy boundary-layer, and its reattachment greatly improves the slat lift efficiency (see paper n° 1 in [8]).

On Figure 23, the interference drag for a typical underwing nacelle configuration is quantified from wind-tunnel measurements: a loss of 1 to 2% of the Aircraft drag is mainly due to a lift reduction at constant incidence, which must be compensated by incidence increase, which generates more induced drag.

At the present time, the major unfavorable interferences between propulsive nacelle and airframe (wing or fuselage) can be detected -and then improved- by computing a theoretical model of the complete Aircraft: for example the panel method is illustrated on Figure 24 (underwing pylon/nacelle/jet interference) and on Figure 25 (rear-fuselage/nacelle interference), see the J.W. Sloof paper in [8]: there is a good agreement between computed and measured detailed pressures in the critical regions between nacelle and main airframe at cruise regime.

In the case of a rear-mounted engines configuration, it is most important to avoid a parasitic supercritical flow thanks to several efficient solutions:

- a local area-ruling with a fuselage contouring (Fig. 25),
- an extensive fairing along the fuselage and a pylon modification, as shown on Figure 26, for a business-jet optimization (see the Withcomb paper in [8]: here the wing trailing-edge and the nacelle were so close that the wing fairing was designed with a "concave" region to obtain a "channel area-rule": the strong shock-wave (inducing a complete flow-separation on the aft-fuselage) was completely removed and the drag-creep was suppressed up to $M = 0.8$ cruise; the same exercise was successfully undertaken during the development of the Dassault Falcon-50 executive Aircraft.

To conclude on these "conventional" propulsive nacelles interfering with the airframe, it is interesting to quantify the potential gains obtained with a better optimization: For an Airbus configuration [7], Figure 27 illustrates these gains, demonstrated on the various parameters acting on the wing/pod/nacelle interference drag at cruise regime.

IV,2 - Turbo-fan installation drag on STOL transport using a powered-lift scheme

Since the discovery of the circulation control on a wing through the "jet-flap" effect in the fifties, it was very attractive to use the large momentum of the turbo-fan engines to induce a substantial lift by deflecting their exhaust flow; the various proposed schemes are illustrated on Figure 28: the two first solutions were successfully tested in flight at low-speed on USAF Military cargo-Aircraft projects with the External-Blown-Flap configuration (EBF-Douglas YC-15) and the upper-Surface-Blowing scheme (USB-Boeing YC-14); this later solution was then applied to an experimental NASA/Boeing four-turbo-fan engine Aircraft (QSRA), which has demonstrated usable lift coefficients around ten in flight!

The third solution, an "over-the-wing" location of the turbo-fan, was first proposed by VFW in Germany [14] and their low-speed wind-tunnel results have shown a much better polar curve than for an usual underwing configuration (Fig. 29).

However, transonic wind-tunnel results were more pessimistic, because the "upper-surface" and the "over-the-wing" nacelle configurations give a quite large installation-drag at cruise regime, due to parasitic shock-waves development. An interesting experimental study by NASA-Langley was undertaken on a transport Aircraft model, to compare these two configurations (Figure 30): the very large installation drag with symmetrical motorized nacelles was sensibly reduced at cruise regime, $M = 0.8$, by contouring the shape of these nacelles.

The third configuration shown on Figure 30, an "aft-mounted nacelle" fitted on the wing lower-surface, is quite interesting for its low installation-drag compared to a conventional poded solution, but this rear location can induce some difficult structural problem (flutter risk?).

To conclude on these configurations, very attractive for their outstanding STOL capabilities, it must be recognized that their nacelle installation-drag penalties are still too large for an economical application to high-speed transport Aircraft, but a better transonic optimization by CFD seems possible in the future.

IV.3 - Prop-fan installation-drag

The "prop-fan" concept, first developed by NASA and Hamilton-Standard and now in several countries [15] is very attractive for its fuel-saving capability compared to conventional turbo-fan. Substantial gains on propulsive efficiency are already demonstrated on isolated propellers tested in wind-tunnel up to Mach 0.8. But two difficult problems remain to be solved:

- the large aerodynamic interference of their slipstream on the airframe;
- the large near-field noise generated by these highly-loaded propellers with supersonic blade-tip speed.

To minimize both of these problems, an aft-fuselage mounting seems much more attractive than a wing-mounting scheme, as explained on Figure 31.

Indeed some preliminary NASA tests, summarized on Figure 32, show that a tractor single-rotation prop-fan in the front of a swept wing has a very strong effect on the inboard-wing pressures due to swirl and super velocity in the slipstream; a theoretical approach developed at Grumman [16] (based on small perturbation equation coupled with mesh-system embedding and simple planer boundary conditions), gives a good picture of the local flow, including a strong shock-wave; this spanwise shock-wave, followed by a large boundary-layer separation on the wing upper-surface, visualized on Figure 33a, gives an important parasitic drag at cruise regime; further tests with small local contouring around the nacelle and the wing-leading-edge have shown an important reduction on the parasitic drag (Fig. 33b).

IV.4 - Nacelle/Airframe interference on supersonic cruise Aircraft

Flow interference between the propulsive nacelles and the airframe has a vital effect on the aerodynamic efficiency of a supersonic cruise Aircraft, either for a bomber (B-58, B-70, B-1,...) or a SST (Concorde, Tu-144, US SST projects,...).

For an "under-wing nacelles" configuration, as illustrated on Figure 34a (a Boeing SST advanced design, see paper n° 35 by R.M. Kulfan and A. Sigallo, from Boeing in [14]), the nacelle-installed-drag is calculated by a modified linear theory (linear small-perturbation for supersonic flow, and a time-marching solution of the Euler Equations to compute mixed regions of subsonic/supersonic flow including shock-wave locations); this calculated drag is the sum of the friction drag of the nacelles, the net wave-drag, and the lift interference effects. For this aft-nacelle location, there is a very favourable interference lift effect due to the increased pressures on the wing lower-surface, i.e. an effective reduction in wing-body drag-due-to-lift: at moderate lift coefficients, the installed nacelle drag is less than half the isolated nacelle drag level.

Such "compression from nacelles" effect on the wing lower-surface was also very favourable on B-70 and on Concorde.

Furthermore, Figure 34b illustrates some satisfactory comparisons between experimental and calculated shock-wave patterns/pressures on the wing lower-surface; two cases are shown, without and with spillage (inlet mass-flow ratio = 0.8) for a flight Mach number = 1.4.

To conclude, theoretical approaches are already available to understand the supersonic interference effects between nacelles and wing-body, including spilling nacelles and detached shock-waves: it should help the designer to avoid configurations having high inherent interference drag (paper n° 35 in [14]).

V - EXTERNAL STORE/AIRFRAME INTERFERENCE ON MILITARY AIRCRAFT

"The military effectiveness of a combat Aircraft may be measured by the number and the range of weapons it can carry, and by its performance with stores installed" (L. Davies, paper n° 8 in [17]). This statement was also a motivation for a very successful AGARD Fluid Dynamics Panel Working Group (WG-03) in 1976-77 "to study means for reducing the drag and other aerodynamic penalties associated with carrying external stores on both current and future Aircraft" [18].

V.1 - In his introduction, the WG Chairman, Clifford Bore, observed that "when the designer has meticulously reduced the drag of the wing of a combat Aircraft by 2 or 3%, he believes that he has accomplished a significant economy -until he sees arrays of stores provided to hang under the wing, with perhaps 7 times the drag of the wing (Fig. 35b)...; and he is entitled to ask why the standard of aerodynamic cleanliness should change so abruptly halfway down the pylons"(Fig. 35a).

"Very substantial improvements could be made to the overall effectiveness of store-carrying Air-Forces; and when looking at the total life-cycle costs of a combat Aircraft (Fig. 35c), the price to pay for a better design, the development and the tests represent a very small part of the total expenses: 30-40% improvement to the effectiveness/cost ratio of a ground-attack force could be obtained for an investment of around 1% of that benefit!"

In the following paragraphs, a quick survey is given on the drag of various store installations and on possibilities for its reduction.

V,2 - Single stores

The store chordwise position is often the most important parameter for an underwing store configuration; at transonic speed, it is mandatory to examine again the area distribution, as demonstrated on Figure 36: a tank-like store mounted below the wing (paper n° 2 in [18]) gives a very strong drag divergence when located at a rearward location, which increases the area distribution. But in a forward position, the area-rule is improved and the addition of the store actually reduces the total drag above $M = 0.9$.

On Figure 37, the maximum interference drag near Mach 1 can vary from 1 to 3 when moving a typical winged missile from a rear to a forward underwing location! [18].

Wing-tip carriage is often the best option for carriage of slender missiles: Figure 38 presents some interesting detailed results for a sweptback wing research model fitted alternatively with a curved wing-tip and with a cropped square-cut tip on which is mounted a missile and its launcher (see the paper on "External store interference, by A.B. Haines in [8]); the tests given for $M = 0.7$ are typical of those obtained to at least $M = 0.9$:

- the drag increment decreases with C_L , becoming negative above $C_L \sim 0.3$ (Fig. 38a);
- the reduction in the lift-dependent drag correlates with an increased lift for a given incidence (Fig. 38b) both on the inner wing and on the missile system itself; and the total lift is almost the same than with an extended curved wing-tip.

On Figure 38c, it is shown that the wing-tip mounting offers the most attractive installation for both subcritical flight conditions and when crossing Mach 1, when compared with underwing-pylon or fuselage-mounted locations... (see the L. Davies paper in [17]).

V,3 - Multiple store carriage

In some cases, a favourable interference effect is obtained when coupling a great number of small stores, mounted on a pallet below a flat-bottomed fuselage (see Haines paper in [8]): on Figure 39a, it is shown that, above Mach 0.92, the total drag increment, for 4 rows x 5 small stores with flat bases is smaller than the increment for a single row of five stores; even for larger boattailed stores, the lower picture shows that an array of 3 rows of two stores is less than the sum of the free-air drag of the stores in isolation (again a favourable "tandem carriage effect").

On the other hand, Figure 39b shows the adverse interference observed at low C_L when the same large boattailed stores are carried on separate pylons under a 40° sweptback wing: with only one store pylon system, the drag-rise Mach number is already strongly reduced; but with 3 pylon-mounted stores, a strong upswept shock appears between the pylons, which translates in a significant drag creep ahead of the steep drag-rise. This adverse interference is particularly severe with standard triple-carriers mounted under the wing of a combat A/C: a considerable drag increase is shown on Figure 40; $\Delta C_D = 78\%$ ($M = 0.7$) to 136% ($M = 0.9$). A better design, with cleaned-up triple-carriers improve the drag penalty, but mainly at low-speed.

All these results were obtained in transonic wind-tunnels, and it is interesting to show, on Figure 41, that such types of comparative testing in wind-tunnel are in good agreement with flight tests - here on a HSA Buccaneer with three types of underwing stores (see the A.J. Grundy paper in [10]).

V,4 - For a better Airframe/Weapon Integration

To conclude this section, it seems important to show -at last- some interesting efforts to optimize the airframe/weapon integration (Fig. 42):

- a) - The first example deals with the conformal weapons carriage experimentally mounted on a F-4 "Phantom" Airplane (US Navy/Air Force/NASA/Boeing program, see paper n° 2 in [18]); the conformal carriage adaptor fairing contains 3 rows of 4 racks = 12 bombs/500 pounds.

The Flight performance comparisons with this carriage and with a conventional system (2 triple ejector racks on wing pylons + 1 multiple ejector rack on centerline pylon) show that :

- At subsonic cruise regime ($M = 0.7-0.8$) the specific range is reduced by 6% and 20% respectively when compared with the clean F-4 A/C
 - At low altitude dash $M = 0.8$, the specific range is reduced by 2% and 31%
 - With the conformal carriage the flight envelop is much less limited than with conventional carriage.
- b) - The second example deals with the development of the "Fast pack" conformal carriage mounted on the sides of the fuselage/under the wing of the Mc-Donnell F-15 [18]. The fuel capacity of these two streamlined packages is between those of two and three external fuel tanks. The wind-tunnel results, confirmed in flight, have shown that the two conformal Fast packs reduce the subsonic drag of the clean F-15, and produce much less parasitic drag at transonic/supersonic regimes than with the external tanks (much better area-ruling).

Thanks to the fuel contained in the Fast packs:

- The Air Superiority Mission radius is doubled when compared with the clean configuration;
- The loiter time at 50 NM and the payload for an Air-to-Ground Mission to 275 NM increase about three-fold'

Finally, it is still possible to cruise at $M > 2$ with this conformal carriage.

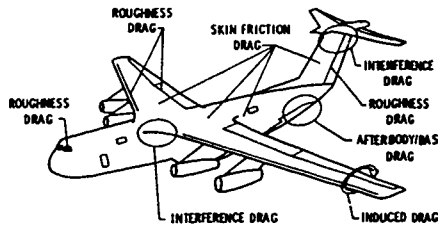
- c) At the design stage, the manufacturer can integrate a large weapon - or fuel tank, under the fuselage to optimize the A/C area-rule; such successful designs were made on the Mirage IV by Dassault and on the B-58 Bomber by G.D.

REFERENCES

- 1 - J.N. HEFNER, D.M. BUSHNELL
An overview of concepts for Aircraft drag reduction.
AGARD R-654 "Special Course on Concepts for Drag Reduction", (1977)
- 2 - Ph. POISSON-QUINTON
Energy Conservation Aircraft Design and Operational Procedures.
AGARD Lecture Series LS-96, (1978)
- 3 - J.H. PATERSON et al
A Survey of Drag Prediction Techniques Applicable to Subsonic and Transonic Aircraft Design.
AGARD CP-124, "Conference on Aerodynamic Drag", (1973)
- 4 - Anon.
Aircraft Excrescence Drag.
AGARD AG-264, (1981)
- 5 - L. GAUDET, K.G. WINTER
Measurements of the Drag of some Characteristic Aircraft Excrescences Immersed in Turbulent
Boundary Layers.
AGARD CP-124, (1973)
- 6 - Anon.
MBB/Transport Div. ; private communication, (April 1985)
- 7 - Anon.
Aerospatiale/Aircraft Div.; private communication, (April 1985)
- 8 - Special Course on Subsonic/Transonic Aerodynamic Interference for Aircraft.
AGARD R-712, (1983)
- 9 - Ch. E. JOBE
Prediction of Aerodynamic Drag.
US-AFWAL/FDL TM-84-203, (July 1984)
- 10 - G.W. WEBBER
Aerodynamic Development for Efficient Military Cargo Transports (Lockheed-Georgia)
AIAA Paper n° 83-1822, (1983)
- 11 - J. SEDDON
Aerodynamics of the Helicopter Rear-Fuselage Upsweep.
8th European Rotorcraft Forum, (Sept. 1982)

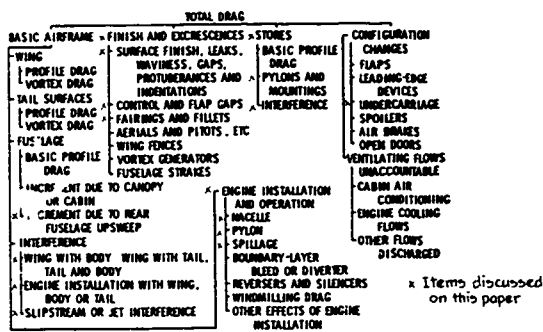
Further Studies in Helicopter Body Aerodynamics.
9th European Rotorcraft Forum, (Sept. 1983)
- 12 - R.T. WHITCOMB
A Study of the Zero-Lift Drag-Rise Characteristics of Wing-Body Combinations near the Speed of
Sound.
NACA Rep. 1273, (1956)
- 13 - R.T. WHITCOMB
Transonic Empirical Configuration Design Process.
AGARD R-654, (1977)
- 14 - Anon.
Aerodynamics of Powerplant Installation.
AGARD CP-301, (1981)
- 15 - Anon.
Aerodynamics and Aeroacoustics of Propellers.
AGARD CP-366, (1985)
- 16 - C.W. BOPPE, B.S. ROSEN
Computation of Prop-Fan Engine Installation Aerodynamics.
ICAS Paper 84-5.5.3, (Sept. 1984)
- 17 - Anon.
Performance Prediction Methods.
AGARD CP-242, (May 1978)
- 18 - Anon.
Drag and Other Aerodynamic Effects of External Stores.
AGARD AR-107, (Nov. 1977)
(Note: several papers are "NATO RESTRICTED")
- 19 - Anon.
Flight/Ground Testing Facilities Correlation.
AGARD CP-187, (1975)

Fig 1 The VARIOUS DRAG COMPONENTS

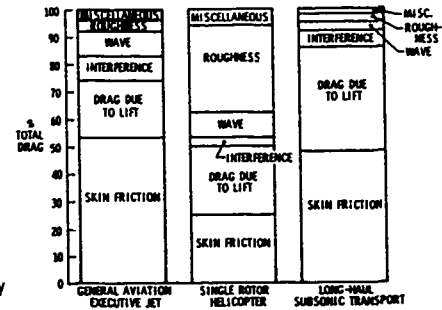


(a) Aircraft drag.

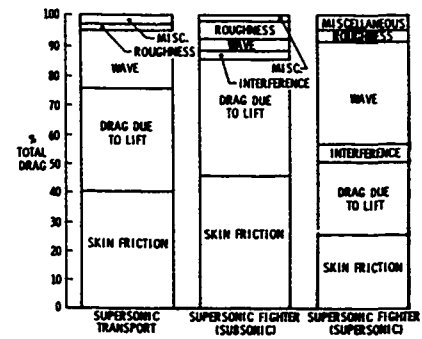
Ref NASA Langley
AGARD
R 654(1)
Paper nr 1



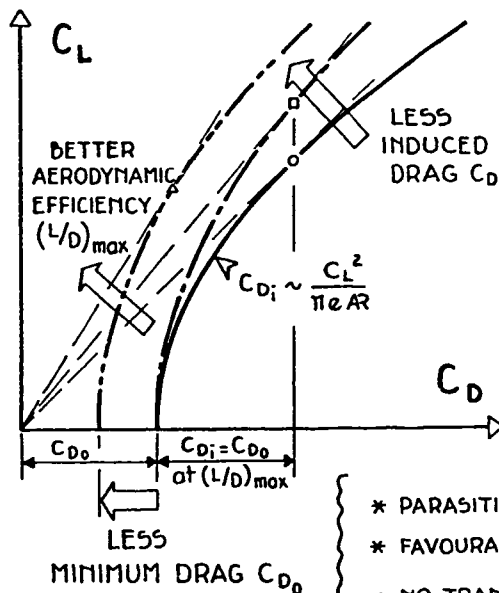
(b) Conventional aircraft drag breakdowns for shock-free flow outside ground effect.



(c) Drag buildup of typical subsonic aircraft configurations.



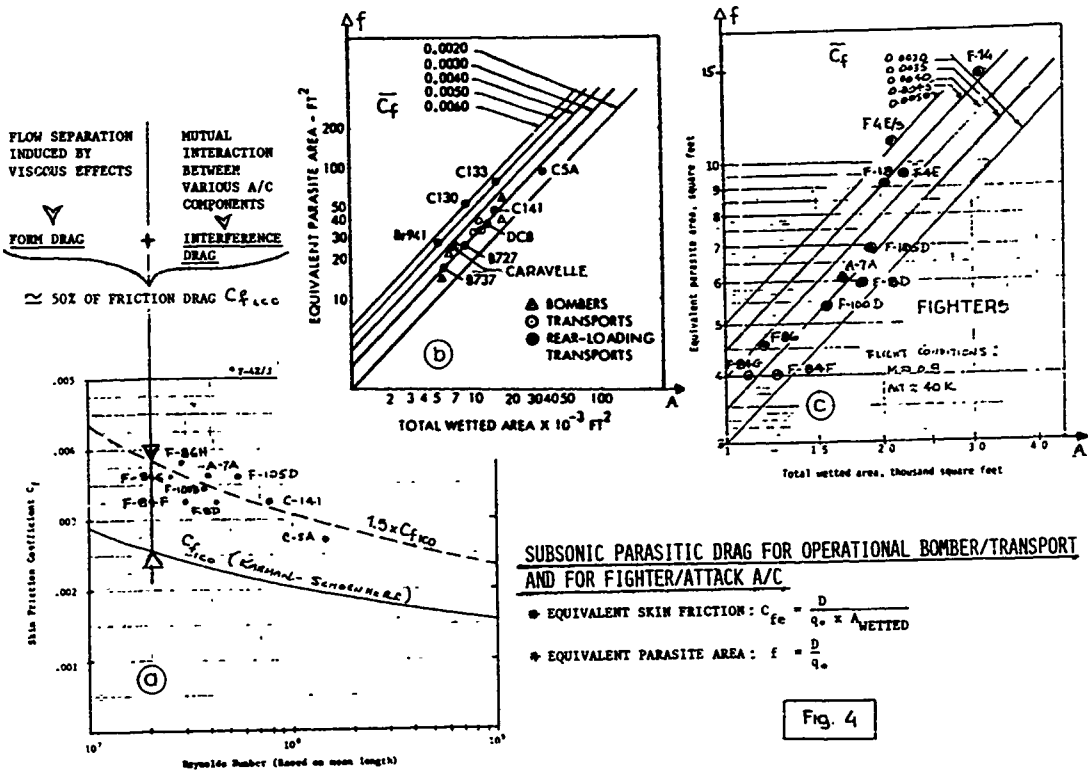
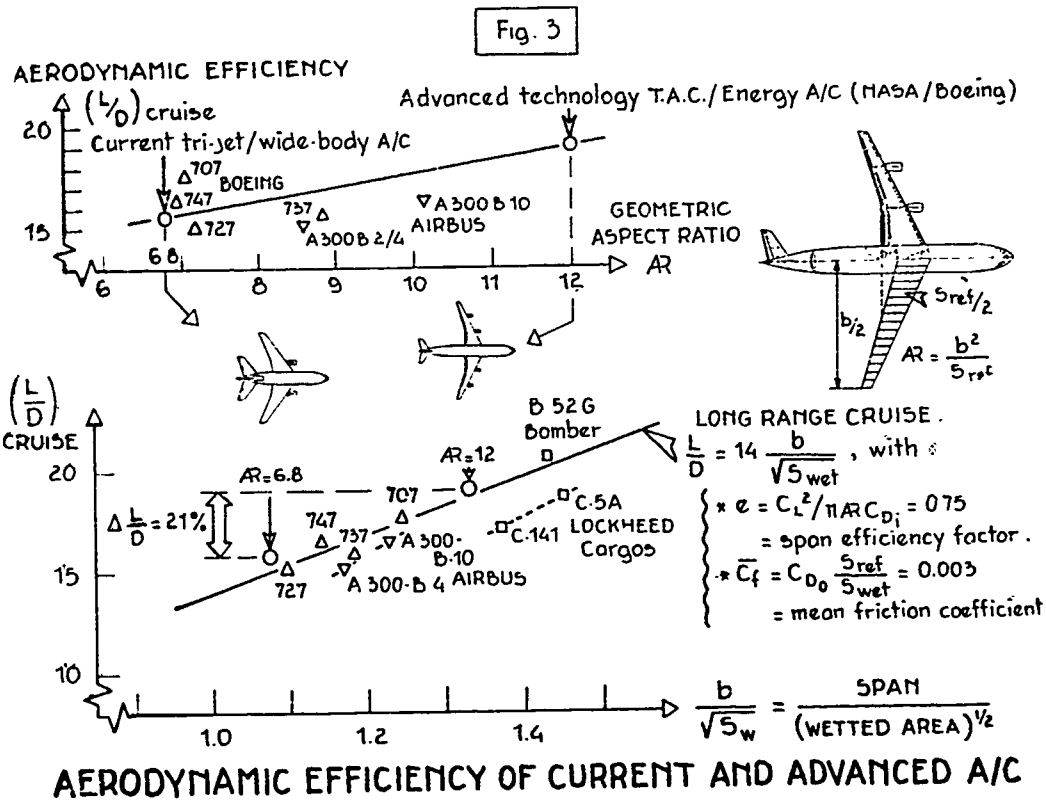
(d) Drag buildup of typical supersonic aircraft configurations.



- * LARGER 'EFFECTIVE' ASPECT RATIO (AR) (Wing tip extension, winglets, engine-airframe integration, ...).
- * BETTER SPAN EFFICIENCY FACTOR (e) (Twist and camber optimization, variable camber, less parasitic drag increase with α , less trim drag, ...).

- * PARASITIC AND INTERFERENCE DRAG REDUCTION.
- * FAVOURABLE REYNOLDS NUMBER EFFECT FOR VERY LARGE A/C.
- * NO TRANSONIC DRAG AT CRUISE.
- * LAMINAR FLOW CONTROL WITH BOUNDARY-LAYER SUCTION.

Fig 2 POLAR CURVE IMPROVEMENT



DRAG IN COUNTS, 1 COUNT = 0.0001

CONTRIBUTION	$\frac{\Delta C_D}{C_D}$
● ANTENNAE	.53
● WINDSHIELD WIPER	.16
● ANTI-COLLISION LIGHT	.01
● JOINTS/STEPS/GAPS	2.73
● EXPOSED FLAP TRACKS	1.60
● APU EXHAUST OUTLET	.02
● BUMPS/BLISTERS/PROTRUSIONS	1.05
● DOORS	.26
● VENTS/PRESSURIZATION LEAKS/AIR COND. I/O	2.30
● WAVINESS/FALLINGS/MISC.	.42
TOTAL	9.08 ≈ 3.5 % OF TOTAL DRAG

Fig 5 Estimates of typical roughness drag contributions for a long-haul cruise aircraft. (Lockheed C 5A Strategic Cargo Aircraft).

Fig 6 SUMMARY OF VARIOUS PARASITIC DRAG : STEPS, RIDGES, GAPS

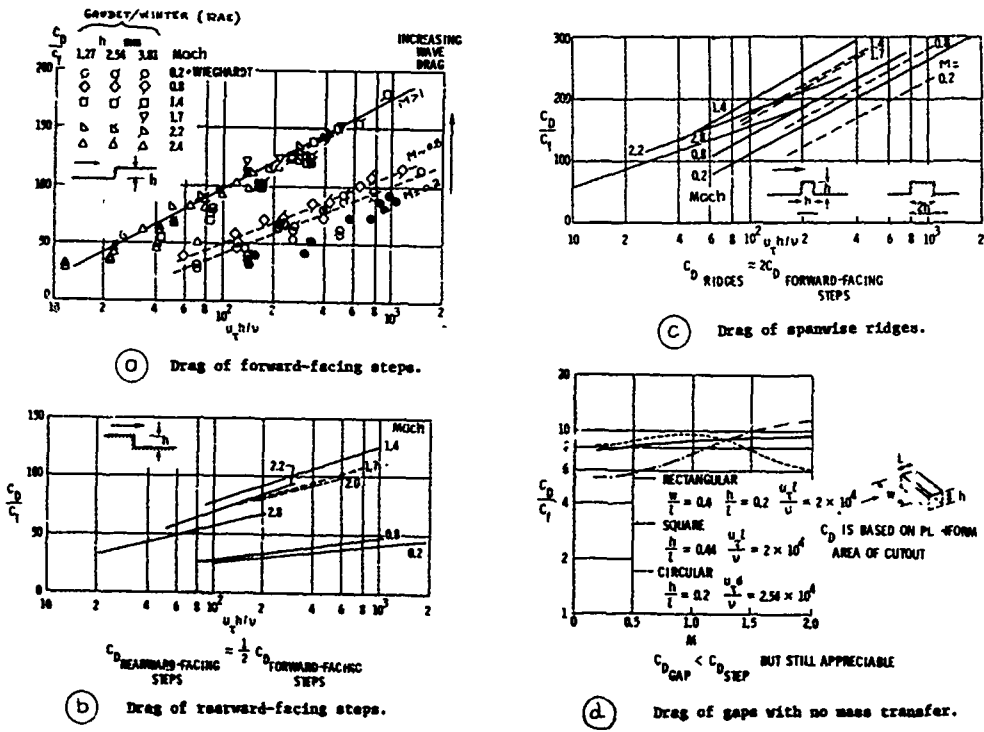
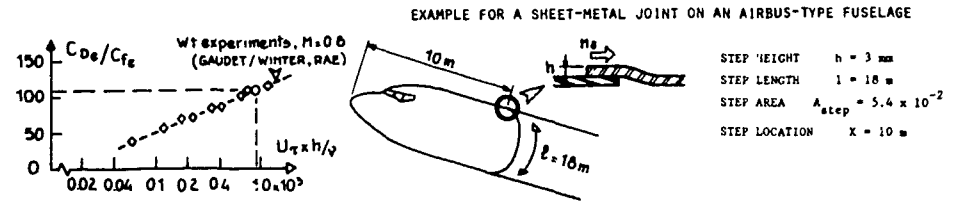


Fig 7

(a) PARASITIC DRAG OF A FORWARD-FACING STEP AT M = 0.8 CRUISE



BOUNDARY-LAYER COMPUTATION AT CRUISE M = 0.8

- * Edge of B L { Mach Number $M_{\delta_x} = 0.8$
 Dynamic press $q_{\delta}/q_{\infty} = 1.0$
- * Local skin-friction $C_{f \text{ local}} = 0.0016$
- * Reynolds number based on step height h , and local friction velocity U_{π}

$$\frac{U_{\pi} h}{\nu} = \frac{U_{\pi} x}{\nu} \times \frac{h}{x} = 3 \times 10^6 \times \frac{3 \times 10^{-3}}{10} = 900$$

$$\frac{C_{De}}{C_{fe}} = A (M_{\delta_x}) \times \log \frac{U_{\pi} h}{\nu} - B (M_{\delta_x})$$

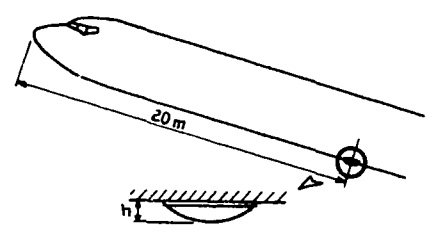
$$= 60 \log 900 - 70 = 107.25$$

PARASITIC DRAG FOR ONE STEP (3 mm x 18000 mm), REFERED TO $A_{\text{ref}} = 200 \text{ m}^2$

$$C_D = D/q_{\infty} A_{\text{ref}} = \frac{C_{De}}{C_{fe}} \times C_{f \text{ local}} \times \frac{q_{\delta}}{q_{\infty}} \times \frac{A_{\text{step}}}{A_{\text{ref}}} = 107.25 \times 0.0016 \times 1.0 \times \frac{5.4 \times 10^{-2}}{200} = 0.46 \times 10^{-4}$$

(b) PARASITIC DRAG OF AN ANTI-COLLISION-LIGHT ON THE BOTTOM OF AN AIRBUS-TYPE FUSELAGE

- LIGHT HEIGHT $h = 75 \text{ mm}$
- FRONTAL AREA $A_f = 0.005 \text{ m}^2$
- LIGHT LOCATION $\lambda = 20 \text{ m}$
- $\bar{C}_D = 0.3$ (HOERNER)



BOUNDARY-LAYER COMPUTATION

- THICKNESS $\delta_x = 110 \text{ mm}$
- Dyn press. $q_{\delta}/q_{\infty} = 1.08$
- Velocity profile exponent $n = 4.5$
- Effective dynamic pressure

$$\frac{q_{\delta}^{\text{eff}}}{q_{\delta}} = \frac{n}{n+2} \left(\frac{h}{\delta} \right)^{2/n}$$

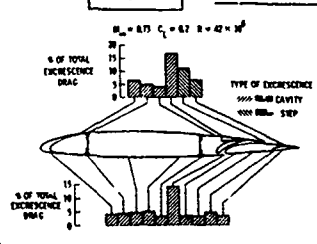
$$= \frac{4.5}{6.5} \times \left(\frac{75}{110} \right)^{0.44} = 0.584$$

PARASITIC DRAG, REFERED TO $A_{\text{ref}} = 200 \text{ m}^2$:

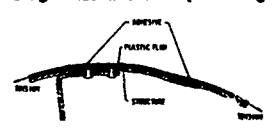
$$C_D = D/q_{\infty} A_{\text{ref}} = \bar{C}_D \times \frac{q_{\delta}^{\text{eff}}}{q_{\delta}} \times \frac{A_f}{A_{\text{ref}}}$$

$$= 0.3 \times 0.584 \times 1.08 \times \frac{0.005}{200} = 0.047 \times 10^{-4}$$

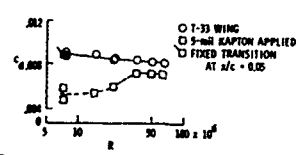
Fig 8 EXCRESCENCE DRAG ON WING AND ITS REDUCTION



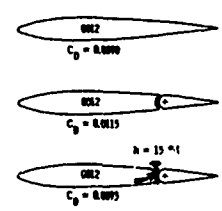
(a) Roughness drag breakdown for a typical medium-range subsonic transport wing.



(b) Application of plastic coatings to reduce roughness drag.

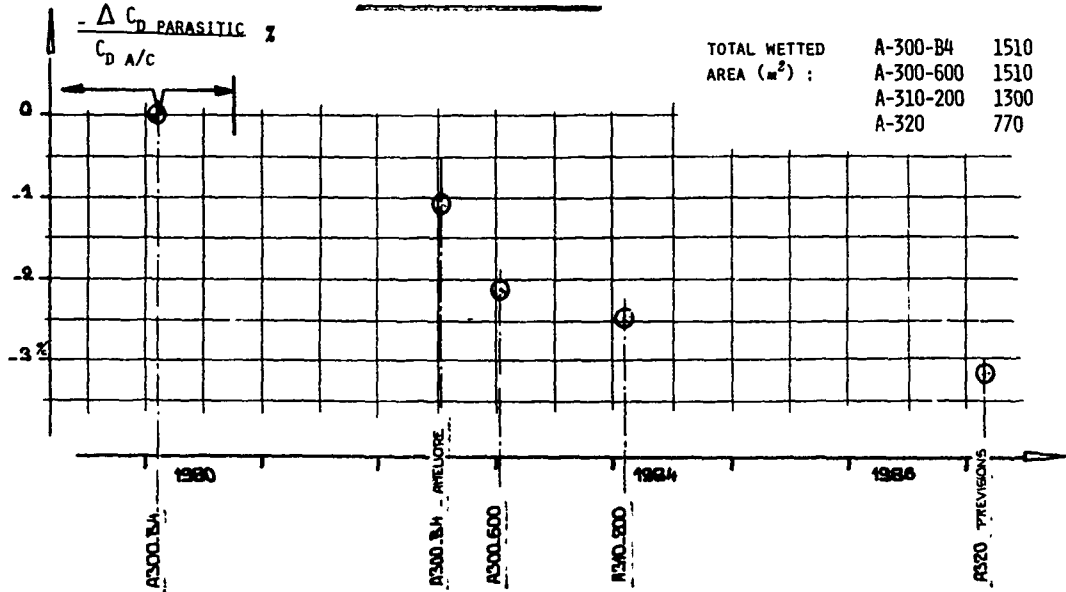


(c) Drag reduction with Kaptan coating.



(d) Drag reduction of control surface gap.

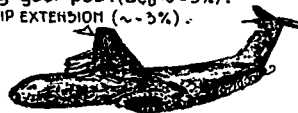
Fig 9 EVOLUTION OF THE PARASITIC DRAG (EXCRESCENCES, SURFACE DEFICIENCIES,...) ON THE AIRBUS A/C FAMILY



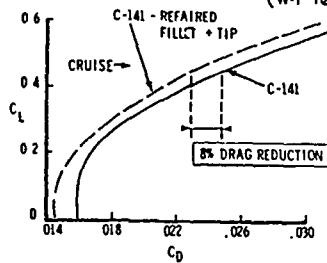
MAIN SOURCES : * HOERNER - FLUID DYNAMIC DRAG
 * ENGINEERING SCIENCES DATA UNIT (AERODYNAMICS)
 + VISCOUS EFFECT

Ref. AEROSPATIALE DIV AVIONS

- * REDUCTION OF PARASITIC VORTICES at the wing-fuselage juncture and around landing gear pod. ($\Delta C_D \sim -5\%$).
- * WING TIP EXTENSION ($\sim -5\%$).



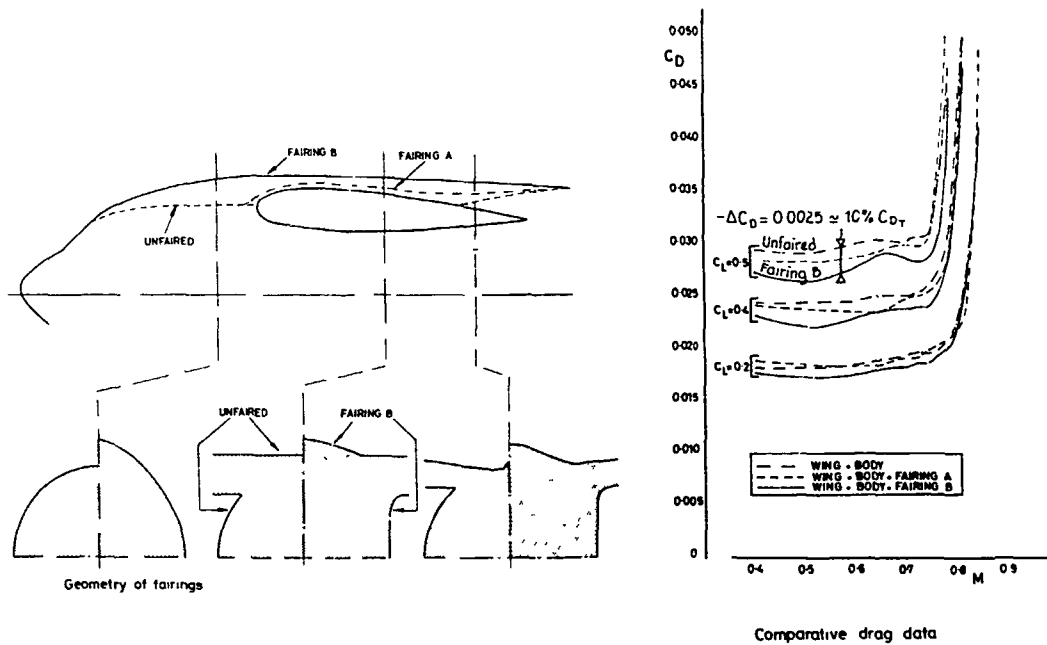
USAF. Jet cargo C-141 : clean-up (w.t tests)



- * FUEL SAVING FOR C-141 FLEET : 82,000,000 GALLONS PER YEAR
- * ESTIMATED COST OF MODIFICATION : 277 A/C \$11,000,000 (Year 1976) (1 YEAR'S FUEL SAVING)

Fig 10 ESTIMATED INTERFERENCE DRAG REDUCTION on an EXISTING CARGO AIRCRAFT.

Fig 11 WING BODY FAIRING RESEARCH HIGH WING SUBSONIC TRANSPORT



AERODYNAMIC INTERFERENCE COMPUTATION
 for TRANSPORT A/C WING/FUSELAGE OPTIMIZATION.

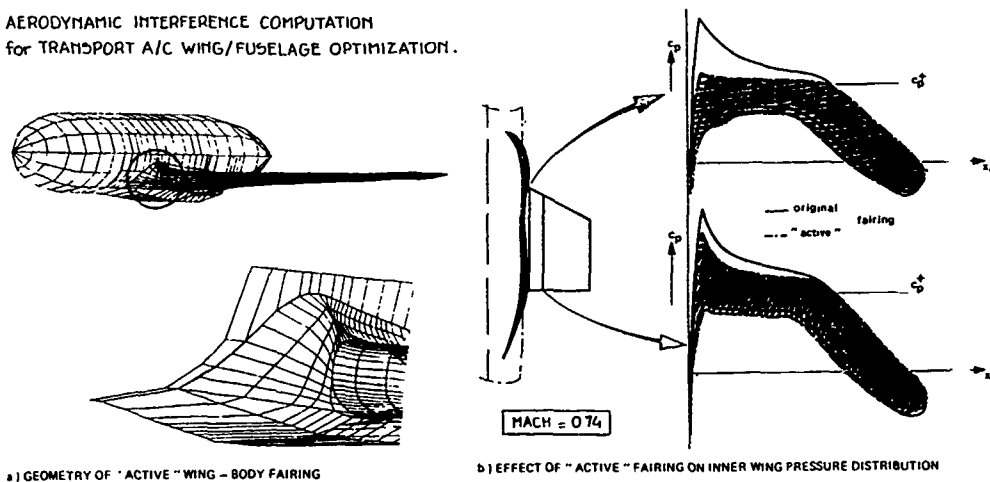


Fig 12 "ACTIVE" SHAPING of WING-FUSELAGE FAIRING by PANEL METHOD (NLR)
 (Area-ruled fairing to reduce superevelocities over the inner wing).

Fig 13 PARASITIC DRAG REDUCTION THROUGH WING ROOT FAIRING ON AIRBUS-TYPE TRANSPORT A/C AT CRUISE

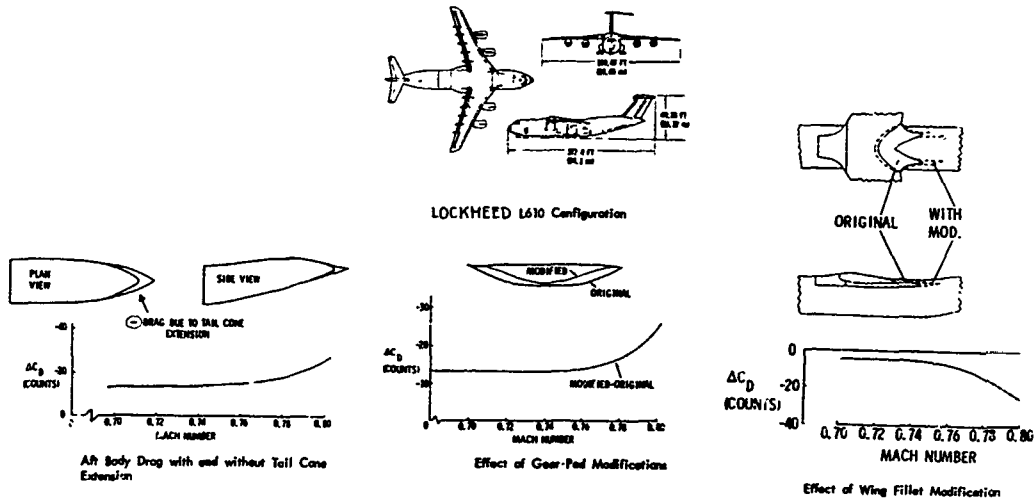
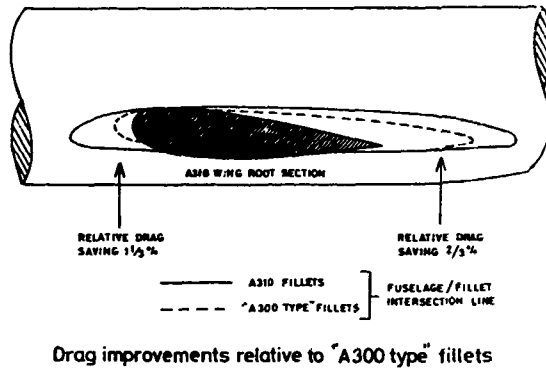
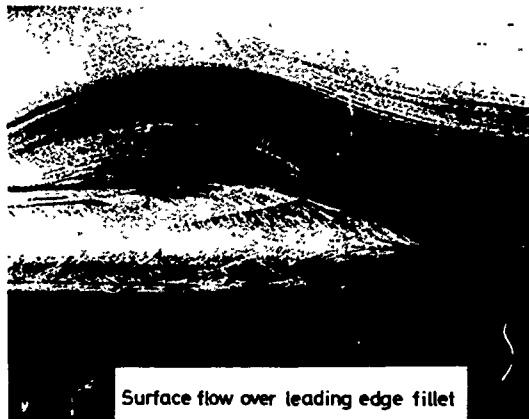
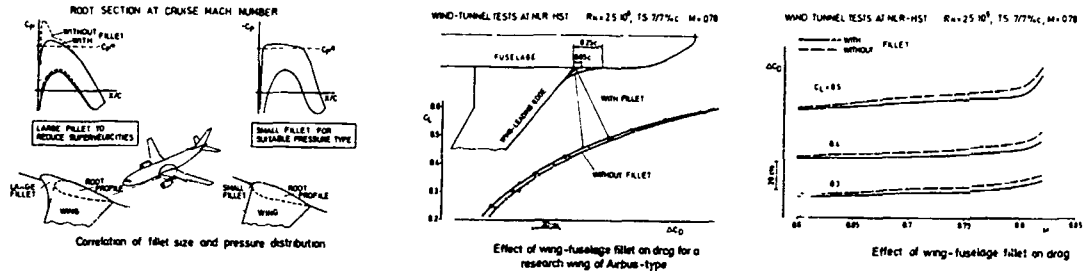


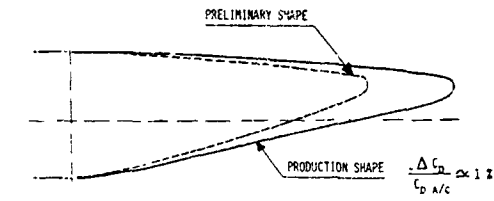
Fig 14 FUSELAGE DRAG IMPROVEMENT of a MILITARY CARGO A/C during preliminary design : WIND-TUNNEL TRANSONIC TESTING
Result : TOTAL $\Delta C_D \approx -50$ counts , at cruise conditions .

Fig 15

REAR-FUSELAGE SHAPE OPTIMIZATION IN WIND-TUNNEL

AEROSPATIALE-AERO DPT

a) ATR-42 COMPUTER A/C



b) CONCORDE SST

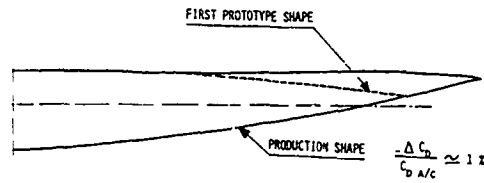
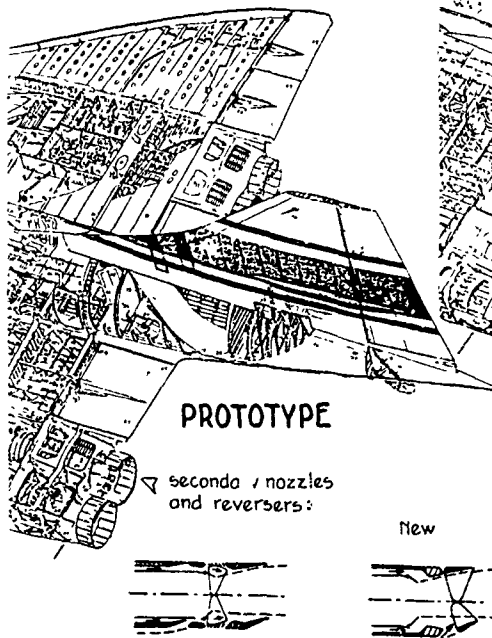


Fig 16

DRAG REDUCTION PROGRAMME on CONCORDE SST



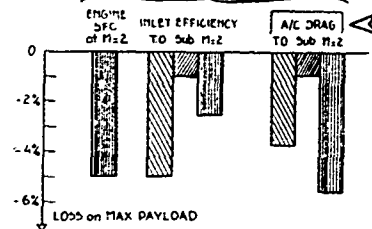
a) EXTENDED REAR-FUSELAGE

PRODUCTION

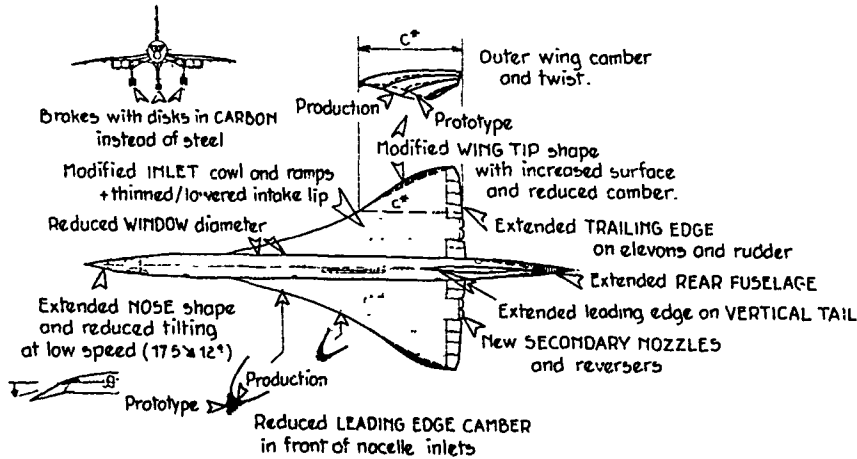
Extended rear fuselage

b) IMPACT on PAYLOAD for:

1% loss on



CONCORDE PERFORMANCE SENSITIVITY to various parameters.



c) MAIN AIRFRAME MODIFICATIONS on CONCORDE SST between the Prototype and the Production A/C.

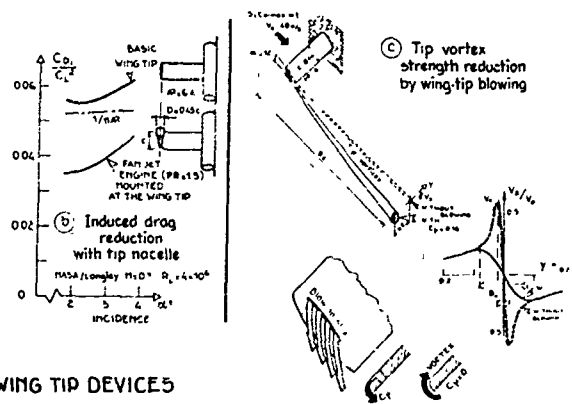
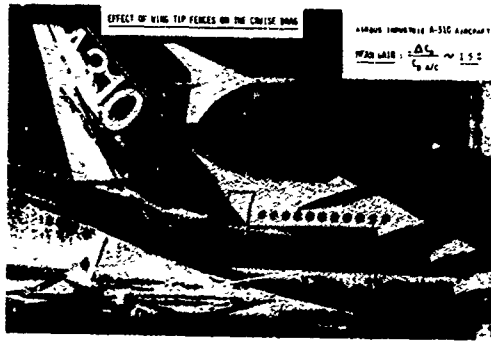
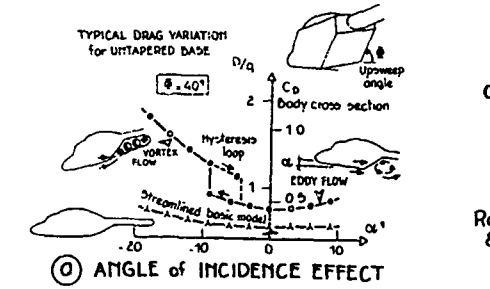
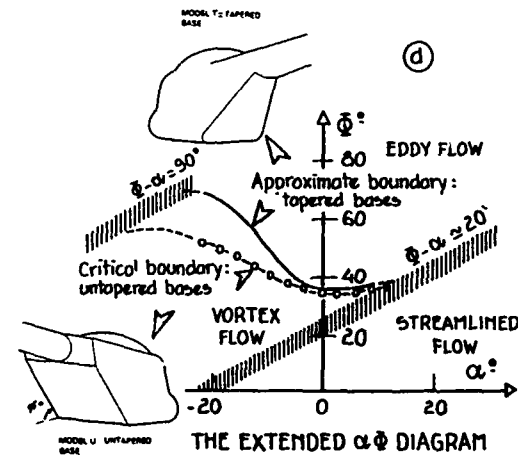
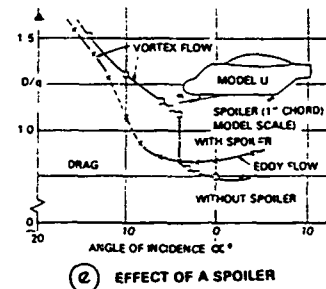
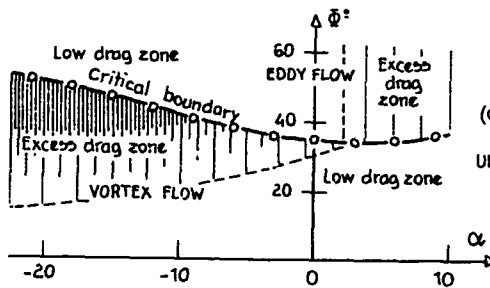
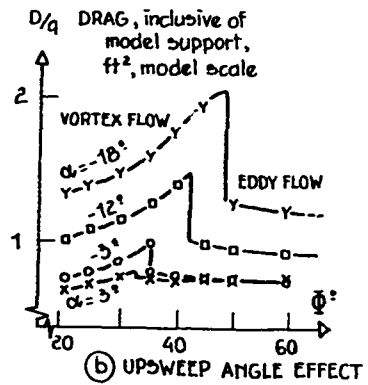


Fig 17 DRAG REDUCTION through WING TIP DEVICES



UPSWEEP EFFECT on FLOW REGIMES and on PARASITIC DRAG for a HELICOPTER FUSELAGE
 Ref.) J. SEDDON, 1982
 8th Europ. Rotorcraft Forum



SOLUTIONS to REDUCE the PARASITIC DRAG:

Ref.) J. SEDDON 9th European Rotorcraft Forum (1983)

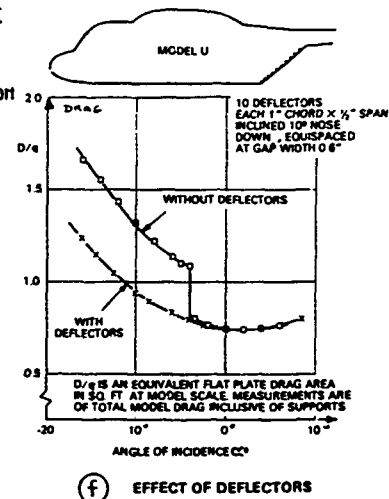
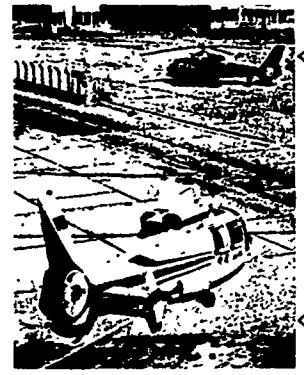


Fig. 18 AERODYNAMICS of the HELICOPTER REAR FUSELAGE:
 UPSWEEP EFFECT and ANGLE of INCIDENCE EFFECT
 Frontier between 2 regimes:
 -Vortex flow
 -Eddy flow

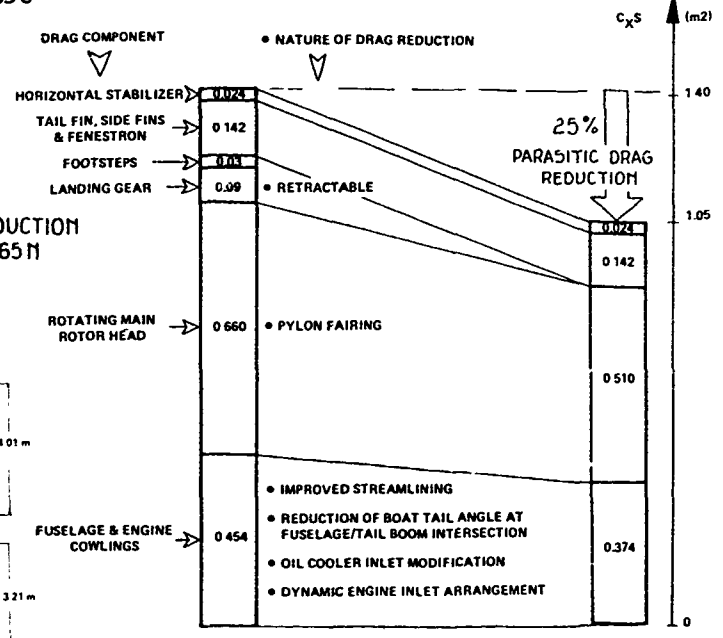
Fig. 19



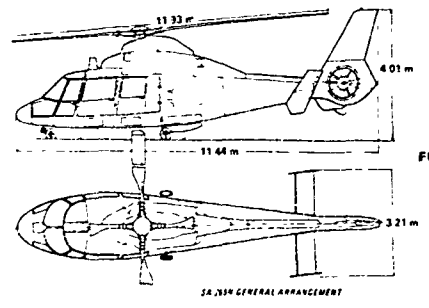
DAUPHIN Prototype SA 365 C

PRODUCTION SA 365 M

PARASITIC DRAG REDUCTION PROGRAMME on the SA 365 helicopter "Dolphin".

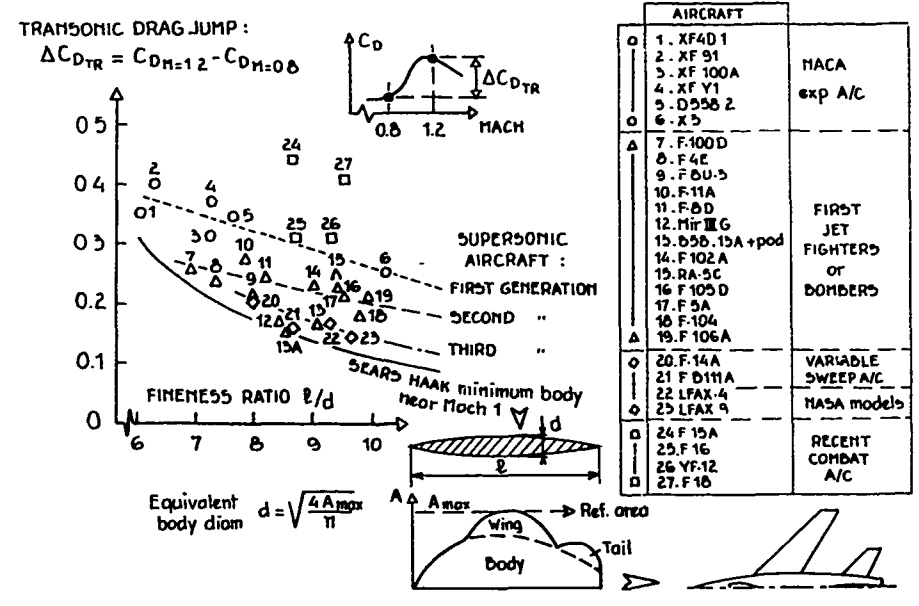


NOTE: The parasitic drag absorbs about 50% of the cruise power.



AEROSPATIALE "DAUPHIN" PROTOTYPE → PRODUCTION (SA 365 C) (Costguard 366 G and SA 365 M)

Fig 20 WAVE DRAG : The PRICE to PAY for CROSSING the SONIC BARRIER .



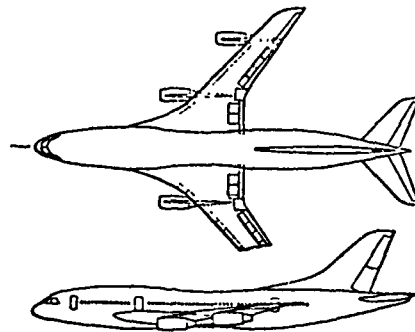
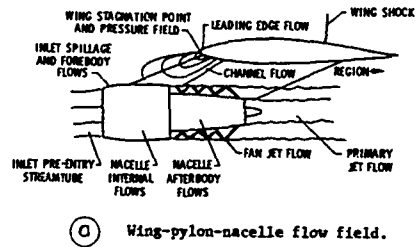
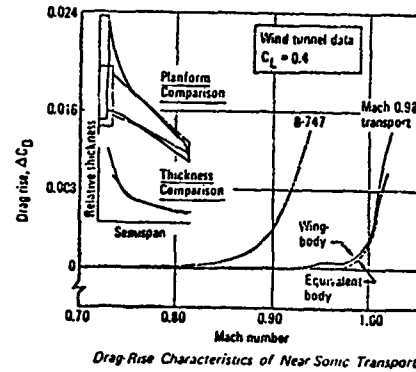
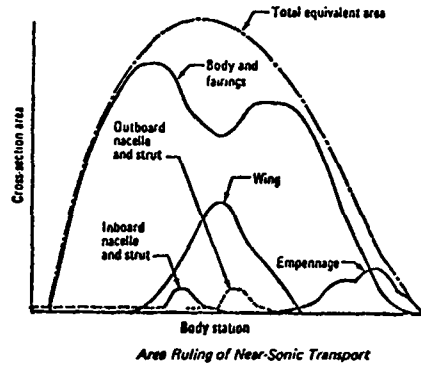
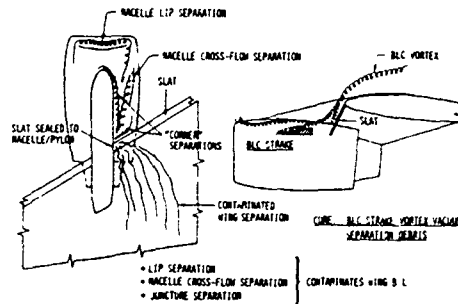


Fig 21

SONIC AREA-RULE
INTEGRATED to a
"NEAR-SONIC" TRANSPORT PROJECT
(Boeing Co)
and drag rise ($M_D = 0.98$) compared
with a B 747 ($M_D = 0.87$).

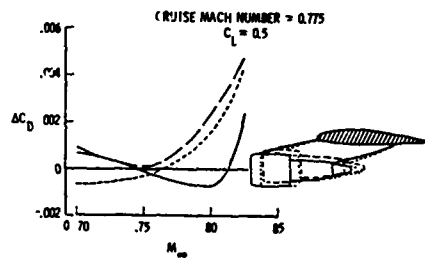


(a) Wing-pylon-nacelle flow field.

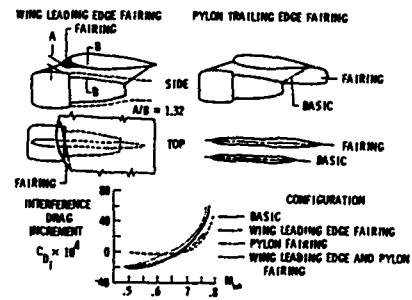


(d) Adverse viscous interference at subcritical high-lift conditions

Fig 22 WING/TURBO-FAN INTERFERENCE for an UNDER-WING CONFIGURATION

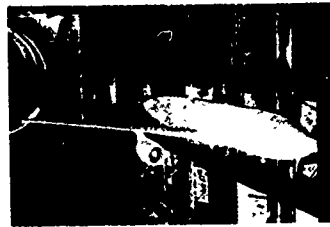


(b) Effect of underwing engine positioning on interference drag.



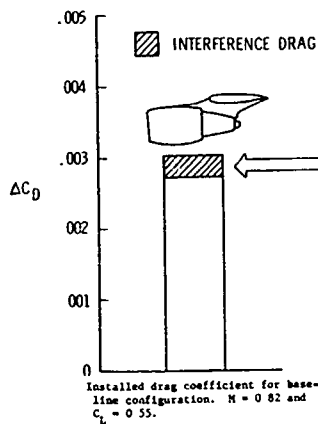
(c) Effect of wing leading-edge fairing and pylon trailing-edge fairing on nacelle-wing interference drag.

Fig 23



Photograph of transport model with high aspect ratio supercritical wing and powered turbofan engines

NASA Langley, 8ft Transonic Tunnel.



INTERFERENCE DRAG between FAN-ENGINE POD and WING on a TRANSPORT AIRCRAFT

- * WIND-TUNNEL HALF MODEL :
 - AR = 10 wing
 - Powered nacelle with A.T.P.S.

* MACELLE INSTALLATION DRAG :

$$\Delta C_D = C_D(\text{nacelle + pylon + wing + fuselage}) - C_D(\text{wing + fuselage})$$

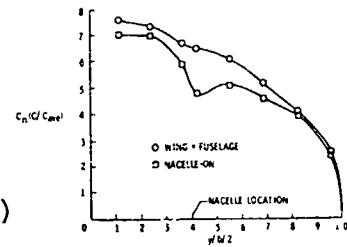
* INTERFERENCE DRAG :

$$= \Delta C_D - C_D(\text{isolated nacelle + pylon})$$

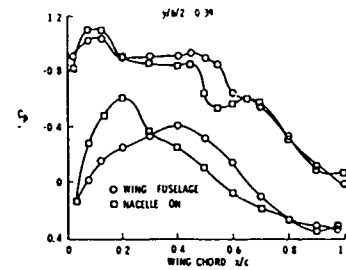
≈ 1 to 2% of A/C DRAG

⇒ This loss is due to a LIFT REDUCTION at CONSTANT α , to be compensated by a $\Delta\alpha \rightarrow \Delta C_D$ induced

Ref NASA (1983)

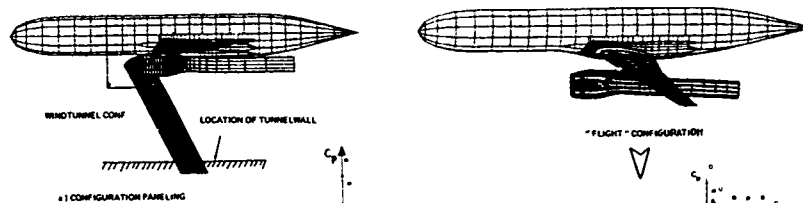


Effect of engine nacelles on span-load distribution. $M = 0.80$, $\alpha = 2.75^\circ$ and $NPR = 1.5$



Effect of engine nacelles on wing pressure distributions. $M = 0.80$, $\alpha = 2.75^\circ$ and $NPR = 1.5$

Fig 24

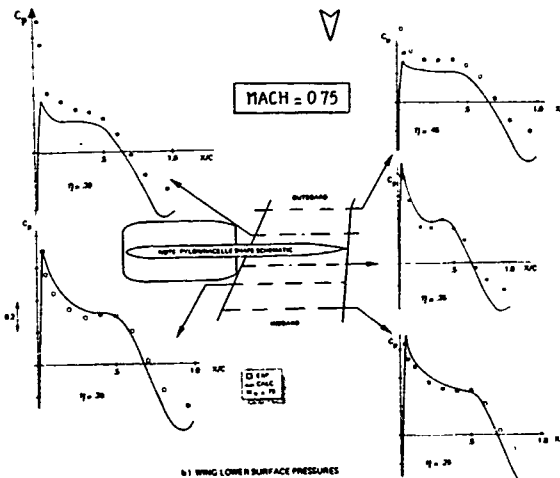


UNDERWING PYLON/MACELLE/JET INTERFERENCE COMPUTATION (NLR, Panel method)

* Flight configuration tested on half-model with a faired inlet and a strut with compressed air supply for jet simulation

* Computation on the flight configuration with jet representation.

Ref.) J.W. DLOOF, AGARD R 712 (1983) Special course on Sub-transonic Aerodynamic Interference for A/C (8).



WING LOWER SURFACE PRESSURES

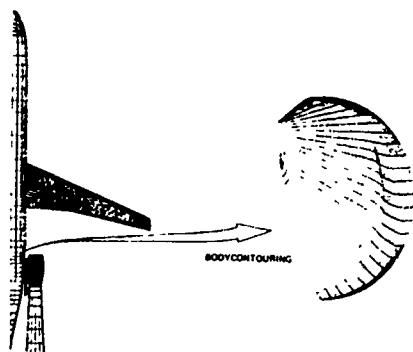
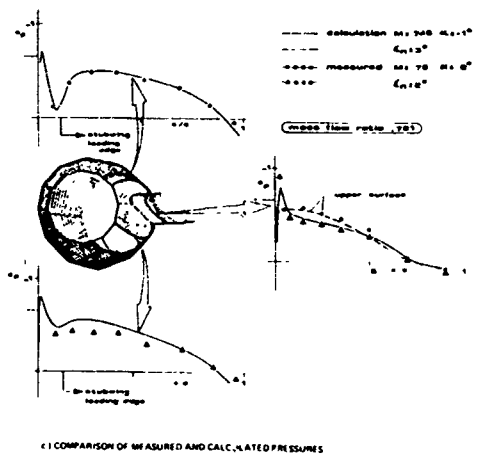
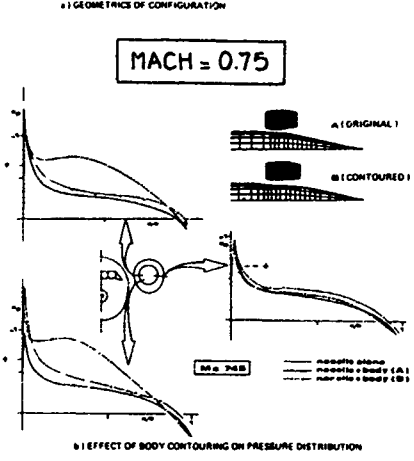


Fig 25

AERODYNAMIC INTERFERENCE COMPUTATION for a TRANSPORT A/C with REAR MOUNTED ENGINES

Minimization of superelevations in the passage between rear-mounted nacelle and fuselage, using NLR panel method computation.

Ref) J.W. SLOOF (NLR) - AGARD R 712 (1965).



(b) EFFECT OF BODY CONTOURING ON PRESSURE DISTRIBUTION

(c) COMPARISON OF MEASURED AND CALCULATED PRESSURES

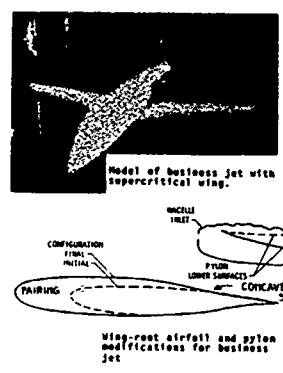
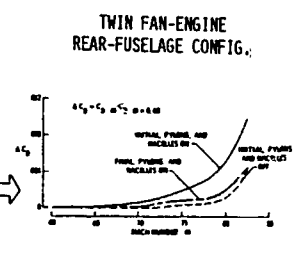
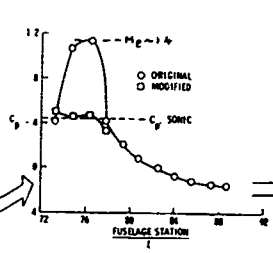


Fig 26 CRUISE DRAG IMPROVEMENT of an EXECUTIVE JET through WING/NACELLE FAIRING



- Pressure distributions on side of fuselage of business jet, $M = 0.80$

Effects of wing-root and pylon modifications on drag-rise characteristics for business jet, $C_L = 0.25$.

Fig 27

INFLUENCE OF VARIOUS GEOMETRICAL PARAMETERS ON WING/POD/PYLON INTERACTION DRAG IN CRUISE FOR AN AIRBUS CONFIGURATION

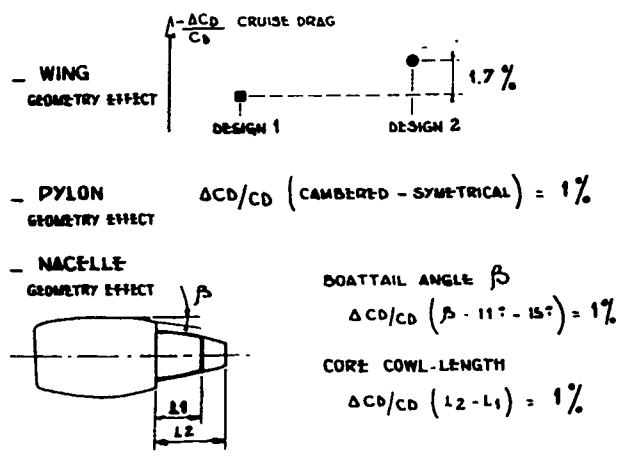


Fig 28

HOW TO USE A JET-ENGINE TO INDUCE AERODYNAMIC LIFT?

HIGH BYPASS RATIO FAN ENGINES/TRANSPORT A/C TURBO-JET/COMBAT A/C

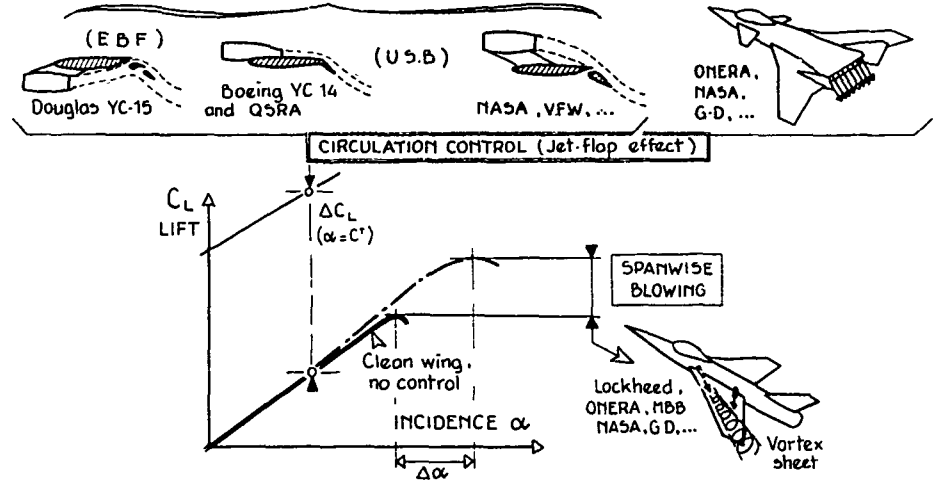
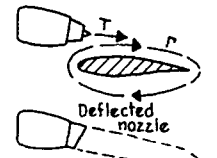
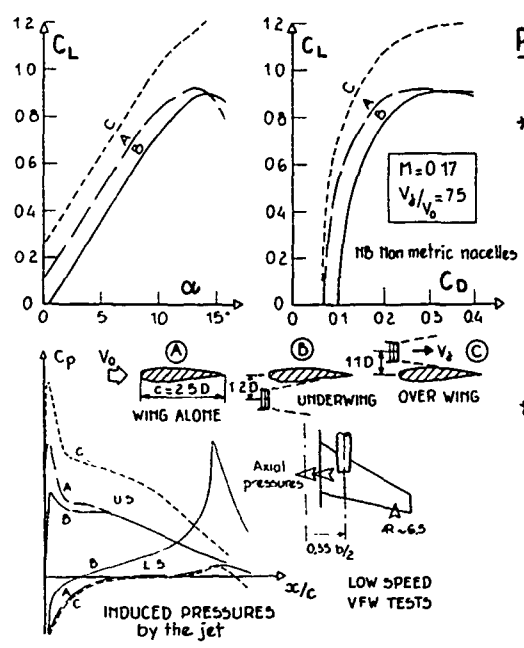


Fig 29

PROPULSIVE NACELLE INTERFERENCE WING

* "Over-the-wing" location, increases the circulation over the wing



* and induces a jet flap effect if the jet is deflected over the high lift system.

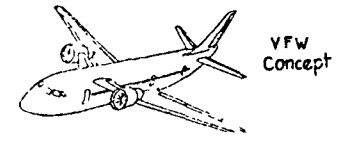


Fig 30

NASA-Langley. PROPULSION INSTALLATION for TURBO-FAN TRANSPORTS



Photograph of model with upper-surface nacelles in Langley 16-Foot Transonic Tunnel

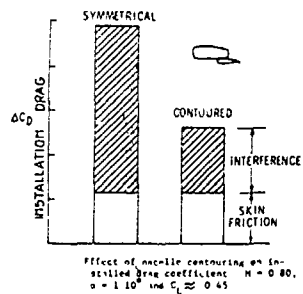


Photograph of model with over-the-wing nacelles in the Langley 16-Foot Transonic Tunnel

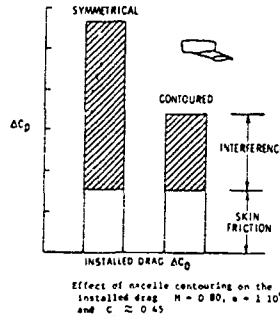


Photograph of model with aft-mounted nacelle in Langley 16-Foot Transonic Tunnel

NACELLES on UPPER-SURFACE ...



OVER the WING ...



AFT-MOUNTED/LOWER SURF.

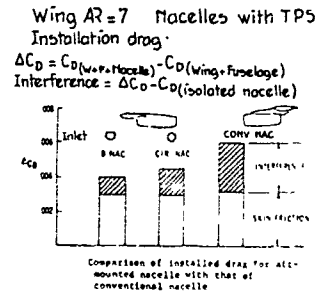
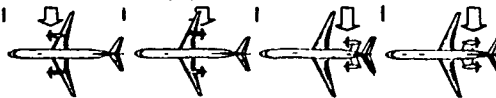


Fig 31

PROP-FAN/AIRFRAME INTERFERENCE at TRANSONIC SPEED

POSITIVE ASPECTS	<ul style="list-style-type: none"> Down flap effect = STOL performance Wing boundary-layer re-energized Better inlet efficiency. 	<ul style="list-style-type: none"> Propeller acoustic signature behind the passenger cabin, but still acoustic fatigue on fuselage and tails. Better inlet efficiency.
NEGATIVE ASPECTS	<ul style="list-style-type: none"> High speed slipstream on the wing: possible shock waves = Δ Drag swirl flow = Δ for single rot propeller Strong noise on passenger cabin 	<ul style="list-style-type: none"> Mild wing wake: Transonic channel flow between nacelle/pylon/fuselage (blockage?) Engine exhaust on propeller

Note: Counter-rotation prop-fan configuration gives better efficiency, no more swirl behind prop, but more near field noise.



PROP-FAN PROPULSION SYSTEMS ON TRANSPORT AIRCRAFT, 0.75 & 1.0 & 0.80.

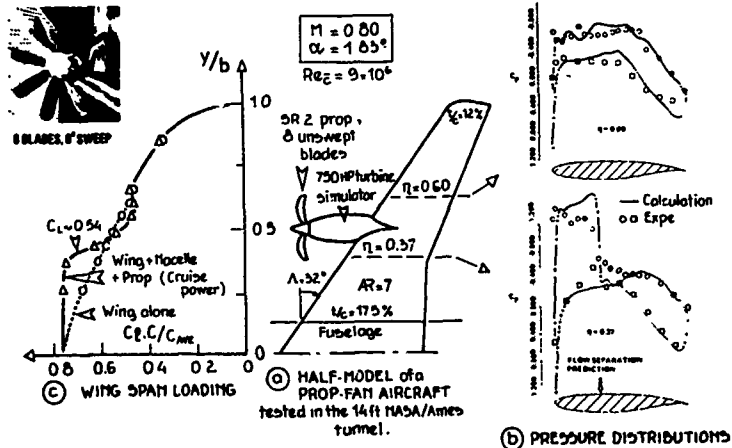


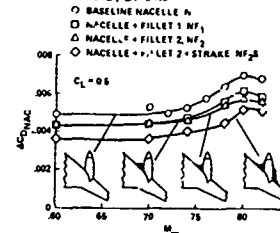
Fig 32 PROP-FAN SLIPSTREAM EFFECT on a SWEEP-WING at CRUISE $M = 0.8$.



Fig 33 POWERED NACELLE/ SWEEP WING INTERACTION.

(a) UPPER SURFACE FLOW SEPARATION behind the shock wave at $M=0.8$, inducing parasitic drag.

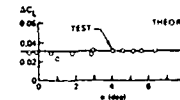
(b) SOLUTIONS:
 - Contoured nacelle
 - Leading edge extension
 - LE fillets/strake



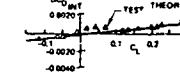
Wind Tunnel Model Features



FAVOURABLE Interference Lift



Interference on Nacelle



Interference on Wing Body

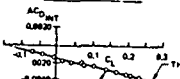
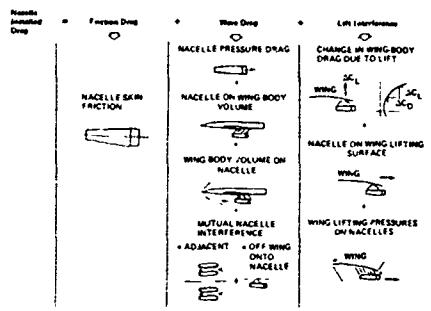


Fig 34a AIRFRAME / NACELLES INTERFERENCE on a 55T AIRCRAFT PROJECT (Boeing, 1971)



Nacelle Installed Element Drag Components

FAVOURABLE Nacelle Installed Drag

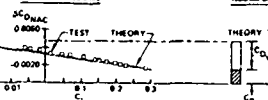
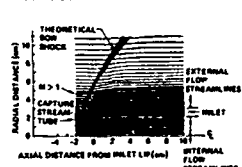
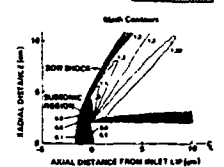
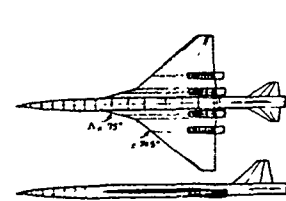
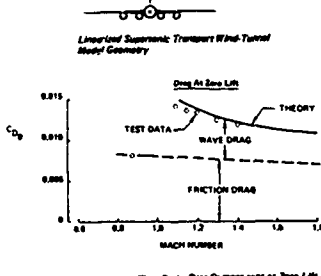


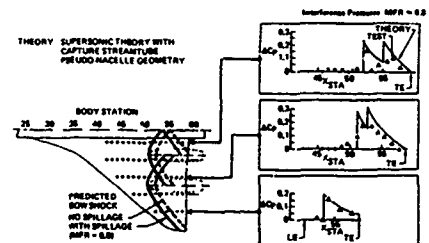
Fig 34b AIRFRAME / NACELLES AERO INTERFERENCE PREDICTIONS on a 55T AIRCRAFT PROJECT and COMPARISON with WIND-TUNNEL TESTS at MACH $M=1.4$, $\alpha=0$.



Mixed-Flow Analysis Results at Mach 1.4 and a Mass Flow Ratio of 0.7

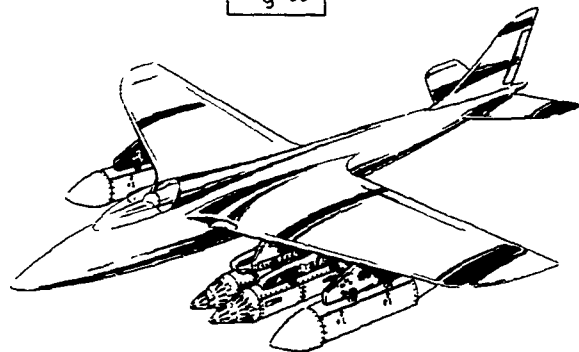


Wing-Body Drag Components at Zero Lift



Effect of Normal Shock Settings on Isolated Nacelle Pressures and Wing Lower Surface Pressures at Mach 1.4, Zero Angle of Attack and a Mass Flow Ratio of 0.6

Fig 35



WHY SHOULD THE AERODYNAMIC CLEANLINESS CHANGE AT THE PYLON?

SIGNIFICANCE OF STORE DRAG AND DRAG REDUCTIONS

LIFE CYCLE COST AIRCRAFT



WHERE THE COSTS GO

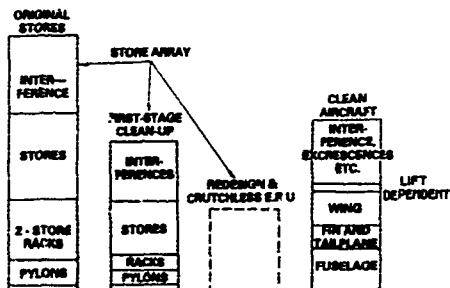
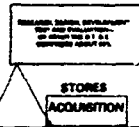


Fig 36

CORRELATION OF DRAG NEAR $M = 1.0$ AND CROSS-SECTIONAL AREA DISTRIBUTIONS (FROM AERIALIA TESTS)

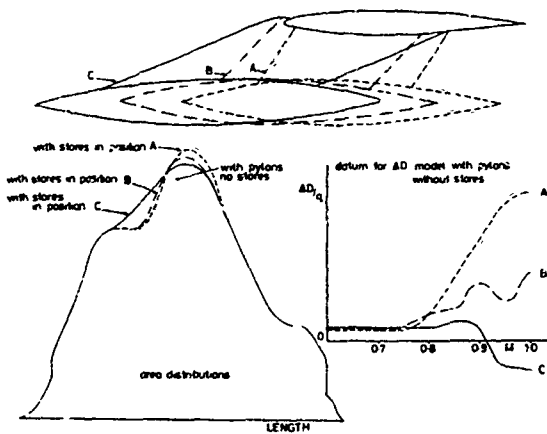


Fig 37

BELOW 65 THICK 53° L. E. SWEEP WING (FROM TESTS AT A.R.A.)

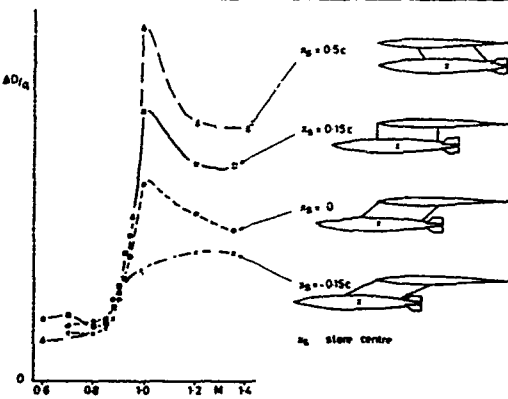
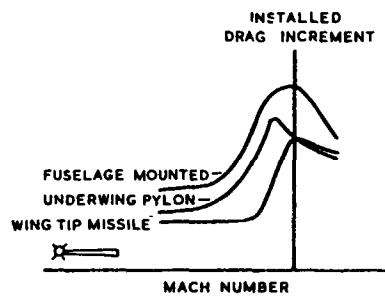
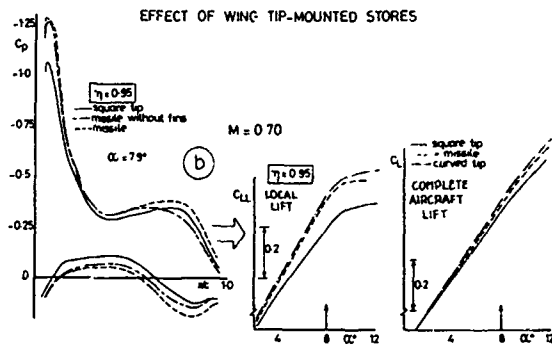
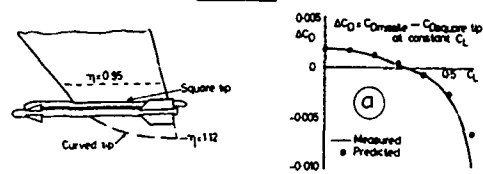


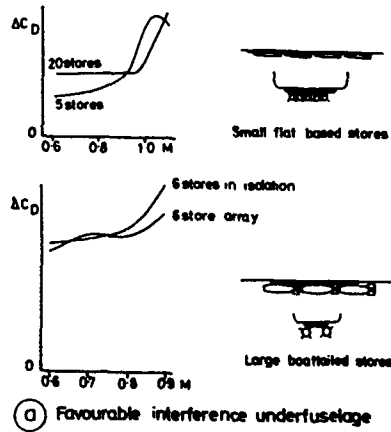
Fig 38



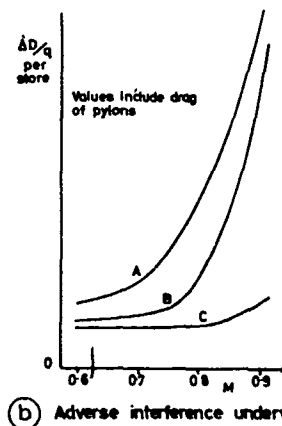
(c) Installed Drag of Missile Plus Launcher as a Function of Carriage Position

Fig 39

EXAMPLES OF FAVOURABLE AND ADVERSE INTERFERENCE FOR MULTIPLE STORE CARRIAGE



- A 3 stores on separate pylons per wing
- B Single store per wing
- C Free air drag



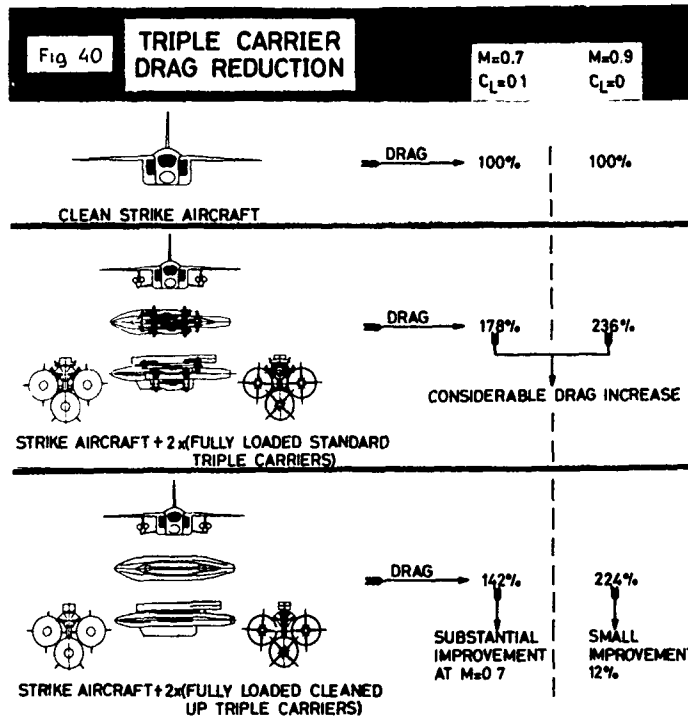


Fig 41

FLIGHT/TUNNEL COMPARISON OF THE INSTALLED DRAG OF WING-MOUNTED STORES (HSA BUCCANEER, AGARD-CP-187)

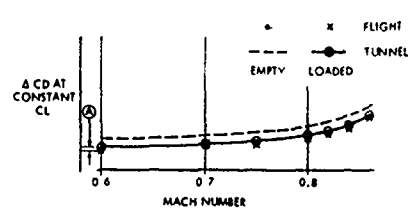
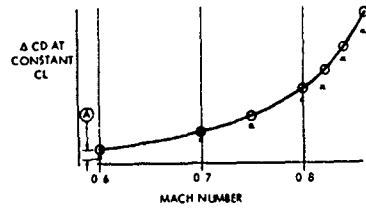
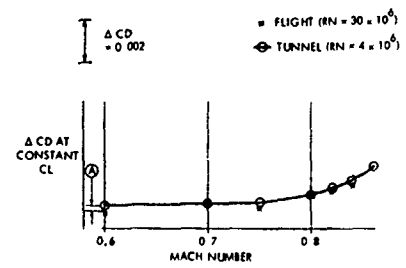
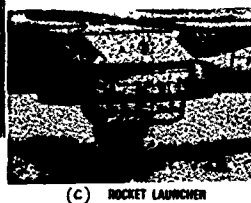
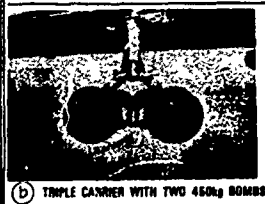
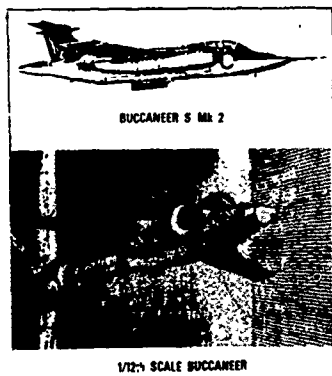
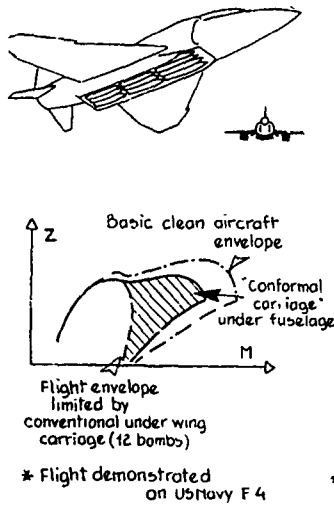
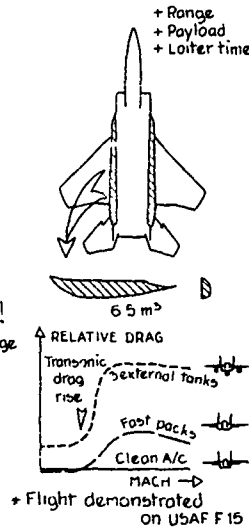


Fig 42 AIRFRAME/WEAPON INTEGRATION

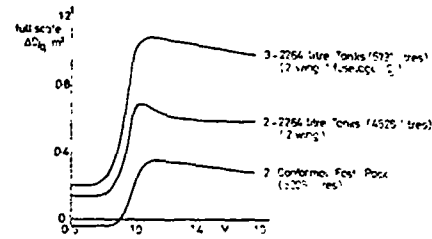
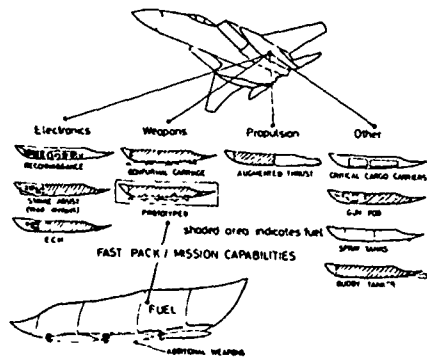
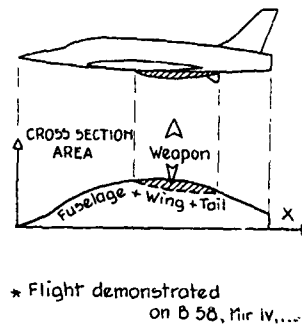
(a) MULTIPLE STORES



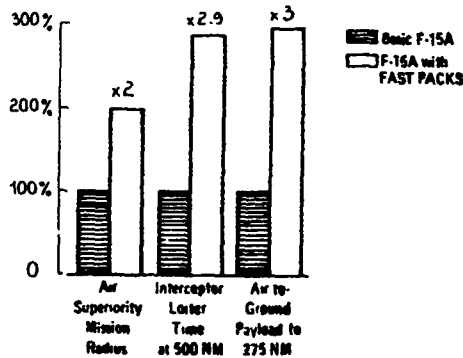
(b) "FAST" PACKS" CONTAINERS



(c) SEMI-IMMERSED LOAD UNDER FUSELAGE



TYPICAL REDUCTIONS IN DRAG INCREMENT
F15 - CONFORMAL CARRIAGE



RECENT DEVELOPMENTS IN THREE-DIMENSIONAL WAKE ANALYSIS

by

J.E.Hackett
A.Sugavanam
Dept. 72-66 Zone 404
Lockheed Georgia Co
Marietta, GA 30063
USA

Significant advances in the determination of drag and its components (viscous, vortex, "source", "blockage", etc.) have been made in recent years. These were triggered by the reduction of the vortex drag integral to a wake integral by Maskell in the early 1970's. In 1979, Wu, Hackett, and Lilley broadened the basis for Maskell's results and, in 1984, Hackett and Sugavanam devised methods which make it suitable for use in the near-wake of wind tunnel models.

The present paper reviews these advances and provides a consistent derivation, starting from a simple form of the momentum equations, which include the best and least restrictive assumptions and procedures. The paper concludes with a practical example.

INTRODUCTION

Though wake integration procedures have been used routinely to determine the profile drag of airfoil sections for very many years, there have been relatively few instances of applications in three dimensional flows. Not only is there an order of magnitude more traverse points to contend with, if the time-honored Betz wake integral is used (Ref 1), but the three dimensional nature of the flow makes the perturbations small and difficult to measure accurately.

Betz reduced the domain of integration to the wake for profile drag but crossflow drag integration still involved the entire crossflow plane. In 1972, E. C. Maskell (Ref 2) made a major contribution by reducing this integral, also, to wake form. At the same time he pointed out the omission, by Betz, of an axial-flow perturbation term and he appears to have been also the first to include the effects of tunnel boundary constraint. Maskell recognized the existence of source-like terms in the crossflow integration, which were (and still are) whole-plane integrals, but he showed them to be small in the far-wake of the model.

Maskell's form of the three dimensional wake drag integral was implemented in the mid-1970's as a collaborative effort between Lockheed-Georgia and Professor J. C. Wu, of the Georgia Institute of Technology. Reference 3 gives a rederivation of Maskell's results, using different analysis methods, together with experimental checks for some simple attached flow cases. This was followed by a further collaborative effort, under NSF sponsorship, in which the methods were applied to the more difficult cases of a stalled wing and an idealized car shape (See Ref 4). Near-field measurements were included in these studies.

The Reference 4 work confirmed the need for near-field traverses. In measurements in the wake of a car-model for example, it was found there was sharp reduction in vortex drag within one or two car lengths. Other significant features were also lost at downstream locations. This caused a reawakening of interest in the "source-term" crossflow drag associated, in this case with flow closure behind the car. The most recent work, described in Reference 5, returns to the fact that the source term is a whole-field integral. A procedure designed to circumvent this difficulty is introduced.

The analyses discussed above are largely incremental in nature and in some cases the references are difficult to obtain. The need has been expressed to lay out the complete theoretical development, starting with Betz, in a single document. That is the intent of the present paper. An attempt will be made, while doing this, to clarify unfamiliar features and to use engineering-oriented analyses where possible.

Consecutive analyses will be given which parallel those of Betz (Ref 1), Maskell (Ref 2), Wu, et al (Ref 3), and finally Hackett and Sugavanam (Ref 5). Improved versions of the original proofs will be used where appropriate. Thus Maskell's proof will be employed for the Betz result - so picking up the u_2 -squared term - and Wu's more general proof will be used for Maskell's crossflow drag integral. Finally, "Nett" and "Gross" forms of the wake drag integral equation, defined in Reference 5, will be introduced. The paper concludes with a practical example.

NOMENCLATURE

a	(Fig 3) Vertex core radius (ft)
A	(Fig 3) Tunnel radius (ft)
A	(elsewhere) Tunnel Area (ft ²)
C _D	Drag Coefficient
D	Drag (lbs)
D ₁	Crossflow drag (Figure 8) calculated using vorticity and stream function (Eqn 24)
D ₂	Crossflow drag (Figure 8) calculated using the integral of crossflow kinetic energy (Eqn 2C)
D ₃	Drag (usually thrust, Figure 8) associated with the quantity u ² (See Eqns 3 and 4)
\bar{D}	Mean of D ₁ and D ₂ (lbs)
f	Source density (ft ² /sec/ft ²)
H	Total pressure (lbs/ft ²)
n	Normal-to-surface direction
P ₁ , P ₂	Static pressure at planes 1 and 2 (lbs/ft ²)
Q	Source strength (ft ³ /sec)
r	(Fig 6) Radius of integration (ft)
T ₁	Components of the drag integral (See Equations 2A, 2B, 2C)
T ₂	
T ₃	
U ₀	Velocity far-upstream in the tunnel test section (ft/sec)
U ₁	Axial velocities in planes 1 and 2
U ₂	
U ₂	(Fig 1) Velocity which, on replacing U ₂ , increases total pressure at plane 2 from H ₂ to H ₀
U _e	Sum of U ₀ and u _b
u, v, w	Perturbations to mainstream velocity (note, u=U-U ₀ , see Pqn 3) (ft/sec)
u _b	"blockage" velocity, see Equations (13A) and (13B), (ft/sec)
x, y, z	rectangular Cartesian coordinates (it)
Γ	Total circulation (ft ² /sec)
ξ	Axial (i.e. x-wise) vorticity (sec ⁻¹)
ψ	Stream function (ft ² /sec)
φ	Velocity Potential (ft ² /sec)
μ	Doublet strength (ft ⁴ /sec)
σ	Source density (ft ² /sec/ft ²)
ρ	Fluid density (slugs/ft ³)

AXIAL FLOW INTEGRATIONSDerivation of the Betz form of the Wake Integral

If we consider two planes at x₁, upstream and x₂, downstream of a model situated in a constant-section wind tunnel (Figure 1), then the drag on the model can be expressed from momentum considerations as

$$D = \iint_A (p_1 + \rho U_1^2) dy \cdot dz - \iint_A (p_2 + \rho U_2^2) dy \cdot dz \quad \text{----- (1)}$$

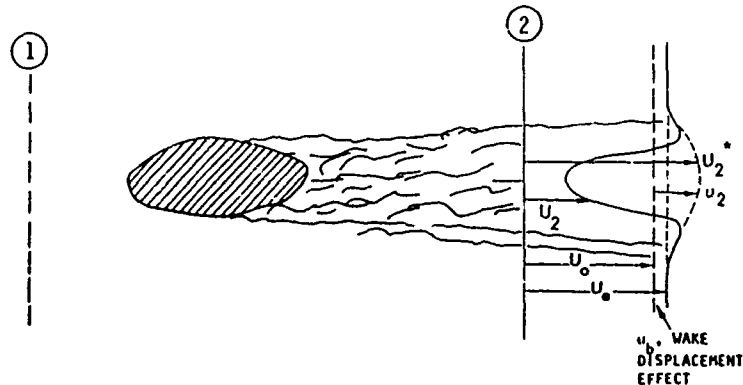


Figure 1. Definitions of Wake Quantities

where p and U are static pressure and axial velocity respectively (see Figure 1) in a flow of constant density ρ in a tunnel of cross sectional area A . Since A includes the tunnel boundary layer, tunnel wall skin friction is implicitly included in D . It is possible to avoid this region in most practical cases unless ground effect is being investigated.

For steady incompressible flow,

$$H = p + \frac{1}{2} \rho (U^2 + v^2 + w^2)$$

or

$$p + \frac{1}{2} \rho U^2 = H - \frac{1}{2} \rho (v^2 + w^2)$$

giving, from (1)

$$D = \iint_A \left\{ H_1 - \frac{1}{2} \rho (v_1^2 + w_1^2) + \frac{1}{2} \rho U_1^2 \right\} dy \cdot dz - \iint_A \left\{ H_2 - \frac{1}{2} \rho (v_2^2 + w_2^2) + \frac{1}{2} \rho U_2^2 \right\} dy \cdot dz$$

For x_1 at an upstream location, $H_1 = H_0$, the mainstream value.

Thus

$$\begin{aligned} D &= \iint_M \{H_0 - H_2\} dy \cdot dz + \frac{1}{2} \rho \iint_A (U_1^2 - U_2^2) dy \cdot dz + \frac{1}{2} \rho \iint_A \{ (v_2^2 + w_2^2) - (v_1^2 + w_1^2) \} dy \cdot dz \\ &= I_1 + I_2 + I_3 \end{aligned} \quad (2)$$

Where, by definition,

$$I_1 = \iint_M \{H_0 - H_2\} dy \cdot dz \quad (2A)$$

$$I_2 = \frac{1}{2} \rho \iint_A (U_1^2 - U_2^2) dy \cdot dz \quad (2B)$$

$$I_3 = \frac{1}{2} \rho \iint_A \{ (v_2^2 + w_2^2) - (v_1^2 + w_1^2) \} dy \cdot dz \quad (2C)$$

Of these, only I_1 is a wake integral (i.e. $H_2 < H_0$)

We next define a fictitious velocity U^* (Figure 1), first introduced by Betz

$$H_0 = p + \frac{1}{2} \rho \{U^{*2} + v^2 + w^2\} \quad (3)$$

also define

$$u = U^* - U_0$$

At plane 2, for example, U_2^* is an axial velocity in the wake which exceeds the true velocity U_2 as needed to restore H_2 to H_0 . U_2^* may therefore be thought of as an equivalent potential flow velocity: it becomes equal to U_2 in the potential flow outside the wake.

We now seek to reduce T_2 to a wake integral. We shall deal first with the general case for U , which may represent either U_1 or U_2 . Consider the identity:

$$\begin{aligned} \iint_A \{U_0^2 - U^2\} dy, dz &= \iint_A \{U_0^2 - U^{*2}\} dy, dz + \iint_M \{U^{*2} - U^2\} dy, dz \\ &= P + Q \end{aligned}$$

Now, Q , a wake integral, is given by

$$Q = \iint_M \{U^{*2} - U^2\} dy, dz = \iint_M \{U^* - U\} \{U^* + U\} dy, dz$$

Re-expressing P :

$$P = - \iint_A \{U^* - U_0\}^2 dy, dz + 2U_0 \iint_A \{U_0 - U^*\} dy, dz$$

and using

$$\iint_A U_0 dy, dz = \iint_A U dy, dz \quad (\text{continuity}) \quad \text{and} \quad (U^* - U_0) = u \quad (\text{by definition})$$

we obtain

$$P = - \iint_A u^2 dy, dz - 2U_0 \iint_M \{U^* - U\} dy, dz$$

and finally

$$\begin{aligned} P + Q &= \iint_A (U_0^2 - U^2) dy, dz \\ &= \iint_M (U^* - U) (U^* + U - 2U_0) dy, dz - \iint_A u^2 dy, dz \quad \text{----- (4)} \end{aligned}$$

Applying (4) at planes 1 and 2, to obtain T_2 , we get

$$\begin{aligned} T_2 &= \frac{1}{2} \rho \iint_M (U_2^* - U_2) (U_2^* + U_2 - 2U_0) dy, dz - \frac{1}{2} \rho \iint_A u_2^2 dy, dz \\ &\quad - \frac{1}{2} \rho \iint_M (U_1^* - U_1) (U_1^* + U_1 - 2U_0) dy, dz + \frac{1}{2} \rho \iint_A u_1^2 dy, dz \end{aligned}$$

Since $H_1 = H_0$, $U_1^* = U_1$ so the third term is zero, leaving

$$\begin{aligned} T_2 &= \frac{1}{2} \rho \iint_M (U_2^* - U_2) (U_2^* + U_2 - 2U_0) dy, dz + \frac{1}{2} \rho \iint_A (u_1^2 - u_2^2) dy, dz \\ &= T_{2A} + T_{2B} \end{aligned} \quad (5)$$

where

$$\begin{aligned} T_{2A} &= \frac{1}{2} \rho \iint_M (U_2^* - U_2) (U_2^* + U_2 - 2U_0) dy, dz \\ T_{2B} &= \frac{1}{2} \rho \iint_A (u_1^2 - u_2^2) dy, dz \end{aligned}$$

The first term, T_{2A} , is the original Betz result. T_{2B} , which is not a wake integral, was derived by Maskell

Maskell's Axial Perturbation Term, T_{2B}

The perturbation u complies with the conventional definition only in non-viscous regions. In viscous regions, it exceeds the normally-defined value by an amount which depends upon the local total pressure deficit

There are two possible approaches for determining the term T_{2B} , designated "Net" and "Gross" by Hackett and Sugavanam in Reference 5. In the first, which represents Maskell's analysis, a tunnel blockage form is derived which is applicable for downstream traverse locations. The "Gross" approach evaluates the u -perturbation term directly, but in a manner consistent with the crossflow terms. This makes it applicable in the near field where flow closure, for example, gives apparent crossflow drag in potential flow.

We shall start with a description of Maskell's blockage interpretation of the axial perturbation term. The "Gross" approach will be discussed later.

Maskell's Blockage Term

Maskell postulates a model represented by a simple, planar horseshoe vortex on the tunnel center plane together with a line source at the bound vortex position and, by implication, a sink far downstream as needed for continuity. Appropriate images are added to represent conditions in a rectangular tunnel test section.

Figure 2 shows the symmetries which result in the axial flow velocities. The u -component induced by the the model source i.e. u_s is symmetric in z and anti-symmetric in x ; u_b , due to the bound vortex, is anti-symmetric in z but symmetric in x ; the downstream sink provides an axial velocity, u_b , which is uniform throughout the test section. The trailing legs of the horseshoe vortices do not contribute to axial velocity.

Using this potential flow model, we may express the perturbation velocities at the upstream and downstream planes as

$$\begin{aligned} u_1 &= u_{S1} + u_{B1} + u_b & u_2 &= u_{S2} + u_{B2} + u_b \\ u_{S1} &= -u_{S2} & u_{B1} &= +u_{B2} \end{aligned} \quad (6)$$

$$\begin{aligned} u_S^+ &= u_S^- & u_B^+ &= u_B^- \end{aligned} \quad (7)$$

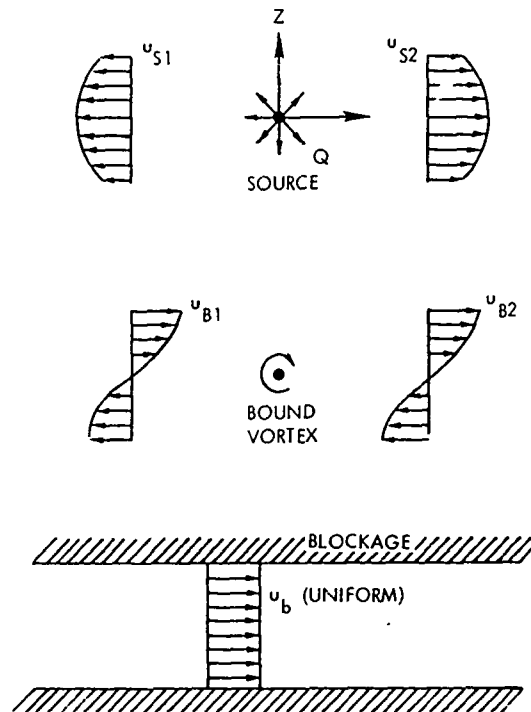


Figure 2. Symmetries Assumed in Maskell's Analysis

and

$$u_b = \text{const.} \quad \text{-----} \quad (8)$$

where the superscripts denote the sign of z .

On forming the sum $(u_1^2 - u_2^2)$ it is obvious that all squared terms cancel, leaving, on substituting into (5),

$$\begin{aligned} T_{2B} &= \frac{1}{2} \rho \iint_A (u_1^2 - u_2^2) dy \cdot dz \\ &= \frac{1}{2} \rho \iint_A \{ (2u_{S1}u_{B1} - 2u_{S2}u_{B2}) + (2u_{B1}u_b - 2u_{B2}u_b) + (2u_bu_{S1} - 2u_bu_{S2}) \} dy \cdot dz \end{aligned} \quad \text{-----} \quad (9)$$

If we pair $(+x_2, +z_2)$ with $(-x_1, -z_1)$ terms in (9), symmetry assures that the first bracket integrates to zero. The second bracket also has a zero integral, from (6) and (8). This leaves

$$\begin{aligned} T_{2B} &= \frac{1}{2} \rho \iint_A (2u_bu_{S1} - 2u_bu_{S2}) dy \cdot dz \\ &= -2 \rho u_b \iint_A u_{S2} dy \cdot dz \quad \text{-----} \quad (10) \end{aligned}$$

on using (6)

Figure 3 shows source-induced and blockage-induced velocities. It is obvious that, to return conditions far-upstream to their nominal value, the total flux from Q_s must be absorbed by the downstream sink Q_b . Hence $Q_s = Q_b$. As defined above, u_s and u_b are the direct effects of Q_s and Q_b respectively. Also, half the flux from Q_s flows to its right and half to its left, and similarly for the flux into Q_b .

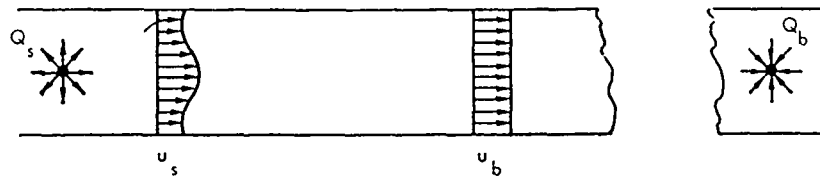


Figure 3. Source-Induced and Blockage Velocities

Thus

$$\iint_A u_s dy \cdot dz = \frac{1}{2} Q_s \quad \text{and} \quad u_b A = \frac{1}{2} Q_b$$

And, since $Q_b = Q_s$,

$$\iint_A u_s dy \cdot dz = u_b A$$

so, from (10)

$$T_{2B} = -2\rho u_b \iint_A u_s^2 dy \cdot dz = -2\rho u_b^2 A \quad \text{----- (11)}$$

The total source-sink flow between Q_s and Q_b is

$$Q = \iint_A u_s dy \cdot dz + u_b A = 2u_b A$$

 Q may also be defined from the velocity profiles as

$$Q = \iint_A (U_2^* - U_0) dy \cdot dz = \iint_M (U_2^* - U_2) dy \cdot dz$$

$$\text{since} \quad \iint_A U_0 dy \cdot dz = \iint_A U_2 dy \cdot dz \quad \text{for continuity}$$

Thus on equating the two expressions for Q , we obtain

$$u_b = \frac{1}{2} \cdot \frac{1}{A} \iint_M (U_2^* - U_2) dy \cdot dz \quad \text{----- (12)}$$

(12) may be used to evaluate u_b in (11), and hence T_{2B} . This, too, is now in wake integral form.Alternative forms for the Axial Flow Terms

We substitute (11) into (5) to obtain the first form. Thus

$$T_{2A} + T_{2B} = \frac{1}{2} \rho \iint_M (U_2^* - U_2) (U_2^* + U_2 - 2U_0) dy \cdot dz - 2\rho u_b^2 A \quad \text{----- (13A)}$$

where u_b is given by (12). Also, we may also substitute for u_b directly from (12), to give

$$\begin{aligned}
 T_{2A} + T_{2B} &= \frac{1}{2} \rho \iint_M (U_2^* - U_2) (U_2^* + U_2 - 2U_0 - 2u_b) dy \cdot dz \\
 &= \frac{1}{2} \rho \iint_M (U_2^* - U_2) (U_2^* + U_2 - 2U_e) dy \cdot dz \quad \text{----- (13B)}
 \end{aligned}$$

on defining $U_e = U_0 + u_b$

Though the second term in (13A) is not a tunnel correction in the usual sense, it is related to the model-dependent wake blockage. This is further discussed in Reference 5. It should also be noted that the first term is purely viscous and the second is a potential flow effect. We shall see later that this is important in analyses of near-field traverses.

CROSSFLOW INTEGRATIONS

Reduction to the Maskell form

The crossflow term, T_3 , from (2) is

$$T_3 = \frac{1}{2} \rho \iint_A ((v_2^2 + w_2^2) - (v_1^2 + w_1^2)) dy \cdot dz \quad \text{----- (14)}$$

There are at least three published analyses of the crossflow term. Those by Maskell (Ref 2) and by Hackett and Sugavanam (Ref 5) are generally similar and rely upon symmetry arguments similar to those used above. However, the analysis by Wu, et al will be followed here because it is less restrictive.

In all of the more recent analyses, the measured crossflow is resolved into vorticity-dependent and source-dependent components. Consider a stream function ψ that describes the vorticity-dependent component of the crossflow and a velocity potential ϕ for the source-related part. The governing equations are

$$\frac{\partial^2 \psi}{\partial y^2} + \frac{\partial^2 \psi}{\partial z^2} = -\xi \quad \text{----- (15)}$$

and

$$\frac{\partial^2 \phi}{\partial y^2} + \frac{\partial^2 \phi}{\partial z^2} = f \quad \text{----- (16)}$$

where ξ is the x-component of vorticity and f is the source density in the crossflow plane. Since the vorticity and source density are independent experimental quantities the stream function and velocity potential in (15) and (16) respectively are unrelated.

The boundary conditions, applied at the tunnel surface are

$\psi = 0$ and $(\partial\phi/\partial n = 0)$ (i.e. $v_n = 0$) where n is normal to the tunnel surface. Application of the boundary conditions will be discussed in a later section.

If v and w are measured crossflow velocities, then we may write

$$v = \frac{\partial\psi}{\partial z} + \frac{\partial\phi}{\partial y} \quad \text{and} \quad w = -\frac{\partial\psi}{\partial y} + \frac{\partial\phi}{\partial z}$$

from which

$$v^2 = v \left(\frac{\partial\psi}{\partial z} + \frac{\partial\phi}{\partial y} \right) \quad \text{----- (17A)}$$

$$w^2 = w \left(-\frac{\partial\psi}{\partial y} + \frac{\partial\phi}{\partial z} \right) \quad \text{----- (17B)}$$

We may also write

$$v \frac{\partial \psi}{\partial z} = \frac{\partial}{\partial z} (\psi v) - \psi \frac{\partial v}{\partial z}, \quad v \frac{\partial \phi}{\partial y} = \frac{\partial}{\partial y} (\phi v) - \phi \frac{\partial v}{\partial y} \quad (18A)$$

$$-w \frac{\partial \psi}{\partial y} = \frac{\partial}{\partial y} (-\psi w) + \psi \frac{\partial w}{\partial y}, \quad w \frac{\partial \phi}{\partial z} = \frac{\partial}{\partial z} (\phi w) - \phi \frac{\partial w}{\partial z} \quad (18B)$$

Substituting from (18A) into (17A) and from (18B) into (17B), summing and regrouping the terms yields

$$\begin{aligned} (v^2 + w^2) &= \left\{ \psi \left(\frac{\partial w}{\partial y} - \frac{\partial v}{\partial z} \right) - \phi \left(\frac{\partial v}{\partial y} + \frac{\partial w}{\partial z} \right) \right\} \\ &\quad + \left\{ \left(-\frac{\partial}{\partial y} (\psi w) + \frac{\partial}{\partial z} (\psi v) \right) + \left(\frac{\partial}{\partial y} (\phi v) + \frac{\partial}{\partial z} (\phi w) \right) \right\} \end{aligned}$$

However, $\left(\frac{\partial w}{\partial y} - \frac{\partial v}{\partial z} \right) = \xi$ and $\left(\frac{\partial v}{\partial y} + \frac{\partial w}{\partial z} \right) = f$

So

$$\frac{1}{2} \rho \iint_A (v^2 + w^2) dy dz = \frac{1}{2} \rho \iint_A (\psi \xi - \phi f) dy dz + R \quad (19)$$

where

$$R = \frac{1}{2} \rho \iint_A \left\{ \left(-\frac{\partial}{\partial y} (\psi w) + \frac{\partial}{\partial z} (\psi v) \right) + \left(\frac{\partial}{\partial y} (\phi v) + \frac{\partial}{\partial z} (\phi w) \right) \right\} dy dz$$

Applying the divergence theorem yields

$$R = -\frac{1}{2} \rho \oint_b (\psi v_t) ds + \frac{1}{2} \rho \oint_b (\phi v_n) ds \quad (20)$$

where s is the running coordinate around the boundary b and v_t and v_n are the tangential and normal velocity components there.

If we choose b to lie on the tunnel boundary then, for solid walls, $v_n = 0$. Without loss of generality we may also assign $\psi = 0$ to the crossflow streamline at the tunnel wall. Hence, from (20), $R = 0$ and (19) becomes

$$\frac{1}{2} \rho \iint_A (v^2 + w^2) dy dz = \frac{1}{2} \rho \iint_A (\psi \xi - \phi f) dy dz \quad (21)$$

Using this result (14) becomes

$$T_3 = \frac{1}{2} \rho \iint_W \psi_2 \xi_2 dy dz + \frac{1}{2} \rho \iint_A (\phi_1 f_1 - \phi_2 f_2) dy dz \quad (22)$$

The first term is a wake integral because vorticity exists only in the model wake. The ξ_1 term disappears for the same reason.

The fact that no assumption of symmetry was required in the above derivation shows that Maskell's result is more general than his analysis indicates.

COMBINED WAKE INTEGRALS

"Net" and "Gross" Forms

Using symmetry arguments for the crossflow similar to those used above for the axial flow (see also Figure 2), Maskell showed that the source term in (22) is zero in the far wake. (Further details may also be found in reference 5, Appendix A.)

Putting Equations (13) and (22) in (2) then gives the final (Maskell) forms, namely

$$D = \iint_W (H_0 - H_2) dy \cdot dz + \frac{1}{2} \rho \iint_W (U_2^* - U_2) (U_2^* + U_2 - 2U_0) dy \cdot dz + \frac{1}{2} \rho \iint_W \psi_2 \xi_2 dy \cdot dz \quad \text{---- (23A)}$$

or, alternatively (using (13B) instead of (13A))

$$D = \iint_W (H_0 - H_2) dy \cdot dz + \frac{1}{2} \rho \iint_W (U_2^* - U_2) \gamma (U_2^* + U_2 - 2U_0) dy \cdot dz + \frac{1}{2} \rho \iint_W \psi_2 \xi_2 dy \cdot dz \quad \text{----- (23B)}$$

The entire integration, in either form, is now confined to the wake.

Equations (23A) and (23B) were derived for the far-wake. If applied too close to the model, two types of error occur. Firstly, the blockage velocity integral (12) may include solid-blockage or other potential flow effects. Usually u_b (or U_e) will be increased and the drag from (23A) or (23B) will decrease. The second effect of near-field application is the neglect of source-induced crossflow, which offsets the previous effect in potential flow.

It is apparent that both (23A) and (23B) lack a positive term (the source-crossflow drag) and, in (23B), the positive and negative contributions cannot be distinguished. For this reason, Hackett and Sugavanam characterized these equations as the "Net" form of the wake integral. Their "Gross" form removes the preceding difficulties and is applicable in the near field: the derivation follows

The "Gross" Form

Using Equations (2) and (5), we may write,

$$D = \iint_W (H_0 - H_2) dy \cdot dz + \frac{1}{2} \rho \iint_W (U_2^* - U_2) (U_2^* + U_2 - 2U_0) dy \cdot dz + \frac{1}{2} \rho \iint_A (u_1^2 - u_2^2) dy \cdot dz + \frac{1}{2} \rho \iint_A \{ (v_2^2 + w_2^2) - (v_1^2 + w_1^2) \} dy \cdot dz$$

The only assumption in the above equation is that W applies only to the model wake, i.e. the tunnel wall boundary layers are thin. For the "Gross" analysis we place plane 1 far upstream, where u , v and w perturbations vanish.

This leaves

$$D = \iint_W (H_0 - H_2) dy \cdot dz + \frac{1}{2} \rho \iint_W (U_2^* - U_2) (U_2^* + U_2 - 2U_0) dy \cdot dz + \frac{1}{2} \rho \iint_A \{ v_2^2 + w_2^2 - u_2^2 \} dy \cdot dz$$

or, using (22) for the crossflow terms and the condition $x_1 \rightarrow \infty$

$$D = \iint_W (H_0 - H_2) dy \cdot dz + \frac{1}{2} \rho \iint_W (U_2^* - U_2) (U_2^* + U_2 - 2U_0) dy \cdot dz + \frac{1}{2} \rho \iint_W \psi_2 \xi_2 dy \cdot dz - \frac{1}{2} \rho \iint_A \psi_2 f_2 dy \cdot dz - \frac{1}{2} \rho \iint_A u_2^2 dy \cdot dz \quad \text{----- (24)}$$

$$\text{The Source Drag Integral} = \iint_A \phi_2 f_2 \, dy \, dz - \iint_A u_2^2 \, dy \, dz$$

One consequence of avoiding Maskell's symmetry arguments and conducting an analysis for near field application is that the last two terms in (24) are not wake integrals (This is contrary to the heading on P6 of Ref 5, which is incorrect). By definition, flow in the model's near-wake will include source-like perturbations not only in the viscous region, but also in the potential flow outside of this. We may examine the fourth and fifth terms of (24) in terms of the limiting case of potential flow. Clearly, (24) should evaluate to zero in this case.

In potential flow, $H_0 = H_2$ and $U_2^* = U_2$ so the first two terms vanish. The third term, concerning trailing vorticity, includes no axial effects and is independent of the source crossflow. Only the fourth and fifth terms remain so it becomes obvious that these source and axial flow perturbation terms must be complementary.

If these terms are integrated to infinity, in free air, or to the tunnel walls in bounded flow the correct zero drag result is obtained, in principle, without difficulty. In practice, the outer flow perturbations are too small to be measured and integrated accurately, even if taken. The crux of the near field wake integration problem thus concerns the evaluation of the source terms over the whole cross-section from measurements only over limited traverse areas.

EVALUATION OF WAKE-CROSSFLOW INTEGRALS

The evaluation of the first two terms of Equation (24) is relatively straightforward provided that proper care is taken to ensure that the integrand is zero at the wake edges. Emphasis will therefore be made, in what follows, to the three remaining, less-familiar terms.

In the far-wake, the vortex-drag is likely to be the only appreciable crossflow term. This will therefore be considered first.

The Far-Wake

Figure 4 shows the procedure currently employed to evaluate the vorticity-induced crossflow (i.e. vortex drag) integral. Local vorticity is determined from crossflow gradients (Step 1) and used to calculate normal velocities at the tunnel boundary. In Step 2, imposition of the zero normal flow condition (Figure 5) yields a distribution of boundary vorticity. This is used with measured vorticity, in Step 3, to recalculate the crossflow velocities. The distribution of stream function, calculated in Step 4, then leads to the crossflow drag integration in Step 5.

In Step 4, it is important to set stream function to zero at the boundary, to achieve the condition $R=0$ in Equation (20). This is done by using a 'double-tunnel' imaging technique (Figure 5) which avoids integrating from a region containing wall singularities. The importance of treating the boundary properly is illustrated in Figure 6. Here, the crossflow drag integration for a Rankine vortex is

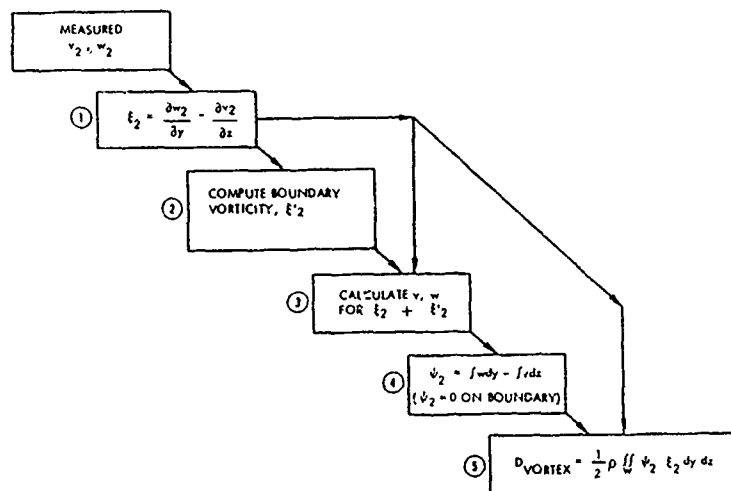


Figure 4. Evaluation Procedure for Vortex Drag

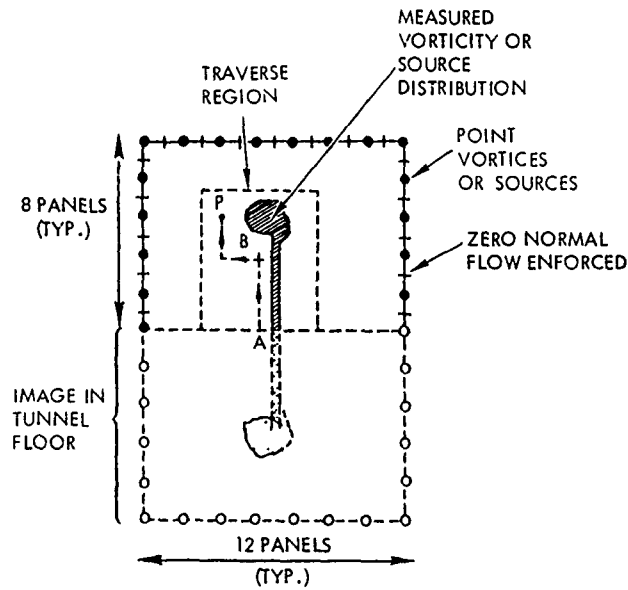


Figure 5. Establishment of the Tunnel-Wall Boundary Condition

illustrated for two circular tunnels, of three and five times the vortex radius respectively. The Betz, kinetic energy integral is continuous to the respective boundary locations. However the integrand for the Maskell, vorticity-stream function form is restricted to the vortex core and it is the imposition of the boundary condition that discriminates between the two tunnels. This underlines need to treat the boundary properly. The example also shows the compactness of Maskell's form. A more complete discussion is given in Reference 5.

The above procedure may appear unnecessarily elaborate for far-field application since, in the absence of sources, the recalculation of crossflow velocities should yield the measured results. However, even in the far-wake, source effects or data scatter may remain which can compromise the evaluation of stream function, by making it non-unique. Steps 2 and 3 thus have an incidental smoothing and filtering effect.

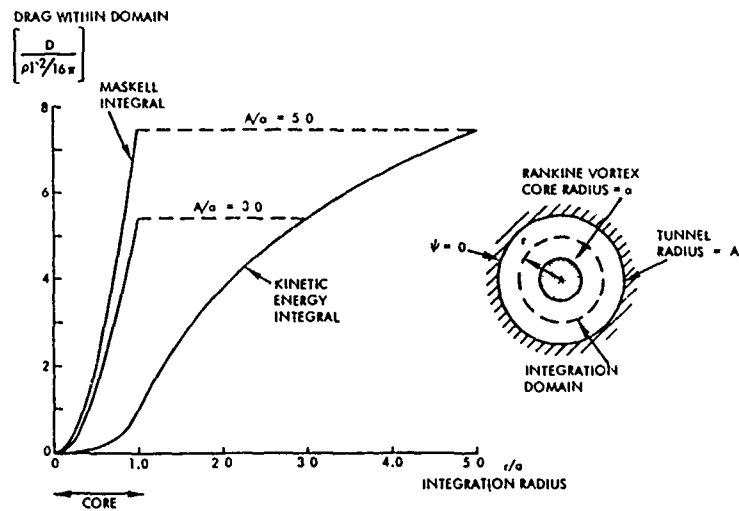


Figure 6. Evaluation of Vortex Drag for an Idealized Case

The Near-Wake

Analyses of the near wake are of practical importance because the flow is more readily related to model features. Here the details have not been blurred by viscosity or rearranged significantly by convection.

The distinctive feature of the near-wake integral is the appearance of source-crossflow and source-axial-flow integrals. Though the source-crossflow integral in the Maskell form is similar to the one for vortex-crossflow, the flow physics and the mathematics differ significantly.

All wake vorticity originates at the model surface so the vortex-induced-crossflow integral is inherently confined to the wake. Source effects, in contrast, relate largely to the potential flow and are widely distributed. This is illustrated in Figure 7 which shows the distribution of apparent source strength in a traverse plane, caused by an upstream source and by a doublet. For both cases, there is a strong local region of apparent sources near the tunnel axis and an extensive region of apparent sinks outside of this. It may be shown that integration of the apparent source strength over the whole field gives a total of zero in both cases.

The above situation contrasts sharply with the vortex crossflow integral, which is very concentrated (Figure 6). To the scale of Figure 7, a practical traverse would have roughly unit radius, and most of the apparent sink region would be missed. A model of the outer region is therefore needed.

The method currently used to evaluate source-crossflow drag parallels that for vortex drag. Source density replaces vorticity in Figures 4 and 5 and source-panels are used at the boundary. Zero-normal-flow is achieved at the wall, as required by the condition $R=0$ in Equation 20. However this representation of the flow physics is somewhat unsatisfactory because the region between the traverse boundary and the tunnel wall is devoid of sinks. These "missing" sinks are, in effect, moved out to the boundary when the boundary condition is applied. For this reason, a normal velocity jump to zero outside the boundary is introduced by the above procedure.

A further difficulty concerns the choice of datum for velocity potential. This arises because the zero normal flow condition defines potential gradient but not potential level. If the total singularity strength integrates to zero (as for vorticity in the double-tunnel, Figure 5) then an arbitrary constant added to the flow function "washes out" in Step 5. This does not occur for sources because there is no sign change on imaging. With or without the image (Figure 5), the "missing sinks" create a problem by making it necessary to define explicitly a datum for velocity potential. Currently, velocity potential is arbitrarily set to zero at the center of the image line (i.e. near 'A' in Figure 5). The rationale for this involves a matched axial- and crossflow integration procedure (Reference 5) which will be reviewed below.

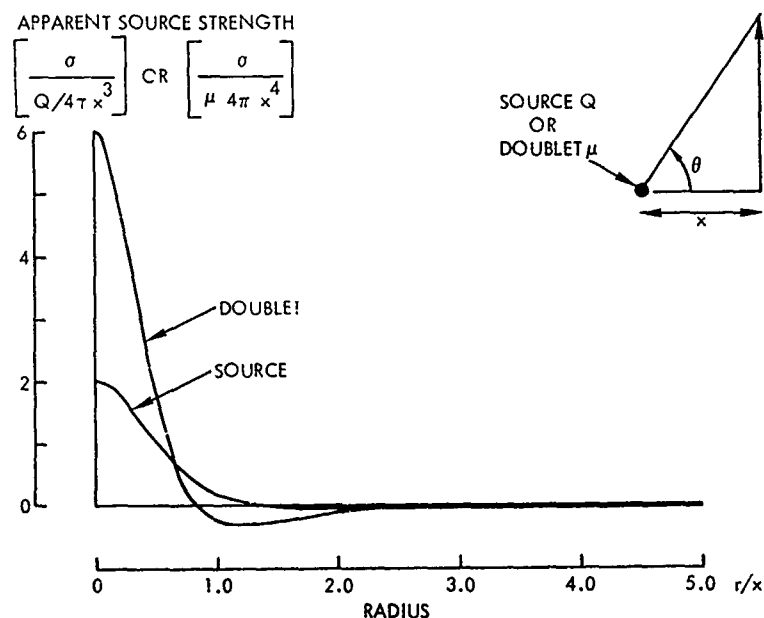


Figure 7. Distributions of Apparent Source Strength for an Axisymmetric Source and a Doublet

The Matched-Integration Procedure for Source-Drag

In the theoretical development, we saw that the source-crossflow and the axial flow perturbation integrals are complementary in the sense that they sum to zero in potential flow. However, this does not occur on a point-by-point basis. If the integrations are performed directly on the squares of perturbation velocities it is found that the thrust from the axial flow term is concentrated near the tunnel axis while the offsetting crossflow drag is located in the outer field. Figure 8 shows this for the flow of Figure 7. The axial perturbation integral, D_3 , builds negatively much more rapidly than the crossflow term, D_2 builds positively. It is evident that a limited-radius integration, to $(r/x)=1$ say, will lead to serious errors if based solely upon D_2 and D_3 .

The crossflow integral increases much more rapidly if Maskell's form is used (see D_1 in Figure 8). In fact, some overshoot occurs. It is shown in Reference 5 that \bar{D} , the mean of D_1 and D_2 is identically equal in magnitude to D_3 . In consequence, the correct result (zero drag) is obtained for all integration radii if $(\bar{D} + D_3)$ is evaluated. This result is exact for the source and a good approximation for an axially-directed doublet. Application of the procedure to a sphere in potential flow shows an order of magnitude reduction in apparent drag coefficient given by a near-field integration (Reference 5).

DISCUSSION

Much of the preceding analysis has concerned source effects. This has arisen largely because this aspect remains the weakest and least-understood feature of near-wake analysis. To place the matter in perspective, however, it should be observed that present experience suggests that the viscous and the vortex terms are dominant in most flows of practical interest, even in the near-wake. In most cases, the net source drag has been found to be a few percent of the total drag.

The present emphasis on the source term relates also to the fact that it is difficult to evaluate accurately. Small, viscosity-dependent source effects must be evaluated as the difference between much larger crossflow and axial flow perturbations which are driven by potential flow effects such as model thickness. Small individual errors in these terms or the failure to use consistent integration procedures can readily cause errors which are comparable to the true source drag.

The above difficulties in evaluating near-wake source effects arise because traverse areas are restricted by practical considerations. More specifically, it is the fact that the measured region is likely to contain unbalanced sources or vortices which gives rise to the difficulty. Appropriate use of an image plane can remove the difficulty for vortices but can not resolve the source problem.

The present procedures restore the source-sink balance when the tunnel boundary condition is applied. As mentioned earlier, this has the effect of moving unmeasured sources (usually sinks) to the tunnel boundary and causes a physically unrealistic jump in normal velocity there.

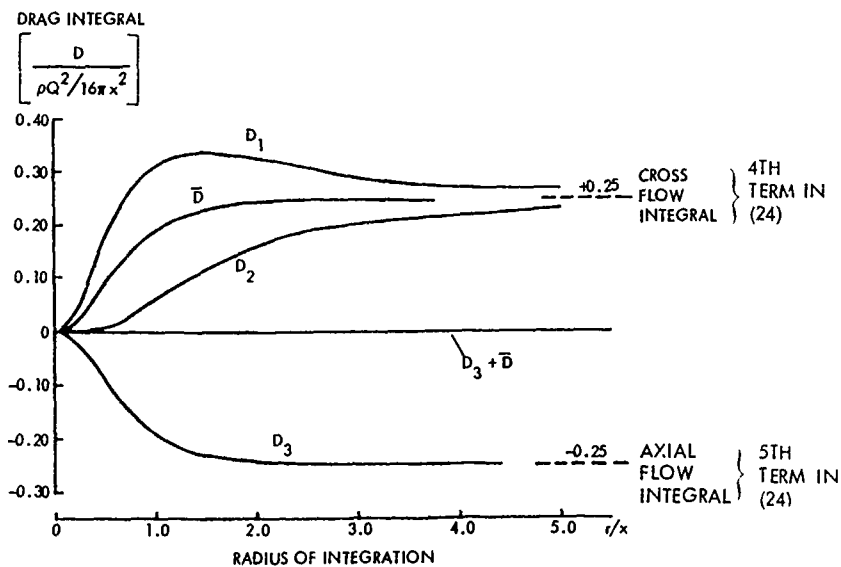


Figure 8. Effect of Traverse Radius and Integration Technique on the Apparent Drag of a Source

It is clear that a better representation of the source flow between the traverse boundary and the tunnel wall is required before the near-field analysis can be considered complete. Pending this and only because experience shows source drag to be generally small, the present approach can be considered adequate.

A TEST EXAMPLE

Figure 9 shows the results of wake measurements made in the Lockheed-Georgia 30- x 43-inch low speed wind tunnel. The model is a 15.4% scale replica of a version of the 1983 Ford Thunderbird. The car length, width and height were 30.41-, 10.81-, and 8.18-inches respectively. The traverse plane is located 30 inches aft of the model center, defined midway between front and back wheels. A rake of 7-orifice pneumatic probes was used with 0.375 inches between centers. The ground was fixed and no boundary layer control was applied.

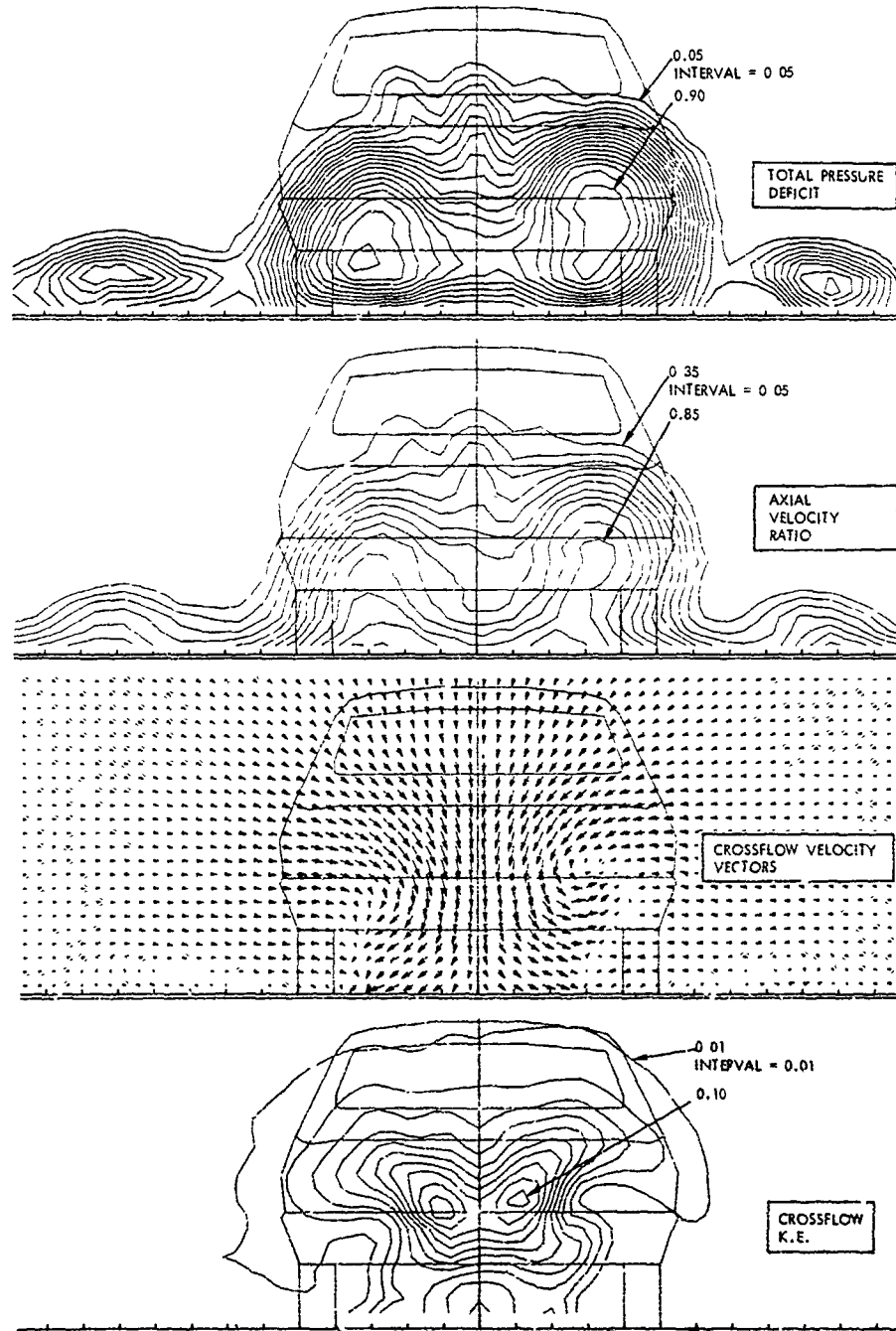


Figure 9. Distributions of Primary Quantities

Though the traverse plane is only 1-inches aft of the back bumper, some wake distortion has occurred. The main wake has been swept downwards and parts have been swept outwards along the floor by a trailing vortex pair. This is apparent in both total pressure deficit and axial velocity measurements (Figure 9, upper). The crossflow kinetic energy is strongest between the vortices and extends beyond the viscous wake (Figure 9, lower).

Figure 10 shows derived quantities, the vortex and source densities, and their associated crossflow velocity fields. Both vortex density ($\Gamma = \text{vorticity}$) and source density contours are less smooth than the basic measurements because they are derived from y - and z -derivatives of crossflow velocities. However on integrating for vortex- and source-induced velocities smooth data is again obtained. This resolution of the measured vectors (Figure 9) brings out source-induced components (Figure 10) which were not apparent before. (A more complicated example of this is discussed in Reference 5.) Line integrations of vortex-induced and source-induced crossflow velocities, starting from the tunnel floor as indicated previously, gives the stream function and velocity potential distributions respectively as needed for the crossflow drag integrations.

Figure 11 shows plots of the integrand distributions for viscous, vortex-crossflow, source-crossflow and source-axial-flow drag. A striking feature is the strong reduction in magnitude for each successive component. The peakiness of the crossflow drag integrands in Maskell's form (Figure 11) may be compared with the kinetic energy form (Figure 9), which is for the total crossflow.

The total drag given by wake integration exceeds that given by the balance which supports the car model. This is thought to arise because of the presence of the fixed wind tunnel floor and its boundary layer. Despite this, it is apparent from Figure 12 that very consistent results are obtained across a wide range of configurations and drag coefficients. This consistency extends from a low drag shape, the Probe IV and variants at zero-yaw to a yawed production car. In fact, some of the inconsistencies which can be seen for the Thunderbird have been traced to slightly undersized traverse areas employed in early tests.

CONCLUSIONS

A complete derivation has been given of the most recent form of the three dimensional wake integral for drag, including near-field terms. Conditions for validity are discussed and the importance of representing the tunnel boundary properly is emphasized. Attention is also drawn to the need to treat source-related axial flow and source-induced crossflow terms consistently. A "matched integration" procedure is described for doing this.

The weakest feature, nonetheless, concerns the (usually small) source-crossflow term. Improved methods are required to represent the weak but extensive sink field which lies outside practically-sized traverse areas. Current methods place these at the tunnel boundary and lack realism.

Analysis of the drag of a model of a Ford Thunderbird car shows strong successive reductions in magnitude for the viscous, vortex, source-crossflow and source-axial flow components of the drag integral.

ACKNOWLEDGEMENTS

The authors wish to thank Mrs. J. T. Allen for typing this report and Mr. J. Patrick, Jr. for assistance in preparing the wake plots. Review comments by Dr. Gino Sovran and Mr. Jack Williams are also greatly appreciated.

REFERENCES

1. A. Retz, "A Method for Direct Determination of Profile Drag" (German). *Z. Flugtechn. Motorluftschiffahrt*, 16 (1925). (See also *Modern Developments in Fluid Dynamics* (ed. S. Goldstein), Vol. I (Oxford, 1938) pp. 258-260.)
2. E. C. Maskell "Progress Towards a Method of Measurement of the Components of the Drag of a Wing of finite Span" Royal Aircraft Establishment Technical Report 72232, January 1973.
3. J. C. Wu, J. E. Hackett and D. E. Lilley "A General Wake Integral Approach for Drag Determination in Three-Dimensional Flows" AIAA Paper No. 79-0219 (Revised). Presented at the 17th Aerospace Sciences Meeting, New Orleans, January 1979.
4. J. E. Hackett and J. C. Wu "Drag Determination and analysis from Three-Dimensional Wake Measurements" ICAS Paper No. 82-644, presented to the 13th ICAS Congress, Seattle, August 1982 (Text not available).

- 5 J. E. Hackett and A. Sugavanam "Evaluation of a Complete Wake Integral for the Drag of a Car-Like Shape" SAE Paper No. 840577, February 1984 (See SAE SP569, 1984)
- 6 J. E. Hackett, J. E. Williams and J. Patrick, Jr "Wake Traverses behind Production Cars and their Interpretation" SAE Paper No. 850280, February 1985.
- 7 T. H. Halstaff and G. W. Brune "An Investigation of Civil Transport Afterbody Drag using a Three-Dimensional Wake Survey Method" AIAA Paper No. 84-0614, January 1984

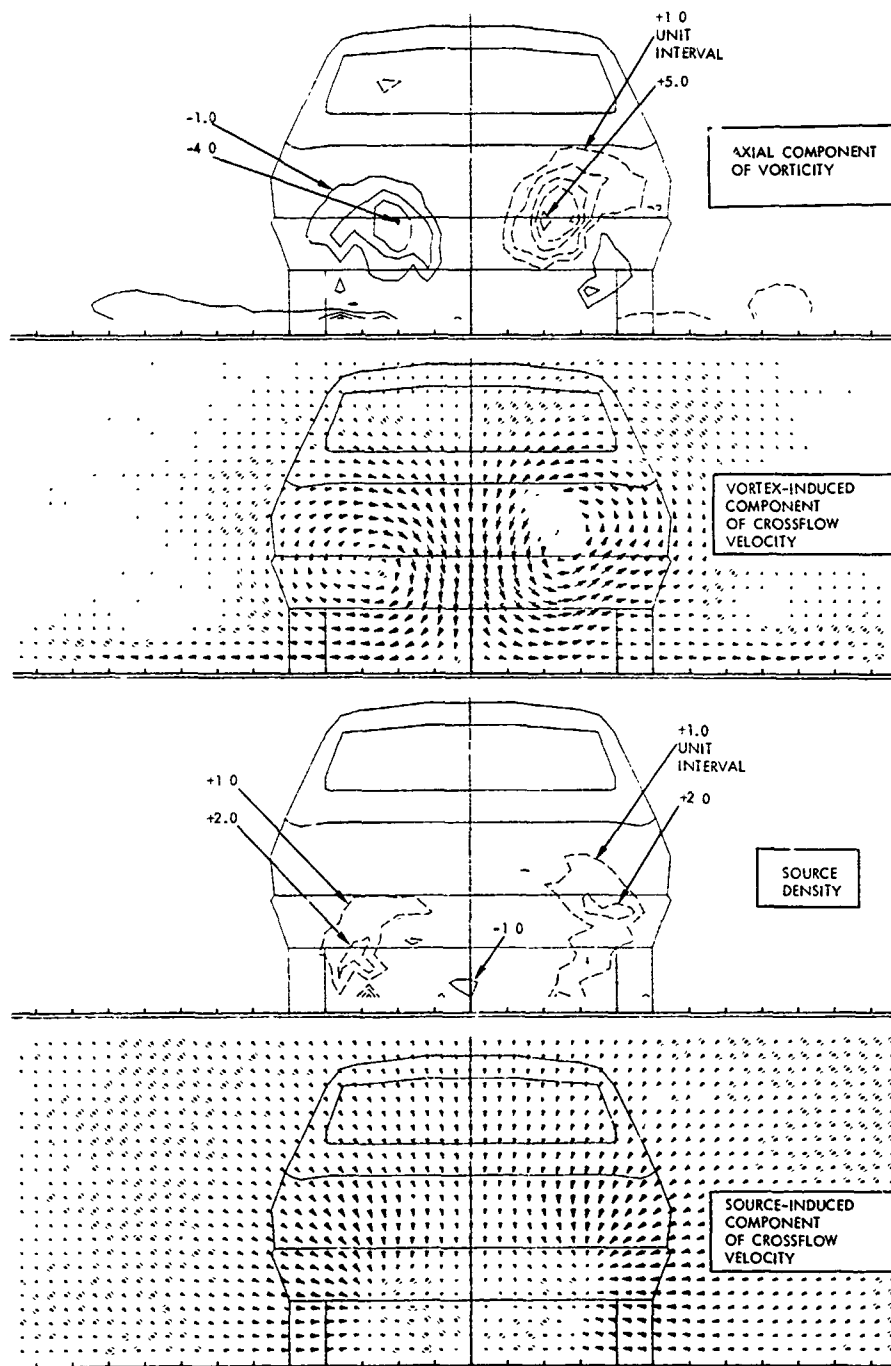


Figure 10. Distributions of Derived Quantities

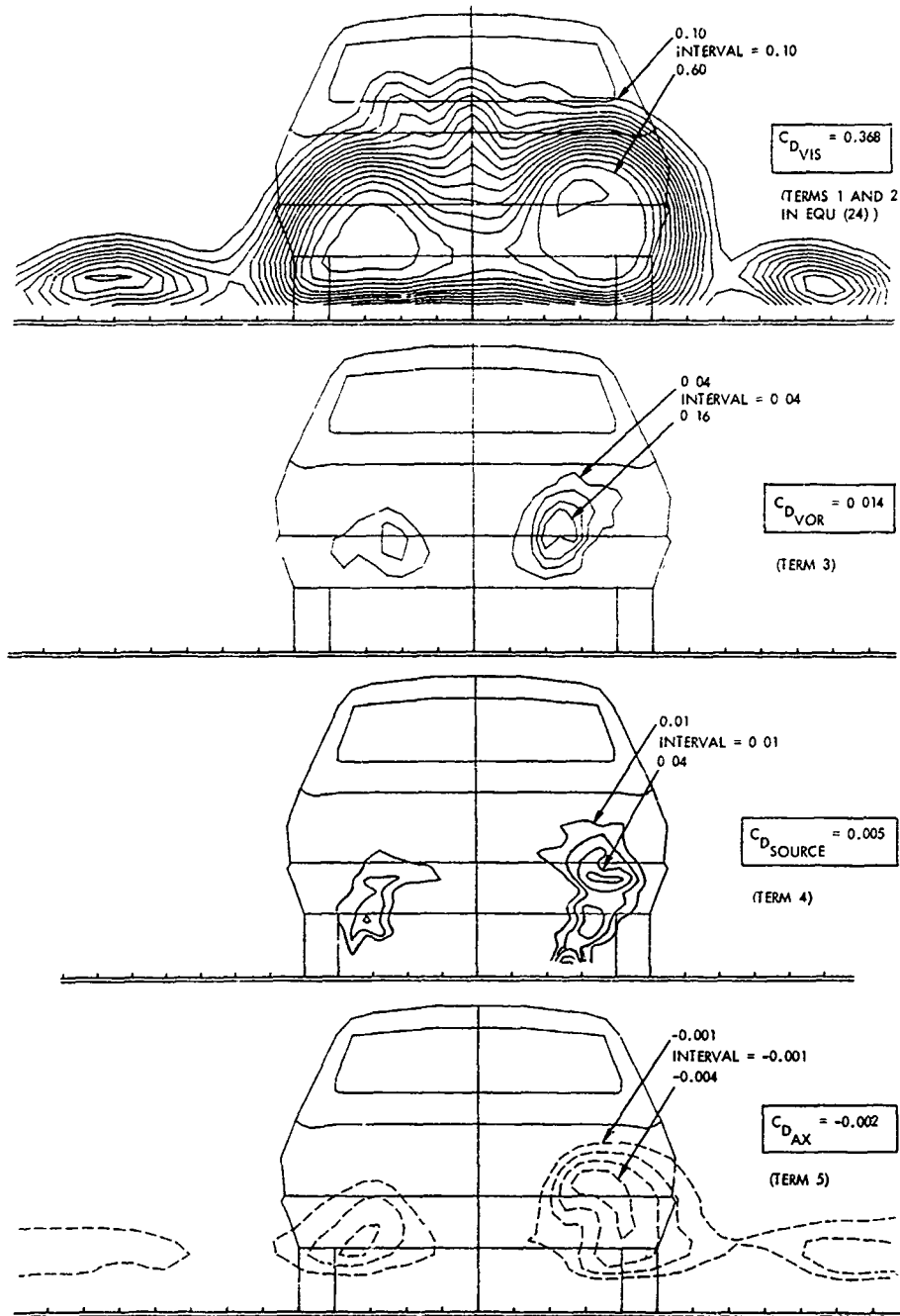


Figure 11. Distributions of Drag Integrand

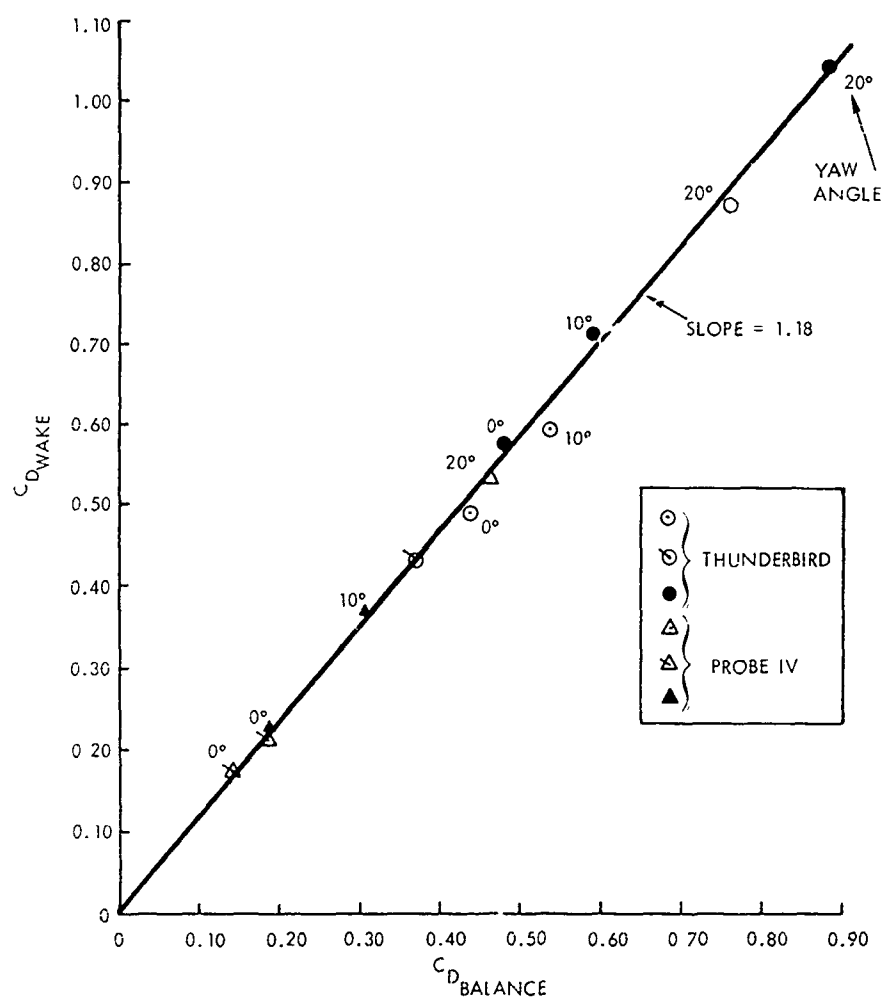


Figure 12. Correlations Between Balance Drag and Wake Integration Results for Selected Car Models

PREDICTION OF THE DRAG OF WINGS AT SUBSONIC SPEEDS BY
VISCOUS/INVISCID INTERACTION TECHNIQUES

by

R.C. Lock

Royal Aircraft Establishment
Farnborough, Hampshire, GU14 6TD, UK

SUMMARY

After a brief introduction (section 1), in section 2 alternative ways of calculating the drag of an aerofoil or wing are discussed, and it is concluded that, at the present time, the 'far-field' approach is both more accurate and more informative. In this approach, the total drag is split into three components, wave (C_{D_W}), vortex (C_{D_V}) and viscous (C_{D_V}), and it is shown how simple methods for estimating these components can be derived. In section 3 a brief account is given of the modern technique of viscous-inviscid interaction, concentrating on methods in which an accurate inviscid code is coupled with an 'integral' method for calculating the viscous shear layers (boundary layer and wake). Recent advances are described which should improve the overall accuracy and allow more difficult cases, where boundary layer separation is present, to be treated successfully. In section 4 some methods of this type for aerofoils in two dimensions are summarised, and their accuracy assessed by comparison with experiment, including examples where flow separation takes place. Finally, in section 5 an experiment on a particular wing-body combination, typical of a modern transport aircraft design, is chosen to show how an analysis of the drag can be performed by using the experimental pressure distribution as input to theoretical methods for calculating the separate wave, vortex and viscous components of drag.

1 INTRODUCTION

In spite of the enormous advances that have been made during the past 20-25 years in the development of numerical methods for calculating the flow fields, both inviscid and viscous, over aircraft shapes or their components, there has been relatively little progress in the application of these methods to the estimation of the overall drag, particularly at high subsonic speeds. The aircraft designer still relies almost exclusively on wind tunnel tests for this purpose, with appropriate guidance from theory in making the extrapolation to full-scale Reynolds number when this is necessary. Yet to be able to make such estimates *ab initio*, by purely theoretical means, would have all the advantages in speed, flexibility and versatility that are justifiably claimed for 'CFD' methods in general.

The main reason for this disappointing lack of progress is that it is often much easier to obtain apparently satisfactory agreement with experiments as regards the pressure distribution or the boundary layer development on a wing, than to predict the overall drag to the high standard of accuracy required for practical performance estimates: one or two per cent for a commercial transport, perhaps rather less exacting for military aircraft where however the complexity of the shapes involved is even greater. In particular, it is clear that a purely inviscid method is of no use for this purpose in itself; nor can one expect to use it simply to provide the input to a suitable boundary layer method from which it might be hoped to obtain an estimate of the viscous contribution to the drag, for addition to the inviscid components separately obtained. It is essential to use only methods in which the effect of viscosity is taken into account from the beginning. Such methods may range in complexity from those in which the full (time-averaged) Navier-Stokes (NS) equations are solved over the whole flow field, to those employing the so-called 'viscous-inviscid interaction' (VII) technique, in which a suitable inviscid flow method is combined iteratively with a method for calculating the development of the boundary layers and wake. In this Paper, only methods of the second (VII) type will be considered, since at the present time they have reached a higher stage of development and assessment than those of the NS class, which are not only more lengthy in execution (particularly for three-dimensional problems), but are also of uncertain accuracy as regards drag prediction, even in two dimensions.

The scope of the Paper is restricted to cases where the free-stream Mach number is subsonic, so that the contribution of the wave-drag component, though often significant, is not of the dominant importance that is usually the case at supersonic speeds; relatively simple means may therefore be used to estimate it. Although the treatment is mainly restricted to flows in which the boundary layers remain attached over most of the wing, the possibility of extending the same computational techniques to deal with appreciable amounts of rear separation is also discussed.

The plan of the Paper is as follows: in section 2, alternative approaches to the problem of calculating the overall drag of a wing are discussed, with emphasis on the 'far-field' method, whereby the drag can be split into three components - viscous (C_{D_V}), vortex or 'induced' (C_{D_I}) and wave (C_{D_W}).

Simple approximations to all three of these components are then described so that they can be estimated from calculations (or measurements) on or near the wing itself. Section 3 is concerned with VII techniques which can be used to obtain the information required to calculate these components of drag. Here, the entrainment method is used to calculate the development of the boundary layer and wake, and a brief account is given of recent improvements to it which are needed for accurate estimation of the overall forces. Techniques are considered next for coupling with a suitable method for the external inviscid flow, and the basis of the 'direct' and 'semi-inverse' iterative procedures is explained. In

sections 4 and 5 some recent 'VII' methods are described, first for aerofoils in two dimensions (section 4) and then for wings and wing-body combinations (section 5); and the accuracy of these methods for predicting the pressure distribution and overall forces is assessed by comparison with experiment. For aerofoils, the examples include some where appreciable boundary layer separation is present. In three dimensions a particular wing-body combination has been chosen, typical of a modern transport aircraft design, and it is shown how an analysis of the drag can be made by using the experimental pressure distribution as input to programs for calculating the separate viscous, vortex and wave-drag components.

2 ALTERNATIVE METHODS FOR CALCULATING THE DRAG OF A WING

2.1 The direct method

There are two basically different ways by which the drag of a wing may be estimated. The first may be called the 'local' or 'direct' method, in which one takes the calculated distribution of pressure and skin friction over the wing surface, and then integrates the appropriate component of these local stresses to obtain the total drag.

Thus the total drag coefficient C_D is

$$C_D = C_{D_p} + C_{D_f} \quad (1)$$

where the pressure and skin friction drag coefficients C_{D_p} and C_{D_f} are given respectively by

$$C_{D_p} = \frac{1}{S} \int_{\text{span}} dy \oint C_p dz \quad (2)$$

the inner integral being taken round the section contour,

$$C_{D_f} = \frac{1}{S} \int_{\text{span}} dy \int_{\text{chord}} C_f dx \quad (3)$$

the inner integral being taken over upper and lower surfaces of the local wing section. Here S is the wing area and conventional 'wind' axes are used, with x in the streamwise direction and y spanwise.

Unfortunately this method - though obvious and direct - is subject to numerical errors because of the difficulty of calculating the pressure component, C_{D_p} , with sufficient accuracy. Even for a symmetrical aerofoil at zero incidence in subcritical, inviscid flow, the correct (zero) value of C_D comes about by the cancellation of two relatively large (of order (t/c)) thrust and drag components. Thus it is essential to take great care in choosing the distribution of sufficient panels or mesh points near the leading and trailing edges of the section, and ensuring that the local pressures near the stagnation point(s) are calculated with adequate accuracy. This latter point is particularly relevant to numerical methods for solving the Euler equations, where spurious entropy errors generated near the leading edge may lead to corresponding errors in the local pressures. For viscous flows, another crucial region is the rear part of the aerofoil, where the pressures are substantially modified by the growth of the boundary layers and by the 'sink' effect of the near wake, which must therefore be carefully modelled.

For lifting aerofoils or wings there is another, perhaps less obvious, potential source of error, caused by the possibility - even probability - that the value of the inviscid lift coefficient C_L , at a given value of the angle of incidence α , may be appreciably underestimated. It is often found that, even so, the predicted pressure distribution is indeed close to the correct one for the particular value of C_L (rather than α). If this is the case, then we can obtain a rough estimate of the corresponding error in C_D in the following way, at least for inviscid subcritical flow in two dimensions. Suppose that, at an angle of incidence α , the predicted pressure distribution is actually that appropriate to a lower incidence $\alpha - \delta\alpha$. Now for the correct solution at angle α , we have

$$0 = C_D = C_T \cos \alpha + C_N \sin \alpha = C_T + C_L \alpha \quad \text{for small } \alpha,$$

where C_T and C_N are the tangential and normal force coefficients, respectively along and normal to the chord of the aerofoil. Thus we should have

$$C_T = -C_N \tan \alpha = -C_L \alpha,$$

while in fact

$$C_T = -C_L(\alpha - \delta\alpha).$$

It follows that, instead of the correct value (zero) for C_D , a value

$$\begin{aligned}\delta C_D &= C_L \delta \alpha && \text{will actually be predicted} \\ &= C_L \delta C_L / a_0 ,\end{aligned}$$

where a_0 is the lift curve slope $dC_L/d\alpha$.

If then the error in C_L is ρC_L , the error in C_D will be $\rho C_L^2/a_0$.

Since $a_0 \approx 6$, this means that even a 1% error in C_L will produce 4 'counts'* of spurious drag at $C = 0.5$; and such a standard of accuracy is extremely difficult to achieve, particularly in three dimensions where problems associated with the far-field boundary conditions can easily lead to much greater relative errors in C_L , and hence also in C_{D_p} .

In spite of the reservations mentioned above, it remains true that for some problems, particularly those involving extensive vortex-type flow separations, there is no sensible alternative to this direct approach to the calculation of drag. In many cases, however, which include both transport and combat aircraft at all but the more extreme regions of their flight envelope, the second, so-called 'far-field' approach has several attractive features, both as regards accuracy and the insight which it can provide into the sources of drag. The basic formulae involved in this method, obtained by considering the flux of momentum across a large control surface surrounding the aircraft, are obtained in the next section, together with certain simplifications and approximations which are convenient to use in practice.

2.2 The calculation of drag by the far-field approach

Consider first an inviscid flow, with or without shock waves. We take a control surface C bounded by a plane normal to the x axis far upstream of the wing, a similar plane T downstream, and by an outer cylindrical surface S of radius R with generators parallel to the x axis. Then, by the momentum theorem, the drag D is given by

$$D = \iint_T (p_\infty - p_T + \rho_\infty U_\infty^2 - \rho_T U_T^2) dydz + \iint_S \rho U V_n dS \quad (4)$$

where V_n is the normal component of velocity on S into the control volume.

The equation of continuity gives (when multiplied by U_∞)

$$\iint_T U_\infty (\rho_\infty U_\infty - \rho_T U_T) dydz + \iint_S \rho U_\infty V_n dS = 0 .$$

Subtracting this from equation (4), we get

$$D = \iint_T \{ p_\infty - p_T + \rho_\infty U_T (U_\infty - U_T) \} dydz + \iint_S \rho V_n (U - U_\infty) dS \quad (5)$$

Now let the radius R of the surface S tend to infinity. When the free stream is subsonic both V_n and $U - U_\infty$ are at most of order R^{-2} ; when it is supersonic they become identically zero as soon as the circle in which S intersects T lies outside the shock system produced by the wing. Hence the second integral in equation (5) approaches zero, and we obtain the familiar formula** (dropping the suffix T)

$$D = \iint_T \{ p_\infty - p + \rho U (U_\infty - U) \} dydz \quad (6)$$

* 1 count corresponds to $C_D = 10^{-4}$

** The above proof is taken from Ref 1. An alternative is to suppose that the outer surface S is a large wind tunnel with solid walls, whose radius R is subsequently allowed to tend to infinity. In that case, the integrals involving V_n are identically zero.

or

$$C_D = \frac{1}{S} \iint_T \left\{ -C_p + \frac{2\rho U}{\rho_\infty U_\infty} \left(1 - \frac{U}{U_\infty}\right) \right\} dydz \quad (6a)$$

where S is the wing area and C_p the pressure coefficient $(p - p_\infty)/(\frac{1}{2}\rho_\infty U_\infty^2)$. The next step is to express C_p and ρ/ρ_∞ in terms of the velocity components (U, V, W) on T and the total head (stagnation pressure) H , which will differ from its upstream value H_∞ if shock waves are present. The energy equation (assuming constant enthalpy) can be written in the form

$$\frac{\gamma p}{\rho} + \frac{1}{2}(\gamma - 1)q^2 = \frac{\gamma p_\infty}{\rho_\infty} + \frac{1}{2}(\gamma - 1)U_\infty^2 \quad (7)$$

where $q^2 = U^2 + V^2 + W^2$.

Dividing both sides by $a_\infty^2 \left(= \frac{\gamma p_\infty}{\rho_\infty} \text{ or } \frac{U_\infty^2}{M_\infty^2} \right)$ and rearranging, this becomes

$$1 + \frac{1}{2}(\gamma - 1)M_\infty^2 \left(1 - \frac{q^2}{U_\infty^2}\right) = \frac{p/p_\infty}{\rho/\rho_\infty} = \frac{T}{T_\infty} \quad (8)$$

Now $\frac{T}{T_\infty} = \frac{T/T_t}{T_\infty/T_t}$, where T_t is the total (stagnation temperature);

$$\text{and } \frac{T}{T_t} = \left(\frac{p}{H}\right) \left(\frac{\rho}{\rho_t}\right)$$

$$= \left(\frac{p}{H}\right)^{\frac{\gamma-1}{\gamma}} \quad \text{from the isentropic relation } \frac{p}{\rho^\gamma} = \frac{H}{\rho_t^\gamma}$$

(H being the pressure when the flow is brought to rest isentropically).

$$\text{Similarly } \frac{T_\infty}{T_t} = \left(\frac{p_\infty}{H_\infty}\right)^{\frac{\gamma-1}{\gamma}},$$

$$\text{so that } \frac{T}{T_\infty} = \left(\frac{p/p_\infty}{H/H_\infty}\right)^{\frac{\gamma-1}{\gamma}} \quad (9)$$

$$\begin{aligned} \text{Hence } \frac{p}{p_\infty} &= \frac{H}{H_\infty} \left(\frac{T}{T_\infty}\right)^{\frac{\gamma}{\gamma-1}} \\ &= \frac{H}{H_\infty} \mathcal{S}^{\frac{\gamma}{\gamma-1}} \end{aligned} \quad (10)$$

$$\text{where from equation (8) } \mathcal{S} = 1 + \frac{1}{2}(\gamma - 1)M_\infty^2 \left(1 - \frac{q^2}{U_\infty^2}\right)$$

$$\text{Now } C_p = -\frac{2}{\gamma M_\infty^2} \left(\frac{p}{p_\infty} - 1\right),$$

$$\text{so that } C_p = -\frac{2}{\gamma M_\infty^2} \left(\frac{H}{H_\infty} \mathcal{S}^{\frac{\gamma}{\gamma-1}} - 1\right) \quad (11)$$

Also, from equation (9), since $\frac{T}{T_\infty} = \frac{p/p_\infty}{\rho/\rho_\infty}$,

$$\begin{aligned} \text{we have } \frac{\rho}{\rho_\infty} &= \left(\frac{p}{p_\infty}\right)^{\frac{1}{\gamma}} \left(\frac{H}{H_\infty}\right)^{\frac{\gamma-1}{\gamma}} \\ &= \frac{H}{H_\infty} \mathcal{S}^{\frac{1}{\gamma-1}}, \quad \text{from equation (10).} \end{aligned} \quad (12)$$

Substituting the relations (11) and (12) for C_p and $\frac{\rho}{\rho_\infty}$ into equation (6a), we obtain

$$C_D = \frac{1}{S} \iint_T \left\{ \frac{2}{\gamma M_\infty^2} \left[1 - \left(\frac{H}{H_\infty}\right) \mathcal{S}^{\frac{\gamma}{\gamma-1}} \right] + \frac{2U}{U_\infty} \left(1 - \frac{U}{U_\infty} \right) \left(\frac{H}{H_\infty}\right) \mathcal{S}^{\frac{\gamma}{\gamma-1}} \right\} dydz$$

$$\text{where } \mathcal{S} = 1 + \frac{1}{2}(\gamma-1)M_\infty^2 \left(1 - \frac{q^2}{U_\infty^2} \right). \quad (13)$$

Note that this formula is exact and is in fact true for any plane T behind the trailing edge of the wing. To reduce it to a more familiar and manageable form we confine our attention to flows with subsonic free stream ($M_\infty < 1$), and now assume that the plane T is at 'downstream infinity'. Consider the nature of the flow in this 'Trefftz' plane T_∞ . If we write $U/U_\infty = 1 + u$, $V/U_\infty = v$, $W/U_\infty = w$, then the non-dimensional perturbation velocity (u, v, w) is produced by two causes:

- (a) the flow induced by the trailing vortex sheet, associated with the vortex ('induced') drag; and
- (b) the downstream effect of any shock waves that are present on the wing, associated with the wave drag.

As regards (a), we can assume that the streamwise component u is much smaller* than v or w , so that $u = 0(v^2 + w^2)$, while the shock waves will produce a deficit in U/U_∞ of order $(1 - H/H_\infty)$. Thus we can assume that u is of order $(v^2 + w^2)$ or $(1 - H/H_\infty)$, whichever is the larger. On T_∞ , we can certainly assume that $|1/2(\gamma-1)M_\infty^2(1 - q^2/U_\infty^2)| < 1$, and hence expand the terms involving \mathcal{S} in equation (13) by the binomial theorem. If we retain terms up to order u^2 or $(v^2 + w^2)^2$, we get first, from equation (11),

$$\begin{aligned} C_p &= \frac{2}{\gamma M_\infty^2} \left(\frac{H}{H_\infty} - 1\right) + \frac{H}{H_\infty} \left[\left(1 - \frac{q^2}{U_\infty^2}\right) + \frac{1}{4}M_\infty^2 \left(1 - \frac{q^2}{U_\infty^2}\right)^2 + \dots \right] \\ &= \frac{2}{\gamma M_\infty^2} \left(\frac{H}{H_\infty} - 1\right) + \frac{H}{H_\infty} \left[-(2u + v^2 + w^2) - u^2 + \frac{1}{4}M_\infty^2(2u + v^2 + w^2)^2 + 0(u + v^2 + w^2)^3 \right] \end{aligned} \quad (14)$$

and from equation (12)

$$\frac{\rho}{\rho_\infty} = \left(\frac{H}{H_\infty}\right) \left[1 - \frac{1}{2}M_\infty^2(2u + v^2 + w^2) + 0(u + v^2 + w^2)^2 \right]. \quad (15)$$

Substituting from equations (14) and (15) into equation (6a), we obtain

$$C_D = \frac{1}{S} \iint_{T_\infty} \left[\frac{2}{\gamma M_\infty^2} \left(1 - \frac{H}{H_\infty}\right) + \frac{H}{H_\infty} \left\{ (v^2 + w^2) - u^2(1 - M_\infty^2) - \frac{1}{4}M_\infty^2(v^2 + w^2)^2 \right\} \right] dydz \quad (16)$$

the error involving terms in u^3 , $u^2(v^2 + w^2)$, $u(v^2 + w^2)^2$ and $(v^2 + w^2)^3$.

* Note that u is not identically zero (as is sometimes assumed), even in shock-free flow, because the vortex filaments in the wake will not in general be precisely normal to the plane T_∞ , and hence will cause a small non-zero streamwise component of velocity perturbation normal to it (cf Ref 17).

Equation (16) can be written in the alternative form

$$C_D = \frac{1}{S} \iint_{T_\infty} \left[\frac{2}{\gamma M_\infty^2} \left(1 - \frac{H}{H_\infty} \right) + (v^2 + w^2) - \left(1 - \frac{H}{H_\infty} \right) (v^2 + w^2) - \frac{H}{H_\infty} \left\{ u^2 (1 - M_\infty^2) + \frac{1}{4} M_\infty^2 (v^2 + w^2)^2 \right\} \right] dydz \quad (16a)$$

$$\text{Thus } C_D = C_{D_W} + C_{D_1} + \text{smaller terms, of order } \int (1 - H/H_\infty)(v^2 + w^2), \int u^2 \text{ and } \int (v^2 + w^2)^2 \quad (17)$$

where $C_{D_W} = \frac{2}{\gamma M_\infty^2 S} \iint_{T_\infty} \left(1 - \frac{H}{H_\infty} \right) dydz$ is the wave-drag coefficient

and $C_{D_1} = \frac{1}{S} \iint_{T_\infty} (v^2 + w^2) dydz$ is the vortex ('induced') drag coefficient.

Note that the error in the familiar formula (17), comprising the second line of equation (16a), is essentially negative (ie equation (17) overestimates the drag) and contains terms of order $C_{D_W} C_{D_1}$, $C_{D_W}^2$ and $\frac{1}{4} M_\infty^2 C_{D_1}^2$. For a transport aircraft at subsonic speeds, the wave drag will usually be smaller than the induced drag, so that the third higher order term - which vanishes when $M_\infty \rightarrow 0$ - will be the most important. For an aircraft of aspect ratio 8, flying at $M_\infty = 0.8$ at $C_L = 0.5$, the value of $\frac{1}{4} M_\infty^2 C_{D_1}^2$ is approximately 2×10^{-5} so that the anticipated error is negligible.

For a viscous flow, in the absence of shock waves or trailing vorticity, pressure on the downstream plane T_∞ will be unperturbed, so that equation (6) gives immediately for the viscous drag coefficient.

$$C_{D_V} = \frac{2}{S} \iint_{T_\infty} \frac{\rho U}{\rho_\infty U_\infty} \left(1 - \frac{U}{U_\infty} \right) dydz$$

$$= \frac{2}{S} \int_{\text{span}} \theta_\infty dy \quad (18)$$

$$\text{where } \theta_\infty = \int_{-\infty}^{\infty} \frac{\rho U}{\rho_\infty U_\infty} \left(1 - \frac{U}{U_\infty} \right) dz$$

is the momentum thickness far downstream in the wake.

In the general case we can therefore assume, again only to first order, that the total drag is given by

$$C_D = C_{D_W} + C_{D_1} + C_{D_V} \quad (19)$$

the error being of the order of squares and products of the individual terms, none of which should normally exceed 1 drag count.

However, in the real flow behind a lifting wing (even without shock waves), the situation is complicated by the fact that the rolling up of the trailing vortex sheet interacts with the viscous dissipation of the turbulent wake, making it extremely difficult to separate uniquely the 'viscous' and 'vortex' contributions to the drag, as investigated by Maskell². When shock waves are present, their contribution to the drag will certainly be included in a measurement by a total head traverse of the wake (cf Ref 1), but it is difficult or impossible to separate the wave drag from the viscous component.

There are better prospects for this approach when the flow is calculated by the VII technique, as recommended in the present Paper (see section 3 below). For the fact that the flow field calculation is split up into separate viscous and inviscid components means that, in effect, the same can be done as regards their drag components. In practice it is usually inconvenient, and possibly inaccurate, to use the 'Trefftz' plane analysis implied by equations (17) and (18) in its direct form. Instead, we show in the next three subsections how each component can be approximated by a calculation on, or near, the wing

surface itself. For this purpose it is sufficient to consider the separate components alone, in the absence of the other two.

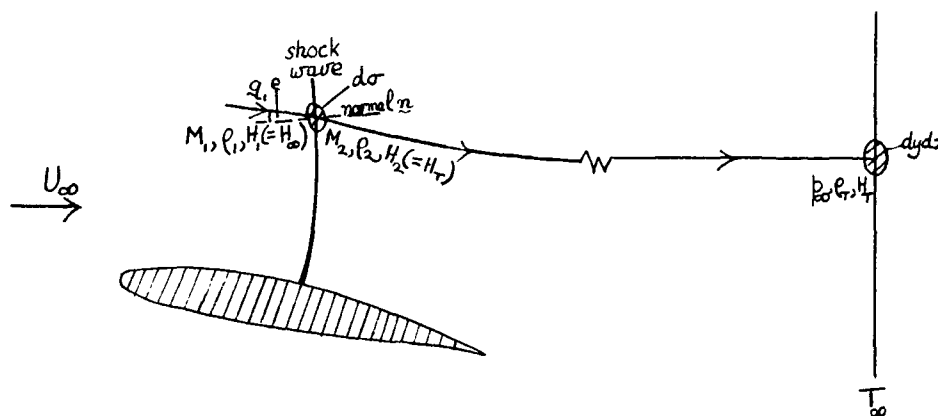
2.2.1 Wave drag

The objective here is to express the wave drag as an integral over the forward surface(s) of the shock(s), first exactly and then to various degrees of approximation. We start by noting that, in the absence of trailing vorticity, we can assume that on the downstream plane T_∞ the pressure is constant, equal to p_∞ , and that $V = W = 0$. Thus from equation (6a), with $C_p = 0$, we have (reintroducing the suffix T to denote values on T_∞)

$$C_{D_w} = \frac{1}{S} \iint_{T_\infty} \frac{2\rho_T U_T}{\rho_\infty U_\infty} \left(1 - \frac{U_T}{U_\infty}\right) dydz \quad (20)$$

while from equation (11)

$$\frac{U_T}{U_\infty} = \left[1 - \frac{2}{(\gamma-1)M_\infty^2} \left\{ \left(\frac{H_\infty}{H_T}\right)^{\frac{\gamma-1}{\gamma}} - 1 \right\}\right]^{\frac{1}{2}} \quad (21)$$



In order to express the wave drag as an integral over the upstream surface of the shock, we can trace a streamtube forward from T_∞ until it meets the shock, as shown in the sketch above. The equation of continuity shows that

$$\rho_1 q_{1n} d\sigma = \rho_T u_T dydz \quad \text{on } T_\infty,$$

where $d\sigma$ is an element of area on the shock, suffix 1 refers to conditions just upstream of the shock and $q_{1n} = q_1 \cdot n = |q_1| \cos \epsilon$ is the velocity component normal to it.* Now the total head is conserved along a streamline (except where it passes through a shock), so that the ratio H_∞/H_T appearing in equation (21) can be written in conventional shock notation as H_1/H_2 . This ratio is given as a function of M_{1n} ($= M_1 \cos \epsilon$), the component of upstream Mach number normal to the shock, by the equation

$$\frac{H_1}{H_2} = \left\{ \frac{(\gamma-1)M_{1n}^2 + 2}{(\gamma+1)M_{1n}^2} \right\}^{\frac{\gamma}{\gamma-1}} \left(\frac{2\gamma M_{1n}^2 + 1 - \gamma}{\gamma+1} \right)^{\frac{1}{\gamma-1}} = \left(\frac{M_{1n}^2 + 5}{6M_{1n}^2} \right)^{3.5} \left(\frac{7M_{1n}^2 - 1}{6} \right)^{2.5} \quad \text{for } \gamma = 1.4 \quad (22)$$

and since the flow upstream of the shock is isentropic, the mass-flow ratio ($\rho_1 q_{1n} / \rho_\infty U_\infty$) is given by

* Note that in three-dimensional flow neither the normal to the shock nor the upstream velocity vector q_1 will, in general, lie in a plane $y = \text{constant}$ (as shown in the sketch), nor will the stream tube downstream of the shock; but this does not affect the validity of the argument given above.

$$\frac{\rho_1 q_{1n}}{\rho_\infty U_\infty} = \frac{M_{1n}}{M_\infty} \left\{ \frac{1 + \frac{1}{2}(\gamma - 1)M_\infty^2}{1 + \frac{1}{2}(\gamma - 1)M_1^2} \right\}^{\frac{\gamma+1}{2(\gamma-1)}} = \frac{M_{1n}}{M_\infty} \left(\frac{5 + M_\infty^2}{5 + M_1^2} \right)^3 \quad (23)$$

Combining these results and substituting in equation (20), we obtain finally

$$C_{D_W} = \frac{1}{S} \iint_{\text{shock}} C_D^i d\sigma$$

$$\begin{aligned} & \leftarrow \frac{2\rho_1 q_{1n}}{\rho_\infty U_\infty} \rightarrow +1 - U_T/U_\infty \longrightarrow \\ \text{where } C_D^i &= \frac{2M_{1n}}{M_\infty} \left(\frac{5 + M_\infty^2}{5 + M_1^2} \right)^3 \left\{ 1 - \left[1 + \frac{5}{M_\infty^2} \left(1 - \frac{(5 + M_{1n}^2)}{6M_{1n}^2} \left(\frac{7M_{1n}^2 - 1}{6} \right)^{\frac{5}{7}} \right)^{\frac{1}{2}} \right] \right\} \end{aligned} \quad (24)$$

which expresses the wave drag exactly (for a single shock) as an integral over the forward face of the shock. [The proof given above is similar to that due to van der Vooren and Slooff.]

This expression could of course be used directly to calculate the wave drag, in conjunction with an accurate numerical solution of the Euler equations coupled with a suitable shock detection scheme. However, we have already seen (section 2.2.1) that in the general case, when vortex and viscous drag components have also to be taken into account, we cannot expect - and therefore do not need - more than first-order accuracy in estimating any one component. So we can now consider various ways of simplifying and approximating equation (24).

First, it is instructive to express equation (24) in terms of the jump in entropy across the shock wave, $\Delta S = S_2 - S_1$.

Now the specific entropy S is defined as $c_v \ln(p/\rho^\gamma)$,

where c_v is the specific heat at constant volume;

$$\text{so } \Delta S/c_p = \ln \left(\frac{p_2/p_1}{(\rho_2/\rho_1)^\gamma} \right) = \ln \left(\frac{H_1}{H_2} \right)^{\gamma-1} \quad \text{from equation (12),}$$

$$\text{or } \left(\frac{H_1}{H_2} \right)^{\frac{\gamma-1}{\gamma}} = \exp(\Delta S/c_p).$$

Hence, from equation (21)

$$\frac{U_T}{U_\infty} = \left[1 - \frac{2}{(\gamma-1)M_\infty^2} \left\{ \exp(\Delta S/c_p) - 1 \right\} \right]^{\frac{1}{2}}$$

If we now assume that $\Delta S/c_p$ is small, then a Maclaurin expansion gives, to second order,

$$1 - \frac{U_T}{U_\infty} = \frac{\Delta S/c_p}{(\gamma-1)M_\infty^2} \left[1 + \frac{\Delta S/c_p}{2(\gamma-1)M_\infty^2} \right] \quad (25)$$

so that, to first order,

$$C_{D_W} = \frac{2}{(\gamma-1)M_\infty^2 S} \iint_{\text{shock}} \frac{\rho_1 q_{1n}}{\rho_\infty U_\infty} (\Delta S/c_p) d\sigma \quad (26)$$

$$= \frac{2}{\gamma M_\infty^2 S} \iint_{\text{shock}} \frac{\rho_1 q_1}{\rho_\infty U_\infty} \ln \left(\frac{H_1}{H_2} \right) d\sigma \quad (26a)$$

a standard formula which has been used by several authors^{6,7}.

$$\text{Equation (26) is equivalent to} \quad D = \frac{T_\infty}{U_\infty} \iint_{\text{shock}} \Delta S \rho_1 q_1 d\sigma \quad (26b)$$

a result originally due to Oswatitsch⁴ (adapted as an integral over the shock).

An alternative formula, which is equally simple and in fact more accurate for high subsonic Mach numbers, can be derived by writing $H_\infty/H_T (= H_1/H_2) = 1 + h$ in equation (21) and expanding in powers of h . We obtain, again to second order,

$$1 - \frac{U_T}{U_\infty} = \frac{h}{\gamma M_\infty^2} \left[1 + \frac{h}{2\gamma M_\infty^2} (1 - M_\infty^2) \right] \quad (27)$$

so that to first order

$$C_{D_W} = \frac{2}{\gamma M_\infty^2 S} \iint_{\text{shock}} \frac{\rho_1 q_1}{\rho_\infty U_\infty} \left(\frac{H_1}{H_2} - 1 \right) d\sigma \quad (28)$$

By comparing equation (27) with equation (25), we see that the relative error in formula (28) is $(1 - M_\infty^2)$ times the corresponding error in equation (26a). Equation (28) is therefore the preferred formula; it may be written in the form

$$C_{D_W} = \frac{1}{S} \iint_{\text{shock}} C_D^i d\sigma \quad (28a)$$

where

$$C_D^i = F(M_\infty) G(M_1, M_{1n}) ,$$

$$F(M_\infty) = \frac{1}{0.7} \left(\frac{1 + 0.2 M_\infty^2}{M_\infty} \right)^3$$

and

$$G(M_1, M_{1n}) = \frac{M_{1n}}{(1 + 0.2 M_1^2)^3} \left\{ \left(\frac{M_{1n}^2 + 5}{6 M_{1n}^2} \right)^{3.5} \left(\frac{7 M_{1n}^2 - 1}{6} \right)^{2.5} - 1 \right\} .$$

As an example of the accuracy of this formula, it is found⁵ that for a case with $M_\infty = 0.75$, $M_{1n} = 1.4$ (a value high enough to cause shock-induced separation) the error in C_D^i is only 1.2%.

The technique suggested above, whereby the wave drag is estimated as an integral taken over the forward surface of the shock wave(s), is reasonably easy to implement in two dimensions provided that a satisfactory numerical 'field' method for solving the Euler or full potential* (FP) equations is available. The main problem is to devise a suitable algorithm for detecting the shock waves; and here one can fortunately rely on the fact that the factor G in C_D^i is of order $(M_{1n} - 1)^3$, which means that shocks (or parts thereof) for which $M_{1n} < 1.05$ (say) are of negligible importance - or, to put it more crudely, "if you can't detect it easily it doesn't matter".

Two alternative schemes for shock detection have been found useful, in either case applying the test on each successive circumferential line of the coordinate grid following the flow from leading edge to trailing edge, starting from the aerofoil surface and working outwards. In the first, the shock is detected by looking for the first occurrence of a compressive jump in local (supersonic) Mach number between successive grid points exceeding some suitable small (but not too small) value, say 0.05; in the second, one looks for the pair of successive grid points in the supersonic flow region at which this jump is the overall maximum. In most cases it has been found that the shock positions specified by these two schemes differ by not more than one mesh interval in the streamwise direction, and are often identical.

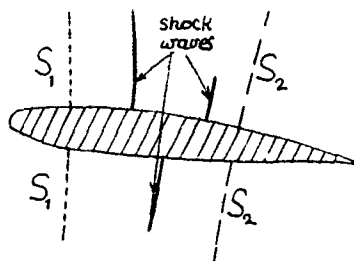
* A FP method is considered satisfactory in this respect if it is capable of predicting the true position and strength of the shock waves to adequate accuracy (cf Ref 10).

With either method, it is important to avoid the detection of spurious shocks by checking that the flow just downstream of the chosen point is subsonic; it is also desirable to take into account the possibility of more than one shock of appreciable strength may be present on one surface of the aerofoil.

Schemes of this type have been used by Jones and Firmin⁷ (RAE) and Bocfi and Billing (ARA)⁶, in conjunction with finite difference methods for solving respectively the transonic small perturbation and the full potential equations. In both cases the shock waves have been treated as though they were indeed true physical ('Rankine-Hugoniot') shocks, ignoring the mathematically different properties of the non-physical 'shocks' that occur in isentropic, irrotational flows; that is, equation (26a) has been used without modification to determine the drag. This assumption is certainly reasonable in the case of the ARA method, which uses the program of Garabedian et al⁸, to calculate the inviscid flow, as modified by Lock¹⁰ to improve the representation of shock waves. They also make the further approximation that the flow direction upstream of the shock may be assumed to be normal to it: that is, they take M_{1n} to be M_1 . Any error involved here will be in the direction of overestimation, since clearly $M_{1n} \leq M_1$. Such evidence as is available (eg ref 11) suggests that this error is unlikely to exceed 5% in C_{Dw} .

In three dimensions a scheme similar to that described above is much more difficult to implement, particularly when multiple shocks are present, as they often are. If the only numerical method available is for potential flow, there is little alternative*. However, if a solution of the full Euler equations is available, it is preferable to make direct use of the fact that the entropy (or total head) is conserved along streamlines that do not pass through shock waves, in the following way (see Ref 13)

In deriving equation (24) above, we may replace the integral over the shock surface σ by one over any suitable surface S_2 downstream of all shock waves (but not intersecting the wake), as shown in the sketch below.



Thus, without approximation,

$$C_D = \frac{2}{\rho_\infty U_\infty} \iint_{S_2} \left\{ 1 - \left[1 - \frac{2}{(\gamma-1)M_\infty^2} \left(\frac{u_\infty}{H} \right)^{\frac{\gamma-1}{\gamma}} - 1 \right]^{\frac{1}{2}} \right\} \rho \underline{q} \cdot \underline{n} \, d\sigma \quad (29)$$

Eliminating \mathcal{F} from equations (10 and (12) above, we see that H is given in terms of the basic variables p and ρ by

$$\frac{H_\infty}{H} = \frac{(p/p_\infty)^{\frac{1}{\gamma-1}}}{(\rho/\rho_\infty)^{\frac{\gamma}{\gamma-1}}} \quad (30)$$

Equation (29) is nominally exact; but unfortunately in most numerical solutions of the Euler equations, spurious changes in entropy (or H) appear ahead of any shock waves, probably generated by discretisation errors near the leading edge. Even so, it is often found that the jump in entropy through the shock wave is still predicted with reasonable accuracy (see for example Ref 11), and we can take advantage of this fact by subtracting from equation (29) the corresponding integral taken over a similar contour S_1 ahead of the shocks (see sketch above). Thus we take finally

$$C_D = \frac{2}{\rho_\infty U_\infty} \iint_{S_2-S_1} \left\{ 1 - \left[1 - \frac{2}{(\gamma-1)M_\infty^2} \left\{ \frac{(p/p_\infty)^{\frac{1}{\gamma}}}{\rho/\rho_\infty} - 1 \right\} \right]^{\frac{1}{2}} \right\} \rho \underline{q} \cdot \underline{n} \, d\sigma; \quad (31)$$

the integral over S_1 , ought of course to be zero, but if it is not then subtracting it will improve the overall accuracy, as shown by Yu et al¹³ in both two and three dimensions. Earlier Sells¹⁴ had used a similar scheme with advantage in two dimensions, using a numerical method in which the spurious entropy errors were much larger than it is now possible to achieve (eg Refs 15 or 16). Even with the best

* Yu et al¹³ have tried various possibilities, involving integration of momentum flux round contours enclosing the shocks: but they were concerned with fully conservative potential flow solutions, which will depart progressively from reality as the shock strength increases.

methods, it is important not to take the contours S_2 and S_1 too close to the shock, and also to check for spurious entropy oscillations in the streamwise direction; if these do occur, then the values for

$(p/p_\infty)^{1/2}/(\rho/\rho_\infty)$ used in equation (31) should be averaged over a few grid points along streamwise grid lines. Thus, although this technique for calculating the wave drag is extremely promising, it does require further extensive checks on accuracy, first in two and then in three dimensions, before full reliance can be placed on it.

Returning now to the approximations which were discussed earlier (equation 28(a)), it is possible to make a further simplification which reduces the evaluation of wave drag to a process involving only a knowledge of the pressure (or Mach number) distribution on the wing surface just ahead of the shock, and yet still retains a useful degree of accuracy. This can be done in the following way.

In two dimensions, we may assume as a first approximation that the shock is normal to the aerofoil surface and that the oncoming flow vector intersects the shock at right angles. Then equation (28a) becomes

$$C_{D_W} = \frac{F(M_\infty)}{c} \int_{\text{shock}} G(M_1) dn \quad (32)$$

$$\text{where } F = \frac{1}{0.7} \left(\frac{1 + 0.2M_\infty^2}{M_\infty} \right)^3, \quad G = \frac{M_1}{(1 + 0.2M_1^2)^3} \left\{ \left(\frac{M_1^2 + 5}{6M_1^2} \right)^{3.5} \left(\frac{7M_1^2 - 1}{6} \right)^{2.5} - 1 \right\},$$

c is the aerofoil chord and n is the distance along the outward normal at the foot of the shock. The next step is to simplify the expression for G by using a two term polynomial in $(M_1 - 1)$. Although the obvious thing to do is to use the Maclaurin expansion

$$G = \frac{7 \times 5^4}{8 \times 3^6} \left\{ (M_1 - 1)^3 - 2(M_1 - 1)^4 \right\} = 0.750(M_1 - 1)^3 - 1.500(M_1 - 1)^4, \quad (33)$$

it is in fact greatly preferable to choose the coefficients of $(M_1 - 1)^3$ and $(M_1 - 1)^4$ so as to fit exactly the correct formula when $M_1 = 1.2$ and 1.3 (values which are typical of the cases of greatest practical interest). We therefore take

$$G = 0.68(M_1 - 1)^3 - 0.85(M_1 - 1)^4; \quad (34)$$

the table below shows the superior accuracy that this gives when $M_1 > 1.1$

M_1	Exact (equation 32)	equation (33)	G equation (34)
1.1	0.000616	0.000600	0.000595
1.2	0.00407	0.00360	0.00408
1.3	0.0114	0.00810	0.0115
1.4	0.0226	0.00960	0.0218
1.5	0.0372	0	0.0319

We can now write equation (32) in the form

$$C_{D_W} = \frac{F(M_\infty)}{c} \int_1^{M_{10}} \frac{G(M_1)}{-dM_1/dn} dM_1 \quad (35)$$

where M_{10} is the value of M_1 on the surface of the aerofoil, just ahead of the shock.

We use a Maclaurin expansion for dM_1/dn :

$$\frac{dM_1}{dn} = \left. \frac{dM_1}{dn} \right|_{n=0} + n \left. \frac{d^2 M_1}{dn^2} \right|_{n=0} + \dots$$

The leading term can be obtained as follows.

We have $M = q/a$ (where a is the local speed of sound),

$$\text{so that } \frac{1}{M} \frac{\partial M}{\partial n} = \frac{1}{q} \frac{\partial q}{\partial n} - \frac{1}{a} \frac{\partial a}{\partial n}.$$

Differentiating equation (7) with respect to n , and noting that $\gamma p/\rho = a^2$,

$$\text{we get } a \frac{\partial a}{\partial n} + \frac{1}{2}(\gamma - 1)q \frac{\partial q}{\partial n} = 0,$$

$$\text{so that } \frac{1}{M} \frac{\partial M}{\partial n} = \left(1 + \frac{1}{2}(\gamma - 1)M^2\right) \frac{1}{q} \frac{\partial q}{\partial n}.$$

Now the flow ahead of the shock is irrotational,

$$\text{so that } \frac{1}{q} \frac{\partial q}{\partial n} \Big|_{h=0} = -\kappa_w,$$

where κ_w is the local surface curvature, reckoned positive if the aerofoil is convex upwards*.

$$\text{Hence } \frac{\partial M_1}{\partial n} \Big|_{h=0} = -\kappa_w M_{10} \left\{1 + \frac{1}{2}(\gamma - 1)M_{10}^2\right\}. \quad (36)$$

Substituting in equation (35), we obtain at once, to a first approximation,

$$\begin{aligned} C_{D_w} &= \frac{F(M_\infty)}{c \kappa_w} \frac{\left\{\frac{0.68}{4}(M_{10} - 1)^4 - \frac{0.85}{5}(M_{10} - 1)^5\right\}}{M_{10} \left\{1 + \frac{1}{2}(\gamma - 1)M_{10}^2\right\}} \\ &= \frac{0.243}{c \kappa_w} \left(\frac{1 + 0.2M_\infty^2}{M_\infty}\right)^3 \frac{(M_{10} - 1)^4 (2 - M_{10})}{M_{10}(1 + 0.2M_{10}^2)} \\ &= \mathcal{F}(M_\infty, M_{10}) / (c \kappa_w), \quad \text{say.} \end{aligned} \quad (37)$$

The accuracy of this formula has been assessed^{5, 11} by comparison with values of the following:

- (a) the wave drag coefficient C_{D_w} obtained by integrating along the shocks using equation (26a), applied to calculations by the FP code of Garabedian et al^{8, 9},
- (b) the pressure drag coefficient C_{D_p} obtained both by an Euler code¹⁶ and the same FP code; these calculations have been made at zero lift to minimise errors of the type described on pages 2 and 3 above.

The latter procedure (b) is clearly the more satisfactory, provided only that the accuracy of the pressure drag calculations can be relied on; and this can be checked by examining the values of C_{D_p} at subcritical conditions. Two typical examples (from Ref 11) are shown in Figs 1(a) and (b), for the symmetrical NACA 0012 and cambered RAE 2822 aerofoils (both 12% thick) respectively; the latter being at $\alpha = 2^\circ$ to give $C_L = 0$. The following points may be noted:

- (i) the values of C_{D_p} shown here have been obtained by subtracting the subcritical values (about 0.0002 for the Euler code, less for the FP code) from the calculated values;
- (ii) when this is done, there is excellent agreement between the two methods, so that there is little doubt about the correct values of the wave drag for these two test cases,
- (iii) the approximate formula (37) overestimates the drag, by about 25% for NACA 0012 and 10% for RAE 2822,
- (iv) it is only the approximate method which is capable of predicting the relative magnitude of the contributions to the wave drag of the strong shock on the lower surface of the cambered RAE 2822 aerofoil and the weaker shock on the upper surface (see Fig 1(b)).

* The opposite sign convention is used in boundary layer theory (section 3).

Similar assessments have been made^{5, 11} (mostly using FP techniques) for a variety of aerofoils. The general conclusion is that the error of the approximate formula (37) lies in the band -10% to +30%, so that the tendency observed above for it to slightly overestimate the wave drag is confirmed.

The usefulness of this approximation would obviously be increased if a counterpart could be found in three dimensions. Unfortunately this does not seem possible in the general case; but what can be done is to derive the corresponding result for an infinite swept wing of constant section, and then apply it on a 'strip theory' basis to a real tapered wing.

Consider an infinite wing with sweep angle Λ and streamwise chord c in an inviscid flow with freestream Mach number M . Denoting with a dash(') corresponding quantities for the equivalent two-dimensional flow about an aerofoil having the shape of a section of the swept wing normal to its leading edge, geometrical considerations give

$$c = c' \sec \Lambda ,$$

so that the thickness/chord ratios are related by

$$\frac{t}{c} = \left(\frac{t'}{c'} \right) \cos \Lambda . \quad (38)$$

Simple sweep theory gives

$$M_{\infty} = M'_{\infty} \sec \Lambda \quad (39)$$

and

$$C_p = C'_p \sec^2 \Lambda \quad (40)$$

It follows that the pressure drag coefficients, and hence the wave drags, are related by

$$C_{D_W} = C'_{D_W} \cos^3 \Lambda \quad (41)$$

(since the pressure coefficients are in the ratio $\cos^2 \Lambda$ (40) and the relative thicknesses are in the ratio $\cos \Lambda$ (38)).

Also, the surface curvatures are related by

$$\kappa_W = \kappa'_W \cos^2 \Lambda ,$$

so that

$$c \kappa_W = c' \kappa'_W \cos \Lambda . \quad (42)$$

Now the approximate formula (37) for the equivalent two-dimensional flow gives

$$C'_{D_W} = \frac{1}{(c' \kappa'_W)} \mathcal{F}(M'_{\infty}, M'_{10}) \quad (43)$$

Using equations (39) and (42), it follows that the wave drag coefficient of the swept wing is given by

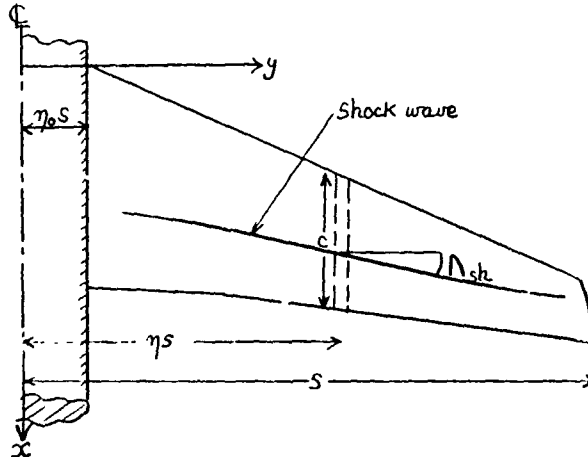
$$C_{D_W} = \frac{\cos^4 \Lambda}{c \kappa_W} \mathcal{F}(M_{\infty} \cos \Lambda, M_{1n}) ; \quad (44)$$

where $M_{1n} (\equiv M'_{10})$, the Mach number component normal to the shock at its foot, can be conveniently obtained from the value of the local pressure coefficient C_{p1} , by the isentropic flow relation

$$M_{1n}^2 = \frac{5 + M_{\infty}^2}{\left(1 + 0.7 M_{\infty}^2 C'_{p1} \right)^{\frac{2}{7}} - 5}$$

$$= \frac{(5 + M_\infty^2 \cos^2 \Lambda)}{(1 + 0.7 M_\infty^2 c_{p1})} - 5 \quad (45)$$

In the case of a tapered swept wing of finite aspect ratio, it is reasonable to assume that conditions ahead of the shock, at any spanwise station, are locally similar - in particular as regards the variation away from the surface of the shock strength and flow direction - to those on an infinite swept wing having the same streamwise section and the same sweep angle as that of the shock at the surface, Λ_{sh} (see sketch).



We can then apply the approximate formula (44) to the strip of the wing between $y = ns$ and $y + \delta y = (n + \delta n)s$, to obtain finally the following formula for the wave drag coefficient of the complete wing:

$$C_{D_W} = \int_{\eta_0}^1 \frac{c(n)}{c} c'_{D_W}(n) dn \quad (46)$$

$$\text{where } c'_{D_W} = \frac{0.243 \cos^4 \Lambda_{sh}}{c_{K_W}} \left(\frac{1 + 0.2 M_\infty^2 \cos^2 \Lambda_{sh}}{M_\infty} \right)^3 \frac{(M_{1n} - 1)^4 (2 - M_{1n})}{M_{1n} (1 + 0.2 M_{1n}^2)}$$

The value of M_{1n} needed in this formula can, in the absence of direct calculation or measurement of the surface flow direction ahead of the shock, be obtained to a consistent standard of accuracy from the infinite wing formula (45), again with Λ replaced by Λ_{sh} .

The accuracy of this approximation is difficult to determine at the present time, because sufficiently reliable results for the wave drag of finite wings by nominally exact techniques are not yet available. Instead, it can be assessed by direct comparison with experiment, as explained in section 5 below. This indeed is its great merit, since no other technique can be used to estimate the spanwise variation of the wave-drag coefficient and its relation to the local shock strength and surface geometry, simply from a knowledge of the surface pressure distribution.

2.2.2 Vortex ('induced') drag

The situation as regards the choice of the best numerical method for calculating the vortex, or 'induced', drag component is less clear than in the case of the wave drag, for which the procedure leading to equation (31) above is both nominally exact and designed to reduce the effect of computational errors. There are perhaps three possibilities, and these are discussed briefly below.

- (1) For inviscid flow, vortex drag = total drag - wave drag,

$$\text{or } C_{D_i} = C_{D_T} - C_{D_W};$$

and so one possibility would appear to be to use the standard pressure/momentum formula (6a), or its equivalent (13), to calculate the total drag by integration over any suitable vertical plane T downstream of the wing trailing edge, and then subtract the previously determined wave drag. However, there seems no reason to expect that this procedure would lead to any greater accuracy in determining C_{D_T} than would a direct integration of pressure over the wing surface. This is confirmed by a two-dimensional calculation quoted by Yu et al.¹³; for a subcritical lifting flow on a NACA 0012 aerofoil,

calculated by an Euler code similar to that of Ref 16, the spurious drag obtained from a downstream pressure/momentum integral was 10 counts, very close to that obtained by a pressure integration over the aerofoil surface (8 counts). Both errors are probably associated with the generation of spurious entropy errors near the leading edge, which are liable to persist downstream into the wake and hence affect the accuracy of the wake integral.

(ii) In a sense, errors of the type just mentioned are analogous to a form of spurious wave drag where none should exist. If then we refer to equation (13) and put $H = H_\infty$, we obtain the formula, valid for shock-free flow,

$$C_{D_i} = \frac{1}{S} \iint_T \left\{ \frac{2}{\gamma M_\infty^2} \left(1 - \mathcal{F}^{\frac{\gamma}{\gamma-1}} \right) - 2u(1+u)\mathcal{F}^{\frac{1}{\gamma-1}} \right\} dydz, \quad (47)$$

$$\text{where } \mathcal{F} = 1 - \frac{1}{2}(\gamma-1)M_\infty^2 \left(\frac{q^2}{u^2} - 1 \right) = 1 - \frac{1}{2}(\gamma-1)(2u + u^2 + v^2 + w^2)$$

and u, v, w are the (non-dimensional) perturbation velocity components. Here, T may be any vertical surface downstream of the trailing edge. It may be worth exploring the use of this formula for calculating the vortex drag, though this does not yet appear to have been attempted. However, it should be noted that for small u, v and w (which will be of the same order of magnitude unless T is far downstream of the wing), the expansion of (47) is

$$C_{D_i} = \frac{1}{S} \iint_T \left\{ v^2 + w^2 - u^2(1 - M_\infty^2) + O(M_\infty^2 u^3) \right\} dydz \quad (48)$$

(this is exact for incompressible flow²). This implies that the correct (zero) value of C_{D_i} for a non-lifting wing must come about by the cancellation of the two non-zero terms $\iint (v^2 + w^2) dydz$ and $(1 - M_\infty^2) \iint u^2 dydz$; so that, once again, numerical errors are probable.

(iii) It therefore seems likely that the most accurate procedure is also the simplest, namely to use the above formula in the 'Trefftz' plane:

$$C_{D_i} = \frac{1}{S} \iint_{T_\infty} \left\{ v^2 + w^2 - u^2(1 - M_\infty^2) \right\} dydz \quad (48a)$$

and to reduce this (approximately) to an integral over the wing span using the following standard analysis.

Following Sears¹⁷, we neglect the rolling up of the trailing vortex sheet so that its cross-section by any plane $T(x = \text{constant})$ remains a horizontal slit (for a wing without dihedral) from $y = -s$ to $+s$, where s is the semi-span of the wing. Far downstream of the wing (T_∞), the upwash at the vortex sheet is of the order $w = -2C_L/(\pi A)$, where A is the aspect ratio (this is exact for elliptic loading): so that the sheet is inclined downwards relative to the x axis at an angle $\alpha_w = 2C_L/(\pi A)$, and hence produces a perturbation in the velocity component in the x direction given by $u = w \alpha_w$. Referring to equation (48a) this means that the ratio of the last term of the integrand to the sum of the first two is less than $4C_L^2/\pi^2 A^2$, which is less than 0.01 even for C_L as high as 1 provided that the aspect ratio A is greater than about 6. It follows that the term in u^2 may be safely neglected, leading to the 'classical' result.

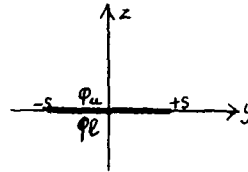
$$C_{D_i} = \frac{1}{S} \iint_{T_\infty} (v^2 + w^2) dydz \quad (49)$$

We can now define a perturbation potential $\phi(y, z)$ in the Trefftz plane T_∞ such that $(v, w) = \text{grad } \phi$ and $\nabla^2 \phi = 0$.

Hence $v^2 + w^2 = \text{grad } \phi \cdot \text{grad } \phi = \text{div}(\phi \text{ grad } \phi)$; and so by Green's theorem

$$C_{D_1} = \frac{1}{S} \oint_{\text{slit}} \phi \frac{\partial \phi}{\partial n} ds$$

$$= \frac{1}{S} \int_{-s}^s -w_0 (\phi_u - \phi_l) dy,$$



where ϕ_u, ϕ_l are the values of ϕ on the upper and lower sides of the slit (see sketch), and $w_0 = \partial\phi/\partial z|_{z=0}$ is the upwash at the slit.

Writing $\phi_u - \phi_l = \Gamma$, the strength of the trailing vortex sheet is $d\Gamma/dy$,

so that

$$w_0 = \frac{1}{2\pi} \int_{-s}^s \frac{d\Gamma}{dy'} \frac{dy'}{y - y'}$$

and hence

$$C_{D_1} = \frac{1}{2\pi S} \int_{-s}^s \Gamma(y) dy \int_{-s}^s \frac{d\Gamma(y')}{y - y'} \quad (50)$$

Finally, the expression for the vortex drag coefficient may be related to quantities calculated (or measured) on the wing surface itself by using the approximation of linearised theory:

$$\Gamma = \frac{L(y)}{\rho_\infty U_\infty^2} = \frac{1}{2} c C_L(y),$$

where c is the local chord and C_L the local lift coefficient,

so that

$$C_{D_1} = \frac{1}{8\pi S} \int_{-s}^s c(y) C_L(y) \int_{-s}^s \frac{d}{dy'} [c(y') C_L(y')] \frac{dy'}{y - y'} \quad (51)$$

And if the spanwise loading $c(y)C_L(y)$ is expressed as a Fourier sine series in $\theta \equiv \cos^{-1}(-y/s)$:

$$c C_L = A_1 \sin \theta + A_3 \sin 3\theta + A_5 \sin 5\theta + \dots,$$

then it can easily be shown that

$$C_{D_1} = \frac{C_L^2}{\pi A} (1 + \delta) \quad (52)$$

where $\delta = (3A_3^2 + 5A_5^2 + \dots)/A_1^2$.

It is clear from the above discussion that the derivation of the 'classical' formula for the vortex drag of a wing involves a number of simplifying assumptions which render it of uncertain accuracy in cases when these assumptions are violated - for example high lift or low aspect ratio; and moreover the absence of reliable theoretical drag data for lifting wings under such circumstances, even with the best numerical methods currently available, makes it impossible to estimate the probable errors involved.

Further details concerning both the theoretical and experimental estimation of vortex drag are given in the Paper by Hackett¹⁸ in the present Lecture Series, and also in Ref 2.

2.2.3 Viscous drag

In two-dimensional flow it may often be sufficient, provided that adequate care is taken in calculating the development of the wake from the trailing edge to 'downstream infinity', simply to use the standard result (equation 18 above):

$$C_{D_V} = 26 \pi / c$$

In three dimensions, however, it is often more difficult to do this with enough accuracy, particularly for lifting cases because of difficulties associated with the edge conditions in the wake behind the wing tips. For this reason - and also in two dimensions when the treatment of the wake is inadequate or even completely absent - it is often more convenient to estimate the viscous drag from a knowledge of the momentum thickness of the boundary layer at, or (preferably) just behind, the trailing edge²¹ and to extrapolate downstream by an extension of the technique first suggested by Squire and Young²¹, due to Cook²⁰ (for two-dimensional compressible flow) and Cooke²⁰ (for infinite yawed wings).

We shall first derive the two-dimensional formula and then show how it can be extended to the three-dimensional case. In two dimensions, the standard momentum integral equation (see section 3 below), in the wake where $C_f = 0$, takes the form

$$\frac{1}{\rho_e U_e^2} \frac{d}{dx} (\rho_e U_e^2 \theta) + H \frac{\theta}{U_e} \frac{dU_e}{dx} = 0, \quad (53)$$

where U_e and ρ_e are the values of the velocity and density at its edge of the wake and H is the shape factor δ^*/θ ; and this may be written

$$\frac{d}{dx} \left[\ln(\rho_e U_e^2 \theta) \right] = -H \frac{d}{dx} (\ln U_e) \quad (53a)$$

Hence, using the suffix T to denote conditions at the trailing edge (or other starting point), we have, integrating equation (53) by parts,

$$\ln \left(\frac{\rho_{eT} U_{eT}^2 \theta_{eT}}{\rho_e U_e^2 \theta} \right) = -H_T \ln \left(\frac{U_{eT}}{U_e} \right) + \int_{H_{eT}}^{H_T} \ln \left(\frac{U_{eT}}{U_e} \right) dH \quad (54)$$

Squire and Young²¹ then made the assumption that H and $\ln(U_e/U_{eT})$ are linearly related in the wake. Some evidence on this point will be presented later.

The value of the integral in equation (54) is therefore $\frac{1}{2}(H_T - H_{eT}) \ln \frac{U_{eT}}{U_e}$ approximately,

$$\text{so that} \quad \frac{\theta_{eT}}{\theta} = \frac{\rho_{eT} U_{eT}}{\rho_e U_e} \left(\frac{U_{eT}}{U_e} \right)^{\frac{1}{2}(H_T + H_{eT} + 4)} \quad (55)$$

where $H_{eT} = 1 + (\gamma - 1)M_{eT}^2$ (see section 3).

It may be more convenient to express equation (55) in terms of the local Mach number M_T ,

$$\text{using} \quad \frac{U_{eT}}{U_e} = \frac{M_T}{M_{eT}} \left(\frac{1 + \frac{1}{2}(\gamma - 1)M_{eT}^2}{1 + \frac{1}{2}(\gamma - 1)M_T^2} \right)^{\frac{1}{2}}$$

and

$$\frac{\rho_{eT}}{\rho_e} = \left(\frac{1 + \frac{1}{2}(\gamma - 1)M_{eT}^2}{1 + \frac{1}{2}(\gamma - 1)M_T^2} \right)^{\frac{1}{\gamma - 1}},$$

giving finally Cook's expression¹⁹

$$\frac{\theta_{eT}}{\theta} = \left(\frac{M_T}{M_{eT}} \right)^{\frac{1}{2}(H_T + H_{eT} + 4)} \left(\frac{5 + M_{eT}^2}{5 + M_T^2} \right)^{\frac{1}{4}(H_T + H_{eT} + 14)}; \quad (56)$$

here the value of M_T may be found from the pressure coefficient C_{pT} by the relation

$$M_T^2 = \frac{5 + M_\infty^2}{\left(1 + 0.7 M_\infty^2 C_{pT}\right)^{2/5}} \quad (57)$$

Evidence concerning the basic assumption involved in this argument is presented in Figs 2 and 3. Fig 2 refers to some measurements made by Cook¹⁹ in the wake of models of two aerofoils (RAE 2814 and 2815), while Fig 3 shows the results of calculations by the lag-entrainment method of Green et al²² for the aerofoils NACA 0012 and RAE 5225. Both the experimental and theoretical results suggest that the relation between $\ln(U_e/U_e)$ and H is indeed satisfactorily linear provided that the value of H at the starting point T does not exceed about 1.8. The error involved in assuming a linear relation all the way from the trailing edge therefore depends on the value of H there; in the most extreme case (Fig 3a), where H is 2.9 at the trailing edge, this results in a slight underestimation of θ_∞ , by about 5%, falling to less than 2% in all the other cases. Moreover, it will be shown later (section 3.1.2) that a more accurate form than equation (53) of the momentum integral equation has a term on the right-hand side,

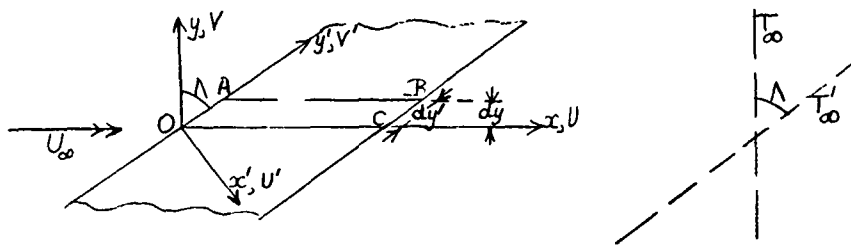
$$\frac{1}{\rho_e U_e^2} \frac{d}{dx} \int_{-\infty}^{\infty} (\overline{\rho u'^2} - \overline{\rho w'^2}) dz,$$

due to the Reynolds normal stresses. The value of this term is approximately

$$\frac{0.07}{\rho_e U_e^2} \frac{d}{dx} \left\{ \rho_e^2 U_e^2 \left(\frac{H-1}{H} \right) \theta \right\},$$

which will be negative in the wake and therefore result in a greater reduction in θ between the trailing edge and infinity than that implied by equation (53); and this has a compensatory effect which causes the formula (56) to be more accurate than would be expected from the figures given above.

In deriving an extension of this method for the case of an infinite yawed wing, of sweep angle Λ , we follow the argument given by Cooke²⁰ for incompressible flow. We start by obtaining an expression for the drag, analogous to equation (6) of section 2.2, in an appropriate coordinate system defined in the sketch below.



$$\text{Equation (6) is } D = \iint_{T_1} (U_\infty - U) \rho U dy dz,$$

and with the swept plane T'_1 this becomes

$$D = \iint_{T'_1} (U_\infty - U) \rho U' dy' dz \quad (58)$$

and since $U = U' \cos \Lambda + V' \sin \Lambda$ this may be written

$$D = \cos \Lambda \iint_{T'_1} \rho U' (U_\infty \cos \Lambda - U') dy' dz + \sin \Lambda \iint_{T'_1} \rho U' (U_\infty \sin \Lambda - V') dy' dz \quad (59)$$

Using the notation of Smith²³, the momentum thicknesses θ_{11} and θ_{21} in the wake are defined as

$$\theta_{11} = \frac{1}{\rho_e U_e^2} \int_{-\infty}^{\infty} \rho U' (U'_e - U') dz \quad (60a)$$

$$\theta_{21} = \frac{1}{\rho_e U_e^2} \int_{-\infty}^{\infty} \rho U' (V'_e - V') dz \quad (60b)$$

where U'_e, V'_e are the values of U' and V' at the outer edge of the wake

and $U_e = \sqrt{(U'_e)^2 + (V'_e)^2}$ is the total external velocity.

[Note that for an infinite yawed wing $V'_e = U_{\infty} \sin \Lambda$ everywhere]

Since the area of the strip ABCD is $cdy' \cos \Lambda$, it follows that the viscous drag coefficient C_{D_V} may be written in the form

$$C_{D_V} = \frac{2}{c} (\theta_{11\infty} + \theta_{21\infty} \tan \Lambda) \quad (61)$$

since at downstream infinity $U_e = U_{\infty}$, $U'_e = U_{\infty} \cos \Lambda$ and $V'_e = U_{\infty} \sin \Lambda$.

As before, the next step is to relate values at downstream infinity to corresponding values at (or just behind) the trailing edge. For this purpose we need the two components of the momentum integral equation in the directions Ox' and Oy' , which for an infinite yawed wing take the form (see Ref 23, equations (2) and (3), setting $h_1 = q = 1$, $d/dy = k_1 = l_1 = C_{f1} = 0$)

$$\frac{1}{\rho_e U_e^2} \frac{d}{dx'} (\rho_e U_e^2 \theta_{11}) + \frac{\Delta_1}{U_e} \frac{dU'_e}{dx'} = 0, \quad (62)$$

$$\text{where } \Delta_1 = \frac{1}{\rho_e U_e} \int_{-\infty}^{\infty} (\rho_e U'_e - \rho U') dz,$$

$$\text{and } \frac{d}{dx'} (\rho_e U_e^2 \theta_{21}) = 0. \quad (63)$$

From equation (63) we obtain immediately

$$\theta_{21\infty} = \frac{\rho_T U_T^2}{\rho_{\infty} U_{\infty}^2} \theta_{21T}. \quad (64)$$

Equation (62) can be put in a form precisely equivalent to the corresponding equation (53) in two dimensions by non-dimensionalising θ_{11} and Δ_1 with respect to U'_e instead of U_e .

$$\text{If then we define } \theta'_{11} = \frac{1}{\rho_e U_e'^2} \int_{-\infty}^{\infty} \rho U' (U'_e - U') dz = \frac{U_e^2}{U_e'^2} \theta_{11} \quad (65a)$$

$$\text{and } \Delta'_1 = \frac{1}{\rho_e U_e'} \int_{-\infty}^{\infty} (\rho_e U'_e - \rho U') dz = \frac{U_e}{U_e'} \Delta_1,$$

$$\text{we obtain immediately } \frac{1}{\rho_e U_e'^2} \frac{d}{dx'} (\rho_e U_e'^2 \theta'_{11}) + \frac{\theta'_{11}}{U_e'} \frac{dU'_e}{dx'} = 0, \quad (66)$$

$$\text{where } H' = \Delta'_1 / \theta'_{11} = U'_e / U_e (\Delta_1 / \theta_{11}) ,$$

and this is identical in form to equation (53). It follows that, provided that the assumption made above regarding the linear variation in the wake of H' with $\ln U'_e$ still holds,

$$\text{then } \frac{\theta'_{11\infty}}{\theta'_{11T}} = \left(\frac{M'_T}{M_\infty \cos \Lambda} \right)^{\frac{1}{2}(H'_T + H'_\infty + 4)} \left(\frac{1 + 0.2M_\infty^2}{1 + 0.2M_T^2} \right)^{\frac{1}{4}(H'_T + H'_\infty + 14)} , \quad (67)$$

$$\text{where } \theta'_{11\infty} = \theta_{11\infty} \sec^2 \Lambda ,$$

$$H'_\infty = 1 + 0.4M_\infty^2 \cos^2 \Lambda ,$$

M'_T can be obtained from equation (45) of section 2.2.1:

$$M_T'^2 = \frac{5 + M_\infty^2 \cos^2 \Lambda}{\left(1 + 0.7M_\infty^2 C_{PT} \right)^{\frac{2}{7}}} - 5 . \quad (68)$$

We need to be able to calculate θ'_{11T} , θ_{21T} and H'_T from the integral quantities, based on external streamline coordinates, that are normally output by a boundary layer program. From Appendix B of Ref 23 we find that

$$\Delta'_1 = \Delta_1 \sec \alpha = \delta_1 - \delta_2 \tan \alpha \quad (69a)$$

$$\theta'_{11} = \theta_{11} \sec^2 \alpha = \theta_{11} - (\theta_{12} + \theta_{21}) \tan \alpha + \theta_{22} \tan^2 \alpha \quad (69b)$$

$$\text{and } \theta_{21} = \theta_{11} \sin \alpha \cos \alpha + \theta_{21} \cos^2 \alpha - \theta_{12} \sin^2 \alpha - \theta_{22} \sin \alpha \cos \alpha \quad (69c)$$

where α is the angle between the external streamline and the direction Ox' (see sketch),

$$\text{given by } \sin \alpha = \sin \Lambda U_\infty / U_e \quad (70)$$

$$\text{or } \cos \alpha = U'_e / U_e ,$$

and δ_1, θ_{1j} are defined in Appendix A of Ref 23, or on page 8-39 below.

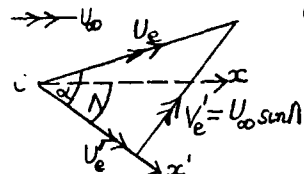
$$\text{Hence } H'_T = \frac{\delta_{1T} - \delta_{2T} \tan \alpha_T}{\theta_{11T} - (\theta_{12T} + \theta_{21T}) \tan \alpha_T + \theta_{22T} \tan^2 \alpha_T} \quad (71)$$

[Note that if the sweep angle Λ is small, so also is α , so that it will often be adequate to take $H'_T = (\delta_1 / \theta_{11T})_T = H_T$, and $H'_\infty = H_\infty$; particularly since equation (67) is only approximate.]

Referring back to equation (61), we see that the drag coefficient is given finally

$$\text{by } C_{D_V} = \frac{2}{c} (\theta'_{11\infty} \cos^2 \Lambda + \theta_{21\infty} \tan \Lambda) \quad (72)$$

$$\text{where } \theta'_{11\infty} = \left(\frac{M'_T}{M_\infty \cos \Lambda} \right)^{\frac{1}{2}(H'_T + H'_\infty + 4)} \left(\frac{5 + M_\infty^2}{5 + M_T^2} \right)^{\frac{1}{4}(H'_T + H'_\infty + 14)} \left\{ \theta_{11T} - (\theta_{12T} + \theta_{21T}) \tan \alpha_T + \theta_{22T} \tan^2 \alpha_T \right\}$$



$$\theta_{21\infty} = \left(\frac{M_T}{M_\infty} \right)^2 \left(\frac{5 + M_\infty^2}{5 + M_T^2} \right)^{\frac{7}{2}} \left\{ \theta_{21T} \cos^2 \alpha_T - \theta_{12T} \sin^2 \alpha_T + (\theta_{11T} - \theta_{22T}) \sin \alpha_T \cos \alpha_T \right\},$$

$$\alpha_T = \sin^{-1} (U_\infty / U_{eT} \sin \Lambda),$$

$$\frac{U_\infty}{U_{eT}} = \frac{M_\infty}{M_T} \left(\frac{5 + M_T^2}{5 + M_\infty^2} \right)^{\frac{1}{2}},$$

$$H_T' = (\delta_{1T} - \delta_{2T} \tan \alpha_T) / \left\{ \theta_{11T} - (\theta_{12T} + \theta_{21T}) \tan \alpha_T + \theta_{22T} \tan^2 \alpha_T \right\},$$

$$H_\infty' = 1 + 0.4 M_\infty^2 \cos^2 \Lambda,$$

$$M_T^{*2} = \frac{5 + M_\infty^2 \cos^2 \Lambda}{\left(1 + 0.7 M_\infty^2 C_{pT} \right)^{\frac{2}{7}}} - 5,$$

$$M_T^2 = \frac{5 + M_\infty^2}{\left(1 + 0.7 M_\infty^2 C_{pT} \right)^{\frac{2}{7}}} - 5,$$

and the integral quantities $\theta_1, \theta_2, \theta_{11}, \theta_{21}, \theta_{12}$ and θ_{22} at the trailing edge are to be obtained from a boundary layer method such as that of Ref 23 or 24.

For a wing of finite aspect ratio, the method described above can be used, on a strip-theory basis, to derive local values of C_{Dv} as a function of spanwise position $n = y/s$; and we can then integrate to get the total viscous drag coefficient of the wing:

$$C_{Dv} = \int_{n_0}^1 \frac{c(n)}{c} C_{Dv}(n) dn. \quad (73)$$

As in the case of the analogous procedure suggested for estimating the wave drag in section 2.2.1, this scheme is likely to be most accurate for wings of high aspect ratio and moderate sweep, and should be used with caution under other conditions.

3 THEORETICAL PRINCIPLES OF VISCOUS/INVISCID INTERACTION TECHNIQUE

In order to be able to calculate the drag of an airofoil or wing, using the techniques described in section 2, to the standard of accuracy - of the order of one per cent - required for practical performance estimates, we need to have available methods of a comparable standard for predicting - at the very least - the detailed pressure distribution and boundary layer development over the wing surface; and in all but the simplest, low speed cases this implies the need for a full flow-field calculation. In principle, this could be achieved either by solving the full time-averaged Navier-Stokes equations (NS), with appropriate turbulence modelling; or by the technique known as 'viscous-inviscid interaction' (VII), whereby separate calculations are made of the viscous shear layers - the boundary layer and wake - and of the external inviscid flow, which are then coupled together in an iterative manner taking into account their mutual interaction.

At the present time, NS methods are certainly more lengthy and sometimes less accurate - for the class of problems with which we are concerned in the present Paper - than those of the 'VII' type; so in this section we shall concentrate entirely on the latter. Here, too, there are choices to be made: the inviscid component could for example be a panel method, a finite difference full potential (FP) method or a finite-volume Euler solver, while for the boundary layers and wake either a 'differential' or an 'integral' method could be used. And since we certainly want to be able to obtain satisfactory results under situations where the assumptions of 'classical' boundary-layer theory are no longer valid, it is important that the method chosen for the viscous part of the flow should be able to deal adequately with what are loosely called 'higher-order' effects. Examples of such 'difficult' situations include the following (see Fig 4):

- flow approaching separation at the trailing edge of a wing, where streamline curvature effects are appreciable and the pressure can no longer be considered to be constant across the boundary layer,

- flows with rear separation where the same effects will extend upstream to forward of the separation point and where the boundary layer cannot be considered 'thin' in the usual sense,
- flow in the interaction region between a shock wave and a boundary layer, where pressure gradients will be large in both streamwise and normal directions.
- interactions between shock-induced and rear separations,
- flows behind the blunt base of a wing or turbine blade, or in the 'cove' region of a slat or flap-fairing, where separations will certainly occur.

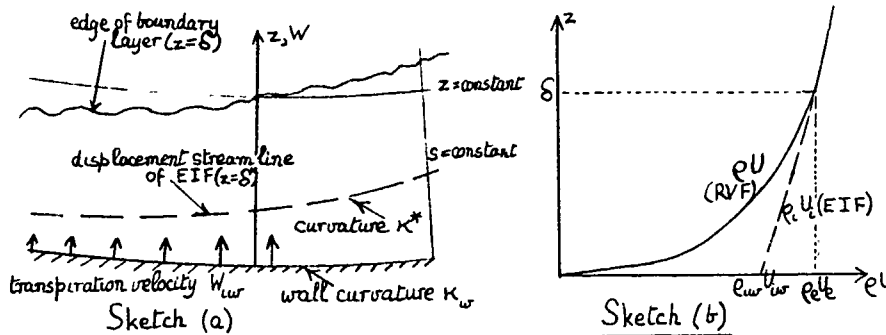
While it is true that only a 'differential' method - which must clearly be of the full NS type - can deal completely with all these situations, it is also true that at the present time no such method has been incorporated into a fully-integrated, practical procedure for calculating the complete flow over an aerofoil or wing. It is therefore important to show how existing 'integral' methods, particularly those involving the entrainment principle, can be extended so that they can be used plausibly in the majority of the situations listed above. A number of relevant reviews of the subject have appeared recently²³⁻³⁰, so that in what follows we shall concentrate on explaining the essential points of the subject, before proceeding in sections 4 and 5 to describe some of the interactive methods that are currently available and to see how well they perform in the task of predicting the overall forces on aerofoils (section 4) and wings (section 5).

3.1 Generalised displacement effect and momentum integral equations

In this section we shall see how the well-established ideas about the displacement effect of a boundary layer, and the momentum integral equation, can be generalised to situations such as those listed above. Initially, we need not make any assumptions regarding the thickness of the boundary layer or the variation of pressure across it; although in practice we shall normally only attempt to allow for departures from first-order boundary layer theory to a fairly rough - but usually adequate - approximation.

It is convenient at this stage to introduce the idea of an equivalent inviscid flow (EIF), which may be defined as a smooth extrapolation of the truly inviscid flow outside the turbulent shear layers into the region which, in the real viscous flow (RVF), is actually occupied by the boundary layers and wake. It is admittedly difficult to define the EIF purely from experimental data; but in an interactive calculation method in which - as is often convenient - the inner boundary conditions for the inviscid flow component continue to be applied on the wing surface itself, the EIF is just the inviscid flow that is actually calculated. This is therefore an example of the numerical technique known as 'zonal', with different systems of equations being solved in adjacent zones and with the solution in one zone overlapping into the other.

The account given below will be restricted to two dimensions; an extension to three dimensions would no doubt be feasible, but the necessary analysis has not yet been completed. Since streamline curvature effects may be important, it is necessary to take into account the curvature of the 'wall' (wing surface), so it is convenient to use orthogonal curvilinear coordinates (s, z), where s is the distance along the wall and z is taken normal to it; the corresponding components of mean velocity are U and W , while the curvature of the wall is κ_w , taken to be positive when concave upwards (see sketch):



On the right is sketched a typical profile of mean mass flow in the boundary layer, ρU , together with the corresponding quantity, $\rho_1 U_1$, in the equivalent inviscid flow; note that the latter is not assumed to be constant as would be the case in standard first-order boundary layer theory. Sketch (a) also shows the displacement surface, $z = \delta^*$, the curvature of which κ^* , is an important quantity in what follows. Since the displacement surface is, by definition, a streamline of the EIF, it follows at once that, to first order, the normal pressure gradient in the EIF is

$$\frac{\partial p_1}{\partial z} = -\kappa^* \rho_e U_e^2 \quad (74)$$

(the suffix e is used to denote values at the outer edge of the boundary layer), while since the EIF is irrotational we have also

$$\frac{\partial U_1}{\partial z} = \kappa^* U_e \quad (75)$$

and

$$\frac{\partial}{\partial z}(\rho_1 U_1) = \kappa^*(1 - M_e^2) U_e \quad (76)$$

Referring to sketch (b), we see that the value of $\rho_1 U_1$ at the wall differs from its value at the outer edge, and that their relative difference is

$$\frac{\rho_e U_e - \rho_{1w} U_{1w}}{\rho_e U_e} = \kappa^* \delta (1 - M_e^2) \quad \text{approximately} \quad (77)$$

3.1.1 The displacement effect

After this preamble, the first step is to derive a generalised expression for the displacement thickness, δ^* , and to show how the displacement effect can be allowed for by introducing a transpiration velocity, W_{1w} , normal to the wall in the EIF. For this purpose - and in the subsequent derivation of the momentum integral equations - it is convenient to use a device introduced by Le Balleur²⁶ and to consider the difference between the equation of continuity in the real viscous flow and the corresponding equation in the equivalent inviscid flow.

Thus

$$\frac{\partial}{\partial s}(\rho_1 U_1 - \rho U) + \frac{\partial}{\partial z} [(1 - \kappa_w z)(\rho_1 W_1 - \rho W)] = 0 \quad (78)$$

If we integrate this across the boundary layer, from $z = 0$ to $z = \delta$, and make use of the fact that, at $z = \delta$, $\rho_1 U_1 = \rho U$ and $\rho_1 W_1 = \rho W$, while at the wall ($z = 0$) $W = 0$, we obtain at once

$$\rho_{1w} W_{1w} = \frac{d}{ds} \int_0^\delta (\rho_1 U_1 - \rho U) dz \quad (79)$$

If then we define the displacement thickness δ^* by

$$\delta^* = \frac{1}{\rho_{1w} U_{1w}} \int_0^\delta (\rho_1 U_1 - \rho U) dz \quad (80)$$

(a natural extension of the standard definition), we have

$$W_{1w} = \frac{1}{\rho_{1w}} \frac{d}{ds} (\rho_{1w} U_{1w} \delta^*) \quad (81)$$

which defines the transpiration velocity at the wall, needed as an inner boundary condition for the inviscid flow calculation to allow for the displacement effect of the boundary layer. Note that, while equation (81) (or its equivalent, equation (79)) is of the same form as that given by Lighthill³¹, its derivation is completely general and makes no assumptions of 'boundary layer' type.

3.1.2 The streamwise momentum integral equation

The next step is to apply the same procedure to the streamwise and normal components of the mean momentum equation for turbulent flow, and thus to derive respectively a generalised form of the von Karman momentum integral equation that forms the basis of all 'integral' methods, and an equation which allows us to take into account the variation of pressure across the boundary layer in the RVF and the way in which this differs from that in the EIF. The details, which are due to East³², are quite complicated (see also Ref 28) and only the main results will be given here. It should be stressed that all the relevant terms in the time-averaged Navier-Stokes equations for turbulent flow are taken into account, including in particular the effects of streamline curvature and Reynolds normal stress, even though in practice some approximations have to be made to reduce the resulting 'integral' equations to manageable form.

First, a generalised momentum thickness θ is defined, such that

$$\rho_{1w} J_{1w}^2 (\theta + \delta^*) = \int_0^\delta (\rho_1 U_1^2 - \rho U^2) dz \quad (82)$$

using equation (80) to define δ^* , this implies that

$$\theta = \frac{1}{\rho_{1w} U_{1w}^2} \int_0^\delta [\rho U (U_{1w} - U) + \rho_1 U_1 (U_1 - U_{1w})] dz \quad (83)$$

Here, the first term is an obvious generalisation of the usual first-order definition, while the second clearly vanishes in standard boundary-layer conditions.

The complete streamwise momentum integral equation then takes the form

$$\frac{1}{\rho_{1w} U_{1w}^2} \frac{d}{ds} (\rho_{1w} U_{1w}^2 \theta) + \frac{\delta^*}{U_{1w}} \frac{dU_{1w}}{ds} - \frac{1}{2} C_f = \kappa_w (\theta + \delta \bar{C}_\tau) + \frac{1}{\rho_{1w} U_{1w}^2} \frac{d}{ds} \left[\int_0^\delta (p_1 - p) dz + \int_0^\delta \overline{\rho u'^2} dz \right] \quad (84)$$

Here, $C_f = \frac{2\tau_w}{\rho_{1w} U_{1w}^2}$ is the skin-friction coefficient,

$$\theta = \frac{1}{\rho_{1w} U_{1w}^2} \int_0^\delta (\rho_1 U_1 W_1 - \rho U W) dz,$$

and $\bar{C}_\tau = \frac{1}{\delta} \int_0^\delta \frac{(-\rho' w')}{\rho_{1w} U_{1w}^2} dz$ is the mean Reynolds stress coefficient.

The terms on the left-hand side of equation (84) are of the familiar form; but note that ρ_{1w} and U_{1w} appear in place of ρ_e and U_e , and this can make an appreciable difference when the curvature of the displacement surface, κ^* , is relatively large, since $(U_e - U_{1w})/U_e = \kappa^* \delta$.

On the right-hand side are four higher-order terms; the first two of these involve the wall curvature κ_w and can usually be safely neglected, except in circumstances in which the wall itself is highly curved in a region where the boundary layer is thick. The next term, involving $\int_0^\delta (p_1 - p) dz$, has to be

estimated by means of the normal momentum equation. It can be shown (cf equation (86), section 3.1.3) that, to a standard of approximation that is adequate for boundary layers close to separation where normal pressure gradients are largest, this integral is given by

$$\int_0^\delta (p_1 - p) dz = \int_0^\delta \overline{\rho w'^2} dz + \kappa^* \int_0^\delta dz \int_z^\delta (\rho_1 U_1^2 - \rho U^2) dz;$$

and East³² suggested that the second integral may be approximated by $\frac{1}{2} \kappa^* \rho_{1w} U_{1w}^2 (\theta + \delta^*)^2$ (see Appendix). The streamwise momentum integral can thus be written in the form

$$\frac{1}{\rho_{1w} U_{1w}^2} \frac{d}{ds} (\rho_{1w} U_{1w}^2 \theta) + \frac{\delta^*}{U_{1w}} \frac{dU_{1w}}{ds} = \frac{1}{2} C_f + \frac{1}{\rho_{1w} U_{1w}^2} \frac{d}{ds} \left[\int_0^\delta \rho (u'^2 - w'^2) dz - \frac{1}{2} \kappa^* \rho_{1w} U_{1w}^2 (\theta + \delta^*)^2 \right], \quad (84a)$$

which should be sufficiently accurate under most of the circumstances of interest.

For equilibrium boundary layers having \bar{H} less than about 2, East and Sawyer³³ found that the values of the Reynolds normal stress integral in equation (84) could be obtained from the empirical relation

$$\int_0^\delta \rho (w'^2 - u'^2) dz = 0.07 \left(\frac{\bar{H} - 1}{\bar{H}} \right) \rho_{1w} U_{1w}^2 \theta,$$

where the transformed shape factor \bar{H} is defined in equation (108) below (section 3.2.2). For higher values of \bar{H} , as separation is approached more closely, the integral is found to increase more rapidly, and the expression

$$\frac{1}{\rho_{1w} U_{1w}^2} \int_0^\delta \rho (w'^2 - u'^2) dz = 0.018 + 0.01 \left(\frac{\bar{H} - \bar{H}_0}{\bar{H}} \right) + 0.25 \left(\frac{\bar{H} - \bar{H}_0}{\bar{H}} \right)^3$$

has been suggested³⁸ as a rough fit to the few available experimental data; here H_0 (≈ 1.3) is the value of H for a constant-pressure boundary layer at the same Reynolds number (see equation (112) below)

3.1.3 The effects of normal pressure gradients

A full account of the results that can be obtained by integrating the normal component of the momentum equation has been given by East³² (see also Ref 28). The main conclusions can be derived more simply by the following argument.

The principal terms in the normal momentum equation can be written

$$\frac{\partial}{\partial z} (p_i - p) = \frac{\partial}{\partial z} (\overline{\rho w'^2}) - (\kappa_i \rho_i U_i^2 - \kappa \rho U^2) \quad (85)$$

where κ is the streamline curvature of the real viscous flow and κ_i that of the equivalent inviscid flow. As explained above (page 3-22), to a first approximation we can assume that κ_i is constant (with respect to z) and equal to κ^* . Integrating equation (85) with respect to z , we obtain

$$p_i - p = \overline{\rho w'^2} + \kappa^* \int_z^\delta (\rho_i U_i^2 - \rho U^2) dz + \int_z^\delta (\kappa^* - \kappa) \rho U^2 dz .$$

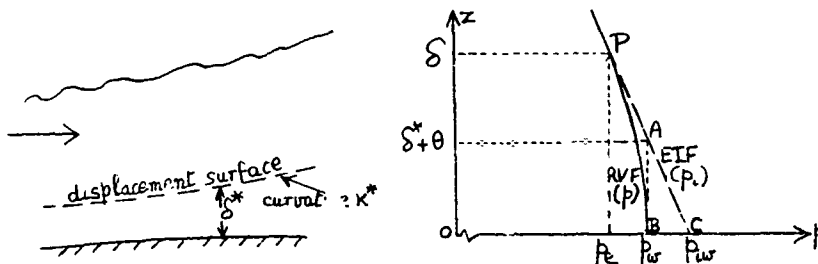
In the second integral, we know that the factor $(\kappa^* - \kappa)$ approaches zero smoothly at the outer edge of the boundary layer, while for boundary layers near separation U^2 will be small over the inner half of the layer. It is therefore reasonable to neglect this integral compared with the first (some numerical evidence on this point is given in the Appendix), and thus to assume that

$$p_i - p \approx \overline{\rho w'^2} + \kappa^* \int_z^\delta (\rho_i U_i^2 - \rho U^2) dz . \quad (86)$$

In particular, at the wall itself we find that the pressures in the two flows (RVF and EIF) differ by an amount given by

$$\frac{\Delta p_w}{\rho_{iw} U_{iw}^2} \equiv \frac{p_{iw} - p_w}{\rho_{iw} U_{iw}^2} = \kappa^* (\theta + \delta^*) \quad (87)$$

The variation of pressure across the boundary layer in the two flows (omitting the Reynolds normal stress term $\overline{\rho w'^2}$ in the RVF) is shown in the sketch.



Note that, to the same degree of approximation, the pressure variation across the entire boundary layer in the real flow is given by

$$\frac{p_w - p_e}{\rho_{iw} U_{iw}^2} = \kappa^* (\delta - \theta - \delta^*) ; \quad (88)$$

for a boundary layer near separation this is about $\frac{1}{2} \kappa^* \delta$. Since this is of the same order as $\Delta p_w / (\rho_{iw} U_{iw}^2)$, it follows that if the pressure variation across the real boundary is significant, then so also is the pressure difference at the wall between the RVF and EIF. Note also that the approximation to $\int_0^\delta (p_i - p) dz$ quoted in section 3.1.2 (see equation (84a)) is equivalent to assuming that this is

equal to the area of the triangle ABC in the sketch above. Another deduction which may sometimes be useful (eg in establishing a 'Kutta' condition for the EIF) is that the wall pressure in the real flow is equal to that in the inviscid flow at A, where $z = \theta + \delta^*$.

The curvature of the displacement surface, κ^* , appearing in the analysis above, may be obtained either from the obvious equation

$$\kappa^* = \kappa_w + \frac{d^2 \delta^*}{ds^2} \quad (89)$$

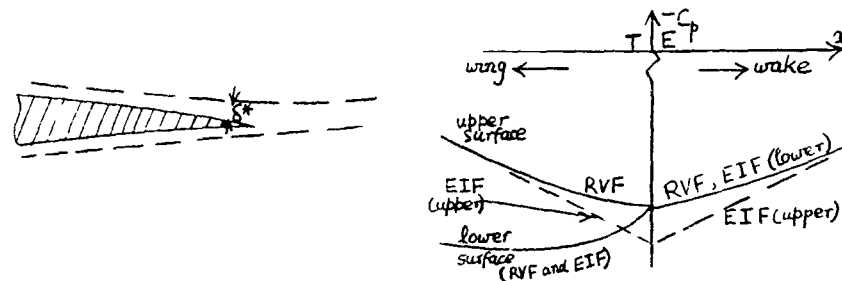
or from its near equivalent (suggested independently by Collyer and Lock^{34, 35} and Le Balleur³⁶)

$$\kappa^* = \kappa_w + \frac{d\Sigma}{ds} \quad (90)$$

where $\Sigma = \frac{1}{\rho_{iw} U_{iw}} \frac{d}{ds} (\rho_{iw} U_{iw} \delta^*)$ is the non-dimensional 'transpiration source strength'.

Equation (87) and the above deductions from it are significant - and not just in a qualitative sense - in establishing when the effects of normal pressure gradients are likely to be of importance in an interactive flow calculation: it is clearly necessary that κ^* , the curvature of the displacement surface, should be relatively large when the boundary layer is at the same time fairly thick. Typical situations in which this is likely to occur are illustrated in the following sketches, which show also the consequent differences of pressure at the wall between the RVF and EIF:

- (a) Near the trailing edge in an attached flow approaching separation

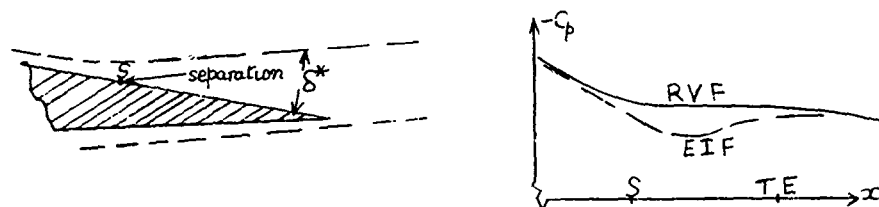


[Here we have assumed that the curvature of the lower displacement surface is negligible.]

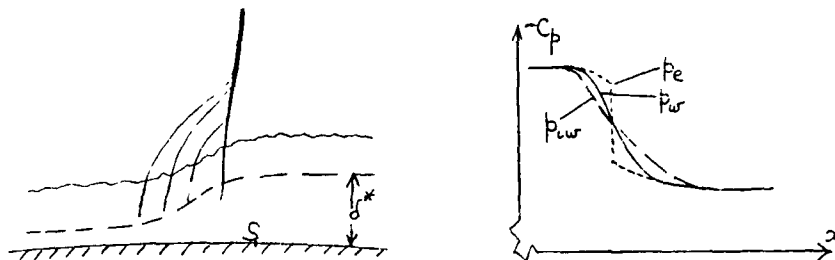
Two points should be noted:

- (i) that the adverse pressure gradient in the EIF near the trailing edge is more severe than that (measured) in the real flow, thus helping to improve the prediction of separation,
- (ii) that a pressure jump is implied along the mean streamline in the wake, and at the trailing edge itself, between the upper and lower parts of the wake in the EIF. The implications of this will be considered in section 3.1.4.

- (b) Near the separation point in a flow near the stall



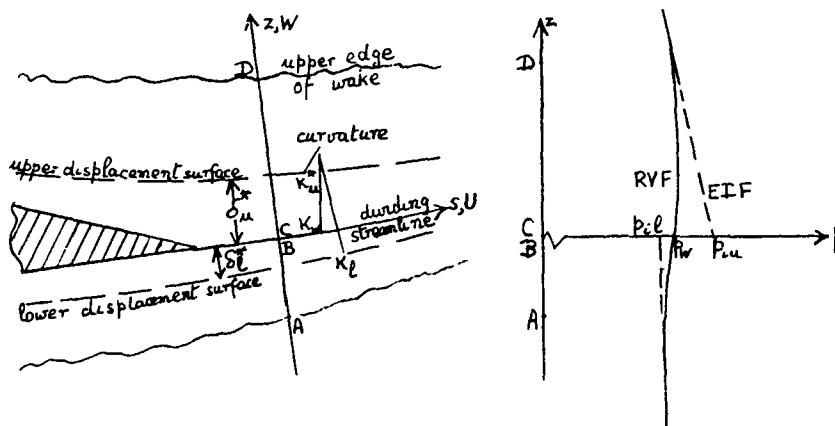
Note that in this case normal pressure gradient effects are expected to be significant only in the immediate neighbourhood of the separation point; downstream of it the displacement thickness will grow almost linearly, so that κ^* will be relatively small.

(c) Near the foot of a shock wave

In this case, although the differences shown in the sketch between the streamwise variation of the pressure at the wall in the real flow (p_w) and in the EIF (p_{iw}), and in the pressure at the edge of the boundary layer (p_e), are qualitatively correct, it is unlikely that the values predicted by the simple theory given above will be of adequate accuracy in this complicated situation.

3.1.4 Jump conditions in the wake

In the near wake we use the coordinate system shown in the sketch below, with s and z measured along and normal to the dividing streamline of the real flow; this line naturally divides the wake into its upper and lower parts, for which the suffices u and l are used. The arguments that were used above in deriving expressions for the transpiration velocity W_{iw} (equation (81)) and the pressure difference Δp_w (equation (87)) depend only on the condition that at the 'wall' the normal component W_w of velocity in the real flow is zero; no use was made of the fact that U_w is also zero there. The same argument can therefore be used without modification in the wake, with the dividing streamline replacing the 'wall', to derive 'jump' conditions across this dividing line for the normal velocity and pressure in the EIF; the second of which forms in effect a replacement to the familiar 'Kutta' condition that is used to fix the circulation, and hence the lift, in a purely inviscid flow calculation.



At the point BC (see left-hand sketch) on the wake line, application of equation (81) to the upper and lower parts of the wake gives

$$v_{iu} = \frac{1}{\rho_{iu}} \frac{d}{ds} (\rho_{iu} U_{iu} \delta^*)$$

and

$$W_{il} = -\frac{1}{\rho_{il}} \frac{d}{ds} (\rho_{il} U_{il} \delta^*); \quad (\text{measuring } W \text{ as shown in the sketch})$$

so that a jump ΔW_w is required in the component of velocity normal to the wake, given by

$$\Delta W_w \equiv W_{iu} - W_{il} = \frac{1}{\rho_{iu}} \frac{d}{ds} (\rho_{iu} U_{iu} \delta^*) + \frac{1}{\rho_{il}} \frac{d}{ds} (\rho_{il} U_{il} \delta^*) \quad (91)$$

[The reason why ρ_i and U_i are not necessarily the same on the upper and lower sides of the wake line will appear immediately.]

Similarly, a double application of equation (87) (see right-hand sketch) gives

$$p_w - p_{iu} = -\kappa_u^* \rho_{iu} U_{iu}^2 (\delta_u^* + \theta_u)$$

and

$$p_w - p_{il} = +\kappa_l^* \rho_{il} U_{il}^2 (\delta_l^* + \theta_l),$$

where $\kappa_u^* = \kappa_w + \frac{d^2 \delta_u^*}{ds^2}$ and $\kappa_l^* = \kappa_w - \frac{d^2 \delta_l^*}{ds^2}$ are the curvatures of the upper and lower parts of the displacement surface (considered positive if concave upwards) and κ_w is the curvature of the wake line. It follows that a jump in pressure is needed in the EIF at the wake line, in order to match the variation of pressure across the wake in the real flow (full line in right-hand sketch), given by

$$\Delta p_w \equiv p_{iu} - p_{il} = \kappa_u^* \rho_{iu} U_{iu}^2 (\delta_u^* + \theta_u) + \kappa_l^* \rho_{il} U_{il}^2 (\delta_l^* + \theta_l). \quad (92)$$

For computational purposes it is usually more convenient to express this in terms of a jump in the streamwise component of velocity, U_1 . Since this jump may be considered to be small, the usual assumptions of linearised theory give

$$\Delta U_{iw} \equiv U_{iu} - U_{il} = -\kappa_u^* U_{iu} (\delta_u^* + \theta_u) + \kappa_l^* U_{il} (\delta_l^* + \theta_l). \quad (93)$$

Equations (91) and (92) or (93) provide the jump conditions needed to represent the interaction of the viscous wake with the equivalent inviscid flow. Two points are of interest in this connection:

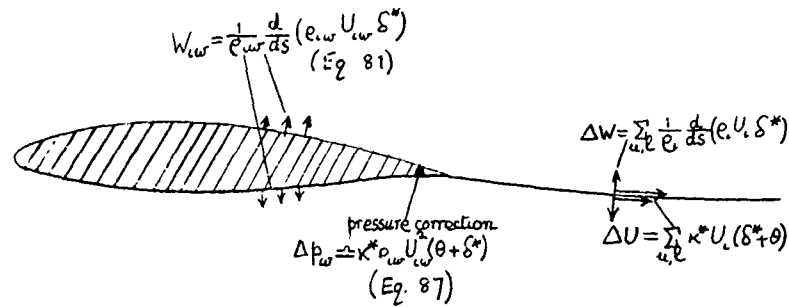
(i) referring back to sketch (a) or page 26, we see that the pressure jump in the wake, implied by equation (92), leads to a discontinuity in pressure in the EIF at the trailing edge, given in fact by the value of the right-hand side of equation (92) there. This discontinuity will be the same, whether the trailing edge is approached from ahead or behind, provided only that κ_u^* and κ_l^* are continuous across the trailing edge. Now in principle we can think of the displacement surface as the dividing stream surface of an inviscid flow (the EIF) produced by a certain distribution of sources and sinks on the surface of the wing and along the wake; so in a mainly subsonic flow this surface, and in particular its curvature, must be mathematically continuous. However, in practice the methods used to compute the development of the boundary layer and wake, involving as they do certain empirical changes in going from the one to the other, may lead to apparent discontinuities in the shape of the net displacement surface at the trailing edge. It will therefore usually be necessary to apply numerical smoothing procedures, certainly to δ^* and possibly also to the pressure, to obtain a satisfactory solution in the trailing edge region.

(ii) In most practical methods for the problem, the question of determining the precise shape of the wake has been avoided, and instead the appropriate jump conditions have been applied on a convenient coordinate line as close to it as possible; this should not normally introduce appreciable errors provided that the two shapes diverge only slowly, because most of the 'wake effects' come from the immediate vicinity of the trailing edge. In this case it is most convenient to derive the two curvatures, κ_u^* and κ_l^* , required in equation (92) or (93), by approximating them as the streamwise rate of change of the net flow direction, relative to fixed cartesian axes, in the EIF just above and below the chosen dividing line:

$$\begin{aligned} \kappa_u^* &= \frac{d}{dx} \left(\phi + \frac{w_{iu}}{U_{iu}} \right) \\ \kappa_l^* &= \frac{d}{dx} \left(\phi + \frac{w_{il}}{U_{il}} \right) \end{aligned} \quad \text{(see sketch)} \quad (94)$$



The conclusion of section 3.1 may be summarised in the following diagram, which shows the full boundary conditions which have to be imposed in the equivalent inviscid flow.



Note that on the wing the curvature effect on the pressure, needed to allow for normal pressure gradients, merely provides a correction to be applied to the pressure calculated in the EIF after an iterative process has converged; but in the wake it forms an essential part of the boundary conditions for the EIF, and therefore has to be determined successively as the interaction proceeds. If all goes well, the resulting corrected pressure distribution should then be smooth and single-valued along the two sides of the wake and, in particular, at the trailing edge - as of course it should be.

3.2 The entrainment methods

The relations derived in section 3.3 are applicable to any 'integral' method for calculating boundary layers, and indeed may be used as a check on the overall accuracy of methods of 'differential' type. In what follows we shall now concentrate on methods which rely on the principle of 'entrainment', first proposed by Head¹, and in particular on the development due to Green et al.² known as the lag-entrainment method.

3.2.1 The entrainment equation

The entrainment equation itself is derived by integrating the mass conservation (continuity) equation across the boundary layer to obtain the direction of flow at its outer edge and hence the rate of entrainment of fluid into it.

We obtain

$$\rho_e W_e = - \int_0^{\delta} \frac{\partial}{\partial s} (\rho U) dz,$$

so that the rate of mass flow into the boundary layer is

$$\rho_e U_e \left(\frac{d\delta}{ds} - \frac{W_e}{U_e} \right) = \frac{d}{ds} \int_0^{\delta} \rho U dz;$$

and this may be written

$$\begin{aligned} \frac{d}{ds} \left\{ \int_0^{\delta} \rho_1 U_1 dz - \int_0^{\delta} (\rho_1 U_1 - \rho U) dz \right\} \\ = \frac{d}{ds} \left\{ \rho_{1w} U_{1w} (\bar{\delta} - \delta^*) \right\} \quad (\text{from equation (80)}) \end{aligned}$$

where

$$\bar{\delta} = \frac{1}{\rho_{1w} U_{1w}} \int_0^{\delta} \rho_1 U_1 dz.$$

Defining the entrainment coefficient by

$$C_E = \frac{1}{\rho_e U_e} \frac{d}{ds} \int_0^{\delta} \rho U dz \equiv \frac{d\delta}{ds} - \frac{W_e}{U_e},$$

we have therefore

$$C_E = \frac{1}{\rho_e U_e} \frac{d}{ds} \left\{ \rho_{1w} U_{1w} (\bar{\delta} - \delta^*) \right\}. \quad (95)$$

In practice, the variation of U_1 across the boundary layer has been neglected, so that the standard entrainment equation

$$C_E = \frac{1}{\rho_{1w} U_{1w}} \frac{d}{ds} \left\{ \rho_{1w} U_{1w} (\bar{\delta} - \delta^*) \right\} \quad (95a)$$

has always been used. This may be written in the alternative form

$$C_E = \frac{1}{\rho_{1w} U_{1w}} \frac{d}{ds} (\rho_{1w} U_{1w} H_1 \theta) \quad (95b)$$

where $H_1 = \frac{\delta - \delta^*}{\theta}$ is the entrainment shape parameter.

The above relation is little more than a definition of the two parameters C_E and H_1 ; the crucial point is how these two parameters are to be determined. In Head's original method³⁷, and in Green's later extension of it to compressible flow³⁹, C_E was defined empirically as a simple function of H_1 ; namely $C_E = 0.03(H_1 - 3.0)^{-0.617}$ over the wing,

with $C_E = 0.4(H - 1)^{0.9}$ in the far wake,

and a smooth blending of the two downstream of the trailing edge (see Ref 39 for details).

In the lag-entrainment method of Green et al²² a more sophisticated procedure was followed, in order to give greater accuracy in boundary layers departing strongly from equilibrium*. For equilibrium boundary layers, for which H_1 is constant, equation (95b) together with the first-order form of the momentum integral equation (84) gives (dropping the suffix on U)

$$(C_E)_{EQ} = H_1 \left[\frac{1}{2} C_f - (H + 1) \left(\frac{\theta}{U} \frac{dU}{ds} \right)_{EQ} \right],$$

where $\left(\frac{\theta}{U} \frac{dU}{ds} \right)_{EQ}$ is chosen to agree with experimental results for incompressible flow :

$$\left(\frac{\theta}{U} \frac{dU}{ds} \right)_{EQ} = \frac{1.25}{H} \left[\frac{1}{2} C_f - 0.0242 \left(\frac{H-1}{H} \right)^2 \right]; \quad (96)$$

so that $(C_E)_{EQ} = H_1 \left[0.0302 \frac{(H+1)(H-1)^2}{H^3} - \frac{1}{2} C_f (0.25 + 1.25/H) \right]. \quad (97)$

For non-equilibrium flows, a further ordinary differential equation is added to determine C_E , based on considerations of the streamwise variation of the maximum shear stress C_T derived from the turbulent kinetic energy equation; this is of the form

$$\theta \frac{dC_E}{ds} = \mathcal{F} \left\{ (C_{T_{EQ}} - C_T), \left(\frac{\theta}{U} \frac{dU}{ds} \right)_{EQ} - \frac{\theta}{U} \frac{dU}{ds} \right\}. \quad (98)$$

The reader is referred to Ref 22 for details, which include modifications to be applied in the wake and to allow for 'secondary influences', the chief of which is the effect of surface curvature on turbulence structure.

At the time when the lag-entrainment method was originally developed, the calculation of separated flow had hardly been contemplated. Now that this is becoming feasible, it is hardly surprising that modifications are needed to some of the empirical features of the method. As regards the equilibrium entrainment coefficient (equation (97)), Melnik and Brook⁴⁰ have recently suggested an alternative definition whereby $(C_E)_{EQ}$ remains roughly constant, about 0.65, for H greater than 3; they also propose some changes to the lag equation (98). Perhaps more important, it has become clear that the definition of H_1 used in the method (see below) becomes progressively less satisfactory as H increases above 2. The derivation of an improved relation between H_1 and H is discussed in the following section.

3.2.2 The entrainment shape factor, H_1

The best way of defining the parameter $H_1 = (\delta - \delta^*)/\theta$ is to make explicit use of information concerning the shape of the mean streamwise velocity profiles in the boundary layer. This has the added advantage that, when the overall calculation is complete, one can then use the calculated values of H_1, H

* A turbulent boundary layer is said to be in equilibrium if the velocity profiles are invariant in the streamwise direction, so that H and H_1 are constant, and if $\frac{d\theta}{ds}, \frac{d\delta^*}{ds}$ and $\frac{s}{U_e} \frac{dU_e}{ds}$ are also constant (implying $U_e \sim s^m$)

etc to deduce the velocity distribution in the boundary layer and, after combination with the results of the inviscid part of the calculation, the entire mean velocity field.

In a recent study⁴¹ the present author has used the following family of velocity profiles, for both attached and separated flows (incompressible):

$$u\left(\equiv \frac{U}{U_e}\right) = u(\zeta; u_\tau, Re_\delta, \chi) = \frac{u_\tau}{\kappa} \left[\ln(\zeta |u_\tau| Re_\delta) + A \right] + C \sin^\chi \left(\frac{1}{2} \pi \zeta \right) \quad (99)$$

where $\zeta = z/\delta$, $u_\tau \left(= \frac{U_\tau}{U_e} \right) = \pm \sqrt{\left(\frac{1}{2} |C_f| \right)}$ (positive for attached, negative for separated flows)

is the non-dimensional skin friction velocity,

$Re_\delta = U_e \delta / \nu$ is the Reynolds number based on boundary layer thickness,

$\kappa = 0.41$, $A = 2.13$ are standard constants of the 'law of the wall',

$$C = 1 - \frac{u_\tau}{\kappa} \left[\ln(|u_\tau| Re_\delta) + A \right] \quad (\text{to give } u(1) = 1),$$

and χ is a third parameter suggested by Cross⁴² which permits a distortion on the shape of the 'wake' function of the standard Coles profile (for which $\chi = 2$) to allow for the effect of strong departures from equilibrium. Cross has shown that, for attached flows, experimental evidence can be correlated by specifying χ as a function of the departure from equilibrium of the non-dimensional velocity gradient $\frac{\theta}{U} \frac{dU}{ds}$ (see equation (96)).

Defining $\Pi = \frac{\theta}{U_e} \frac{dU_e}{ds} - \left(\frac{\theta}{U_e} \frac{dU_e}{ds} \right)_{eq}$, Cross' correlation can be fitted by

$$\chi = 0.7 + 1.3 \exp(250\Pi). \quad (100)$$

Thus χ is less than 2 for strongly retarded flows, greater than 2 for accelerated flows. Equation (99) can be integrated to give the displacement and momentum thicknesses (to first order)

$$\Delta^* \left(= \frac{\delta^*}{\delta} \right) = \frac{u_\tau}{\kappa} + Cf(\chi) \quad (101)$$

$$\text{and} \quad \Theta \left(= \frac{\theta}{\delta} \right) = \Delta^* - 2 \left(\frac{u_\tau}{\kappa} \right)^2 - C^2 \{ 2f(\chi) - f(2\chi) \} - 2 \frac{Cu_\tau}{\kappa} g(\chi) \quad (102)$$

$$\text{where } f(\chi) = 1 - \int_0^{\frac{1}{2}} \sin^\chi \left(\frac{1}{2} \pi n \right) dn = 1 - \frac{1}{\sqrt{\pi}} \frac{\left(\frac{\chi-1}{2} \right)!}{\left(\frac{\chi}{2} \right)!}$$

$$\text{and } g(\chi) = 1 + \int_0^{\frac{1}{2}} \sin^\chi \left(\frac{1}{2} \pi n \right) \ln(n) dn = f(\chi) / (0.434 + 0.288 f + 0.1355 f^2 + 0.142 f^3).$$

Given u_τ , Re_δ and χ we can thus find Δ^* and Θ from equations (101) and (102), and then $H = \Delta^*/\Theta$ and $H_1 = (1 - \Delta^*)/\Theta$.

With this family of profiles, separation ($u_\tau = 0$) occurs when $C = 1$, so that

$$\Delta_{sep}^* = f(\chi), \quad \Theta_{sep} = f(2\chi) - f(\chi)$$

$$\text{and } H = H_{sep} = f(\chi) / \{ f(2\chi) - f(\chi) \}; \quad (103)$$

the value of H at separation increases almost linearly with χ , from $2.7(\chi = 1)$ to $4(\chi = 2)$.

For fully separated flows ($u_\tau < 0$), it has been found⁴¹ that a reasonable fit with reliable experimental data, such as those of Simpson et al⁴³ and D elery⁴⁴, can be obtained provided that χ is allowed to increase relative to its value at separation, χ_{sep} (which will depend on the upstream history of the flow), according to

$$\chi = \chi_{sep} + 0.1(H - H_{sep}) \quad (104)$$

Now the lag-entrainment method uses as independent variables the quantities θ, H and $Re_\theta (= \theta u_e / \nu)$ rather than the basic parameters δ, u_r and Re_δ of the present profile family. To avoid this difficulty, it has been found possible to fit the values of H_1 , calculated from equations (100) and (101) for a range of values of u_r, Re_δ and χ , by the following explicit formula (suggested by Gaudet⁴⁵ for $\chi = 2$):

$$H_1 = \left(\frac{1-f}{f} \right) \left\{ \frac{H_{sep}^{-\beta}}{(F-1)H_{sep} + \beta} \right\} \left\{ F \frac{H^2}{H-\beta} - H \right\} \quad (105)$$

where $f = f(\chi)$, $F = \{2f(\chi) - f(2\chi)\}/f^2(\chi)$, H_{sep} is given by equation (103)

$$\text{and } \beta = 1 + 6.2/(\log_{10} Re_\theta)^{3.3} .$$

This has the property that, as $Re_\theta \rightarrow \infty$, $\beta \rightarrow 1$ and we obtain the 'infinite Reynolds number' formula for H_1 :

$$H_1 = \frac{FH^2}{H-1} - H ; \quad (105a)$$

and for flows approaching and beyond separation, for which u_r is small, this represents a satisfactory approximation to the parameter H_1 . For attached flows, particularly at low Reynolds numbers, the departure of H_1 from its infinite Reynolds number values becomes more significant and should be taken into account.

For flows which do not depart far from equilibrium conditions at separation (so that $\chi_{sep} = 2$ and $H_{sep} = 4$), the relation between H_1 and H implied by equations (104) and (105a) can be approximated by

$$H_1 = 4 + \frac{1}{3}(H-4) , \quad (4 < H < 12) \quad (106)$$

and if for attached flows it is desired to avoid the complications of the full dependence of H_1 on Re_θ and χ implied by equation (105), then the formula suggested by Green³⁹, namely

$$H_1 = 2 + 1.5 \left(\frac{1.12}{H-1} \right)^{1.093} + 0.5 \left(\frac{H-1}{1.12} \right)^{1.093} \quad (H < 4) \quad (10a)$$

provides a reasonable mean approximation to H_1 .

In Fig 5 are plotted a number of the alternative formulae that have been suggested to represent the variation of H_1 with H , together with some relevant experimental data. The former include:

- (a) the results of equations (104) and (105) (with $Re_\theta = 50000$),
- (b) the composite formula of equations (106) and (106a), which is seen to lie close to the result of (a) with $\chi_{sep} = 2.0$,
- (c) the formula normally used in the lag-entrainment method²², namely

$$H_1 = 3.15 + 1.72/(H-1) - 0.01(H-1)^2 \quad (107)$$

together with a modification for separated flows suggested by East et al⁴⁹:

$$H_1 = 4.55 + 295 \exp(-3.325H) \quad (H > 1.8) \quad (107a)$$

The experimental data comprise:

- (i) The attached flow equilibrium data of East and Sawyer⁴⁶, together with values for a separated equilibrium boundary layer measured by Hastings⁵⁰; the agreement with (a) above (with $\chi = 2$) and (b) is good.

- (ii) The low-speed separated flow measurements of Simpson et al.⁴³, which also agree well with (a) and (b).
- (iii) Measurements by Delery⁴⁴ behind a shock-induced separation; these are consistent with (a) with $x_{sep} = 1.5$, as would be expected at a shock wave (here H is replaced by \bar{H} , see below).
- (iv) Low-speed measurements in a strong adverse pressure gradient by East and Hoxey; these were used to define equation (107), and are also seen to correspond closely to equation (105) with $\chi = 1$.

This figure confirms the suggestion that the simple composite formula (b) (equations 106 and 106a) represents a satisfactory mean line through most of the low-speed data. For a shock-induced separation, equations (107) and (107a) seem more satisfactory, at least up to $\bar{H} = 5$, above which the curve should probably be blended into equation (107a).

Finally, for compressible flows Green³⁹ has shown that H should be replaced (in any of the above formulae) by \bar{H} ,

$$\text{where } \bar{H} = \frac{1}{\rho_{1w} U_{1w}} \int_0^{\delta} \rho(U_i - U) dz \quad / \theta \quad \text{is a transformed shape parameter, related to } H \text{ by}$$

$$(H + 1) = (\bar{H} + 1)(1 + rM_e^2/5), \quad (108)$$

where r is the recovery factor, usually taken to be unity, and M_e (or M_{1w}) is the Mach number of the local inviscid flow.

3.3 Skin-friction formulae

The final 'closure condition' required by nearly all 'integral' methods for turbulent boundary layers is the relation used to determine the skin-friction coefficient, C_f , usually as a function of H, Re_θ and (for compressible flow) the Mach number M_e . This has an obvious and immediate impact on the calculation of drag without (as is the case with some of the 'higher-order' effects mentioned in section 3.1 above) any compensatory effects in the wake.

Commonly used skin-friction formulae include the following:

- (i) Ludwig-Tillmann⁵³ (incompressible):

$$C_f = 0.246 Re_\theta^{-0.268} 10^{-0.678H} \quad (109)$$

- (ii) Swafford and Whitfield⁵¹ (incompressible):

$$C_f = \frac{0.3e^{-0.33H}}{(\log_{10} Re_\theta)^{1.74} + 0.31H} + 1.1 \times 10^{-4} [\tanh(4 - 1.14H) - 1] \quad (110)$$

- (iii) Lag-entrainment²²:

First, the following 'flat-plate' (zero pressure gradient) values are calculated:

$$C_{f0} = \left(\frac{0.01013}{\log_{10}(F_R Re_\theta) - 1.02} \right) \left(1 + \frac{33}{Re_\theta} \right) / F_c \quad (111)$$

$$\bar{H}_0 = 1 / \left\{ 1 - 6.55 \left[\frac{1}{2} C_{f0} (1 + 0.04M_e^2) \left(1 + \frac{42}{Re_\theta} \right) \right]^{1/2} \right\} \quad (112)$$

where the compressibility factors F_c and F_R are given by

$$F_c = (1 + 0.2M_e^2)^{1/2}, \quad F_R = 1 + 0.056M_e^2$$

[The factors $(1 + 33/Re_\theta)$, $(1 + 42/Re_\theta)$ are included⁵² to improve the accuracy of the formula for low values of Re_θ .]

$$\text{Then } C_f = C_{f0} \left\{ 0.9 / \left(\frac{H}{H_0} \right) - 0.4 - 0.5 \right\} \quad (113)$$

where H is given by equation (108).

Equation (113) suggests that $C_f = 0$

when $H = H_s = 2.2 H_0$;

and since H_0 (equation 112) varies between 1.2 ($Re_\theta = 10^6$) and 1.6 ($Re_\theta = 500$), this implies that 'separation' is predicted for H between 2.6 and 3.4, depending on Reynolds number. Both these values are lower than the value (4.0) for boundary layers near equilibrium, as implied by the velocity profile family of section 3.2.2 (cf equations (99) and (103)) and confirmed by experiments like that of Simpson et al (Ref 43; see also Ref 47); but they are consistent with values of H at separation that will occur in strongly-retarded boundary layers, with χ less than 2.

(iv) When the flow is separated, equation (113) gives unrealistically high (negative) values of C_f ; and Melnik has recently suggested a modification given by

$$C_f = A \left\{ 1 - \exp[-C(H - H_s)] \right\} \quad (114)$$

with $A = -2.2 \times 10^{-4}$ and $C = -0.28 C_{f0} / (A H_0)$.

This has the same slope as equation (113) at $H = H_s$, and rapidly approaches the value A for $H \gg H_s$, as does Swafford's formula (110).

(v) The method described in section 3.2.2, based on Cross' family of profiles⁴², has its own built-in skin-friction relation, through the basic parameter u_τ : thus

$$C_f = \pm 2u_\tau^2 \quad (+ \text{ for attached, } - \text{ for separated flow}).$$

If H , Re_θ and χ are given, equation (105) can be used to determine H_1 ; then $\Delta^* (= \frac{5\Delta^*}{\delta})$ and Re_δ follow from $\Delta^* = H/(H + H_1)$, $Re_\delta = Re_\theta (H + H_1)$, so that equation (101) can be solved for u_τ to give C_f . [In the examples given below, the 'wall' part of the profile (98) has been modified very near the wall and at the outer edge of the boundary layer to give a better representation of the flow: see Ref 41 for details.]

Values of C_f predicted by these formulae are compared in Figs 6 to 8. First, in Fig 6 we show the predictions for a flat plate (zero pressure-gradient): in the case of methods (i), (ii) and (v) the values of H_0 have been taken from equation (112). If we accept that the formula (110) used in the lag-entrainment method is the most reliable (being based at its two extremes on the recent high Reynolds number data of Winter and Gaudet⁵⁴ and an unpublished analysis of low Reynolds number data by Green⁵⁵), then it is clear that:

- (a) all the other methods require some upward adjustment at values of Re_θ below about 5000, the present method (equations (99) and (101)) less so than the other two;
- (b) the Ludwig-Tillmann formula also underestimates C_f at high Reynolds number but the other two methods are satisfactory.

In Fig 7 we compared the results of the four methods for a moderate value of Re_θ , 10,000. We see that

- (a) the Ludwig-Tillman formula (108) now gives slightly higher values (typically by 1×10^{-4}) than any of the other methods, which all agree closely for $H < 2$.
- (b) the lag-entrainment formula (110-112) predicts the most rapid approach to separation and consequently the lowest values of C_f for $H > 2$;
- (c) unlike any of the others, the present method predicts that dC_f/dH is (almost) zero at separation (actually, it is of order $1/Re_\theta$, see Ref 41); as a result, the shape of the skin-friction curve in the vicinity of separation is appreciably different from the others, even though the numerical differences remain low (less than 2×10^{-4});
- (d) for fully separated flow the experimental evidence is both sparse and of dubious accuracy (see Ref 51, for example); but it seems to be generally agreed that the numerical values of C_f are likely to remain extremely low, so that the mean value -2.2×10^{-4} assumed in methods (ii) and (iv) is a sensible one to take. The present method probably underestimates ($-C_f$) slightly at high Reynolds numbers, but it

does predict a plausible variation with Reynolds number (which is absent from the other formulae), even though there is no experimental evidence on this point.

In Fig 8 is shown the effect on the present method of varying the velocity gradient parameter χ , for $Re_0 = 10^5$ (see equations (100) and (104)). At one extreme, with $\chi = 1$ up to separation (in a strong adverse pressure gradient), separation occurs at $H = 2.8$, so that for $H < H_{sep}$ the skin friction is now lower than that predicted by the lag-entrainment (or other) formula. At the other extreme, with $\chi = 4$ (strong favourable pressure gradient), C_f is higher than its equilibrium value by a similar amount; the overall 'spread' in the values of C_f reaches a maximum of about $\pm 2 \times 10^{-4}$ when $H = 2$ (increasing to $\pm 5 \times 10^{-4}$ when $Re_0 = 1000$).

To sum up this section: it appears that the lag-entrainment formula - and of course the compressibility correction that it contains - is adequate for most purposes (provided that it is suitably modified for separated flow as suggested by Melnik). It would no doubt be desirable to improve its performance in the vicinity of separation and in particular to allow for departures from equilibrium as described above; but since such departures tend to be short-lived it may well be that the overall effect on the prediction of drag will usually be negligible.

3.4 The organisation and numerical stability of an iterative procedure for calculating viscous/inviscid interactions

In the present section we shall consider how best to organise an interactive viscous/inviscid calculation procedure, and explain why, for flows that are sufficiently close to separation, something quite different from the obvious, direct iterative scheme is not simply desirable, but absolutely essential. Such a direct iterative procedure for calculating the viscous flow over an aerofoil - in which we are linking a boundary layer method such as that described in the preceding sections with a suitable inviscid flow solver - can best be described with the aid of a simplified flow diagram (Fig 9). After setting the initial data (M_∞, α , Reynolds number etc), we start, if we are using an iterative (eg finite difference) scheme for the inviscid component of the calculation, by performing a few inviscid iterations to get a rough approximation to the pressure distribution. This is then fed into the boundary layer method, to produce a first estimate of the displacement thickness δ^* and hence of the transpiration velocity W_{iw} (equation (81), which in turn is used to modify the inner boundary conditions for the next inviscid calculation; this will probably comprise a further 5 to 10 iteration: of a relaxation technique or time-stepping procedure. In principle, one will then simply continue round this loop until the whole process converges, as judged for example by the changes in the inviscid velocity distribution U_{iw} and the overall forces. However, it was early discovered⁵⁵ that such a procedure will almost inevitably lead to unstable oscillations which will eventually diverge; so an under-relaxation scheme has to be used: that is, only a fraction ω of the calculated changes to W_{iw} is applied at each iteration. For many years, this relaxation factor ω had to be chosen empirically, but more recently Le Balleur³⁶ has developed an elegant linearised stability analysis of the process, which not only explains why this instability occurs and gets worse as separation is approached, but also indicates how to proceed in cases of fully separated flow when a direct scheme becomes impossible. His analysis is repeated briefly below.

We assume that the matching between the viscous and inviscid components of the method is done through the 'source strength'.

$$\Sigma = \frac{W_{iw}}{U_{iw}} = \frac{1}{\rho_{iw} U_{iw}} \frac{d}{ds} (\rho_{iw} U_{iw} \delta^*) \quad (\text{equation 81})$$

We denote by $\Sigma^{(n)}$ the values of Σ at the nth iteration, and by $\bar{\Sigma}$ the converged value - the 'right answer' - and define an 'error function' for Σ : $\sigma^{(n)} = \Sigma^{(n)} - \bar{\Sigma}$.

Similarly, for the inviscid flow we define $u^{(n)} = \frac{U_{iw}^{(n)} - \bar{U}_{iw}}{U_{iw}}$.

We now perform a locally linearised analysis in which all coefficients in the appropriate differential equations are assumed to be slowly varying (compared with the errors) so that they can be regarded as 'constants'. Thus for the inviscid flow we can define a potential function ϕ such that

$$u = \frac{\partial \phi}{\partial s}, \quad \sigma = \frac{\partial \phi}{\partial z},$$

and then

$$(1 - M^2)\phi_{ss} + \phi_{zz} = 0 \quad (115)$$

where M is the local (inviscid) Mach number. We now suppose that the function ϕ (together with the errors u and σ) is analysed into Fourier components of wavelength $\lambda_1 (= 2\pi/\nu_1)$, and study the growth or decay of a particular component of wavelength λ . The solution of equation (115) which varies as $e^{i\nu s}$ and goes to zero as $z \rightarrow \infty$ is $\phi = Ae^{-\nu B z} e^{i\nu s}$,

where $\beta = \sqrt{1 - M^2}$ (for $M < 1$)*

it follows that

$$u = -i\sigma/\beta \quad (116)$$

or

$$\frac{du}{ds} = v\sigma/\beta$$

For the boundary layer, the momentum and entrainment equations (84a, 95b) can be rearranged to give the source strength Σ in terms of the velocity gradient parameter $\frac{\theta}{U_{iw}} \frac{dU_{iw}}{ds}$:

$$\Sigma = -B \frac{\theta}{U_{iw}} \frac{dU_{iw}}{ds} + C \quad (117)$$

where for incompressible flow

$$B = \frac{(H+1)(H_1 - HH_1')}{(-H_1')}$$

$$C = (H - H_1/H_1') \frac{1}{2} C_f + C_E/H_1'$$

and

$$H_1' \equiv \frac{dH_1}{dH}$$

(the corresponding expressions for compressible flow are given in Ref 28).

Notice that $B \rightarrow \infty$ as $H_1' \rightarrow 0$, that is at the minimum in the (H_1, H) curve (see Fig 5); this explains at once why a direct iterative procedure breaks down at this point, where H (or \bar{H}) = $H_{\min} = 2.7$.

The linearised perturbation form of equation (117) is simply

$$\sigma = -B\theta \frac{d\sigma}{ds}, \quad (118)$$

which shows how the errors in U and Σ are connected through the boundary layer part of the calculation. We can now, by combining equations (116) and (118), see what happens to the error $\sigma^{(n)}$ in one complete cycle of the iteration: the inviscid part gives $\frac{d\sigma}{ds} = v^{(n)}/\beta$, and then the viscous part gives

$$\begin{aligned} \sigma^{(n+1)} &= -B\theta \frac{v}{\beta} \sigma^{(n)} \\ &= \mu \sigma^{(n)} \end{aligned} \quad (119)$$

where $\mu = -B\theta v/\beta$ is the amplification factor of the iterative process. Note that B is positive when $H < H_{\min}$ so μ is negative, indicating an undamped oscillation and implying the need for under-relaxation.

We can in fact at once deduce a suitable 'optimum' relaxation factor, in the following way. We recall that the converged solution, $\bar{\Sigma}$, is given by

$$\bar{\Sigma} = \Sigma^{(n)} - \sigma^{(n)}$$

and also by

$$\bar{\Sigma} = \Sigma^{(n+1)} - \sigma^{(n+1)} = \Sigma^{(n+1)} - \mu \sigma^{(n)}$$

If we eliminate $\sigma^{(n)}$ from these two equations, we obtain

$$\bar{\Sigma} = \frac{\mu}{\mu - 1} \Sigma^{(n)} - \frac{1}{\mu - 1} \Sigma^{(n+1)}$$

* For the corresponding analysis when $M > 1$ see Ref 57.

which may be written
$$\Sigma = \Sigma^{(n)} + \omega(\Sigma^{(n+1)} - \Sigma^{(n)}) \quad (120)$$

with
$$\omega = \omega_{opt} = \frac{1}{1 - \mu} = \frac{1}{1 + \nu B \theta / \beta} \quad (121)$$

That is, the converged solution would be given (in principle!) in one step only, by the 'optimum' relaxation process indicated by equation (120).

Of course, the numerous simplifying assumptions that have been made in deriving equations (120) and (121) mean that they can only be regarded as a guide; and in particular an arbitrary element is introduced by the presence in equation (121) of the wave-number $\nu (= 2\pi/\lambda)$, where λ is the wave length of the error. With any particular numerical method the highest value of ν (lowest λ) will occur when λ is of the order of twice the streamwise step length (panel length or mesh size): that is, $\nu_{max} \sim \frac{\pi}{\Delta s}$, giving

$$\omega_{opt}^{(min)} = \frac{1}{1 + \pi B \theta / (\beta \Delta s)} \quad (122)$$

Equation (122) explains, at least qualitatively, why lower relaxation factors have been found, from experience, to be necessary

- when separation is approached (B becomes larger)
- when the computational grid is refined (Δs becomes smaller)
- when the local Mach number approaches unity (β becomes smaller)
- at lower Reynolds numbers (θ increases)

To proceed beyond the state of intermittent separation ($H \sim H_{min}$), it is clearly necessary to solve the boundary layer equations in an inverse manner: that is, instead of specifying U_{iw} and calculating Σ , we specify Σ and calculate U_{iw} . In order to do this, equation (117) is simply re-written in the form

$$\frac{\theta}{U_{iw}} \frac{dU_{iw}}{ds} = (-\Sigma + C)/B \quad (117a)$$

which clearly remains regular as $B \rightarrow \infty$.

It remains, however, convenient - though not necessarily essential - to continue to calculate the inviscid flow in the usual direct way: that is, also by specifying Σ . So we can proceed as follows: suppose that at the n th iteration we have a current estimate $\Sigma^{(n)}$ of the source strength Σ , with error $\sigma^{(n)}$ as before. We can use this to perform parallel calculations by both the (inverse) boundary layer and (direct) inviscid flow methods, leading to alternative estimates for U_{iw} , which we call U_{iw}^V and U_{iw}^I respectively (V for viscous, I for inviscid). Then we want to estimate the required change in Σ from the difference between U_{iw}^V and U_{iw}^I .

Now Le Balleur's analysis gives at once (for the errors in U_{iw}):

Viscous:
$$\frac{du^V}{ds} = \frac{-\sigma^{(n)}}{B\theta} \quad (\text{cf equation 118})$$

Inviscid:
$$\frac{du^I}{ds} = \nu \sigma^{(n)} / \beta \quad (\text{equation 116})$$

Subtracting these equations, we obtain

$$\sigma^{(n)} = \frac{1}{\nu/\beta + 1/B\theta} \left(\frac{du^I}{ds} - \frac{du^V}{ds} \right)^{(n)}$$

But
$$\Sigma = \Sigma^{(n)} - \sigma^{(n)},$$

and so
$$\Sigma = \Sigma^{(n)} + \frac{B\theta}{\beta + B\nu\theta} \left(\frac{du^V}{ds} - \frac{du^I}{ds} \right)^{(n)} \quad (123)$$

Remembering the definition $u^{(n)} = (U_{iw}^{(n)} - \bar{U}_{iw}) / \bar{U}_{iw}$, equation (123) suggests that the new value of Σ should be taken to be

$$\Sigma^{(n+1)} = \Sigma^{(n)} + \Omega \left[\left(\frac{\theta}{\bar{U}_{iw}} \frac{dU_{iw}}{ds} \right)^v - \left(\frac{\theta}{\bar{U}_{iw}} \frac{dU_{iw}}{ds} \right)^v \right]^{(n)} \quad (124)$$

with $\Omega = \frac{\beta}{v\theta + \beta B^{-1}}$ again depending on the boundary layer quantities B and θ and on the wave number v . Note in particular that Ω remains finite (non-zero) as H goes through H_{\min} and B^{-1} through zero. As before, the lowest value of Ω occurs when $v = v_{\max} = \pi/\Delta s$, and is

$$\Omega_{\min} = \frac{\beta}{\pi\theta/\Delta s + \beta B^{-1}} \quad (125)$$

It has been shown by Williams⁵⁶ that convergence can be obtained more rapidly if a sequence of values $\Omega^{(p)}$ is used in successive iterations,

$$\text{where } \Omega^{(p)} = \frac{\beta}{\pi\theta/(p\Delta s) + \beta B^{-1}}, \quad p = 1, 2, 3, \dots \quad (126)$$

The algorithm given by equation (124) suggests the procedure known as 'semi-inverse' for calculating flows in which separation is likely to occur, as shown in the flow diagram of Fig 10. As explained above, having obtained an initial estimate for Σ (which can in fact be chosen quite arbitrarily), we use this as input to parallel calculations by the direct inviscid method and the inverse boundary layer equations, and then compare the resulting values of the non-dimensional velocity gradient

$$\frac{\theta}{\bar{U}_{iw}} \frac{dU_{iw}}{ds},$$

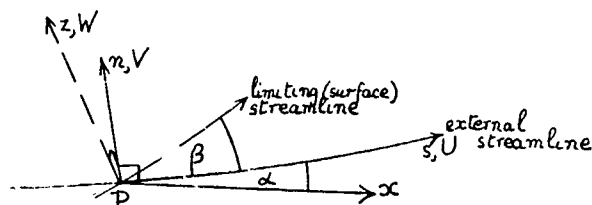
using equation (124) to provide the next value for Σ : the whole process being then repeated until convergence is obtained.

The semi-inverse technique has been used recently by several workers (eg Refs 29, 30, 56, 58 and 59); most of whom have found - perhaps surprisingly - that 'it works equally well for attached as for separated flows, so that no 'switching' between inverse and direct solution of the boundary layer equations is necessary. Some results obtained by this technique will be given in section 4 below.

3.5 Methods for three-dimensional problems

At the present time there is no three-dimensional counterpart of the 'higher-order' features of the analysis described in sections 3.1 to 3.3, nor of the linearised stability analysis of section 3.4. It is therefore necessary to rely in the main on essentially first-order methods, coupled with intuitive ideas based on our experience in two-dimensions. A brief description of the principal equations is given below; for full details the reader is referred to Refs 23, 60 and 61.

For the boundary layer over a wing the most physically-relevant coordinate system on the body surface consists of the projections on the surface of the external streamlines (s) and their normals (n), forming an orthogonal curvilinear system (s, n), together with the surface normals (z). For numerical purposes, however, this is clearly inconvenient since the position of these streamlines is not generally known a priori and indeed will vary during the course of an iterative calculation. It is therefore more convenient to perform the calculations in any suitable (non-orthogonal) surface coordinate system (x, y) (see sketch) and to make the appropriate transformations to and from the (s, n) system; details are given in Ref 23 but the (s, n) system will be used in the equations that follow.



Just as in two dimension, the displacement effect of the boundary layer on the external inviscid flow can be taken into account by introducing a normal 'transpiration' velocity W_{iw} at the surface, given by the equation

$$w_{1w} = \frac{1}{\rho_e} \frac{\partial}{\partial s} (\rho_e U_e \delta_1) - \delta_1 \kappa_s + \frac{1}{\rho_e} \frac{\partial}{\partial n} (\rho_e U_e \delta_2) - \delta_2 \kappa_n \quad (127)$$

$$\text{where } \delta_1 = \frac{1}{\rho_e U_e} \int_0^\delta (\rho_e U_e - \rho U) dz \quad \text{and} \quad \delta_2 = \frac{1}{\rho_e U_e} \int_0^\delta (-\rho V) dz$$

are the 'components' of displacement thickness and κ_s, κ_n are the geodesic curvatures of the lines $s = \text{constant}$ (normals) and $n = \text{constant}$ (streamlines) respectively. [If the (x, y) system is rectangular Cartesian, then $\kappa_s = -\frac{\partial \alpha}{\partial n}$, $\kappa_n = \frac{\partial \alpha}{\partial s}$, where α is the angle between the external streamline and the x direction (see sketch on page 8-38).] Thus κ_s is a measure of the rate of divergence of the streamlines; while since the component of vorticity of the external flow normal to the surface is generally zero, we have $\kappa_n = \frac{1}{U_e} \frac{\partial U_e}{\partial n}$.

The momentum integral equation now has two components, in the s and n directions respectively:

$$\frac{1}{\rho_e} \frac{d}{ds} (\rho_e \theta_{11}) + \frac{1}{\rho_e} \frac{\partial}{\partial n} (\rho_e \theta_{12}) + (H+2) \frac{\theta_{11}}{U_e} \frac{\partial U_e}{\partial s} + \kappa_s (\theta_{22} - \theta_{11}) = \frac{1}{2} C_{fs} \quad (128)$$

and

$$\frac{1}{\rho_e} \frac{\partial}{\partial s} (\rho_e \theta_{21}) + \frac{1}{\rho_e} \frac{\partial}{\partial n} (\rho_e \theta_{22}) + 2\theta_{21} \left(\frac{1}{U_e} \frac{\partial U_e}{\partial s} - \kappa_s \right) + \frac{1}{U_e} \frac{\partial U_e}{\partial n} \{ (H+1)\theta_{11} + \theta_{22} \} = \frac{1}{2} C_{fn} \quad (129)$$

where the momentum thicknesses θ_{ij} are defined by

$$\theta_{11} = \frac{1}{\rho_e U_e^2} \int_0^\delta \rho U (U_e - U) dz, \quad \theta_{12} = \frac{1}{\rho_e U_e^2} \int_0^\delta \rho V (U_e - U) dz,$$

$$\theta_{21} = \frac{1}{\rho_e U_e^2} \int_0^\delta -\rho UV dz, \quad \theta_{22} = \frac{1}{\rho_e U_e^2} \int_0^\delta -\rho V^2 dz,$$

H is the shape factor δ_1/θ_{11} and C_{fs}, C_{fn} are the components of the skin-friction vector in the streamwise and normal directions respectively: $C_{fs} = C_f \cos \beta$, $C_{fn} = C_f \sin \beta$,

where β is the angle between the limiting surface streamline and the external flow direction (see sketch on page 8-38).

The entrainment equation may be written

$$C_E = \frac{1}{\rho_e U_e} \frac{\partial}{\partial s} (\rho_e U_e H_1 \theta) - \frac{1}{\rho_e} \frac{\partial}{\partial n} (\rho_e \delta_2) - H_1 \theta_{11} \kappa_s \quad (130)$$

where $H_1 = (\delta - \delta_1)/\theta_{11}$ is the entrainment shape factor.

As in two dimensions, this may be supplemented⁶⁰ by an additional equation for $\partial C_E / \partial s$ to take into account departures of the boundary layer from equilibrium. Relations similar to their two-dimensional counterparts (see section 3.2.3 above) may be used to define H_1 , normally as a function of H alone. Similarly, the streamwise skin-friction coefficient, C_{fs} , may be defined as a function of H and θ_{11}

by any of the relations given in section 3.2.4. The limitations introduced by these assumptions are however likely to be even more restrictive in three dimensions than in two, as separation is approached and the cross-flow angle β becomes large.

To proceed further, it is necessary to make some assumptions regarding the shape of the cross-flow profile $V(z)$; the integral quantities $\delta_2, \theta_{12}, \theta_{21}$ and θ_{22} can then be expressed in terms of θ_{11} and the cross-flow angle β . In Smith's method²³ it is usually assumed, following Mager⁶², that

$$\frac{v}{U_e} = \left(1 - \frac{z}{\delta}\right)^2 \frac{U}{U_e} \tan \beta \quad (131)$$

together with the 'power-law' streamwise profile $\frac{U}{U_e} = \left(\frac{z}{\delta}\right)^{\frac{1}{2}(H-1)}$.

Equations of the form $\theta_{1j} = f_{1j}(H)\theta_{11} \tan \beta$, $\delta_2 = f(H)\delta_1 \tan \beta$ are then obtained (see Ref 23 for details); so that finally the governing equations (128-130) can be transformed, using the generalised coordinate system (x, y) , into a set of three partial differential equations for the three unknowns θ_{11} , H and β in terms of the given external velocity field (U_e, α) .

Alternatively, in Cross' method⁶³ an explicit family of velocity profiles is assumed from the start, analogous to that used in two dimensions (equation 99, section 3.2.2):

$$\frac{U}{U_e} = \frac{u_\tau}{\kappa} \cos \beta [\ln(\zeta u_\tau Re_\delta) + A] + C \sin^{\chi_s} \left(\frac{1}{2} \pi \zeta\right) \quad (132)$$

$$\frac{v}{U_e} = \frac{u_\tau}{\kappa} \sin \beta [\ln(\zeta u_\tau Re_\delta) + A] + D \sin^{\chi_c} \left(\frac{1}{2} \pi \zeta\right)$$

where $u_\tau = \sqrt{\left(\frac{1}{2} \zeta_f\right)}$ and the coefficients C and D are chosen to give, at $\zeta = 1$, $U/U_e = 1$ and $v/U_e = 0$;

so that $C = 1 - u_\tau/\kappa \cos \beta [\ln(u_\tau Re_\delta) + A]$

and $D = -u_\tau/\kappa \sin \beta [\ln(u_\tau Re_\delta) + A] = (C - 1) \tan \beta$.

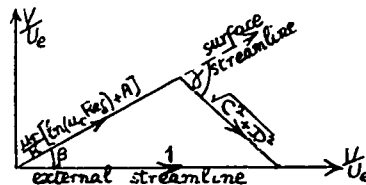
In Cross' original paper the exponents χ_s and χ_c were given by $\chi_s = 2 - \sin^2 \beta$, $\chi_c = 2 - \cos^2 \beta$; but more recently⁶⁴ the definition has been modified empirically to improve the representation of profiles with large values of β , and now he takes

$$\chi_s = \chi(1 - 0.17 \sin^{2.2} \gamma), \quad \chi_c = \chi_s(1 - 0.4 \cos^2 \beta)$$

where γ is the angle between the 'wall' and 'wake' components of velocity at the outer edge of the boundary layer, given by

$$\sin \gamma = \sin \beta / \sqrt{C^2 + D^2} \quad (\text{see sketch})$$

and χ is defined as in two dimensions (equation 100).



With this family of profiles all the integral quantities $\Delta_1 (= \delta_1/\delta)$ and $\theta_{1j} (= \theta_{1j}/\delta)$ can be expressed as functions of u_τ, Re_δ and β ; and no further empiricism is required concerning the definition of H_1 and C_f . The governing equations (128-130) can then be transformed into a system of equations for δ , u_τ and β which form the basic dependent variables of the method.

Whichever method is used, when the external velocity field (U_e, α) is prescribed the result is a set of hyperbolic partial differential equations which may be solved as an initial value problem using a marching procedure⁶⁵. The bounding characteristics of these equations lie roughly in the directions of the external flow and of the skin-friction vector, so that as separation is approached and β becomes large a numerical method of this type will become unstable. It is therefore natural to seek for an inverse technique for solving the boundary layer equations, as has been done so successfully in two dimensions. The obvious thing to try first is to specify the equivalent source strength $\xi = W_{1U}/U_e$, supplemented (since two quantities are needed as input in a three-dimensional problem) by the condition that the component of vorticity normal to the surface in the external inviscid flow is (normally) zero:

$$\xi = \kappa \frac{\partial U_e}{\partial n} = 0 \quad (133)$$

This ' ξ, ζ ' approach has been used, in conjunction with the infinite yawed wing equations, by Smith⁶¹, who was able to considerably improve the prediction of all relevant quantities for the yawed wing experiment of van den Berg and Elsenaar.

Unfortunately, however, it is not immediately applicable in a fully three-dimensional problem, since the governing equations then turn out to be elliptic rather than hyperbolic, so that a standard marching procedure cannot be used. Wigton and Yoshihara have had some limited success by using H and α as input variables; but since to specify α is equivalent, in principle, to specifying U_e as well through the vorticity condition (133), it seems unlikely that this approach will prove of lasting value. More recently Smith⁶⁷ and Cross⁶⁴ have shown that a promising alternative scheme is to specify either H and β , or u_τ and β - that is, to specify both the magnitude and direction of the skin-friction velocity vector - coupled with equation (133) to eliminate cross-flow velocity derivatives. The resulting equations then have real characteristics, all of which lie sufficiently close to the external streamline direction to allow streamwise marching to be used even when the flow is separated.

There remains the problem of discovering a suitable algorithm, analogous to equation (124) in two dimensions, for updating the linking quantities (for example u_τ and β) in a semi-inverse iterative procedure. For this reason it may be preferable^{61,66} to return to the ' Σ, ξ ' approach and face the resulting ellipticity of the equations by using some form of iterative relaxation procedure, which could perhaps be organised in conjunction with the iterations required to couple the boundary layer with the external inviscid flow calculations.

There is no doubt that higher-order effects, analogous to those already identified in two dimensions, will be just as important in three-dimensional flows. In the absence of any more rigorous treatment of the problem, it seems probable that the most important of these effects will continue to be that of pressure gradients normal to the surface, induced by curvature of the streamlines in both the viscous and equivalent inviscid flows. The argument used above (section 3.1.3) in two dimensions can be adapted as follows.

In the inviscid flow we have $\partial p_1 / \partial z = -\kappa_s^* \rho_e U_e^2$, where κ_s^* is the curvature of a section of the displacement surface by a plane normal to the wing surface through the direction of the external streamline. Just as in two dimensions, we can therefore write

$$\frac{\partial}{\partial z} (p - p_1) = \kappa_s^* \rho_e U_e^2 - \rho Q^2, \quad \text{where } Q^2 = U^2 + V^2,$$

$$\text{giving } \Delta p \equiv p_{1w} - p_w = \kappa_s^* \int_0^\delta (\rho_e U_e^2 - \rho Q^2) dz + \int_0^\delta \rho Q^2 (\kappa_s^* - \kappa) dz;$$

so that, neglecting the second integral compared with the first for the same reasons as before, we obtain

$$\begin{aligned} \Delta p &= \kappa_s^* \int_0^\delta (\rho_e U_e^2 - \rho U^2 - \rho V^2) dz \\ &= \kappa_s^* \rho_e U_e^2 (\delta_1 + \theta_{11} + \theta_{22}) \end{aligned} \quad (134)$$

Normally, the term θ_{22} will be small compared with θ_{11} , leaving the obvious generalisation of the two-dimensional formula (87). To evaluate κ_s^* , it may be convenient to use the equivalent of equation (94),

$$\text{namely } \kappa_s^* = \kappa_{ws} + \frac{\partial}{\partial s} \xi, \quad (135)$$

where κ_{ws} is the curvature of the wall along the direction of the external streamline.

The above argument implies that corrections to the pressures p_{1w} calculated for the equivalent inviscid flow will be required both over the wing surface and in the wake, where 'jump' conditions similar to those applied in two dimensions must be imposed in the inviscid part of the calculation. Appropriate modifications must therefore be made to the boundary conditions usually applied in a purely inviscid flow calculation, and this may not always be straightforward, particularly for an Euler method in the wake.

Additional problems, that have no obvious analogue in two dimensions, will occur; for example in corner regions, such as the junction of a wing with a fuselage or pylon, and near the wing tip, where the normal assumptions of thin shear-layer theory are no longer valid. Little progress has yet been made with any of these problems, and it remains to be seen what effect they have on the accuracy of the estimation of the overall drag.

4 PRACTICAL METHODS AND COMPARISON WITH EXPERIMENT: TWO DIMENSIONS (AEROFOILS)

In section 3 a survey was given of recent work on the basic principles and equations that are required in the development of accurate, practical interactive methods for calculating the viscous flow over aerofoils and wings. The emphasis on the problems that occur when boundary layer separation is encountered can be fully justified in the present context by the obvious importance of this phenomenon in the estimation and reduction of drag. In the next two sections we shall describe some recent methods

which make use of these ideas, and compare the results with experimental measurements of local pressures and overall lift and drag: first for aerofoils in two-dimensional flow (section 4), and then for a complete swept-wing-body combination (section 5). In all cases the drag has been calculated by means of the 'far-field' approach described in section 2.2; in two dimensions by purely theoretical methods and in three dimensions by a combination of theory and experiment, as described in section 5. No attempt has been made here to give an exhaustive review* of current methods or computer programs; instead, only those which are directly accessible to the present author have been considered. This is also true of the experimental results that have been used in the evaluation exercise that follows. It cannot be emphasised too strongly that it is just as difficult to measure accurately the pressures and forces on a wing, under precisely known conditions (free stream Mach number, angle of incidence, transition position etc), as it is to calculate them. Particular uncertainties that occur in wind-tunnel tests include:

- Wall constraint corrections: particularly severe with ventilated walls and with the relatively large models that are commonly used in aerofoil tests.
- Difficulties concerned with transition from laminar to turbulent flow: if transition is 'free' then its position is seldom known with adequate accuracy, while if it is artificially 'fixed' then the roughness (or other device) used to do this is liable to cause an appreciable and unknown drag penalty, unless great care is taken.
- Model support interference, particularly in aerofoil tests where the interaction between the main flow and the boundary layers on the side walls can seriously affect the 'two-dimensionality' of the experiment and the effective conditions at the measuring station. To minimise this effect it is essential that the aspect ratio of the model should be high (greater than 2, say), or that other precautions - eg end plates, side-wall suction - should be taken.

It is not of course claimed that the experiments referred to below are ideal in this respect, but at least it is known that considerable care has been taken with regard to all the points referred to above.

4.1 Low speed flow: William's method⁵⁶

This method, for calculating low-speed flows over single aerofoils with rear separation, has the following principal features:

- Inviscid flow calculation: the incompressible panel method of Newling and Butter⁷¹ is used.
- Boundary layers and wake: the lag-entrainment method²² is used, without additional terms in the momentum equation or allowance for normal pressure gradients and wake curvature. The wake thickness effect is however included.
- Equations (106) and (106a) are used to specify the shape factor H_1 .
- Matching between the viscous and inviscid components is done through the 'source strength' Σ , using the 'seal-inverse' scheme described in section 3.4 (equation 124).
- The 'relaxation factor' $\Omega^{(p)}$ is defined by equation (126).

The significance of the last feature is illustrated in Fig 11, which shows for a typical case the effect on convergence rate (judged by the lift coefficient C_L) of the number of values of p (see equation (126)) used in the iterative sequence; the value 4 usually seems to give the best results, with reasonable convergence achieved in about 50 cycles.

Two comparisons with experiment are given below. The first example refers to recent tests made by Hastings⁶⁸ in the 13ft x 9ft wind tunnel at RAE, Bedford, on a 1 metre chord model of the aerofoil NACA 4412 spanning the larger dimension of the working section. The chord Reynolds number of the test was 4.2×10^6 and the Mach number 0.18. The main objective of the experiment was to make detailed measurements of the upper surface boundary layer and near wake under separated flow conditions near the stall, using laser anemometry, but detailed pressure measurements were also taken so that the overall lift could be estimated accurately. Comparisons between measured and predicted values of C_L are given in Fig 12, showing excellent agreement right up to $C_{L \max}$; note the very large effect of viscosity as the stall is approached. At the highest angle of incidence at which measurements were made ($\alpha = 12.2^\circ$) the standard of prediction of the detailed pressure distribution is less satisfactory (not shown here), with separation predicted at $x/c = 0.9$ compared with the value 0.8 measured. Calculations at a slightly higher angle of incidence ($\alpha = 13.5^\circ$) are however in better agreement with experiment, as shown in Fig 13. The development of the displacement thickness is also well predicted (Fig 14) at this incidence, but the values of the momentum thickness, and hence of the shape factor H (Fig 15), are in less good agreement. Unfortunately, reliable measurements of drag are not yet available from this experiment to check the theoretical predictions, but a comparison with the standard results for this aerofoil published by Abbott and von Doenhoff⁷² (Fig 16) show reasonably good agreement near $C_{L \max}$; the discrepancies at lower values of C_L are probably due to uncertainties with regard to transition, which was 'free' in the experiment but assumed fixed on the theory at $x/c = 0.015$ (upper), 0.1 (lower).

The second example refers to tests by Render et al⁶⁹ on a model of the Göttingen 797 aerofoil in the 8ft x 6ft wind tunnel at Cranfield Institute of Technology (CIT), as part of a research programme on wing sections suitable for remotely piloted vehicles (RPVs). At the low Reynolds number (0.7×10^6) of these tests, which were made with transition free, the natural variation with incidence of the transition

* One such review - admittedly now out-of-date - is given in Ref 25.

position on both surfaces is of great importance; in the calculations the transition position was estimated by means of Granville's correlation⁷⁴, unless laminar-separation occurs earlier, when Horton's semi-empirical theory⁷⁴ was used. The model almost completely spanned the wind tunnel, with a small gap at the wing tips to allow balance measurements to be made; the effective aspect ratio of the wing was estimated by repeating the tests with a wing of smaller span and comparing the results, and then corrections were made to reduce the measured forces to infinite aspect ratio conditions. The theoretical and experimental lift curves (Fig 17) are in good general agreement, but $C_{L \max}$ is underestimated by about 0.06 (4%). At the highest angle of incidence, 16° , there is also fair agreement between the detailed pressure distributions (Fig 18), particular with regard to the separation position ($x/c = 0.5$); although the pressures near the trailing edge and on the forward part of the upper surface are slightly overestimated. Bearing in mind the discrepancies in C_L already noted, the standard of drag prediction is also satisfactory (Fig 19), even at $\alpha = 16^\circ$ where the drag level reaches 1000 counts, 10 times its value at low incidences.

4.2 High subsonic flows: the VCK methods

During the past ten years a family of methods has been developed at RAE for calculating compressible, viscous flows over aerofoils up to high subsonic Mach numbers, known by the general abbreviation 'VCK' (standing for 'viscous Garabedian and Korn'). The features common to all these methods include:

- The inviscid flow is calculated by the original method of Garabedian and Korn^{8,9}, modified to improve the representation of strong shockwaves by using a partially-conservative difference scheme.
- For the viscous shear layers the lag entrainment method is used; various modifications to it have been gradually incorporated (see below).
- The coupling between the viscous and inviscid elements of the method is done by means of the surface transpiration technique; jump conditions to allow for both thickness and curvature effects are applied in the wake, along a coordinate line through the trailing edge.

In the original VCK method^{34,35} the following additional features should be noted:

- No 'higher-order' terms were included in the momentum integral equation.
- The original formula for H_1 (equation 107) was used.
- In the expression for skin friction (equations 101-113), the low Reynolds number factors were omitted.
- Some attempt was made to allow for the effect of normal pressure gradients, but not in the logical way described in section 3.1.3.
- The direct iterative technique was used, with constant relaxation factor ω , usually chosen to be about 0.1 or less.

In the 'advanced' version, known as AVCK⁵⁸, the following improvements were made:

- All the additional terms in the streamwise momentum integral equation (84a) are included.
- The low Reynolds number factors are included in the expression for skin friction.
- The effect of streamline curvature on turbulence structure is included (see Ref 22, section 3.3).
- The allowance for the effects of normal pressure gradients (section 3.1.3) is fully incorporated.

As we shall see below, this version generally gives improved results, but at the expense of reduced rate of convergence and range of applicability. Consequently, a 'semi-inverse' version of the method has recently been developed⁵⁹, known as BVCK:

- The displacement thickness δ^* , updated by means of Carter's algorithm⁵⁹

$$\frac{\delta^*(n+1)}{\delta^*(n)} = 1 + \Omega \left(\frac{U^v}{U^i} - 1 \right) \quad (\text{with constant } \Omega),$$

is used as input to the inverse boundary layer equations⁴⁹, rather than the source strength Σ as described above.

- The original (H_1, \bar{H}) relation (106) can be replaced by a near-equivalent of the method described in section 3.2.2 (with $\chi = 2$), and with

$$H_1 = 4 + \frac{1}{3}(H - 4) \quad \text{for } H > 4.$$

4.2.1 RAE 2822 aerofoil

To investigate the accuracy of these methods, experiments on two aerofoils have been selected. The first of these, RAE 2822, is 12% thick with a moderate degree of rear camber (see top of Fig 20), and was

tested in the 8ft x 6ft wind tunnel at RAE Farnborough at a chord Reynolds number of about 6×10^6 (see Ref 75). The model was of 2ft (0.61m) chord and aspect ratio 3.0. Transition was fixed by narrow bands of ballotini, usually at 3% chord on both surfaces; in most cases these were chosen to be of the smallest size needed to be effective, so that any spurious increment to the drag should be minimised. The main objective was to obtain detailed measurements of the boundary layer and near wake, so that relatively few test cases are available; results from four of these are shown in Figs 20 to 25. Case 1 (Fig 20) is a relatively simple example; at $M_\infty = 0.679^*$, $C_L = 0.566$, the flow is just supercritical near the leading edge on the upper surface. The pressure distribution (Fig 20a) is well predicted by the standard VCK method; of the two boundary layer integral thicknesses (Fig 20b) δ^* is slightly better predicted by the advanced (AVGK) version, but there is no perceptible difference in the momentum thickness. As a result the calculated values of C_D are almost identical. The table below contains, in addition to the value $C_{D_V} = 2\theta$ normally used for the drag, the alternative estimate C_{D_T} obtained by summing the integrated pressure and skin friction components.

Values of $C_D \times 10^4$ at $M_\infty = 0.679$, $C_L = 0.566$

	C_{D_V}	C_{D_T}	Experiment
Standard	85.5	82.8	85
Advanced	86.4	84.4	

In this particular case (though by no means always), the values of C_{D_T} and C_{D_V} are in good agreement of each other, and also with the experimental measurement, obtained by a total head traverse of the wake one chord downstream of the trailing edge. There is in fact a slightly more significant discrepancy between the two versions with regard to the value of α required to give the specified value (0.566) of C_L : 1.78° by the standard, 1.92° by the advanced version. There is some uncertainty with regard to the size of the wall interference corrections in this slotted-wall wind tunnel; if the quoted value (-0.065) of the factor δ_0 is used then the corrected angle of incidence is 1.86° .

[It should be noted that an attempt has been made in this and most other cases to allow for the effect of the flow curvature induced by the walls in the vicinity of the model by adding an equal and opposite increment Δz_c to the camber line of the model used in the calculation. Thus, if the interference factor δ_1 , is defined as usual by

$$\delta_1 = \frac{\beta h^2}{C_L c^2} \frac{\partial(W_1/U_\infty)}{\partial(x/c)}$$

(where h is the tunnel height, $\beta = \sqrt{1 - M_\infty^2}$ and W_1 is the induced upwash),

$$\text{then } \Delta z_c/c = A \frac{x}{c} \left(1 - \frac{x}{c}\right) \quad \text{with } A = \frac{1}{2} \frac{\delta_1}{\beta} \frac{C_L(c/h)}{c}$$

The effect of this correction is usually small, and does not always improve the agreement between theory and experiment, but it should certainly be included.]

The next two cases, 7 and 9, are both at a Mach number of about 0.73; in Case 7 ($C_L = 0.66$, $M_\infty = 0.729$) there is a shock wave of moderate strength on the upper surface, a considerably stronger one in Case 9 ($C_L = 0.80$, $M_\infty = 0.734$), though the boundary layer is still attached over the whole chord. The agreement between theoretical and experimental values of pressure (Fig 21) is excellent on the lower surface and good over most of the upper surface; again, there is little difference between the results of the standard and advanced versions. As for Case 1, the advanced version does predict slightly higher values of δ^* (Fig 22), in better agreement with experiment; the values of θ , and hence of the viscous drag coefficient C_{D_V} are almost the same. Again, here is slightly more difference in the predicted lift curves (Fig 23). There is even more uncertainty than for Case 1 with regard to the wall interference corrections on α (see Ref 79), but at least a plausibly good agreement between theory and experiment is indicated. The values of drag shown in Fig 24 have been obtained by adding to the viscous component C_{D_V} the wave drag C_{D_W} calculated by the field integral method of Ref 6 (section 2.2.1, equation 26a); in this case the author's approximate formula (equation 37) gives almost identical results. The agreement with experiment is reasonably satisfactory; there is a slight anomaly in the measurements at $C_L = 0.8$ because the diameter of the ballotini particles used to fix transition in Case 9 was three times that in Case 8, yet the drag is lower.

The last example for this aerofoil, Case 10 - at the same angle of incidence as Cases 8 and 9 but 0.02 higher in Mach number - is the only one of this series in which the shock wave is strong enough to separate the boundary layer at its foot ($x/c = 0.7$), reattaching subsequently at $x/c = 0.8$. As a result, neither of the direct iterative methods (VCK and AVGK) will converge, in spite of the use of the

* A blockage correction of +0.004 has been applied in all the cases shown here.

spurious (H_1, H) relation (106). The semi-inverse version, however, converges without difficulty; but the resulting pressure distribution (Fig 25) is less satisfactory than in the other cases. The shock wave is about 5% chord too far back, and the pressure level behind it is uniformly high by about 0.1 in C_p . The reason for this is that the displacement thickness behind the shock is underestimated; whether this could be remedied by including additional mesh points in the calculations near the foot of the shock, or whether a special treatment of the shock/boundary layer interaction like that proposed by Stanewsky and Inger⁸⁰ is essential, remains to be seen. The momentum thickness is also underestimated, and so as a result is the overall drag: theory, 0.0215 experiment 0.0242.

4.2.2 RAE 5225 aerofoil

The second aerofoil, RAE 5225 (Fig 26), is 14% thick and has considerably more rear camber than RAE 2822. The additional rear loading that this produces involves a severe adverse pressure gradient from 50% to 80% chord on the lower surface, causing high values of H and thus presenting a difficult problem to the boundary layer method. The model, of 25 inches (0.635m) chord and aspect ratio 3.8, was tested in the 8ft x 8ft wind tunnel at RAE Bedford, at Reynolds numbers 6×10^6 and 20×10^6 . There are two features of this experiment which make it particularly suitable as a test case for CFD methods:

(i) Transition was fixed (at 5% chord), by air injection through small holes normal to the surface. This technique causes minimal disturbance to the boundary layer and hence the least possible spurious increment in drag.

(ii) The fact that the wind tunnel has solid walls makes it possible to calculate the wall interference effects - blockage, incidence correction and induced curvature - with a greater degree of precision than that normally possible with ventilated walls, even though some of these corrections will be larger (see Ref 78).

In spite of the more advanced nature of the aerofoil design, at the higher Reynolds number (20×10^6) there is again excellent agreement between calculations of pressure by the standard (VGK) method and the experimental measurements (Fig 27). The four cases shown here are all at a lift coefficient around 0.55, with Mach number progressively increasing from a subcritical case (Fig 27a) through to one where there is a fairly strong shock wave on the upper surface (Fig 27d). At the lower Reynolds number (6×10^6), however, the boundary layers are quite close to separation on both surfaces, and consequently (Fig 28) the standard method (full line) now gives less satisfactory results, both on the lower surface around 70%-80% chord and on the upper surface near the trailing edge; but the situation is much improved by the inclusion of higher order effects (AVGK - broken line).

No boundary layer measurements are available from this experiment, but far more data points were taken than for RAE 2822, and this allows a thorough assessment to be made of the prediction of the overall forces. This is shown in Figs 29 and 30 for the drag and lift respectively, at a free stream Mach number of 0.735. At the higher Reynolds number there is little difference between the values of C_D predicted by the standard and advanced versions, and the agreement with experiment is good, about 1 to 2 counts below the measured values. At $Re = 6 \times 10^6$, however, there is a greater difference between the two versions and even the AVGK method underestimates the drag by 4 to 5 counts (about 5%). The situation with regard to lift (Fig 30) is similar, but the discrepancies in the values of α required for a given value of C_L are relatively somewhat larger than in the case of the drag.

5.1 Methods and results for wing-body combinations

Following up on earlier work⁸⁴ at RAE in which a 'transonic small perturbation' (TSP) inviscid code was successfully coupled with Smith's three-dimensional boundary layer method⁸³, an extension of the same technique - with the inviscid element replaced by the more accurate full potential (FP) code of Forsey and Carr⁸⁵ - has recently been developed by Arthur⁸¹ and Firmin; this is known as the VFP (viscous full potential) method. Its principal features are as follows:

- The inviscid flow is calculated by a modification of the ARA FP method⁸⁵. In this, an 'O-H' grid is formed by conformally mapping (using the fast Fourier technique) the individual wing sections across the span into circles, the fuselage (if present) having been first transformed into a vertical slit in the plane $y = 0$ by a Joukowski transformation. In this non-orthogonal coordinate system a non-conservative (or partially conservative*) finite difference form of the full potential equations is solved by a successive line relaxation iterative scheme.
- The inadequate representation of the front and rear ends of the fuselage is partially remedied by making a separate calculation for the fuselage alone, and from this deriving at each spanwise station a mean Mach number increment, averaged over the chord, which is used to modify the upstream boundary conditions for the wing-body method.
- The boundary layer and wake are calculated by Smith's entrainment method²³, including 'lag' effects⁶⁹. The original equation of Green et al²² (equation 106, section 3.2.2) is used to define H_1 , together with Mager's approximation⁶² for the cross-flow profiles (equation 131, section 3.5). Although both these assumptions are known to be unrealistic as the flow approaches separation, they do have the advantage that numerical stability problems are delayed, thus allowing the use of a direct iterative scheme in situations where it would otherwise break down.
- Matching between the inviscid and viscous components is achieved by modifying the normal boundary conditions in the inviscid code to allow the 'surface transpiration' representation of the

* In the calculations described below (Fig 32), the partially-conservative factor λ was set at 0.5.

displacement effect to be used. Jump conditions in the wake are added to take into account thickness, but not curvature, effects. No other 'higher-order' effects are included.

- The direct iterative technique (section 3.4) is used, with constant relaxation factor ω , normally taken to be between 0.03 and 0.1.
- No allowance is made for the boundary layer on the fuselage, whose drag would therefore need to be estimated by other means.
- Calculations are usually made through a sequence of three meshes, the finest of which has 160 points round the chordal sections, 36 points spanwise and 20 points in the outward normal direction. The outer boundary condition (zero perturbation potential) is nominally applied at 'infinity', but the sparsity of points in the far field can lead to a loss of lift in the inviscid part of the calculation which can be as large as 10% for wings of high aspect ratio.

The example chosen to illustrate the use of this method is a wing-body combination, typical of a modern transport aircraft design, shown in Fig 31. The wing is of aspect ratio 8, the leading edge sweep is 28° and the trailing edge sweep over the outer panel is 14° ; there is a 'crank' in the trailing edge at $\eta (= y/s) = 0.41$, inboard of which the sweep is reduced to 3.5° . The configuration has been tested in the 12ft x 8ft wind tunnel at RAE Bedford in two forms, as a floor-mounted half-model (with half-fuselage) and as a complete model mounted on a conventional rear sting support. The maximum Reynolds numbers (based on mean wing chord) for the two models were 12×10^6 and 6×10^6 respectively; transition was fixed on both surfaces by roughness bands at 5% chord. Detailed pressures were measured at the seven spanwise stations shown in Fig 31, with 36 pressure holes at each station.

Typical results for the half-model at $Re_c = 12 \times 10^6$, $M_\infty = 0.78$ are shown in Fig 32 at two values of the overall lift coefficient C_L , 0.57 and 0.65, at the higher of which the wing is close to its separation boundary. The calculations by the VFP method were matched with experiment as regards C_L rather than α , the values of which are about 0.2° higher than their experimental counterparts. This contrasts with the situation that would have been expected from experience in two dimensions (cf Fig 30) where, with the standard VFK method to which the VFP method most closely corresponds, the corresponding values of α would have been about 0.2° lower than experiment. The reason for this discrepancy is thought to be that, in contrast to the Garabedian and Korn method used in two dimensions, the FP method does underestimate the lift coefficient in inviscid flow for wings of high aspect ratio, as noted above.

In discussing the comparison between theory and experiment shown in Fig 32, two general points may be made first: (a) although on the lower surface the agreement is generally very good, examination of the results ahead of $x/c = 0.5$ suggests that the Mach number increment used to simulate finite-body effects (which varied between 0.013 at the root to 0.006 at the tip) may have been slightly underestimated; and (b) the pressures on the upper surface near the trailing edge are uniformly overestimated, by about 0.05 in C_p . This would have been expected from experience in two dimensions, since the values of \bar{H} near the trailing edge are quite high (>2.5) over most of the span. Looking at the upper surface results at the four successive spanwise stations (1), (3), (5) and (7) included here, we see that at the root (1) there is good overall agreement and that the weak shock occurring at $x/c = 0.4$ at the higher lift coefficient is well predicted. At station (3), near the position of the trailing edge crank, the near-isentropic (apart from a few wiggles) compression over the forward part of the chord is well predicted, as is the weak shock that develops at $x/c = 0.5$ at the higher value of C_L . Behind this shock (and similarly at the two outboard stations) the pressure is apparently overestimated (by about 0.07 in C_p), but it should be noted that there are unexplained discrepancies of that order in this region between the experimental results for the half and full models, admittedly at a lower Reynolds number (6×10^6). At station (5), in the middle of the outer wing panel, the position of the shock - now fairly strong - is perfectly predicted* and so is the pressure ahead of it; and it is this region of the wing that produces most of the wave drag, as we shall see shortly. Behind the shock there are again discrepancies of about 0.05 in C_p but the point made with regard to station (3) still applies. At the outermost station (7) the pressures over the front half of the chord are again well predicted but the shock position is too far back - about 0.05 in x/c at $C_L = 0.57$, 0.1 at $C_L = 0.65$. In fact, at the higher lift coefficient the shock has clearly caused the flow to separate at its foot, to a greater extent even than for Case 10 on the RAE 2822 aerofoil considered in section 4.2; and yet the present method produces nearly as plausible a result as did the semi-inverse BVGK method for the two-dimensional example (cf Fig 25).

This comparison between theory and experiment has been discussed in some detail because no reliable drag measurements could be obtained from the half-model tests; so that for the purpose of assessing the accuracy of drag prediction we must turn to the complete model, for which conventional balance measurements are of course available. Unfortunately, at the lower Reynolds number of these tests (6×10^6), systematic calculations by the VFP method have not yet been made. However, from what we have seen above it is reasonable to assume that its predictions of pressure would be entirely adequate for use in the estimation of drag by the techniques described in section 2, none of which require a knowledge of anything beyond the detailed pressure distribution on the wing. We shall therefore use the measured pressure distribution on the complete model for illustrative purposes, in exactly the same way as would be done in the course of a completely theoretical prediction of drag.

First, the procedure explained in section 2 for estimating the three components of drag - wave, vortex and viscous - will be presented in some detail for $M_\infty = 0.78$, and then results for other Mach numbers will be briefly described. In Fig 33 upper surface pressure distributions measured at this Mach

* see footnote on page 45.

number on the complete model⁸³ are shown for four cases, A to D, covering a range of values* of C_L from 0.32 to 0.66, over which the flow develops from a situation (A) where it is only just supercritical (in the swept wing sense) to one (D) where a shock system has developed on the outer wing strong enough to cause shock-induced separation. The general pattern of flow development is naturally similar to that on the half-model at the higher Reynolds number (Fig 32), but there are some additional features worth mentioning. At the root (station (1)), there is an additional expansion near $x/c = 0.4$ which is thought to be spurious, caused by a small manufacturing imperfection in body shape; it is not present on the half model, and the weak shock wave that it causes extends over only a small part of the wing, so that it can be safely neglected in the estimation of wave drag. Except for this, the whole inner wing panel, from the trailing crank station (3) inboard, remains satisfactorily shock-free up to the highest incidence (D). By contrast, over the outer wing panel a clear shock wave is visible for Case (B), and by Case (D) it is sufficiently strong to cause the boundary layer at its foot to separate, from station (5) ($\eta = 0.65$) out to the tip.

Clearly, there is no difficulty in identifying the shock system, both in position and strength, with sufficient precision to be able to carry out the steps involved in estimating the wave drag by the approximate method given in section 2.2.1, as described below.

5.1 Estimation of wave drag (C_{D_w})

The positions of the shock wave on the wing platform are shown in Fig 34, for the three cases B, C, and D where it can be clearly identified. Note the steady rearward movement of the shock as the incidence increases, except near the tip where this process is reversed by the onset of separation. At each station, therefore, we can determine the local shock sweep Λ_{sh} and upstream pressure coefficient C_{p_1} , and from equation (45) derive M_{1n} , the component of upstream Mach number normal to the shock. Values of M_{1n} are shown in Fig 35; in Case D these reach 1.4 near the tip, again clearly indicating the likelihood of shock-induced separation. Next, the local wave drag coefficients, $C_{D_w}(\eta)$, can be found from equation (46); these are shown in Fig 36. Notice that in Case B, even though the shock on the outer wing could be clearly identified from the pressure distribution (Fig 33), the wave drag that it produces is extremely small. By contrast, in Case D the predicted values of C_{D_w} exceed 170 counts near the tip, but remain small over the inner wing panel. Perhaps more informative is Fig 37, which shows the values of $C_{D_w}(\eta) c(\eta)/\bar{c}$, the effective contribution of a particular station (η) to the overall wave drag. Because of the wing taper, this is seen to peak at $\eta = 0.5$ rather than at the tip where C_{D_w} itself is greatest.

Finally, the local values of Fig 37 can be integrated across the span to obtain the total wave-drag coefficient, C_{D_w} , shown in Fig 38 as it varies with C_L ; in addition to Cases B, C and D described above, results from four intermediate cases are also shown. Clearly, for this Mach number (0.76) the onset of wave drag occurs at $C_L \approx 0.4$; and because the shock wave system is confined to the outer wing panel, the subsequent increase in C_{D_w} is less than half that of the local values shown in Fig 36.

5.2 Estimation of vortex drag (C_{D_i})

The vortex drag coefficients have been obtained in the conventional way described in section 2.2.2, using equation (51). In this formula, the spanwise variation in $C_L(\eta)$ required has been derived from the experimental values of C_L at the seven measuring stations, plotting cC_L/\bar{c} against $\cos^{-1}(\eta)$ and interpolating by the 'cubic/circle' method, as shown in Fig 39. As explained in Ref 83, alternative ways of allowing for the effect of the fuselage on the vortex drag have been investigated; the results showed very little variation in the values of C_{D_i} (1 to 2 counts at most), and the scheme shown in Fig 39, in which the values of cC_L/\bar{c} are simply extrapolated smoothly to $\eta = 0$ and then used in the 'wing-alone' formula (51), is thought to be as accurate as any in this particular case.

The results of these calculations (taken from Ref (83)) are shown in Fig 40 in the form of 'excess vortex drag', defined by subtracting from the actual value the 'ideal' vortex drag coefficient (for

$$\text{elliptic loading), } C_{D_i}^2/(\pi A); \quad \Delta C_{D_i} = C_{D_i} - \frac{C_L^2}{\pi A} = \frac{C_L^2}{\sigma \pi A} \quad (\text{see equation (52)}).$$

It appears that the excess vortex drag remains roughly constant, at between 4 and 5 counts, for values of C_L up to 0.65. If an induced drag factor K is defined in the usual way by $K = C_{D_i} \pi A / C_L^2 = 1 + \delta$, then K is seen to decrease initially as C_L increases, particularly between $C_L = 0.45$ and 0.6. The reason for this is that the appearance of a shock wave on the outer wing initially increases the local lift and hence brings the spanwise load distribution closer to the ideal elliptic shape. For still higher values

* Values of C_L quoted here were obtained from balance measurements.

of $C_L (>0.65)$, the shock-induced separation already noted near the wing tip then reduces the loading there and hence causes the vortex drag factor to increase rapidly.

5.3 Estimation of viscous drag (C_{D_V})

The third component of drag, due to the boundary layer on the wing, is estimated as explained in section 2.2.3. The relevant integral parameters (θ_{ij} etc) at the trailing edge, required in this method, were calculated from the measured chordwise pressure distributions (on both upper and lower surfaces) by an 'infinite tapered wing' version of the lag-entrainment method; this allows for the effects of sweep and taper on the boundary layer development on the assumption that the spanwise variation of pressure distribution is small - clearly a reasonable one in the present case except perhaps very close to the root or tip of the wing. The local values of the viscous drag coefficient, $C_{D_V}(n)$ were then obtained from equation (72) (section 2.2.3).

Fig 41 shows three typical results for $M_\infty = 0.78$. The local values of C_{D_V} (full lines) increases steadily from root to tip, partly because the local chord Reynolds number is decreasing and partly because the adverse pressure gradients on the upper surface become more severe (see Fig 33). The effective local drag contribution, $C_{D_V} c/\bar{c}$ (dashed line), on the other hand, decreases because of the taper effect, so that it is the inner half of the wing which contributes the greater proportion of the viscous drag, in contrast to the situation as regards wave drag.

These viscous drag contributions can now be integrated across the span to obtain the total viscous drag coefficient of the wing, C_{D_V} . The variation of C_{D_V} with C_L at $M_\infty = 0.78$ is shown in Fig 42. Just as in two dimensions (cf Fig 24), there is a slow but steady increase in C_{D_V} as the lift increases. For C_L greater than about 0.55 the calculated values of C_{D_V} become increasingly unrealistic (they actually begin to decrease) because, as we saw earlier, the flow near the tip has started to separate; and under these circumstances it is well known that to use a standard first-order boundary-layer method together with a measured pressure distribution will inevitably lead to serious underestimation of the drag. Instead, a simple extrapolation has been guessed (dotted line); this may well be an underestimate of the rate of increase of viscous drag caused by separation.

5.4 Comparison with experimental measurements of total drag

In Fig 43 are collected together the values of the three components of wing drag obtained in the way discussed in sections 5.1 to 5.3: the wave drag, the vortex (induced) drag and the viscous drag. For eventual comparison with balance measurements on the complete wing-body combination, we need also to know the drag of the body. In the present exercise this has simply been taken from separate balance measurements, on the body alone. This is of course not precisely the same as the drag of the body when the wing is mounted on it, but at subsonic speeds the error involved here is likely to be small. It will be seen from Fig 43 that, over the range of lift coefficient considered here (0 to 0.7) the body drag is effectively constant (about 80 counts) and is close to the viscous drag of the wing. At a value of C_L typical of long-range cruise conditions (say 0.5), the vortex drag is also of a similar size, while as noted in section 5.1 the wave drag is just beginning to become appreciable (less than 10 counts).

We now come to the crucial point: how does the sum of the four drag components,

$$C_{D_T} = C_{D_B} + C_{D_V} + C_{D_i} + C_{D_W} ,$$

estimated in the fairly simple way described above, compare with the total drag measured on the balance? Such a comparison is given below in two ways. Fig 44 show the total drag coefficients, theoretical and experimental, plotted against C_L .

[Note that the value of C_L quoted here, and used in the calculation of the main part, $C_L^2/\pi A$ of the vortex drag, are obtained from the balance measurements rather than from the integrated wing lift.]

We notice first that, for values of C_L below 0.4 when there is no wave drag, the general predicted drag level is about 8 counts (5%) lower than the measured values - a creditable standard of accuracy that would be difficult to better, even in two dimensions, at this Reynolds number (compare with Fig 29) - and that the increase of drag with lift is well predicted by the 'classical' vortex drag theory. For higher values of C_L , as the wave drag appears and starts to increase, the agreement between 'theory' and experiment actually improves, indicating that the wave-drag component is being slightly overestimated by the present approximate method. This point is brought out more clearly in Fig 45, which shows the respective values of

$$\Delta C_D = C_{D_T} - C_L^2/\pi A ,$$

on a larger scale. Here, nearly all the apparent drag increase is due to viscous and wave drag, mostly to the latter.

A similar analysis has been carried out at other Mach numbers by the staff of the Engineering Sciences Data Unit. Comparisons with experiment, analogous to Fig 45, are shown in Fig 46 for $M_\infty = 0.80$ and in Fig 47 for $M_\infty = 0.82$. At the lower Mach number (Fig 46) the conclusions are the same as those given above: at low lift coefficients, between 0.2 and 0.3 where the onset of wave drag occurs, the drag is again underestimated by about 5%, and again the wave drag component appears to be overestimated when it becomes important. The failure to predict the increase in drag for C_L below 0.2, due to wave drag from the lower surface, is largely caused by the sparsity of pressure points in the region of the shock wave (see Fig 31) and the consequent inability to estimate the upstream Mach number properly. At $M = 0.82$ (Fig 47), there is now no condition in which the wave drag disappears completely; as the lift is reduced a shock appears on the lower surface before the one on the upper surface has vanished. At the condition of minimum wave drag ($C_L = 0.25$) the total drag is again underestimated by about 8 counts, but the tendency to overestimate the wave drag at higher values of C_L has disappeared; although the flow has now started to separate near the wing tips when there is less overall wave drag than in the two previous cases, so that what we are seeing may be as much an underestimation of viscous drag as a correct estimator of wave drag.

Similar analyses are also available for $M_\infty = 0.70, 0.74, 0.79$ and 0.81 , and the results of these are summarised in the two concluding figures. Fig 48 shows a 'carpet' of values of the estimated wave-drag coefficient C_{D_w} , plotted against the two variables M_∞ (from 0.70 to 0.82) and C_L (from 0.2 to 0.6); some minor smoothing has been needed to obtain these curves. One point of interest is that, for values of C_L greater than 0.4, appreciable wave drag has already appeared at $M_\infty = 0.70$ (30 counts at $C_L = 0.6$); this remains roughly constant until, at a value of M_∞ depending on C_L , a really rapid rise in wave drag occurs. This unexpected wave drag at the lower Mach numbers is caused by high leading edge suction peaks, leading to shock waves of appreciable strength in the region 5% to 10% chord.

Finally, in Fig 49 the overall 'excess' drag coefficient, $C_{D_T} - C_L^2/\pi A$, is compared with experiment in a similar way. The 'theoretical' results shown here are both including (full line) and excluding (dashed line) the wave drag contribution. The most important feature is that for all values of C_L between 0.2 and 0.6, the variation of drag with Mach number is uniformly well predicted, until the onset of appreciable boundary layer separation over the outer part of the wing (indicated by a broken line). As noted above, the absolute accuracy of the prediction improves with increasing C_L , the deficit being about 8 counts (5% of total drag) at $C_L = 0.2$ decreasing to less than 1% at $C_L = 0.6$. However, as already suggested, this apparent improvement comes about as a result of cancellation of errors: an overestimation of the wave drag compensates for an underestimation of the viscous drag contribution that, for this particular configuration, appears to occur throughout the range of conditions considered - as indeed it does in two dimensions for aerofoils of comparable standard at this rather low Reynolds number (6×10^6), as noted in section 4 above.

Attempts are currently in progress to apply the same technique to wings of lower aspect ratio, typical of military combat aircraft. The same insight into the sources of unwanted drag are still provided but, as might perhaps be expected, preliminary results suggest that the overall errors involved are somewhat greater than those obtained with the example given above. To reduce these to an acceptable level, it will probably be necessary to go to a full 'field' technique for calculating the wave drag (eg equation (31), section 2.2.1), and to improve the representation of viscous effects on both the wing and the fuselage.

6 CONCLUSIONS

- (1) For the class of problems considered in this paper - flows up to high subsonic speeds on conventional wings with a modest degree of separation - it appears at the present time to be more satisfactory, both as regards accuracy and the insight provided to the designer, to estimate the drag by the 'far field' technique (section 2.2) rather than by the more obvious 'direct' method (section 2.1). And the approximations derived in 2.2 allow this to be done with a reasonable degree of accuracy from a knowledge only of the pressure distribution on the wing, as shown in sections 4 and 5.
- (2) Nevertheless, in really difficult cases, for example when extensive regions of separated flow are present, there seems no alternative to the direct approach, used in conjunction with numerical solutions of the full time-averaged Navier-Stokes equations. Authors of CFD codes for such problems should therefore be encouraged to pay much more attention to the prediction of overall forces; so often they appear to be content with demonstrating reasonable overall agreement with regard to (say) the pressure distribution for a given value of C_L , without considering whether the implied values of drag are of even tolerable accuracy.
- (3) Equal attention needs also to be paid to the accuracy of drag measurement; in particular
 - to ensuring that transition is fixed with the minimum unnecessary disturbance to the boundary layer,
 - to improving the accuracy of prediction of the effects of wind-tunnel wall interference or to eliminating them completely and indisputably; and
 - to minimising the interference effects of model support systems or (in two dimensions) of the side-wall boundary layers, and of checking the two-dimensionality of the flow.

(4) In two dimensions a standard of accuracy in drag prediction has been demonstrated which depends, very roughly, on the state of the boundary layer at the trailing edge as measured by the value of the shape factor (R_{τ}) there. If this is less than about 2 the agreement with experiment is excellent, but for higher values the accuracy deteriorates progressively even with the most advanced methods currently available, particularly when boundary layer separation takes place. To remedy this situation, further improvements in our ability to predict separated flows, whether shock-induced or otherwise, are clearly needed.

(5) In three dimensions the relatively simple technique of analysis described in section 2.2, which as shown in section 5 can be applied to measured as well as to calculated pressure data, provides a valuable insight into the sources of the three components of wing drag which in itself should be useful to designers seeking to reduce them. The overall standard of accuracy has been shown to be comparable to that achieved in two dimensions for wings of high aspect ratio (≥ 8 say), but has been found to deteriorate for lower aspect ratios (around 4). Improvements should be possible when full 'field' methods are available for calculating the wave drag, when better account is taken of 'higher-order' effects in boundary layer and viscous-inviscid interaction theory, and when the viscous flow over the fuselage and its interaction with that on the wing are properly treated.

Acknowledgments

I am indebted to my colleagues P.R. Ashill, M.C.P. Firmin, B.R. Williams and R.F. Wood for helpful advice and for providing unpublished results. The views expressed in this Paper are however my own and not necessarily those of the Royal Aircraft Establishment.

Appendix

THE EFFECT OF NORMAL PRESSURE GRADIENTS

As shown in section 3.1.3, the difference between the pressures in the inviscid and viscous flows, due to normal pressure gradients, can be approximated by

$$\Delta p \equiv p_i - p = \kappa^* \int_z^\delta (\rho_e U_e^2 - \rho U^2) dz + \int_z^\delta (\kappa^* - \kappa) \rho U^2 dz \quad (A1)$$

here the normal stress term $\overline{\rho u'^2}$ has been omitted.

We want to show that, for flows approaching separation ($H > 2$, say), the second integral in (A1) is small enough to be neglected. To do this we must first make some assumption about the variation of $(\kappa^* - \kappa)$ across the boundary layer. We know that this must tend smoothly to zero at the outer edge, $z \rightarrow \delta$, at least as fast as $(1 - z/\delta)^2$, and have the value $(\kappa^* - \kappa_w)$ at the wall, $z = 0$. The simplest expression with this property is just

$$\kappa^* - \kappa = (\kappa^* - \kappa_w)(1 - \zeta)^2,$$

where $\zeta = z/\delta$.

If we make this assumption, write $u = U/U_e$ and neglect density changes, then we have

$$\begin{aligned} \Delta p / \kappa^* \delta \rho_e U_e^2 &= \int_\zeta^1 (1 - u^2) d\zeta + \left(1 - \frac{\kappa_w}{\kappa^*}\right) \int_\zeta^1 (1 - \zeta)^2 u^2 dz \\ &= f_1(\zeta) + \left(1 - \frac{\kappa_w}{\kappa^*}\right) f_2(\zeta), \quad \text{say.} \end{aligned} \quad (A2)$$

To evaluate the integrals f_1 and f_2 two alternative simple expressions for the velocity profile can be used:

- the power law profile $u = \zeta^p$, where $p = \frac{1}{2}(H - 1)$; this is sensible for values of H up to about 2,
- the 'wake' term of the Coles profile, $u = 1 - C(1 + \cos \pi\zeta)$, where $C = \frac{2}{3}(H - 1)/H$; this becomes increasingly realistic as separation is approached ($H = 4$).

Results obtained with these two simple profiles are given below.

(a) $u = \zeta^p$

In this case $f_1 = \frac{2p}{2p+1} - \zeta \frac{\zeta^{2p+1}}{2p+1}$ (A3)

and

$$f_2 = \frac{1}{(p+1)(2p+1)(2p+3)} - \frac{\zeta^{2p+1}}{2p+1} + \frac{\zeta^{2p+2}}{p+1} - \frac{\zeta^{2p+3}}{2p+3} \quad (A4)$$

Values of f_1 and f_2 are given in the table below for $H = 2$ and 3.

ζ	$H = 2$			$H = 3$		
	f_1	f_2	f_2/f_1	f_1	f_2	f_2/f_1
0	0.500	0.083	0.17	0.667	0.033	0.05
0.2	0.320	0.068	0.21	0.469	0.031	0.07
0.4	0.180	0.040	0.22	0.288	0.023	0.08
0.6	0.080	0.016	0.19	0.139	0.011	0.08
0.8	0.020	0.002	0.11	0.037	0.002	0.05
1.0	0	0		0	0	

$$(b) \quad u = 1 - C(1 + \cos \pi \zeta)$$

Writing $\pi \zeta = \theta$, the result is

$$f_1 = (1 - A)(1 - \zeta) - B \sin \theta + D \sin 2\theta \quad (A5)$$

$$f_2 = \frac{1}{3} A(1 - \zeta)^3 + B \left\{ (1 - \zeta)^2 \sin \theta - \frac{2(1 - \zeta)}{\pi} \cos \theta - \frac{2}{\pi^2} \sin \theta \right\} \\ + D \left\{ -(1 - \zeta)^2 \sin 2\theta + \frac{(1 - \zeta)}{\pi} \cos 2\theta + \frac{1}{2\pi^2} \sin 2\theta \right\}, \quad (A6)$$

where $A = (1 - C)^2 + \frac{1}{2} C^2$, $B = 2C(1 - C)/\pi$ and $D = C^2/(4\pi)$.

Values of f_1 and f_2 are given in the table below for $H = 2, 3$ and 4 ,

ζ	$H = 2 (C = \frac{1}{3})$			$H = 3 (C = \frac{4}{9})$			$H = 4 (C = \frac{1}{2})$		
	f_1	f_2	f_2/f_1	f_1	f_2	f_2/f_1	f_1	f_2	f_2/f_1
0	0.500	0.079	0.16	0.593	0.041	0.069	0.625	0.030	0.05
0.2	0.325	0.059	0.18	0.397	0.038	0.095	0.425	0.030	0.07
0.4	0.171	0.038	0.22	0.215	0.029	0.135	0.235	0.025	0.11
0.6	0.060	0.016	0.26	0.078	0.014	0.18	0.087	0.013	0.153
0.8	0.008	0.030	0.011	0.002	0.21	0.0125	0.002	0.19	
1.0	0	0		0	0		0	0	

It is clear from these tables that, whichever form of the velocity profile is chosen, the function $f_2(\zeta)$ has a maximum value (at the wall), of about 0.08 for $H = 2$ decreasing to 0.03 for $H = 4$, that is less than $1/6 f_1(0)$ for $H = 2$ or $1/20 f_1(0)$ for $H = 4$. The second term in equation (A2) can therefore be safely neglected compared with the first for $H > 2$; and in particular the validity is confirmed of the approximation suggested in section 3.1.3:

$$\frac{\Delta p_w}{\rho_e U_e^2} = \kappa^* (\theta + \delta^*), \quad (86)$$

where $\Delta p_w = p_{1w} - p_w$.

We can also use the same argument to check the validity of the approximation to $\int_0^\delta \Delta p d\zeta$, required in equation (84a). We find that

$$\int_0^\delta \Delta p d\zeta / (\kappa^* \delta^2 \rho_e U_e^2) = I_1 + \left(1 - \frac{\kappa_w}{\kappa^*}\right) I_2 \quad (A7)$$

where $I_1 = \int_0^1 f_1(\zeta) d\zeta$ and $I_2 = \int_0^1 f_2(\zeta) d\zeta$.

$$\text{For profile (a), } I_1 = \frac{H-1}{2(H+1)}$$

$$\text{and } I_2 = \frac{2}{(H+1)(H+2)(H+3)}$$

$$\text{so that } I_2/I_1 = \frac{4}{(H-1)(H+2)(H+3)},$$

which is less than $1/5$ for H greater than 2.

$$\text{For profile (b), } I_1 = C \left(1 - \frac{4}{\pi^2}\right) - C^2 \left(\frac{3}{4} - \frac{4}{\pi^2}\right)$$

$$\text{and } I_2 = \frac{1}{12} A + \frac{B}{\pi} \left(1 - \frac{12}{\pi} - \frac{D}{2\pi} \right).$$

H	C	I_1	I_2/I_1
2	$\frac{1}{3}$	0.160	0.19
3	$\frac{4}{9}$	0.196	0.105
4	$\frac{1}{2}$	0.211	0.08

As the above table shows, as before $I_2/I_1 < 0.2$ when $H > 2$.

The approximation
$$\int_0^\delta \Delta p d\zeta = \kappa^* \int_0^\delta dz \int_z^\zeta (\rho_e U_e^2 - \rho U^2) dz \quad (A8)$$

is therefore satisfactory. We can now assess the validity of East's suggestion³² that

$$\int_0^\delta \Delta p d\zeta = \kappa^* \rho_e U_e^2 \cdot \frac{1}{2} (\theta + \delta^*)^2.$$

To do this we have to compare I_1 with $\frac{1}{2} \left(\frac{\theta + \delta^*}{\delta} \right)^2$. We obtain the following values:

H	<u>Profile (a)</u>		<u>Profile (b)</u>	
	I_1	$\frac{1}{2} \left(\frac{\theta + \delta^*}{\delta} \right)^2$	I_1	$\frac{1}{2} \left(\frac{\theta + \delta^*}{\delta} \right)^2$
2	$\frac{1}{6}$	$\frac{1}{8}$	0.160	0.125
3	$\frac{1}{4}$	$\frac{2}{9}$	0.196	0.176
4			0.211	0.195
5			0.219	0.205

Bearing in mind that only a rough approximation is required, we see that this is satisfactory for $H > 2$.

REFERENCES

- | <u>No.</u> | <u>Author</u> | <u>Title, etc</u> |
|------------|---|---|
| 1 | C.N.H. Lock
W.F. Hilton
S. Goldstein | Determination of profile drag at high speeds by a pitot traverse technique.
A.R.C. R&M 1971. (1945) |
| 2 | E.C. Maskell | Progress towards a method for the measurement of the components of the drag of a wing of finite span.
RAE Technical Report 72232 (1973) |
| 3 | J. van der Vooren
J.W. Slooff | On inviscid isentropic flow models used for finite difference calculations of two-dimensional transonic flows with imbedded shock waves about aerofoils.
NLR MP 73024U (1973) |
| 4 | K. Oswatitsch | Der Verdichtungsstoss bei der stationären Umströmung flacher Profile.
ZAMM 29, 129-141 (1949).
(see also 'Gas Dynamics', Academic Press, p209) (1949) |
| 5 | R.C. Lock | An approximate method for estimating the wave drag of an aerofoil in subsonic/transonic flow.
RAE Technical Report to be issued (1985) |
| 6 | A. Bocci
Christine Billing | Unpublished work at ARA. |
| 7 | A.F. Jones
M.C.P. Firmin | Unpublished work at RAE. |
| 8 | P.R. Garabedian
D.G. Korn | Analysis of transonic aerofoils.
Comm. Pure App. Math., 24, 841 (1971) |
| 9 | F. Bauer
P. Garabedian
D. Korn | A theory of supercritical wing sections.
Springer-Verlag, Berlin (1972) |
| 10 | R.C. Lock | A modification to the method of Garabedian and Korn.
In 'Numerical methods for the computation of transonic flows with shock waves'.
Fredr-Vieweg and Sohn, Braunschweig (1980) |
| 11 | R.C. Lock | An assessment of methods for calculating the wave drag of aerofoils using an Euler program.
RAE Technical Memorandum Aero 1958 (1984) |
| 12 | J.L. Steger
B.S. Baldwin | Shock waves and drag in the numerical calculation of isentropic transonic flow.
NASA TN D-6997 (1972) |
| 13 | N.J. Yu
H.C. Chen
S.S. Samant
P.E. Rubbert | Inviscid drag calculations for transonic flows.
AIAA Paper 83-1928 (1983) |
| 14 | C.C.L. Sells | Solutions of the Euler equations for transonic flow past a lifting aerofoil
RAE Technical Report 80065 (1980) |
| 15 | C.C. Lytton
(formerly
C.C.L. Sells) | Solution of the Euler equations for transonic flow past a lifting aerofoil - the Bernouilli formulation.
RAE Technical Report 84080 (1984) |
| 16 | A. Jameson
W. Schmidt
E. Turkel | Numerical solutions of the Euler equations by finite volume methods using Runge-Kutta time-stepping schemes.
AIAA Paper 81-1259 (1981) |
| 17 | W.R. Sears | On calculation of induced drag and conditions downstream of a lifting wing.
AIAA J. of Aircraft 11, 191 (1974) |

REFERENCES (continued)

- | <u>No.</u> | <u>Author</u> | <u>Title, etc</u> |
|------------|--|--|
| 18 | J.E. Hackett | Recent developments in three-dimensional wake analysis, vortex drag and its reduction.
AGARD/VKI Lecture Series 'Aircraft drag prediction and reduction' (1985) |
| 19 | T.A. Cook | Measurements of the boundary layer and wake of two aerofoil sections at high Reynolds numbers and high subsonic Mach numbers.
A.R.C. R&M 3722 (1973) |
| 20 | J.C. Cooke | The drag of infinite swept wings.
A.R.C. Current Paper 1040 (1969) |
| 21 | H.B. Squire
A.D. Young | The calculation of the profile drag of aerofoils.
A.R.C. R&M 1838 (1937) |
| 22 | J.E. Green
D.G. Weeks
J.W.F. Brooman | Prediction of turbulent boundary layers and wakes in compressible flow by a lag-entrainment method.
A.R.C. R&M 3791 (1973) |
| 23 | P.D. Smith | An integral prediction method for three-dimensional compressible turbulent boundary layers.
A.R.C. R&M 3739 (1974) |
| 24 | P.D. Smith | A calculation method for the turbulent boundary layer on an infinite yawed wing in compressible, adiabatic flow.
RAE Technical Report 72193 (1972) |
| 25 | R.C. Lock | A review of methods for predicting viscous effects on aerofoils and wings at transonic speeds.
AGARD CP-291, Paper 2 (1980) |
| 26 | J.C. le Balleur | Calcul des écoulements a forte interaction visqueuse au moyen de method de couplage.
AGARD CP-291, Paper 1 (1980) |
| 27 | R.E. Melnik | Turbulent interactions on airfoils at transonic speeds - recent developments.
AGARD CP-291, Paper 10 (1980) |
| 28 | R.C. Lock
M.C.P. Firmin | Survey of techniques for estimating viscous effects in external aerodynamics. In 'Numerical methods in aeronautical fluid dynamics' (ed P.L. Roe). Academic Press (1982) |
| 29 | J.C. le Balleur | Strong matching method for computing transonic flows including wakes and separations: lifting aerofoils.
La Recherche Aerospatiale 1981-3 (1981) |
| 30 | J.C. le Balleur | Numerical flow calculation and viscous-inviscid interaction techniques. In 'Recent advances in numerical methods in fluids'.
Pineridge Press (1984) |
| 31 | M.J. Lighthill | On displacement thickness.
J.Fl.Mech. 4, p383 (1958) |
| 32 | L.F. East | A representation of second-order boundary layer effects in the momentum integral equation and in viscous-inviscid interactions.
RAE Technical Report 81002 (1981) |
| 33 | L.F. East
W.G. Sawyer
C.R. Nash | An investigation of the structure of equilibrium turbulent boundary layers.
RAE Technical Report 79040 (1979) |

REFERENCES (continued)

- | <u>No.</u> | <u>Author</u> | <u>Title, etc</u> |
|------------|---|---|
| 34 | M.R. Collyer | An extension to the method of Garabedian and Korn for the calculation of transonic flow past an aerofoil to include the effects of a boundary layer and wake.
RAE Technical Report 77104 (1977) |
| 35 | M.R. Collyer
R.C. Lock | Prediction of viscous effects in steady transonic flow past an aerofoil.
Aero.Qu, <u>30</u> , 485 (1979) |
| 36 | J.C. le Bailleur | Couplage visqueux-non visqueux: analyse du problème incluant décollements et ondes de choc.
La R ch. Aerospatiale, No. 1977-6, 349 (1977) |
| 37 | M.R. Head | Entrainment in the turbulent boundary layer.
A.R.C. R&M 3152 (1960) |
| 38 | R.C. Hastings | Private communication. |
| 39 | J.E. Green | Application of Head's entrainment method to the prediction of turbulent boundary layers and wakes in compressible flow.
RAE Technical Report 72079 (1972) |
| 40 | R.E. Melnik
J.W. Brook | The computation of viscous/inviscid interaction on airfoils with separated flow.
Proc. 3rd Symposium on Numerical and Physical Aspects of Aerodynamic Flows, California State University, Long Beach, pp 1-21 to 1-37 (1985) |
| 41 | R.C. Lock | Velocity profiles for turbulent boundary layers in two dimensions.
RAE Technical Report to be issued (1985) |
| 42 | A.G.T. Cross | Boundary layer calculations using a three parameter velocity profile.
British Aerospace (Brough) Note YAD 3428 (1980) |
| 43 | R.L. Simpson
Y.J. Chew
B.C. Shivaprasad | The structure of a turbulent boundary layer.
J.F.M., <u>113</u> , 23 (1983) |
| 44 | J.A. D lery | Experimental investigation of turbulence properties in transonic shock/boundary-layer interactions.
AIAA Journal, <u>21</u> , No.2, 180 (1983) |
| 45 | L. Gaudet | Private communication |
| 46 | L.F. East
W.G. Sawyer
C.R. Nash | An investigation of the structure of equilibrium turbulent boundary layers.
RAE Technical Report 79040 (1979) |
| 47 | S.J. Kline
J.C. Bardina
R.C. Straun | Correlation of the detachment of two-dimensional turbulent boundary layers.
A.I.A.A. Journal, <u>21</u> , No.1, 68 (1983) |
| 48 | L.F. East
R.P. Hoxey | Low-speed three-dimensional turbulent boundary-layer data.
A.R.C. R&M 3653 (1969) |
| 49 | L.F. East
P.D. Smith
P.J. Merryman | Prediction of the development of separated turbulent boundary layers by the lag-entrainment method.
RAE Technical Report 77046 (1977) |
| 50 | R.C. Hastings
K.G. Moreton | An investigation of a separated equilibrium turbulent boundary layer.
In 'Laser anemometry in fluid mechanics', Lodon-Instituto Superior Tecnico, Lisbon (1984). |
| 51 | T.W. Swafford | Analytical approximation of two-dimensional separated turbulent boundary-layer profiles.
A.I.A.A. Journal, <u>21</u> , No.6, 923 (1983) |

- 52 J.G. Green A note on the turbulent boundary layer at low Reynolds numbers in compressible flow at constant pressure. Unpublished RAE Paper.
- 53 H. Ludwig
W. Tillmann Untersuchungen über die Wand schubspannung in turbulenten Reifungsschichten. Ing.Archiv., 17, 288-299 (1949) (English translation in NACA Technical Memorandum 1295)
- 54 K.G. Winter
L. Gaudet Turbulent boundary layer studies at high Reynolds numbers at Mach numbers between 0.2 and 2.8. RAE Technical Report 70251 (1970)
- 55 B.J. Powell The calculation of the pressure distribution of a thick cambered aerofoil at subsonic speeds including the effect of the boundary layer (1967)
- 56 B.R. Williams The prediction of separated flow using a viscous-inviscid interaction method. ICAS Paper, 84-23.2 (1984)
- 57 R.C. Lock Optimum relaxation factors for 'semi-inverse' viscous/inviscid interaction schemes for subsonic or supersonic flows. RAE Paper to be issued (1985)
- 58 D.J. Weeks
R.F. Wood
P.R. Ashill Improvements to the VGR method and developments of a semi-inverse version. RAE Paper to be issued (1985)
- 59 J.E. Carter A new boundary layer inviscid iteration technique for separated flows. A.I.A.A. Paper 79-1450 (1979)
- 60 P.D. Smith Calculations with the three-dimensional lag-entrainment method. Proc. SSPA-ITC Workshop on Ship Boundary Layers (1981)
- 61 P.D. Smith Direct and inverse integral calculation methods for three-dimensional turbulent boundary layers. Aero.Journal of R.Ae.Soc., 88, 155 (1984)
- 62 A. Mager Generalisation of the boundary layer momentum integral equations to three-dimensional flows, including those of rotating systems. NACA Report 1067 (1951)
- 63 A.G.T. Cross Calculation of compressible three-dimensional turbulent boundary layers with particular reference to wings and bodies. British Aerospace (Brough) Report YAD 3379 (1979)
- 64 A.G.T. Cross Private communication.
- 65 B. van den Berg
A. Elsenaar Measurements in a three-dimensional incompressible turbulent boundary layer in an adverse pressure gradient under infinite swept wing conditions. NLR Technical Report 720920 (1972)
- 66 L. Wigton
H. Yoshihara Viscous-inviscid interactions with a three-dimensional inverse boundary layer code. Second Symposium on Numerical and Physical Aspects of Aerodynamic Flows, Long Beach, California (1983)
- 67 P.D. Smith Private communication.
- 68 R.C. Hastings
B.R. Williams Studies of the flow field near a NACA4412 aerofoil at nearly maximum lift. Third Symposium on Numerical and Physical Aspects of Aerodynamic Flows, Long Beach, California, Paper 7-23 (1985)
- 69 P.M. Render
J.L. Stollery
B.R. Williams Aerofoils at low Reynolds numbers - prediction and experiment. Third Symposium on Numerical and Physical Aspects of Aerodynamic Flows, Long Beach, California, Paper 7-39 (1985)

REFERENCES (concluded)

<u>No.</u>	<u>Author</u>	<u>Title, etc</u>
70	B.R. Williams	The calculation of the flow about aerofoils at low Reynolds numbers suitable for remotely piloted vehicles. RAE Report to be issued (1985)
71	J.C. Newling	An improved two-dimensional multi-aerofoil program. BAe (Manchester) Report HSA-MAE-R-FDM-0007 (1977)
72	I.H. Abbott A.E. von Doenhoff	Theory of wing sections. Dover Publications (1949)
73	P.S. Granville	The calculation of the viscous drag of bodies of revolution. David Taylor Model Basin Report 849 (1953)
74	H.P. Horton	A semi-empirical theory for the growth and bursting of laminar separation bubbles. A.R.C. Current Paper 1073 (1967)
75	P.H. Cook M.A. McDonald M.C.P. Firmin	Aerofoil RAE 2822: pressure distributions and boundary layer and wake measurements. AGARD AR 138 Paper A6 (1979)
76	P.R. Ashill J.L. Fulker D.J. Wicks	Air injection: a method for fixing boundary layer transition and investigating scale effects. RAE Technical Report to be issued (1985)
77	D.J. Weeks P.R. Ashill	Tests on aerofoils of advanced design. RAE Technical Report to be issued (1985)
78	P.R. Ashill D.J. Weeks	A method for determining wall-interference corrections in solid-wall wind tunnels from measurements of static pressure at the walls. AGARD-CP-335, Paper 1 (1982)
79	M.C.P. Firmin P.H. Cook	Disturbances from ventilated tunnel walls in aerofoil testing. AGARD-CP-348, Paper 8 (1983)
80	E. Stanewsky M. Nardanan G.R. Inger	The coupling of a shock boundary layer interaction module with a viscous-inviscid computation method. AGARD-CP-291, Paper 4 (1980)
81	M.T. Arthur	A method for calculating subsonic and transonic flow over wings and wing-fuselage combinations with an allowance for viscous effects. A.I.A.A.-84-0428 (1984)
82	P.R. Ashill P.D. Smith	An integral method for calculating the effect on turbulent boundary layer development of sweep and taper. RAE Technical Report 83053 (1983) (also Aero. J. of R.Ae.Soc., March 1985)
83	P.R. Ashill J.L. Fulker	Methods for calculating viscous drag and vortex drag of wing-body configurations from measurements of static pressure on the wing. RAE Technical Report to be issued (1985)
84	M.C.P. Firmin	Calculation of transonic flow over wing-body combinations with an allowance for viscous effects. AGARD CP-291, Paper 8 (1981)
85	C.R. Forsey M.P. Carr	The calculation of transonic flow over three-dimensional swept wings using the exact potential equations. DGLR Symposium on 'Transonic Configurations', Bad Harzburg. DGLR Paper 78-064 (1978)
86	M.D. Hodges P.R. Ashill P.D. Cozens R.C. Lock	Application to a particular model of an approximate theory for determining the spanwise distribution of and total wave drag on a swept wing. Unpublished ESDU Paper (1984)

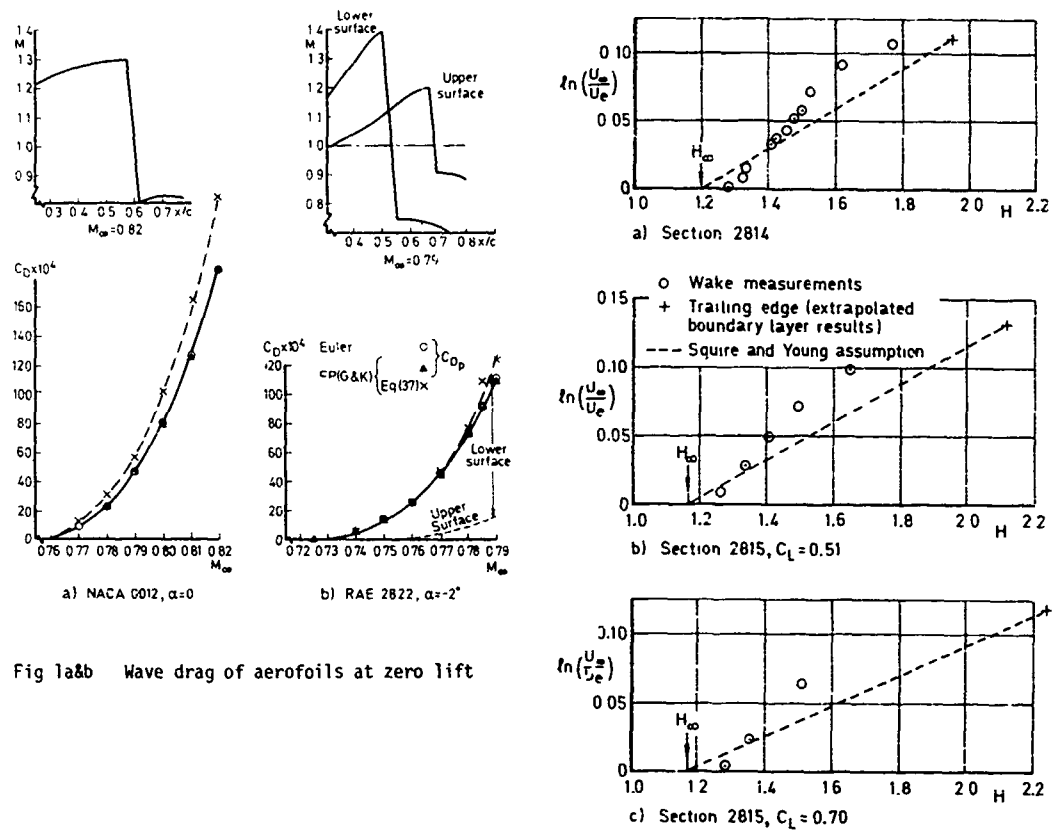


Fig 1a&b Wave drag of aerofoils at zero lift

Fig 2a-c Comparison of wake data with Squire and Young assumption:
(i) Experiment

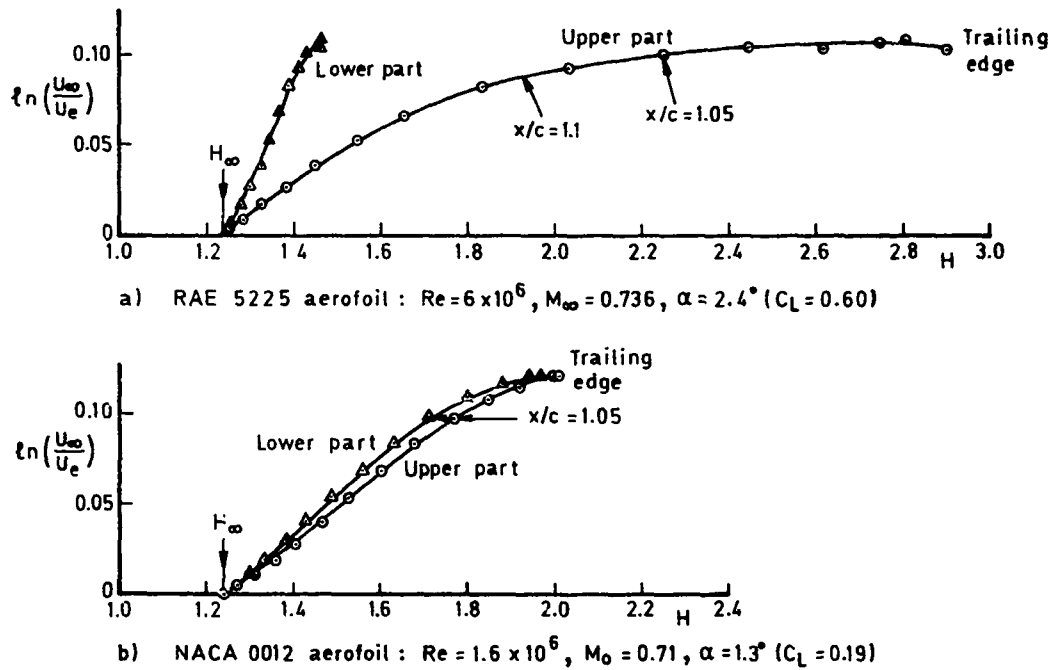


Fig 3a-b Comparison of wake data with Squire and Young assumption: (ii) Theory

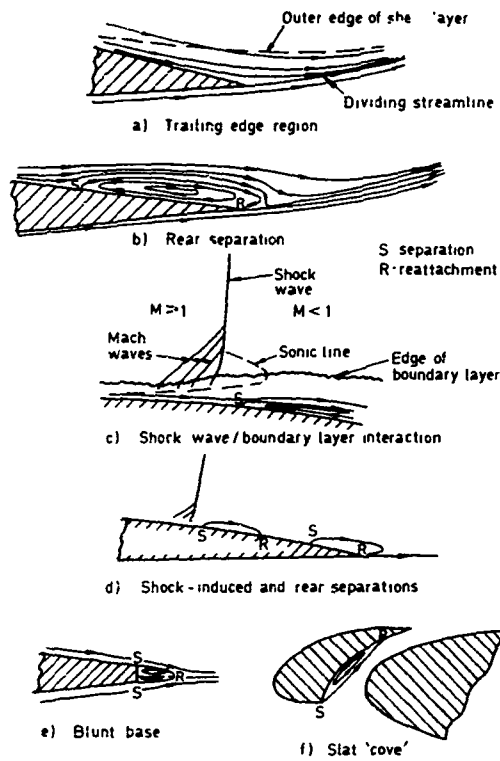


Fig 4a-f Flows in which first-order boundary-layer assumptions are invalid

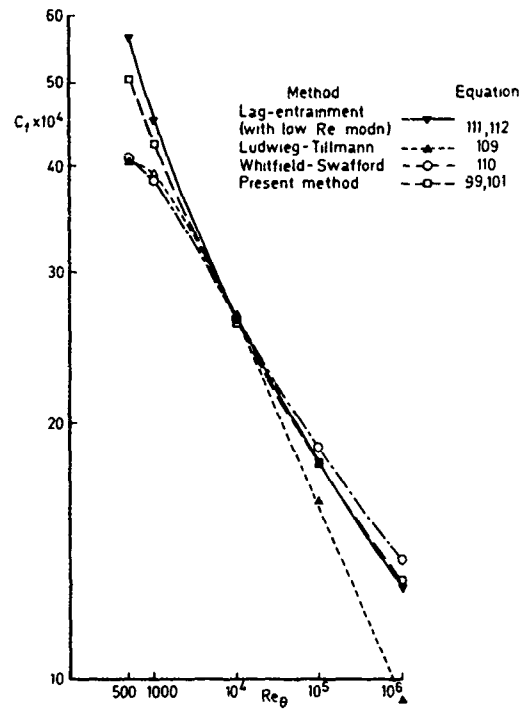


Fig 6 Flat-plate skin-friction values

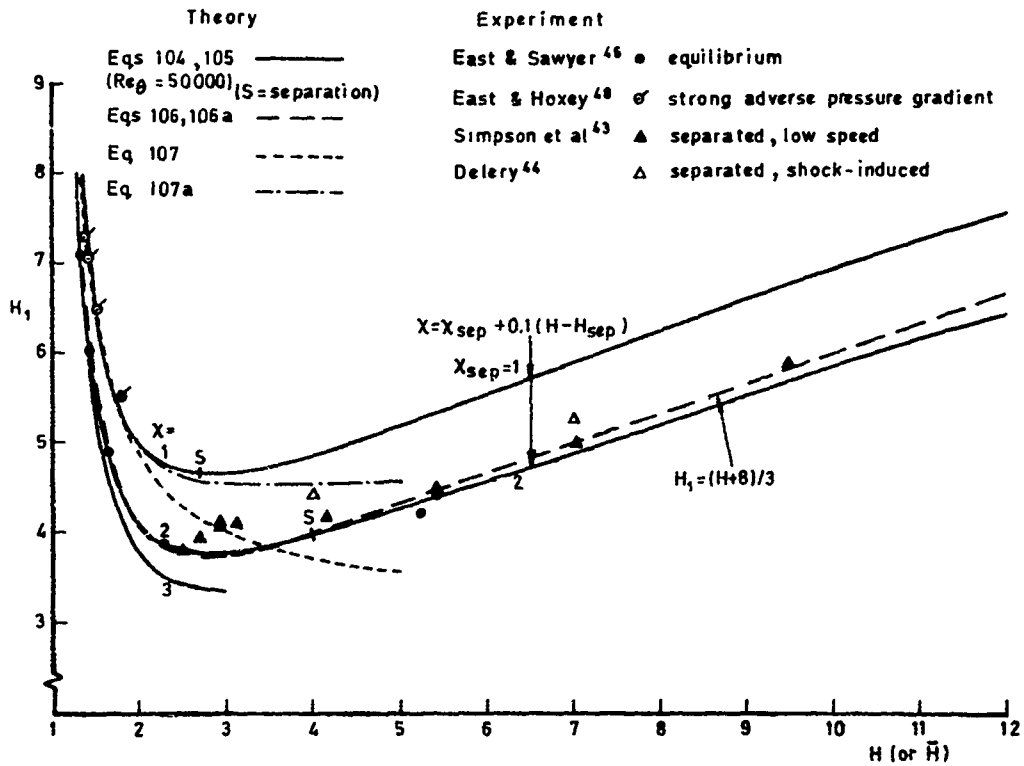
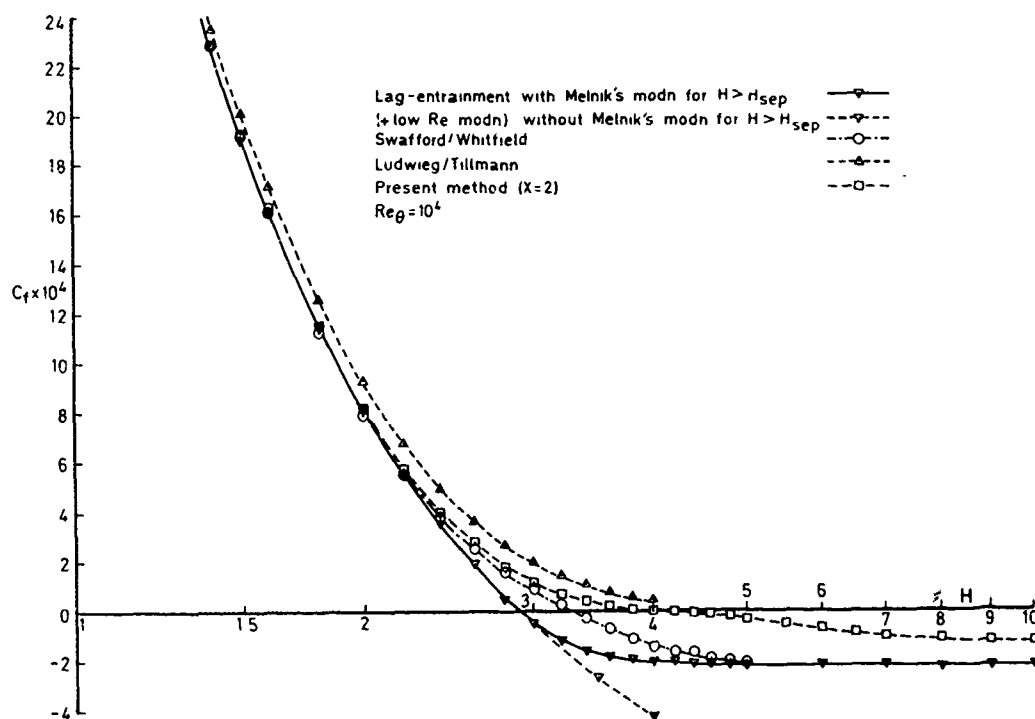
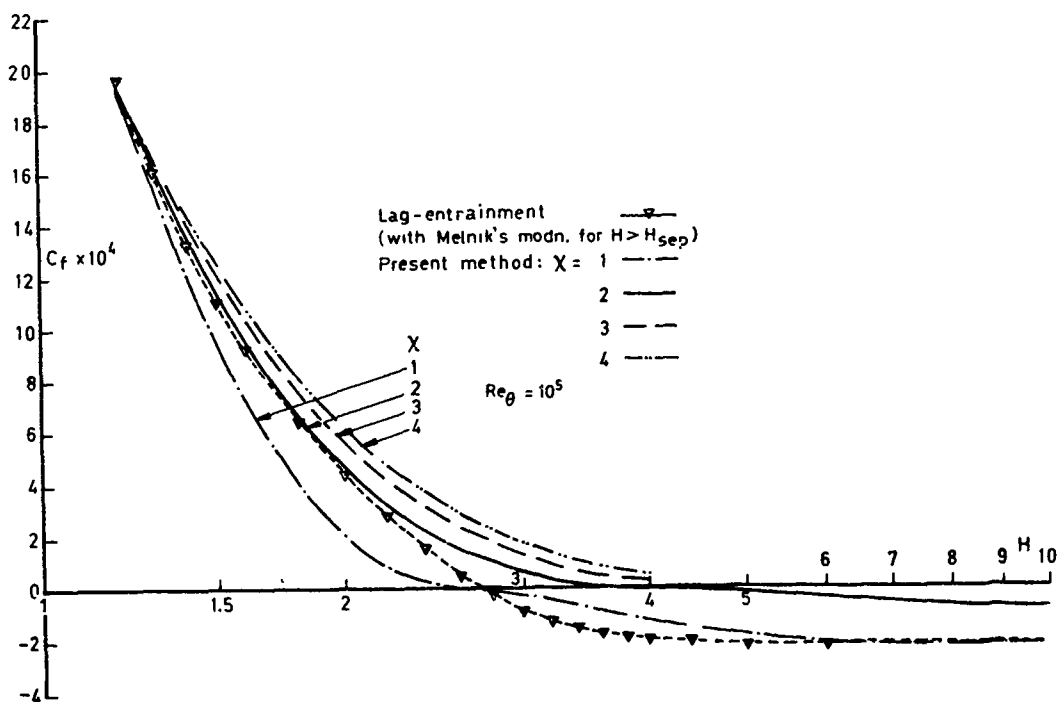


Fig 5 Variation of H_1 with H (or R)

Fig 7 Skin-friction formulae: $Re_{\theta} = 10^4$ Fig 8 Skin-friction: Effect of parameter χ : $Re_{\theta} = 10^5$

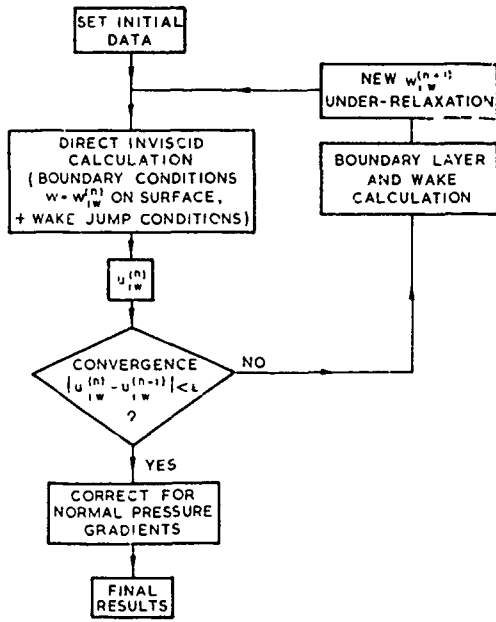


Fig 9 Flow diagram for direct iterative calculation

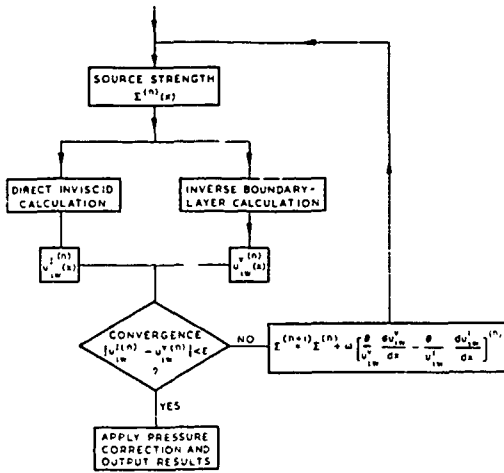


Fig 10 Flow diagram for semi-inverse scheme

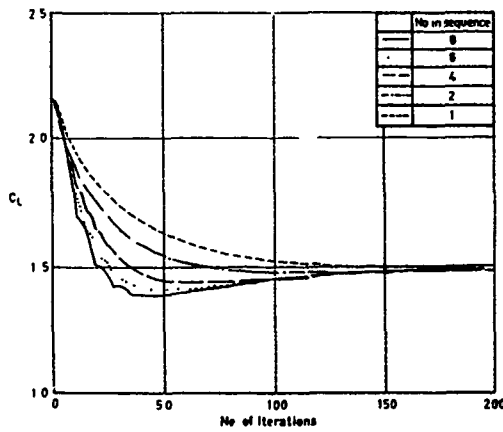


Fig 11 Study of convergence rate

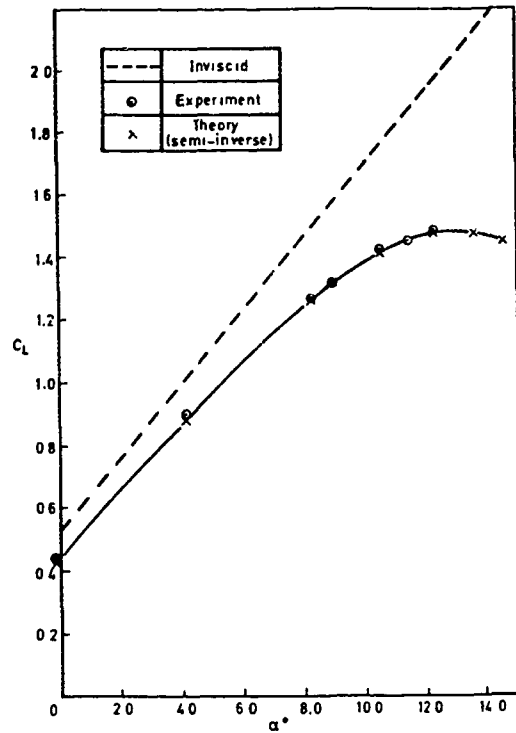


Fig 12 NACA 4412 aerofoil: Variation of C_L with α

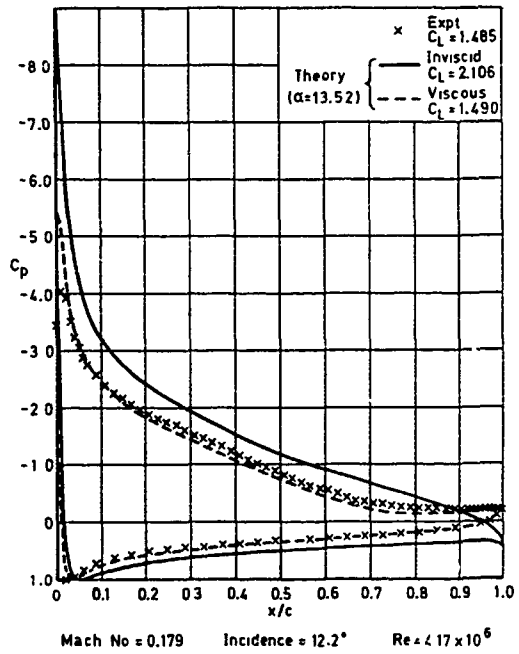


Fig 13 NACA 4412 aerofoil: Pressure distribution

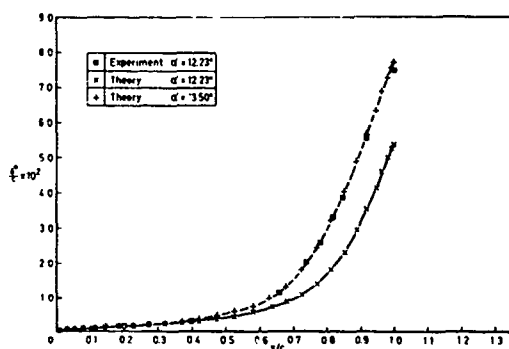


Fig 14 NACA 4412 aerofoil: Displacement thickness on upper surface

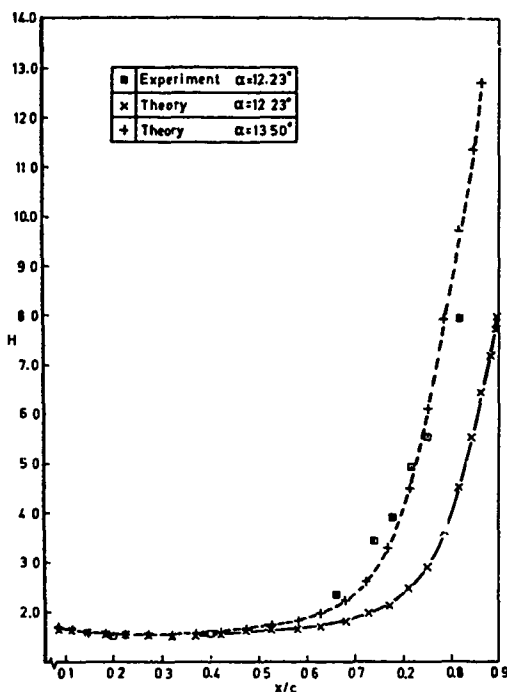


Fig 15 NACA 4412 aerofoil: Variation of H on upper surface

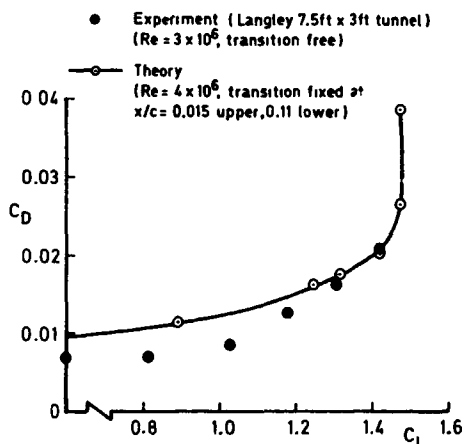


Fig 16 NACA 4412 aerofoil: Variation of C_D with C_L

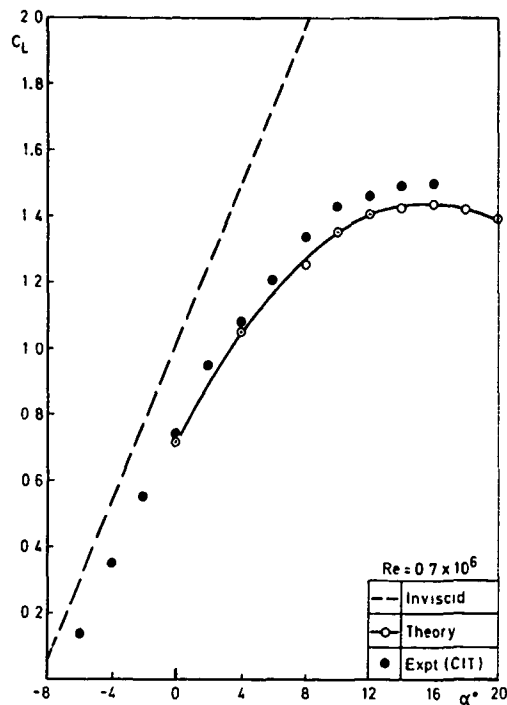


Fig 17 Gottingen 797 aerofoil: Lift curves

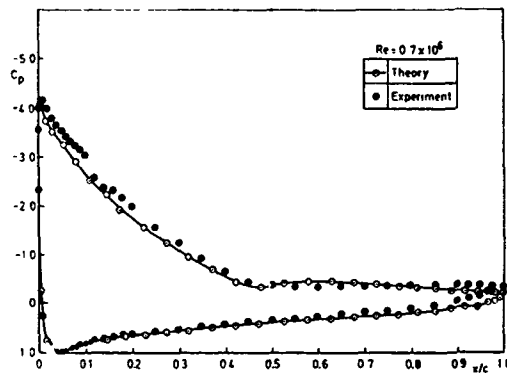


Fig 18 Gottingen 797 aerofoil: Pressure distribution, $\alpha = 16^\circ$

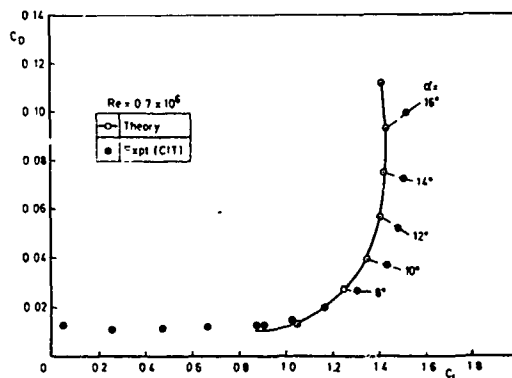


Fig 19 Gottingen 797 aerofoil: Drag curves

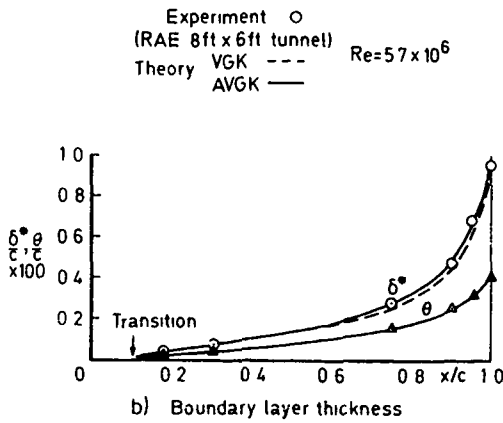
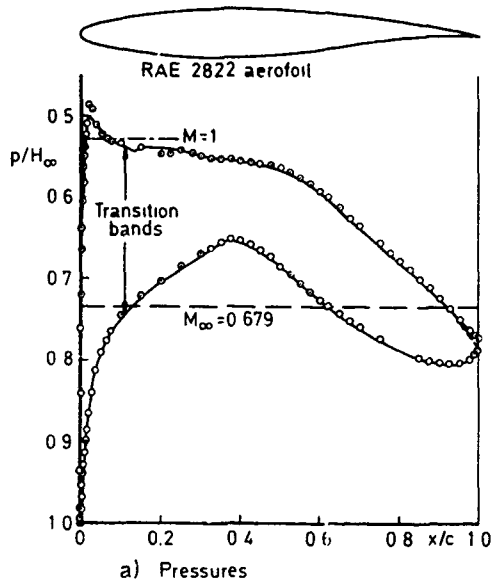


Fig 20a&b RAE 2822 aerofoil: Case 1
 $M_\infty = 0.679, C_L = 0.566$,
Pressure distribution.

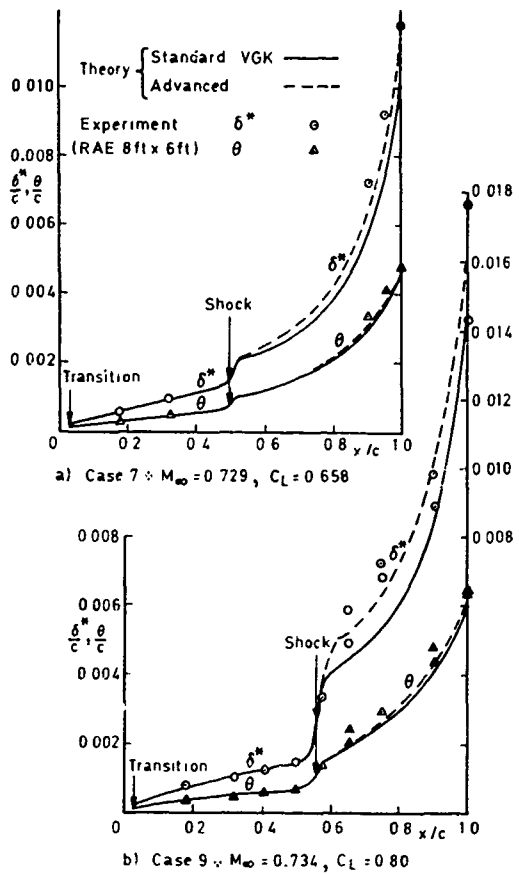


Fig 22a&b RAE 2822 aerofoil:
 $M_\infty \approx 0.73, Re = 6.5 \times 10^6$
Boundary layer thickness.

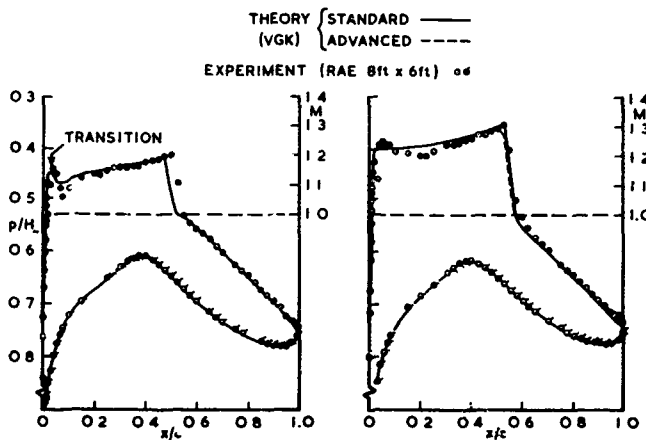


Fig 21a&b RAE 2822 aerofoil: $Re = 6.5 \times 10^6$
(a) Case 7: $M_\infty = 0.729, C_L = 0.658$
(b) Case 9: $M_\infty = 0.734, C_L = 0.803$

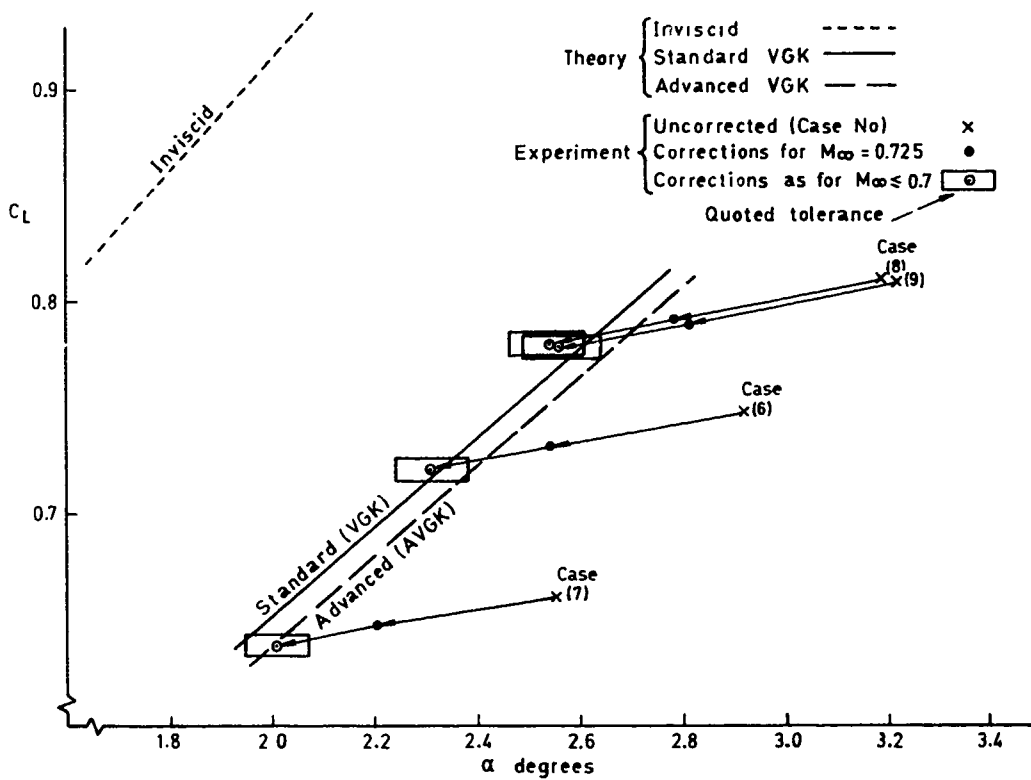


Fig 23 RAE 2822 aerofoil: $M_\infty \approx 0.73$
Lift curves

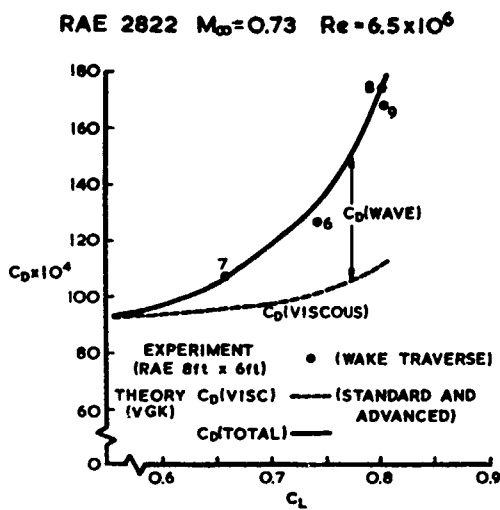


Fig 24 RAE 2822 aerofoil: $M_\infty \approx 0.73$
Drag curves

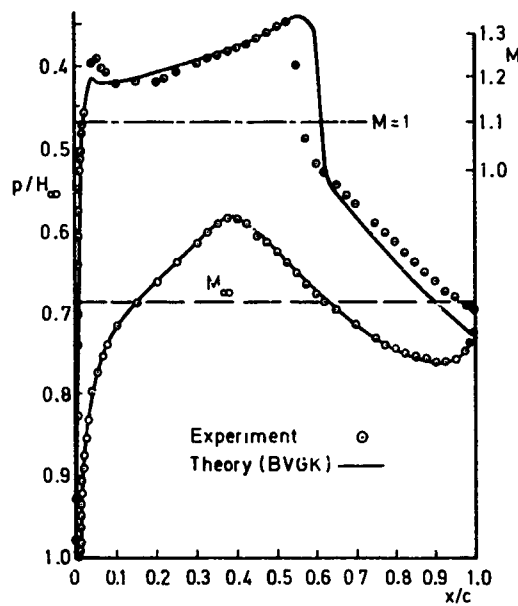


Fig 25 RAE 2822 aerofoil:
Case 10: $M_\infty = 0.753$, $C_L = 0.74$
Pressure distributions

RAE 5225 $\frac{t}{c} = 0.140$

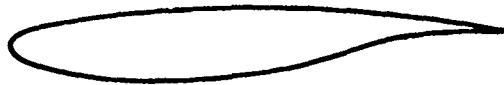


Fig 26 RAE 5225 aerofoil

RAE 5225 PRESSURE DISTRIBUTIONS—COMPARISON BETWEEN VGK THEORY AND MEASUREMENT $Re = 20 \times 10^6$

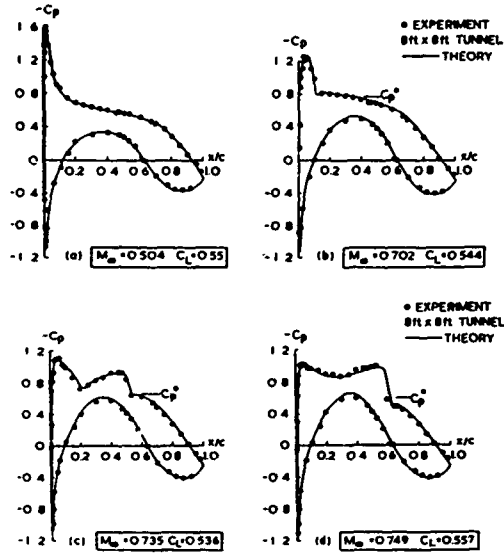


Fig 27a&b RAE 5225 aerofoil. Pressure distributions $C_L \approx 0.55$, $Re = 20 \times 10^6$

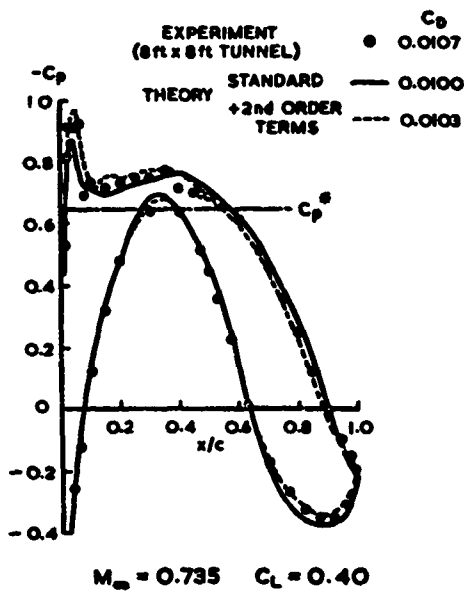


Fig 28 RAE 5225 aerofoil: Comparison between VGK theory and measurement, $Re = 6 \times 10^6$

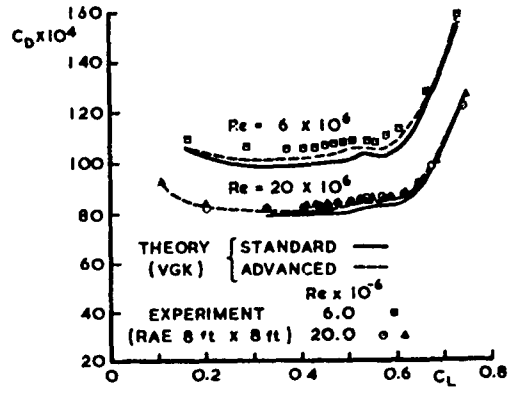


Fig 29 RAE 5225 aerofoil: Variation of C_D with C_L , $M_\infty = 0.735$

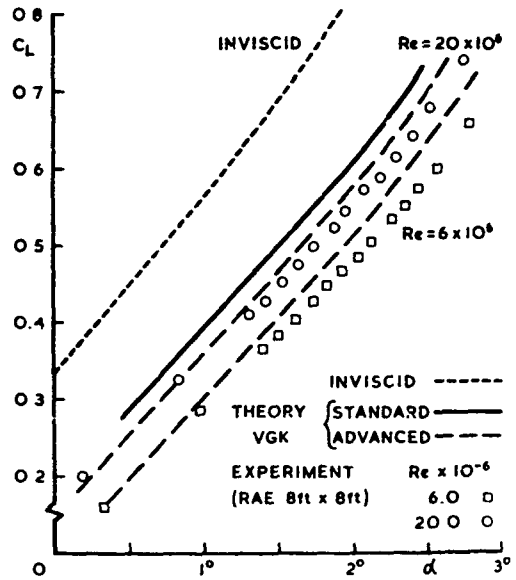


Fig 30 RAE 5225 aerofoil: Variation of C_L with α , $M_\infty = 0.735$

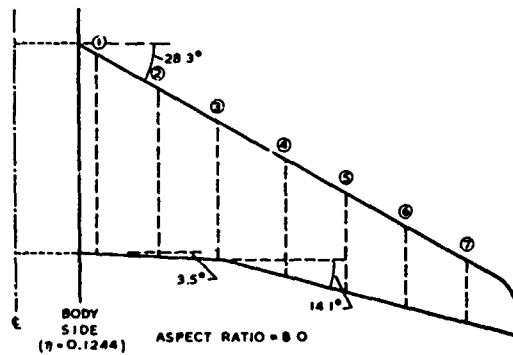


Fig 31 Wing-body (1)

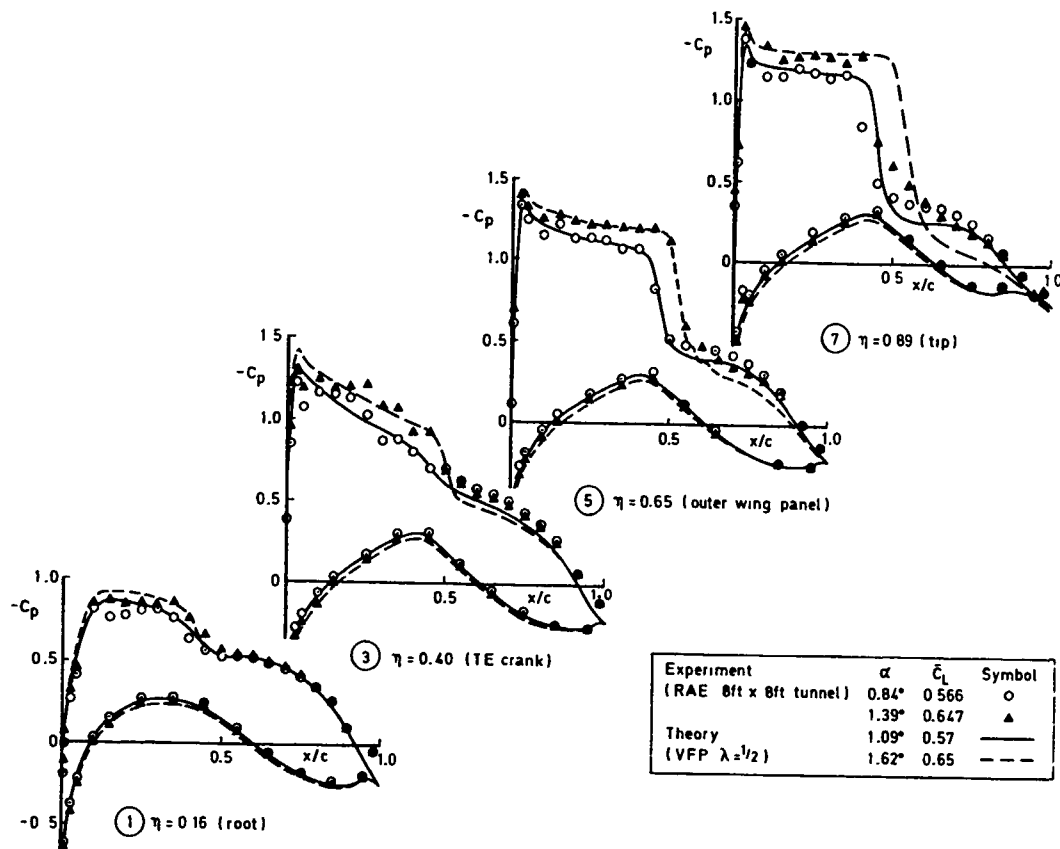


Fig 32 Wing-body (1): Half-model pressures, $M_\infty = 0.78$, $Re_c = 12 \times 10^6$

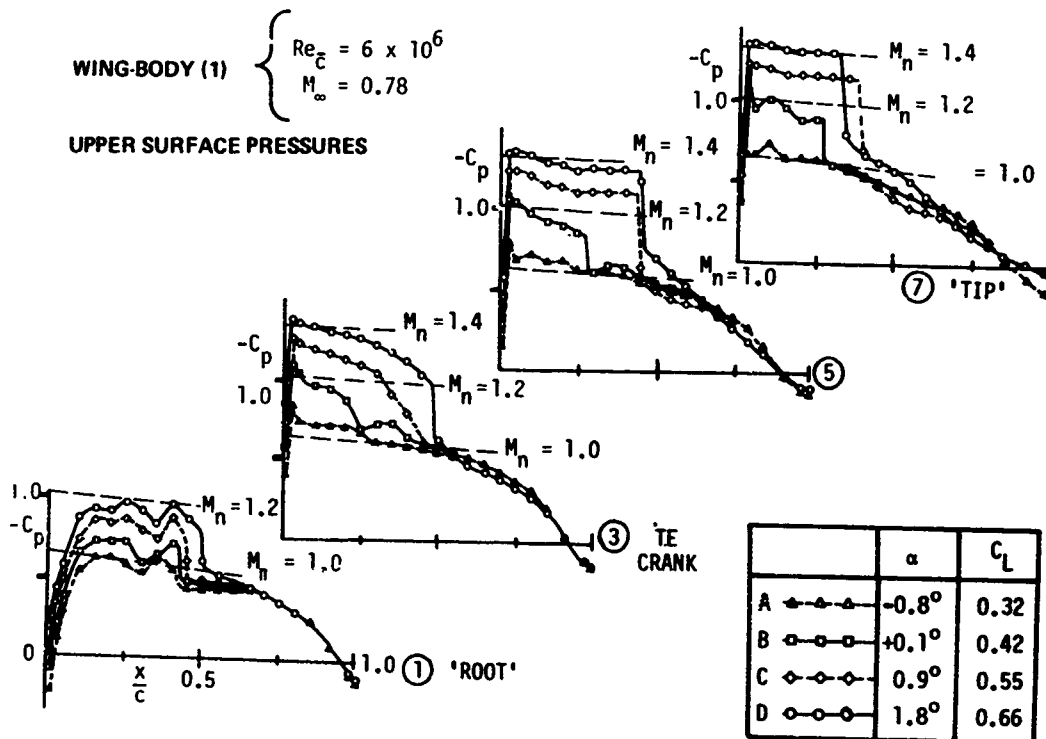


Fig 33 Wing-body (1): Complete model pressures, $M_\infty = 0.78$, $Re_c = 6 \times 10^6$

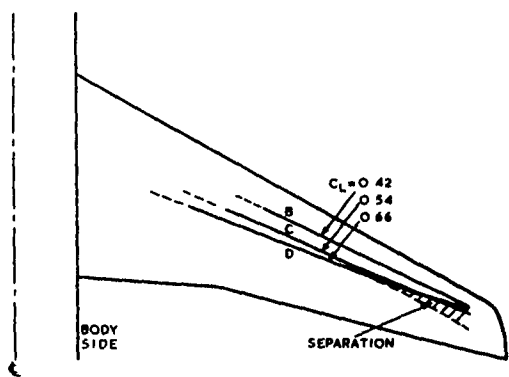


Fig 34 Wing-body (1): Snock positions $M_\infty = 0.78$

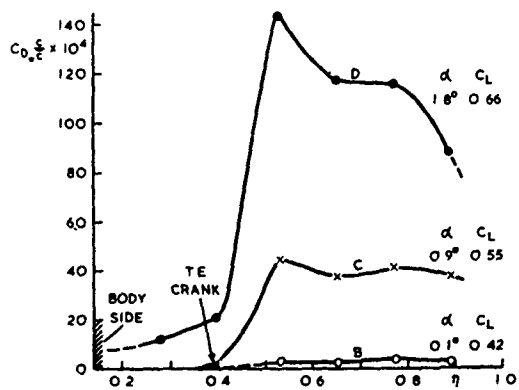


Fig 37 Wing-body (1): Local contributions to wave drag: $C_{D,w}/C_L$

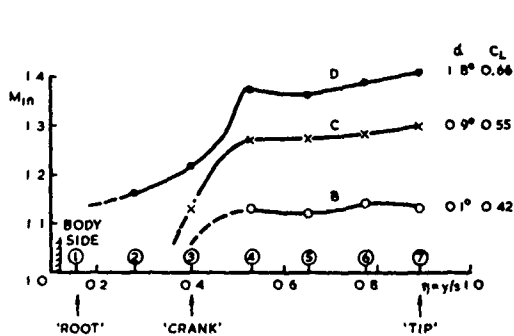


Fig 35 Wing-body (1): Shock upstream Mach numbers

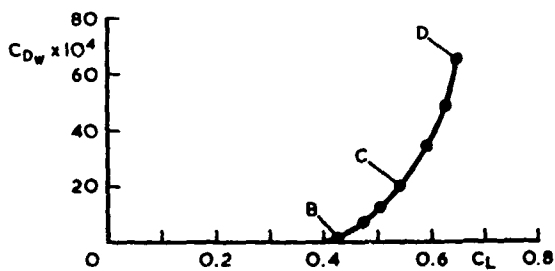
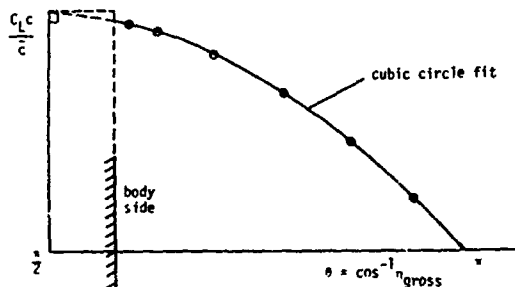


Fig 38 Wing-body (1): Wave drag, $M_\infty = 0.78$

A. INTERPOLATION OF LOAD DISTRIBUTION



B. VORTEX DRAG AND LIFT DETERMINED BY USING MUTHOPP'S METHOD OF GAUSSIAN QUADRATURE

Fig 39 Method used to determine vortex drag

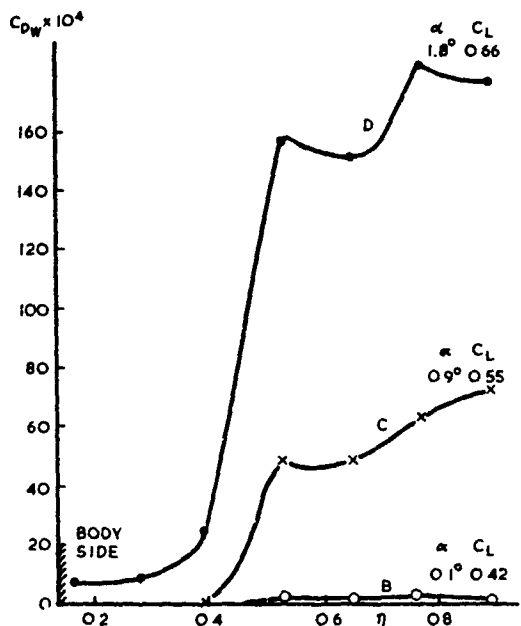


Fig 36 Wing-body (1): Local wavedrag: $C_{D,wave}^{(n)}$

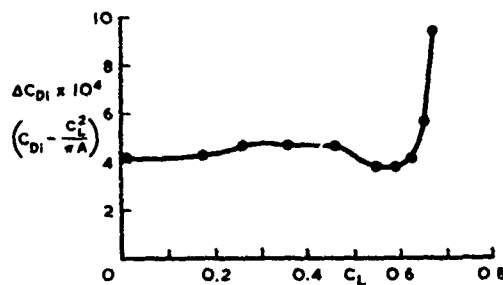
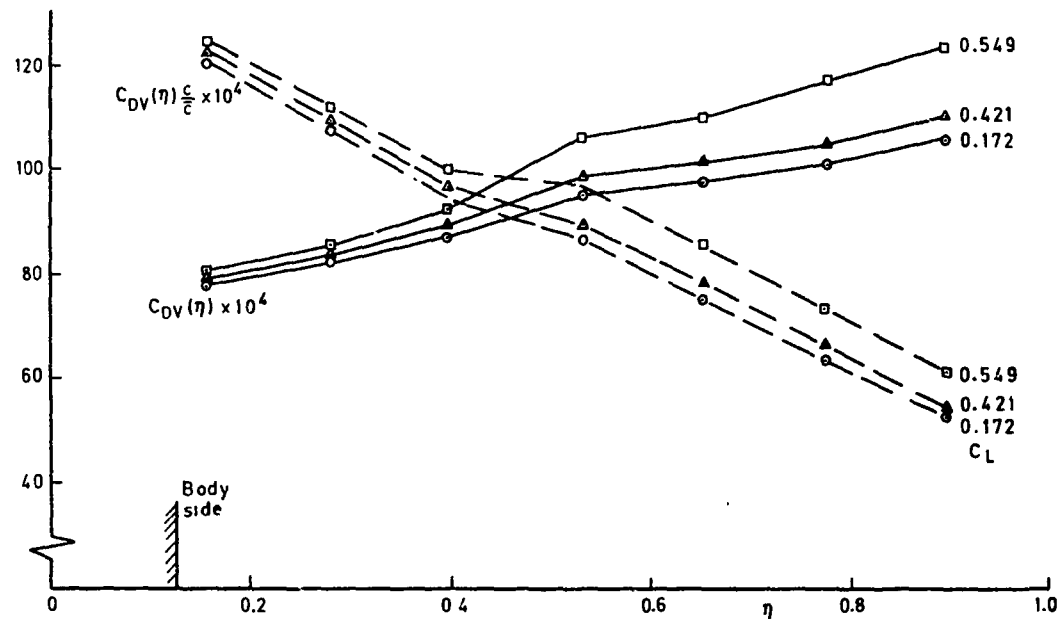
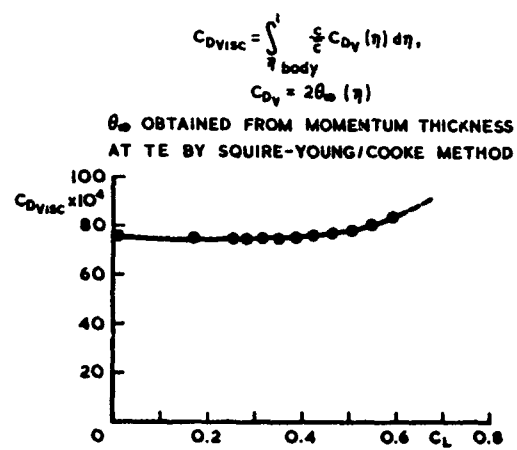
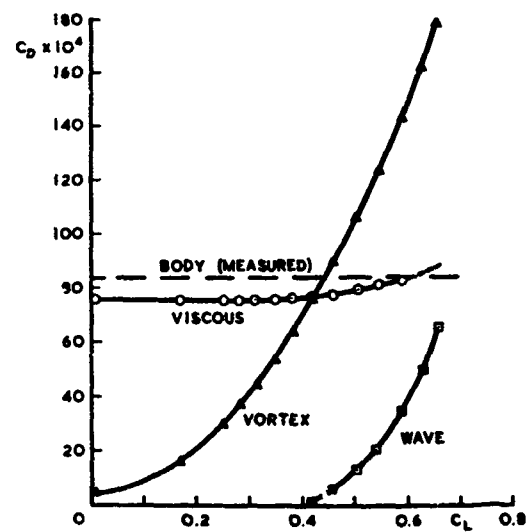


Fig 40 Wing-body (1): Vortex drag, $M_\infty = 0.78$

Fig 41 Spanwise variation of viscous drag, $M_\infty = 0.78$ Fig 42 Wing-body (1): Viscous drag, $M_\infty = 0.78$ Fig 43 Wing-body (1): Drag components, $M_\infty = 0.78$, $Re = 6 \times 10^6$

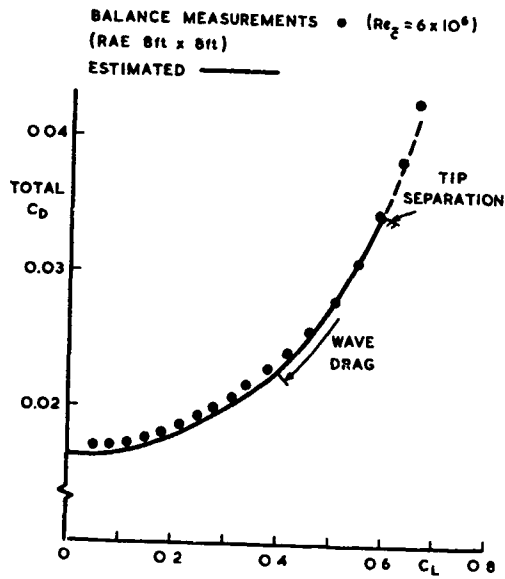


Fig 44 Wing-body (1): Total drag, $M_{\infty} = 0.78$

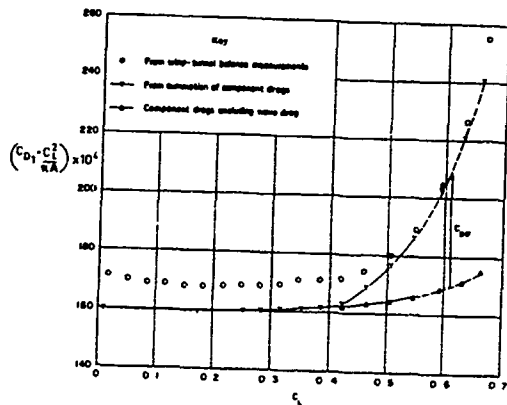


Fig 45 Comparison of estimated and measured drag, $M_{\infty} = 0.78$

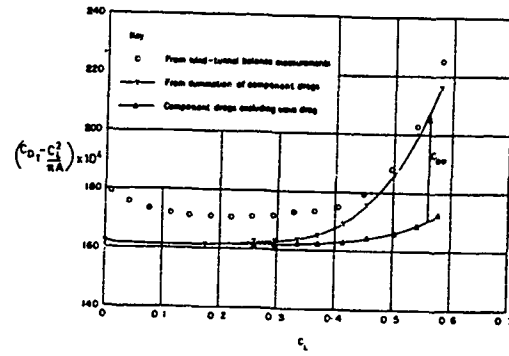


Fig 46 Comparison of estimated and measured drag, $M_{\infty} = 0.80$

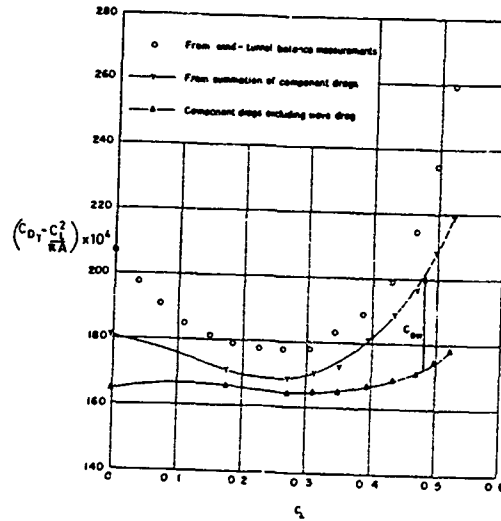


Fig 47 Comparison of estimated and measured drag, $M_{\infty} = 0.82$

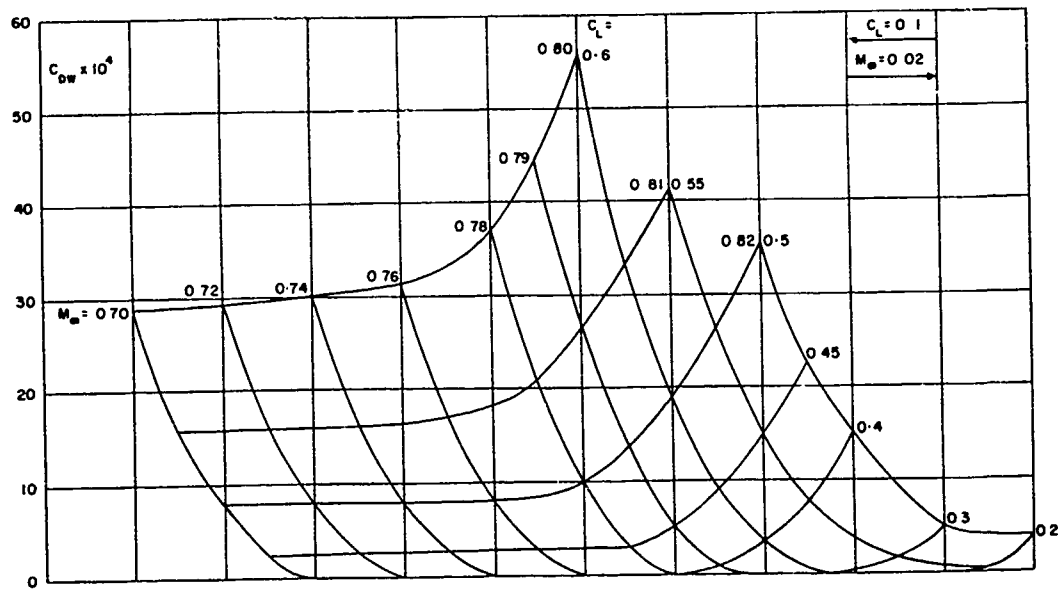


Fig 48 Carpet of estimated wave drag

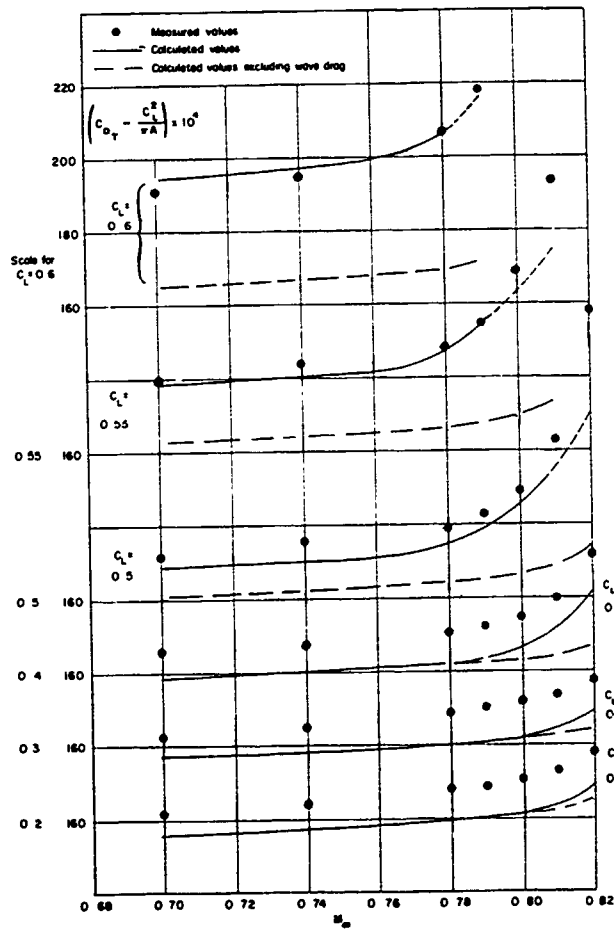


Fig 49 Variation of $C_D - \frac{C_L^2}{\pi A}$ with M_∞ at constant C_L

**TRANSONIC DRAG RISE AND DRAG REDUCTION
BY ACTIVE/PASSIVE BOUNDARY LAYER CONTROL**

by

E. Stanewsky and P. Krogmann

Institut für Experimentelle Stromungsmechanik
Deutsche Forschungs- und Versuchsanstalt
für Luft- und Raumfahrt e.V.
D-3400 Göttingen, FRG

SUMMARY

Accurate drag prediction and efficient drag reduction are, particularly in the transonic speed range, paramount to the future of economical aircraft design and operation. In the present paper the prediction of drag based on high-speed wind tunnel results will be discussed with emphasis being placed on problems associated with testing at transonic speeds and the transfer of low Reynolds number wind tunnel results to full-scale aircraft conditions. This discussion is preceded by a more general consideration of the drag development associated with compressibility and viscosity and the viscous-inviscid interaction of the flow on an aerodynamic configuration. The second part of the paper treats drag reduction methods which are mainly based on active and passive boundary layer control by means of slots and perforated strips utilized to either draw material from and/or add material to the boundary layer. It may be concluded that (a) present transonic drag prediction methods need further improvement, especially at off-design conditions, and (b) some of the approaches to boundary layer control considered may be quite efficient in increasing aircraft aerodynamic performance.

Re	Reynolds number, $U_\infty c / \nu_\infty$
Re_θ	Reynolds number based on momentum thickness
S	entropy
S_{ref}	wing reference area
t	airfoil thickness
T_s	transonic sensitivity parameter
U, V	velocity
W	airplane weight
x, y, z	coordinates
α	angle of incidence
δ	boundary layer thickness
δ_1	displacement thickness
ν	kinematic viscosity
ρ	density
τ	wall open area ratio

Subscripts

B	buffet onset
d.r., D	drag rise
j	blowing
L	local
R	location of tripping device
s	shock
T. E.	trailing edge
1	condition ahead of shock
2	condition behind shock
-	free stream conditions

NOMENCLATURE

A_{wet}	wetted area
b	span
b_s	span of suction region
c	chord
C_D	drag coefficient
C_{D_M}	compressibility drag
C_{D_P}	profile (parasite) drag
C_L	lift coefficient
$C_{L_{MC}}$	max. cruise lift coefficient
C_N	normal force coefficient
C_f	skin friction coefficient
C_p	pressure coefficient
c_p^*	c_p at sonic condition
$C_Q = \dot{m} / (\rho_\infty U_\infty b_s c)$	suction coefficient
$c_{\mu_j} = m_j V_j / q_\infty c$	momentum coefficient
D	drag
FS	component form parameter
h	roughness height
H	test section height; shape factor
L	lift
\dot{m}	mass flow rate
M	Mach number
p	pressure

Abbreviations

150 K	carborundum with grain size 150
ct(s)	drag counts (1 ct = 0.0001 in C_D)

Further symbols are explained within the text

1. INTRODUCTION

The state-of-the-art in aircraft drag prediction as of 1973 is summarized in the proceedings of the AGARD-Symposium "Aerodynamic Drag" [1]. Further detailed treatments of this subject are contained in the AGARD-Lecture Series "Prediction Methods for Aircraft Aerodynamic Characteristics" of 1974 [2]. The latest summary is a survey and critical review of the present state-of-the-art entitled "Thrust and Drag: Its Prediction and Verification" which will be published in the AIAA Progress in Astronautics and Aeronautics Series [3]¹). Where applicable to the transonic speed range, the present contribution on drag prediction will draw considerably on the contents of these references.

A summary of research in the field of drag reduction up to about 1979 is contained in another volume of the aforementioned AIAA series entitled "Viscous Flow Drag Reduction" [4]. In the present context furthermore to be mentioned are two AGARD sponsored events, viz., a Special Course on "Concepts for Drag Reduction" [5], and the latest, a Symposium on "Improvement of Aerodynamic Performance Through Boundary Layer Control and High Lift Systems", held in 1984 [6].

There is certainly no need to outline here in detail the importance of an accurate drag prediction and an efficient drag reduction to aircraft design and to cruise and off-design performance. This subject will therefore only briefly be addressed when considering the transonic drag development in Chapter 2. In this chapter we will also treat in a similarly brief manner the characteristics of transonic flow, the general drag buildup and the effects of Mach number and Reynolds number on drag. It is quite likely that other authors of the present Lecture Series will follow a similar approach; however, in order to keep the present paper self-contained, this more general discussion is retained.

Drag prediction is here understood as the prediction based on low Reynolds number wind tunnel results. Chapter 3 of this paper is accordingly concerned with the problems associated with low Reynolds number transonic wind tunnel testing: Boundary layer transition, transition fixation, wall and sting interference and its corrections and the transfer of experimental results thus obtained to full-scale aircraft conditions. Also briefly considered are specific flow diagnostic studies. Drag reduction, treated in Chapter 4, is restricted to the reduction by active and passive boundary layer control mainly administered by means of slots and perforated strips utilized to either draw material from and/or add material to the boundary layer.

1) The authors are indebted to the principle editor of this work, Prof. Eugene E. Covert of MIT, for providing them with an early copy of the manuscript.

2. TRANSONIC DRAG DEVELOPMENT

2.1 General Considerations

One dominant design goal, at least for commercial transport aircraft at high subsonic cruise speeds, is low fuel consumption which is equivalent to operating the aircraft near the maximum $M_{\infty}(L/D)$ since

$$\frac{\text{FUEL CONSUMPTION}}{\text{DISTANCE}} = \frac{\text{SFC}}{U_{\infty}} \times \frac{W}{L/D}$$

where SFC is the specific fuel consumption, W is the aircraft total weight, $U_{\infty}(M_{\infty})$ is the cruise speed and L/D is the lift to drag ratio. The aerodynamic performance parameter $M_{\infty}(L/D)$ increases with increasing Mach number until the drag rise due to the growing compressibility drag (mainly wave drag) is no longer offset by the Mach number increase, Fig. 1 [7]. The curves in Fig. 1 indicate the performance parameters attainable with today's transonic technology. Their maximum values and form are dependent on the quality of the aerodynamic design (mainly the wing design) and, of course, on the specific design requirements. It can easily be recognized how the topic of the present paper relates to the optimization of the performance parameter since the latter requires

- cruise at transonic Mach numbers,
- the accurate prediction of drag and the drag - divergence Mach number - and, of course, other aerodynamic parameters - and
- the reduction of drag either by active or passive boundary layer control methods which might be incorporated in future aircraft developments.

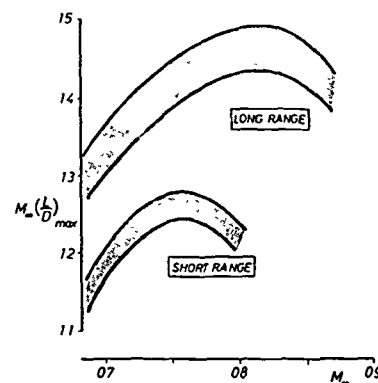


Fig. 1: Performance Parameter of Commercial Transport Aircraft, Ref. 7

While commercial transport aircraft are almost exclusively designed for fuel efficiency, tactical military aircraft encompass a vast spectrum of operational requirements, Fig. 2 [8]. For example, wings designed for efficient transonic cruise and maneuver may also be required to have the capability to accelerate rapidly to supersonic speeds and exhibit efficient performance in that range, demands which actually call for different wing characteristics. However, for aircraft with strong emphasis on transonic operation, sufficient similarity in wing design exists so that all that is said for commercial transports holds, to a large degree, also for tactical military airplanes.

2.2 Transonic Flow Characteristics

Transonic or supercritical airfoils or wings typically exhibit a large supersonic region on the upper surface while the freestream velocity is still subsonic. At the design (cruise) condition, the upper surface flow decelerates to subsonic velocities either through an isentropic recompression or via a weak shock wave, Fig. 3a [9]. In designing such a wing, one would like to maximize the supersonic flow region on the upper surface to produce the desired lift coefficient while, at the same time, minimizing the shock/recompression strength in order to keep the viscous interaction weak, hence the drag low.

As the freestream Mach number or angle of attack is increased beyond the design point, stronger shock waves develop on the wing upper surface resulting at a certain strength directly or indirectly in a flow separation. As is indicated in Fig. 3b [10], direct shock-induced separation is restricted to a separation bubble originating at the foot of the shock and closing upstream of the trailing edge while an indirect separation originates at the trailing edge caused - in most instances - by the weakening of the boundary layer due to the shock wave. The various combinations

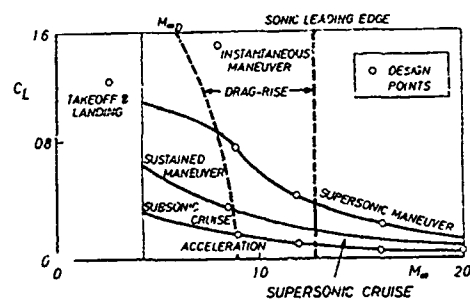


Fig. 2: Typical Performance Map for Fighters, Ref. 8

in the onset and development of separation possible with increasing Mach number or angle of attack were classified by H.H. Pearcy et al. in 1968 [11]. These strong shock wave boundary layer interactions not

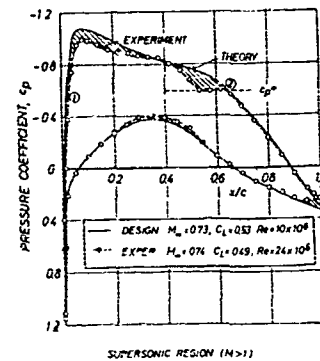


Fig. 3a: Shock-free Pressure Distribution at the Design Condition. Airfoil DFVLR 48080

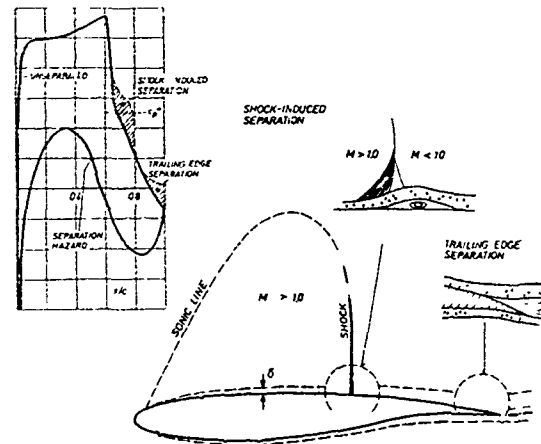


Fig. 3b: Types of Transonic Flow Separations.

only cause a rapid increase in drag, they also constitute a major source of significant scale effects in wind tunnel tests which make the transfer of low Reynolds number wind tunnel results to full-scale aircraft conditions, as will be shown later, so problematic.

The drag contribution of the wing is, in essence, the contribution responsible for the Mach number dependence of the overall drag. Before considering the relation between the flow development described above and this Mach number dependence, i.e., the transonic drag behavior, it is deemed sensible to first consider briefly the elements comprising total drag.

2.3 Drag Buildup

The resultant aerodynamic force caused by a flight vehicle's motion with respect to the atmosphere is the sum of the pressure or normal forces and the tangential or skin friction forces acting on the vehicle's surface. These forces are resolved into lift, i.e., the aerodynamic reaction perpendicular to the flight path, and drag, i.e., the component of the total force that opposes motion in the flight path direction.

In almost any approach to drag prediction and analysis, the total drag at cruise is considered to consist of three major elements:

- Minimum profile drag (basic parasite drag) at a lift coefficient different from zero
- Lift dependent induced drag
- Compressibility drag, i.e., the drag increase with Mach number.

The first two contributions are generally taken at subcritical Mach numbers, typically $M_{\infty} \leq 0.60$. As indicated in Fig. 4 [3][12], the basic parasite drag comprises

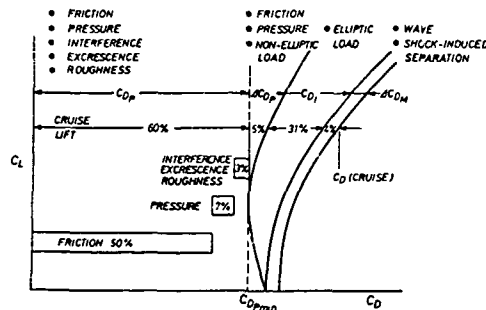


Fig. 4: Transonic Aircraft Drag Buildup, Ref. 3, 12

friction and pressure (form) drag and drag resulting from interferences between the different aircraft components and from excrescences and roughness. The lift dependent drag contains a contribution, ΔC_{D_i} , which accounts mainly for the effect of increasing lift, i.e., load on the boundary layer, on the friction and form drag. The major lift dependent component is, of course, the vortex drag, generally referred to as induced drag which is due to the finite span of the wing.

Increases in airplane drag coefficient as the Mach number is increased towards the cruise point and beyond are commonly referred to as compressibility drag, the latter being associated with the formation of local regions of supersonic flow, mainly on the wing. One must, however, realize that it also includes, in reality, in addition to the wave drag and any drag due to shock-induced separation, the variation of

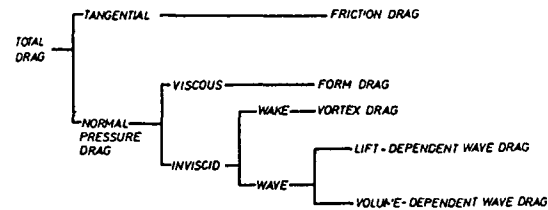


Fig. 5: Components of Aircraft Drag

the skin friction, form and vortex drag with Mach number [13]. This indicates that the simple classification of aircraft drag as depicted in Fig. 4 is somewhat artificial and reflects the (past) state-of-the-art, though still applied, in drag prediction methodology. Butler [14] suggests a drag break-down more directly associated with the basic causes for drag and closely related to the physics of the flow, Fig. 5. As computational methods - and the diagnostic tools in wind tunnel tests - become more powerful such a drag classification as base for predictive and analysis methods seems much more appropriate.

In the context of the present paper the prediction of drag will only be considered for those drag elements (Fig. 4) needed to relate low Reynolds number wind tunnel results to full-scale conditions.

2.4 Mach Number Dependence (Compressibility Drag)

Compressibility drag is, as noted above, mainly associated with the wing, the latter accounting for about 63% of the total drag of a commercial transport aircraft [7]. It is configuration dependent: A highly loaded wing associated with a smaller wing area will exhibit a different drag behavior than a large wing with correspondingly lower lift coefficients. To demonstrate the drag development with increasing Mach number - as well as the Reynolds number dependence in the next section - it is convenient to utilize a supercritical airfoil tested in a wide range of Reynolds numbers, for which detailed pressure distribution and wake measurements are available [9]. The compressibility drag development on a two-dimensional airfoil is quite similar to the one occurring on a complete aircraft provided the wing section characteristics are the same.

The development of compressibility drag with increasing Mach number at constant lift coefficient can be separated into four segments, Fig. 6: First, there is a gradual increase in drag that can occur before any substantial supersonic velocities arise ($M_{\infty} < 0.70$). It follows a somewhat more pronounced increase (drag-creep) leading to a plateau, typical of many transonic airfoils, as larger regions of supersonic flow and shock waves form and start to move downstream. In particular, the increase in the vicinity of $M_{\infty} = 0.75$ is associated with the development of a double shock in the mid-chord region resulting in stronger shock losses. As the double shock system

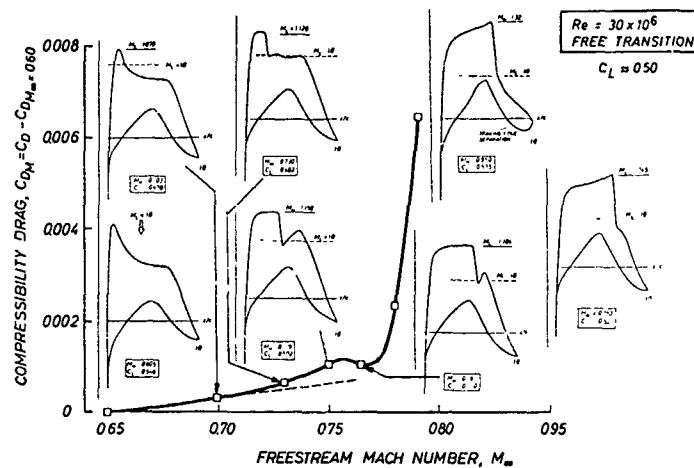


Fig. 6: Transonic Drag Development-Compressibility Drag.
Airfoil CAST 10-2/DOA2

resolves into a single shock, a slight reduction in drag occurs with increasing freestream Mach number despite the higher shock-upstream Mach number. The third region is characterized by the transition from the more gradual drag increase to the steeper drag rise ($M_\infty < 0.78$), this development being due to a further increase in shock strength (wave drag) and an excessive thickening of the boundary layer resulting in a higher form drag. Finally, there is the very steep drag rise, usually starting when the shock-upstream Mach number exceeds $M \approx 1.25$ and separation starts to develop. Note, that for complete aircraft configurations the Mach number at which this steep drag rise commences may also be influenced by interference drag situations.

The sum of the compressibility drag curves at constant lift coefficient, Fig. 7, leads to the drag-divergence or drag-rise boundary for a specific aircraft configuration. Criteria used to determine this boundary are, as indicated in Fig. 7,

$$C_{DD} = C_{D_{M_\infty}} = 0.60 + \Delta C_{DM}$$

where C_{DD} is the drag coefficient at drag rise and ΔC_{DM} , commonly taken to be 0.002, is the increase in compressibility drag above the drag level at $M_\infty = 0.60$, and

$$(\partial C_D / \partial M_\infty)_{C_L} = \text{const.} = 0.10$$

Both criteria must be applied judiciously if large amounts of drag creep are present (see curves at lift coefficients of $C_L = 0.50$ and 0.70 , respectively). Fig. 8 shows, as a summary, the drag-rise boundary in the well-known $C_L - M_\infty$ -diagram. Also depicted is the buffet boundary which is completely associated with flow separation thus limiting the maximum possible cruise lift coefficient ($C_{LMC} \approx C_{LB} / 1.3$).

At the cruise condition compressibility drag constitutes about four percent of the total drag (Fig. 4). This seems a rather unimportant contribution compared to the other drag elements, mainly friction and form drag and (subsonic) lift dependent drag. However, such an interpretation is misleading since compressibility drag sets, as is indicated by the drag-rise behavior, the boundary up to where fuel efficient flight can be performed [7]. This boundary, as well as the drag level, must be predicted with a high degree of accuracy: Assuming an accuracy of $\Delta C_D = 0.0001$ (see Section 3.1 and Ref. 15) requires, translated to the airfoil considered, the Mach number near the drag-rise boundary to be determined with an accuracy of $\Delta M_\infty = 0.003$.

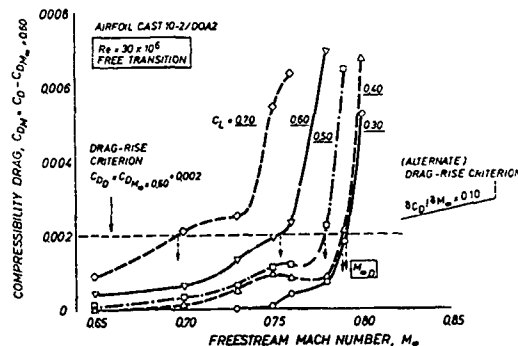


Fig. 7: Transonic Drag Development and Drag-Rise Boundaries

2.5 Reynolds Number Dependence

The Reynolds number capability of today's operational large transonic wind tunnels (except NTF [16]) is substantially less than required for correctly "duplicating"

the full-scale aerodynamics of current and future aircraft. The Reynolds number deficiency would not, however, constitute a major problem if only viscous drag was affected. In reality, scaling problems arise due to the influence of the Reynolds number on

- the boundary layer (displacement) thickness and hence the effective wing contour - supercritical sections may be sensitive to changes in that parameter,
- pressure gradient induced boundary layer separation, the latter occurring, for instance, in the low Reynolds number wind tunnel tests but not, or to a lesser degree, in flight, and
- shock-induced boundary layer separation.

These Reynolds number dependent changes in the flow development not only affect lift but in an intricate way, that seems no longer predictable by conventional means, also drag and the drag-rise Mach number. In what follows, some examples of Reynolds number effects shall be presented, again utilizing results obtained with the supercritical airfoil introduced in the previous section.

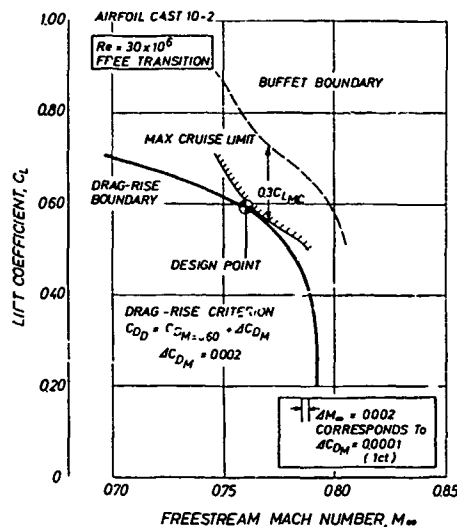


Fig. 8: Drag-Rise and Buffet Boundaries

Airfoil drag at subcritical conditions consists, following Fig. 4, of the minimum profile drag, i.e., mainly friction and form drag at some optimum lift coefficient, and the lift dependent contribution of the friction and form drag. This dependence can, according to Ref. 17, be written as

$$C_D = (C_f)_0 \frac{A_{wet}}{S_{ref}} \cdot FS \cdot F(C_L)$$

where C_{f0} is the skin friction coefficient at optimum lift, A_{wet} and S_{ref} are the wetted surface area and the reference area, respectively, FS is the (empirical) form factor accounting for form drag and $F(C_L)$ is a factor representing the lift dependence. It will be shown later that a quite similar procedure is still being used in extrapolating wind tunnel results to full-scale conditions.

A comparison of the predicted drag, using the above equation together with numerical values given in Ref. 17, and the measured drag at the subcritical Mach number $M_\infty = 0.60$ ($C_L = 0.50$) is presented in Fig. 9 [9]. It can be seen that at $Re \geq 10 \times 10^6$ the predicted and measured trends in the Reynolds

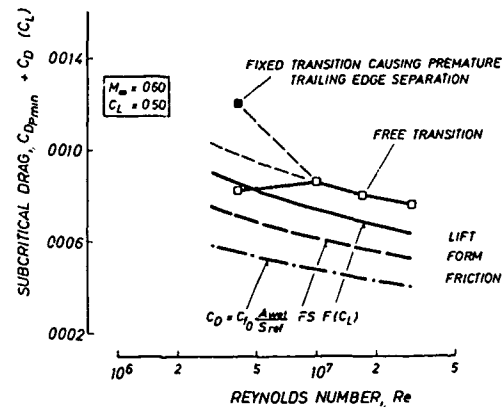


Fig. 9: Drag Dependence on Reynolds Number at Subcritical Conditions. Airfoil CAST 10-2/DOA2

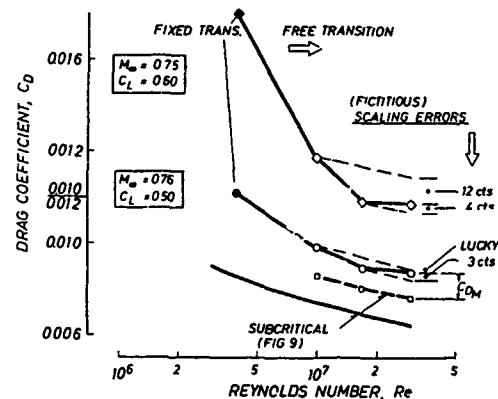


Fig. 10: Drag Dependence on Reynolds Number at Supercritical Conditions. Airfoil CAST 10-2/DOA2

number dependence agree quite well, implying that here the change in skin friction coefficient dominates. (The form parameter is only represented by a constant factor!) At the lower Reynolds numbers some deviations occur: With transition fixed a premature trailing edge separation develops due to the thick initial boundary layer, while in the case of free transition large regions of the flow are still laminar.

At supercritical freestream conditions the Reynolds number dependence of drag no longer follows the trend given by the skin friction coefficient, Fig. 10. At the lower Reynolds numbers form drag due to partial separation dominates. As the Reynolds number is increased, the separation disappears and the displacement thickness is reduced

resulting in a rapid drag decrease. At the higher Reynolds numbers ($Re > 17 \times 10^6$) the shock strength increases due to improved conditions at the trailing edge. The shock losses become larger, partly because the shock associated pressure gradients close to the surface are no longer weakened by the thick boundary layer, and compensate to some extent the positive effects of the Reynolds number on displacement thickness and skin friction. (Note, that also the "sudden" effect of surface roughness on skin friction may contribute to such a trend in the Reynolds number dependence.) The shift in the dominance of the various drag components results in a drag dependence that can, as indicated in Fig. 10 by the dash-dotted lines, no longer be predicted by classical methods.

The development of the compressibility drag with Mach number is also Reynolds number dependent, Fig. 11. Both, the drag-creep and the drag-rise Mach number are influenced: The initial drag-creep is reduced as the Reynolds number is increased, since the higher Reynolds number boundary layer can better negotiate the more severe loads associated with the increasing Mach number, and the drag-divergence Mach number is here shifted to higher values. It is indicated in Fig. 12 that the influence of the Reynolds number on the drag-rise is, however, lift dependent. A pronounced reversal of the Reynolds number dependence can be observed at $C_L = 0.60$ and the higher Reynolds numbers which may, as was indicated

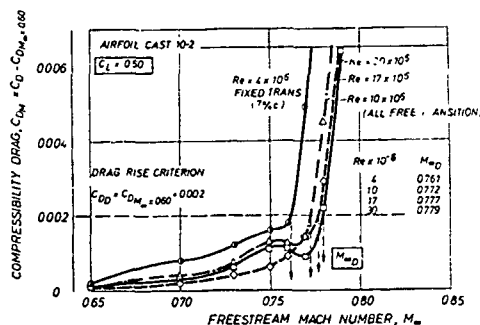


Fig. 11: Reynolds Number Effect on Compressibility Drag and Drag-rise Mach Number

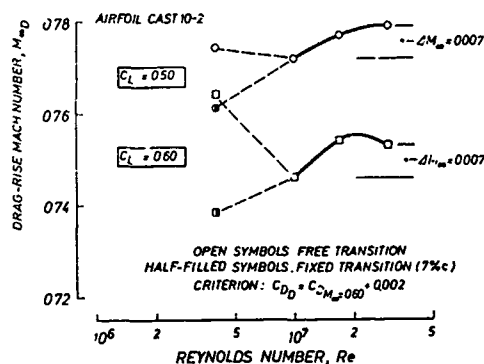


Fig. 12: Reynolds Number Effect on Drag-rise Mach Number

above, be due to the varying balance in the interaction between the outer inviscid flow and the boundary layer as the Reynolds number is increased.

A note of caution, complicating matters, must be introduced: There exists some evidence that the Reynolds number dependence of the drag-rise Mach number may, in part, be due to the effect of the Reynolds number on the effective wind tunnel wall characteristics, the latter being more pronounced for perforated than for slotted wall wind tunnels [18]. The topic of wall interference effects will again be addressed in the next chapter.

3. DRAG PREDICTION BASED ON HIGH-SPEED WIND TUNNEL TESTS

The wind tunnel is considered an indispensable tool for the development of forecasts for the full-scale aerodynamic characteristics as well as for the configuration optimization [12]. The effect of the free-stream conditions, such as Mach number and angle of attack and, unfortunately only to a limited degree, the Reynolds number on the lift and drag of complete configurations and aircraft components can most rapidly and easily be obtained by wind tunnel tests. The wind tunnel can also be used for specific diagnostic flow studies on almost any aircraft component or any sensible combination of components. In all studies flow visualization on the various aircraft surfaces and in the surrounding flow field can be performed to aid in the design process, particularly of the wing, and the concurrent drag analysis. Considering today's demands, a confident prediction of the aircraft performance can only be made through the integration of all types of information from the wind tunnel - pressure data, force data, flow visualization studies - together with, and this is especially true for the transonic speed range, the maximum correlation with full-scale results on similar configurations.

In the present chapter only the drag prediction based on wind tunnel results will be considered with emphasis placed on the discussion of

- the difficulties arising in such wind tunnel tests due to wall and support interferences and the low Reynolds number capacities of the wind tunnels involved and on
- extrapolating the low Reynolds number wind tunnel results to full-scale conditions.

Conventional, generally semi-empirical prediction methods will only be considered as they are employed today to scale the said wind tunnel results. Specific diagnostic flow studies (see, e.g., Ref. 19) will also not be treated in any detail.

Fig. 13 gives an indication of the time when the wind tunnel tests enter the design cycle, starting with exploratory tests of the airfoil and the wing. Intensive wind tunnel tests with the complete configura-

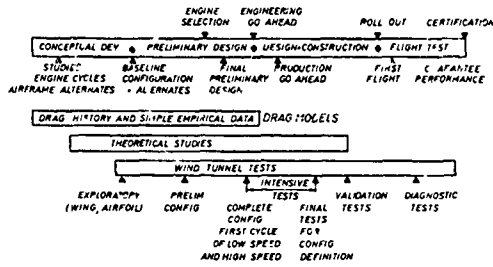


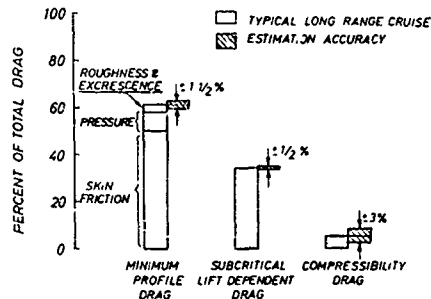
Fig. 13: Airplane Development Schedule, Ref. 12

tion commence shortly before the final design phase. The wind tunnel investigations end with diagnostic studies, if required, as a result of open questions arising during the flight test program. Also shown in Fig. 13 is the relative time span of theoretical studies whose main role today is the provision of a more rapid convergence of the (best) aerodynamic design.

3.1 Accuracy Achieved and Accuracy Required

To determine the accuracy with which the drag at full-scale conditions can be predicted requires extensive flight tests and a very thorough analysis of flight data. Very few reports are published which attempt the total comparison between prediction and flight test results - a glorious exception is, for instance, Ref. 17 - reasons being that (1) such a venture requires a considerable "hardware" effort and expert technical attention and that (2) the data gathered are considered highly proprietary since they contribute significantly to a company's "know-how" [12].

From the information available it seems that for a long range transport minimum profile drag and subcritical lift dependent



L/D Level Achieved	$M_{\infty D}$	Rating
±3%	±0.002	Amazing
±5%	±0.004	Very Good
±7%	±0.006	Average
±10%	±0.010	Below Average

Fig. 14: Drag Source and Estimation Accuracy for a Long Range Transport Aircraft, Ref. 12

drag - to use the drag buildup of Fig. 4 - can be estimated with a fairly high degree of accuracy, viz., ±1.5% and ±0.5%, respectively, while the prediction of compressibility drag is believed to be accurate within ±3%, Fig. 14. So, the ability in predicting the total drag seems quite high - as long as one remains far enough off the drag-divergence boundary: Near cruise the prediction of the drag level is coupled to the determination of the drag-rise Mach number. Assuming the average prediction capability given in Fig. 14, i.e., $\Delta M_{\infty D} = \pm 0.006$, results at the drag-rise Mach number for the design lift coefficient of a modern transport aircraft in a change in the total drag level of about ±3% which, incidentally, corresponds to the accuracy that seems attainable in flight tests [3]. Note, that the numbers quoted reflect the situation as of 1974. With the wind tunnel based methods of drag prediction described below, one is likely (?) to do better than this.

An outline of accuracy requirements and the resulting demand on wind tunnel flow quality, including the requirements for setting the freestream conditions and the demand placed on wall interference correction methods, is given in Ref. 15. Here, it is distinguished between the requirements for

- small configurational changes, i.e., fairings, wing/pylon arrangements, etc.,
- major configurational changes, for instance, different wing geometries,
- assessment of computational methods and
- the prediction of the performance of complete configurations.

Concerning drag, for the first three categories an accuracy of $\Delta C_D = \pm 0.0001$ (±1 ct) was quoted by various industry and research sources to be required, while for the determination of the absolute drag level the situation is somewhat relaxed and an accuracy of about $\Delta C_D = \pm 3$ cts, corresponding to an accuracy of about ±1% for a large commercial transport, was seen adequate. The latter requires an accuracy in the determination of the drag-rise Mach number of approximately $\Delta M_{\infty D} = \pm 0.003$ which in the rating of Fig. 14 settles somewhere between "Amazing" and "Very Good". The latter are, of course, 1974 (?) - standards. A summary of the most stringent flow quality and data accuracy requirements given in Ref. 15 is presented in Table I.

3.2 Wind Tunnel Testing Techniques

Wind tunnel testing techniques have been developed, in part, to cope with the inadequacies resulting from the fixed suspension of a sub-scale model at sub-scale Reynolds numbers in an airstream bounded by test section walls of some kind. For accurate drag prediction one must first overcome the "known" deficiencies of the wind tunnel and only then be concerned with extrapolating the results to full-scale conditions.

Item	Description	Value
w/U_∞	Flow angle	$\pm 0.01^\circ$
$(d(w/U_\infty))/d(x/c)$	Flow curvature	$\pm 0.03^\circ/\text{chord}$
$id(w/U_\infty)/dn$	Spanwise variation in flow angle	$\pm 0.1^\circ$
$dM/d(x/L)$	Mach gradient	$\pm 0.0006 \text{ M}$
Item	Description	2x Value
P_0	Stagnation pressure	$0.001 P_{fs}$
P	Static pressure	$0.001 P_{fs}$
T_0	Stagnation temperature	$0.01 T_0$
M	Mach number	0.002
α	Angle of attack	0.01°
F_N	Normal force	$0.0008 F_{N_{des}}$
F_C	Chord force	$0.0008 F_{C_{des}}$

des = design fs = full scale
w = normal velocity component

Note: The basis is an accuracy requirement in drag prediction of $\Delta C_D = \pm 0.0001$ (1 count)

Table 1: Flow quality and data accuracy requirements, Ref. 15

3.2.1 Transition fixing

Due to the large difference in Reynolds number between wind tunnel and flight there may be a considerable difference in the boundary layer development on the model as compared to the actual aircraft (see 2.5). While the boundary layer on a large aircraft is generally fully turbulent - disregarding here laminar flow aircraft - extensive regions of laminar flow may exist at the low wind tunnel Reynolds numbers ($Re < 10 \times 10^6$). The size of the laminar regions depends strongly on the wind tunnel environment, mainly noise and turbulence level and structure, the model roughness and the (streamwise) pressure gradients on the model surfaces, thus on freestream Mach number and angle of attack. The latter is indicated in Fig. 15 [9] using the supercritical airfoil previously considered as an example. One observes that drag variations up to $\Delta C_D = 0.002$ (20 cts) occur due to the upstream movement of the transition point with increasing angle of attack.

Due to the wide range possible in transition location, it seems that today the only feasible way for an accurate drag prediction is the fixation of the boundary layer transition near the leading edge of the wing and other aerodynamic surfaces. 1) This has, however, the disadvantage that one must deal with a relatively thick, though turbulent, boundary layer which may cause premature separation and hence increased form drag and a lower drag-rise Mach number (see Fig. 11). It seems that, as a result, one must, at least in the vicinity of the cruise point, design the wing in such a way that even at the low wind tunnel Reynolds number separation is avoided. This may, of course, lead to a very conservative wing design.

1) Note, that a remotely controllable transition location together with adequate transition monitoring devices, such as surface hot-film elements [20], would avoid a "permanent" forward transition fixation.

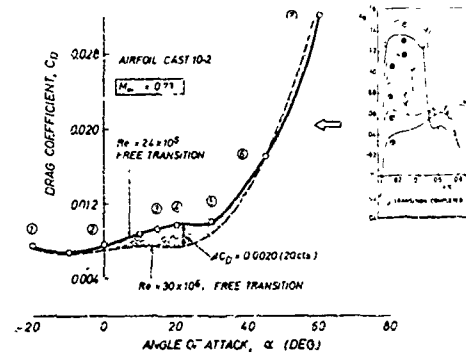


Fig. 15: Effect of Transition Point Location on Total Drag

It was, nevertheless, agreed, at least among the European airframe manufacturers, to follow common procedures in placing transition fixing devices, the position of the roughness element for the purpose of drag prediction selected to be near the wing leading edge, Fig. 16 [21]. It is beyond the scope of this paper to consider the simulation of high Reynolds number flow behavior by aft-fixation, the latter being, for instance, applied in the case of the determination of buffet onset. The reader is here referred to Ref. 9, 22 and 23.

The application of a transition strip - sparsely distributed carborundum grains or ballotini glass beads are commonly used today - requires some skill; however, experience has shown that a once selected and optimized strip can be reproduced confidently. "Optimizing" means to select the "correct" trip size for the model and test conditions considered: Reynolds number at the trip location, Mach number and/or angle of attack or a certain range of these parameters since one is generally not inclined to change the trip location beyond the

PREDICTION OF	TYPE OF BOUNDARY LAYER FIXATION
ZERO-LIFT PITCHING MOMENT (C_{m_0})	FREE TRANSITION
NEUTRAL-POINT POSITION (dC_m/dC_L)	FORWARD FIXATION
DRAG	FORWARD FIXATION
BUFFET ONSET	TRIPPING DEVICE AT ABOUT 15%c UPSTREAM OF SHOCK LOCATION

Fig. 16: Transition Fixation/Location Methodology, Ref. 21

scope indicated in Fig. 16. Correct trip size or critical roughness height implies that the laminar/turbulent transition occurs immediately at the tripping device without introducing additional "roughness" drag.

There are several means of checking whether the trip selected meets the above requirements. One commonly used technique is based on the sublimation process which depends on the difference in heat transfer between laminar and turbulent boundary layers using, for instance, Acenaphthene as an agent [21]. Other methods include the observation of the variation of a suitable aerodynamic parameter, such as drag or trailing edge pressure, with Reynolds number [24], the use of surface pressure holes [25] or, as will be demonstrated below, the application of the surface hot-film technique [20].

Both, "underfixing" the boundary layer, where transition occurs somewhere downstream of the trip, and "overfixing" it, where the viscous layer becomes too thick, have their influence on drag, Fig. 17:

- Underfixing has a negligible effect at the lower lift coefficients (cruise lift) if the trip size is underrated by one grain size on the carborundum grit scale. However, considering the free transition results, one recognizes the great potential for error. Comparing the free and fixed transition results at the higher C_L -values, one realizes that here the roughness element is not at all successful in promoting transition giving most favorable, though erroneous, results.
- Overfixing the boundary layer by one grain size has the same negligible influence as underfixing it except for the adverse influence at the above-cruise lift coefficients. Overfixing by two sizes, however, results in a drag penalty at cruise of about 5 cts which cannot be tolerated.

One must, of course, remember that the "correct" roughness height does not imply the correct simulation of full-scale flow behavior. It is just the prerequisite for the correct scaling of drag. The effect of under/overfixing on lift is depicted in Fig. 18.

As already indicated in Fig. 17, optimizing the tripping device for cruise conditions (zero penalty drag) may lead to an underfixed boundary layer at higher angles of attack - which again suggests the need for a remotely controllable trip. This is due to the stronger acceleration of the flow resulting in an increased stability of the laminar boundary layer. The development is demonstrated in Fig. 19 utilizing results of surface hot-film measurements on a sheared wing, Fig. 19a [25]. With free transition (left column of Fig. 19b), the flow stays laminar up to about 45 % chord. It follows a region of intermittent laminar/turbulent boundary layer behavior and finally, at $x/c = 0.65$, a fully turbulent viscous layer. At an angle of attack of $\alpha = 2^\circ$ and transition fixed at 4 % chord (right column), a turbulent boundary layer is present at and downstream of the first hot-film station, i.e., 8 % chord. At an increased angle of attack of $\alpha = 6.8^\circ$ (center column), a laminar boundary layer prevails downstream of the trip followed by an intermittence region with transition to turbulent flow being completed only at about 50 % chord. The highly unsteady flow behavior indicated at $x/c > 0.50$ is due to shock oscillations. It

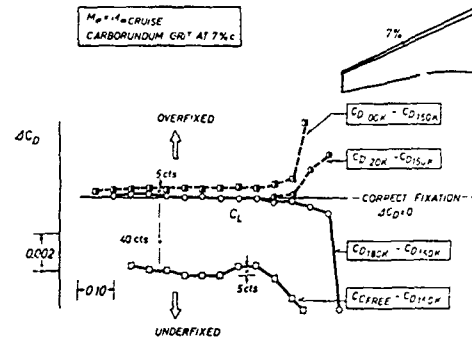


Fig. 17: Effect of Roughness Height on Drag for a Transport Configuration, Ref. 21

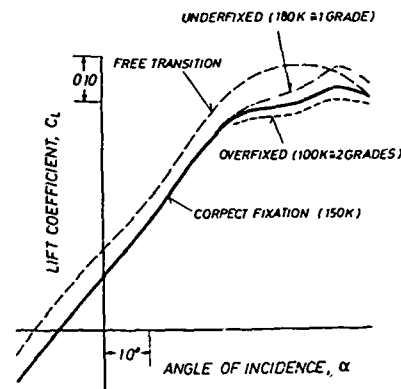


Fig. 18: Effect of Roughness Height on Lift for a Transport Configuration, Ref. 21

should be noted here, that more research concerning transition fixation devices and techniques is needed.

One problem still to be addressed is the selection of the initial roughness height prior to the first tunnel entry. Today, there exists, of course, considerable experience with the tunnel operators and the aircraft manufacturer's teams responsible for the wind tunnel tests with empirical correlations having been successfully established [23]. Originally, the initial trip selection was mainly based on the work of Braslow et al. (see, for instance, Ref. 27) according to which the grit size (of carborundum) was chosen such that the Reynolds number based on local flow conditions and nominal grit height was $Re_k > 600$. Here, one recent research effort to determine the critical roughness height should be mentioned: Michel and Arnal of ONERA/CERT carried out fundamental studies on a flat plate for zero and positive and negative pressure gradients, investigating a great number of different size tripping devices and measuring the boundary layer development for all configurations [28]. As a practical result, they were able to plot the critical grain size required for fixing transition at the roughness location, Fig. 20. They found, furthermore, that the roughness drag associated with an "optimized" grit strip is about $\Delta C_{Dk} = 0.0002$ (2 cts). It must, however, be pointed out that

the roughness elements considered were, against common practice, densely packed. The results of the basic studies were successfully applied to transition fixing on a supercritical airfoil.

For military combat aircraft at full-scale conditions transition is likely to occur at or near the leading edge of the wing, so that for the drag prediction in sub-scale wind tunnel tests a forward transition fixation is frequently employed.

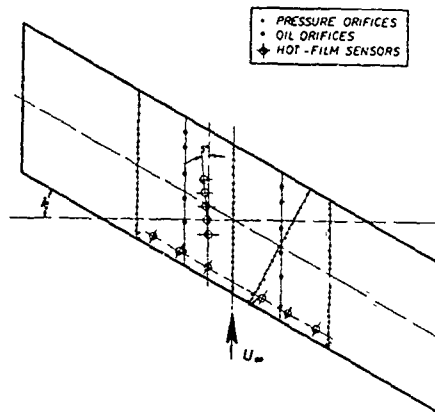


Fig. 19a: Sheared-wing Instrumentation

Fig. 19b: Surface-hot-film Signals for Laminar, Transitional and Turbulent Boundary Layers on a Sheared Wing

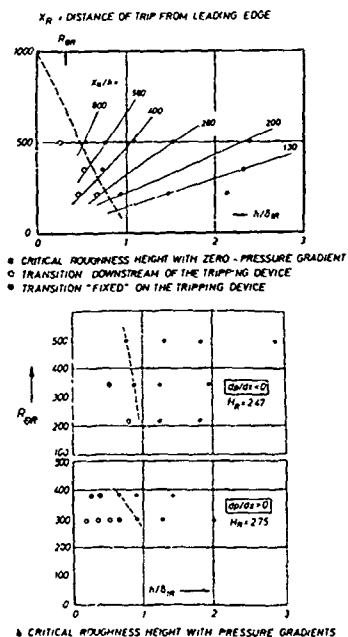
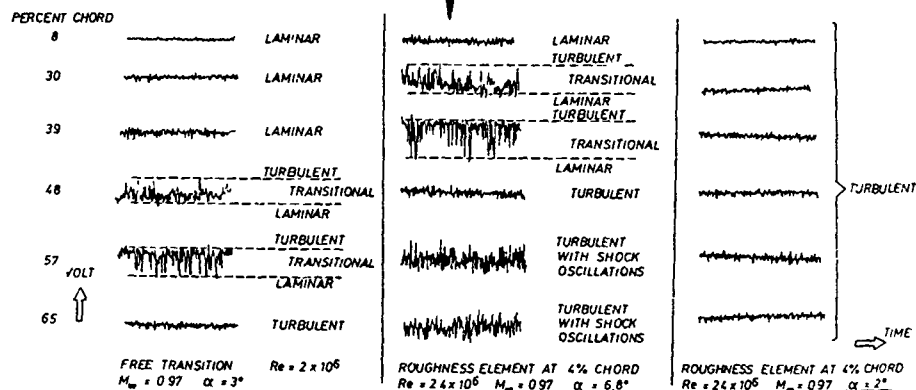


Fig. 20: Critical Roughness Height, Ref. 28

3.2.2 Wind tunnel wall interference

It is obvious that the constraints imposed by the wind tunnel walls - unless they are fully adapted - may influence the flow about a model thus inducing deviations from free-air flow in the measured freestream conditions and the forces and moments acting on the model. Major aerodynamic problems may arise from

- solid and wake blockage effects, introducing a disturbance flow velocity in streamwise direction which may vary over the model length,
- lift interference effects (upwash and streamline curvature), mainly introducing a disturbance velocity normal to the freestream direction, and
- shock wave reflections at the walls at $M_{\infty} > 1$.

Nearly all aspects of test section walls, wall interference effects and correction methods are treated in detail in Ref. 29 (ventilated test section walls), Ref. 30 (classical correction methods), Ref. 31 (modern approaches to wall interference) and Ref. 32 (two-dimensional wall interference).

Both, blockage and lift interference may affect drag and the effective drag-rise Mach number as a result of the longitudinal disturbance velocity distribution and its level. Inaccuracies in the angle of attack enter the drag prediction due to the fact that the forces measured by the internal balance are normal and tangential forces that must be converted into lift and drag. The data accuracies that must be maintained by the combination wall interference/wall correction are listed in Table 1. It is believed that these demands cannot be met by classical correction methods.

At transonic speeds the blockage and lift interference effects on drag and drag-divergence Mach number may be quite severe. This is demonstrated in Fig. 21 again using the previously cited supercritical airfoil as an example. In this figure, the Reynolds number dependence of the drag-divergence Mach number at $C_L = 0.50$, originally plotted in Fig. 12, is compared with corresponding data obtained with two different sized models of the same airfoil in the NASA 0.3-m Transonic Cryogenic Wind Tunnel (TCT) [18]. In the lower Reynolds number range agreement exists in the gradients, while the level in the drag-rise Mach number is widely different. The latter is, at least in part, due to differences in the magnitude of wall interference. It seems that the effective freestream Mach numbers for the larger models (height/chord = 4) are lower than indicated by the respective curves. At the higher Reynolds numbers - $Re > 10 \times 10^6$ - a deviation in trends occurs in addition to the difference in level. One possible explanation: The effective wall open area ratio increases with Reynolds number more strongly for the perforated CFWT than in the case of the slotted TCT resulting for the former in a pronounced reduction in the effective freestream Mach number. At the lower Reynolds numbers this process is masked by the dominance of viscous effects. The drag-rise behavior, determined from uncorrected wind tunnel results, demonstrates the need for adequate correction procedures.

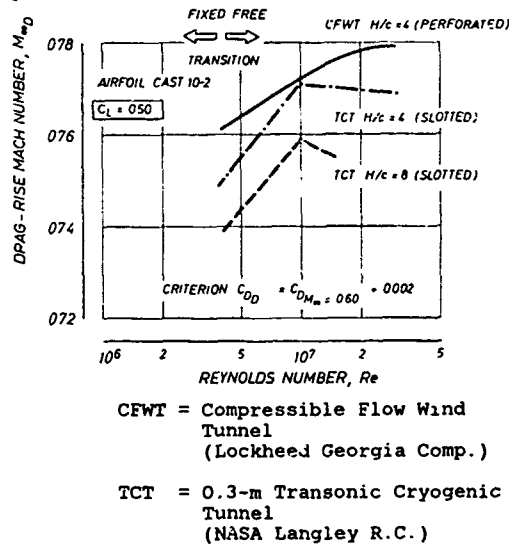
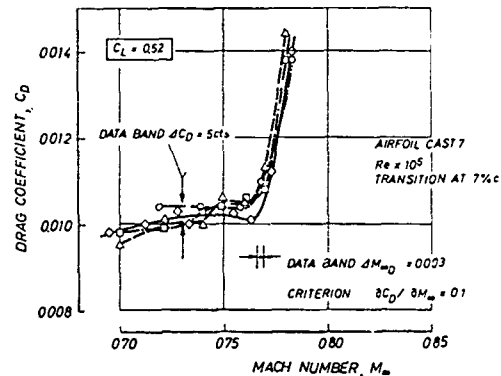


Fig. 21: Reynolds Number Dependence of Drag Rise and Wall Interference

Correction procedures have been applied to the freestream conditions and the aerodynamic coefficients of the results depicted in Fig. 22 [33]. This figure shows the compressibility drag of the airfoil CAST 7/DOA1 near the design lift coefficient ($C_L = 0.52$) determined in four different wind tunnels. One observes that deviations in drag level with respect to the adaptive wall wind tunnel T2 (ONERA), considered essentially interference free, is about $\Delta C_D = \pm 0.0003$ prior to the drag divergence, while the spread in the drag-divergence Mach number is $\Delta M_{\infty D} = 0.003$. This is judged to be the best one can achieve today in two-dimensional non-adaptive wall wind tunnel tests.



Tunnel	Wall Type	τ (%)	H/C
○ S3Ma	Perforated	9.7	3.9
△ TWB	Slotted	2.35	3.0
□ ARA	Slotted	3.2	3.6
◇ T2	Adaptive	---	1.9

Fig. 22: Airfoil Drag Behavior Determined in Various Wind Tunnels

One can minimize wall interference effects in the following ways: 1) Reduce model size (blockage $< 0.5\%$), utilize partially open wind tunnel walls optimized for zero blockage (2-d tests) or zero lift interference (3-d tests), apply appropriate correction methods, i.e., correction methods based on measured boundary conditions [31] or, ultimately, use adaptive wall wind tunnels. As an example of the considerable merit of such a tunnel, Fig. 23 [34] presents the drag polar determined in the adaptive wall rubber-tube wind tunnel of the DFVLR [35] for a generic fighter aircraft with slats and flaps deployed. The data are compared to results obtained with the identical model in the DFVLR 1 x 1 m² Transonic Wind Tunnel Göttingen (TWG) and the 1.6 x 2.0 m² High Speed Tunnel of the NLR (HST), the latter being considered interference free. The small adaptive wall test section of 0.8 m diameter (0.50 m²) provides results, especially in the minimum drag and positive lift range, in close agreement with the data of the much larger HST, while the TWG indicates a noticeable deviation from these data ($\Delta C_{D_{min}} = 12$ cts).

1) Listed in the order of "sophistication"

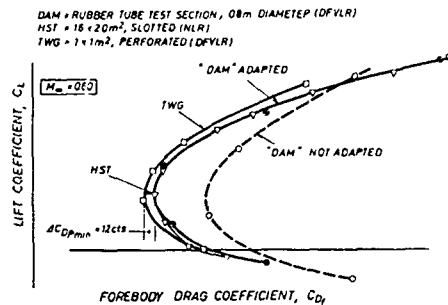


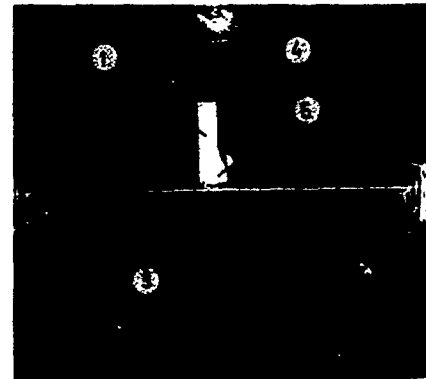
Fig. 23: Drag Polar of a Generic Fighter Model: Comparison of Conventional and Adaptive Wall Results

Today, most large transonic wind tunnels have partially open slotted or perforated test section walls. In the past, it was believed that in these tunnels for "reasonable size models" at moderate lift coefficients wall interference was negligible, hence most aircraft configuration experiments did not include any corrections for wall interference [36]. However, for the more advanced transonic configurations with substantial regions of supersonic flow it seems no longer possible to neglect wall interference effects and the best (correction) procedure available must be applied.

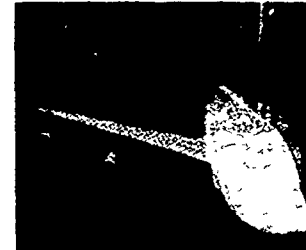
3.2.3 Support interference effects

There exist various arrangements to suspend a model in the test section of a wind tunnel mainly dependent on the purpose of the tests. Some model support systems are illustrated in Fig. 24 [9][36]. Fig. 24a shows the typical setup for airfoil tests, here with a probe mounted for extensive boundary layer and wake surveys, the latter to determine the airfoil drag components. Support interferences result mainly from the interaction of the model and its flow field with the side-wall boundary layer. It is indicated in Ref. 37 that these effects can be neglected if aspect ratios - tunnel width/model chord - greater than two are employed. Half-model tests, Fig. 24b, may in general be used if model details must be resolved that cannot otherwise be achieved. Typical examples, mainly related to wing flow, are investigations of winglets, wing/pylon/nacelle interferences, the interference due to simulated propulsion systems employing, e.g., Turbine Powered Simulators (TPS) (see 3.2.4), and completely new wing designs. The support interference is in essence restricted to the fuselage. The half-model approach is generally not well suited to predict absolute drag levels [38]. For production type aircraft developments, sting mounted models are generally employed, Fig. 24c.

A significant amount of uncertainty in the drag prediction may be introduced by sting suspension systems, several of which are sketched in Fig. 25 [12]. Each of the different mounting systems introduces a dif-



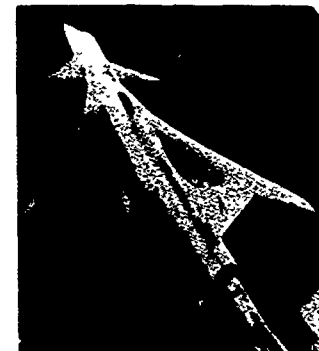
- ① Probe drive
 - ② Airfoil
 - ③ Probe support and probe
 - ④ Sting support
 - ⑤ Sting
 - ⑥ Rotatable discs
 - ⑦ Schlieren window
 - ⑧ Perforated walls
- a) Airfoil model test setup, (Ref 9)



b) Half-model Test Setup, Ref. 36



Lockheed C-5A aircraft



Grumman advanced fighter configuration

- c) Examples of Sting Mounted Models, Ref. 36

Fig. 24: Typical Model Support Arrangements

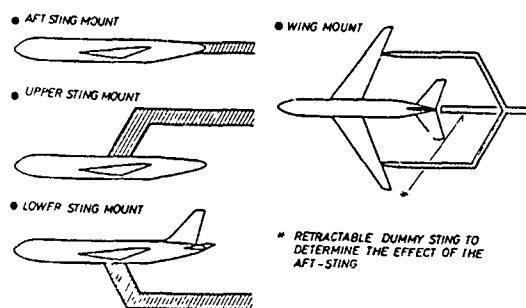


Fig. 25: Typical Model Suspension Systems, Ref. 12

ferent upwash and buoyancy due to its own pressure field and the additional blockage introduced into the wind tunnel test section. (Note, that an adaptive wall wind tunnel also eliminates these interferences.) In addition, and this seems more severe, viscous, form and vortex drag may be generated at the intersections between the model and its support system which must be corrected for. Such corrections may be determined by using various combinations of supports with the same model (Fig. 25). An excellent example of the effort one must invest to determine the interference drag due to the model support is given by Patterson et al. [17] who preferred the lower sting/blade mount (Fig. 25) for the regular tests and used the upper sting mount together with a "dummy" lower blade to determine the interference. Patterson et al. found that the interference drag for the model (C5A)/lower-sting-mount system was approximately six (6) aircraft drag counts at the cruise lift coefficient, or about 2.5 % (?) of the total drag, an amount that cannot be neglected. For further information on sting interference, the reader is referred to Ref. 31.

3.2.4 Component testing and flow diagnostics

An aircraft consists of many components which can initially be tested independent of each other. That way, larger models (or smaller facilities) may be utilized and much more detailed investigations, especially into the physics of the flow, are possible. A good example are airfoils and individual wings where, besides development tests, detailed studies can be performed consisting of surface pressure, boundary layer, field and wake measurements using either conventional probes (Fig. 24a) or more sophisticated LDV-equipment. It is not intended to elaborate further on this "Lecture-series-filling" subject except for a brief outline of procedures used to determine the drag contribution of the propulsion system which is again an area in drag prediction associated with a large amount of uncertainty.

The complete aircraft is in tests used to develop the airframe commonly equipped with flow-through nacelles set at cruise inlet airflow conditions (Fig. 24c). Interactions at the inlet and/or the nozzle of the propulsion system produced by changes of airflow accompanying thrust changes require separate and very careful wind tun-

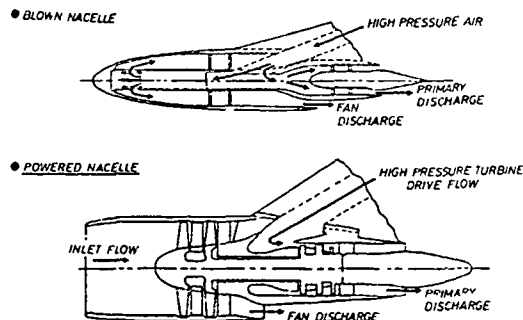


Fig. 26: Propulsion System Simulation, Ref. 12,39

nel testing, preferably using powered nacelles in combination with either complete, possibly, however, half-models, Fig. 26 [12][39]. The drag buildup can here, as proposed in Ref. 12, be associated with the equation

$$C_D = C_D' + \Delta C_{D_{\text{INLET}}} + \Delta C_{D_{\text{THRUST}}}$$

where

- C_D' is equal to the full-scale prediction of drag based on complete model tests with flow-through nacelles, corrected for excrescence drag, trim drag, Reynolds number effects, etc.,
- $\Delta C_{D_{\text{INLET}}}$ is the incremental force due to a variable inlet velocity ratio and
- $\Delta C_{D_{\text{THRUST}}}$ is the incremental force due to the fan and/or the primary exhaust flow (Fig. 26a).

Note, that tests with powered nacelles at cruise conditions are only carried out if the effect of the exhaust jet on the aircraft flow field is expected to be significant. For the determination of $\Delta C_{D_{\text{INLET}}}$, tests with throttled flow-through nacelles might suffice. (For the effect of the propulsion system on the aircraft flow field and test procedures see, e.g., Ref. 40).

The influence of the power plant installation on drag is obtained as shown in the drag polar buildup of Fig. 27 [12], also indicating one possible drag/thrust interface: Given is the drag polar obtained with flow-through nacelles at the cruise inlet velocity ratio corrected as indicated above

and with the nacelle internal drag removed, the latter, for instance, calculated with the measured internal pressure distribution. Added or subtracted (inlet lip suction dominates) will be the contribution due to the change in inlet velocity ratio, V_1/V_{∞} , obtained from tests with varying inlet mass flow. The thrust effect is determined by blowing at varying rates relative to the ram pressure ratio of the flow-through nacelle at cruise conditions. It should be noted that when using powered nacelles, the wind tunnel balance registers the difference between thrust and drag. The thrust is accounted for by calibration results obtained with the TPS in static tests. The latter are described in some detail in Ref. 39 and 41.

3.3 Extrapolation of Wind Tunnel Results to Full-Scale Conditions

The process of transforming wind tunnel test results to full-scale aircraft performance data in the transonic flight regime is one of the main and most difficult tasks of aircraft design. It is so important since errors in the prediction of cruise drag can have serious consequences for the manufacturer due to the stringent requirement to guarantee performance data within close margins in order to be competitive [7]. Erroneous load prediction may, in addition, cause grave re-design problems.

For the scaling process, based on already corrected (for wall and support interferences) wind tunnel data, several operations are necessary to arrive at the full-scale aircraft drag: (1) The model data must be "adjusted" due to one or two orders of magnitude difference in Reynolds number between wind tunnel and flight. (2) Drag items which cannot be simulated in the model test - surface roughness, excrescences, etc. - must be assessed. (3) Corrections for thrust effects must be applied. Today, basically two approaches to full-scale aircraft performance prediction from wind tunnel measurements are being pursued.

3.3.1 The direct scaling method

The drag components comprising the total drag (Fig. 4) can be split into the minimum profile drag (parasitic drag) and the lift and Mach number dependent drag, the latter including trim drag which is, however, generally not accounted for in the drag polars established in the wind tunnel:

$$C_D = C_{D_{Pmin}} + \Delta C_D(C_L; M_{\infty})$$

In the direct scaling approach, the second term is directly transferred to the actual aircraft, although this term might be highly Reynolds number dependent. The first term can be split into its components

- friction and pressure (form) drag,
- interference/intersection drag,
- roughness/excrescences drag accounting for steps, gaps, rivets, antennae, canopy, lights, roughness different from the model, etc. and

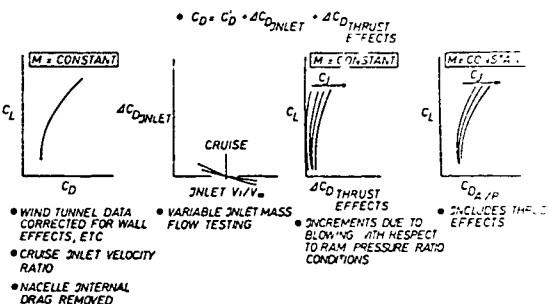
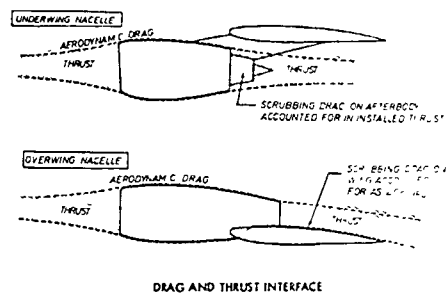


Fig. 27: Drag Polar Buildup Procedure, Ref. 12

- ventilation drag accounting for air conditioning, cooling and other vents.

All of the above drag increments may be subject to Reynolds number effects; however, in the direct method only the skin friction drag is adequately treated. The overall methodology of the approach is sketched in Fig. 28 taken slightly modified from Ref. 21: Basically, the skin friction at the wind tunnel Reynolds number for all components is removed from the total drag and similarly is the skin friction drag at the full-scale Reynolds number added using results based on flat plate calculations. The form or pressure drag can be treated in the same way. It is, however, as will be seen below, generally being accounted for by a multiplicative factor to the skin friction drag which is mainly based on empirical data. The procedure implies that

$$\frac{C_{D_{Pmin}}}{C_f} \text{ Wind tunnel} = \frac{C_{D_{Pmin}}}{C_f} \text{ Full-scale}$$

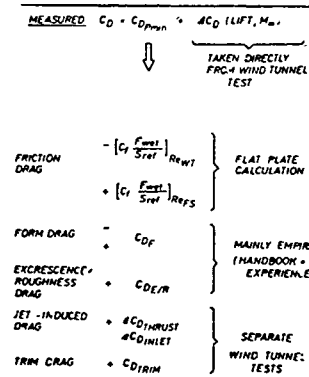


Fig. 28: The Direct Scaling Method

Roughness is dealt with by assuming a certain "sand grain roughness" for the actual aircraft on which the skin friction coefficient at the flight Reynolds number is based [3], while the excrescence drag to be added is obtained from handbook-type sources as, for instance, Ref. 42 (also see Ref. 43). Jet-induced drag is obtained as described in the previous section. Trim drag, resulting from the fact that, in flight, all forces must be balanced is also determined in (separate) wind tunnel tests with control surfaces deflected.

The main effect of the Reynolds number on drag is, as indicated above, obtained through relations based on some flat plate skin friction laws. For the laminar part - known for the model due to the effort put into transition fixing - there exists little controversy in using the Blasius formula derived from the exact solution to the laminar boundary layer equations for zero pressure gradient [3]:

$$C_f = 1.32824/Re^{1/2}$$

For the turbulent boundary layer various correlations exist, Fig. 29 [3]: One observes that a very significant change in C_f - hence in predicted drag - can occur in scaling from wind tunnel to flight ($Re = 3 \times 10^6 \rightarrow Re = 40 \times 10^6$) if different correlations are used. Patterson et al. [17] have shown, however, that the Karman-Schonherr formula

$$C_f^{-1/2} = 4.13 \log (Re \cdot C_f)$$

where Re is the Reynolds number based on a typical component length, e.g., the wing reference chord, constitutes a good representation of existing experimental results. A relatively new relation for the compressible turbulent skin friction, developed by White and Christoph [44] and reported in Ref. 12,

$$C_f = 0.42/\ln^2 (0.056 \times Re),$$

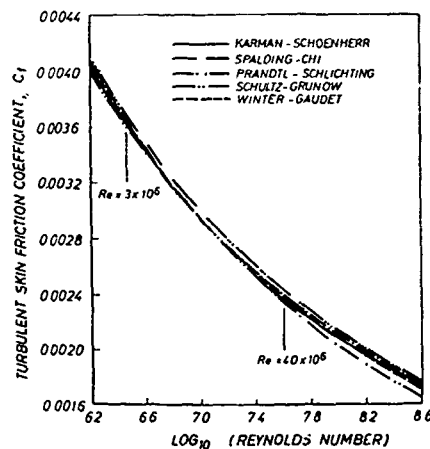


Fig. 29: Comparison of Empirical Flat Plate Skin Friction Formulae for Incompressible Turbulent Flow, Ref. 3

is supposed to be accurate to within ± 4 percent in a Reynolds number range between $Re = 10^5$ and 10^9 .

The form drag resulting from the effect of the non-zero pressure gradient (aircraft component thickness) is, as mentioned above, commonly accounted for by a multiplicative factor applied to the skin friction drag for each component, hence

$$\Delta C_{D_{Pmin}} = C_f \frac{A_{wet}}{S_{ref}} \cdot FS$$

with FS being the component form or shape factor. Formulae/graphs for determining the form factors for all aircraft components are given, for instance, in Ref. 42, 45 and 46 (also see Ref. 12) along with their application in drag determination. It must, however, be realized that the form drag follows the same dependence on Reynolds number as the skin friction which may, as is indicated in Fig. 10, lead to considerable errors in the predicted full-scale aircraft drag.

The deficiencies pointed out above together with the fact that the Reynolds number influence on all other drag components (e.g., lift dependent and compressibility drag) is not at all accounted for, led to the introduction of a further (complementary) method for the prediction of the full-scale aerodynamic characteristics of a new design.

3.3.2 The reference scaling method

The reference method utilizes the experience gained in a company in wind tunnel and flight tests and the correlation of the data sets obtained in these tests. Best use of the method can, of course, be made if the aircraft to be developed is in many aspects similar to an earlier configuration tested in the whole range of Reynolds numbers up to flight conditions. It is especially advantageous if the fuselage stays quite similar in shape as in an aircraft family concept such as Airbus [7]. Here, most(!) prerequisites for a successful application of the method are met, viz., the (near) identity for the reference and the new aircraft of

- wind tunnel, wind tunnel balance and model support,
- model scale, fuselage and model material (aeroelastic effects),
- transition location, Mach and Reynolds number.

Using the same wind tunnel, support and model scale will, of course, put less emphasis on wind tunnel wall and support correction procedures.

The basic principle of the present scaling methodology, first introduced in 1975 [47], is sketched in Fig. 30 taken slightly modified from Ref. 21. The changes in aerodynamic drag between wind tunnel and flight test of the known aircraft are transferred to the new design. Prior to this transfer, the reference full-scale data are stripped of drag components not present on the wind tunnel model and/or particular to either

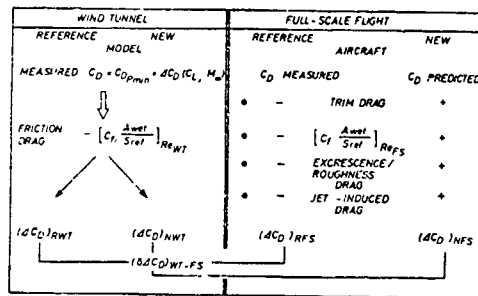


Fig. 30: The Reference Scaling Method

aircraft, such as for instance trim drag, roughness drag, jet-induced drag and skin friction drag. After adjusting the new configuration wind tunnel data, these drag items, determined for the new design, will be added to give the final "predicted" drag coefficient for the new aircraft. The accuracy in drag prediction attainable with this method seems quite high. There is, however, no published evidence that it will meet the accuracy requirements given in Section 3.1.

There are still some major drawbacks inherent in the method as it is applied today: Conventional semi-empirical means are used to determine the skin friction drag, assuming that the form drag stays essentially the same for both aircraft. Also assumed is, of course, that the lift and Mach number dependent drag follow similar trends for the reference and the new design as the Reynolds number is increased. If the wing section characteristics are drastically altered, however, as was done in going from conventional to supercritical wings (technology jump), the approach cannot provide the necessary accuracy.

3.3.3 Higher order reference method

Fig. 31(a) [7] compares the pressure distributions of two wing sections, designated reference and projected aircraft, at the design lift coefficient and a Mach number above the design, where mainly the shock location and the rear loading are different. The boundary layer displacement thicknesses computed with these pressure distributions, assuming transition from

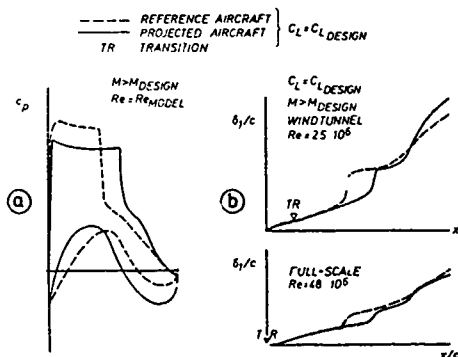


Fig. 31: Representative Pressure and Boundary Layer Developments for a (Conventional) Reference and a New Wing Design, Ref. 7

laminar to turbulent flow to occur at the leading edge at full scale and at 15% chord for the model Reynolds number, are shown in Fig. 31b. One observes essential differences in the development of the displacement thicknesses at the wind tunnel and at the full-scale Reynolds number which are, as far as the outer inviscid flow is concerned, mainly due to the stronger (upper surface) rear adverse pressure gradients and the more aft shock location in case of the projected wing section. While, at the model Reynolds number, the boundary layer on the projected wing increases so strongly that the displacement thickness at the trailing edge is larger for the new wing than for the reference wing, at the full-scale Reynolds number the reverse is true. When scaling by the conventional reference method, this behavior would lead to an overly pessimistic prediction of the full-scale lift to drag ratio, the drag-rise Mach number and separation, hence buffet onset. The "Reynolds number sensitivity" of a configuration thus plays a crucial role in scaling by the reference method that must in some way be accounted for. Fig. 32 depicts the Reynolds number sensitivity of wing sections with regard to drag. It was established in Ref. 9, based on experimental results, that this sensitivity depends on the freestream Mach number, i.e., the type of pressure distribution, and certain geometric parameters representing the upper surface rear adverse pressure gradients and the trailing edge angle. It is indicated below how such curves can bridge the gap between any reference and new wing section when scaling by the reference method.

An improvement of the reference method is outlined in Fig. 33 [7]. In addition to the "DELTA" obtained from wind tunnel and flight test results for the reference aircraft, calculations must be performed for the reference as well as the projected aircraft (wing) at model and full-scale Reynolds numbers. This will indicate essential differences in the sensitivity between the two configurations considered which may then be accounted for by theoretical or empirical corrections, the latter attainable from graphs like the one shown in Fig. 32. Note, that the curves of Fig. 32 may also be used to check the Reynolds number sensitivity of any wing design.

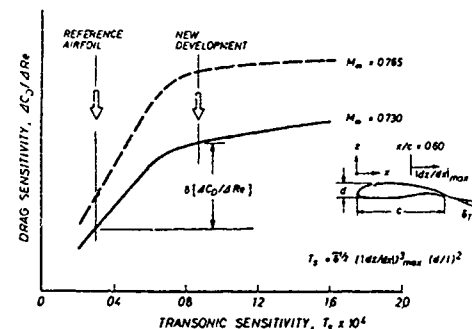


Fig. 32: Reynolds Number Sensitivity and "Technology" Drag Increment

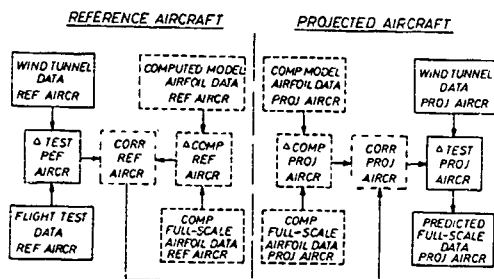


Fig. 33: Higher Order Reference Method, Ref. 7

Alternately, knowing the sensitivity may allow the selection of more realistic test conditions, implemented, for instance, by a more aft fixation of transition, in the low Reynolds number wind tunnel tests. In the case of Fig. 31 this would mean that the boundary layer growth across the shock and

the sustained rear adverse pressure gradients would be less pronounced at the wind tunnel Reynolds number. The integration of advanced computational methods into the scaling process may thus allow in the future

- a more reliable scaling of low Reynolds number wind tunnel results in the case of different wing sections for the reference and the projected aircraft, which is in part due to a more realistic transition fixation on the wing in the wind tunnel experiments.

The latter requires, however, as outlined above, for a successful application the development of new transition fixing techniques.

In concluding this section it should be noted that there exists, at present, the AGARD Working Group O9 "Boundary-layer Control and Simulation in Wind Tunnels" which is concerned with the very subject of this chapter.

4. TRANSONIC DRAG REDUCTION BY ACTIVE/PASSIVE BOUNDARY LAYER CONTROL

4.1 General Remarks

One of the principal objectives of present-day airplane design is the optimization of the aerodynamic efficiency parameter $M \times L/D$. Typically, this performance parameter increases with Mach number, as was shown in Fig. 1, until the transonic drag rise associated with the occurrence of local supersonic flow regions and shock waves offset the Mach number increase [13]. On the other hand, the direct operational costs (DOC) of a commercial transport decrease gradually with increasing cruise Mach number to a minimum near $M_{\infty} = 0.80$ for a transcontinental airplane.

Wing sweep enabled the optimum cruise Mach number to be increased when conventional airfoil sections were used, but increased the structural weight of an airplane as well. In comparison to earlier designs improved airfoil technology allows - for the same cruise Mach number - the wing sweep to be reduced, the relative thickness of the airfoil section and the wing span to be increased. Less wing sweep increases the low speed performance and reduces the structural weight. A thicker wing increases the fuel volume, hence the range, and increased wing span reduces the lift dependent induced drag.

Appreciable performance advantages are obtained by utilizing (so-called) supercritical airfoil sections. Due to an extended supersonic region on the upper surface and a highly cambered aft portion these airfoils produce substantially higher lift for a given thickness and drag at high subsonic Mach numbers. In addition, the drag-divergence Mach number is appreciably increased for a given thickness, Fig. 34. Instead of increasing the cruise speed at the same wing sweep and thickness, the current trend for commercial airplanes is to reduce the sweep angle with the above mentioned potential of increasing thickness and aspect ratio [13][48].

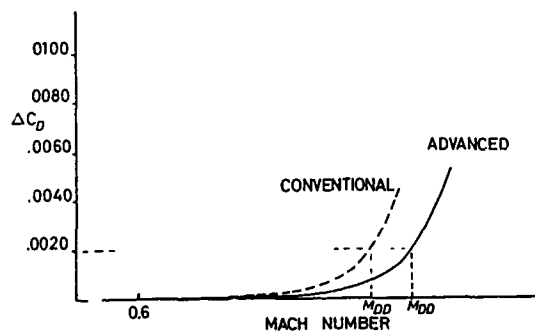


Fig. 34: Drag Rise of Conventional and Advanced Transonic Airfoil

A typical total drag buildup for a long range transport airplane at cruise conditions has been described earlier in the present paper, Fig. 4, showing the basic drag (mainly friction and form drag) to be about 57 percent and the induced drag to be about 31 percent of the total drag. The largest potential in reducing total drag lies, of course, in the reduction of friction and induced drag. Corresponding drag reduction methods have been described variously in the literature, [49] through [55], and are the topic of several papers of the present Lecture Series [56]. The compressibility drag, mainly wave drag associated with the occurrence of shock waves on the upper wing surface, contributing in this example 4 percent to the total drag, may be minimized by utilizing shock-free airfoil design [57][58]. However, during a given flight the cruise lift coefficient may vary by as much as $AC_L = 0.1$, and such deviations from the design point will immediately cause shock waves, although weak, to occur on the wing, and the total drag will correspondingly increase through increased wave drag and possibly higher form drag due to shock induced separations on the wing. Since the wing and its components contribute as much as two-thirds to the total drag of the airplane at cruise conditions, [13], the off-design characteristics of an airfoil have to be carefully determined, and it is worthwhile to look for or consider means of drag reduction at off-design conditions in order to improve the airfoil section performance in this regime.

To influence the flow development most favorably, a sound physical understanding of the flow phenomena to be affected is necessary. Because of the complexity and mixed character of the transonic airfoil flow (supersonic regions embedded in a subsonic flow, and possibly separated regions) which is strongly influenced by viscous effects, it is useful to consider the relevant flow features first for the two-dimensional case. We shall give, in the following, a brief description of the nature and the effects of normal shock boundary layer interaction on transonic airfoils. This will be followed by a consideration of methods which may be used to affect this interaction and a presentation of representative experimental results.

4.2 Transonic Shock Boundary Layer Interaction

4.2.1 Two-dimensional flow

The flow about a supercritical airfoil at high subsonic speed is characterized by the relatively large supersonic region on the upper surface which, at the design condition, is terminated by a near isentropic recompression (shock-free design) or by weak shock waves, Fig. 3, hence the wave drag is minimized. With increasing freestream Mach number or incidence the shock strength is increased and the shock position shifts downstream simultaneously. This progressive rearward extension of the supersonic flow as the terminating shock moves downstream over the upper surface is an essential feature of the flow development on a supercritical airfoil. During this process, the boundary layer ahead of the shock grows thicker, allowing viscous

interaction effects to become more pronounced. While in the outer inviscid flow the pressure increases nearly discontinuously across the shock, this steep pressure rise is smoothed in the boundary layer because the overall pressure rise is partly transmitted upstream through the subsonic part of the boundary layer. This causes the streamlines at the front of the interaction region to diverge, generating compression waves in the outer supersonic flow field, thus thickening the boundary layer in the shock region strongly ("viscous wedge").

As the shock strength is further increased, either by Mach number or incidence, the rearward movement of the shock is slowed down by the progressively thickening boundary layer until, at a certain shock strength, the boundary layer can no longer negotiate the pressure gradient imposed by the shock and separates, forming a separation bubble. Although the boundary layer velocity profiles may not have fully recovered even after 50 boundary layer thicknesses downstream of reattachment, the consequences on the overall flow and airfoil loading are usually not serious [59]. However, when the shock fails to re-establish subsonic flow immediately downstream, the separation bubble expands rapidly towards the trailing edge [9][60][61][62].

Sustained adverse pressure gradients downstream of the shock, most likely to occur on present-day highly loaded aft-cambered airfoils, will either amplify the effects of shock-induced separation or cause a trailing edge separation to occur first which may lead to different combinations in the development of the two types of separation [11]. In any case, significant effects on the steady-flow loading and the overall flow development on the airfoil are generally observed when severe separation occurs at the trailing edge which is indicated by a rapidly decreasing trailing edge pressure. Due to displacement effects of the separated region, the downstream movement of the shock is reversed, and any fluctuations of the trailing edge pressure, arising from the inherent unsteadiness of the separated flow, may lead to shock oscillations with corresponding fluctuations in overall loading (buffet-onset) [63][64][65][66].

It was one of the major findings in the very early experiments on transonic shock boundary layer interaction of Ackeret et al. [67] and Liepmann [68] that the shock wave patterns and pressure distributions are strongly dependent on the state of the boundary layer. For a constant Mach number the interaction between a normal shock in the outer flow with a laminar boundary layer results in the formation of a λ -shock system, the interaction region extending about 15 to 100 boundary layer thicknesses upstream. Shock-induced separation occurs at lower shock strength than for the turbulent case, and the extents of interaction and separated regions are strongly Reynolds number dependent. For a turbulent boundary layer the interaction region is much smaller, only 5 to 15 boundary layer thicknesses, higher shock strengths can be negotiated without separation and the shock turbulent boundary layer interaction is less sensitive to Reynolds number vari-

ations. Further details on this topic may be found in Refs. 63, 69 and 70.

Since in almost all practical cases on transonic aircraft wings the boundary layer is turbulent from or from near the leading edge, we will be mainly concerned with turbulent shock boundary layer interaction and its control, though laminar interaction will be of some importance on airfoils with laminar flow control (LFC) or natural laminar flow (NLF).

4.2.2 Three-dimensional flow

The flow development about a three-dimensional wing is much more complicated than in the two-dimensional or quasi two-dimensional (infinitely swept airfoil) case [71][72][73]. Although significant features of two-dimensional shock boundary layer interaction may be utilized as a guide in swept wing design, [74][75][76], the flow field on a swept wing at high subsonic speeds is almost unpredictable due to strong spanwise flow components, shock waves, vortex systems, separating and reattaching flows. An airplane designer, therefore, has to rely on wind tunnel experiments despite of all the inherent shortcomings as scale effects, wall interferences etc., outlined in Chapter 3, [22][36][77][78][79]. It is difficult to give a general description of the three-dimensional swept wing flow, because of the numerous parameters characterizing each particular case: wing sweep angle, thickness, aspect and taper ratio, camber and twist distribution.

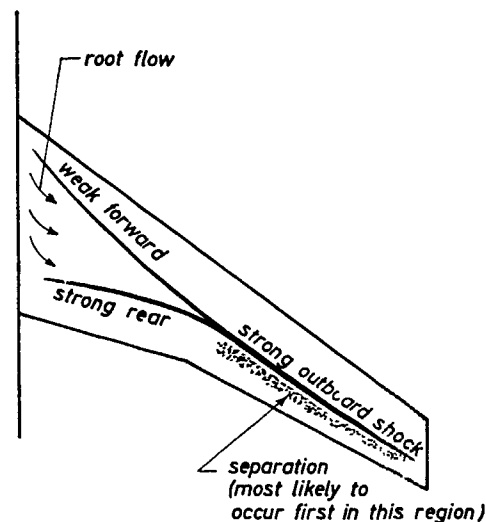


Fig. 35: Three-Dimensional Swept Wing Flow Pattern

A typical flow pattern on a swept wing at high subsonic speed is sketched in Fig. 35, exhibiting the characteristic three-shock system. A weak shock originates near the leading edge of the wing root and extends downstream and outboard. A second, stronger shock is formed near the trailing edge of

the inboard wing and merges with the forward shock somewhere in the mid-span region to form a strong outboard shock extending to the wing tip. The inboard shocks are strongly affected by the root flow, and some of this influence can even be transmitted to the outboard shock near the merging point. Shock-induced separation is most likely to occur in the region at and downstream of the strong outboard shock. For high aspect ratio wings the flow over the outboard wing is most analogous to ideal swept wing flow and hence to two-dimensional flow models.

4.3 Active and Passive Boundary Layer Control

The idea of boundary layer control (BLC) for the purpose of improving airfoil performance is almost as old as modern aerodynamics. A comprehensive history of boundary layer control research in various countries and descriptions of different BLC methods, many of which are suitable for transonic application, are presented in Ref. 49. It is beyond the scope of the present paper to discuss in detail all the methods which might be or have been applied for transonic drag reduction. In the following we will concentrate mainly on methods which affect the shock turbulent boundary layer interaction and related phenomena by different means.

In the context of this paper BLC methods for the purpose of transonic drag reduction have been classified into two main categories: Methods requiring an additional energy source for accomplishing the desired control effect have been named "active", and devices affecting the flow development simply by their presence in the flow, without any need for additional energy, have been named "passive".

4.3.1 Active boundary layer control

It was shown above that the transonic drag rise is mainly due to increasing wave drag with growing shock strength and increasing form drag, caused by shock-induced or trailing edge separation. Viscous effects, causing shock-induced separation to occur at a certain shock strength, limit the increase of wave drag at high subsonic speed, while the form drag may grow excessively. The greatest potential in reducing the transonic drag rise, therefore, lies in the reduction of form drag by delaying or preventing separation.

Transonic flight speeds were still far from a practical application when Regenscheit [80] in 1941 proposed to reduce the strong drag rise, which had been observed in wind tunnel experiments on airfoils at near sonic speeds, by boundary layer suction in the region of shock-induced separation. First experiments on a circular arc airfoil with suction applied through a single slot substantiated this hypothesis. Considerable drag reductions with increasing suction mass flow rates were obtained at $M_\infty = 0.8$ and 0.90 . The most effective slot location was found to be at 70 percent chord at the foot of the shock. Similar investigations were reported a few years later in 1943 by Fage and Sargent [81].

In view of improving the off-design characteristics of a supercritical airfoil by slot suction within the shock region, theoretical studies were made and subsequent experimental investigations were carried out in the DFVLR 1m x 1m Transonic Wind Tunnel [82][83] [84][85]. A two-dimensional model of the VFW-VA-2 airfoil section, not particularly designed for suction application, was equipped with a 0.6 mm wide suction slot at 58.5 percent chord. The airfoil and its general arrangement in the wind tunnel is sketched in Fig. 36 a and b. In order to simulate realistic boundary layer properties at the shock boundary layer interaction region for a freestream chord Reynolds number of 2.5×10^6 , the boundary layer was tripped at 30 percent chord on the upper surface and at 25 percent chord on the lower surface [9] [36]. Lift and drag coefficients were evaluated from surface pressure and wake impact pressure measurements, respectively. Further information on the flow development as obtained from boundary layer probe measurements at selected angles of attack and at different chordwise positions. Monitoring the RMS-value of the airfoil root bending moment on an oscillograph and simultaneous Schlieren observations during the measurements enabled the onset of buffet to be detected.

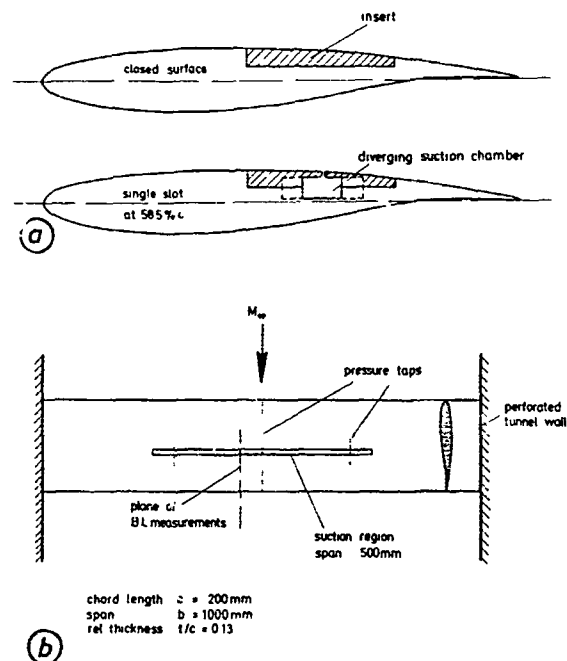


Fig. 36: a) VFW-VA-2 Single Slot Airfoil
b) Model Arrangement (top view)

Lift and drag coefficients obtained at $M_\infty = 0.76$ for different suction rates, ranging from $C_Q = 0$ to 8×10^{-4} , are shown in Fig. 37. The effectiveness of single slot suction at flow conditions where strong shock boundary layer interactions are present is clearly demonstrated. At higher incidence the drag is considerably reduced and, in

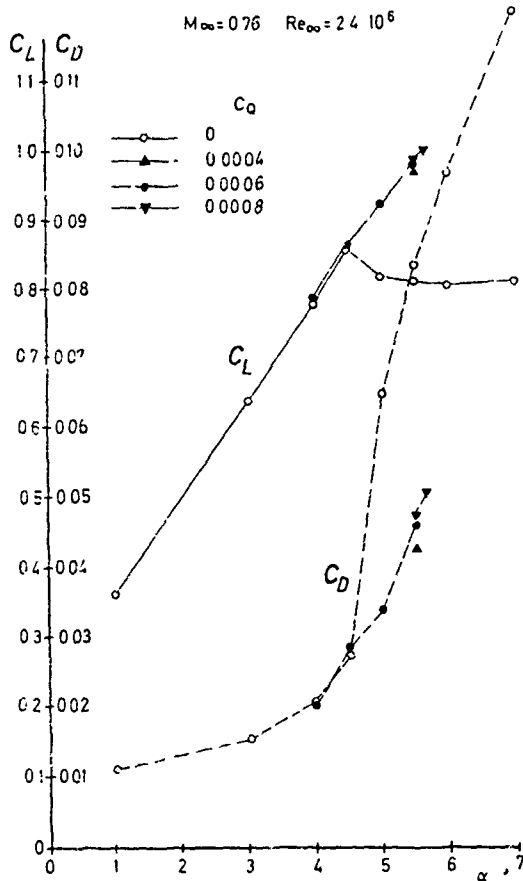


Fig. 37: Effect of Single Slot Suction on Lift and Drag, $M_\infty = 0.76$

addition, the lift is most favorably increased by suction. At a slightly higher Mach number $M_\infty = 0.78$, Fig. 38, these favorable effects become less pronounced. The drag is at high incidences still reduced however, at lower incidences suction even increases the drag. This, at a first glance, unexpected result may be explained by surface pressure distribution and boundary layer measurements taken at corresponding angles of attack, $\alpha = 4^\circ$ and 5° .

The measured velocity profiles in the shock region at $\alpha = 4^\circ$, Fig. 39, reveal that with suction the boundary layer thickness, and correspondingly the displacement thickness, is considerably reduced at the suction slot location, causing the following effects: The shock is allowed to displace rearward to the suction slot, the interaction region over which the shock pressure rise takes place is reduced, and, in spite of the greater shock strength, no shock-induced separation bubble occurs, which is obviously present for the non-suction case. For this particular flow condition the reduction of form drag due to reduced displacement effects is apparently exceeded by the increase of friction and wave drag, caused by fuller velocity pro-

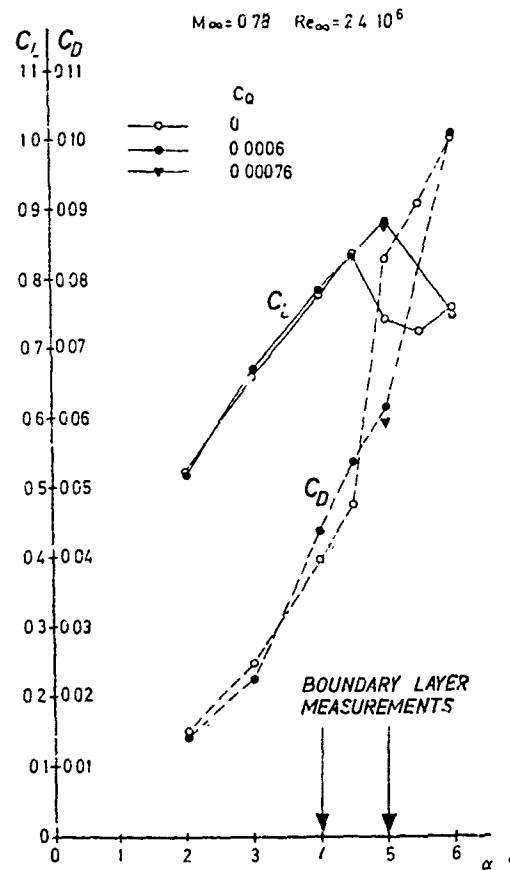


Fig. 38: Effect of Single Slot Suction on Lift and Drag, $M_\infty = 0.78$

files over the rear of the airfoil and by greater shock strength, respectively.

For $\alpha = 5^\circ$, Fig. 40, the shock location, without suction applied, has moved far upstream, inducing separation over the entire aft section of the airfoil up to the trailing edge, as indicated by the pressure distribution and negative trailing edge pressure. The most favorable effect of suction is demonstrated by the pressure distributions and boundary layer thicknesses for the non-suction and suction case. With suction applied, the shock is located at the suction slot; the low pressure coefficient ahead of the shock represents a local Mach number of $M_1 \approx 1.44$ which normally would lead to total separation from shock to the trailing edge. Due to the thin boundary layer approaching the shock location and suction applied in the shock boundary layer interaction region, the flow is able to negotiate the downstream adverse pressure gradients without severe separation at the trailing edge.

Since the effectiveness of single slot suction is dependent on the shock location, it was expected that the range of effectiveness (Mach number and incidence) could be extended by applying suction through two

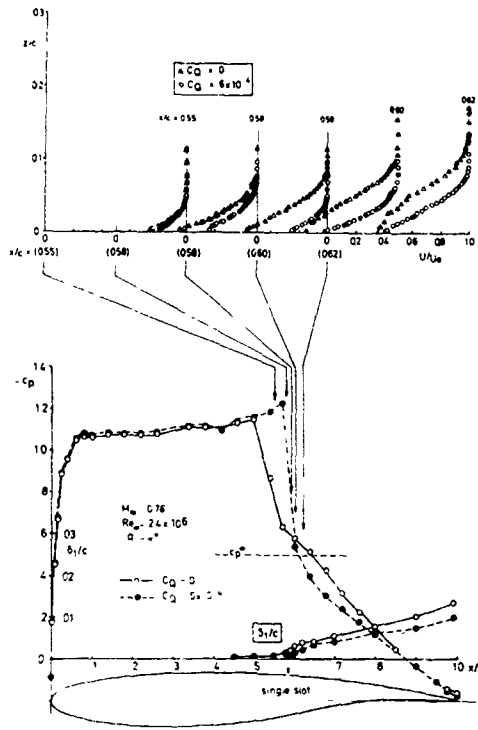


Fig. 39: Boundary Layer Properties and Pressure Distributions on Single Slot Suction Airfoil, $M_\infty = 0.78$, $\alpha = 4^\circ$

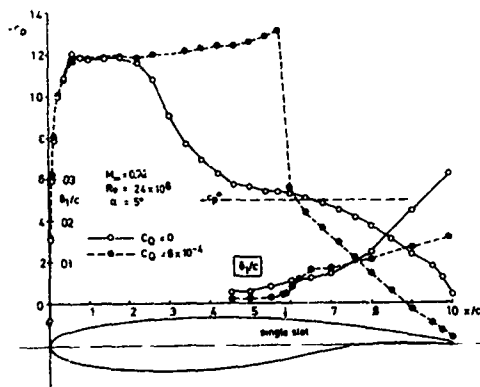


Fig. 40: Pressure Distributions and Displacement Thicknesses on Single Slot Suction Airfoil, $M_\infty = 0.78$, $\alpha = 5^\circ$

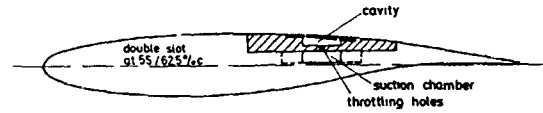


Fig. 41: VFW-VA-2 Double Slot Airfoil

slots rather than one. The two-dimensional airfoil was correspondingly equipped with two slots, Fig. 41, at 55 and 62.5 percent chord, respectively, which were connected to one common suction chamber [86]. Lift and drag curves, shown in Figs. 42 and 43, obtained at $M_\infty = 0.76$ and 0.78 without and with suction applied, exhibit only minor effects of suction. These results are, at first glance, surprising. A comparison of Fig. 42 and 37 reveals, however, that even for the non-suction case the drag of the double slot airfoil at high incidence is considerably lower than that of the single slot airfoil. A further comparison, viz., of corresponding pressure distributions at $M_\infty = 0.78$ and $\alpha = 5^\circ$, Fig. 44 and 40, may give, preliminary, an explanation for these differences. On the single slot suction airfoil without suction at $\alpha = 5^\circ$ the flow was totally separated from the shock to the

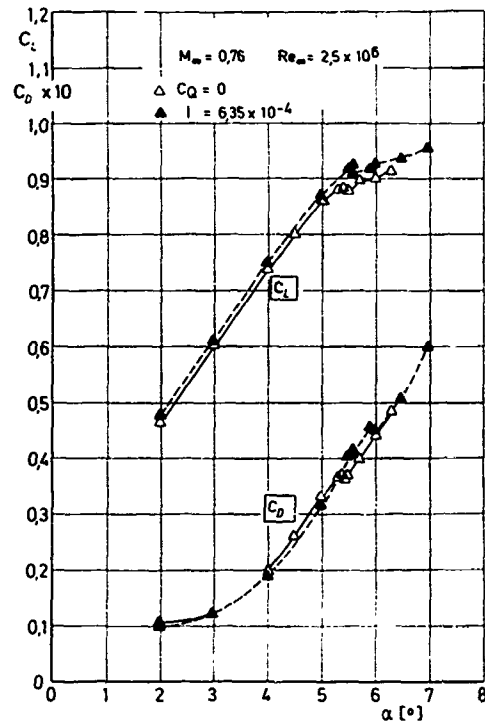


Fig. 42: Effect of Double Slot Suction on Lift and Drag, $M_\infty = 0.76$

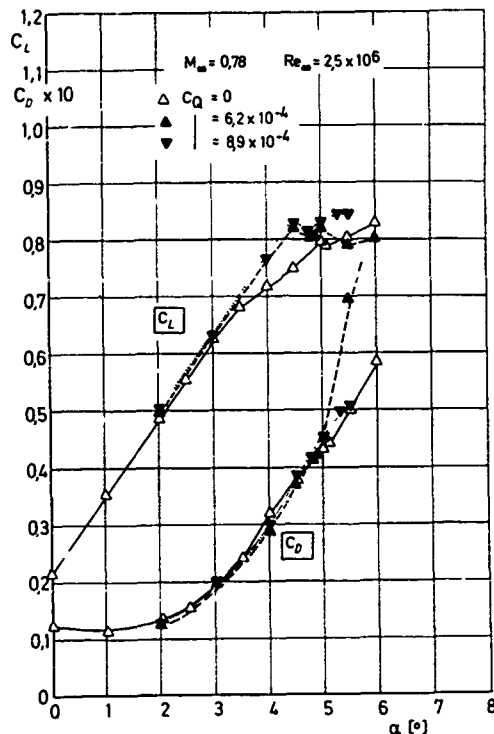


Fig. 43: Effect of Double Slot Suction on Lift and Drag, $M_\infty = 0.78$

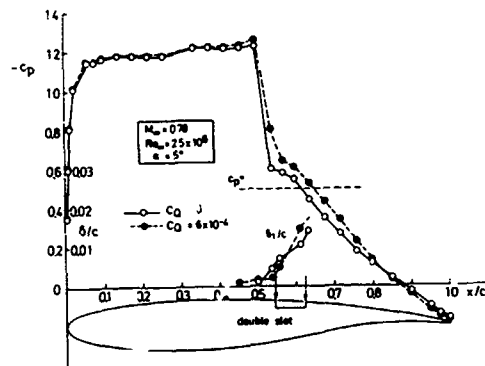


Fig. 44: Pressure Distributions and Displacement Thicknesses on Double Slot Suction Airfoil, $M_\infty = 0.78$, $\alpha = 5^\circ$

trailing edge, causing an excessive drag rise. In contrast, on the double slot airfoil without suction applied the flow at the trailing edge is attached and only a local separation bubble can be detected from the surface pressure distribution. This most favorable effect of the double slot/cavity arrangement shall be described in more detail in a later section.

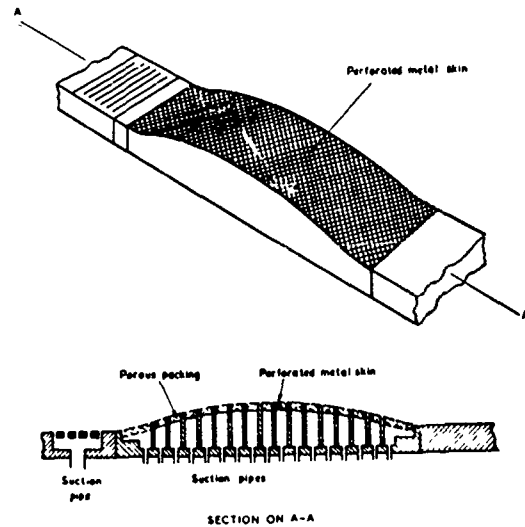


Fig. 45: Distributed Suction Model (Ref. 62)

In order to prevent or reduce shock-induced separation effects, distributed suction may be applied as well, either locally or over the entire airfoil surface. In experiments described by Pearcy [62] a "bump" model, Fig. 45, subdivided into a large number of suction compartments (to prevent spurious inflow and outflow under external pressure gradients), covered with a perforated metal skin, was used. At a fixed Mach number, with suction applied, the shock was appreciably displaced rearward due to reduced boundary layer thickness, and no significant separation effects were observed. Similar investigations of Wedemeyer [87] on two-dimensional airfoils having porous surfaces of sintered metal showed that the shock-boundary layer interaction region was considerably reduced by boundary layer suction, and the overall flow development was altered towards a better agreement with inviscid flow theory. In utilizing such arrangements with extended area suction, it seems, however, from a present-day point of view, more advantageous to adjust the suction distribution such as to laminarize the flow and gain a (large) friction drag reduction.

Instead of affecting the turbulent boundary layer upstream of the shock, significant separation effects may as well be reduced by applying local area suction in the shock region or downstream. An NACA 64 A 010 airfoil section with a plain flap of 30 percent chord and a perforated suction area, extending from 69 to 90 percent chord, was used in the investigations of Smith and Walker, [88], Fig. 46. The suction area was varied and the greatest drag reduction was obtained by suction over the area from 69 to 72.5 percent chord. Typical pressure distributions and boundary layer profiles (at $x/c = 0.85$) without and with suction applied are depicted in Fig. 47 a and b. With suction the shock is displaced rearward to the suction region (marked by the

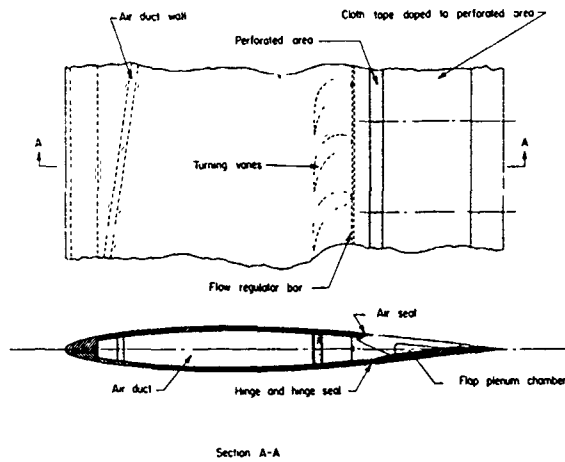


Fig. 46: NACA 64 A 010 Airfoil with Area Suction Flap, (Ref. 88)

shaded strip), the extent of the interaction region is reduced, approaching the inviscid step-pressure-rise, the pressure recovery behind the shock and at the trailing edge is much better than for the non-suction case, and there is no indication of separation, though the shock strength is increased. The improvement in boundary layer development due to suction is demonstrated by the velocity profiles at 85 percent chord, Fig. 47 b. However, increased skin friction due to fuller velocity profiles along with increased wave drag due to greater shock strength lessen the effect of suction on total drag reduction, especially at conditions where no significant separation effects are present. Therefore, only at higher incidences were appreciable drag reductions obtained. Since at a constant lift coefficient for the model with the surface closed drag reductions of the same order were gained by deflecting the flap, indicating the merits of airfoils with variable camber [89], Smith and Walker considered area suction of no great importance. In the opinion of the present authors, the suction area was too far aft relative to the shock locations, as to be fully effective either in the "active" or "passive" mode.

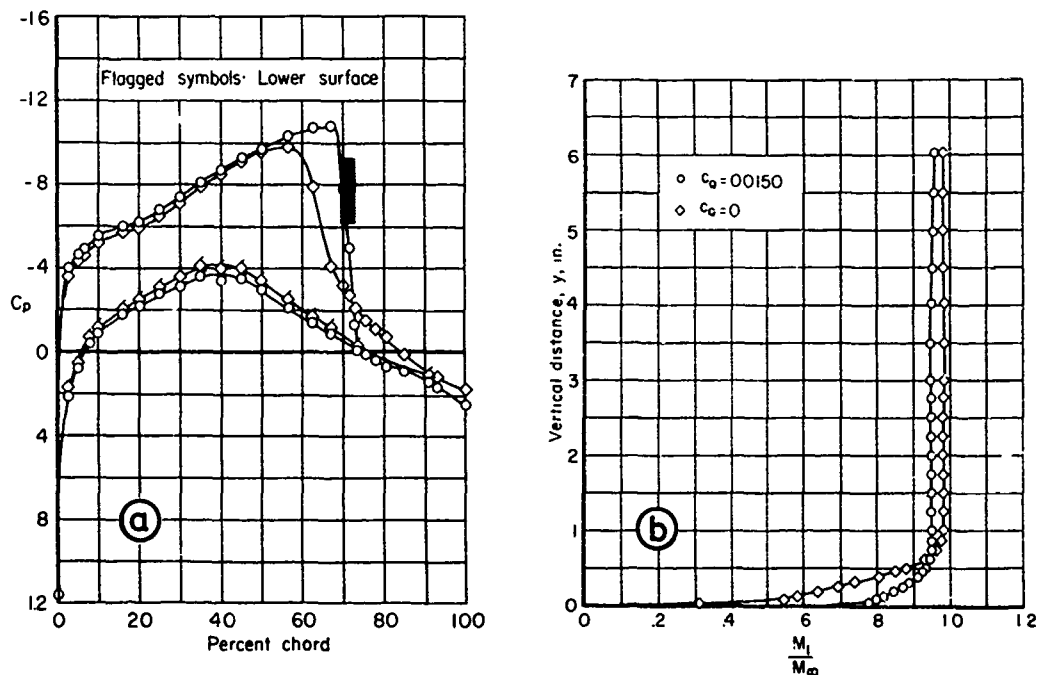


Fig. 47: Effect of Local Area Suction on Pressure Distribution and Velocity Profiles, $M_\infty = 0.8$ (from Ref. 88)

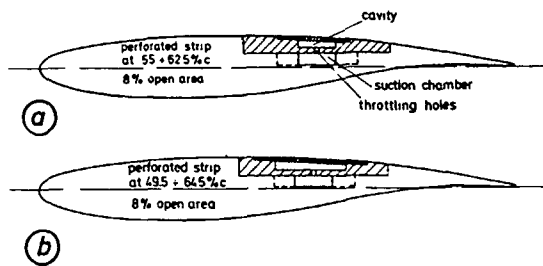


Fig. 48: VFW-VA-2 Local Area Suction Airfoils

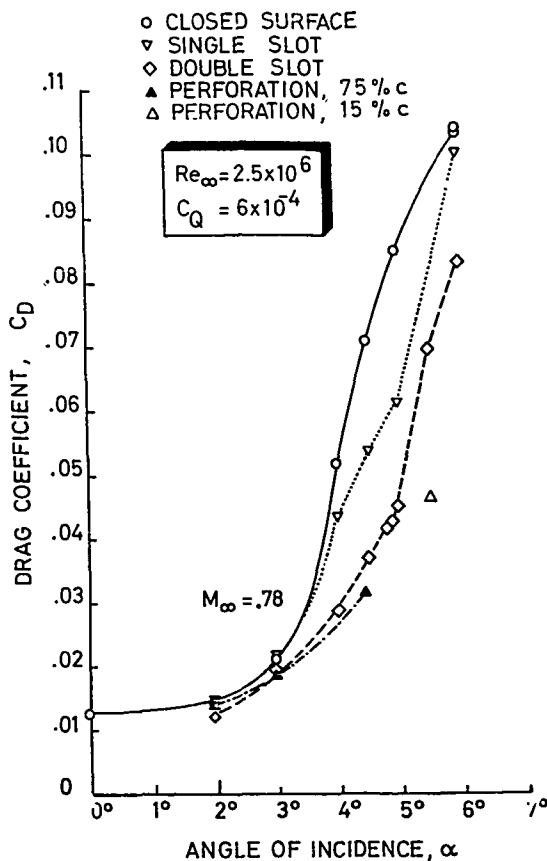


Fig. 49: Effect of Different Suction Methods on Airfoil Drag

Similar investigations on the supercritical airfoil section mentioned earlier, equipped with a 7.5 percent chord wide perforated suction area, Fig. 48 a, were performed in the DFVLR 1m x 1m Transonic Wind Tunnel. The drag reductions obtained on this model with suction, compared to the non-suction case, were only small [90]. Compared with results of the solid-surface

airfoil, however, the drag is substantially reduced, as demonstrated in Fig. 49. Included in this figure are also the results obtained with single slot and double slot suction applied. A reference measurement at $\alpha = 5.5^\circ$ with suction applied through a 15 percent chord wide perforated area extending from 50 to 65 percent chord, Fig. 48 b, confirms the trend of the results of the narrower perforation. It has, however, to be noted that the main drag reduction is due to an inherent passive effect of the perforation/cavity and double slot/cavity arrangement.

Since the largest improvements are gained at high incidences, it is obvious that the onset of shock oscillations (buffet onset) may be favorably affected by area suction. Experiments of Finke [91] on a conventional and a circular-arc airfoil showed that shock oscillations resulting from severe separation could be totally suppressed by area suction, though high suction rates were necessary. The effect of suction on the buffet boundary of the supercritical airfoil with 7.5 percent chord wide perforation is shown in Fig. 50. Lift coefficients at the onset of unsteady shock motion, observed from the increase of the RMS-value of the airfoil root bending moment and from Schlieren observations, are plotted as function of the freestream Mach number. Compared to the solid-surface airfoil the onset of buffet is considerably delayed to higher Mach numbers or higher lift, respectively. With increasing Mach number the growing passive effect of the perforation, without suction applied, becomes evident.

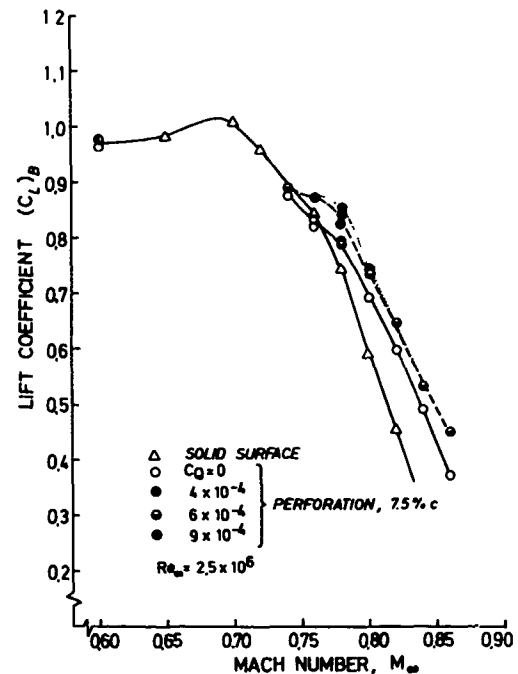


Fig. 50: Effect of Area Suction on Buffet Boundary

In contrast to boundary layer suction, where low energy air flow near the wall is removed, thus increasing the fullness of the velocity profiles and thinning the boundary layer which then will be less susceptible to separation, the near-wall flow may as well be energized by appropriate means. One method in common use is to generate streamwise vortices by suitably shaped protuberances (passive device) or by discrete air jets, Fig. 51, described in detail in Refs. 62 and 70. These vortices transfer low energy air up from the boundary layer into the outer flow and high energy air from the outer flow into the boundary layer, thus separation may be suppressed or the reattachment process promoted. These devices are, of course, mainly suited to reduce form drag in the vicinity of the drag-rise boundary.

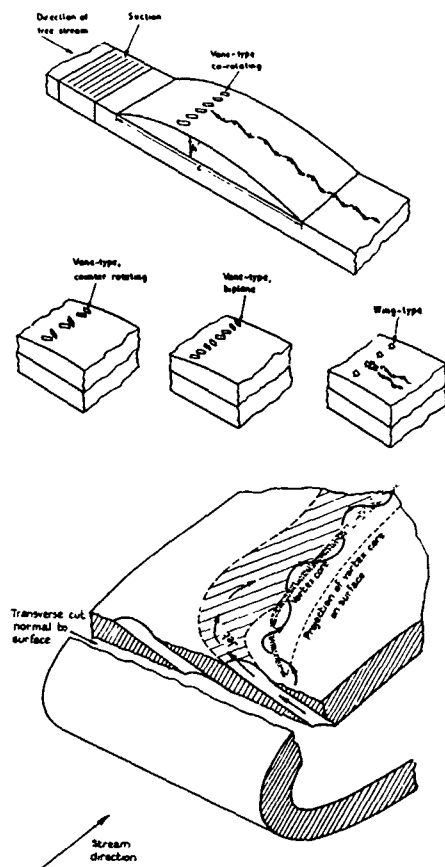


Fig. 51: Vortex Generators

Another approach of energizing the near wall boundary layer flow is blowing a high velocity streamwise jet tangentially through a narrow spanwise slot along the surface, Fig. 52, which may delay separation or promote an earlier reattachment. Improvements obtained on a conventional airfoil in different flow regimes by slot blowing at 15 percent chord are demonstrated in Fig. 53 [63]. Similar improvements were observed on a half-airfoil with slot blowing in the shock region at 70 per-

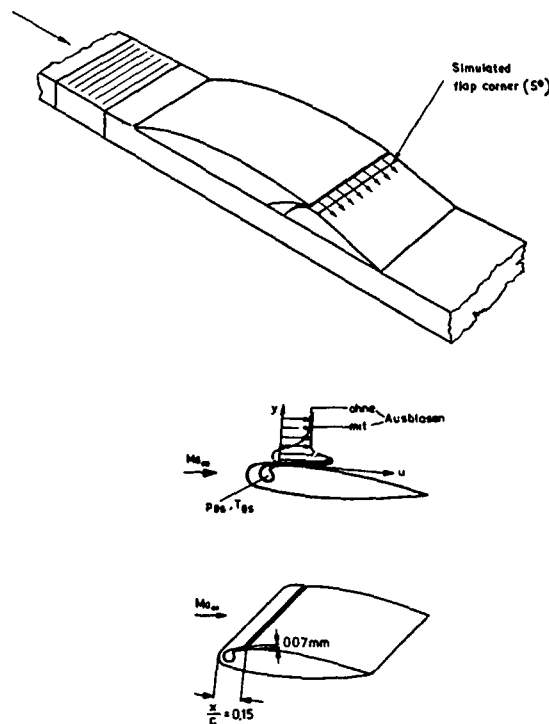
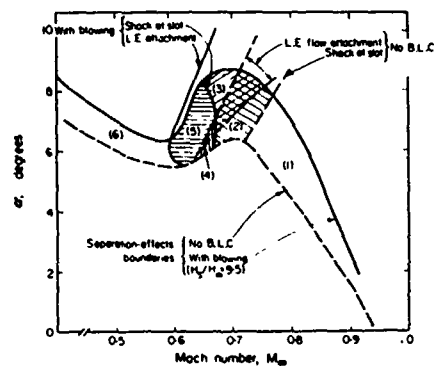


Fig. 52: Tangential Slot Blowing



- Type of Improvement
- (1) Suppression of separation downstream of slot
 - (2) Ditto, after movement of shock from upstream to downstream of slot
 - (3) Flow attachment at leading edge to shock downstream of slot
 - (4) Accelerated reattachment of shock-induced separation upstream of slot
 - (5) Ditto, after flow attachment at leading edge
 - (6) Accelerated reattachment of leading-edge separation

Fig. 53: Improvements Obtained in Several Flow Regimes by Blowing from a Single Slot at 0.15c (from Ref. 62)

cent chord. For a shock position just upstream of the slot, the application of a small blowing quantity resulted in a fairly rapid reattachment of the flow with a substantial pressure rise. At higher blowing

rates the pressure recovery at the trailing edge, too, was considerably improved. Furthermore, experiments of Finke [91] on an NLR-airfoil showed that unsteady shock oscillations could be completely suppressed by employing slot blowing at either 15 percent or at 60 percent chord.

Combining slot blowing with a favourable contouring downstream for "active diffusion control" [92] may be employed in order to improve the performance characteristics of a transonic airfoil. The primary device of active diffusion control, schematically shown in Fig. 54, is the "antiseperation tailored contour" (ATC) downstream of the blowing slot in the boundary layer energizing region, followed by a severe diffusion step. If the boundary layer existing at the slot location is properly energized, significant diffusion over a short distance should be possible. In order to prove this hypothesis, Haight and Mask [92] investigated the aerodynamic characteristics of a cruise (7 C) and a maneuver (7 M) configuration of a seven percent thick transonic antiseperation tailored contour (TATC) airfoil, Fig. 55, comparing the results with corresponding Whitcomb-type and a conventional NACA 64 A 406 airfoils.

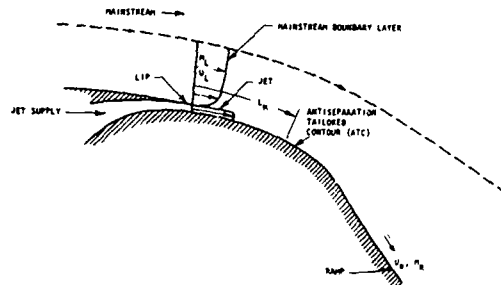


Fig. 54: Schematic of ATC Active Diffusion Control Device (from Ref. 92)

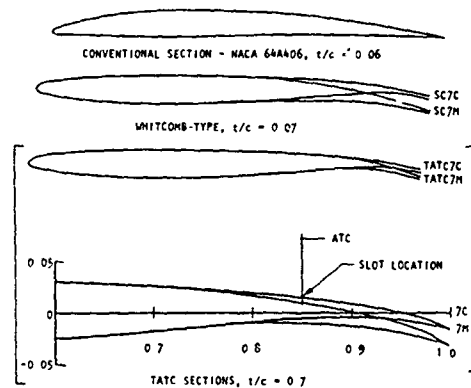


Fig. 55: Baseline and TATC Section Geometries (from Ref. 92)

Typical variations of the pressure distributions of the maneuver configuration with blowing are presented in Fig. 56 for $M_\infty = 0.80$, $\alpha = 3^\circ$. With increasing blowing rates the shock location is displaced progressively rearward causing the normal force coefficient to be increased by $\Delta C_N = 0.16$. Without blowing a trailing edge separation is indicated by the negative trailing edge pressure. Blowing results in a better pressure recovery at the trailing edge without the flow separating.

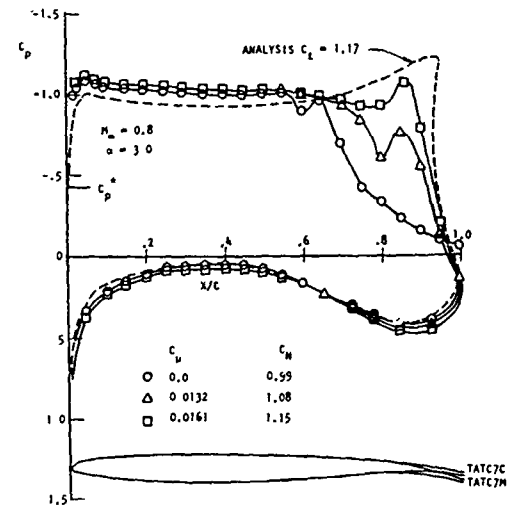


Fig. 56: TATC7M Pressure Distribution Data at Blowing, $M_\infty = 0.8$, $\alpha = 3.0$. (from Ref. 92)

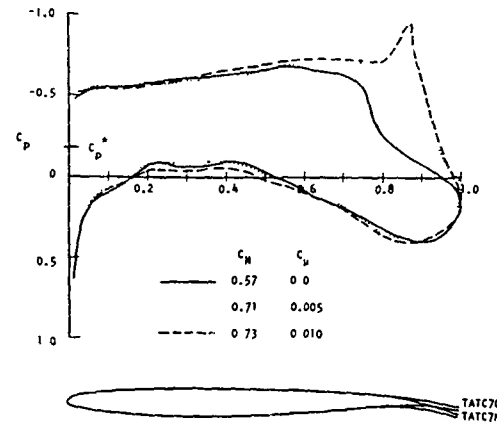


Fig. 57: TATC7C Pressure Distribution Data at Blowing, $M_\infty = 0.9$, $\alpha = 2$ deg. (from Ref. 92)

For the cruise configuration at $M_\infty = 0.90$, $\alpha = 2^\circ$, Fig. 57, a blowing jet momentum coefficient $C_\mu = 0.005$ suffices to displace the shock pressure rise downstream of the blowing slot, increasing the normal force coefficient by $\Delta C_N = 0.14$. Further increasing the blowing quantity has - with

the exception of a distinct spike in the pressure distribution at the slot location - a negligible effect. On the contrary, higher friction drag and wave drag due to increased shock strength may even increase the total drag.

For the cruise configuration TATC 7C airfoil the total drag ($C_D + C_{\mu}$) is plotted in Figs. 58 and 59 as function of Mach number for $C_L = 0.40$ and 0.60 , respectively. Conventional airfoil data and analytically predicted results for a Whitcomb-type airfoil are added in the figures for reference.

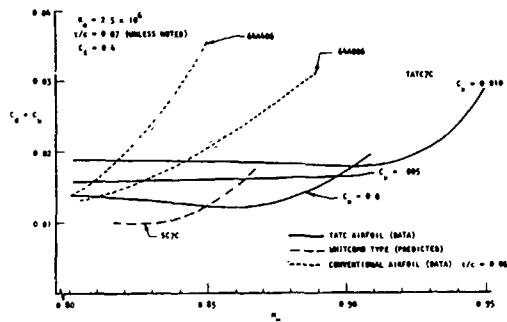


Fig. 58: Cruise Drag Divergence, $C_L = 0.40$ (from Ref. 92)

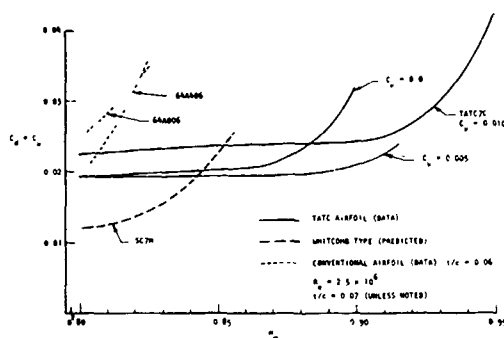


Fig. 59: Cruise Drag Divergence, $C_L = 0.60$ (from Ref. 92)

The onset of drag divergence at $C_L = 0.40$, Fig. 58, is delayed to appreciably higher Mach numbers relative to conventional airfoil data and baseline Whitcomb calculations. However, considerably higher pre-divergence drag levels are observed, although the $C_{\mu} = 0$ curve approaches the lower drag levels. Blowing slot step drag for $C_{\mu} = 0$ and non-optimized blowing may contribute to these effects, since C_{μ} accounts for 25 to 50 percent of the total drag.

At higher C_L , Fig. 59, the performance at $C_{\mu} = 0.005$ exceeds that at either $C_{\mu} = 0$ or 0.010 for all Mach numbers, indicating the existence of an optimum blowing quantity. In any case, the drag rise occurs, at considerably higher Mach numbers than for comparable conventional and Whitcomb-type airfoils. Disadvantageous is still the

fairly high drag level at pre-divergence Mach numbers which might be reduced by variable geometry, refinements in the blowing rates, and the reduction of blowing slot drag.

Experiments of Haight et al., cited in Ref. 92, showed that the application of active diffusion control on a 12 percent thick airfoil resulted in similar improvements of the drag divergence Mach number as demonstrated above. Furthermore, corresponding estimates, using existing engine technology, showed the C_{μ} required, even for maneuvering, to be well within the limits of engine bypass bleed or even of compressor bleed.

Active diffusion control, employing combined blowing and contouring may also be applied to laminar flow control (LFC) or natural laminar flow (NLF) airfoils, suppressing separation in the very strong adverse pressure gradient region near the trailing edge. A corresponding two-dimensional airfoil, integrating laminar flow stabilization by pressure gradient shaping, and active diffusion control technique near the trailing edge, was designed by Mask, [93], for $M_{\infty} = 0.6$ and a chord Reynolds number of $Re = 40 \times 10^6$, Figs. 60 and 61. So far, results of full scale Reynolds number experiments defining maximum transition Reynolds number and environmental influences on transition, but no particular drag measurements were published.

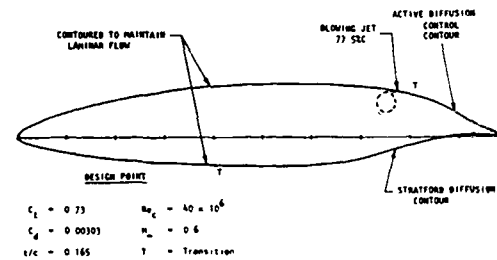


Fig. 60: ATC/Laminar Airfoil Design (from Ref. 93)

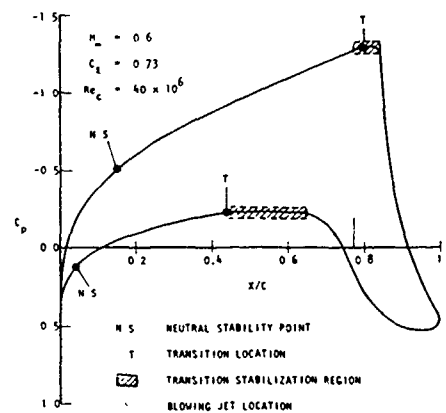


Fig. 61: ATC/Laminar Airfoil Design Pressure Distribution (from Ref. 93)

It has been shown above that each of the active boundary layer control methods can be beneficial to transonic airfoil performance. No attempt will be made here to give a general assessment of the different active BLC methods or give a recommendation for a particular method, because the transonic airfoil flow development is so strongly dependent on so many parameters. A particular BLC method may be successful in improving the aerodynamic characteristics of one airfoil, but may fail if it is applied in the same manner to a different airfoil shape. To achieve the optimum effectiveness of a BLC method, it has to be thoroughly examined for and integrated in the airfoil design process.

4.3.2 Passive boundary layer control

The most economic means of boundary layer control for the purpose of drag reduction are those which do not require additional energy or energy consumption devices to be effective, as compressors or pumps for blowing and suction, respectively. The inherent drag, if present, of the control device itself should be as low as possible in order to gain maximum effectiveness, and, a crucial point for some active BLC methods, the control device should quite easily to be incorporated into an aircraft wing and require the least amount of maintenance. In the context of the present paper, we shall not consider passive means of drag reduction which are well established, as for example vortex generators energizing the boundary layer flow, contour tailoring, area ruling, natural flow laminarization or means of boundary layer transition control [94][95], but will place emphasis on a most promising method of transonic airfoil drag reduction which has been investigated independently at different locations in recent years.

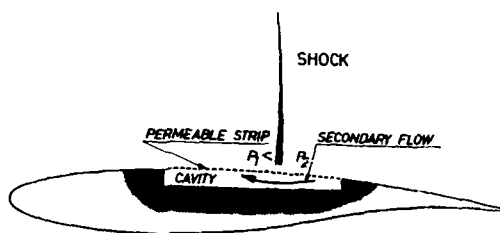


Fig. 62: Schematic of Passive Shock-Boundary Layer Interaction Control

The basic idea of this method is to place a permeable surface with a cavity underneath on a transonic airfoil at a chordwise position where normally a shock wave would occur, Fig. 62. Due to the strong pressure rise across the shock in the external flow a secondary flow through the permeable surface and cavity is induced. Decelerated boundary layer air at higher pressure downstream of the shock is forced to flow through the permeable surface into the cavity and out into the low pressure region upstream of the shock. By this effect the shock pressure rise at the wall is spread in chordwise direction over the width of the permeable surface, reducing the shock

strength and the pressure and velocity gradients across the shock. The consequences of such "passive" arrangement on transonic airfoil flow development will be discussed below by typical analytical and experimental results.

Utilizing transonic small disturbance theory the flow about a NACA 0012 airfoil section at zero incidence with a perforated surface from close to the leading edge to the trailing edge was studied analytically by Savu et al. [96][97][98]. Assuming the cavity pressure to be constant and introducing a porosity distribution as shown in the lower part of Fig. 63, the resulting pressure distribution was calculated for a Mach number $M_\infty = 0.82$. The original solid-airfoil pressure distribution for this Mach number shows a clearly defined shock at about 40 percent chord. In the calculated pressure distribution for the porous-surface airfoil the recompression over the rear of the airfoil is apparently shockless. This pressure distribution corresponds to that of an equivalent solid airfoil shown at the bottom of Fig. 63,

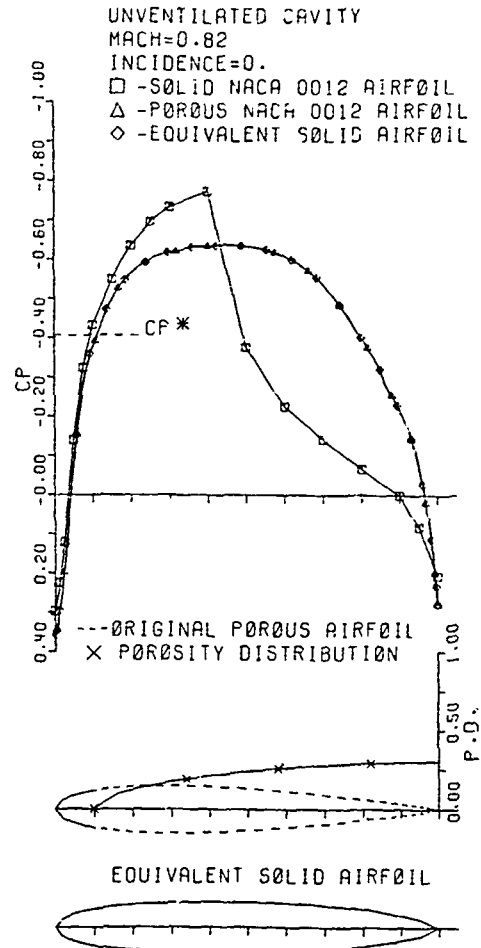


Fig. 63: Pressure Distributions on the Original Solid, the Porous, and Equivalent Solid Airfoil (from Ref. 98)

indicating how the effective contour of the airfoil is changed by the secondary flow through the perforated surface. In principle, any porosity distribution may be introduced in order to obtain a desired pressure distribution (or equivalent solid airfoil shape).

These results from inviscid flow theory are promising, but have to be validated by a more complete flow model including viscous effects, especially the complex interaction between the shock and the boundary layer, and by experiments. The latter were restricted to Schlieren visualizations, [96], which verified that in a range of Mach numbers the formation of a shock wave could apparently be suppressed. A residual shock appearing at higher Mach numbers was still much weaker than on the solid surface, indicating that the wave drag should be greatly reduced. No pressure distribution measurements and in particular drag measurements have been published so far.

For practical application it might be difficult to incorporate a permeable surface with a cavity underneath over a wide portion of the chord into an airfoil. Furthermore, it can be suspected that a wide-chord perforated area may be detrimental to subcritical and low speed performance due to increased skin friction. On a suggestion of Mr. D. Bushnell and Dr. R. Whitcomb of NASA Langley Research Center experiments were made at Rensselaer Polytechnic Institute by Bahl et al. [99] and Nagamatsu et al. [100][101] on a circular-arc and 14% thick supercritical airfoils (mounted as half-airfoil on the tunnel floor) using 25 to 30 percent chord-wide perforated surface/cavity arrangements at the shock location. Exploratory surface pressure distribution measurements, wake impact pressure data and Schlieren observations indicated appreciable drag reductions on the porous-surface airfoils, though a small loss of lift was observed. The original normal shock on the solid surface was changed to a lambda (λ) shock system by the porous surface, and a variation of cavity depth from 0.75 in. to 0.25 in. revealed an increased effectiveness for the shallower cavity [99]. In subsequent experiments on 14 percent thick NASA supercritical airfoils, 0.25 in. deep cavities were used.

Drag coefficients of the 14% thick (tunnel floor mounted) airfoils are plotted as function of Mach number in Fig. 64, Refs. [100] [101]. A porosity of 1.4 percent, based on total airfoil area (5.6 percent open, based on porous area), fails to reduce the total drag. For all Mach numbers tested, increased drag, relative to the closed-surface airfoil, is observed. With 2.8 percent porosity (11.2 percent open, based on porous area), however, the drag at higher Mach numbers is substantially reduced on both airfoils. At lower Mach numbers (subcritical, or the shock being located upstream of the perforated region), the drag coefficients are considerably higher than on the closed surface, presumably due to increased friction drag of the relatively coarse perforation (hole diameter 0.64 mm, model chord 101.6 mm).

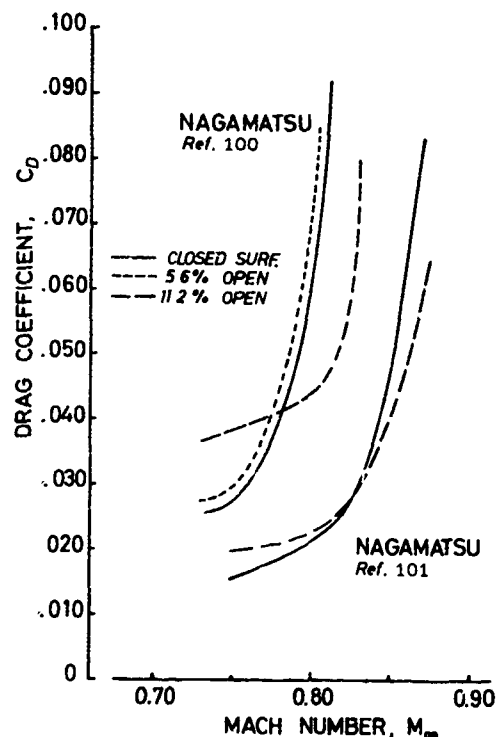


Fig. 64: Passive Effect of Porosity/Cavity Arrangement on 14% Thick Airfoil Drag (Refs. 100, 101)

As a logical consequence of the investigations at DFVLR on active boundary layer control by suction through a double slot and a 7.5 percent chord wide perforation, Refs. 86 and 90, the passive effects of these devices, i.e. without suction applied, was also investigated, Refs. 102, 103, 104 and 105. First experimental results for the aforementioned supercritical airfoil VFW-VA-2, equipped with a 15

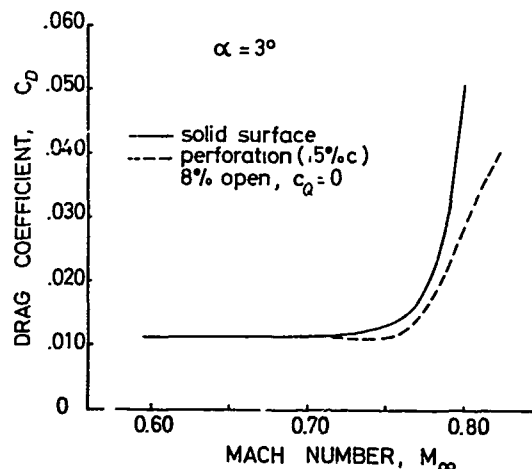


Fig. 65: Passive Effect of Perforation/Cavity Arrangement on VFW-VA-2 Airfoil Drag

percent chord wide perforated region ranging from 50 to 65 percent chord, were reported in Ref. 106, they will be supplemented in here. The perforation (8 percent open, based on perforated area) was electron-beam drilled with hole diameters of 0.3 mm, giving a very smooth surface. Drag coefficients at constant α versus Mach number, Fig. 65, show that for subcritical Mach numbers no drag penalties arise from the perforation/cavity arrangement which, at higher Mach numbers, becomes fully effective and reduces the total drag substantially by shifting the drag rise to a higher Mach number. In the entire range of Mach numbers and incidences, essentially no disadvantageous effects of the perforation were observed.

For three relevant Mach numbers close to the design Mach number the drag coefficients of the airfoils with perforation/cavity (15% c) and with double slot/cavity arrangement (slots at 55 and 62.5% c, connected to a common cavity) are plotted against angle of attack in Fig. 66 along with corresponding solid-surface data. For subcritical conditions at $M_{\infty} = 0.74$ and low incidence the drag is by no means affected by the presence of either the perforation or the double slot/cavity arrangement. With shock waves occurring in the flow field the passive devices become effective, reducing the drag at high incidence by more than 50 percent. For the higher Mach numbers the drag is even at low incidence reduced; an explanation will be given below by discussing characteristic flow features. It is remarkable that the double slot/cavity arrangement is almost as effective as the perforation/cavity device. The differences appearing between the two corresponding drag curves result obviously from the fact that the two slots were only 7.5 percent chord apart while the perforated region was 15 percent chord wide.

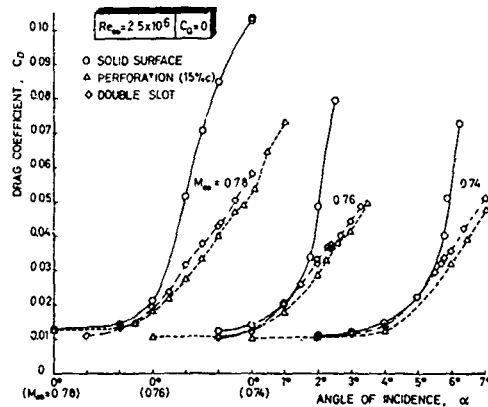


Fig. 66: Drag Coefficients of VFW-VA-2 Airfoil with Different Passive BLC Devices

In comparison to the solid-surface airfoil, both passive devices improve the drag-rise boundary most favorably. Lift coefficients at drag rise, obtained from drag versus Mach number curves at constant lift, using the $\Delta C_D = 0.002$ criterion, are plotted in Fig. 67 and Fig. 68 against Mach number. At constant Mach number the lift at drag rise is significantly increased, or at constant lift coefficient the drag rise is substantially shifted to higher Mach numbers.

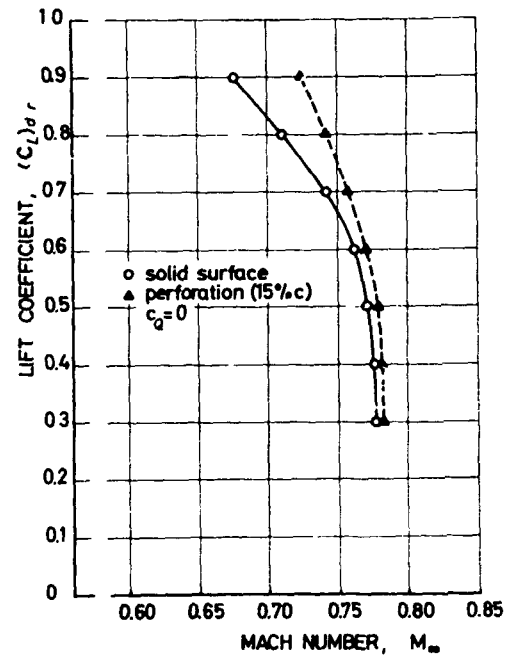


Fig. 67: Effect of Perforation/Cavity Arrangement on Drag-Rise Boundary

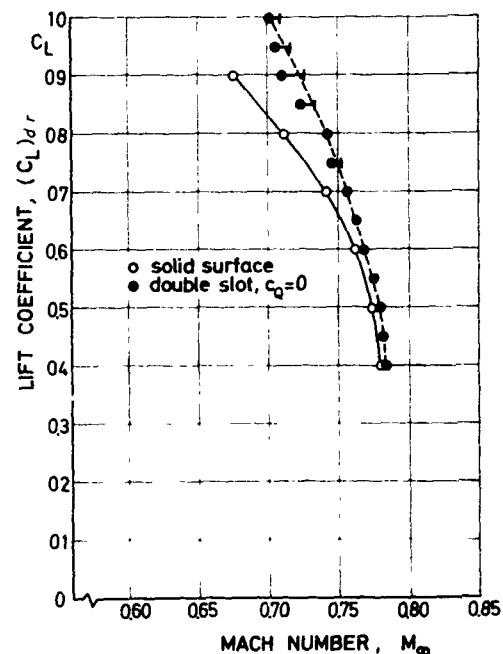


Fig. 68: Effect of Double Slot/Cavity Arrangement on Drag-Rise Boundary

The importance of the aerodynamic performance parameter $M \times L/D$ has been emphasized above. How the lift-to-drag ratios are affected by the perforation and double slot/cavity arrangement is depicted in Fig. 69. In the entire range investigated L/D , compared with corresponding solid-surface data, is considerably increased due to the passive effect of both devices, substantiating their potential of improving the airfoil performance at design conditions ($C_L \sim 0.5$ to 0.6) as well as at off-design.

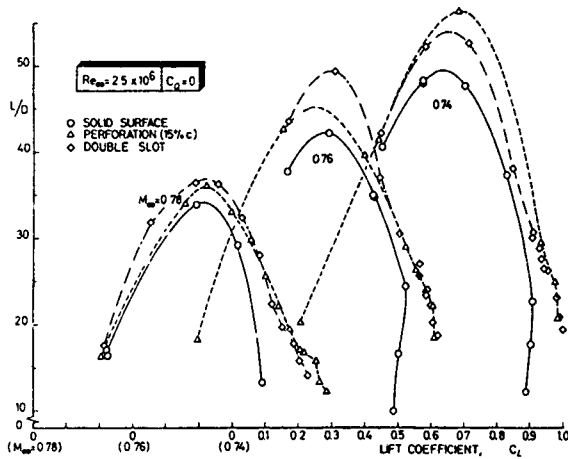


Fig. 69: Effect of Passive BLC Devices on Performance Parameter L/D

So far, only improvements of the global aerodynamic characteristics of the airfoil due to the presence of the passive devices have been demonstrated but the mechanism and effects causing these improvements still need some further explanation. Since no direct experimental information on the secondary flow in and around the passive devices is available at present, the improvements gained can only be interpreted indirectly by the effects of the secondary flow on characteristic flow features.

For characteristic stages in the flow development over the airfoil at the constant Mach number $M_{\infty} = 0.78$, different effects of the perforation/cavity arrangement, in comparison with the solid-surface airfoil, are illustrated in Fig. 70. Compression waves at an angle corresponding to the local Mach numbers, obtained from the surface pressure distributions (shown at left) in the interaction region, have been drawn at the edge of an assumed boundary layer to give an impression of the different shock patterns.

The severe shock pressure rise at $\alpha = 2^\circ$ on the solid-surface airfoil is weakened on the perforation/cavity airfoil due to the pressure equalizing effect of the flow through the perforated surface and cavity. By this the pre-shock Mach number is lowered and the pressure rise is spread over the perforated region (indicated in the pressure distribution by the shaded region). The latter will cause a less strong boundary layer thickening, thus reducing the form drag in addition to the wave drag reduction resulting from the

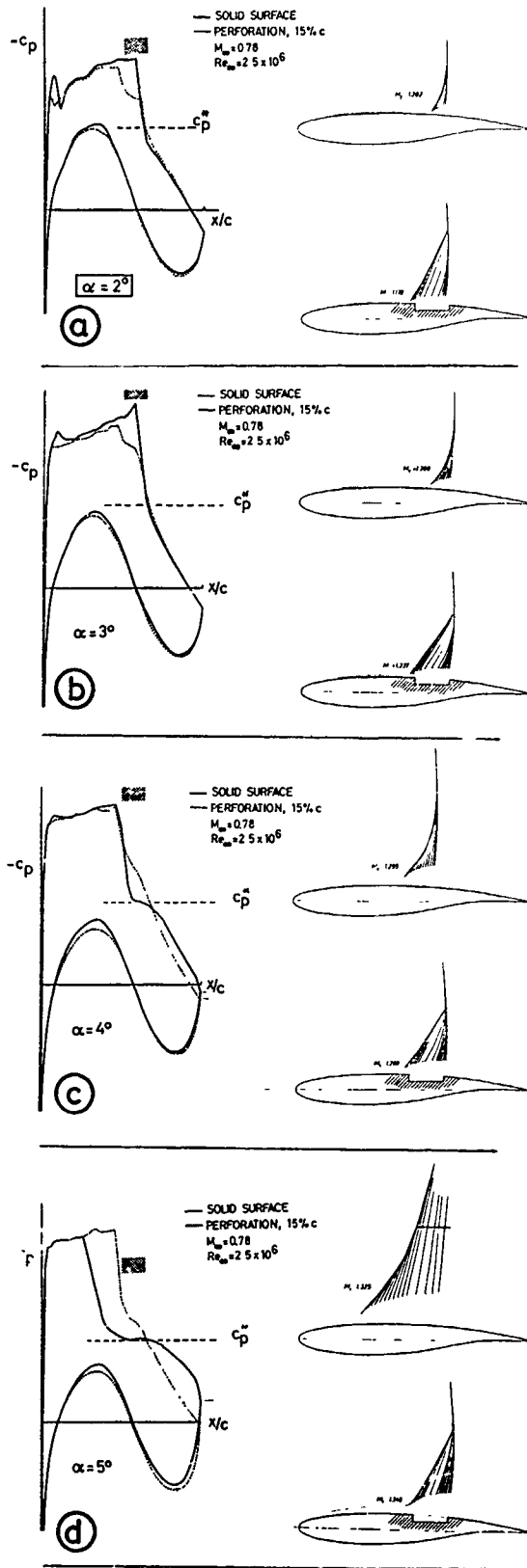


Fig. 70: Pressure Distributions and Schematic Shock Patterns

reduced shock strength. It is suspected that the additional boundary layer thickening due to outflowing mass at the upstream part of the perforation is offset (for continuity reason) by the inflow over the rear part. The counteracting effects of the thinner boundary layer over the rear of the airfoil and possibly roughness of the perforation (increased friction drag) are obviously smaller than the effects of reduced shock strength and displacement thickness. Hence a (small) drag reduction is gained even at low incidence, as was seen in Fig. 66.

At slightly higher incidence, $\alpha = 3^\circ$, the maximum shock strength ($M_1 = 1.008$) is reached on the solid-surface airfoil which the boundary layer can negotiate without detrimental shock-induced or trailing edge separation. Therefore, maximum wave drag reduction is attained at this stage by the perforation/cavity arrangement. The larger pressure difference over the perforated region, indicated by the higher shock-upstream Mach number, causes stronger in- and outflow velocity components, the latter inducing stronger compression waves which coalesce to an oblique shock, merging in the outer flow with the terminating normal shock.

Further increasing the incidence to $\alpha = 4^\circ$ results in an upstream movement of the normal shock on the solid-surface airfoil, causing a shock-induced separation, clearly indicated in the corresponding pressure distribution. The slightly lower pressure coefficient at the trailing edge signals separation to be present there, but from the mere pressure distribution it cannot be clearly distinguished whether this separation is caused by the shock-induced separation bubble extending to the trailing edge or by the rear adverse pressure gradients. On the perforation/cavity airfoil the surface pressure increases steadily from immediately upstream of the perforation to the trailing edge, and neither shock-induced nor trailing edge separation is evident. Since the shock strength is about the same for both airfoils, the effect of the perforation on wave drag ceases at this stage and the form drag reduction, due to suppressed separation, prevails; the total drag reduction at this point (see Fig. 66) is about 47 percent.

Severe separation effects become visible for the solid-surface airfoil at $\alpha = 5^\circ$. Monitoring the RMS-value of the airfoil root bending moment and Schlieren observations during the experiments revealed shock oscillations to be present and the flow to be totally separated from the shock to the trailing edge. The (mean) pressure distribution shows the shock location far upstream and indicates the severe separation by the negative trailing edge pressure coefficient. Though on the perforated model trailing edge separation was evident too, the shock location was steady (and remained steady even for incidences up to $\alpha = 7^\circ$), located at the front of the perforated region, thus substantiating, in addition to the large drag reduction (53 percent), the great potential of the passive device in affecting the onset of buffet. It seems likely that the mutual interaction of the shock and the separated trailing edge flow is interrupted or greatly suppressed by the perforation/cavity arrangement and the corresponding secondary flow. At this angle

of attack ($\alpha = 5^\circ$) the wave drag on the perforated airfoil is no longer reduced but, due to higher shock strength, even increased, and the large drag reduction (seen in Fig. 66) has to be exclusively attributed to a reduction of form drag.

The entropy production across a shock wave may be taken as some measure for the wave drag. Utilizing normal shock relations, the effectiveness of the perforation/cavity arrangement in reducing the wave drag relative to the solid surface airfoil is illustrated in Fig. 71 for a range of Mach numbers and incidences. The behavior corresponding to the curve for $M_\infty = 0.78$ has been described in the example above and it is seen that the curves for differing Mach numbers follow a similar trend viz., the wave drag reduction diminishing with increasing incidence, and the wave drag being increased on the perforated airfoil above a certain angle of attack. From the above example it was furthermore seen that different shock displacement behavior on the two airfoil models was responsible for this trend.

NORMAL SHOCK:

$$\frac{\Delta S}{R} = -\ln \left\{ \frac{\left[\frac{\gamma+1}{2\gamma M_1^2 - (\gamma-1)} \right]^{\frac{1}{\gamma-1}} \left[\frac{(\gamma+1)M_1^2}{(\gamma-1)M_1^2 + 2} \right]^{\frac{\gamma}{\gamma-1}} \right\}$$

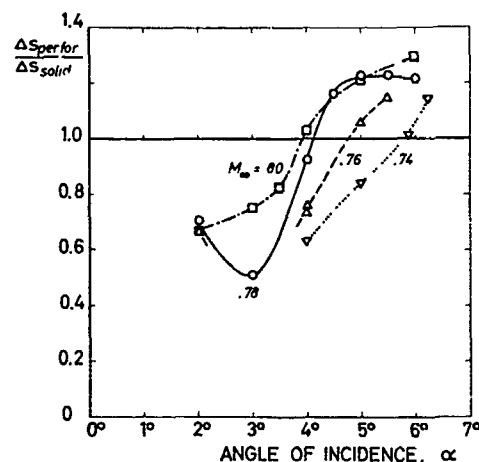
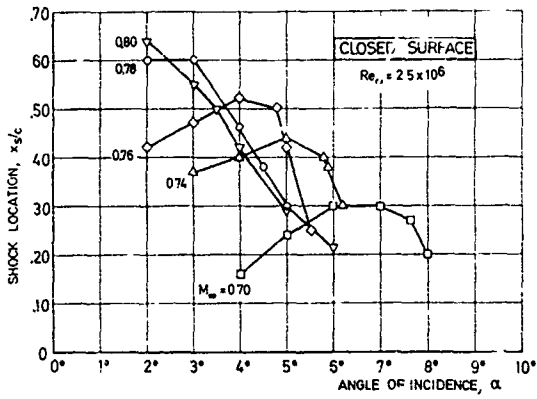


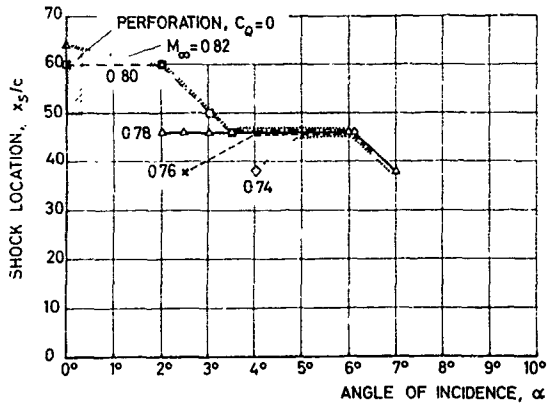
Fig. 71: Relative Entropy Production

The shock movement on the closed-surface airfoil for different Mach numbers is depicted in Fig. 72a as function of angle of attack, exhibiting at lower Mach numbers the generally observed downstream movement with increasing incidence to a most rearward position, and then a rapid upstream movement. For the higher Mach numbers the shock is at low incidence already located fairly aft on the airfoil and shifts upstream with increasing angle of attack.

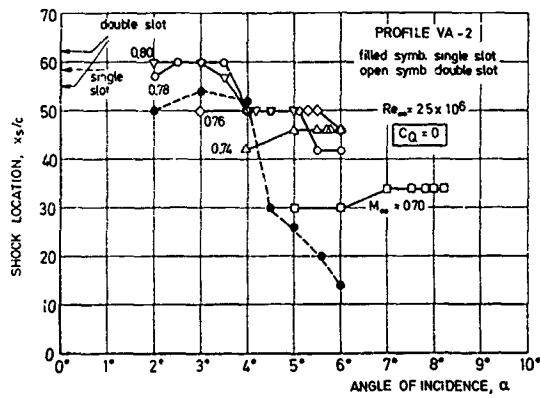
It may be noted that the "shock location" is defined here as the beginning of the surface pressure rise (most upstream point of the shock boundary layer interaction region). Since the spacing of the pressure measuring orifices in this region was 4 percent chord, uncertainties in the shock position of about 3% chord are likely.



a) Closed Surface

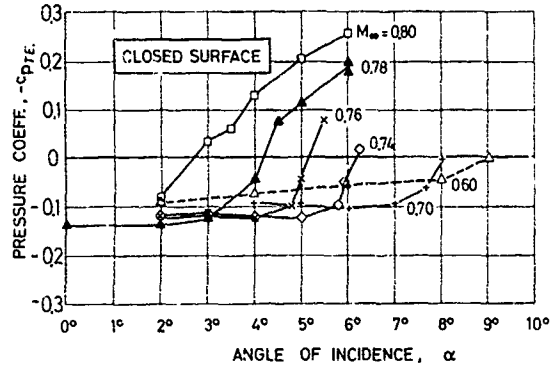


b) Perforation/Cavity

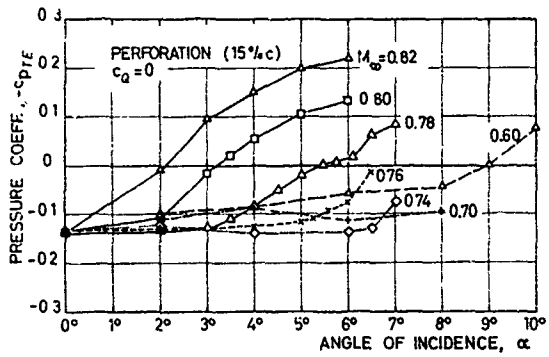


c) Double Slot/Cavity

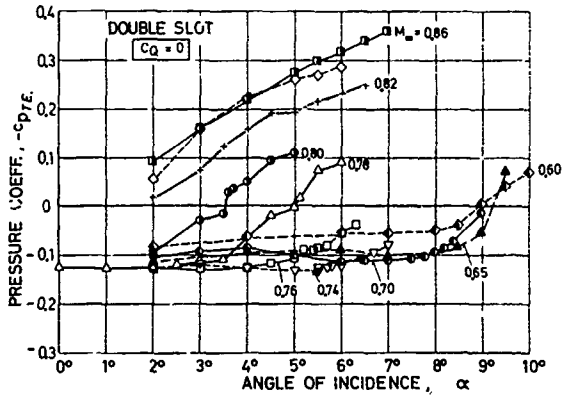
Fig. 72: Shock Locations



a) Closed Surface



b) Perforation/Cavity



c) Double Slot/Cavity

Fig. 73: Trailing Edge Pressures

It was mentioned above, and seen in Fig. 70, that the passive device has a strong influence on the shock position. This is illustrated for the perforated airfoil at different Mach numbers in Fig. 72 b. For the two lower Mach numbers the upstream movement of the shock is, at higher incidences, delayed over a certain range of angles of attack. For $M_{\infty} = 0.78$ the shock pressure rise starts immediately upstream of the perforated surface/cavity region in a range from $\alpha = 2^\circ$ to 6° , and is then slowly shifted upstream. The aft fixation of the shock at the higher incidences results, due to the increased supersonic region, in an appreciable gain in lift which, in addition to the observed total drag reductions, contributes most favorably to the improvements in the performance parameter L/D (Fig. 69). The overall boundary layer thickening in the interaction region is obviously reduced, permitting the shock to remain located at a most rearward position.

A similar effect of the combined suction and blowing on the shock location is observed on the airfoil with double slot/cavity arrangement, Fig. 72 c. At low incidence the shock is positioned between the two slots and shifts upstream of the front (blowing) slot with increasing incidence. Here, it is fixed over a range of angles of attack, thus causing the observed improvements of the airfoil aerodynamic characteristics, viz., lift-to-drag ratio, drag rise, and the onset of buffet.

It was established earlier that a rapidly decreasing trailing edge pressure indicates the presence of significant separation at the trailing edge. A comparison of Fig. 73 a and Fig. 72 a reveals that for the closed-surface airfoil the divergence of trailing edge pressure is associated with a rapid upstream movement of the shock, and vice versa, demonstrating the strong interaction between the shock and separated trailing edge flow. Comparisons of the corresponding data in Fig. 73 b and Fig. 72 b for the perforation/cavity airfoil and Fig. 73 c and Fig. 72 c for the double slot/cavity airfoil substantiate the assumption that the interaction between the shock and the separated trailing edge flow is largely suppressed by the passive arrangements. The trailing edge pressure coefficient has decreased well below zero before the shock location is affected. Furthermore, with passive BLC devices, the trailing edge pressure divergence is less pronounced which lets one conclude that separation effects are less severe.

The main effects of the passive devices may be summarized by the schematic flow models in Fig. 74. On the solid-surface airfoil the boundary layer in the interaction region is severely thickened due to the strong pressure rise across the shock and due to the displacement effect of the shock-induced separation bubble. After reattachment the boundary layer velocity profiles do not fully recover thus being still highly susceptible to separation in a downstream adverse pressure gradient. The presence of a passive BLC device, here perforation/cavity, has the following effects on the flow development. If the shock is located on the perforation the shock pressure rise is spread over the width of the perforated region by the pressure equalizing effect of the (self-adjusting)

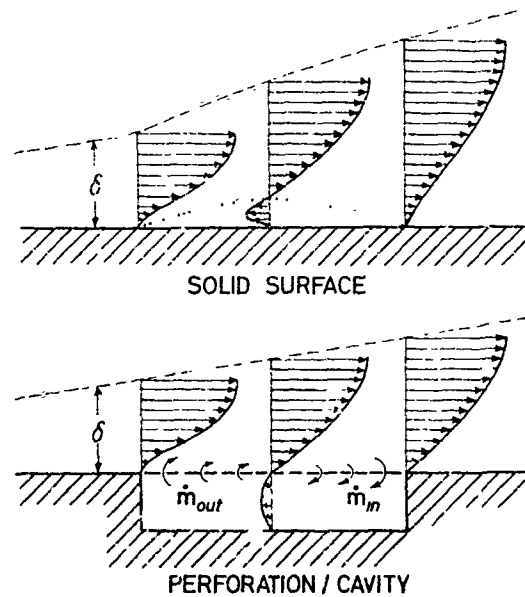


Fig. 74: Effect of Passive Device on Transonic Flow Development

secondary flow through the surface and cavity, thus reducing the adverse pressure gradient and the shock strength. By these effects and, partly, since the region of reversed flow is displaced beneath the airfoil contour, the overall boundary layer thickening in the interaction region is drastically reduced. The thickening of the boundary layer at the front of the perforation due to outflowing mass is offset downstream by the same amount of mass flowing into the cavity. A "healthier" velocity profile, less susceptible to separation, enters the downstream region of adverse pressure gradients. Furthermore, the flow issuing from the holes of the perforation may act as some kind of air jet vortex generators altering the small scale turbulence within the boundary layer, thus additionally affecting the separation behavior, favorably, but this is still speculative.

5. CONCLUDING REMARKS

Accurate drag prediction and efficient drag reduction are, particularly in the transonic speed range, paramount to the future of economical aircraft design and operation. In the present paper the prediction of drag based on high-speed wind tunnel results was discussed, emphasizing problems associated with testing in the transonic speed range and with the extrapolation of low Reynolds number wind tunnel results to full-scale aircraft conditions. Drag reduction methods were treated, emphasizing active and passive boundary layer control mainly based on direct modifications of the wing surface, such as slots and perforations, utilized to either draw material from and/or add material to the boundary layer.

The accurate determination of the transonic drag rise, mainly caused by wave drag due to shock waves occurring in the flow and increased form drag due to boundary layer thickening and, ultimately, separation, requires the wind tunnel as an indispensable tool since theoretical methods are still inadequate. Concerning the testing techniques employed in low Reynolds number wind tunnel experiments, improvements are, however, necessary: Transition fixation is required to provide reliable results upon which the extrapolation of wind tunnel data can firmly be based. Here, further research is needed to develop devices, preferably remotely adjustable, that ensure transition to occur at the trip location - or, if suitable sensing elements can be employed, at any desired location - without generating additional drag and over- or underfixing the boundary layer as the freestream conditions are changed. Also, but not only, with respect to the new generation high Reynolds number wind tunnels, must wall interference correction procedures based on measured boundary conditions be further developed - or adaptive wall wind tunnel techniques improved to become feasible for large facilities throughout the transonic range - in order to meet the overall accuracy demanded for the drag prediction of future aircraft. Concerning scaling methods, better results seem possible by replacing or supplementing the direct scaling approach, based on accounting for Reynolds number effects on drag through flat plate skin friction computations, by the reference scaling method. The latter requires, however, close similarity between the reference and the new aircraft design; it seems to fail if essential differences exist in the Reynolds number sensitivity of the two configurations considered. Here, again, more research is needed with the objective of understanding the Reynolds number sensitivity of transonic configurations dependent on their geometry so that empirical and computational procedures may successfully be included into the scaling process. There is a close coupling between the latter and the most realistic simulation of full-scale flow behavior at low Reynolds numbers, for instance, by aft transition fixation or other boundary layer manipulating devices.

It was shown in Chapter 4 that appreciable improvements in the aerodynamic performance of supercritical airfoils at design and off-design conditions can be achieved by applying either active or passive boundary layer control methods. Active BLC methods, having the disadvantage of requiring external power to be effective, which has to be accounted for in the overall drag breakdown, reduce the form drag by preventing undesirable boundary layer thickening (suction) or separation by energizing the near wall boundary layer flow (blowing). Furthermore, the shock location and the effective camber may be favorably altered by the reduced boundary layer displacement thickness effects, thus increasing the lift which contributes, in addition to the reduced drag, to the improvement in the performance parameter L/D . However, care has to be taken that the control device produces no drag penalty at subcritical speeds.

This statement holds, of course, as well for the passive BLC methods described above. Utilizing the most favorable effect of a secondary flow through a permeable surface and a cavity or plenum underneath, placed at the shock location, substantial wave and form drag reductions, especially at highly off-design conditions, were obtained by different investigators. It may be worthwhile to note that these improvements were gained on supercritical airfoils neither designed for the application of boundary layer control nor were the extent of the permeable surface, the porosity and the cavity depth optimized. Therefore, further improvements may be expected on appropriately designed airfoils with optimized passive control devices. It is anticipated that full-scale flight tests on a swept wing, recently initiated [107], will validate the improvements due to passive BLC also for three-dimensional flows.

ACKNOWLEDGEMENT

The preparation of the paper was preceded by a detailed discussion of the contents of the chapter on transonic drag rise with Messrs. Hilbig, Anders and Mantel of MBB-UT (Bremen) whose valuable suggestions are gratefully acknowledged. The research on BLC at DFVLR reported here was conducted in close cooperation with Prof. Thiede of MBB-UT (Bremen). Finally, we would like again to express our appreciation to Prof. E.E. Covert for providing us with an early copy of the manuscript of Ref. 3.

6. REFERENCES

1. AGARD Conference Proceedings No. 124 on "Aerodynamic Drag", AGARD-CP-124, Oct. 1973.
2. AGARD Lecture Series No. 67 on "Prediction Methods for Aircraft Aerodynamic Characteristics", AGARD-LS-67, May 1974.
3. Covert, E.E. (Principle Editor), "Thrust and Drag: Its Prediction and Verification", AIAA Progress in Astronautics and Aeronautics, Vol. 99, to be published in 1985.
4. Hough, G.R. (Editor), "Viscous Drag Reduction", AIAA Progress in Astronautics and Aeronautics, Vol. 72, 1980.
5. AGARD Special Course on Concepts for Drag Reduction, AGARD Report No. 654, June 1977.
6. AGARD Conference Proceedings No. 365 on "Improvement of Aerodynamic Performance Through Boundary Layer Control and High Lift Systems", AGARD-CP-365, August 1984.
7. Krenz, G., "Transonic Configuration Design" in AGARD-R-712, Special Course on Subsonic/Transonic Aerodynamic Interference for Aircraft, July 1983, Paper No. 10.

8. Bradley, R.G., "Practical Aerodynamic Problems - Military Aircraft" in Progress in Astronautics and Aeronautics, Vol. 81, Transonic Aerodynamics, 1982.
9. Stanewsky, E., "Interaction between the outer inviscid flow and the boundary layer on transonic airfoils", Thesis D 83, Technical University Berlin, 1981 (also see Z. Flugwiss. Weltraumforsch. 7 (1983), Heft 4, pp. 242-252).
10. Boehe, R.D., Stanewsky, E., "Measurement with the VFW Airfoil Va2 with Flow-through Nacelle at Transonic Speeds", BMET Ziviles Komponentenprogramm LFK 7511, Report No. 9, Sept. 1977.
11. Pearcey, H.H., Osborne, J. and Haines, A.B., "The Interaction Between Local Effects at the Shock and Rear Separation - a Source of Significant Scale Effects in Wind-tunnel Tests on Airfoils and Wings" in AGARD-CP-35, Sep. 1968, Paper No. 11.
12. Bowes, G.M., "Aircraft Lift and Drag Prediction and Measurement" in AGARD-LS-67, Prediction Methods for Aircraft Aerodynamic Characteristics, May 1974, Paper No. 4.
13. Lynch, F.T., "Commercial Transports - Aerodynamic Design for Cruise Performance Efficiency" in AIAA Progress in Astronautics and Aeronautics, Vol. 81, Transonic Aerodynamics, 1982.
14. Butler, S.F.J., "Aircraft Drag Prediction for Project Appraisal and Performance Estimation" in AGARD-CP-124, Aerodynamic Drag, Oct. 1973, Paper No. 6.
15. Steinle, F. and Stanewsky, E., "Wind Tunnel Flow Quality and Data Accuracy Requirements", AGARD Advisory Report No. 184, Nov. 1982.
16. McKinney, L.W., "Operational Experience with the National Transonic Facility" in AGARD-CP-348, Wind Tunnels and Testing Techniques, Feb. 1984, Paper No. 1.
17. Paterson, J.H., Mac Wilkinson, D.G. and Blackerby, W.T., "A Survey of Drag Prediction Techniques Applicable to Subsonic and Transonic Aircraft Design" in AGARD-CP-124, Aerodynamic Drag, Oct. 1973, Paper No. 1.
18. Stanewsky, E., Demurie, F., Ray, E.J. and Johnson, C.B., "High Reynolds Number Tests of the CAST 10-2/DOA2 Transonic Airfoil at Ambient and Cryogenic Temperature Conditions" in AGARD-CP-348, Wind Tunnel and Testing Techniques, Feb. 1984, Paper Nr. 10.
19. Hackett, J.E. and Sugavanam, A., "Recent developments in three-dimensional wake analysis" in AGARD-VKI Special Course on Aircraft Drag Prediction and Reduction, May 20-23, 1985.
20. Meier, H.U. and Kreplin, H.-P., "Experimental Investigation of the Boundary Layer Transition and Separation on a Body of Revolution" Z. Flugwiss. Weltraumforsch. 4 (1980), Heft 2, pp. 65-71.
21. Burgsmüller, W., "Transition Fixation for the Wing Development of Commercial Transport Aircraft at High Speeds" in Grenzschicht Steuerung und Transitionsfixierung, DFVLR (DGLR)-Mitt. 84-17, 1984, pp. 55-79.
22. Blackwell, J.A., "Effects of Reynolds number and Boundary Layer Transition Location on Shock-induced Separation" in AGARD-CP-35, Transonic Aerodynamics, 1968, Paper No. 21 (also see: Proceedings of the 11th ICAS, 1978, Vol. 1, pp. 370-383 and Ref. 36).
23. Elsenaar, A., "Experiences with Transition Fixation in the High-Speed-Regime at NLR" in Grenzschichtsteuerung und Transitionsfixierung, DFVLR(DGLR)-Mitt. 84-17, 1984, pp. 33-54.
24. Stanewsky, E., "Transition Fixing and Simulation of High Reynolds Number Flow at Transonic Velocities" (same as Ref. 23, pp. 115-129).
25. van den Berg, B., "Transition Detection Using Surface Pressure Holes" (same as Ref. 23, pp. 131-138).
26. Stanewsky, E., Hefer, G. and Freimuth, P., "Preliminary Investigation of Three-dimensional Shock Boundary Layer Interaction on a Sheared Wing", 2nd STAB-Workshop, DFVLR-Zentrum Köln-Porz, 18.-19.9.1984.
27. Braslow, E.L., Hicks, R.M. and Harris, R.V., Jr., "Use of Grit-Type Boundary Layer Transition Trips on Wind Tunnel Models", NASA TN D-3579, 1966.
28. Michel, R. and Arnal, D., "Investigation of the Conditions for Tripping Transition with Roughness Elements and their Influence on Boundary Layer Development" (same as Ref. 23, pp. 103-113) also see: Arnal, D., "Description, Measurement and Prediction of Transition in Two-dimensional Incompressible Flow" in AGARD-VKI Special Course on Stability and Transition of Laminar Flows, March 26-30, 1984, Paper No. 2.
29. Göthert, B.H., "Transonic Wind Tunnel Testing", AGARDograph No. 49, Pergamon Press, New York, Oxford, London, Paris, 1961.
30. Garner, H.C. et al. "Subsonic Wind Tunnel Wall Corrections", AGARDograph 109, 1966.
31. AGARD Conference Proceedings No. 335 "Wall Interference in Wind Tunnels", AGARD-CP-335, Sep. 1982.
32. Mokry, M., Chan, Y.Y. and Jones, D.J., "Two-dimensional Wind Tunnel Wall Interference", AGARDograph No. 281, Nov. 1983.
33. Elsenaar, A. and Stanewsky, E., "A Report of a GARTEur Action Group on Two-dimensional Transonic Testing Methods" in AGARD-CP-335, Wall Interference in Wind Tunnels, 1982, Paper No. 5.

34. Kuczka, D., Wedemeyer, E. and Heddergott, A., "Measurement of Interference-free Data in an Adaptive Wind Tunnel with Flexible Walls", DFVLR-IB 222-84 A 46, 1984.
35. Heddergott, A. and Wedemeyer, E., "Deformable Adaptive Wall Test Section for Three-dimensional Wind Tunnel Testing", 14th Congress of ICAS, Sept 9-14, 1984, Toulouse, France, Paper No. 84-2.1.2.
36. Blackwell, J.A., "Experimental Testing at Transonic Speeds" in AIAA Progress in Astronautics and Aeronautics, Vol. 81, Transonic Aerodynamics, 1982.
37. Ganzer, U., Stanewsky, E. and Ziemann, J., "Sidewall Effects on Airfoil Tests", AIAA-Journal, Vol. 22, No. 2, Feb. 1984, p. 297.
38. Boersen, S.J. and Elsenaar, A., "Half-model Testing in the NLR High Speed Wind Tunnel HST: Its Technique and Application" in AGARD-CP-348, Wind Tunnels and Testing Techniques, Feb. 1984, Paper No. 23.
39. Beclé, J.P., Coste, J. and Leynaert, J., "New Turbo Powered Simulation Calibration Bench and Ejector Tests" (same as Ref. 38, Paper No. 29)
40. AGARD Special Course on Subsonic/Transonic Aerodynamic Interference for Aircraft, AGARD Report 712, July 1983, Papers No. 13, 14, 15 and 16.
41. Binder, B., Melzer, E. and Wulf, R., "The New Calibration Tank for Engine Simulators at DFVLR Göttingen" in AGARD-CP-348, Wind Tunnels and Testing Techniques, Feb. 1984, Paper No. 28.
42. Hoerner, S.F., "Fluid Dynamic Drag" published by S.F. Hoerner, 1965.
43. Young, A.D., Patterson, J.H. and Jones, J.L., "Aircraft Excrescence Drag", AGARD-AG-264, July 1981.
44. White, F.M. and Christoph, G.H., "A Simple New Analysis of Compressible Turbulent Two-dimensional Skin Friction Under Arbitrary Conditions", AFFDL-TR-70-133, 1971 (also AFFDL-TR-72-163, Nov. 1972).
45. Haak, D.E., USAF Stability and Control DATCOM, Revised, April 1978.
46. Snodgrass, R.R., "A Computerized Method for Predicting Drag and Lift for Aeronautical Systems," ASD-ENF-TM-76-1, Oct. 1976.
47. Pelagatti, C., Pilon, J.C. and Bardaud, J., "Analyse critique des comparaisons des résultats de vol aux prévisions de soufflerie pour des avions de transport subsonique et supersonique" in AGARD-CP-187, June 1975.
48. Swihart, J.M., "The Next Generation of Commercial Aircraft - The Technological Imperative", 12th Congress of ICAS, Oct. 12-17, 1980, Munich, FRG.
49. Lachmann, G.V., "Boundary Layer and Flow Control", Vol. I, Vol. II, Pergamon Press, Oxford, 1961.
50. Schlichting, H. "Boundary Layer Theory", 7th Edition, Mc Graw-Hill, New-York, 1979.
51. Hefner, J.M., Bushnell, D.M., "An Overview of Concepts for Drag Reduction", in Ref. [5], Paper No. 1.
52. Bushnell, D.M., "Turbulent Drag Reduction for External Flows", AIAA 21st Aerospace Sciences Meeting, Jan. 10-13, 1983, Reno, Nev., Paper No. 83-0227.
53. Whitcomb, R.T., "Methods for Reducing Subsonic Drag Due to Lift", in Ref. [5], Paper No. 2.
54. Pfenninger, W., "Laminar Flow Control, Laminarization" in Ref. [5], Paper No. 3.
55. Thomas, A.S.W., "Aircraft Drag Reduction Technology", in Ref. [6], Paper No. 11.
56. AGARD-VKI Special Course on "Aircraft Drag Prediction and Reduction", May 20-23, 1985, Rhode-Saint-Genese, Belgium.
57. Nieuwland, G.Y., Spee, B.M., "Transonic Shock-Free Flow, Fact or Fiction?", in AGARD-CP-35, Transonic Aerodynamics, Sept. 1968, Paper No. 1
58. Whitcomb, R.T., "Review of NASA Supercritical Airfoils", 9th Congress of the International Council of the Aeronautical Sciences, Aug. 25-30, 1974, Haifa, Israel.
59. Seddon, J., "The Flow Produced by Interaction of a Turbulent Boundary Layer with a Normal Shock Wave of Strength Sufficient to Cause Separation", RAE Technical Memorandum, No., Aero 667, March 1960.
60. Pearcey, H.H., "Some Effects of Shock-Induced Separation of Turbulent Boundary Layers in Transonic Flow Past Aerofoils", ARC R&M No. 3108, 1955.
61. Pearcey, H.H., "The Occurrence and Development of Boundary Layer Separations at High Incidences and High Speeds", ARC R&M No. 3109, 1955.
62. Pearcey, H.H., "Shock-Induced Separation and its Prevention by Design and Boundary Layer Control", in Ref. [49], Vol. II. pp. 1166-1344.
63. Pearcey, H.H., "A Method for the Prediction of the Onset of Buffeting and other Separation Effects from Wind Tunnel Tests on Rigid Models", AGARD Report 223, Oct. 1958.
64. Finke, K., "Unsteady Shock Wave-Boundary Layer Interaction on Profiles in Transonic Flow", AGARD-CP-168, Flow Separation, May 1975.
65. Thomas, F., Redeker, G., "A Method for Calculating the Transonic Buffet Boundary Including the Influence of Reynolds Number", AGARD-CP-83, April 1971, Paper No. 3.

66. Vanino, R., Wedemeyer, E., "Wind Tunnel Investigation of Buffet Loads on Four Airplane Models", AGARD-CP-83, April 1971, Paper No. 34.
67. Ackeret, J., Feldmann, F., Rott, N., Untersuchungen an Verdichtungsstoßen und Grenzschichten in schnell bewegten Gasen", Mitteilungen aus dem Institut für Aerodynamik der ETH Zurich, No. 10, 1946.
68. Liepmann, J.W., "The Interaction Between Boundary Layer and Shock Waves in Transonic Flow", Journ. of the Aeron. Sciences, Vol. 13, No. 12, Dec. 1946, pp. 623-637.
69. Haines, A.B., Holder, D.W., Pearcey, H.H., "Scale Effects at High Subsonic and Transonic Speeds, and Methods for Fixing Boundary Layer Transition in Model Experiments", ARC R&M 3012, 1954.
70. Green, J.E., "Interactions Between Shock Waves and Turbulent Boundary Layers", Progress in Aerospace Sciences, Vol. 11, 1970, pp. 235-340, Pergamon Press, Oxford, 1970.
71. Yoshihara, H., Zonars, D., "The many Facets of 3-D Transonic Shock-Induced Separation", AGARD-CP-168, Flow Separation, May 1975, Paper No. 42.
72. Yoshihara, H., "Subsonic/Transonic Viscous Interactions", AGARD Report No. 712, Special Course on Subsonic/Transonic Aerodynamic Interference for Aircraft, May 1983.
73. Monnerie, B., "Flow Field Aspects of Transonic Phenomena", AGARD Advisory Report No. 82, Chapter 3, 1975.
74. Pearcey, H.H., "The Aerodynamic Design of Section Shapes for Swept Wings", in Advances in Aeronautical Sciences, Vol. 3, pp. 277-322, Pergamon Press, Oxford, 1962.
75. Lock, R.C., Rogers, E.W.E., "Aerodynamic Design of Swept wings and Bodies for Transonic Speeds", in Advances in Aeronautical Sciences, Vol. 3, pp. 253-276, Pergamon Press, Oxford, 1962.
76. Haines, A.B., "Factors Affecting the Choice of a Three-Dimensional Swept Wing Design for High Subsonic Speeds", AGARD-CP-35, Transonic Aerodynamics, 1968, Paper No. 16.
77. Loving, D.L., "Wind Tunnel-Flight Correlation of Shock-Induced Separated Flow", NASA TN-D-3580, Sept. 1966.
78. Hall, M.G., "Scale Effects in Flows over Swept Wings", AGARD-CP-83, 1971, Paper No. 1.
79. Green, J.E., "Some Aspects of Viscous-Inviscid Interactions at Transonic Speeds, and their Dependence on Reynolds Number", AGARD-CP-83, 1971, Paper No. 2.
80. Regenscheit, B., "Versuche zur Widerstandsverringerng eines Flugels bei hoher Mach'scher Zahl durch Absaugung der hinter dem Gebiet unsteady Verdichtung abgelösten Grenzschicht", ZWB-FB-1424, Juli 1941, english translation: NACA TM 1168, July 1947.
81. Fage, A., Sargent, R.F., "Effect on Airfoil Drag of Boundary Layer Suction Behind a Shock Wave", ARC R&M, No. 1913, 1943.
82. Thiede, P., "Supercritical Airfoil Flow Control by Slot Suction in the Shock Region", Proceedings of the 5th USAF/FRG DEA Meeting, April 1980, AFFDL-TR-80-3088.
83. Thiede, P., Dargel, G., "Erweiterung des Einsatzbereiches von transsonischen Profilen durch lokale Grenzschichtabsaugung", Rufo IV, Auftr. Nr. T/RF 41/70021/71420, 1980.
84. Krogmann, P., "Druckverteilungs- und Grenzschichtmessungen an einem überkritischen Profil mit Grenzschichtabsaugung durch einen Einzelschlitz", DFVLR IB 222 81 A 06.
85. Stanewsky, E., Krogmann, P., Thiede, P., Dargel, G., "Stoß-Grenzschicht-Interferenz und ihre Beeinflussung durch Grenzschichtabsaugung", DGLR Symposium: Stromungen mit Ablosung, Nov. 1981, Stuttgart, FRG.
86. Krogmann, P., "Untersuchungen an einem überkritischen Profil mit Grenzschichtabsaugung im Stoßbereich über einen Doppelschlitz", DFVLR IB 222 83 A 25 (to be published 1985).
87. Wedemeyer, E., "Experimentelle Untersuchungen über den Einfluß der Grenzschicht auf die Ausbildung des Verdichtungsstoßes an verschiedenen gekrümmten Wänden", AVA Bericht 61 A 50 (1961).
88. Smith, D.W., Walker, J.H., "Tests of an Area Suction Flap on an NACA 64 A 010 Airfoil at High Subsonic Speeds", NASA TN D-310, May 1960.
89. Hilbig, H., Wagner, H., "Variable Wing Camber for Civil Transport Aircraft", Proceedings of the 14th Congress of ICAS, Sept. 1984, Toulouse, France, Paper No. 84-5.2.1.
90. Krogmann, P., "Untersuchungen an einem überkritischen Profil mit Grenzschichtabsaugung im Stoßbereich über einen perforierten Streifen", DFVLR IB 222 82 A 37, published as: DFVLR-FB 85-15.
91. Finke, K., "Stoßschwingungen in schallnahen Strömungen", VDI-Forschungsheft 580, VDI-Verlag, Düsseldorf (FRG), 1977.
92. Haight, C.H., Mask, R.L., "Transonic Maneuver/Cruise Airfoil Design Employing Active Diffusion Control, in Ref. [4], pp. 187-211.
93. Mask, R.L., "Low Drag Airfoil Design Utilizing Passive Laminar Flow and Coupled Diffusion Control", in Ref. [4], pp. 212-232.
94. Reshotko, E., "Drag Reduction by Cooling in Hydrogen Fueled Aircraft", Journ. of Aircraft, Vol. 16, No. 9, 1979, p. 584.

95. Reshotko, E., "Control of Boundary Layer Transition", AIAA Shear Flow Control Conference, March 12-14, 1985, Paper No. 85-0562.
96. Savu, G., Trifu, O., Dumitrescu, L.Z., "Suppression of Shocks on Transonic Airfoils", Proceedings of the 14th International Symposium on Shock Tubes and Shock Waves, Aug. 1983, Sidney, Australia, pp. 92-101.
97. Savu, G., Trifu, O., "Porous Airfoils in Transonic Flow" AIAA Journal, Vol. 22, No. 7, July 1984, pp. 989-991.
98. Savu, G. "Drag Reduction of Transonic Airfoils", Meeting abstract: EUROMECH 181 Colloquium, August 29-31, 1984, Saltsjobaden, Sweden.
99. Bahi, L., Ross, J.M., Nagamatsu, H.T., "Passive Shock Wave/Boundary Layer Control for Transonic Airfoil Drag Reduction", AIAA 21st Aerospace Sciences Meeting, January 1983, Reno, Nev., Paper No. 83-0137.
100. Nagamatsu, H.T., Orozco, R.D., Ling, D.C., "Porosity Effect on Supercritical Airfoil Drag Reduction by Shock Wave/Boundary Layer Control", AIAA 17th Fluid Dynamics, Plasma Dynamics, and Lasers Conference, June 1984, Snowmass, Col., Paper No. 84-1682.
101. Nagamatsu, H.T., Dyer, R., Ficarra, R.V., "Supercritical Airfoil Drag Reduction by Passive Shock Wave/Boundary Layer Control in the Mach Number Range .75 to .90", AIAA 23rd Aerospace Sciences Meeting, Jan. 1985, Reno, Nev., Paper No. 85-0207.
102. Krogmann, P., Thiede, P., "Aktive und passive Beeinflussung der Stoß-Grenzschicht-Interferenz an überkritischen Tragflügeln", 4. DGLR Symposium Strömungen mit Ablösung, Oct. 1983, Göttingen (FRG), Also: DEVLR IB 222 83 A 26 (1983).
103. Krogmann, P., Stanewsky, E., Thiede, P., "Effects of Suction on Shock/Boundary Layer Interaction and Shock-Induced Separation", Journ. of Aircraft, Vol. 22, No. 1, 1985, pp. 37-42.
104. Thiede, P., Krogmann, P., Stanewsky, E., "Active and Passive Shock/Boundary Layer Interaction Control on Supercritical Airfoils", in Ref. [6], Paper No. 24.
105. Krogmann, P., Stanewsky, E., Thiede, P., "Transonic Shock-Boundary Layer Interaction Control", Proceedings of the 14th Congress of ICAS, Sept. 1984, Toulouse, France, Paper No. 84-2.3.2.
106. Krogmann, P., "Drag Reduction Through Active or Passive Shock-Boundary Layer Interaction Control", EUROMECH 181 Colloquium, Aug. 29-31, 1984, Saltsjobaden, Sweden.
107. Bertelrud, A., "Passive Shock Modification in Flight", EUROMECH 181 Colloquium, Aug. 29-31, 1984, Saltsjobaden, Sweden.

REPORT DOCUMENTATION PAGE

1. Recipient's Reference	2. Originator's Reference	3. Further Reference	4. Security Classification of Document								
	AGARD-R-723	ISBN 92-835-1507-2	UNCLASSIFIED								
5. Originator	Advisory Group for Aerospace Research and Development North Atlantic Treaty Organization 7 rue Ancelle, 92210 Neuilly sur Seine, France										
6. Title	AIRCRAFT DRAG PREDICTION AND REDUCTION										
7. Presented at											
8. Author(s)/Editor(s)	Various		9. Date July 1985								
10. Author's/Editor's Address	Various		11. Pages 272								
12. Distribution Statement	This document is distributed in accordance with AGARD policies and regulations, which are outlined on the Outside Back Covers of all AGARD publications.										
13. Keywords/Descriptors	<table> <tr> <td>Aerodynamic drag</td> <td>Turbulence</td> </tr> <tr> <td>Laminar flow</td> <td>External stores</td> </tr> <tr> <td>Skin friction</td> <td>Nacelles</td> </tr> <tr> <td>Boundary layer</td> <td></td> </tr> </table>			Aerodynamic drag	Turbulence	Laminar flow	External stores	Skin friction	Nacelles	Boundary layer	
Aerodynamic drag	Turbulence										
Laminar flow	External stores										
Skin friction	Nacelles										
Boundary layer											
14. Abstract	<p>The Special Course on Aircraft Drag Prediction was sponsored by the AGARD Fluid Dynamics Panel and the von Kármán Institute and presented at the von Kármán Institute, Rhode-Saint-Genèse, Belgium, on 20—23 May 1985 and at the NASA Langley Research Center, Hampton, Virginia, USA, 5—9 August 1985.</p> <p>The course began with a general review of drag reduction technology. Then the possibility of reduction of skin friction through control of laminar flow and through modification of the structure of the turbulence in the boundary layer were discussed. Methods for predicting and reducing the drag of external stores, of nacelles, of fuselage protuberances, and of fuselage afterbodies were then presented followed by discussion of transonic drag rise. The prediction of viscous and wave drag by a method matching inviscid flow calculations and boundary layer integral calculations, and the reduction of transonic drag through boundary layer control are also discussed.</p>										

<p>AGARD Report No. 723 Advisory Group for Aerospace Research and Development, NATO AIRCRAFT DRAG PREDICTION AND REDUCTION Published July 1985 272 pages</p> <p>The Special Course on Aircraft Drag Prediction was sponsored by the AGARD Fluid Dynamics Panel and the von Kármán Institute and presented at the von Kármán Institute, Rhode-Saint-Genèse, Belgium, on 20-23 May 1983 and at the NASA Langley Research Center, Hampton, Virginia, USA, 5-9 August 1985.</p> <p>The course began with a general review of drag reduction</p> <p>P.T.O</p>	<p>AGARD Report No. 723 Advisory Group for Aerospace Research and Development, NATO AIRCRAFT DRAG PREDICTION AND REDUCTION Published July 1985 272 pages</p> <p>The Special Course on Aircraft Drag Prediction was sponsored by the AGARD Fluid Dynamics Panel and the von Kármán Institute and presented at the von Kármán Institute, Rhode-Saint-Genèse, Belgium, on 20-23 May 1983 and at the NASA Langley Research Center, Hampton, Virginia, USA, 5-9 August 1985.</p> <p>The course began with a general review of drag reduction</p> <p>P.T.O</p>	<p>AGARD Report No. 723 Advisory Group for Aerospace Research and Development, NATO AIRCRAFT DRAG PREDICTION AND REDUCTION Published July 1985 272 pages</p> <p>The Special Course on Aircraft Drag Prediction was sponsored by the AGARD Fluid Dynamics Panel and the von Kármán Institute and presented at the von Kármán Institute, Rhode-Saint-Genèse, Belgium, on 20-23 May 1983 and at the NASA Langley Research Center, Hampton, Virginia, USA, 5-9 August 1985.</p> <p>The course began with a general review of drag reduction</p> <p>P.T.O</p>	<p>AGARD Report No. 723 Advisory Group for Aerospace Research and Development, NATO AIRCRAFT DRAG PREDICTION AND REDUCTION Published July 1985 272 pages</p> <p>The Special Course on Aircraft Drag Prediction was sponsored by the AGARD Fluid Dynamics Panel and the von Kármán Institute and presented at the von Kármán Institute, Rhode-Saint-Genèse, Belgium, on 20-23 May 1983 and at the NASA Langley Research Center, Hampton, Virginia, USA, 5-9 August 1985.</p> <p>The course began with a general review of drag reduction</p> <p>P.T.O</p>
<p>AGARD Report No. 723 Advisory Group for Aerospace Research and Development, NATO AIRCRAFT DRAG PREDICTION AND REDUCTION Published July 1985 272 pages</p> <p>The Special Course on Aircraft Drag Prediction was sponsored by the AGARD Fluid Dynamics Panel and the von Kármán Institute and presented at the von Kármán Institute, Rhode-Saint-Genèse, Belgium, on 20-23 May 1983 and at the NASA Langley Research Center, Hampton, Virginia, USA, 5-9 August 1985.</p> <p>The course began with a general review of drag reduction</p> <p>P.T.O</p>	<p>AGARD Report No. 723 Advisory Group for Aerospace Research and Development, NATO AIRCRAFT DRAG PREDICTION AND REDUCTION Published July 1985 272 pages</p> <p>The Special Course on Aircraft Drag Prediction was sponsored by the AGARD Fluid Dynamics Panel and the von Kármán Institute and presented at the von Kármán Institute, Rhode-Saint-Genèse, Belgium, on 20-23 May 1983 and at the NASA Langley Research Center, Hampton, Virginia, USA, 5-9 August 1985.</p> <p>The course began with a general review of drag reduction</p> <p>P.T.O</p>	<p>AGARD Report No. 723 Advisory Group for Aerospace Research and Development, NATO AIRCRAFT DRAG PREDICTION AND REDUCTION Published July 1985 272 pages</p> <p>The Special Course on Aircraft Drag Prediction was sponsored by the AGARD Fluid Dynamics Panel and the von Kármán Institute and presented at the von Kármán Institute, Rhode-Saint-Genèse, Belgium, on 20-23 May 1983 and at the NASA Langley Research Center, Hampton, Virginia, USA, 5-9 August 1985.</p> <p>The course began with a general review of drag reduction</p> <p>P.T.O</p>	<p>AGARD Report No. 723 Advisory Group for Aerospace Research and Development, NATO AIRCRAFT DRAG PREDICTION AND REDUCTION Published July 1985 272 pages</p> <p>The Special Course on Aircraft Drag Prediction was sponsored by the AGARD Fluid Dynamics Panel and the von Kármán Institute and presented at the von Kármán Institute, Rhode-Saint-Genèse, Belgium, on 20-23 May 1983 and at the NASA Langley Research Center, Hampton, Virginia, USA, 5-9 August 1985.</p> <p>The course began with a general review of drag reduction</p> <p>P.T.O</p>

<p>technology. Then the possibility of reduction of skin friction through control of laminar flow and through modification of the structure of the turbulence in the boundary layer were discussed. Methods for predicting and reducing the drag of external stores, of nacelles, of fuselage protuberances, and of fuselage afterbodies were then presented followed by discussion of transonic drag rise. The prediction of viscous and wave drag by a method matching inviscid flow calculations and boundary layer integral calculations, and the reduction of transonic drag through boundary layer control are also discussed.</p> <p>ISBN 92-835-1507-2</p>	<p>technology. Then the possibility of reduction of skin friction through control of laminar flow and through modification of the structure of the turbulence in the boundary layer were discussed. Methods for predicting and reducing the drag of external stores, of nacelles, of fuselage protuberances, and of fuselage afterbodies were then presented followed by discussion of transonic drag rise. The prediction of viscous and wave drag by a method matching inviscid flow calculations and boundary layer integral calculations, and the reduction of transonic drag through boundary layer control are also discussed.</p> <p>ISBN 92-835-1507-2</p>
<p>technology. Then the possibility of reduction of skin friction through control of laminar flow and through modification of the structure of the turbulence in the boundary layer were discussed. Methods for predicting and reducing the drag of external stores, of nacelles, of fuselage protuberances, and of fuselage afterbodies were then presented followed by discussion of transonic drag rise. The prediction of viscous and wave drag by a method matching inviscid flow calculations and boundary layer integral calculations, and the reduction of transonic drag through boundary layer control are also discussed.</p> <p>ISBN 92-835-1507-2</p>	<p>technology. Then the possibility of reduction of skin friction through control of laminar flow and through modification of the structure of the turbulence in the boundary layer were discussed. Methods for predicting and reducing the drag of external stores, of nacelles, of fuselage protuberances, and of fuselage afterbodies were then presented followed by discussion of transonic drag rise. The prediction of viscous and wave drag by a method matching inviscid flow calculations and boundary layer integral calculations, and the reduction of transonic drag through boundary layer control are also discussed.</p> <p>ISBN 92-835-1507-2</p>

AGARD

NATO  OTAN

7 RUE ANCELLE • 92200 NEUILLY-SUR-SEINE
FRANCE

Telephone 745 08.10 • Telex 610176

DISTRIBUTION OF UNCLASSIFIED
AGARD PUBLICATIONS

AGARD does NOT hold stocks of AGARD publications at the above address for general distribution. Initial distribution of AGARD publications is made to AGARD Member Nations through the following National Distribution Centres. Further copies are sometimes available from these Centres, but if not may be purchased in Microfiche or Photocopy form from the Purchase Agencies listed below.

NATIONAL DISTRIBUTION CENTRES

BELGIUM

Coordonnateur AGARD — VSL
Etat-Major de la Force Aérienne
Quartier Reine Elisabeth
Rue d'Evere, 1140 Bruxelles

CANADA

Defence Scientific Information Services
Dept of National Defence
Ottawa, Ontario K1A 0K2

DENMARK

Danish Defence Research Board
Ved Istraetsparken 4
2100 Copenhagen Ø

FRANCE

O.N.E.R.A. (Direction)
29 Avenue de la Division Leclerc
92320 Châtillon

GERMANY

Fachinformationszentrum Energie,
Physik, Mathematik GmbH
Kernforschungszentrum
D-7514 Eggenstein-Leopoldshafen

GREECE

Hellenic Air Force General Staff
Research and Development Directorate
Holargos, Athens

ICELAND

Director of Aviation
c/o Flugrad
Reyjavik

UNITED STATES

National Aeronautics and Space Administration (NASA)
Langley Research Center
M/S 180
Hampton, Virginia 23665

ITALY

Aeronautica Militare
Ufficio del Delegato Nazionale all'AGARD
3 Piazzale Adenauer
00144 Roma/EUR

LUXEMBOURG

See Belgium

NETHERLANDS

Netherlands Delegation to AGARD
National Aerospace Laboratory, NLR
P.O. Box 126
2600 AC Delft

NORWAY

Norwegian Defence Research Establishment
Attn: Biblioteket
P.O. Box 25
N-2007 Kjeller

PORTUGAL

Portuguese National Coordinator to AGARD
Gabinete de Estudos e Programas
CLAF
Base de Alfragide
Alfragide
2700 Amadora

TURKEY

Department of Research and Development (ARGE)
Ministry of National Defence, Ankara

UNITED KINGDOM

Defence Research Information Centre
Station Square House
St Mary Cray
Orpington, Kent BR5 3RE

THE UNITED STATES NATIONAL DISTRIBUTION CENTRE (NASA) DOES NOT HOLD STOCKS OF AGARD PUBLICATIONS, AND APPLICATIONS FOR COPIES SHOULD BE MADE DIRECT TO THE NATIONAL TECHNICAL INFORMATION SERVICE (NTIS) AT THE ADDRESS BELOW.

PURCHASE AGENCIES

Microfiche or Photocopy

National Technical
Information Service (NTIS)
5285 Port Royal Road
Springfield
Virginia 22161, USA

Microfiche

ESA/Information Retrieval Service
European Space Agency
10, rue Mario Nikis
75015 Paris, France

Microfiche or Photocopy

British Library Lending
Division
Boston Spa, Wetherby
West Yorkshire LS23 7BQ
England

Requests for microfiche or photocopies of AGARD documents should include the AGARD serial number, title, author or editor, and publication date. Requests to NTIS should include the NASA accession report number. Full bibliographical references and abstracts of AGARD publications are given in the following journals:

Scientific and Technical Aerospace Reports (STAR)
published by NASA Scientific and Technical
Information Branch
NASA Headquarters (NIT-40)
Washington D.C. 20546, USA

Government Reports Announcements (GRA)
published by the National Technical
Information Services, Springfield
Virginia 22161, USA



Printed by Specialised Printing Services Limited
40 Chigwell Lane, Loughton, Essex IG10 3TZ

ISBN 92-835-1507-2